LEVEL II

PROJECT MANAGER SMOKE/OBSCURANTS
DRCPM-SMK-T
ABERDEEN PROVING GROUND, MD. 21005

AD A104760

VOLUME I, UNCLASSIFIED SECTION

of the

PROCEEDINGS

of the

SMOKE/OBSCURANTS SYMPOSIUM V

held at

HARRY DIAMOND LABORATORIES
ADELPHI, MARYLAND 20783
28, 29, & 30 APRIL, 1981

Sponsored by the

OFFICE OF THE PROJECT MANAGER
SMOKE/OBSCURANTS

OPM SMOKE/OBSCURANTS
TECHNICAL REPORT
DRCPM-SMK-T-001-81
(VOLUME I, pgs. 1-422)

UNCLASSIFIED

PROCEEDINGS OF THE SMOKE/OBSCURANTS SYMPOSIUM V

UNCLASSIFIED SECTION VOLUME I

Edited by:
Rush E. Elkins
R. H. Kohl
University of Tennessee Space Institute
Tullahoma, Tennessee

OFFICE OF THE PROJECT MANAGER SMOKE/OBSCURANTS 1981

UNCLASSIFIED

PAGES _____

ARE

MISSING

IN

ORIGINAL

DOCUMENT

UNCLASSIFIED

SECURITY CLASSIFICATION OF THIS PAGE *(When Data Entered)*

REPORT DOCUMENTATION PAGE

READ INSTRUCTIONS BEFORE COMPLETING FORM

1. REPORT NUMBER: DRCPM-SMK-T-001-81	2. GOVT ACCESSION NO.: AD-A104 760
3. RECIPIENT'S CATALOG NUMBER:	
4. TITLE *(and Subtitle)*: Volumes I & II of the UNCLASSIFIED SECTION, PROCEEDINGS OF THE SMOKE/OBSCURANTS SYMPOSIUM V, Held at [illegible], 28, 29, & 30, April 1981, Sponsored by PM Smoke/Obscurants. Vol II	5. TYPE OF REPORT & PERIOD COVERED: Special Report
	6. PERFORMING ORG. REPORT NUMBER:
7. AUTHOR(s): Editors: Rush E. Elkins and R. H. Kohl of the University of Tennessee Space Institute	8. CONTRACT OR GRANT NUMBER(s):
9. PERFORMING ORGANIZATION NAME AND ADDRESS: Project Manager Smoke/Obscurants, Aberdeen Proving Ground, MD 21005	10. PROGRAM ELEMENT, PROJECT, TASK AREA & WORK UNIT NUMBERS:
11. CONTROLLING OFFICE NAME AND ADDRESS: PM Smoke/Obscurants, Attn: DRCPM-SMK-T, Aberdeen Proving Ground, MD 21005	12. REPORT DATE: July, 1981 13. NUMBER OF PAGES: 960 Vol. I, 460; Vol II, 500.
14. MONITORING AGENCY NAME & ADDRESS *(if different from Controlling Office)*:	15. SECURITY CLASS. *(of this report)*: UNCLASSIFIED 15a. DECLASSIFICATION/DOWNGRADING SCHEDULE:

16. DISTRIBUTION STATEMENT *(of this Report)*

Unlimited

DTIC

17. DISTRIBUTION STATEMENT *(of the abstract entered in Block 20, if different from Report)*

Unlimited

18. SUPPLEMENTARY NOTES

19. KEY WORDS *(Continue on reverse side if necessary and identify by block number)*

Battlefield Environment, Screening, Smoke, Obscurant, Obscurants, Obscuration, Dust, Battlefield Obscurants, Smoke Obscuration, Dust Clouds, Smoke Clouds, Smoke Plumes, WP, RP, White Phosphorus, Red Phosphorus, Phosphorous Smoke, HC, Obscured Visibility Environment, DIRT I, DIRT II, DIRT III,

20. ABSTRACT *(Continue on reverse side if necessary and identify by block number)*

This report consists of sixty-seven papers in two volumes (I & II) which, with the eight papers of DRCPM-SMK-T-002-81 and the eight papers of DRCPM-SMK-T-003-81 (Limited Distribution) comprise the Proceedings of the Smoke/Obscurants Symposium V. Papers in this section fall into the following subject areas: A. Testing, Instrumentation and Methodology; B. Modeling; C. Smoke/Obscurants Technology and Hardware Development; D. Doctrine and Training, Concepts and System Evaluation and Analysis.

DD FORM 1 JAN 73 1473 EDITION OF 1 NOV 65 IS OBSOLETE

UNCLASSIFIED

SECURITY CLASSIFICATION OF THIS PAGE *(When Data Entered)*

19. Key Words

Smoke Week II, H^3S, Proceedings, Symposium, Electro-optics, Electro-optics Countermeasure, Thermal Imaging, Lidar, Sensor, Tank Thermal Sight, TTS, Nightsight, Laser, Ultraviolet, Visible, Near IR, IR, Mid IR, Far IR, Infrared, Smoke Models, Dust Models, Obscuration Models, Smoke Deployment, Smoke Field Tests, Combat Obscuration, Smoke Test Data, Diffusion of Smoke, Gaussian Plumes, Smoke Test, Dust Test, Imaging Sensor, Crater, Cratering Parameters, Particle Sizing, Partical Size Measurement, Interferometric Particle Sizing, Millimeter Wave Propagation, Millitary Smokes, Backscatter Coefficient, Extinction Coefficient, Attenuation, Transmission, Laboratory Smoke, Field Smoke, Smoke Munitions, Screening Smokes, Obscurant Munitions, VEESS, Vehicle Exhaust Smoke, Smoke Projectile, Large Area Smoke Screening, Smoke Disseminators, Instant Smoke Disseminators, Common Military Smokes, Smoke Compositions, Condensational Growth, Relative Humidity Effects, Employment of Smoke, Night Vision, Tank, Concentration Length Product, Tactical Smoke, Spectral Transmittance, Transmittance, CL, CL Profiles, Inventory Smoke, Transmissometers, Smoke . Aerosol Working Group, Antitank, Laser Seeker, Obscurant Performance, Instantaneous Smoke Screening, Cold Environment, COPPERHEAD, Health Hazards, Obscurant Technology, Multispectral Screening, Smoke Toxicology, Gaming, Dirty Battlefield, Scenario, Scenario Analysis, Bi-modal Size Distribution, Propagation of CO_2 laser radiation, Phosphoric Acid, Stochastic Models, Obscurant Technology, High Wind Smoke Screening, SNOW-ONE, Optical Transmission, Millimeter Wave Transmission, IR Screening, Dusty Infrared Test Series, Dusty Infrared Test III, Smoke/Obscurants Measurements, Smoke/Obscurant Variability, Obscurant Field Data, Instrumentation Cluster, Obscurant Field Testing, Spectrophones, Fog Oil, Background Measurement Spectroradiometer, High Power Laser, CO_2 Laser, Laser Beam, Clearing by Laser Beam, Depolarization, Electro-Optical Test Facility, Smoke Munition Expenditure, BETS, Tailored Soils, Dust Observations, Tropics Dust, Soil Parameters, HE, Radiometer Measurements, Transmission Measurement, Cloud Geometry, Smoke Cloud Geometry, Dust Cloud Geometry, Two-Perspective Geometry, KWIK, KWIK Phase I, ACT II, BELDWSS, Laser Designator, Artillery Produced Dust, Dispersion of Obscurants, Error Bounds , Extinction by Smokes, Light Scattering, Irregular Particles, Smoke Persistency, Multicompnent Oil Smokes, Oil Smokes, SCREEN, EOSAEL 80, Target Acquisition Probability, Path Luminance, Background Luminance, Windblown Dust, Aerosol Materials, IR Obscuring Materials, Pyrotechnic Infrared Screening, Multistage Chaff Rocket, 2.75 Inch Rocket, Clutter Rejection, Laser Semi-Active Missile Systems, Felt Wedge, Diesel Fuel Obscurant, Inhalation Toxicology, Inhaled Aerosols, M18 Grenades, Colored Smoke, Nontoxic Smoke, Alkali Halide Smoke, XM49, XM49 Smoke Generator, Helicopter Smoke Grenade, Laser Induced Smoke, Multispectral Chaff, Training, Training Smoke, MILES, Small Unit Tactics, Operational Smoke Concept, SAWG, SAWG Concepts Study, Battlefield Environment Obscuration Handbook, Obscurant Countermeasure.

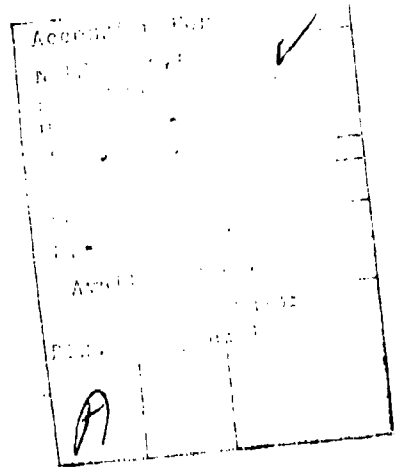

CONTENTS OF THE PROCEEDINGS#

UNCLASSIFIED SECTION

TECHNICAL REPORT DRCPM-SMK-T-001-81

VOLUME I

The Proceedings of the Smoke/Obscurants Symposium V are divided into the Unclassified Section, Volumes I and II (DRCPM-SMK-T-001-81), the Confidential Section (DRCPM-SMK-T-002-81) and the Restricted Addendum (DRCPM-SMK-T-003-81).

* Indicates that paper was presented in the Symposium (presenter is underlined).

[1] Papers A-5 and A-6 were presented in a joint presentation

Contents of Volume I (continued)

[2] Due to the absence of the author, only a few viewgraphs from this paper were presented at the end of the presentation of paper A-9.

[P] On this and following papers "p" indicates the paper was presented in the Preliminary Session.

[3] Some aspects of this paper appeared in the presentation of the following paper.

Contents of Volume I (continued)

[4] Indicates a presented standby paper. Standby papers were not indicated on the Agenda. Paper A-27 was presented in the Preliminary Session.

Contents of Volume I (continued)

VOLUME II

Contents of Volume II (continued)

Contents of Volume II (continued)

Contents of Volume II (continued)

CONFIDENTIAL SECTION

TECHNICAL REPORT DRCPM-SMK-T-002-81

Contents of the Proceedings (continued)

RESTRICTED ADDENDUM#

TECHNICAL REPORT DRCPM-SMK-T-003-81

The Restricted Addendum is a Confidential document whose distribution is limited to U. S. Government Agencies. All other requests for the Addendum must be referred to PM Smoke/Obscurants, DRCPM-SMK-T, Aberdeen Proving Ground, MD 21005

FOREWORD

The Smoke/Obscurants Symposium V, held on 28, 29 and 30 April 1981 is the fifth sponsored by my office and held at the Harry Diamond Laboratories. Fifty-two papers were presented at this Symposium. This number is only 60 percent of the acceptable papers that were submitted. In order that all papers of merit and/or interest might come to the attention of the Smoke/Obscurant and Electro-Optical communities, all such papers are included in these Proceedings.

The Proceedings of the Smoke/Obscurants Symposium V are being published in three parts. These are an Unclassified Section, Volumes I and II of Technical Report DRCPM-SMK-T-001-81; a Confidential Section, Technical Report DRCPM-SMK-T-002-81; and a Restricted Addendum, Technical Report DRCPM-SMK-T-003-81.

From the comments received from attendees, Smoke Symposium V was an outstanding success, as was its predecessors. As in previous years, however, it remains our challenge to convert the developing technical information discussed in the Symposia and Proceedings into fielded combat capabilities. In this regard an ever-increasing emphasis must be placed on doctrine and training and the development of smoke and obscurants in tactical scenarios.

Appreciation is due Major General Light for his keynote address highlighting the past year's events and outlining our future challenges. We wish to thank the organizers, the authors, the editors, the participants and the presenters for their contributions to the success of this Symposium and its Proceedings. Finally, I wish to express my appreciation to Harry Diamond Laboratories and ERADCOM for continuing to host the Symposium.

SAMUEL L. EURE
Colonel, CmlC
Project Manager

KEYNOTE ADDRESS:
SMOKE SYMPOSIUM V

MG Allen H. Light, Jr.
Commander, ARRADCOM
Dover, New Jersey 07801

Good Afternoon Ladies and Gentlemen!

It is a great pleasure for me to be here and to have the opportunity to address the Army's Fifth Smoke Symposium. This is the first Smoke Symposium that I have been able to attend. I have been informed that, thus far, each Symposium has been better than the previous one. This Symposium, which began in 1977 as a small forum for discussions on Army smoke materiel and the direction which the Smoke/Obscurants program should move, has grown in size and importance. Today, it provides the principal medium for discussing and disseminating technical and operational information on the effects of both man-made and natural obscurants on electro-optical devices. Smoke Symposium V is a very important event, and I thank you for your participation. I especially acknowledge the attendance and participation of our Allies.

Over the past year, as shown in Figure 1, several significant accomplishments and actions have occurred which provide new strength and direction to the Army Smoke/Obscurants program. First there was a management realignment last summer in which the Office of the Project Manager Smoke/Obscurants was assigned to my command, ARRADCOM. For the first time, PM Smoke is a member of the same command as the development laboratories which have primary responsibility for smoke/aerosol technology and smoke material developments--Chemical Systems Laboratory and Large Caliber Weapons Systems Laboratory. That management change and other actions which I will subsequently mention will make 1980-81 as significant for the Smoke/Obscurants program as was 1976, when the Army Vice Chief of Staff directed the establishment of OPM-Smoke.

Perhaps the most significant and far-reaching event was the 1980 Chemical Systems Program Review, which, for brevity, we call the CSPR. The Vice Chief of Staff of the Army hosted a review of the Army's chemical warfare, chemical and biological defense and smoke systems in May of 1980. At that review, I chaired a general officer panel which was concerned with smoke operations. New thrust and emphasis have been placed on the Army smoke program as a result of the CSPR. Figure 2 summarizes the key smoke and obscurants actions which will be directed by the Army's Chemical Action Plan. In response, ARRADCOM elements must have new and enhanced programs created to meet future threats and to provide new capabilities to the Army.

In the case of the smoke program, the Chemical Systems Program Review identified a need to enhance and expedite our planned developments in infrared defeating munitions and materials, with particular attention to our capability to project those materials on enemy forces. The CSPR also identified the need for preparation of an enhanced Smoke Technology Base Program to intensify the search for better IR defeating materials. The Smoke Tech Base Program plan has been prepared, staffed within DARCOM and TRADOC, and briefed at HQ, ARRADCOM and HQ, DARCOM. The program plan will be forwarded through channels for approval.

TRADOC, in their response to the directions of the Chemical Systems Program Review, took certain actions. The most significant for the smoke program was the approval of a smoke operational concept. TRADOC published a concept for the employment of smoke in September 1980. This document is pivotal in insuring that the Army is prepared to effectively use obscurants in battle and, at the same time, cope with the rigors of operations under obscured conditions. In the smoke concept, several roles for the application of smoke have been reemphasized and several new applications for smoke have been identified. They will impact both on the smoke technology program and the material development program in the coming years. The smoke concept also provides a foundation for the integration of the employment of smoke into combined arms tactics and doctrine. One of the priority recommendations of the Chemical SPR action plan is to use the concept as a foundation for a revision of "How to Fight" manuals to insure that the integrated employment of smoke and obscurants is included in those manuals.

We see growing from these actions increased needs for materiel support for training. COL Eure's office is now studying requirements and planning for the support. One action which will place heavy demands for support of training in obscured environments is the National Training Center. The past year has seen tremendous progress towards the implementation of the National Training Center Concept by a combined TRADOC/FORSCOM management team. The National Training Center will provide unparalleled opportunity for training our soldiers under realistic battlefield conditions, including smoke. Not only will units be able to maneuver through realistic scenarios using their principal weapons systems in a combined arms approach, but they will be able to do so under conditions as realistic as is safely achievable using modern technology. The center will provide soldiers an opportunity to experience obscured environments as well as to employ obscurants in a tactical setting. Short of actual combat, the Army has never had the training opportunity such as that presented at the National Training Center.

With respect to force structure, we have recently seen a number of concepts implemented. I want to briefly mention the Rapid Deployment Force (RDF), the High Technology Test Bed, and some of the other force structure changes which are impacting on the Army Smoke/Obscurants Program.

First the RDF. The formation of the RDF presents some definite advantages for the Army in light of the objectives of having a highly mobile, yet highly survivable strike force. PM Smoke has been invited by OSD to participate in RDF matters and has devoted a considerable amount of thought and initiative in identifying smoke munitions/material which can enhance the survivability of forces such as the RDF. We look forward to continued efforts to this end.

The High Technology Test Bed, operated by the 9th Infantry Division, Fort Lewis, Offers unique opportunities to evaluate new force structure concepts and materiel to support those concepts. In the future, we hope to have the opportunity to test smoke systems such as the smoke grenade launchers, the visual through near-IR L8A1 grenade, the SM76 far-infrared defeating grenade, the SM49 smoke generator, and other smoke devices and concepts using the High Technology Test Bed as a vehicle for those evaluations. Those evaluations will clearly demonstrate the contribution smoke can make to enhance survivability.

Other force structure changes include formation of the 2d Chemical Battalion (Smoke Generator) and approval of Army 86 concepts. The Army 86 concepts include significant increases in smoke force structure in the form of increased smoke generator companies and battalion headquarters and headquarters detachments at the corps level. The Division 86 concept includes provision for a smoke generator platoon at the division level as a part of the Division 86 NBC Company.

In September of this year, the Army is scheduled to activate a chemical smoke generator battalion, which is the first smoke generator battalion the Army will have had for almost 10 years. See Figure 3. Formation of the Second Chemical Battalion, comprised of four separate smoke generator companies and battalion headquarters and headquarters detachment, will provide improved smoke employment capabilities sorely needed by the Army. The Second Chemical Battalion elements will be stationed throughout the country. Besides providing substantial combat smoke capability in the event of

deployment of the Battalion, the units will also provide a substantial asset for the training of Army units under obscured conditions.

Our Smoke Materiel Development Program is continuing to show good progress. We can provide more effective screening and obscuration in the visual and near-infrared regions of the spectrum with the application of the submunition concept to smoke ammunition. The submunition concept provides more smoke for longer duration, markedly reducing the logistics burden which standard smoke ammunition imposes upon battlefield commanders. 1981 saw the initial production of our first smoke submunition ammunition item, the M259, 2.75 inch smoke rocket. The M259 will give the army a new and exceptionally effective smoke capability. This year another submunition ammunition item, the XM819 81MM mortar round, began full scale engineering development, and the XM825 155MM smoke projectile will begin DTII/OTII testing. For far-IR screening and obscuration, advanced development continues on the XM76 grenade and XM49 generator systems, which will provide our first far-infrared screening capabilities. Next year, we will be initating advanced development programs on other IR defeating systems and will provide an IR candidate and participate in the NATO field trials.

Field experiments and field tests are of great significance to the Smoke/Obscurants and Electro-Optical community. The most comprehensive field test conducted over the past year was Smoke Week III, which was held in August 1980 at Eglin Air Force Base. There were 42 different obscurant trials conducted, using 18 obscurants in which 35 electro-optical devices were evaluated. Among the many accomplishments was the demonstration of the effectiveness of improved laser guided projectile logic.

Smoke Weeks concentrate on intentional, man-made obscuration. Two other tests were performed in the field this year which concentrated on natural and unintentional obscuration. The first, sponsored by the Corps of Engineers, was the Scenario Normalization for Operations in Winter Obscuration and the Natural Environment (Snow I Series). The second, the Dusty Infrared Transmission Test III, DIRT III, sponsored by the Atmospheric Sciences Laboratory, was conducted at Folt Polk, Louisiana. In the first test, we were concerned primarily with the effect of snow and other forms of winter natural obscuration on the propagation of electromagnetic radiation. In the second, propagation of electromagnetic radiation through the dust and debris that results from artillery explosions was evaluated. Presentations, scheduled to be given later in the Symposium, will highlight results of those tests.

Has Obscurants/EO field testing increased the combat readiness of the Army? From all indications, I believe so. The field soldier has benefitted. Changes in obscuring materials and dissemination techniques tested at the Smoke Weeks are being provided to the soldier in the field in various forms to enable him to evade detection by enemy target acquisition devices and to neutralize ATGM's. Modelers, wargamers, and major systems developers have also benefitted. Improvements, being made to COPPERHEAD and TOW as a result of testing in obscurants, will turn misses into hits. HELLFIRE will be capable of destroying more enemy tanks because of changes brought about by testing in battlefield obscurants. Finally, our own target acquisition and detection devices will have their operational performance envelope more clearly defined.

In the next two days, you will have the opportunity to hear many fine papers presented by experts in their fields. It is my fervent hope that you will find your interest stimulated, your curiosity piqued, some of your conclusions questioned, and certainly your knowledge broadened. A lot of information will be beamed in your direction. However, it is extremely important that eveyone keep the goal clearly in focus--that goal being to provide an improved combat capability for US and Allied forces. As you leave this Symposium, ask yourself, "What have I learned here which can be converted into an enhanced combat capability?" If one clear and practical idea comes to mind, then I would consider Smoke Symposium V to have been a success. I give you my best wishes to that end.

SMOKE PROGRAM ACCOMPLISHMENTS

- MANAGEMENT REALIGNMENT
- CHEMICAL SPR
- FORCE STRUCTURE ACTIONS
- MATERIEL DEVELOPMENT PROGRAMS
- COUNTERMEASURES TESTING

SMOKE SYMPOSIUM V

FIGURE 1. SMOKE PROGRAM ACCOMPLISHMENTS

KEY CSPR SMOKE AND OBSCURANT ACTIONS

DOCTRINE	• PREPARE AND APPROVE SMOKE CONCEPT • INTEGRATE SMOKE EMPLOYMENT INTO MANUALS
EQUIPMENT	• DEVELOP IR DEFEATING SYSTEMS • EXPEDITE DEVELOPMENT OF IMPROVED VISUAL AND NEAR IR DEFEATING SYSTEMS • EXPEDITE APPLICATION OF PROTECTIVE SMOKE SYSTEMS TO THE COMBAT VEHICLE FLEET
TRAINING	• ACCOMPLISH ARTEP PRIMARY MISSION TASKS IN SMOKE • INCLUDE SMOKE PLAY AT NATIONAL TRAINING CENTER • DEVELOP SIMULATIONS WHICH INCLUDE OBSCURATION FOR TRAINING WITH ELECTRO-OPTICAL DEVICES
FORCE STRUCTURE	• ACTIVATE MORE SMOKE COMPANIES AND BATTALION HEADQUARTERS • INCLUDE SMOKE GENERATOR CAPABILITY IN DIVISIONS • MOUNT SMOKE GENERATOR COMPANIES IN TRACKED VEHICLES

FIGURE 2. KEY CSPR SMOKE AND OBSCURANT ACTIONS

2d CHEMICAL BATTALION (SG)

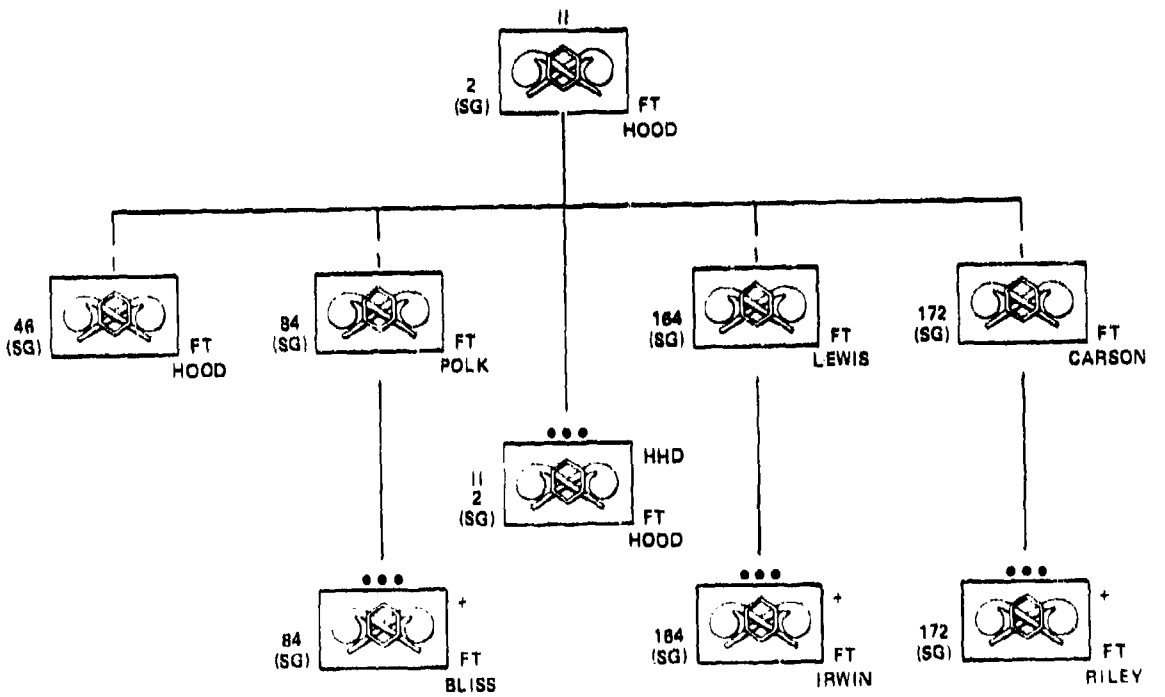

FIGURE 3. 2d CHEMICAL BATTALION (SG)

REMARKS AT THE CLOSING: SMOKE/OBSCURANTS SYMPOSIUM V

COL (Ret.) Henry R. Shelton
Systems Planning Corp.
Arlington, VA 22209

When I started the PM Smoke office six years ago, I found three diverse communities within the Army that had their own parochial interests. First, the technical community of sub-cultures devoted to smoke development, modeling, and testing. Second, the user, who knew he had a problem but not what it was all about. Somewhere in between was a third community made up of design engineers who were working on sophisticated sensors and guidance systems.

The last three days I have listened to outstanding scholastic presentations from the technical community, but the alarming trend seems to be emphasis on a precise scientific answer to very imprecise activities. Secondly, there appears to be a lack of communications with the user. What I mean by that comment is the scientific community must tell the user how these technological breakthroughs can be used to solve user deficiencies. One exception to these caustic comments is in the test area where the Martin-Marietta presentation on the fix to the COPPERHEAD seeker was an excellent example of the payoff from Smoke Week testing. In this example, hardware performance was tested in a field environment, deficiencies recorded, and engineering solutions undertaken to improve seeker performance without trying to scientifically define every detail of the problem.

Next, I am most concerned about the imbalance in the representation at this symposium in the lack of user representatives and the design engineers. This is not intended as a criticism of the presentations given by representatives of the US Army Chemical School and MICOM, but the facts remain that they were overshadowed by sheer numbers of technically oriented papers.

This leads to what I believe to be a two-way problem. The first, the science and technology community failure to communicate to the user technological opportunities and what they might contribute on the battlefield. The second, the user community's failure to communicate the specific battlefield conditions where obscurants could be used as a combat multiplier. This includes broad requirements in terms that the science and technology community can understand.

In conclusion, I have a prediction to make. That is, the resource support of the tech base, which has been substantial in the last few years, will evaporate due to its own hot air unless the user is brought into focus.

CLOSING REMARKS:
SMOKE SYMPOSIUM V

COL Samuel L. Eure
Project Manager, Smoke/Obscurants
Aberdeen Proving Ground, Maryland

Gentlemen:

I won't take too much of your time. I'm sure you want to get on the road.

Thank you for your participation in Smoke Symposium V. Thanks to you we can declare the Symposium a success. I want to especially thank the authors and presenters for their time and efforts. I also want to recognize Dr. Ron Kohl and his crew from the University of Tennessee Space Institute for their superb job in organizing and conducting this Symposium. Dr. Kohl wanted me to be sure to also recognize the stand-by presenters. They prepared talks with little assurance of being able to present them. Their availability contributed significantly to the success of the Symposium.

Dr. Kohl has said that we are a community which "Lets it all hang out". This may have startled some of you who have not been to Smoke Symposiums previously. I believe that this attitude is one of the factors which contributes to the success of the Symposium and our programs.

I thought you might be interested in some statistics which demonstrate the success of Smoke Symposium V. Over 200 people attended the Symposium in spite of the severe travel restrictions we are now experiencing. These people represented over twenty government agencies from eight major commands and all four services. Twenty-three government contractors and four academic institutions were represented. In addition, allies from 7 nations have joined us. I am particularly pleased with the participation of these contractors, institutions, and allies. This breadth of representation is a part of the formula which creates successful gatherings like this.

I would appreciate any suggestions you might have for improving future symposiums. Your completion of the reaction form which you will find in your folder will be a great help toward this end. Gary Nelson, my right hand countermeasures man, Dr. Kohl, or I would also be glad to discuss any ideas you might have. I have one suggestion which I'd like to send back with our TRADOC representatives. We badly need more input in the training and doctrine area to round out the Symposium. You might be thinking of ways to encourage the trainers and tactitions to submit papers and participate in future Symposiums.

One last point before I close the symposium.

Figure 1 shows events of interest to all of you during the coming year. These are some of the events which I hope will result in contributions to future Smoke Symposia. I look forward

FUTURE EVENTS

SMOKE WEEK IV PLANNING MEETING	REDSTONE ARSENAL, AL	20 - 21 MAY 81
FIELD OBSCURANTS DATA WORKSHOP	APG, MD	16 - 18 JUN 81
JTCG/ME SAWG MEETING	APG, MD	9 - 11 JUN 81
SNOW ONE SYMPOSIUM	CRREL, HANOVER, NH	4 - 5 AUG 81
SNOW ONE A PLANNING MEETING	CRREL, HANOVER, NH	6 AUG 81
SMOKE WEEK IV	REDSTONE ARSENAL, AL	2 - 6 NOV 81
SNOW ONE A	CAMP ETHAN ALLEN, VT	DEC - FEB 82
SMOKE SYMPOSIUM VI	HDL, ADELPHI, MD	APR 82

FIGURE 1. EVENTS OF INTEREST.

to seeing many of you at these events.

With that, I declare Smoke Symposium V officially closed. Again, my sincere thanks for your participation. Please drive carefully and have a safe trip home.

AGENDA*

for the

PRELIMINARY SESSION

(U.S. Citizens Only)

of the

SMOKE/OBSCURANTS SYMPOSIUM V

Tuesday Morning
28 April 1981

Harry Diamond Laboratories
2800 Powder Mill Road
Adelphi, Maryland 20783

TUESDAY MORNING 28 APRIL 1981

0745 - 0840		Registration
0840		Administrative Announcements

Paper From
AREA A. TESTING, INSTRUMENTATION AND METHODOLOGY

0845	A-11.	SAM Launch Cloud Interference with E-O Surveillance by George Buckle, Naval Ordnance Station, Charles R. Cundiff and W. Roy Price, Office of Missile Electronic Warfare - 20

Papers From
AREA C. SMOKE/OBSCURANT TECHNOLOGY AND HARDWARE DEVELOPMENT

0840	C-15.	Novel Multispectral Screening Materials by Richard Kenley, Gerald August, Marie Comas, and Zoila Reyes, SRI International - 15
0940	C-6.	Evaluation of Multispectral Screening Smoke Generators by James J. Savage and Roy E. Shaffer, Chemical Systems Laboratory - 15
1005	C-7.	Redispersal of Multispectral Obscuring Fibers by Paul L. Bachman, Aerodyne Research, Inc. - 15
1030	COFFEE BREAK	
1100	C-8.	IR Screening Smoke Development by D. R. Dillehay, Thiokol- 10
1120	C-13.	COPPERHEAD/HELLFIRE Seeker Performance in Battlefield Obscurants (Smoke Week III) by Ray Schneider, Missile Command - 10
1140	C-12.	COPPERHEAD Performance on the Modern Dirty Battlefield by Howard E. Weaver and George D. Minto, Martin-Marietta Corp. - 20

*Scheduled times assume full utilization of all time periods alloted for papers and discussion. The schedule will be allowed to slip forward in time in order to end the day earlier or to add another paper.

Preliminary Session (Continued)

Paper From
AREA D. DOCTRINE AND TRAINING, CONCEPTS AND SYSTEM EVALUATION AND ANALYSIS

1210 D-5. Warsaw Pact Irritant Smokes - A New Dimension in Combat by Frank Poleski, Foreign Science and Technology Center and LTC John Bulger, Office of the Project Manager, Smoke/Obscurants - 10

1230 END OF PRELIMINARY SESSION
(Lunch available in Cafeteria)

AGENDA*

for the

SMOKE/OBSCURANTS SYMPOSIUM V

Tuesday Afternoon, 28 April 1981
through
Thursday, 30 April 1981

Harry Diamond Laboratories
2800 Powder Mill Road
Adelphi, Maryland 20783

TUESDAY AFTERNOON 28 April 1981

1300 - 1330	Registration
1330	Welcome to Smoke/Obscurants Symposium V COL Samuel L. Eure Project Manager, Smoke/Obscurants
	Introduction of Keynote Speaker by COL Eure
	Keynote Address MG Allen H. Light, Jr. Commander, ARRADCOM
1400	Administrative Announcements

AREA A. TESTING, INSTRUMENTATION AND METHODOLOGY

1405 A-1.	High Wind Smoke Screening by Stephen L. Cohn, Atmospheric Sciences Laboratory (ASL) - 15
1430 A-2.	A First Look at SNOW-ONE Results by George W. Aitken, U. S. Army Cold Regions Research and Engineering Laboratory (CRREL) - 15
1455 A-3	An Overview of Smoke Week III by Gary Nelson, Office of the Project Manager, Smoke/Obscurants - 10
1515 Coffee Break	
1535 A-4.	Results from United Kingdom Electro-Optics Sensors at Smoke Week III by S. Briam, P. H. Davies, P. Griffith, K. Hulme, J. Payne and P. Richardson, Royal Signals and Radar Establishment - 20 (presented by W. A. Shand)

*Scheduled times assume full utilization of all time periods alloted for papers and discussion. The schedule will be allowed to slip forward in time in order to end the day earlier or to add another paper.

Tuesday afternoon 28 April 1981 (continued)

AREA A. (continued)

1605	A-5. & A-6.	Combined Presentation: Description of a System for the Measurement of Optical and Millimeter Wave Transmission Through Battlefield Environments by R. J. Keyes and Results of Simultaneous Transmission Measurements at MMW and Various Optical Frequencies in a Battlefield Environment by R.J. Sasiela, Massachusetts Institute of Technology, Lincoln Laboratory - 20
1635	A-7.	155 mm Smoke Projectile - Field Test by Nissim Dayan, MOD/R&D, Israel - 15
1700	A-8.	Canadian Program in Anti-IR Screening Aerosols by R. E. Kluchert, Defense Research Establishment Valcartier, Canada - 15
1725	End of First Day	

WEDNESDAY 29 APRIL 1981

0745 - 0815		Registration and Badge Pick Up

AREA A. (continued)

0815	A-12.	Estimation of Precision of Smoke/Obscurants Measurements and Product Variability by James F. O'Bryon, JTCG/ME Smoke Aerosol Working Group- 15
0840	A-13.	A Data Reduction Technique for Field Data by Marvin Smith, Keith Jones and P. Kittikul, Oklahoma State University - 15
0905	A-34.	Infrared Measurements with the MIDAS III Radiometer During Smoke Week III Tests by A. G. Geiser, Cincinnati Electronics - 15
0930	A-15.	Data Obtained from the Smoke Week III Instrumentation Cluster by W. Michael Farmer, University of Tennessee Space Institute - 20
1000	A-16.	Battlefield Smoke/Dust Parameters Measured In-Situ Using Spectrophones by G. W. Bruce, Y. P. Yee, A. V. Jelinek, L. M. Moore and N. Richardson, ASL - 10
1020	Coffee Break	
1040	A-17.	In-Situ Measurements of Phosphorus Smokes During Smoke Week III by D. M. Garvey, G. Fernandez, C. W. Bruce and R. G. Pinnick, ASL- 10
1100	A-19.	Particle Size and Infrared Absorption Measurements of IR Smokes During Smoke Week III by R. G. Pinnick, G. Fernandez, C. W. Bruce, D. M. Garvey and B. D. Hinds, ASL - 10
1120	A-20.	Thermal Radiance of Smokes and Battlefield Fires by T. W. Cassidy and W. E. Stump, Night Vision and Electro-Optics Laboratory - 20
1150	A-21.	The Infrared Characterization of Smokes and Obscurants Utilizing the Honeywell Background Measurement Spectroradiometer by J. R. Bryson, M. J. Flanagan, Honeywell and D. R. Snyder, Eglin AFB - 15
1215	A-23.	Propagation of a High Power Pulsed Laser Through Battlefield Aerosols by Thomas G. Miller, U. S. Army Missile Command (MICOM) - 15

xxx

Wednesday 29 April (Continued)

1240 Lunch

Beginning at 1310 the 14 minute film "Dusty Infrared Test Series" (paper A-9 by Bruce Kennedy, ASL) will be shown. This will be followed by a few viewgraphs on the Dusty Infrared Test - III (Paper A-10 by Bruce Kennedy, ASL). Both will be presented by Frank Niles, ASL.

AREA B. MODELING

1340	B-1.	Temporal Characterization of Smoke and Dust Cloud Geometry by Processing of Two-Perspective Video Images by George R. Blackman, ASL - 15
1405	B-2.	Munition Expenditure Model Verification, KWIK Phase I by Ricardo Pena, ASL - 15
1430	B-3.	Comparisons Between the Upgraded Model ACT II and Recent Smoke Week Tests by Robert Sutherland, ASL - 15
1455	Coffee Break	
1515	B-4.	Battlefield Environment Laser Designator Weapon System Simulation (BELDWSS) Test and Simulation Results by Robert Yates, MICOM - 20
1545	B-7.	Sensitivity of Calculated Transmittances in Artillery Produced Dust Clouds to Variations in Model Inputs by Melvin G. Heaps and Donald W. Hoock, ASL - 15
1610	B-8.	Parameterization of the Dispersion of Battlefield Obscurants by W. D. Ohmstede and E. B. Stenmark, ASL - 15
1635	B-9.	Error Bounds for Smoke Obscuration Models by Marvin D. Smith, James R. Rowland and D. Mark Anderson, Oklahoma State University - 15
1655	B-10.	MMTRN: Millimeter Wave Propagation for Rain, Fog, and Snow Extinction and Gaseous Absorption by Douglas R. Brown, ASL - 10
1715	End of Second Day	

THURSDAY 30 APRIL 1981

AREA B. (continued)

0745 - 0815		Registration and Badge Pick Up
0815	B-11.	Extinction by Smokes at Visible, Infrared and Millimeter Wavelengths by Janon Embury, Chemical Systems Laboratory (CSL) - 20
0845	B-12.	Some Aspects of Light Scattering from Clouds of Regularly and Irregularly Shaped Particles by D. K. Anker, Logica Ltd, United Kingdom - 15
0910	B-13.	A Semiquantitative Model for the Prediction of the Persistency of Multicomponent Oil Smokes by Glenn O. Rubel, CSL - 20
0940	B-14.	A New Look at the Chemical Modeling of White Phosphorus and Hexachloroethane Smokes by Barbara W. Levitt, Omega Science and Research Technologies, and Leonard W. Levitt, University of Texas at El Paso - 10

Thursday 30 April (continued)

AREA C. SMOKE/OBSCURANT TECHNOLOGY AND HARDWARE DEVELOPMENT

1000	C-1.	The Optical Properties of Phosphorus Smoke in the 7-14 Micrometer Infrared by Merrill E. Milham, CSL - 15
1025	Coffee Break	
1045	C-2.	Replacement of HC Smoke by Michael D. Smith, CSL - 10
1105	C-3.	Smoke/Obscurants Health Effects Research by CPT David L. Johnson and James C. Eaton, U.S. Army Medical Bioengineering Research and Development Laboratory - 15
1130	C-4.	An Investigation of Aerosol Materials that Obscure in the Mid- to Far Infrared by Clyde L. Witham, Richard A. Kenley and Kenneth M. Sancier, SRI International - 15
1155	C-9.	Pyrotechnic Infrared Screening Mechanisms by Joseph A. Domanico, CSL - 15
1220	C-26.	Optimization Assessment of Chemically Non-Reactive Obscurants for Vehicle Self-Protection by John F. Ebersole and Thomas F. Spaulding, Aerodyne Research, Inc. - 15
1245	Lunch	
1345	C-10.	Multistage, Chaff, 2.75" Rocket Warhead by William G. Rouse, CSL - 10
1405	C-11.	Clutter Rejection Techniques for Laser Semi-Active Systems by Huey F. Anderson, MICOM, and Robert J. Polge, University of Alabama, Huntsville, - 15

AREA D. DOCTRINE AND TRAINING, CONCEPTS AND SYSTEM EVALUATION AND ANALYSIS

1430	D-1.	Training Smoke Considerations (MILES System) by Robert Frickel, CSL - 15
1455	Coffee Break	
1515	D-2.	The Effect of Smoke in Small Unit Tactics by Bruce W. Fowler, MICOM and CPT James Price, U.S. Army Missile and Munitions Center and School - 20
1545	D-3.	Smoke Employment: An Operational Concept by John W. Scully and MAJ Peter B. Harrington, U.S. Army Chemical School - 15
1610	D-6.	Development of the Battlefield Environment Obscuration Handbook by Robert E. Turner, Science Applications, Inc. - 15
1635	End of Symposium	

ATTENDANCE LIST:
SMOKE SYMPOSIUM V
28 - 30 APRIL 1981

NAME	ORGANIZATION	PHONE
AITKEN, George	CRREL	AV 684-3357
AKERS, Charles	Calspan	(716)634-3697
ALONGI, J.		
ANDERSON, David	ARRADCOM APG	AV 584-2180
APODACA, Gilbert		AV 258-1816
ARPKE, Charles	Oklahoma St Univ	
BACHMAN, Paul	Aerodyne	
BAER, LeRoy	CSL	AV 584-1652
BAILEY, Ronald	CAA	AV 295-1652
BAITY, Warren	TECOM	
BALDWIN, A.	ITTRI	(202)296-1610
BAUER, Ernest	IDA	
BECHTOL, T.	BRL	
BENDER, Frank	CSL	
BEYTH, Werner	CSL	AV 584-2890
BOWLER, Mark		(714)759-5697
BOWMAN, Eugene	UTSI	
BROMLEY, Donny	CSL	AV 584-3388
BROWN, Douglas	ASL	AV 258-3681
BROWN, Morris	Andrews AFB	AV 858-5181
BROWN, Roland	CSL	
BRUCE, Charles	ASL	AV 258-1585
BUCKLE, George	Naval Ord Stn	AV 364-4398
BULGER, John	PM Smoke	AV 283-2804
BURGESS, Eldon	DPG	AV 789-5346
CAMPBELL, Frederick	APG	
CARELLA, Robert	Barnes Eng	
CHESNOV, Gilbert	ARRADCOM	AV 880-2884
COBB, Henry	Ft Hood	AV 737-9008
COHEN, Herbert	APG	AV 283-2965
COHN, Stephen	ASL	AV 258-5624
COLEMAN, Sheryl	PM Smoke	AV 283-5355
COMER, Roger	MICOM	AV 746-2246
CUNDIFF, Charles	EWL	
CURCIE, Sanford	Analytics	(201)542-8383
CURCIO, Joseph	NRL	
CURRIE, Bill	Calspan	(615)455-2611
DAUM, Gaalen	BRL	AV 283-4509
DEPERCIN, Fernand	Ft McNair	(202)272-0259
DECKER, William	Ft Huachuca	AV 879-6883
DEE, William	CSL	AV 584-2922
DEKINDER, Robert	PM Smoke	AV 283-5411
DICKINSON, George	PM Smoke	AV 283-2804/4249
DILLEHAY, D.	Long Horn Army Depot	(214)679-2543
DINERMAN, Carl	Nav Wpn	AV 482-1992
DIVIS, Dale		
DOMANICO, Joseph	CSL	
DOHERTY, Robert	ARRADCOM APG	AV 584-2760
DOUGHERTY, Edward	PM Smoke	AV 283-5759
DOWLING, James		
DUDLEY, Edward	HDL	
EATON, James	Ft Detrick	AV 343-7207
EBERSOLE, John	Aerodyne	(617)275-9400
ELKINS, Allen		
EMBURY, Janon	ARRADCOM APG	AV 584-4256
ERICKSON, Merlin	CSL	AV 584-2390
ETHERTON, David	David Taylor Naval Base	AV 281-2352
EURE, Samuel	PM Smoke	AV 283-2804

Attendance List (continued)

NAME	ORGANIZATION	PHONE
EVANS, Kenneth		
FARMER, W.	UTSI	AV 340-5011*
FITCHEK, Joseph	Analytics	(215)657-4100
FRICKEL, Robert	ARRADCOM APG	AV 584-3854
FRIDLUND, Lind	BDM Corp	AV 244-0436
GANDY, Woodrow	TRADOC Ft Hood	AV 737-9125
GEISER, Albert	Cincinnati Elec	(513)563-6000
GERARD, Sidney	CRREL	AV 684-3447
GLEASON, Thomas		(703)841-8974
GREEN, John	PM Smoke	AV 283-5411
GREENBERG, Melvin	David Taylor Naval Base	
GREENLEAF, William		(205)837-7200
GRIFFIN, James	HDL	
GROSS, Deanna	PM Smoke	AV 283-5759
GUIDA, Ed	ARRADCOM	AV 880-5444
HABER, George	HDL	AV 290-3167
HAGY, Mara	PM Smoke	AV 283-4249
HANLEY, James	Calspan	(716)632-7500
HANLON, William	HEL	
HARWELL, Kenneth	UTSI	AV 340-5011*
HATTERY, Walter	HDL	
HENRY, Mary	Ft Detrick	AV 343-7207
HOLMBERG, Robert	Oakridge Opns Tenn	
HOLST, Gerald	ARRADCOM APG	AV 584-2326
HOOCK, Donald	ASL	AV 258-3951
HOOVER, Charles	Norden Systems	
HUFFMAN, Paul	Univ of Dayton	(513)229-3921
HUMPHREY, Robert	HDL	AV 290-3130
HESS George		(206)773-9678
HARTMAN, Clarence	ARRADCOM	AV 880-2374
INGRAM, David	TRADOC Ft Monroe	AV 680-3441
INGRAM, John	Ft McNair	
JOHNSON, David	Ft Detrick	AV 343-7207
KASAI, Kenneth	PM Smoke	AV 284-4249
KENDALL, Arthur		(614)239-3263
KENLEY, Richard	SIR Int CA	
KERN, Harry	CSL	AV 584-2577
KLIMEK, Walter	PM Smoke	AV 283-5411
KOHL, Ronald	UTSI	AV 340-5011*
KOURY, Robert	CAA	
KRIST, Kathryn	UTSI	AV 340-5011*
KUBINSKY, Stanley		AV 258-3749
LAGRANGE, Arthur	BRL	AV 283-4509
LAMONTAGNE, Joseph	Barnes Engineering	
LICHTENBERGER, Frederick	PM CAWS	AV 880-2502
LOVE, Gary	Ft Ord	AV 929-7092
LOWE, Laban		
LUN, Michael	APL	(301)953-7100
MACK, Eugene	Calspan	(716)631-6782
MAGUIRE, Thomas	Geor-Centers Inc	(301)423-3332
MANION, Francis	HDL	AV 290-2430
MANNING, Joseph	Optimetrics	(313)973-1177
MARCHETTI, Robert	AMSAA	AV 283-4260
MARTIN, John		AV 283-5278
MASON, James		(601)634-2601
MCCOSKEY, Robert	HDL	AV 394-2300

*Ask for UTSI, Extension 246

Attendance List (continued)

NAME	ORGANIZATION	PHONE
MELAND, Tor	Litton Mellonics	AV 920-8822
MILHAM, Merle	CSL	AV 584-3859
MILLER, Thomas	Redstone Arsenal	AV 746-8271
MONTGOMERY, Willard	Lockheed	(205)837-1800
MORGENTHAU, Frederick	PM Smoke	AV 283-4716
MOSKOWITZ, Lionel	NRL	AV 297-4873
MUTCHLER, Paul	American Air Filter	(314)993-5880
NASH, Carolyn	DCS Corp	(703)522-8300
NELSON, J. Gary	PM Smoke	AV 283-5411
NEMARICH, Joseph	HDL	AV 290-3130
NETTE, Robert		
NILES, Franklin	ASL	AV 258-3721
NORTON, James	CSL	
O'BRYON, James	AMSAA	AV 283-2981
OSTROWSKI, Peter	Geo Centers Inc	(301)423-3332
OTTO, Charles	TSM Smoke	AV 552-3489
PALUGHI, Donald	CSL	AV 584-3061
PENNSYLE, Ronald	CSL	AV 584-3570
PEREZ'ESANDI, Jose	NSWC	AV 394-2785
PEPPER, William	HDL	AV 280-3160
PILIE, Rowland		
PINKLEY, Larry	Nichols Rsch Corp	(205)883-1140
PINNICK, Ronald	ASL	AV 258-5634
PINSON, Lewis	UTSI	AV 340-5011*
PORUBCANSKY, Thomas	WPAFB	AV 785-5922
PRIBYL, William	CSL	AV 584-2837
REALE, Ronald	CAA	AV 295-5300
REDFORD, Joseph		AV 693-1309
REITZ, Richard	BRL	AV 283-2424
RITTER, Albert	Nav Elec Sys	AV 692-2395
ROBERTS, Earl	USA Infantry Bd	AV 546-3813
ROCHA, Domingo		AV 290-3170
ROGERS, William	Nav Ord Stn	AV 364-4884
ROGNE, Timothy	Optimetrics, Inc	(313)973-1177
ROSEN, Melvin	Melonics	(703)920-8822
ROUSE, William	CSL	AV 584-3079
ROWLAND, James	OK St	(405)624-5172
RUBEL, Glenn	CSL	
RUHGE, Justin		(805)968-3511
SASIELA, Richard	MIT	(617)862-5500
SAVAGE, James	CSL	
SCALES, John	HDL	AV 280-3160
SCHNEIDER, Raymond	MICOM	AV 746-7499
SCHNEPFE, Robert		
SCULLY, John	CML Sch	AV 869-5569
SHAW, David	So Ctr for Elec Engr Ed	(717)831-3059
SHELTON, Henry	Systems Planning Corp	(703)842-2903
SILVERSTEIN, J.		AV 290-3170
SINDONI, Orazio	CSL	
SINGER, Abraham	ERADCOM	AV 290-3160
SKEEN, Charles	Hughes Helicopters	
SMALLEY, Howard	PM Smoke	AV 283-5411
SMITH, Frederick	Optimetrics	(313)973-1177
SMITH, Loranzo	BDM Corp	(505)848-5000
SMITH, Marvin	OK St	(405)624-5711
SMITH, Nicholas	MPC McClean	(703)734-1410
SNELSON, Alan		

*Ask for UTSI, Extension 246

Attendance List (continued)

NAME	ORGANIZATION	PHONE
SNIDER, Donald	ASL	AV 258-4450
SPAULDING, Thomas	Aerodyne	AV 589-0800
STAMPER, Herman	AMSAA	AV 283-5539
STEEDMAN, Joseph	UTSI	
STENMARK, Ernest	ASL	AV 258-4650
STEUBING, ED	CSL	
STRICKLAND, Richard		
STUMPFEL, Charles	BRL	
SUTHERLAND, Robert	ASL	AV 258-7951
SZTANKAY, Z.	HDL	AV 290-3130
TARNOVE, Theodore	CSL	AV 584-2577
THOMAS, Albert	SRI	(205)323-6592
TRACY, David	Kirtland AFB	AV 244-9926
TRAINO, Joseph	PM Smoke	AV 283-4249
TURNER, Robert	Sci Appl	(313)662-3261
VAN DE WAL, Anthony	PM Smoke	AV 283-4716
WADE, Clarence	Ft Detrick	AV 343-2036
WATANABE, Steven	McDonnell Douglas	(714)896-5016
WATKINS, Melvin	MRJ, Inc	AV 385-0763
WELLMAN, Ronald	HDL	
WELNER, Victor	AVRADCOM	AV 693-1353
WEAVER, Howard		(305)277-4718
WHITING, Lawrence	TECOM	AV 283-2775
WIDENHOFER, Gene	MICOM	AV 746-3609
WILKINS, Eugene	Vought Corp	(214)266-3489
WOLFHARD, Hans	Inst Def Analysis	(703)558-1850
ZWEIBAUM, Frederic	Barnes Engr.	(203)348-5381

FOREIGN VISITORS

AUSTRALIA

WYLLIE, David

CANADA

KLUCHERT, Rolf
LEVESQUE, Jules
LUMSDEN, Wayne

FRANCE

BARET, Robert
LOTTE,
LOUCHET, Jean
MIRGUET, Georges

GERMANY

COHEN, Donald
KRONE, Une
SCHEUNEMANN, Winfried
SKORNA, Geisher
STEINICKE, Wolfgang

ISRAEL

DAYAN, Nissam
KERTES, Agnes
DAR-RAFEL, Tamar
PERETZ, Matitiahu

NETHERLANDS

FERNIG, P.
HOFFMANS, D.

UNITED KINGDOM

ANKERS, David
EVANS, Alan
MONK, Graham
SHAND, William

PROCEEDINGS PAPERS BY AUTHOR

Papers presented at the Symposium are indicated by an asterisk (*).
Papers presented at the Preliminary Session of the Symposium are indicated by a superscript "p".
Papers presented by the indicated author are underlined.

PROCEEDINGS PAPERS BY ORGANIZATION

Papers presented at the Symposium are indicated by an asterisk (*).
Papers presented at the Preliminary Session of the Symposium are indicated by a superscript "p".
Papers where the presenter was from the indicated organization are underlined.
Papers from a foreign country are listed under the country name also.

AREA A

TESTING, INSTRUMENTATION AND METHODOLOGY

HIGH WIND SMOKE SCREENING

Stephen L. Cohn
Atmospheric Sciences Laboratory
White Sands Missile Range, New Mexico

ABSTRACT

Smoke screening is a valuable military tactic used to deny enemy acquisition of friendly forces. Up until this time, it has been believed that smoke screening at wind speeds in excess of 17 knots is impractical (Army Training Circular 6-20-5) because of the expected high munition expenditure rate needed to establish and maintain a screen. This has important inplications in battle planning, since high winds frequently occur over areas of the order of hundreds of kilometers.

Phase I of the KWIK Evaluation Test was designed to test a real time smoke munition expenditure algorithm known as KWIK (Cross Wind Integrated Concentration). On September 18, 1980, during Phase I, winds between 17-40 knots were encountered during eight trials. Preliminary examination of available data suggests that the trials conducted during this high wind episode produced excellent screens with a reasonable expenditure of munitions.

1. INTRODUCTION

The use of chemical smokes in the battlefield for obscuration or screening is a valuable tool which can deny the enemy acquisition of friendly forces. For obscuration, smoke is placed on or near the enemy with the primary purpose of minimizing his vision both within and beyond his position area. For screening, smoke is placed on the battlefield to deceive or confuse the enemy as to the activities of the maneuver elements.

In the deployment of smoke, the commander must give consideration to the weather in the target area. The two most important meteorological factors are atmospheric stability and wind (speed and direction). These factors influence the rate of vertical and horizontal spread of a smoke cloud. Under unstable or lapse conditions, a smoke cloud will disperse rapidly, causing high munition expenditure. With stable or inversion conditions, a smoke cloud will tend to keep its integrity over a relatively long period of time, thus requiring low munition expenditures. If the atmospheric conditions are between stable and unstable, it is considered neutral and still favorable for smoke usage.

Army Training Circular 6-20-5 entitled "Field Artillery Smoke" details the deployment of smoke under various meteorological regimes. As indicated in this circular, wind speeds under 2 knots or in excess of 17 knots are considered unfavorable for smoke screening or obscuration. Under the light wind regime ($\leq$2 knots), the wind direction is likely to be variable over space and time, rendering smoke munitions relatively useless. Under the high wind regime (>17 knots) it is believed that excessive munition expenditures would be required due to the quick dispersal of the smoke plume.

Phase I of the KWIK Evaluation Test was designed to test a real time smoke munition expenditure algorithm known as KWIK (Cross Wind Integrated Concentration). On September 18, 1980, during Phase I,

winds between 17-40 knots were encountered during eight trials. The available data indicate that the trials conducted during this high wind episode produced excellent screens with a reasonable expenditure of munitions.

2. BACKGROUND

Phase I of the KWIK Evaluation Test was conducted at Dugway Proving Grounds during July and September of 1980. The Horizontal Grid (Figure 1) located about 20 kilometers west of the post area was utilized for all trials. The grid was oriented with the major axis on a NE-SW line so that the prevailing winds would be normal to the grid. The smoke impact area (Figure 1) consisted of seventeen rows with each row containing three lines. Each line contained four M116 HC cannisters (3 M1's and 1 M2), whihc simulates a dynamically fired M116BE projectile. The lines utilized for a given trial (as determined by KWIK) were detonated two minutes apart, simulating an initial volley with two sustaining volleys. The screen was always calculated for 500 meters in length and six minutes in duration.

Meteorological measurements were made from two 10 meter towers on either side of the smoke impact area (Figure 1) and from one 32 meter tower located near the observation post (Figure 1). Temperature, wind speed and and wind direction were measured at 2 and 10 meter levels on the small towers and at 2, 10, 16, and 32 meter levels on the large tower. Dewpoint temperature was measured at the 2 meter level on all towers. All of these parameters were monitored continuously before and during each trial. Standard airway hourly observations were made at the weather station located in the Ditto technical area about 10 kilometers east of the grid. All of this information was utilized for each trial.

3. WEATHER ANALYSIS

In some parts of the world, including western Europe, high winds are not necessarily localized phenomena. When associated with large scale weather systems, they can persist for days over regions of the order of hundreds of kilometers. The high winds observed in the course of this investigation were part of such a large scale system extending over much of the central United States.

At 1200Z (0500 MST) on September 18, 1981, a ridge at 500 mb and 700 mb was centered over the central and eastern portions of Utah (Figures 2, 3). At 850 mb (Figure 4) a weak short wavewas entering the western portion of the state. At the surface (Figure 5), a cold front extended from a 1005 mb low in southeast Washington to just north of Utah and eastward to 1013 mb low over southwest Nebraska. From

there, it extended northeast into a 1009 mb low over northern Minnesota. A 1017 mb high was centered over southwest Colorado and 1023 mb high was centered just to the north of North Dakota.

The combination of the low level short wave (850 mb) with the proximity of the surface cold front with a developing low pressure system gave the horizontal grid a steadily increasing wind from the southeast during the morning hours. As the upper level ridge moved east during the day, the winds at all levels from the surface to 500 mb (Figures 2, 3, 4, 6) backed to the southwest. The 1002 mb surface low (Figure 6) along with the upper level support increased the wind speed as the day progressed. Thus the winds on the grid were light to moderate from the southeast early in the day and became moderate to strong from the southwest late in the day. There was no precipitation in the region during this period.

4. RESULTS

Trials 23 through 30 were conducted at wind speed in excess of 17 knots as shown in Table 1. The KWIK model uses a modified Pasquill stability scheme which gives six stability categories which are:

A - Highly Unstable

B - Unstable

C - Slightly Unstable

D - Neutral

E - Stable

F - Moderately Stable

As can be seen in Table 1, with the high wind speeds encountered, the stability remained neutral throughout the seven trials. Photographic records of the trials also indicate a neutral stability.

The number of munitions calculated for the six minute screens ranged from 18 to 45, with the higher figure calculated during a near gale with a quartering/headwind direction. A typical scenario would involve 1/3 of the total munitions expended for establishing the screen and two sustaining firings of 1/3 each to maintain the screen.

The screen characteristics are indicated in Table 2. The buildup time is defined as the time needed to obscure all targets from the observer's view. The length of the screen is the time after initiation of the test for a target to become visible to one or more of the observers. The total effective screening time is the total time that all targets were continually screened from all observers.

A-1

For the seven trials, the mean buildup time was 28.75 seconds with a mean effective screening time of 6 minutes and 17 seconds. In all cases, once the screen had formed there were no apparent holes until the screen began to break up at the end of the trial.

5. CONCLUSIONS

There are several possible reasons for the successful screening at high wind speeds. One very plausible explanation is that as the wind speed increases, the vegetation flattens, changing the effective roughness length. This lowering of the roughness length would change the dispersion parameters which are critical to the correct calculation of munition expenditures. Examining Table 1, it is noted that the actual number of munitions that successfully detonated was always less than the number calculated. Since all of the screens were successful, this overprediction of needed munitions could be due to wind modified roughness length.

Another possibility is the homogeneity of the terrain at Dugway. It is possible that over heterogeneous terrain or terrain with extensive vegetation, such as a forest, the increased turbulence at higher wind speeds would preclude the use of smoke.

A third possibility is a change in the efficiency of continuous burning smoke munitions during high winds. An increase of available oxygen to the munition could conceivably improve the efficiency.

Regardless of the reason or combination of reasons for the high wind smoke screening, further investigation is warranted. Western Europe and other strategically important parts of the world are frequently subject to large areas of high wind speeds. If future experiments confirm that smoke screening at high speeds is feasible, then a change in doctrine would be indicated. This could give friendly forces an advantage in future confrontations utilizing smoke.

TABLE 1. WIND SPEED (WS) VS MUNITION EXPENDITURES CALCULATED

TRIAL #	WS(M/S)	STABILITY	# DETONATED	# CALCULATED	DIRECTION
23	9-12	D	17	18	CROSS
24	8.8-12	D	16.75	18	CROSS
25	9.7-13	D	17	18	CROSS
26	8.7-12	D	15.75	18	CROSS
27	11.7-15.5	D	20	21	Quarter
28	12.8-18	D	25.5	27	Quarter
29	12.3-19.5	D	25.5	27	Quarter
30	15-20	D	41*	45	Quarter

*Calculated during high wind

TABLE 2. SCREEN CHARACTERISTICS

TRIAL #	BUILDUP TIME	LENGTH OF SCREEN	TOTAL EFFECTIVE SCREENING TIME
23	30 SEC	6:40	6:10
24	30	6:50	6:20
25	40	6:40	6:00
26	42	6:45	6:03
27	15	6:55	6:40
28	28	6:50	6:22
29	30	6:40	6:10
30	15	6:45	6:30
MEAN	28.75	6:46	6:17

A-1

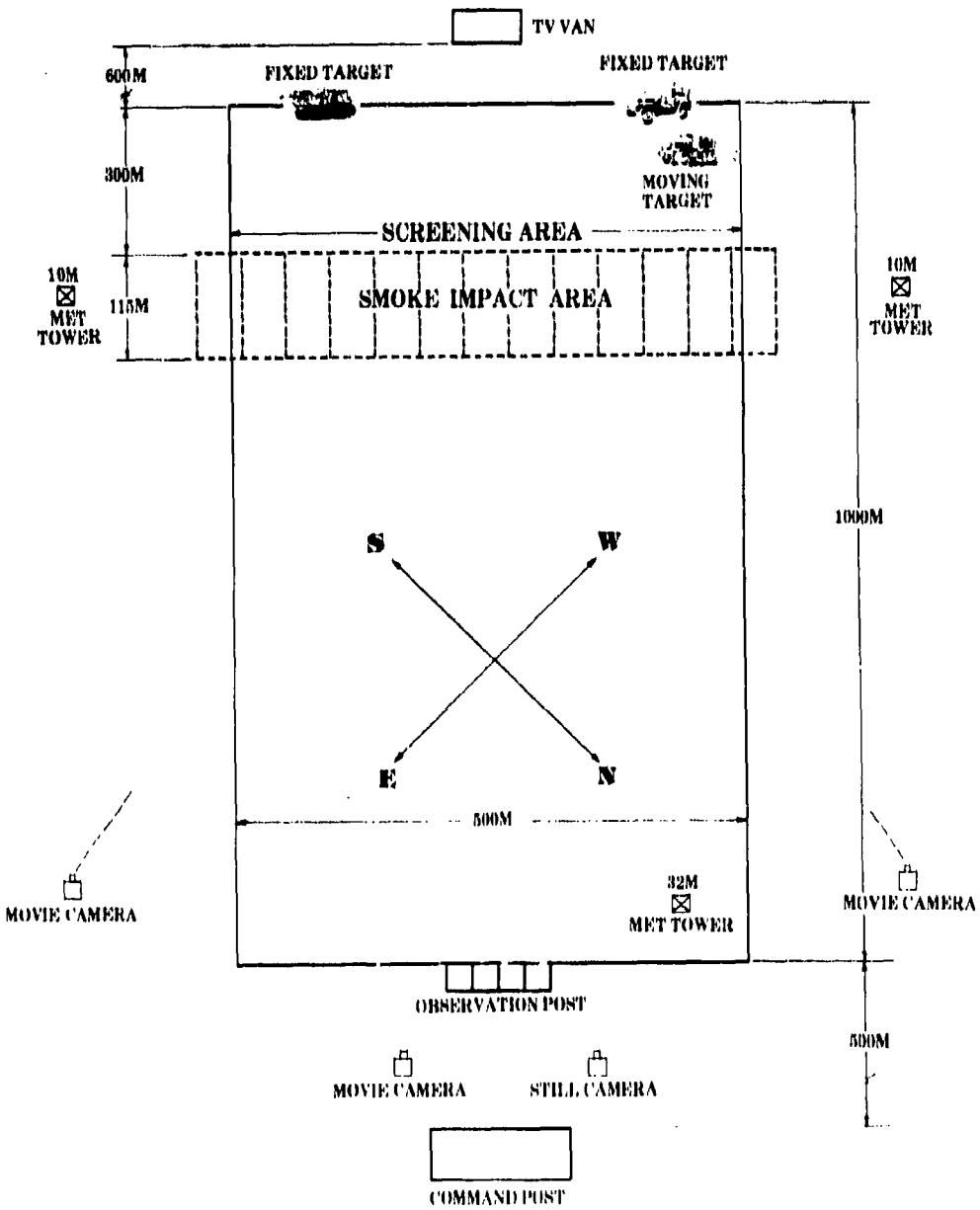

FIGURE 1. TEST GRID FOR KWIK SMOKE TESTS PHASE I DPG, UTAH

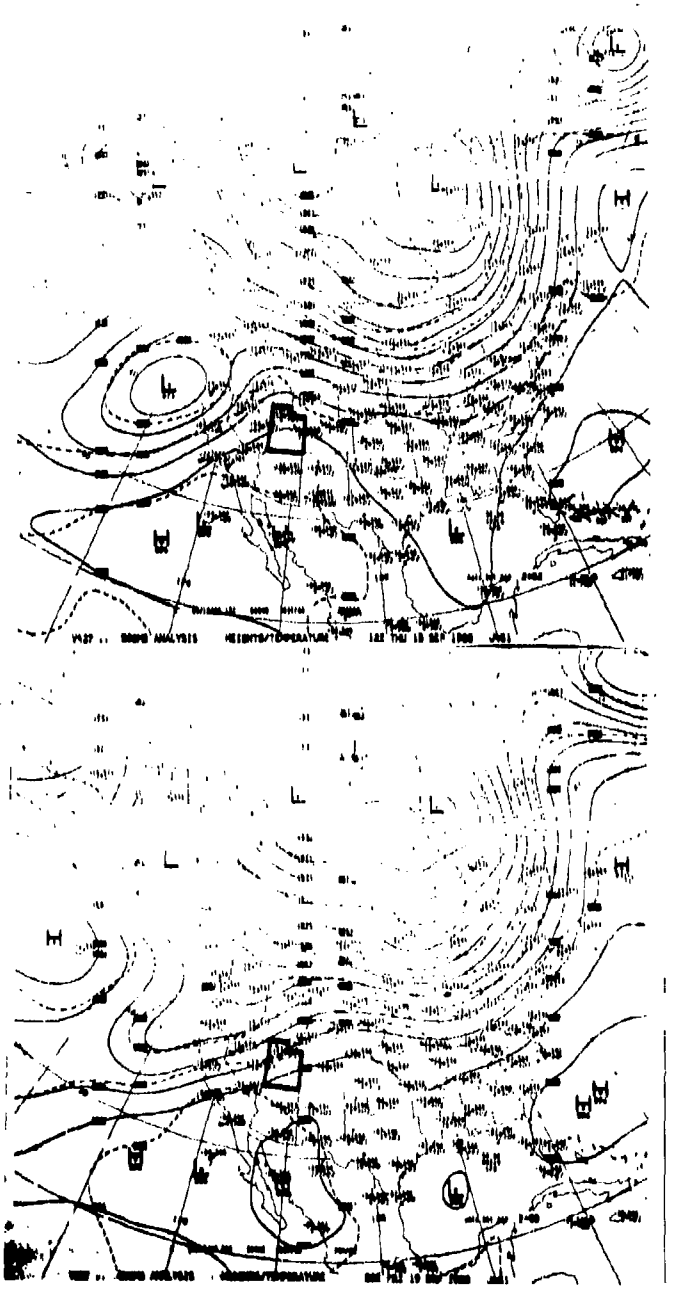

FIGURE 2. 500 mb SYNOPTIC ANALYSIS. This is a reproduction of the National Weather Service 500 mb analysis for 18-19 September at 12 zulu and 00 zulu respectively.

A-1

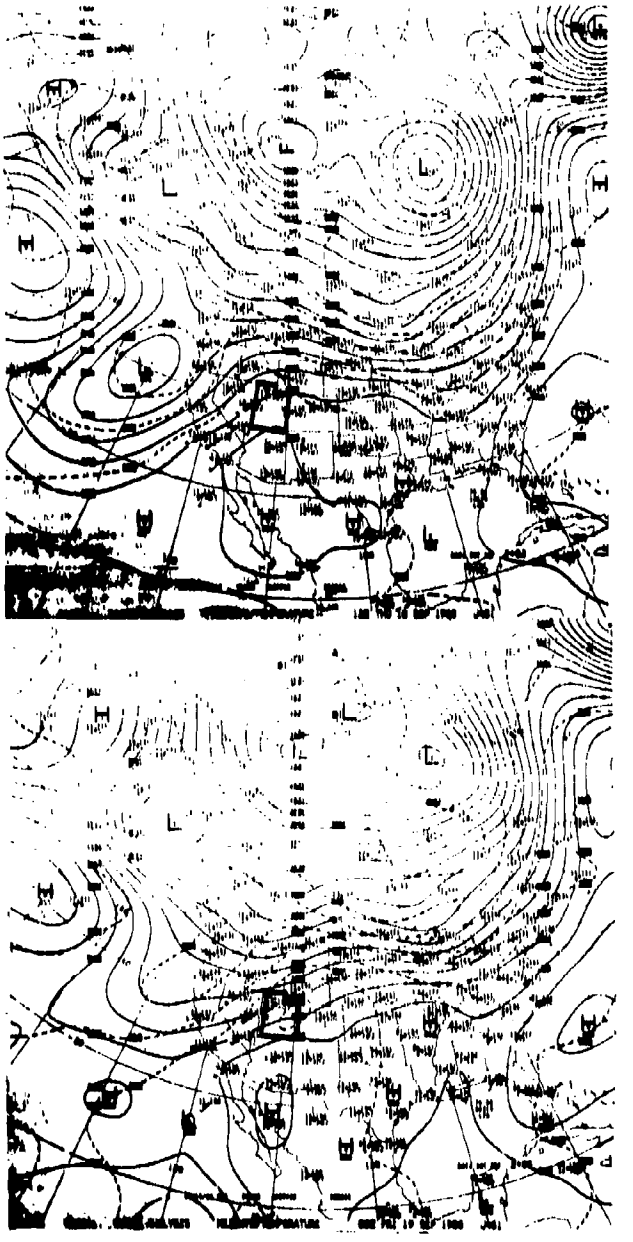

FIGURE 3. 700 mb SYNOPTIC ANALYSIS. This is a reproduction of the National Weather Service 700 mb analysis for 18-19 September at 12 zulu and 00 zulu respectively.

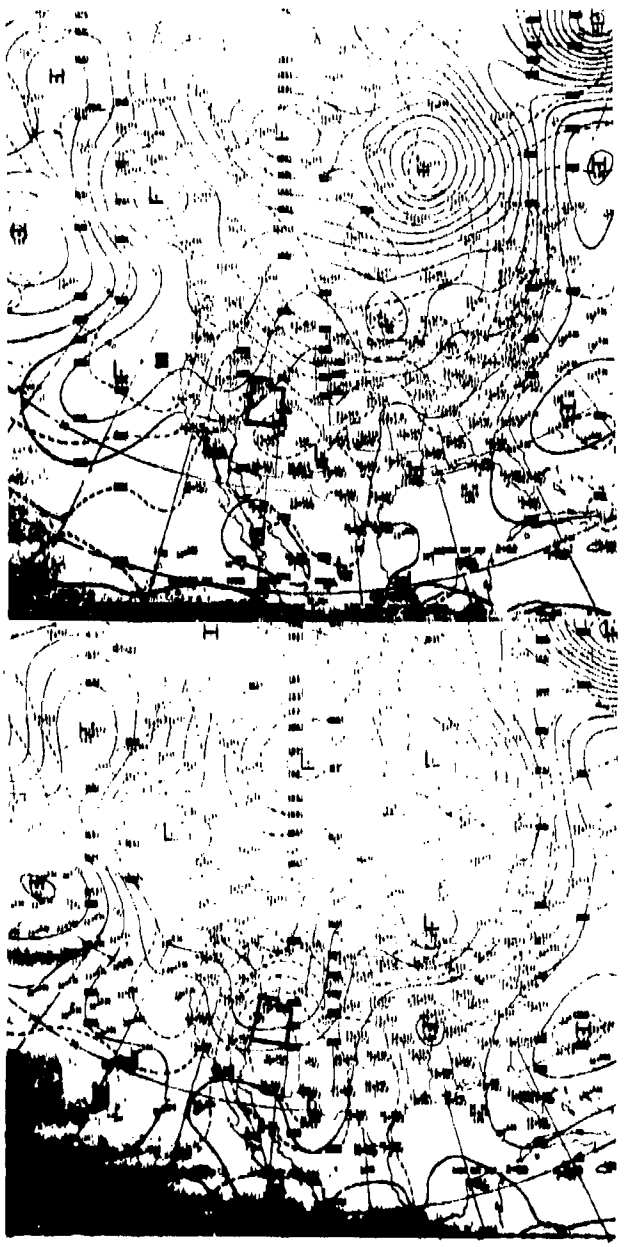

FIGURE 4. 850 mb SYNOPTIC ANALYSIS. This is a reproduction of the National Weather Service 850 mb analysis for 18-19 September at 12 zulu and 00 zulu respectively.

A-1

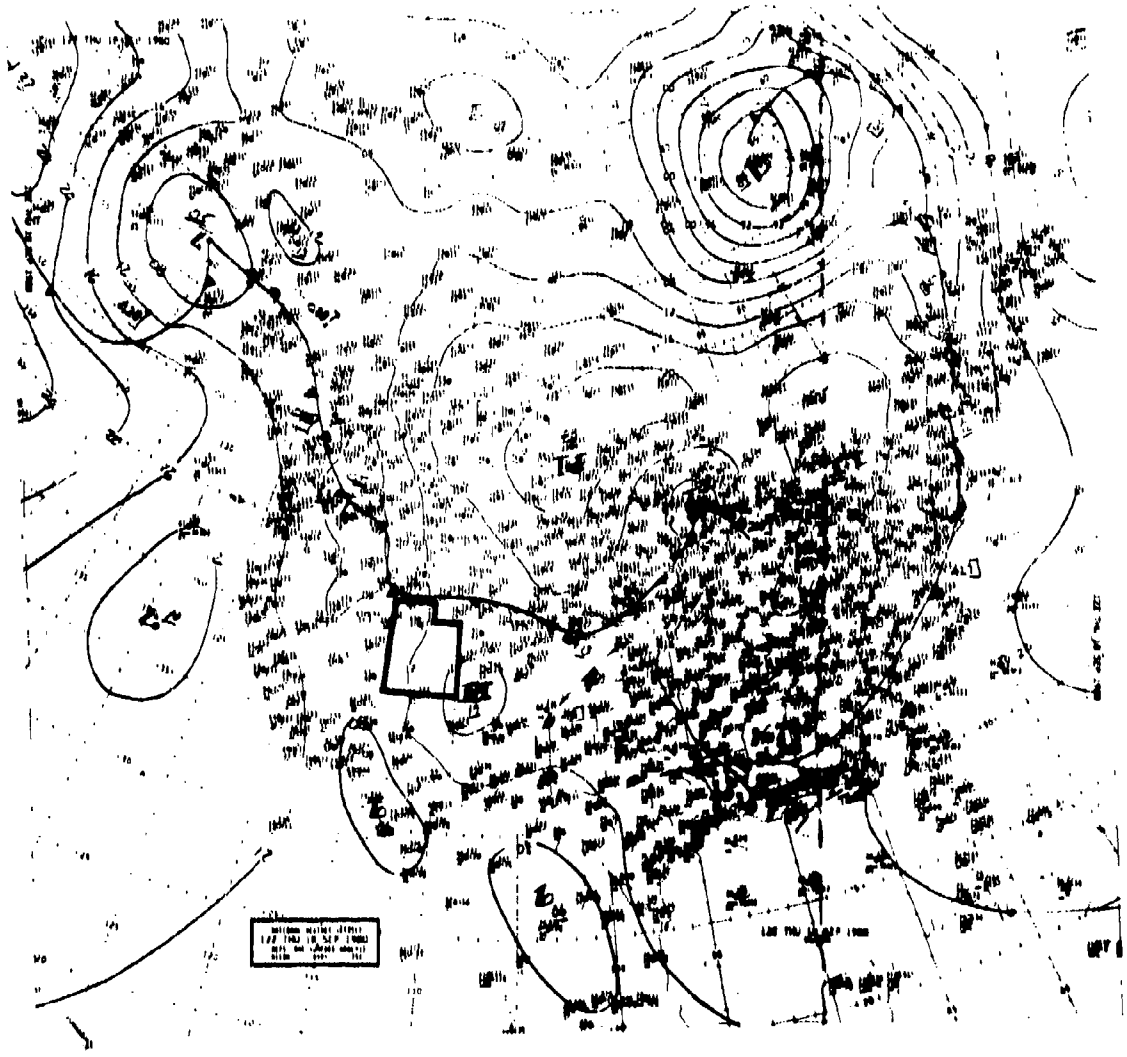

FIGURE 5. 12 ZULU SURFACE SYNOPTIC ANALYSIS
This is a reproduction of the National Weather Service surface analysis for 18 September at 12 zulu.

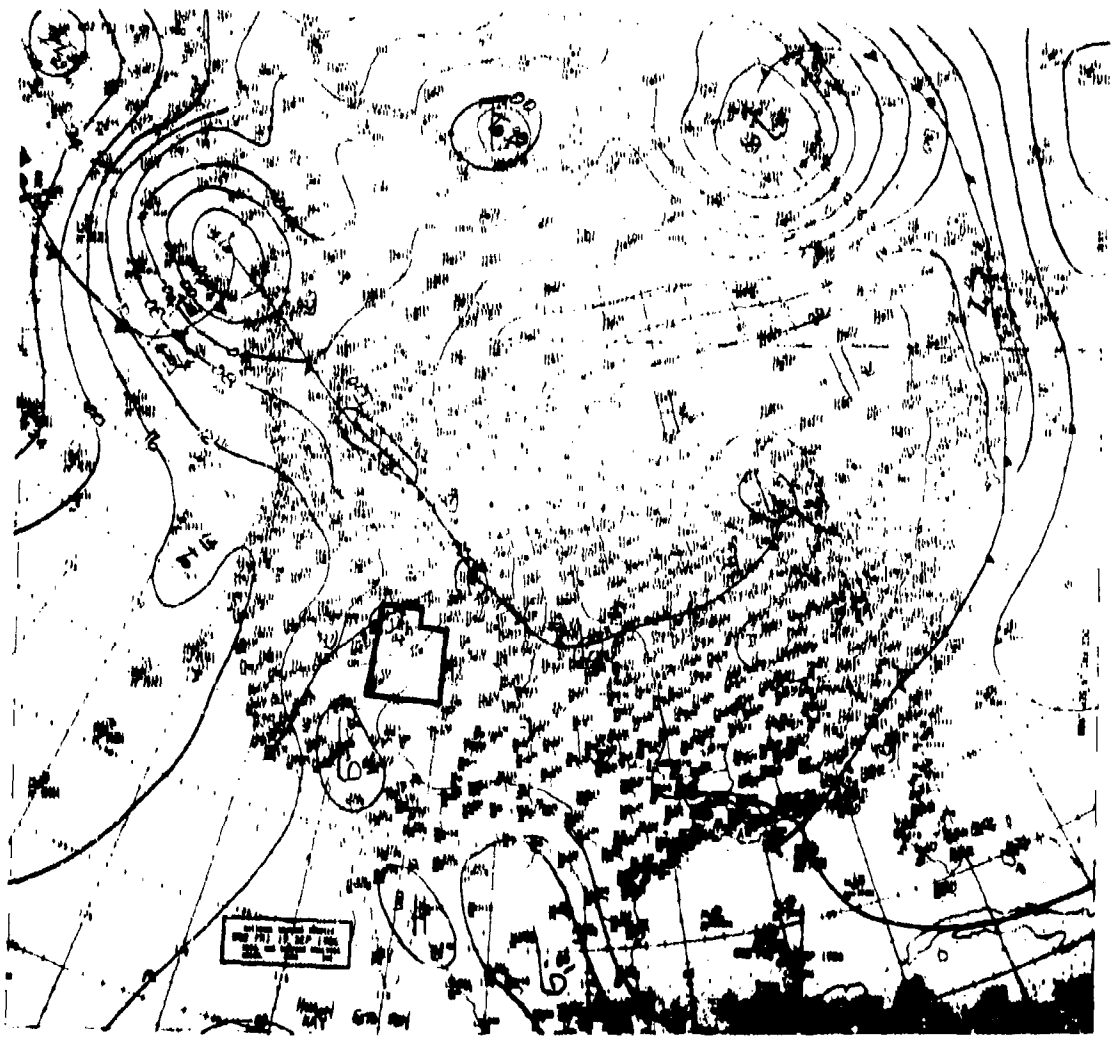

FIGURE 6. 00 ZULU SURFACE SYNOPTIC ANALYSIS
This is a reproduction of the National Weather Service surface analysis for 19 September at 00 zulu.

A FIRST LOOK AT SNOW-ONE

George W. Aitken
U.S. Army Cold Regions Research and Engineering Laboratory
Hanover, New Hampshire

ABSTRACT

SNOW-ONE was the first in a series of major field experiments conducted to evaluate the performance of electro-optical systems under winter conditions and to establish the comprehensive data base needed by the modeling and development community. It was conducted near Burlington, Vermont, starting on 5 January 1981. Fourteen DOD agencies and/or their contractors conducted measurement programs during SNOW-ONE. This paper presents a "first-look" summary of the experiment. It describes the methodology adopted to characterize the environment, including data from several state-of-the-art devices used to characterize airborne snow. A brief summary of the work accomplished by a number of the participants is included, and information is provided on the final form and availability of the results.

1. INTRODUCTION

The SNOW-ONE Field Experiment was the first in a planned series of winter exercises. It was conducted between 5 January and 20 February 1981 at the Vermont Army National Guard Camp Ethan Allen Training Center near Burlington, Vermont. Figure 1 is an aerial view of the SNOW-ONE site, looking east. Figure 2 is a plan view of the site with major features identified.

The objectives of SNOW-ONE were to begin establishing a comprehensive data base containing information on electromagnetic energy propagation through falling and blowing snow, to investigate the influence of the characteristics of snow (both falling and on the ground) on signature measurements, and to conduct studies of seismic and acoustic energy propagation. The agencies that were represented at SNOW-ONE are listed in Table I. As you can see, a broad range of interests were represented. These included a human factors study conducted by the U.S. Marine Corps, the performance of smokes and smoke-characterizing instrumentation, signature measurements in the infrared and near-mm wavelengths, atmospheric propagation measurements from the visible through near-mm wavelengths, and seismic/acoustic vehicle signature measurements.

The purpose of this paper is to present a preliminary summary of SNOW-ONE. As this paper is being written, information from the agencies that were represented at SNOW-ONE is just starting to become available. Therefore, this summary is not complete, and analyses of the data obtained are not attempted. The participants will be providing their results to CRREL as they become available. These will be

Table 1. SNOW-ONE Participating Agency List.

Participant	Measurement
CRREL:	Met., Micro-met., Aerosol Size/Distribution/Concentration, Vertical Met. Profile, Snow Cover Characterization/Chemistry
AFATL:	IR Top-attack Signature Measurements Seismic/Acoustic Signature Measurements
ASL:	Met., Micro-met., Acoustic Sounder, Aerosol Size/Distribution, Visible and IR Transmission
AVCO:	ERAM, Assault Breaker
AVRADA:	10.6-μm Transmission and Signature Measurements
BRL:	MM-Wave Transmission, 35-GHz Top-attack Signature Measurements
CSL:	Smoke Test Support
DPG:	Smoke Particle Size/Distribution/Chemistry, Visible and IR Transmission
HDL:	MM-Wave Transmission
MICOM:	10.6-μm Transmission, GLLD, Copperhead and Hellfire Seekers
NRL:	Visible and IR Transmission
USMC:	MULE, Human Factors Study
UTSI:	Aerosol Size/Distribution, IR Extinction
PM SMOKE/OBSCURANTS:	Technical Support and Assistance

FIGURE 1. Aerial view of the SNOW-ONE site, looking east.

used to correlate snow characterization parameters with propagation measurements and system performance. A report containing this information is scheduled for completion in June. Samples of the data collected by CRREL and some other agencies are presented here as examples of the type of information that will be forthcoming. A few preliminary results that appear to be significant are discussed.

2. METEOROLOGY

One of the most important measurement programs conducted during SNOW-ONE was the environmental characterization work carried out by CRREL and the U.S. Army Atmospheric Sciences Laboratory (ASL). Temperature, dew point, wind speed and wind direction were measured at heights from 2 to 32 m above the ground near the West and East Pads and to a 21-m height at Midpoint (see Fig. 2). In addition, temperature and humidity profiles were obtained to a height of 1,000 m above the ground using a tethered balloon, and frequent rawinsonde flights were conducted. A view of the east meteorological tower operated

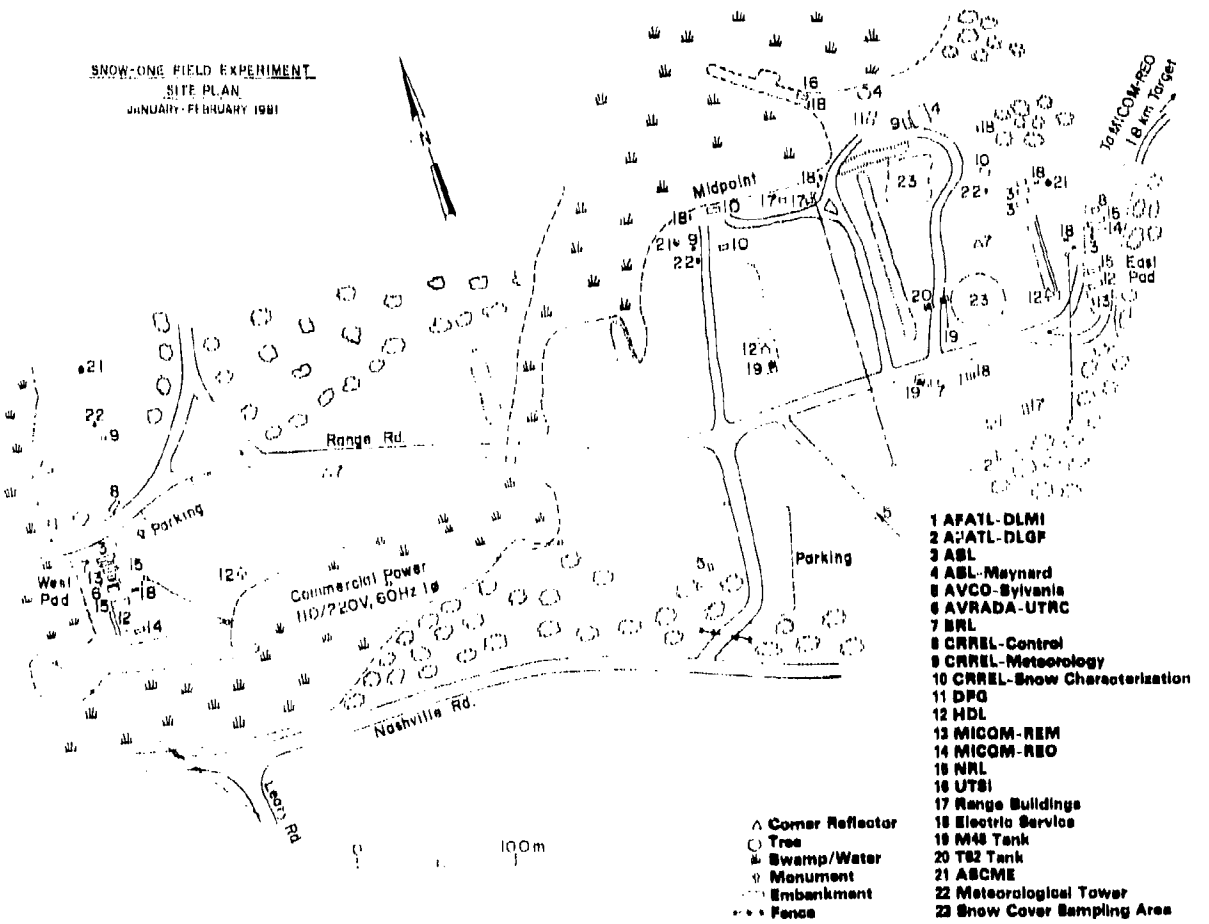

FIGURE 2. Site plan. The primary line of sight from the West Pad to the East Pad was about 640 m in length.

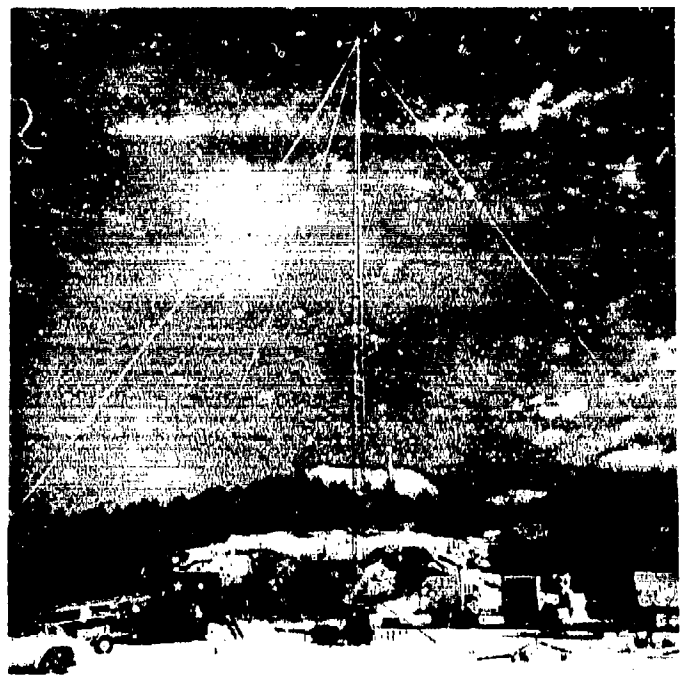

FIGURE 3. Meteorological tower 32 m high at east end of site. Note three-axis wind sensors at all levels.

by ASL is shown in Figure 3. The vans in the background are a part of ASL's Transportable Atmospheric Characterization System (TACS).

Typical meteorological data obtained from tower-mounted sensors during a snowstorm that occurred on 8-9 February are presented in Figures 4 and 5. The curves cover the time period from 0400 on 8

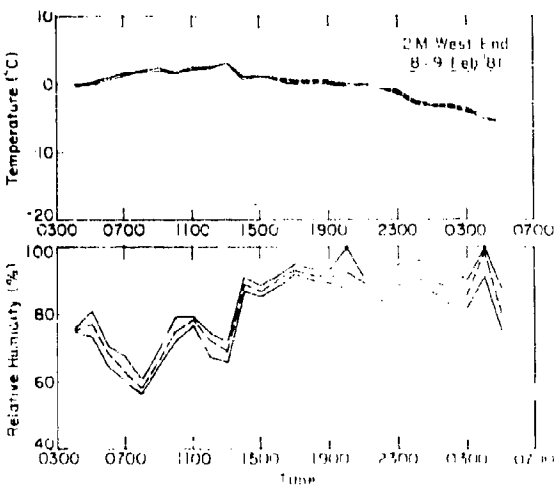

FIGURE 4. Temperature and relative humidity data at 2-m height at west end of site. Curves are the maximum, average and minimum readings obtained during the first 20-minute period of each hour.

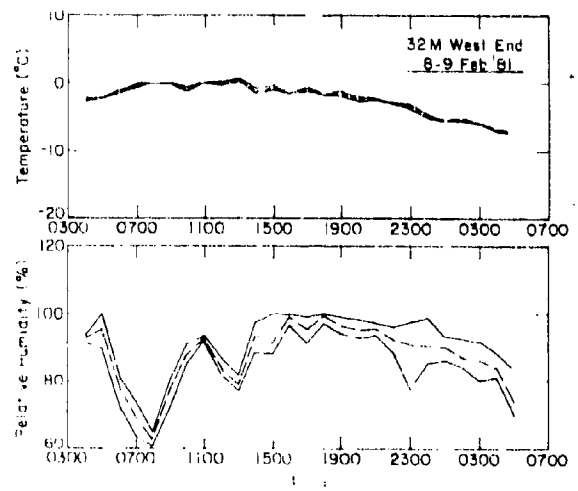

FIGURE 5. Temperature and relative humidity data at 32-m height at west end of site. Curves are the same as Fig. 4.

TABLE II. Example of Wind Data Obtained at SNOW-ONE (0100-0400, 9 Feb 81).

Time	Location	Resultant wind		Max wind		Avg wind
		Dir deg	Speed m/s	Dir deg	Speed m/s	speed m/s
040:01:00	2M WEST END	180.9	1.8	203.4	3.1	2.0
040:01:00	4M WEST END	52.2	1.5	74.1	3.7	1.7
040:01:00	8M WEST END	339.1	1.6	347.7	5.1	2.3
040:01:00	16M WEST END	0.0	0.0	0.0	4.9	2.4
040:01:00	32M WEST END	298.0	10.0	293.1	13.3	10.7
040:01:00	2M CENTER	285.2	1.8	2[illegible].6	4.0	2.1
040:01:00	4M CENTER	230.7	1.8	17[illegible].1	3.9	2.2
040:01:00	8M CENTER	303.1	1.8	286.5	4.3	2.1
040:01:00	21M CENTER	317.1	3.4	313.4	13.4	3.7
040:02:00	2M WEST END	203.0	[illegible].6	179.6	3.1	1.7
040:02:00	4M WEST END	36.6	1.3	9.5	3.0	1.5
040:02:00	8M WEST END	348.8	1.5	321.1	3.6	2.2
040:02:00	16M WEST END	0.0	0.0	0.0	3.3	2.0
040:02:00	32M WEST END	308.1	9.3	307.7	11.7	10.5
040:02:00	2M CENTER	318.9	2.[illegible]	350.5	4.3	2.9
040:02:00	4M CENTER	242.3	1.9	269.0	4.2	2.2
040:02:00	8M CENTER	324.1	2.[illegible]	299.2	4.3	2.7
040:02:00	21M CENTER	320.5	4.8	322.7	10.1	5.4
040:03:00	2M WEST END	155.8	2.0	164.3	4.3	2.2
040:03:00	4M WEST END	65.8	1.5	53.8	3.7	1.8
040:03:00	8M WEST END	334.7	2.0	341.4	4.1	2.5
040:03:00	16M WEST END	0.0	0.0	0.0	6.2	2.5
040:03:00	32M WEST END	274.3	10.6	279.0	17.9	11.8
040:03:00	2M CENTER	274.5	2.6	303.5	4.9	2.9
040:03:00	4M CENTER	195.3	2.1	180.4	3.6	2.3
040:03:00	8M CENTER	285.1	2.6	277.6	4.7	2.8
040:03:00	21M CENTER	283.0	5.2	314.3	17.9	5.7
040:04:00	2M WEST END	132.3	1.8	142.3	3.9	2.0
040:04:00	4M WEST END	89.7	1.7	86.3	5.4	1.9
040:04:00	8M WEST END	293.1	2.4	280.7	4.8	2.6
040:04:00	16M WEST END	0.0	0.0	0.0	5.6	2.8
040:04:00	32M WEST END	268.6	11.3	257.0	17.6	11.4
040:04:00	2M CENTER	259.5	2.3	230.1	4.[illegible]	2.8
040:04:00	4M CENTER	176.5	2.1	160.2	3.7	2.4
040:04:00	8M CENTER	277.2	2.5	266.5	4.7	2.8
040:04:00	21M CENTER	274.6	4.3	267.5	11.3	4.6

February through 0500 on the 9th. This was the longest-lasting snowstorm that occurred during SNOW-ONE and it also produced some of the heaviest concentrations of snow in the air. Snowfall was light and intermittent prior to 1300 hours on the 8th. At that time, coincident with the increase in relative humidity noted in Figures 4 and 5, snow began falling continuously. The snowfall increased to moderate intensity during the night and finally stopped shortly after 0500 on the 9th. An examination of the 2- and 32-m temperature data shows that this was a relatively warm storm, as the temperature at 2 m didn't drop below the freezing level until after about 2100 hours on the 8th. The temperature at 32 m, however, was below the freezing level except for one sample interval at 1300 hours. Typical wind data for this same storm are given in Table II.

3. SNOW CHARACTERIZATION

Standard meteorological and/or micro-meteorological measurements cannot be used alone to adequately characterize a snowstorm. The size, size distribution and type of individual snow crystals or snowflakes are also required, as is a measure of the concentration of snow in the air at any time. Complete characterization must also include documentation of any other obscurant present while it is snowing, such as haze or fog.

Characterization of snow in the air during SNOW-ONE was accomplished using a number of different techniques. The type (or "habit") of the snow crystals or flakes was determined periodically by catching crystals on a black velvet pad and examining them under a microscope (Figure 6). The continuous replicator shown in Figure 6 was used to obtain a record of the change in crystal type with time. It operates by moving formvar-coated 35-mm-wide film beneath a small opening in its top. Snow crystals fall through the opening onto the film and are coated with formvar through surface attraction; then the formvar coating is dried, leaving a 3-dimensional image (replica) of the crystal.

Snow crystals were also "caught" on formvar-coated glass slides at regular intervals during snowstorms. The continuous replicator, because of its fixed film drive speed and restricted sample area, does not provide data suitable for size distribution calculations, but the crystal replicas on glass

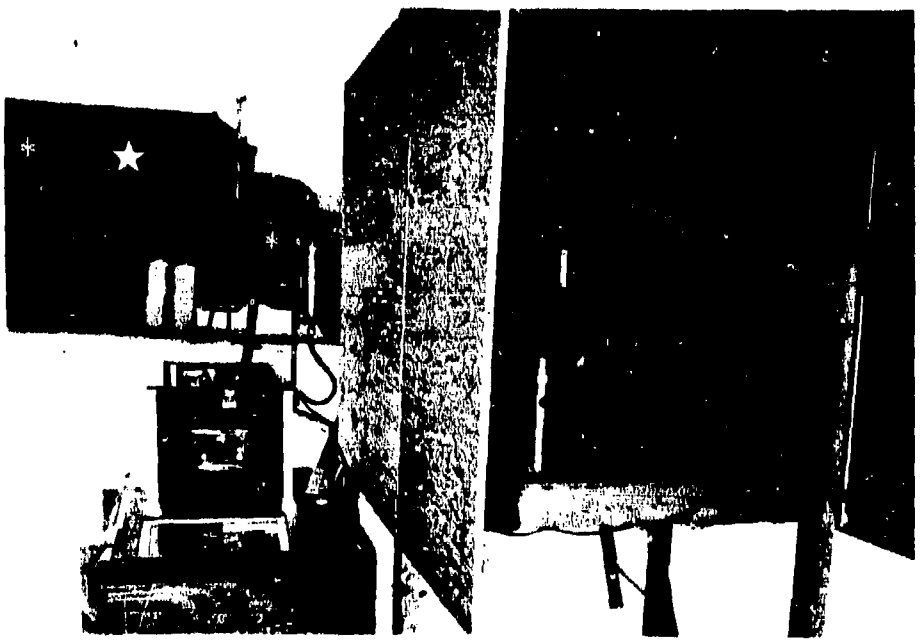

FIGURE 6. Basic snow characterization equipment. Device on the left is a continuous replicator that provides a record of crystal types.

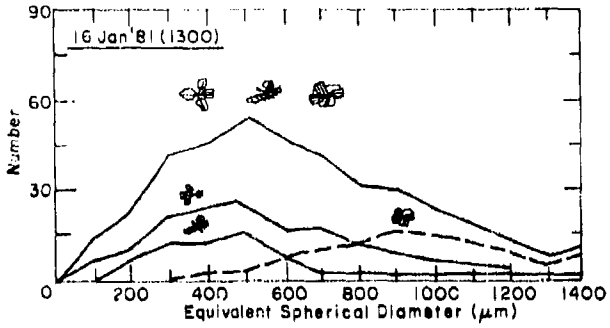

FIGURE 7. Snow crystal size distributions obtained using samples caught on formvar-coated glass slides. The symbols indicate three different crystal types (l. to r.): side-planes, scale-like side-planes, and a combination of side-planes, bullets and columns. The top curve represents a cumulative size distribution for the three crystals shown, plus some relatively small number of other crystals of miscellaneous types that were also present. The three lower curves are size distributions for specific crystal types.

slides can be used for this purpose. Examples of size distributions from these replicas are shown in Figure 7. The size in this case is computed by tracing the outline of the particle, and then computing an equivalent circular diameter from the area obtained. It is easy to see that, when attempts are made to correlate data from propagation measurements that are dependent on particle size with snow crystal size distributions, breaking down the data by crystal type could be very important. This is illustrated by (as one example) the difference in the peak diameter for the cumulative curve from that (dashed line) for the crystals classified as a combination of side planes, bullets and columns.

The snow characterization methods discussed above are very time-consuming and have other limitations as well. Among these limitations is the need for long sampling times to obtain enough crystals for statistically significant size distributions when using the glass slide method. This problem can be eliminated, at least in theory, by utilizing electro-optical particle size measuring systems that are now available. Both CRREL and ASL operated this type of instrumentation at SNOW-ONE. Figure 8 shows two such systems operated by ASL. These probes provide a 2-dimensional image of particles passing between the two arms located on their left end. The probe in the foreground with the arms skewed outward from its longitudinal axis has a size range from 200 to 6400 μm in 200-μm steps, while the one in the rear has a range from 25 to 800 μm in 25-μm steps. During measurement periods, the probes are oriented in elevation and azimuth so that snow falls directly through the sampling area rather than at some angle to it.

The electro-optical probes operated by CRREL are shown in Figure 9. The two with the large intake horns are two-dimensional gray probes. Unlike a standard two-dimensional probe, they provide an indication of the transmittance through the particles that are imaged. These probes are adjustable in elevation and are slaved to a wind direction sensor for automatic azimuth control. In addition, a high air flow is maintained through the sample volume by a fan-driven aspiration system to provide a known particle velocity. The image formed by these probes is a direct function of particle velocity and, for

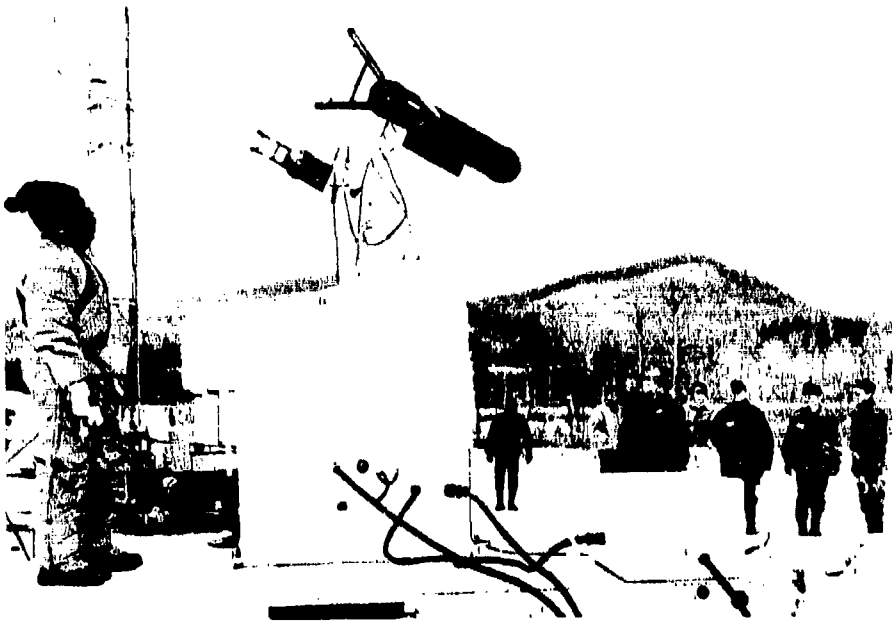

FIGURE 8. Two-dimensional electro-optical particle size measurement systems operated by the Atmospheric Sciences Laboratory.

FIGURE 9. Forward scattering probe (left) and two-dimensional gray probes with aspirators operated by CRREL.

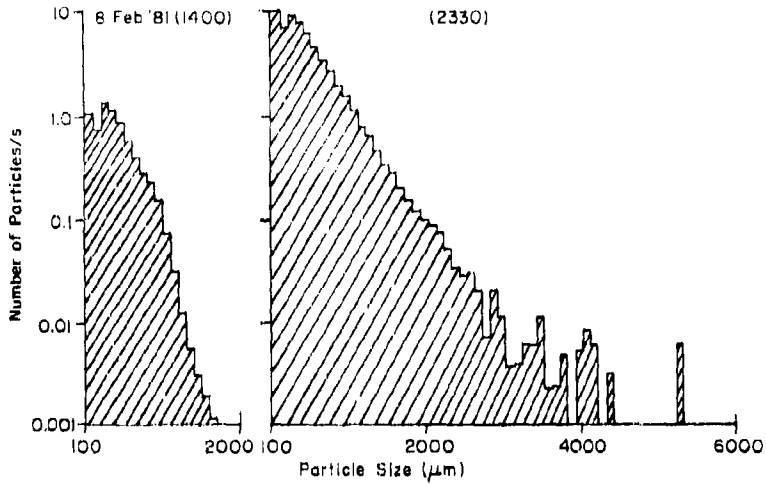

FIGURE 10. Snow crystal size distributions obtained using 100 to 6400 μm aspirated two-dimensional-gray electro-optical probe.

non-spherical particles like snow crystals, a true image analysis can be accomplished only if this velocity is known. These probes cover the size ranges of 5 to 320 um and 100 to 6400 μm in 5- and 100-μm steps, respectively.

The probe on the far left in Figure 9 is a forward scattering probe with a size range of 0.5 to 45 μm. It is used to monitor the size and size distribution of fog that may occur concurrently with a snowfall. This probe is also aspirated and has a long tube on its intake (left) end to preclude snowflakes from being drawn into it.

These types of particle measurement systems can provide size distributions over relatively short time intervals because of the relatively high flow rates through them. Typical size distribution data obtained using the 100 to 6400 μm probe are given in Figure 10. These data represent 20-minute averages starting at the time indicated. Data were obtained for time intervals as small as 20 s, but these are not yet available in a suitable format for presentation. In this case, the size was computed by assuming that the width of the particle was equal to its diameter and that the particle was spherical. This is, of course, an oversimplification in the case of snow. Analyses are in progress to develop more realistic, but still manageable, sizing algorithms for this type of data. It is also planned to attempt comparison of the data obtained using both aspirated and unaspirated probes. Aspirated probes have the advantage of a known particle velocity, but they may also contribute to reorientation or breaking up of some particles, thus producing a biased size distribution.

FIGURE 11. Holographic camera.

All of the characterizing methods discussed above have some potential drawbacks. For instance, they may damage the snow crystals, or some key parameter like particle fall velocity may be unknown. The holographic camera shown in Figure 11 has the potential to eliminate these drawbacks. It can obtain a true picture of a snowstorm without disturbing any of the crystals and, using a double-pulse, mutiple-exposure technique, fall velocities can be determined. The sample volume of this particular camera (the first of its kind suitable for field-portable operation) is a 4 in. diameter cylinder, 10 in. long, located between the two arms protruding from the rear of the camera. A 50 mjoule ruby laser is used to make the hologram. A number of holograms of snowflakes were made using this camera during SNOW-ONE. Analysis of these images is extremely time consuming, however, and a standard methodology for this is currently under development. Future plans for this camera include configuring it to look at the same sample volume at the same time as a two-dimensional electro-optical probe to compare performance of the two systems.

One indication of the severity of the weather that occurred during SNOW-ONE is illustrated in Figure 12. The trailer in which the holographic camera was kept when not in use was blown on its side during a severe wind and rain storm on 11 February. Peak wind speeds were estimated at greater than 70 knots.

FIGURE 12. Storm damage to holographic camera.

As noted earlier, one of the measurements required to adequately characterize a snowstorm is snow concentration. The actual concentration of snow (or, if you prefer, ice) in the air cannot be obtained by measuring accumulation on the ground because of the different fall velocities of different snow crystals, which can vary from less than 50 to more than 250 cm/s (O'Brien, 1970). Also, the time resolution of an accumulation-on-the-ground measurement is much too coarse for the needs of the electro-optical community.

Stallabrass (1976) described an electromechanical device consisting of a cyclone separator mounted on a whirling arm (Figure 13) that appeared to offer a relatively straightforward means of making the concentration measurement. A schematic of the collection head portion is presented in Figure 14. Air and snow are ingested through the nozzle as the arm is turned at 130 rpm. The snow is melted by electric heaters and the melt water is forced out through a calibrated hypodermic needle. The drops are counted as they break a beam of light shining on a photo-transistor. The volume of the individual drops

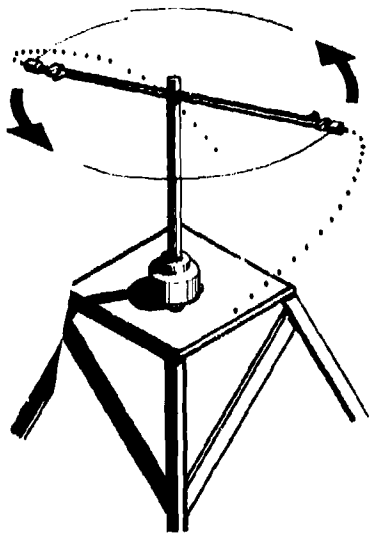

FIGURE 13. Airborne Snow Concentration Measuring Equipment (ASCME).

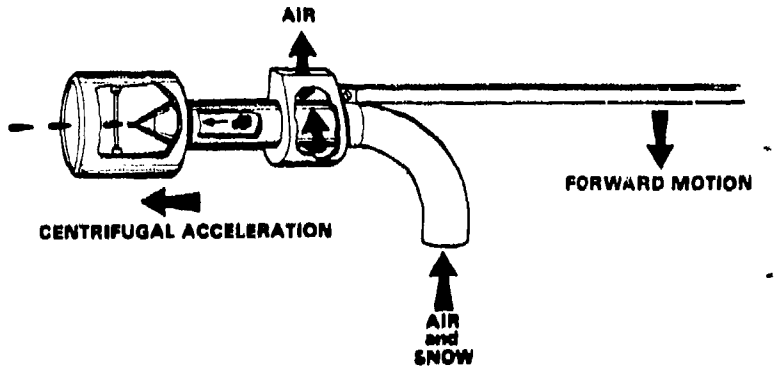

FIGURE 14. Schematic of ASCME collection head.

FIGURE 15. ASCME installed at Midpoint site. Researcher is pointing to the input tube of the collection head.

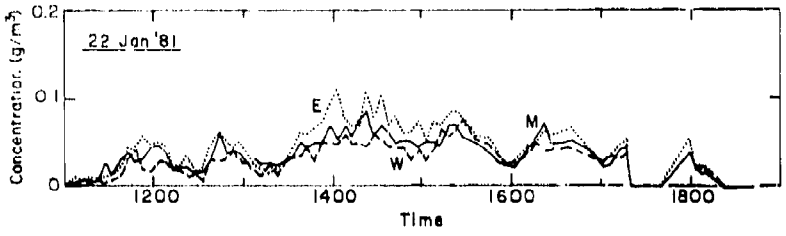

FIGURE 16. ASCME data for 22 Jan 81. E, W and M refer to East Pad, West Pad and Midpoint locations.

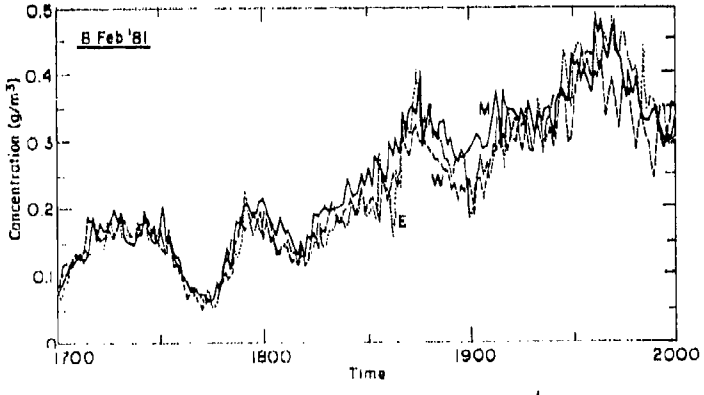

FIGURE 17. ASCME data for 8 Feb 81.

can be calculated from knowledge of the needle dimensions and the centrifugal force on the drop. Summing the number of drops over a given time period provides a measure of ice concentration during that period.

A significant number of refinements were made to Stallabrass's original configuration, particularly in the design of an airfoil to minimize turbulence at the collection head and in the electronics package. Three of the redesigned devices, designated Airborne Snow Concentration Measuring Equipment (ASCME), were operated at SNOW-ONE. Figure 15, a picture of the ASCME located at Midpoint site, shows the airfoil used to minimize turbulence at the intake.

Figures 16 and 17 illustrate ASCME data typical of a light snowstorm and a light-to-moderate storm, respectively. These data clearly show that both a wide range in amplitude and a high rate of amplitude change characterize the concentration of snow in the air.

In addition to characterizing snow in the air, measurements were also made to describe snow on the ground. These included measurements of depth, density, hardness and crystal description. The liquid water content was also monitored using both cold and hot calorimetric techniques.

4. ATMOSPHERIC PROPAGATION MEASUREMENTS

A primary objective of SNOW-ONE was to obtain electromagnetic propagation data from visible through near mm wavelengths in a well defined winter environment. Most of these measurements were made along the primary, 640 m long line of sight between the West and East Pads shown in Figure 2. The 4- and 8-inch Barnes transmissometers shown in Figure 18 were used to obtain data at 0.44-0.7, 3.8 and 8-12 μm by ASL. These were mounted at the West Pad and used a collimated visible and black body source located on the East Pad.

Visible and infrared propagation measurements were also made by the Naval Research Laboratory (NRL). They made narrowband measurements using a Fourier Transform Spectrometer in the 2-12 μm spectral region and broadband measurements at 0.55, 1.06, 3.0 and 10.37 μm. The receiver used for the broadband measurements is shown in Figure 19. This receiver was mounted on the West Pad and used a searchlight mounted on the East Pad for a source. Typical data obtained using this system during a snowstorm on 22 January are given in Figures 20 and 21. Snow concentration data from the ASCME located at the Midpoint site are included for reference. A complete record of ASCME data for this snowstorm is given in Figure 16 and, as noted earlier, the intensity of this storm was light and the concentration of snow in the air was quite low. Transmissions at 1.06 and 3.0 μm were also obtained by NRL during those same time periods

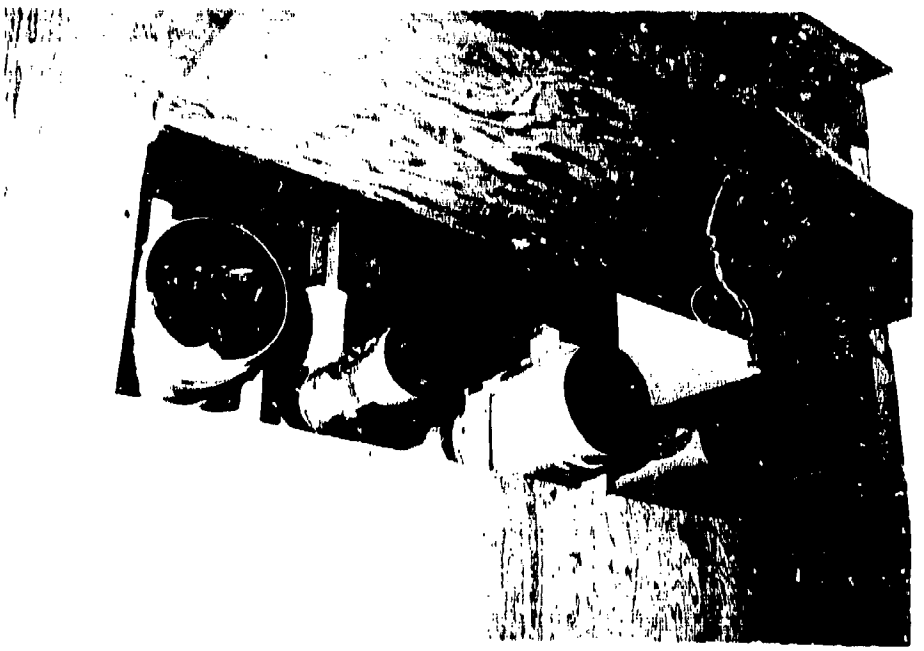

FIGURE 18. Four- and eight-inch Barnes transmissometers operated by ASL.

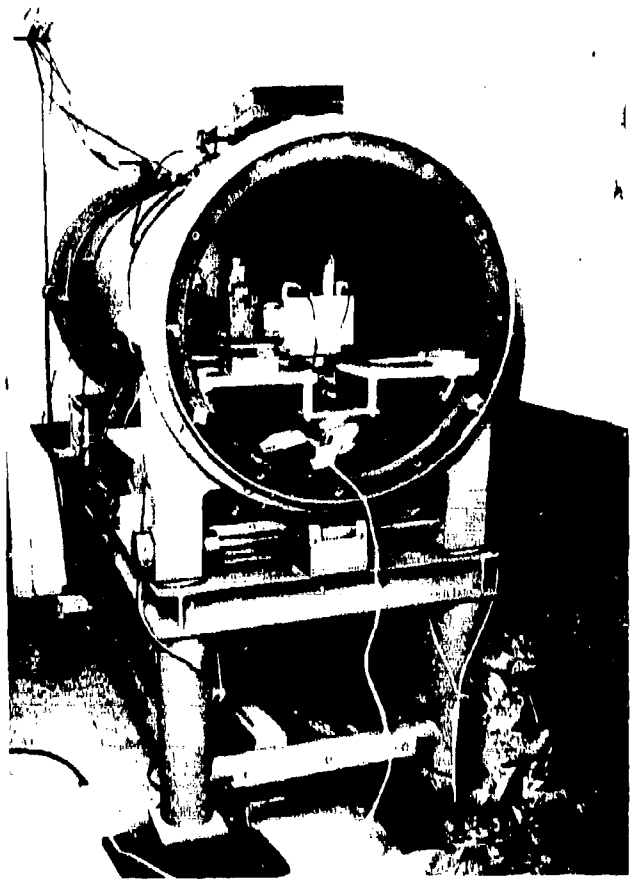

FIGURE 19. NRL broadband transmissometer receiver.

but were not plotted, as the 1.06-μm data were very close to those obtained at 0.55 μm, and the 3.0-μm data closely track those at 10.37 μm.

These data can be used to illustrate a typical problem encountered by the analyst in trying to explain variations in transmission during snowstorms. The data for the 1130-1230 time period (Figure 20) indicate a decrease in transmission early in the period, followed by relatively constant transmission, followed by a slight increase at the end of the data set. The ASCME data do not follow this same trend, suggesting that a change in snow concentration was not the primary factor influencing the changes in transmission that were observed. Moving on to the 1250-1350 period, again the ASCME data do not appear to be strongly related to the transmission data shown.

An examination of the snow crystals for these two time periods shows that they were principally spatial dendrites with some aggregates (flakes) greater than 1 cm in diameter (Redfield, 1981). A

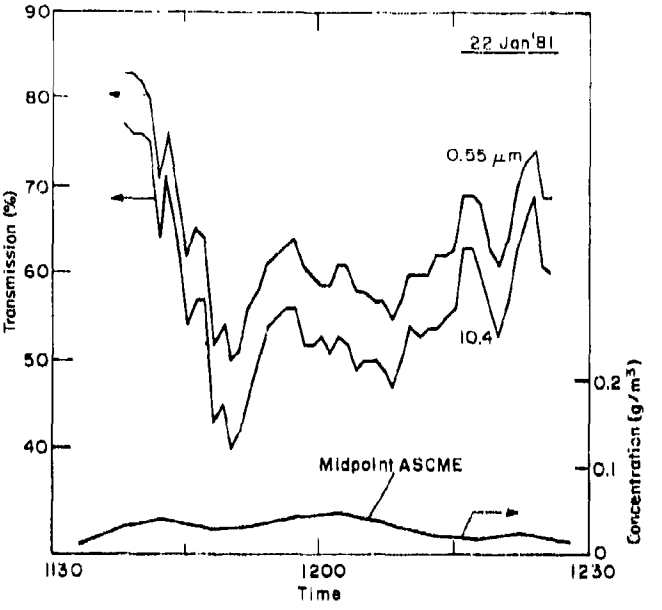

FIGURE 20. Comparison of transmission and snow concentration data.

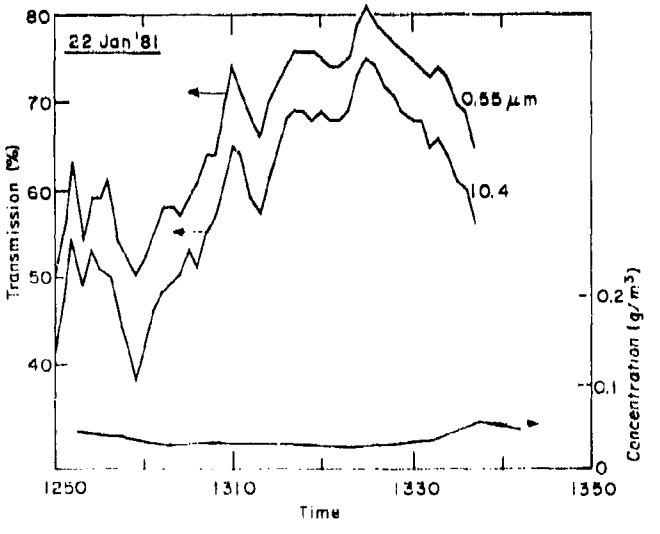

FIGURE 21. Comparison of transmission and snow concentration data.

greater number of these large aggregates was observed after 1300. This observation is corroborated by data obtained using the 100 μm resolution electro-optical probe.

This probe recorded a greater number of particles during the 1200-1220 period than during the 1300-1320 period. As this probe did not "see" the large aggregates that were falling, and the concen-

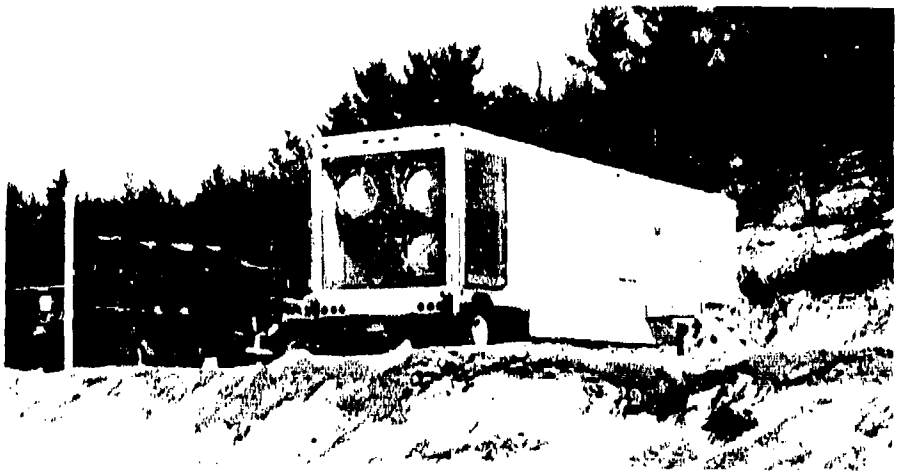

FIGURE 22. Transmitter van for Mobile Measurement Facility located on the East Pad.

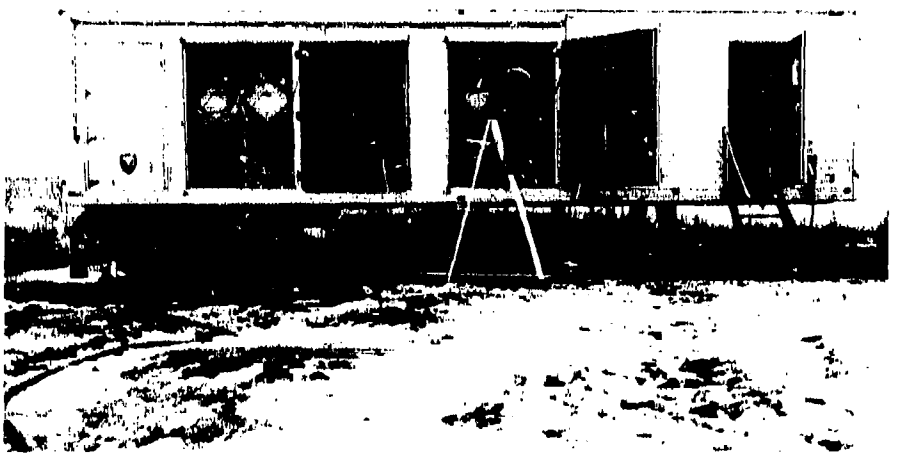

FIGURE 23. Receiver van for Mobile Measurement Facility located on the West Pad.

tration of snow in the air remained about the same, this information corroborates the qualitative observations that there were more large aggregates during the later time period.

In addition, the forward scattering probe data for this period show a slightly higher concentration of fog during 1200-1220 than later on. Therefore, it appears that the low transmission during the 1145-1215 time period (relative to that from 1105-1130) was caused by a greater number of small crystals in the air together with a slightly higher concentration of fog droplets.

Two groups conducted near-mm wave propagation experiments during 33DW-ONE. Harry Diamond Laboratory (HDL), utilizing their Mobile Measurement Facility (MMF), made transmission and backscatter measurements at 94, 140 and 250 GHz. Figures 22 and 23 show the transmitter and receiver vans for the

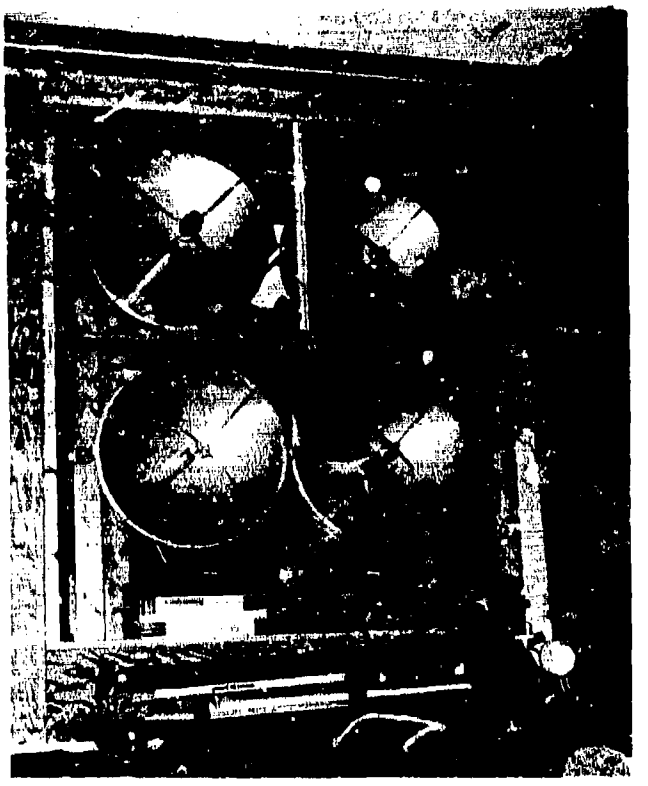

FIGURE 24. Transmit/receive antennas for BRL near-mm-wave measurements located on the West Pad.

MMF. The Ballistic Research Laboratory (BRL) conducted mm wave propagation measurements at 35, 95, 14[illegible] and 217 GHz over a 914 m path length using the antenna array shown in Figure 24 with corner reflectors mounted along the line of sight.

There were two Ground Laser Locator Designators (GLLD) that were used at SNOW-ONE by MICOM, one with and one without the AN/TAS-4 night sight (Figure 25). They were used with the Copperhead and Hellfire seekers (Figure 26) to develop rule-of-thumb operational procedures, obtain estimates of maximum lock-on range versus snowfall rate, and obtain backscatter/false target data during snowfall.

The GLLD's were located at the west end of the SNOW-ONE site. From that location they were used to designate 8-ft-square, OD painted wooden targets located on the East Pad, 640 m away, and on a hill 1800 m to the east-northeast. Both of these targets were equipped with a heat tape to allow location with the night sight. In addition, some measurements were made using both a U.S. M48A5 and a Soviet T62 tank as targets (Fig. 27).

FIGURE 25. GLLD's in use. Unit on right is equipped with AN/TAS-4 night sight.

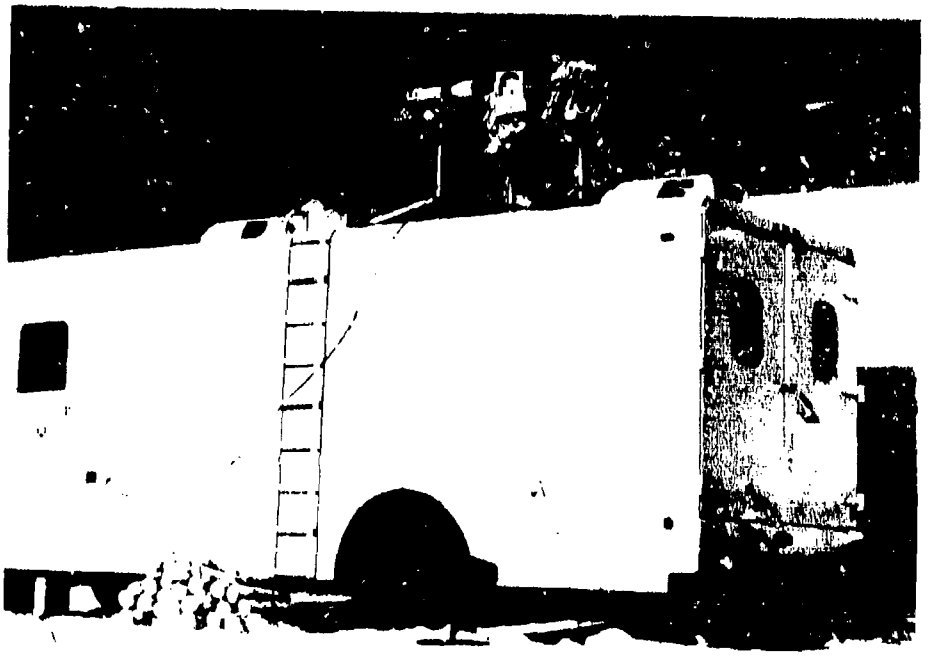

FIGURE 26. Copperhead (far right) and Hellfire (center) missiles mounted on top of MICOM instrument van. Note firewood supply.

FIGURE 27. U.S. M48A5 tank (background) and Russian T62 tank used as targets for the signature measurements.

FIGURE 28. MULE setup at MICOM GLED site for comparison test with GLED.

The Modular Universal Laser Equipment (MULE) was also used to check its compibility with the seekers (Figure 28).

5. SIGNATURE MEASUREMENTS

The instrumentation shown in Figure 29 was used by personnel from the Air Force Armament Laboratory to obtain signature measurements in the 3-5 and 8-12 μm portion of the infrared spectrum. The cameras on the pole were used to look down from various heights up to 27.5 m at both the M48A5 and the T62 tank. Typical data obtained using this system are shown in Figure 30. This is a thermogram of the idling M48A5 taken with the 3-5 μm camera. The two spikes in the foreground are the signatures of heat lamps used for calibration. The large spike at the left rear is the tank's exhaust.

Signature measurements were also conducted by BRL using a 35-GHz solid state CW radar with polarization diversity mounted on top of a 15 m high pole. In this case the test objectives were to make radar backscatter measurements from snow surfaces and to evaluate the effects of snow cover on armored targets. Measurements were made using both parallel and cross polarization techniques.

FIGURE 29. Instrumentation used to obtain infrared target signatures. Pole in middle extends to 27.5 m in height and carries 3-5 and 8-12 μm passive infrared cameras.

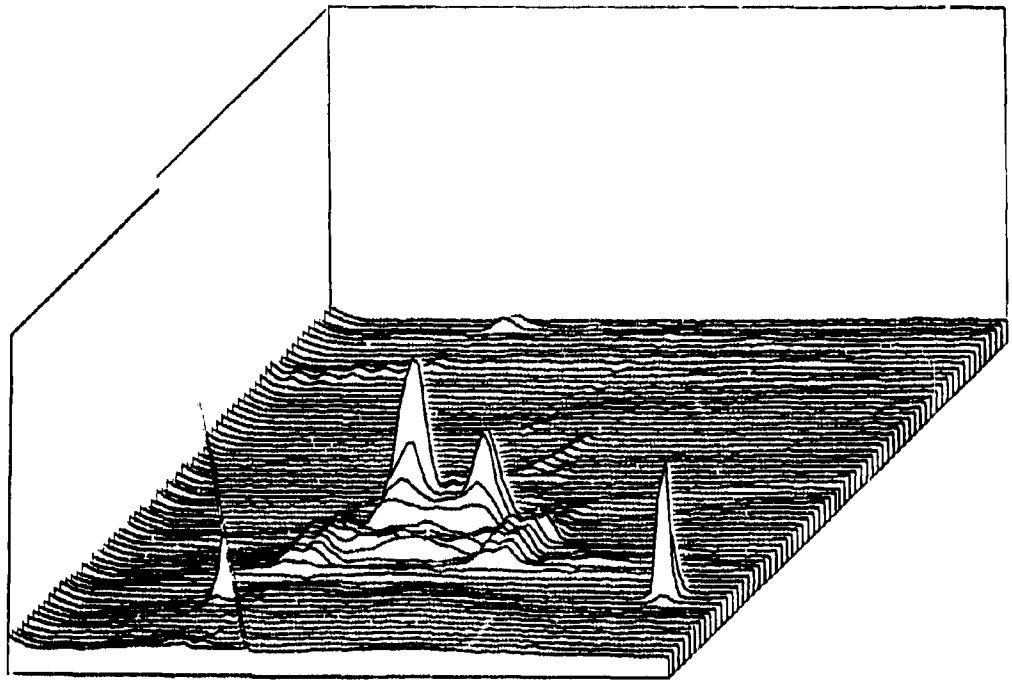

FIGURE 30. Typical signature data obtained using the 3-5 μm camera looking at an M48A5 tank against a snow background.

6. SMOKE CHARACTERIZATION

Preliminary evaluation of smoke characterization instrumentation was also conducted during SNOW-ONE. Fog oil, PEG 200, and four IR screeners were dispensed by Chemical System Laboratory personnel using the equipment shown in Figure 31. The fogger (left) was used to dispense fog oil and the PEG 200. The other materials were dispensed using the device in the center, which was assembled using parts from the XM49 smoke generator. A small amount of WP smoke was also released using wedges from the XM825, 155 mm round. In all, 12 smoke trials were conducted, all under clear conditions. Unfortunately, it was not possible to maintain an on-site smoke capability long enough to conduct operations during a snowfall or under very cold conditions.

A major objective of the smoke experiment was to evaluate the performance of current smoke-characterizing instrumentation in a winter environment in advance of any major winter smoke test. Figure 32 is a view of some of this instrumentation operated by the Dugway Proving Ground (DPG) Safari Team. In addition to the chemical impingers, aerosol photometers, and a particle size analyzer used by DPG, additional measurements, including some using the University of Tennessee Space Institute particle

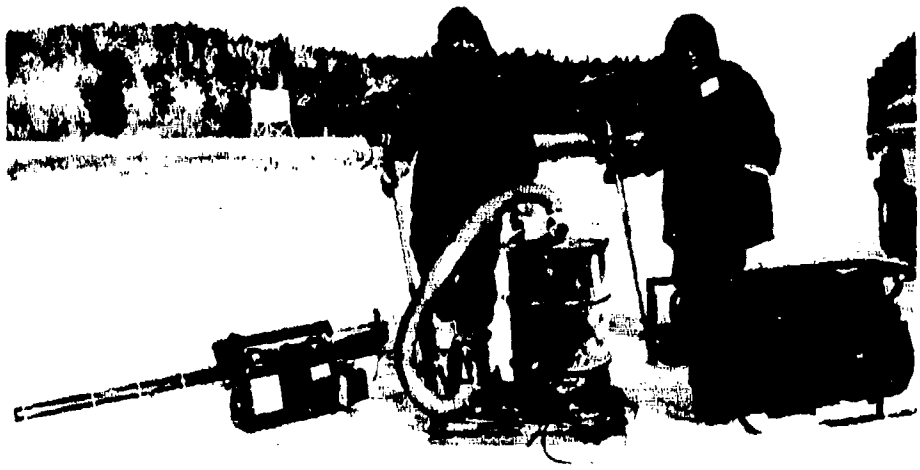

FIGURE 31. Smoke dispensing equipment. From left to right: a commercial fogger, a prototype dispenser using XM 49 generator parts, and the M3A3 generator.

FIGURE 32. Smoke sampling equipment deployed at SNOW-ONE by DPG Safari Team.

FIGURE 33. UTSI particle size interferometer.

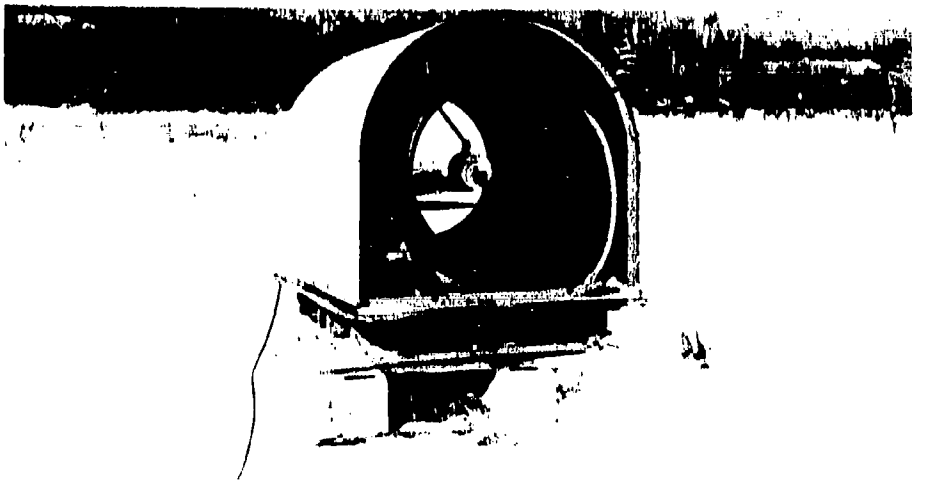

FIGURE 34. Source for DPG 0.4-0.7 and 3.4 μm transmissometer.

size interferometer shown in Figure 33, were also made. Effectiveness of the smokes was measured using a Barnes short path transmissometer operating in the 2.5-14 μm band. In addition, transmission measurements were made in the 0.4-0.7 and 3.4 μm spectral bands. The source and receiver for that transmissometer, which were mounted at opposite ends of a 100 m long instrumented path, are shown in Figures 34 and 35 respectively.

Figure 36 shows one of the smoke trials using WP wedges.

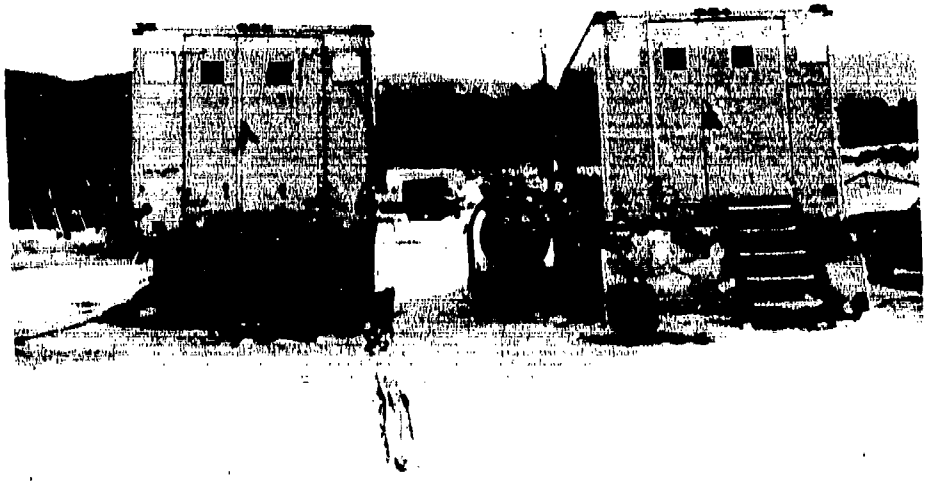

FIGURE 35. Receiver for DPG transmissometer.

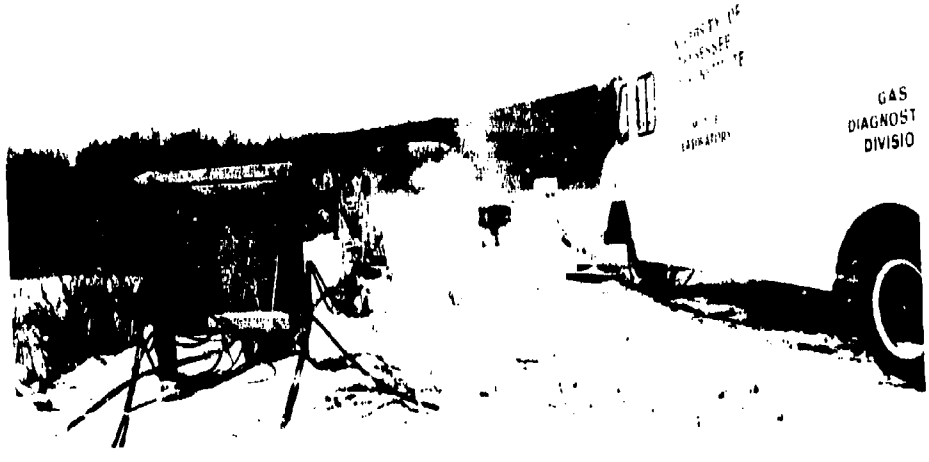

FIGURE 36. WP smoke trial.

FIGURE 37. The two loads required to transport the MULE.

7. HUMAN FACTORS STUDY

The USMC conducted a human factors exercise at the SNOW-ONE site and adjoining areas using the MULE. They were interested in seeing what types of problems might be encountered during movement, setup and operation of the MULE in a winter environment. This exercise was directed by the USMC Operations Test and Evaluation Activity at Quantico. The troops involved were from Camp Pendleton. Transporting the MULE requires two men, each with a load of approximately 100 lb, as shown in Figure 37. After setup, it was difficult to operate with gloves on (Figure 38). Battery life was also extremely limited, even at the relatively moderate temperatures (+5 to -15°C) encountered during this test phase.

FIGURE 38. Typical MULE deployment. Note that operator has removed his gloves.

8. PRELIMINARY RESULTS

Up to this point, is has been possible to discuss some of the measurement programs that were conducted at SNOW-ONE without saying too much relative to results or conclusions. There was little choice in this approach, as this paper had to meet a 10 April 81 deadline, and, essentially, no final results were available prior to that date. However, there are several areas where important preliminary results are emerging.

First, performance of the state-of-the-art snow characterization instrumentation used at SNOW-ONE was very good. High frequency mass concentration measurements were made for the first time in both rain and snow in combination with propagation measurements across a wide frequency spectrum. These, together with both mechanical, photographic and electro-optical (e/o) particle size measurements will allow significant advances to be made in understanding of the performance of e/o systems performance in a winter environment. One example: mass concentration alone does not determine e/o system performance in falling snow. The size and size distribution of the snow must also be considered, as must the potential presence of other obscurants.

Second, a snow cover can pose problems for the operation of both infrared and mm wave target location and tracking systems. This appears particularly true at mm wavelengths where changes in snow characteristics over relatively short time periods resulted in large (≈20 db) changes in backscatter (Hauerle, 1981).

Next, transportation and operation of the USMC MULE (Modular Universal Laser Equipment) was very difficult under winter conditions. Individual loads are heavy (>100 lb), the equipment is difficult to operate with gloves on, and battery life was extremely short.

Finally, visible through far infrared transmission appears to degrade at about the same time in falling snow. Transmission in the infrared appears to be affected slightly more than that in the visible, possibly because of strong water absorption in the infrared (Curcio, 1981). Moderate snowfall significantly attenuated transmission at short ranges (640 m), to the extent of complete system degradation (Butterfield, 1981). Attenuation in light snowfall was sufficient to suggest a reduction in the maximum range capabilities of some systems.

9. SUMMARY

In the interests of time and space, and because at this time a great deal of the needed data are unavailable, I have not mentioned all of the measurement programs conducted at SNOW-ONE. And I fear I may not have done justice to some of those I did mention. A report summarizing all of these measurement programs and containing analyses of data for selected times, together with an index to all the data available, is scheduled for completion in June. A detailed discussion of the results will take place at a symposium to be held at CRREL on 4-5 August 81.

The next major winter field program, SNOW-ONE A, is scheduled to begin in early December 1981 at the SNOW-ONE site in Vermont. A planning meeting for SNOW-ONE A will be held at CRREL on 6 August. Preliminary plans for SNOW-TWO, which will emphasize smoke performance in a winter environment, will also be discussed at the 6 August meeting. SNOW-TWO is tentatively scheduled for January—February 1983.

10. ACKNOWLEDGMENT

I thank Bob Redfield and Sid Gerard of CRREL for reviewing this paper, and all of the people who survived SNOW-ONE for making it possible. SNOW-ONE is a part of the Corps of Engineers Winter

Battlefield Obscuration Research Program. This program is being coordinated by CRREL for the Directorate of Research and Development, OCE, under DA Project 4A762730AT42.

11. REFERENCES

Bauerle, D. (1981) Personal communication, 3 March.

Butterfield, E. (1981) Personal communication, 31 March.

Curcio, J.A. (1981) Personal communication, 19 March.

O'Brien, H.W. (1970) Visibility and light attenuation in falling snow, Journal of Applied Meteorology, Vol. 9, No. 4, Aug.

Redfield, R. (Ed.) (1981) SNOW-ONE: Preliminary test results, CRREL Internal Report 715, April (Draft).

Stallabrass, J.R. (1976) The airborne concentration of falling snow, National Research Council of Canada, DME/NAE Quarterly Bulletin, 1976(3), 1, 29.

AN OVERVIEW OF SMOKE WEEK III

Gary Nelson
Office of the Project Manager, Smoke/Obscurants
Aberdeen Proving Ground, Maryland 21005

ABSTRACT

An eight minute film describing Smoke Week III will be shown. This will serve as an introduction and orienting background for the many papers which follow in this Symposium dealing with the measuring techniques used and observations made during Smoke Week III.

The film shows the topography of the area in which the test was conducted, the instrumentation of participants, aerosol dissemination methods and devices, and one or two examples of the smoke trials as they develop. The instrumentation cluster used in Smoke Week III and a field calibration of the instruments in that cluster are also shown. The film reviews the major positions, including the target area, instrumentation cluster and grid, and the 0.8 km and 1.7 km positions.

DESCRIPTION OF A SYSTEM FOR THE MEASUREMENT OF OPTICAL AND MILLIMETER WAVE TRANSMISSION THROUGH BATTLEFIELD ENVIRONMENTS*

Robert J. Keyes
Massachusetts Institute of Technology
Lincoln Laboratory
P.O. Box 73; Lexington, Massachusetts 02173

ABSTRACT

Simultaneous measurements of the propagation of radiations at .6328μm, 0.904μm, 10.6μm and 3mm have been carried out over the past year at Camp Edwards, MA through natural atmospheres and simulated battlefield environments (smoke, dust and explosions). These measurements of radiation attenuation over near identical paths for all wavelengths were designed to provide the data base necessary for the optimal design of a battlefield communication system. This report describes the transportable systems used in these tests, including the pertinent parameters associated with the transmitters, receiving sensors, digital and analog recording systems, and auxiliary sensors which produce passive infrared imagery with an AGA camera and measure C_n^2 at the HeNe wavelength. The geometric layouts of the various tests are also discussed along with a description of the environmental conditions. Analysis of these data is presented in the following paper by R. Sasiela.

1. INTRODUCTION

During the past spring and summer, a variety of simultaneous atmospheric transmission measurements at wavelengths of .6328μm, 0.904μm, 10.6μm and 3mm were conducted at Camp Edwards, MA using a mobile measurement system developed under Army support. These data, recorded on digital tape, were subsequently computer analyzed in order to assess the impact of natural and battlefield environments on potential question and answer communication systems. This report describes the parameters of the measurements system and the pertinent aspects of the field tests that were conducted.

The system is installed in two large vans (transmitter and receiver) that carry their own sources of power and communications. For tests, the vans can be positioned at the terminal points of selected paths and the transmission of that path can be measured at the various wavelengths under a variety of natural and battlefield conditions. Figure 1 shows a block diagram of the total measurement system. The optical

*This work was sponsored by the Departments of the Army and the Air Force. "The U.S. Government assumes no responsibility for the information presented."

radiation sources indicated in Figure 1 are co-boresighted on a single optical platform that can be accurately pointed in the desired direction with the aid of a gunsight telescope. The 3mm source (12 inch dish) and pointing scope were located beside the optical mount and boresighted in the same direction. A TV antenna atop each van provided a common time reference pulse from a local commercial broadcasting station which was used to synchronize the optical radiation pulses and the receiver electronics at 1500Hz. The millimeter wave system was operated cw.

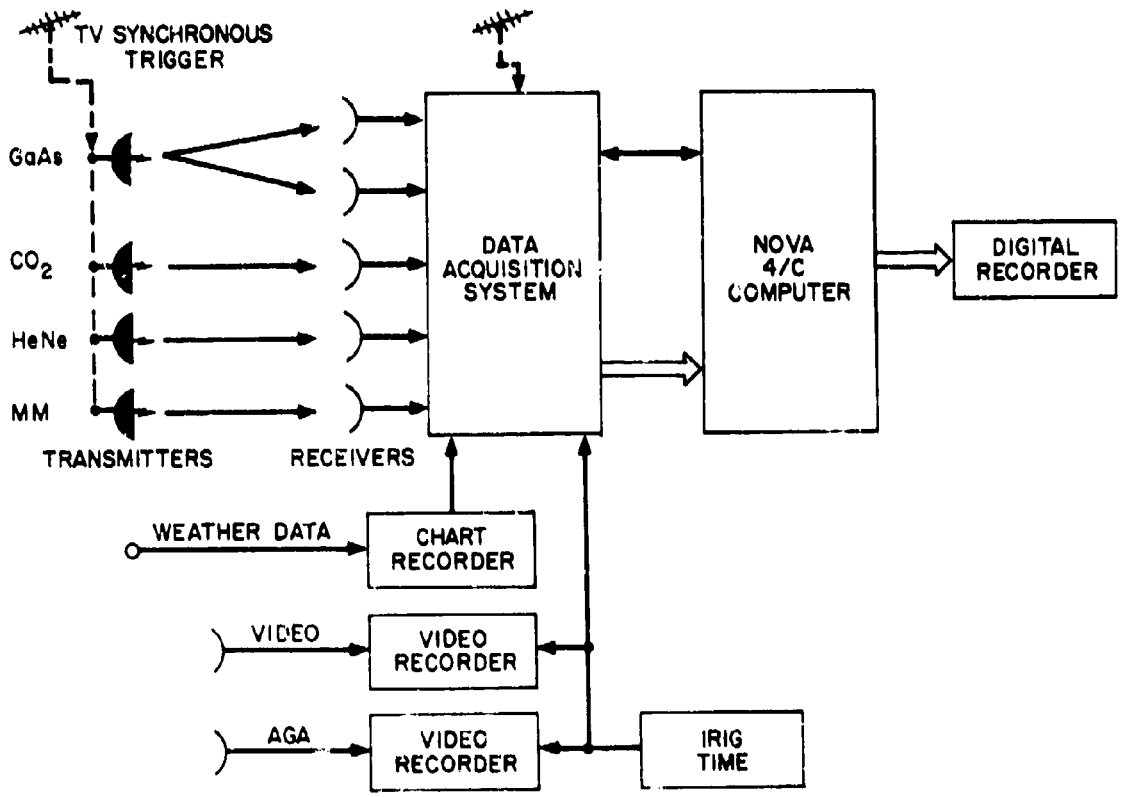

FIGURE 1. A BLOCK DIAGRAM OF THE MEASUREMENT SYSTEM FOR THE EXPERIMENTAL FIELD SITE.

The radiation receivers, also co-located and boresighted, were housed in the second van along with the recording and monitoring systems. Except for the GaAs radiation there is one receiver for each wavelength. Two receivers, whose spatial separation was controllable, were provided at 0.904μm in order to study the effects of spatial diversity on fading phenomena due to atmospheric turbulence. The sensor signals are amplified to a level of 10 volts peak-to-peak before entering the analog

and digital recording systems. For digital recording, peak hold circuits triggered by the TV reference pulse were used prior to 12 bit digitization. The analog signals were recorded on a 14 channel system (not shown) along with voice comments and IRIG time. The analog data was used primarily as a backup to the digital systems and as a "quick-look" capability for editing purposes. Real time monitoring of signals from the prime sensors was obtained via oscilloscope displays.

In addition to the prime sensor measurements, meteorological data (temperature, humidity, rain rate, wind speed and direction) from a portable weather station were digitized and recorded. A video tape system which was also boresighted to the prime sensors provided a visual image of the test path. During all battlefield environment tests an AQA recording camera provided LWIR images of the area and of calibrated thermal sources in the field of view. Communications between the various instrument stations were conducted over radio except during recording runs. It was observed that radio transmissions interfered with data recording. During measurement periods, hardwire military field telephones were used for communication. Table I gives some of the pertinent parameters of the prime radiation transmitters and receivers.

TABLE I. TRANSMITTER/RECEIVER PARAMETERS

TRANSMITTERS					RECEIVERS			
Wavelength	Average Power (watts)	Peak Power (watts)	PRF (Hz)	Beam Angle (mrad)	FOV (rad)	Aperture (cm)	Sensitivity (SNR=1)	Bandwidth (Hz)
0.6328μm	0.5×10^{-3}	10^{-3}	1,500	1 to 6	7×10^{-3}	3.5	10^{-13}w/Hz$^{1/2}$	2,500
0.904μm	0.012	30	1,500	7	1.0	5.0	10^{-12}w/Hz$^{1/2}$	2,500
10.6μm	1.0	2.0	1,500	14	.01	2.5	10^{-12}w/Hz$^{1/2}$	2,500
3mm	0.01	cw	cw	13	0.18	1.7	6×10^{-18}w/Hz	10

2. FIELD MEASUREMENTS

The battlefield environments of interest can be broken down into two broad categories: natural and man-generated. The natural environments are dictated by the vagaries of local meteorological conditions and hence require extended periods of time to encompass the wide variety of conditions that might be present on a battlefield. The man-generated environments (smokes, dust, explosions) were under our direct control and hence measurements of these conditions were conducted over short time periods of intensive testing (2 days). Table II presents a summary of the propagation tests carried out at the Camp Edwards site. R. Sasiela will discuss the computer analysis of this data and its significance to BIFF systems in these spectral regions in the following paper.

TABLE II. CAMP EDWARDS BIFF PROPAGATION EXPERIMENTS

1. HC Smoke	Two twenty-minute tests using military smoke pots with total visible obscuration
2. White Phosphorus	Two tests using smoke grenades deployed from tank launcher
3. Vehicular Dust	Eight tests with high visible attenuation generated by dragging a hurricane fence over propagation path
4. 105mm Shell Explosions	Two tests with 5 shells exploded at 2 second intervals producing high attenuation at all wavelengths
5. Natural Atmospheric Turbulence	Optical data recorded at various turbulence levels with 600 and 1200m path lengths
6. Turbulence in Rain and Fog	One test with 8 dB/km visible attenuation
7. Spatial Diversity Tests	Data recorded at various separations of GaAs receivers

RESULTS OF SIMULTANEOUS TRANSMISSION MEASUREMENTS AT MMW AND VARIOUS OPTICAL FREQUENCIES IN A BATTLEFIELD ENVIRONMENT*

R. J. Sasiela

Massachusetts Institute of Technology
Lincoln Laboratory
Lexington, Massachusetts 02173

ABSTRACT

Simultaneous transmission measurements have been made at 0.904, 0.6328, and 10.6 microns, and 3mm wavelengths. Various impediments to transmission including turbulence, explosives, HC smoke, phosphorus grenades, dust and fog were introduced into the transmission path. Results of the data analysis will be presented which include relative attenuation, temporal and spatial effects, and a comparison of the turbulence data with theory.

1. INTRODUCTION

This report describes the analysis of data taken in various natural and battlefield environments to determine the effect of obscurants on a communication system. Measurements were taken at 0.6328, 0.904, and 10.6 micrometers and at 92.7GHz with the system described by R. Keyes in the previous paper. These frequencies were chosen because for covert communications they have the advantage of having a narrow beamwidth with modest aperture size and they respond differently to battlefield obscurants.

The bit error rate is a measure of the effectiveness of a digital communication system. On a dirty battlefield the error rate is affected not only by the attenuation produced by the obscurants but also by scintillation-induced fading. It has been shown[1] that under turbulence conditions likely to be encountered, optical systems can require a 10-30dB increase in required signal level in order to achieve rates comparable to those achieved in the absence of turbulence. A question addressed in this report is whether the effects of obscuration and scintillation are independent or whether scintillation level is a function of the obscuration.

Additionally, the time history of the obscuration is examined to see what is the best strategy in repeating a message to increase the probability of reception.

*This work was sponsored by the Departments of the Army and the Air Force.

"The U.S. Government assumes no responsibility for the information presented".

2. EXPERIMENTAL SYSTEM

The portable system used to make the measurements is described in detail in the previous paper by R. Keyes. Briefly, the system consists of two trucks, one containing the transmitters the other the receivers and recording equipment. The transmitters used were a CO_2 laser operating at 10.6 micrometers, a HeNe laser operating at 0.6328 micrometers, a GaAs laser operating at 0.904 micrometers, and a MMW system operating at 92.7GHz. The receiver truck contained receivers for all the above frequencies and a computer controlled recording system. Each signal was digitized by a 12 bit A/D converter and recorded at a 1500Hz rate.

The beamwidth of the transmitted signal was much larger than the receiver apertures. The signal to noise ratio in the receivers with no obscurants present was greater than the 36dB instantaneous dynamic range of the recording system. An analog display system was used to set gain levels and help to verify proper systems operation before digital recording started.

The time history of the signal transmission was recorded for each experiment and subsequently analyzed. From this data, we determined the scintillation level with and without obscurants and the relative attenuation measured by all sensors. In addition, the time history of the transmissivity was examined to determine the best strategy for repeating messages.

3. TURBULENCE DATA

Data was taken with no obscurants present and compared to theory, both to verify the data taking and reduction process and to gather scintillation data which could be compared to the scintillation data with obscurants present. The amplitude of the return is expected to have a log-normal distribution. Over a path of uniform turbulence when the turbulence integrated along the path is not too strong, the variance of the log intensity for a spherical wave is equal to[2]:

$$\sigma_I^2 = 0.5\ C_n^2\ k^{7/6}\ L^{11/6}$$

where C_n^2 is the refractive index structure constant,

k is the wavenumber, $2\pi/\lambda$,

and L is the path length

The above formula applies to a point detector or one much smaller than the Fresnel length ($\sqrt{2\lambda L}$), which is the average size of the turbulence cells at the receiver. For larger apertures as in this experiment, the measured scintillation is reduced by an aperture averaging effect. For low angular beam divergence and turbulence levels not close to saturation (conditions which applied in these experiments), a good approximation to the true log - intensity variance, σ_I^2, measured by an aperture of diameter d, can be found from the measured value, σ^2, by solving the equation[1]

$$\exp(\sigma^2) - 1 = \xi\,(\exp(\sigma_I^2) - 1)$$

where $$\xi = (\lambda L/d^2) \,/\, [\,1 + (\lambda L/d^2)\,]$$

Scintillation measurements were taken on various days. A typical time plot of a sensor return is shown in Figure 1. The histograms of the return intensity for the HeNe, GaAs, and CO_2 sensors for the same time are compared to a log-normal intensity curve with the same standard deviation as the data in Figures 2, 3, and 4. The agreement is very good. Another way of plotting the data, which accentuates the returns which lie in the tail of the curve, is shown in Figure 5. This contains a plot of the GaAs data on log probability paper out to ± 3 standard deviations.

Along with the digital measurements, a bar chart at the transmitters was viewed through an optical telescope at the receivers to measure the "seeing" conditions. This measurement can be used to get an estimate of C_n^2, since at visible wavelengths the resolution, Res_V, is approximately equal to

$$Res_V = \lambda_V / r_{oV}$$

where r_o is Fried's coherence diameter, which is related to C_n^2 by[3]

$$r_o^{-5/3} = 0.159 k^2 L\, C_n^2.$$

Using 0.6 micrometers as the wavelength, one obtains

$$C_n^2 = 1.87 \times 10^{-12}\ Res_V^{5/3}/L$$

where the resolution is measured in arc-seconds.

The value of C_n^2 measured by all sensors should be the same at any time. A comparison of results for various days and times of day is given in Figure 6. The agreement is very good for all sensors. There was no effort to make seeing

measurements at the time the scintillation data was taken. On day three the sky was partly cloudly and the value of C_n^2 changed rapidly as the sun came out. This could account for the anomalous seeing measurement which was taken 8 minutes before the scintillation data was recorded.

4. WHITE PHOSPHORUS SMOKE

White phosphorus smoke clouds were generated by firing smoke grenades from a tank launcher. This experiment and the following ones had a 600 meter propagation path. The transmitted signal versus time for the HeNe, GaAs and CO_2 laser systems are shown in Figures 7, 8, 9. There was no effect on the MMW signal. The lowest signal which could be measured was 0 counts. To indicate how many points had zero counts, all these points are plotted as a random number between 0 and minus 1. The region of high attenuation lasted several minutes. There were no holes in the smoke; however, there were large variations in the attenuation occurring on a time scale of about 10 seconds.

An examination of the scintillation amplitude does not show any significant change as the attenuation changed. Therefore for white phosphorus smoke, the effects of attenuation and scintillation are additive in producing an increase in bit error rate.

The relative attenuation of the different sensors can be found by plotting the signal level of one sensor versus another for each pulse. This is shown for GaAs vs HeNe in Figure 10 and GaAs vs CO_2 in Figure 11. The relative attenuation is found from the slope of the line drawn through the points. Doing this, one finds that HeNe has 2.1 times the extinction coefficient of GaAs while the CO_2 laser has 0.15 times that of GaAs. As previously mentioned, the MMW system had no attenuation. Therefore the HeNe laser signal is very sensitive to white phosphorus smoke, the GaAs laser system is moderately affected, while the CO_2 laser system is only slightly affected.

5. DUST

Dust was generated by driving a truck which was dragging a wire fence along a dirt road that crossed the transmission path of the sensors. Figures 12, 13 and 14 show the time history of the HeNe, GaAs and CO_2 laser returns for one run with the plots starting just after the truck passed through the field of view. The MMW signal is not shown because once again it was unaffected by the obscurant. The time duration of the dust effect, which is 40 seconds in this case, is highly dependent on weather conditions.

Notice that the scintillation initially decreases as the attenuation increases. The scintillation was examined more closely at various levels of attenuation and the results are summarized in Table I. For 7dB of GaAs attenuation there is a reduction of the scintillation in the 3 laser sensors. The scintillation then rises rapidly as the attenuation increases. For the HeNe laser the reduction in scintillation when the GaAs attenuation is 7dB almost compensates for the reduced signal level,

Table I. Variance of Log Intensity for Various Levels of Dust Produced Attenuation

GaAs Attenuation (db)	HeNe	GaAs	CO_2
0	.145	.063	.017
7	.087	.041	.013
10	.16	.10	.025

so that low levels of dust do not affect the bit error rate significantly. Since the scintillation rate with no attenuation is lower for GaAs and the CO_2 system, the reduction of scintillation is not as significant at this attenuation level. For the GaAs system, the reduction in scintillation reduces the attenuation effect by 2dB, while it has hardly any effect for the CO_2 sensor. Since the scintillation still increases with frequency of the signal, it produces a more detrimental effect on the higher frequencies.

The attenuation varied over 10dB in periods of about 5 seconds. In an actual battlefield situation, the source of the generators of dust would be generally local and may be transitory. Therefore, a strategy of repeating the message every several seconds would be the most effective in getting the message through.

The extinction coefficient is found by plotting one sensor's data versus the other in Figure 15 and 16. From these the extinction coefficients are found to be the same for the HeNe and GaAs while CO_2 is 0.7 of the other two. Therefore, the effect of dust is about the same for all these laser systems with CO_2 having a slight advantage. Dust has no effect on the MMW signal.

6. HC SMOKE

The hexachloroethane (HC) smoke was generated by military smoke pots. There was total visible obscuration for several minutes at a time under the conditions of the

test. Attenuation levels greater then 30dB were recorded for both the GaAs and HeNe lasers. Figures 17, 18 and 19 are plots of the HeNe, GaAs and CO_2 signals versus time during a period when the smoke was dissipating and transmission holes were developing in the smoke. There was no effect of the smoke on the MMW signal during this entire test. Figures 20 and 21 are relative attenuation plots of the GaAs signal versus HeNe and CO_2. From these, one determines that HeNe has 1.2 times and CO_2 has less than .02 times the extinction coefficient of GaAs.

During some periods of the test, the GaAs and HeNe attenuations were greater than 30dB for over a minute. There is no effective strategy to use in this situation to get the signal through. As the smoke is dissipating, the attenuation experiences rapid changes in level over periods of several seconds. In this situation, repeating the signal when the target was visible, which was about every second in these tests, would be the most effective strategy.

The relative scintillation level did not change much with attenuation and the effects of scintillation and attenuation would have an additive effect on the bit error rate.

7. ARTILLERY SHELLS

To simulate an artillery shell landing in the transmission path, 105mm shells were buried 2 feet underground between the transmitters and receivers. At the time of shell detonation the transmission fell to zero for all sensors, indicating that the attenuation is greater than 30dB. This total obscuration lasted for approximately 1.5 seconds followed by a rapid recovery to a level with about 10dB attenuation. The transmission then gradually recovered to the non-obscurant level in 5-10 seconds. Figure 22 shows the time history of the MMW signal, which is typical of the other sensors. Figures 23 and 24 show a comparison of the GaAs signal to HeNe and CO_2. The attenuation at any time is equal for all the sensors, which indicates that the particles thrown up by the explosions are large compared to all wavelengths and the attenuation is equal to the percentage of the sensors field of view which is obscured by the particles.

Because of the total signal obscuration immediately after the shell explodes, a transmission would have to be repeated several seconds after the burst in order to get a message through. In these experiments the dust produced by the falling debris blew out of the beam so that no effect of dust is present. In the case of shells exploding upwind, there would be dust effects if the ground were not too wet.

7. CONCLUSIONS

A measurement system to record simultaneous measurements at 3 laser frequencies and at 92.7Ghz was built and tested in the field. This system gave results in agreement with theory when atmospheric turbulence was measured. The relative attenuation between the three laser frequencies was measured with white phosphorus smoke, HC smoke, dust and 105mm shell-produced debris in the transmission path. A summary of these measurements is given in Table II.

Table II. Relative Extinction Coefficients of Various Sensors Compared to a GaAs Laser.

	White Phosphorus Smoke	HC Smoke	Dust	Artillery
0.6328 μm	2.1	1.2	1	1
0.904 μm	1	1	1	1
10.6 μm	0.15	<.015	0.7	1
92.7 GHz	0	0	0	≈ 1

The MMW system is the most desirable for a communication system when transmission effects are considered. The CO_2 system is next in desirability because it is affected to only a small degree by white phosphorus and HC smoke and because turbulence effects are not as severe as at the higher frequencies.

The effects of the obscurants are additive to those of turbulence when considering transmission effects except in the case of dust. For low attenuation, the scintillation decreases to reduce the effect of the dust on the communication system. The scintillation reduction is no longer evident once the attenuation exceeds 10dB.

REFERENCES

1. J. Shapiro and R. Harney, "Burst-Mode Atmospheric Optical Communications", National Telecommunications Conference, November 30., December 4, 1980.

2. R. Lawrence and J. Strohbehn, "A Survey of Clear-Air Propagation Affects Relevant to Optical Communications", Proc. IEEE, Vol. 58, No. 10, October 1970.

3. D. L. Fried, "Limiting Resolution Looking Down Through the Atmosphere", Journal of the Optical Society of America, Vol. 56, No. 10, October 1966.

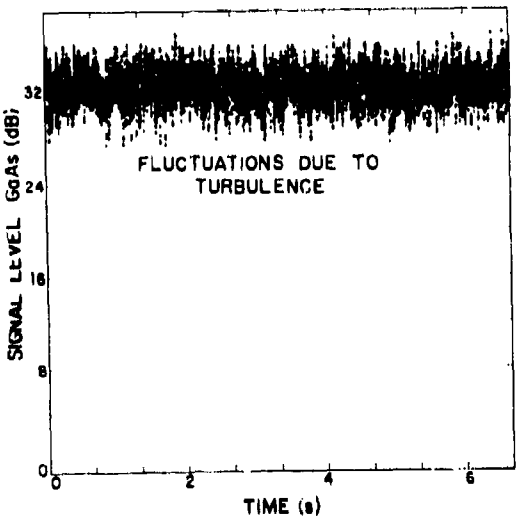

FIGURE 1. GaAs LASER SIGNAL VS. TIME.

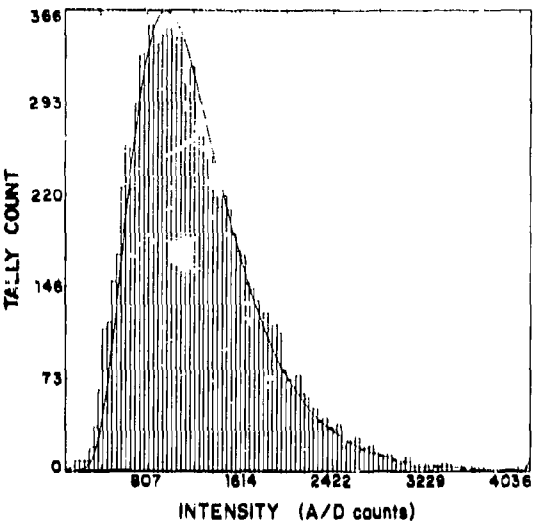

FIGURE 2. INTENSITY HISTOGRAMS OF THE HeNe LASER SIGNAL COMPARED TO A LOG-NORMAL DISTRIBUTION.

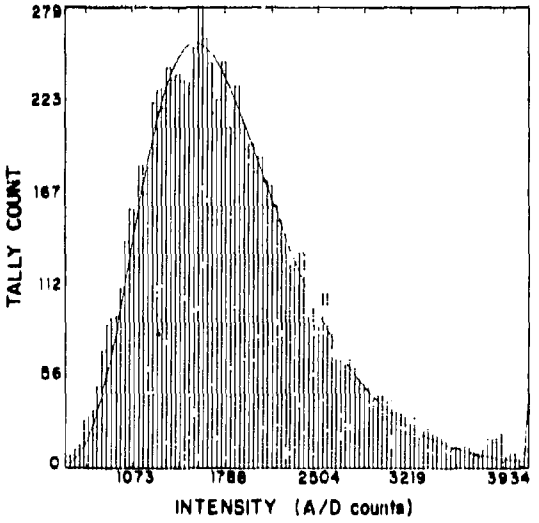

FIGURE 3. INTENSITY HISTOGRAMS OF THE GaAs LASER SIGNAL COMPARED TO A LOG-NORMAL DISTRIBUTION.

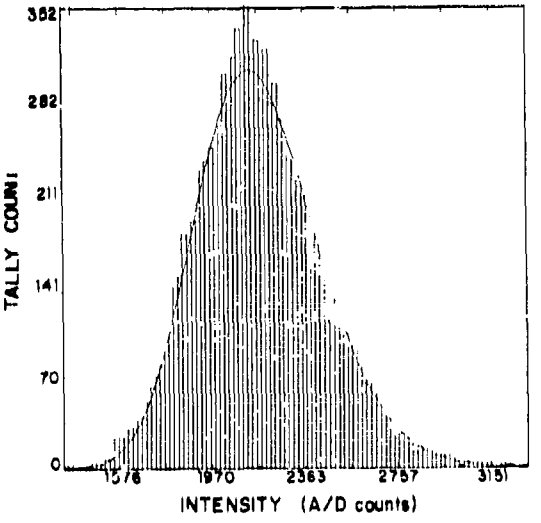

FIGURE 4. INTENSITY HISTOGRAMS OF THE CO_2 LASER RETURN COMPARED TO A LOG-NORMAL DISTRIBUTION.

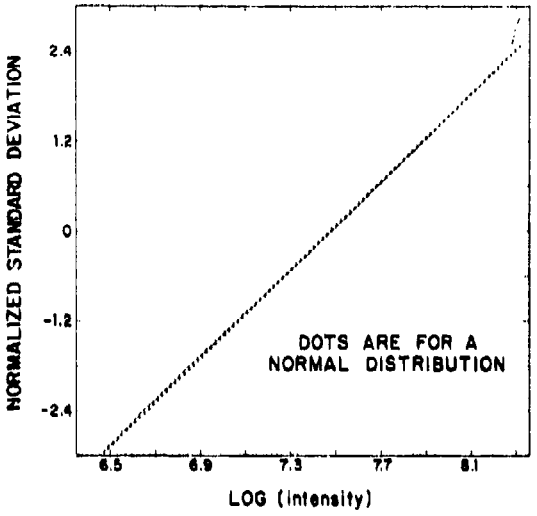

FIGURE 5. STANDARD INVERSE NORMAL DISTRIBUTION PLOT OF THE ln INTENSITY GaAs RETURN.

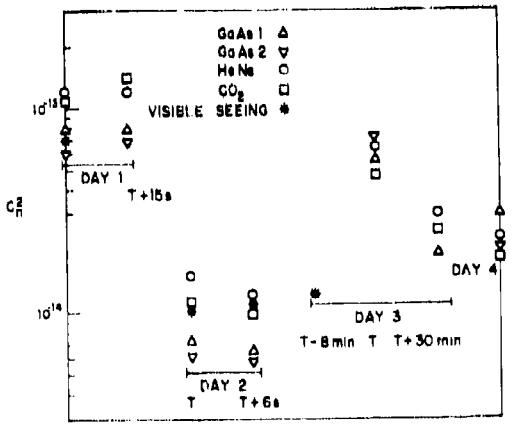

FIGURE 6. VALUES OF C_n^2 DERIVED FROM MEASUREMENTS AT VARIOUS WAVELENGTHS

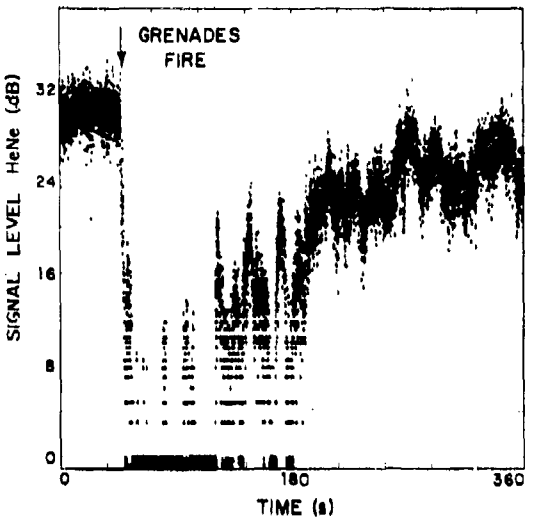

FIGURE 7. TRANSMISSION OF A HeNe LASER SIGNAL IN THE PRESENCE OF WHITE PHOSPHORUS SMOKE.

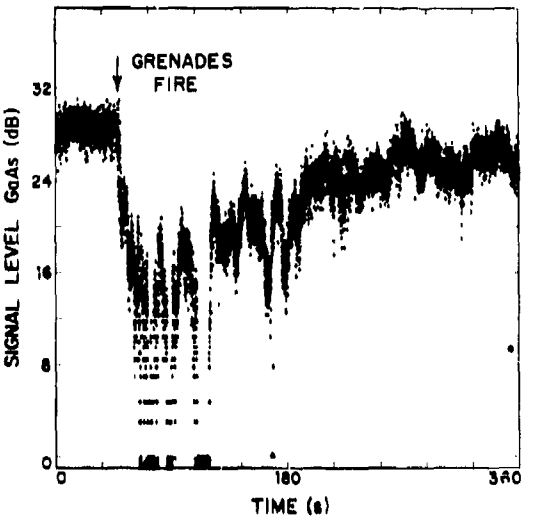

FIGURE 8. TRANSMISSION OF A GaAs LASER SIGNAL IN THE PRESENCE OF WHITE PHOSPHORUS SMOKE.

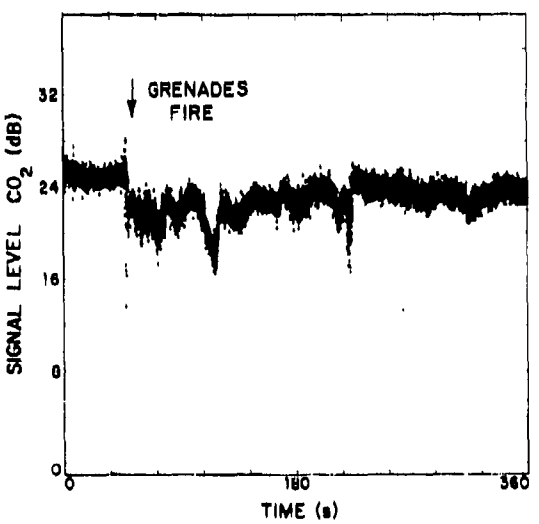

FIGURE 9. TRANSMISSION OF A CO_2 LASER SIGNAL IN THE PRESENCE OF WHITE PHOSPHORUS SMOKE.

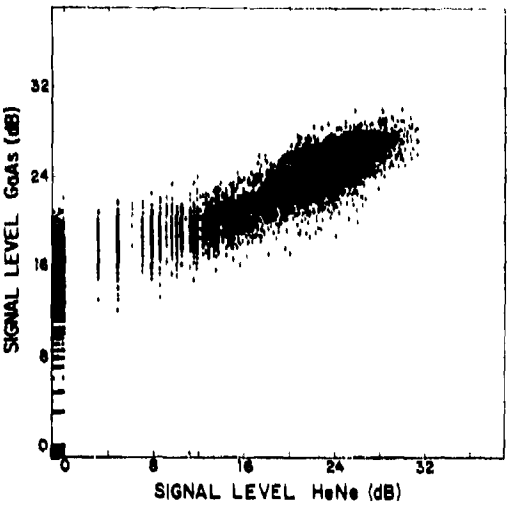

FIGURE 10. RELATIVE TRANSMISSION OF GaAs AND HeNe LASERS IN THE PRESENCE OF WHITE PHOSPHORUS SMOKE.

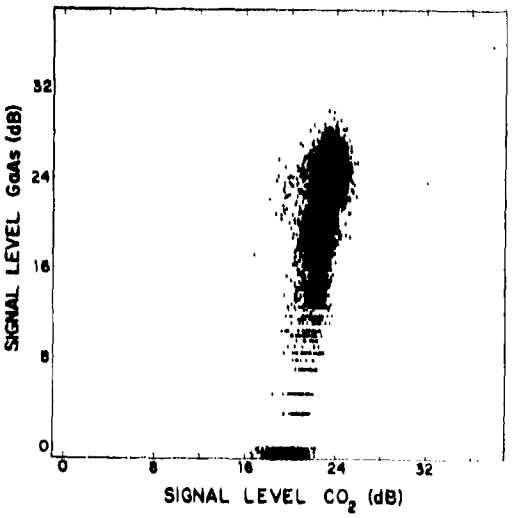

FIGURE 11. RELATIVE TRANSMISSION OF GaAs AND CO_2 LASERS IN THE PRESENCE OF WHITE PHOSPHORUS SMOKE.

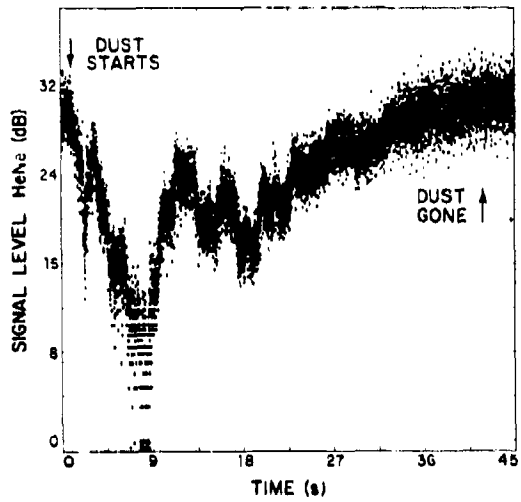

FIGURE 12. HeNe LASER SIGNAL WITH DUST IN THE PATH.

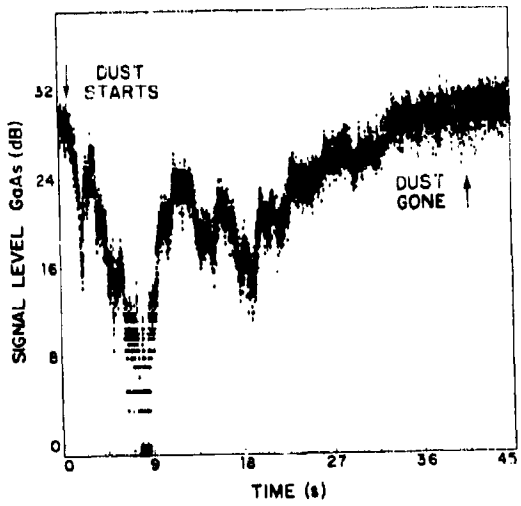

FIGURE 13. GaAs LASER SIGNAL WITH DUST IN THE PATH.

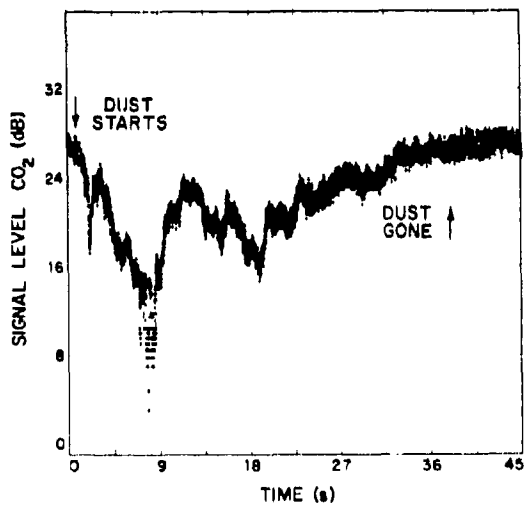

FIGURE 14. CO_2 LASER SIGNAL WITH DUST IN THE PATH.

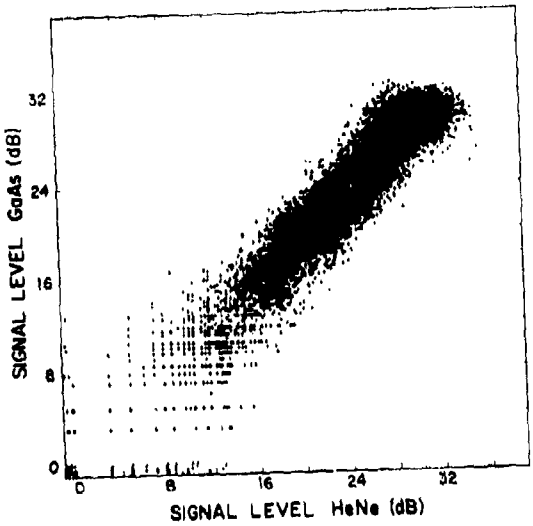

FIGURE 15. RELATIVE TRANSMISSION OF HeNe AND GaAs LASER SYSTEMS WITH DUST IN THE PATH.

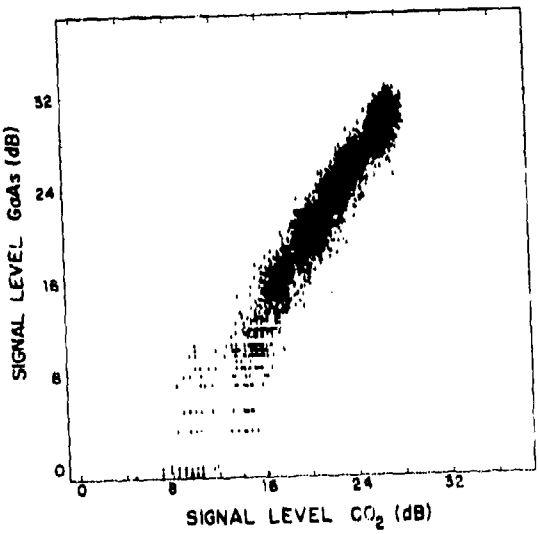

FIGURE 16. RELATIVE TRANSMISSION OF CO_2 AND GaAs LASER SYSTEMS WITH DUST IN THE PATH.

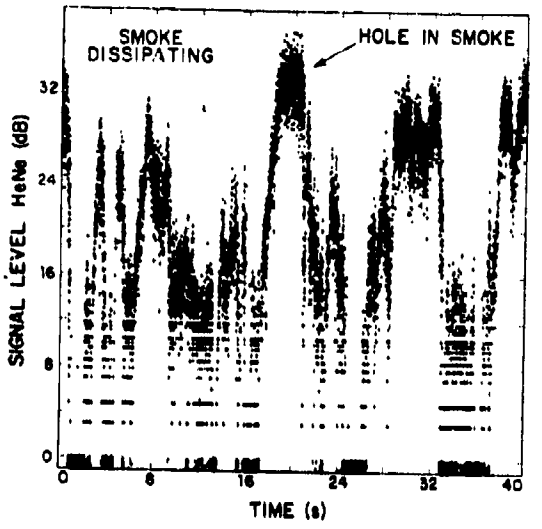

FIGURE 17. HeNe LASER SIGNAL VS. TIME WITH SMOKE PRESENT.

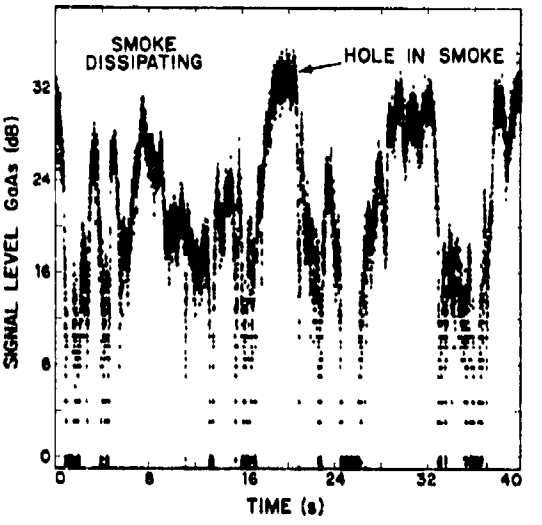

FIGURE 18. GaAs LASER RETURNS VS. TIME WITH SMOKE PRESENT.

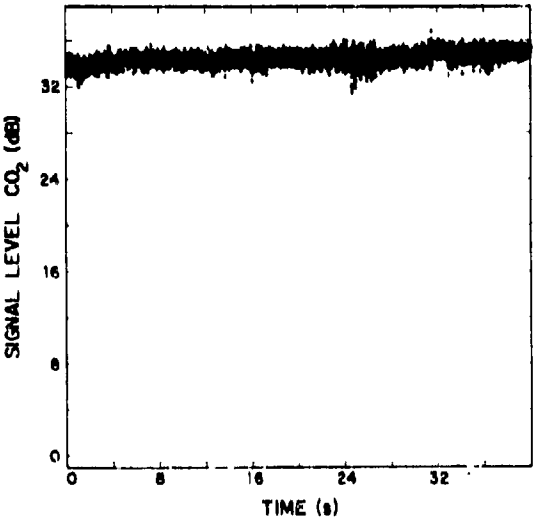

FIGURE 19. CO_2 LASER RETURNS VS. TIME WITH SMOKE PRESENT.

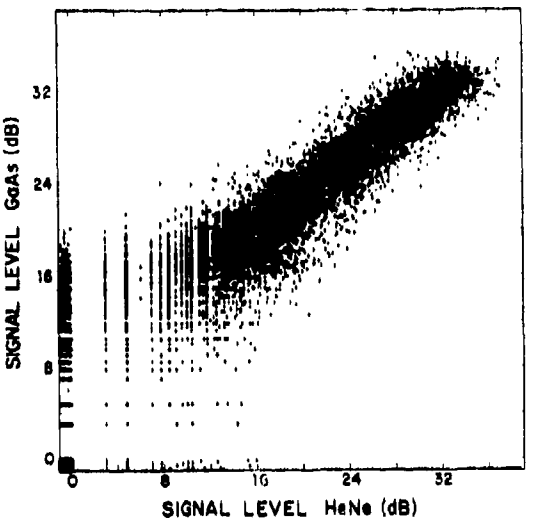

FIGURE 20. RELATIVE TRANSMISSION OF GaAs AND HeNe LASER SYSTEMS WITH SMOKE PRESENT.

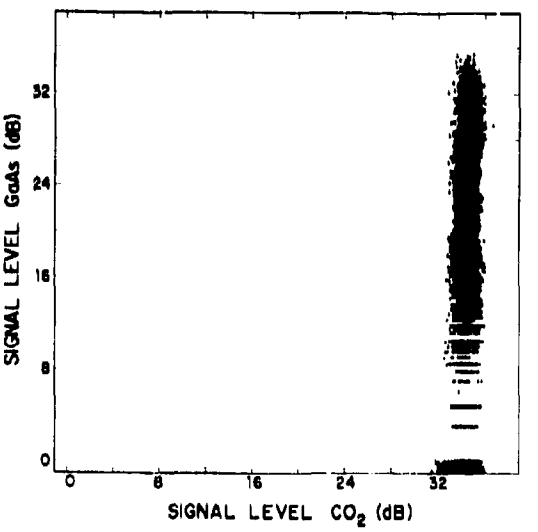

FIGURE 21. RELATIVE TRANSMISSION OF GaAs AND CO_2 LASER SYSTEMS WITH SMOKE PRESENT.

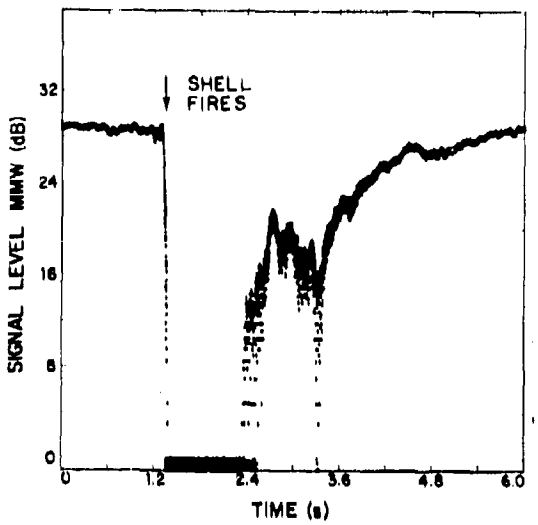

FIGURE 22. TIME HISTORY OF MMW TRANSMISSION WHEN A 105mm SHELL EXPLODES IN THE SIGNAL PATH

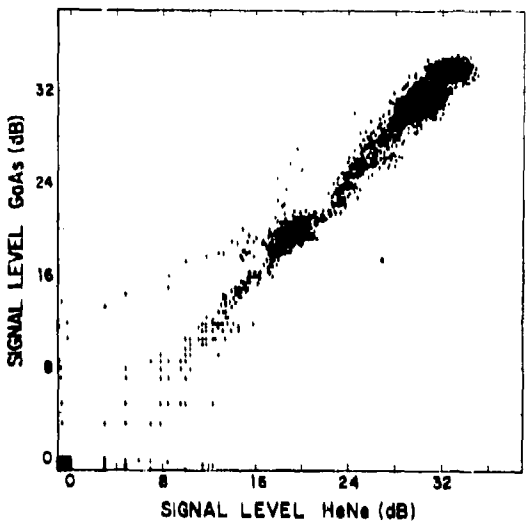

FIGURE 23. RELATIVE TRANSMISSION OF GaAs AND HeNe LASERS WHEN A 105mm SHELL EXPLODES IN THE SIGNAL PATH.

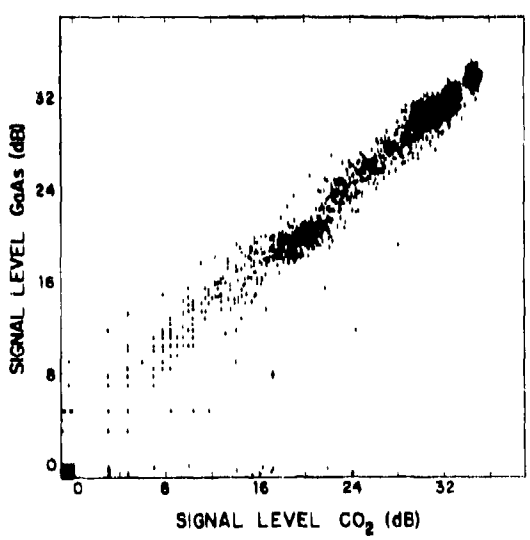

FIGURE 24. RELATIVE TRANSMISSION OF THE GaAs AND CO_2 LASERS WHEN A 105mm SHELL EXPLODES IN THE SIGNAL PATH.

CANADIAN PROGRAM IN ANTI-IR SCREENING AEROSOLS

R. E. Kluchert
Defence Research Establishment Valcartier
Courcelette, Que, Canada

ABSTRACT

The Defence Research Establishment Valcartier has been active over the past three years in the development and testing of IR obscuring aerosols. An instrumented 300 m^3 aerosol test chamber was developed and a series of low-temperature transmission experiments carried out on military screening agents and potential new IR screening materials. A mobile "Laser Cloud Mapper" instrument was commercially developed for the rapid three-dimensional sounding of smoke clouds over the angular limits of 90° azimuth x 10° elevation and over a maximum range-gate of 675 m. Based on a method proposed by Klett, linear extinction coefficients were calculated from digitized backscatter data that were collected during recent field trials with HC and red phosphorus generated smoke clouds. The DREV research activity will continue on cold weather evaluations of candidate IR screening materials. An extensive R&D program is also evolving through research contracts with industry and university. An analysis of the application of screening clouds for the protection of armored vehicles shows that smaller clouds, sequentially disseminated closer to the tank, provide a more efficient screening performance. Proposals are made for collaborative research work with U. S. laboratories.

Requests for copies of this paper (which are Confidential) should be sent to the following address:

Chief of Defense Research Establishment, Valcartier
P. O. Box 8800
Courcelette, Quebec
G0A 1R0; Canada

DUSTY INFRARED TEST SERIES (FILM)

Bruce W. Kennedy
US Army Atmospheric Sciences Laboratory
White Sands Missile Range, New Mexico 88002

ABSTRACT

The Atmospheric Sciences Laboratory has conducted three major field tests to determine the effects of battlefield dust on electro-optical transmission. Dust Infrared Test-I (DIRT-I) was performed at White Sands Missile Range (WSMR) in dry sandy soil utilizing arrays of munitions, high expolsives, and barrage artillery firings. DIRT-II was also conducted at WSMR and consisted of detonations of single projectiles, high explosive charges, and single artillery firings in moist, silty clay. DIRT-IIIA and B were held at Fort Polk, Louisiana, in sandy clay. The first part, DIRT-IIIA, consisted of single explosions of munitions and HE; DIRT-IIIB was single HE detonations in prepared or tailored soils.

A motion picture film entitled "Dusty Infrared Test Series" has been produced describing each test, the instrumentation used, and some results. The 16-mm color film has narration and sound, and the running time is 14 minutes.

DUSTY INFRARED TEST III (DIRT-III) PROJECT SUMMARY

Bruce W. Kennedy
US Army Atmospheric Sciences Laboratory
White Sands Missile Range, NM 88002

ABSTRACT

The Dusty Infrared Test III (DIRT-III) was conducted at Fort Polk, Louisiana, during April-May 1980. The tests were divided into two parts. DIRT-IIIA consisted of explosions of munitions and high explosives in the natural soil. DIRT-IIIB consisted of detonating high explosives on tailored soils. The major purpose of DIRT-IIIA was to measure the transmission of electro-optical and millimeter radiation through dust clouds produced by the explosions. The soil at Fort Polk offered an extreme departure from soils of the previous DIRT-I and DIRT-II tests. DIRT-IIIB tailored soils were sand, silt, clay, and kaolinite that were varied in moisture content from dry to wet. Electro-optical transmission measurements were also made through the dust clouds.

1. INTRODUCTION

The Dusty Infrared Test III (DIRT-III) project was the continuation of a series that started with DIRT-I at White Sands Missile Range (WSMR), New Mexico, October 1978, and DIRT-II at WSMR during July 1979. DIRT-III was conducted at Fort Polk, Louisiana. Each field experiment had unique characteristics, but the purpose of the three projects was to measure the transmission of electro-optical (EO) and millimeter energy through dust clouds produced by high explosive (HE) detonations. Correlative measurements were made of cloud dynamics, soil characteristics, cloud particles, meteorology, and crater size.

Fort Polk was selected for DIRT-III because a radical change of soil and climate were needed. The soil, silty sand and heavy clay, was very moist. The region was surrounded by a pine forest. Air masses varied from continental to maritime and combinations of both. The DIRT-III project was two sequential tests: DIRT-IIIA was performed in the natural soil; DIRT-IIIB was conducted in carefully selected and controlled soils. DIRT-IIIA consisted of static detonations of single HE charges and of foreign and domestic ammunition, while DIRT-IIIB used only uncased HE charges.

2. DIRT-III OVERVIEW

DIRT-IIIA was conducted as a joint project between the Electro-Optics Division, US Army Atmospheric Sciences Laboratory (ASL) and the Explosion Effects Division, US Army Engineer Waterways Experiment Station (WES) between 14-23 April 1980. The location was Range 37, Fort Polk (see figure 1). The WES program was known as Munitions Bare Charge Equivalence-80 (MBCE-80)

DIRT-IIIB, conducted between 28 April and 1 May 1980, was a cooperative effort between ASL and the Environmental Systems Division, Environmental Laboratory, WES. The WES title for the project was Battlefield Environment Tailored Soils (BETS). It was also conducted at Fort Polk.

The objectives of DIRT-IIIA were:

a. Comparison of craters formed by the detonation of artillery munitions, including 105 mm, 155 mm, 122 mm USSR, and 152 mm USSR, with those formed by C-4 explosives in soil conditions and in an atmospheric environment that were significantly different from those of DIRT-I and DIRT-II

b. Measurement of dust cloud growth, movement, and diffusion

c. Soil characterization of the test area

d. Measurement of local meteorology during the test period

e. Determination of EO transmission properties through dust clouds

f. Sampling of particle size distribution in the dust clouds

g. Examination of the explosive equivalence between cased (munitions) and uncased bare charges

DIRT-IIIB was concerned with the influence of various types of soils and moisture content on EO and millimeter energy attenuation. Sand, silt, clay, and kaolin were used as the test materials, and dust clouds were produced by detonating charges of M118 demolition blocks over prepared test pits. Measurements similar to those of DIRT-IIIA were made for DIRT-IIIB. Table 1 summarizes the instrumentation used in support of both projects.

3. SITE CONFIGURATION

Figure 2 contains a legend and shows the layout and coordinates of the project site. Most of the instrumentation was located at the southern portion of the 867-m optical path. The 40-m by 150-m test

area was located closer to the northern end of the path. The nearest detonation to the south instrumentation site was 574 m and the most distant was 724 m. The WSMR digital imagery system and the Colorado State University (CSU) meteorology equipment were just over 400 m in a southeasterly direction and nearly perpendicular to the test area.

The forest surrounding Range 37 was primarily of pine with some hardwood mixture. In preparing for the project, clear lines of sight were cut during January 1980 along and perpendicular to the optical path for photographic and observational purposes. Most trees were very young pine that were 3 to 4 m tall, but some larger trees were also felled. As part of their controlled burning procedure, the US Forest Service burned the grass from the test area in February 1980. However, by the time the DIRT-III project started, grasses had begun to grow. Other than from the necessary vehicular traffic in the test area, the soil was not disturbed.

In spite of tree cutting, the forest played a dominant role in the behavior of prevailing winds. It was for this reason that meteorological measurements were made at four locations. The CSU forest meteorology measurements combined with those of ASL, were made specifically to address this complex problem. (See figure 2, legend items 7, 24, 29, and 38.)

The terrain was gently rolling with the test area about 17 m lower than the south instrumentation site. Figure 3 shows a profile along the optical path.

4. DIRT-IIIA TESTS

Forty-four tests were conducted. All were static detonations of munitions and bare charge C-4 HE. Charges were: (1) placed tangent to the surface (ST) inclined at 20° and rotated at 45° to the optical path, (2) buried so that the top of the charge or projectile was tangent to the ground surface (STB), (3) shallow buried (SB) to depths of approximately 0.75 m, and (4) deep buried (DB) to depths greater than 1 m. Both on-axis and off-axis test locations were used. Table 2 summarizes the test schedule and includes survey location and surface weather observation at the south instrumentation site.

Figure 4 is a photograph comparing the sizes of ammunition used for the tests. Table 3 describes ammunition characteristics.

The 11.9 and 6.8 kg charges of C-4 were made up from individual blocks tapped together. ST and STB packages were inclined at 20° similiary to the projectiles. SB and DB charges were oriented vertically and so were the SB and DB projectiles. Each projectile received approximately 0.2 kg booster charge in the fuze cavity.

5. DIRT-IIIB TESTS

Forty-four tests were conducted. Emphasis was placed on tailored soils and not on charge types, so almost every charge was a 2.27 kg tapped package of military plastic explosive, M118 demolition block. One larger charge of 4.5 kg was used for scaling purposes. All charges were laid horizontally on the surface except for tests TS 43 and TS 44 in which the charges were buried for scaling studies. Table 4 summarized tailored soils tests.

The dry silt and clay were brought to Fort Polk from WES at Vicksburg, Mississippi, by truck. Packaged kaolinite in powdered form was also brought from WES. Sand was acquired locally from a concrete company and had not been subjected to the drying process as had the silt and clay. Test pits were dug with a backhoe and filled with the desired soil.

6. SUPPLEMENTAL TESTS

A number of supplemental tests were conducted aside from the HE dust test. These included:

a. Measurement of fog droplet size and other associated meteorological parameters on 16 April 1980

b. Rain obscuration of visible, infrared, and 95-GHz energy; rain rate and drop size; related meteorological parameters on 17 April 1980

c. Simultaneous measurements of forest meteorology by ASL and CSU instrumentation throughout the night; measurement of 95-GHz scintillation before, during, and after sunset and sunrise on 22 and 23 April 1980

d. Ninety-five GHz backscatter from a 105-mm projectile

e. Obscuration of visible and infrared energy by vehicular dust on 21 April 1980

7. RAINFALL AND DUST

In the springtime, west-central Louisiana is very wet. Fortunately, the weather was fairly cooperative during the tests, but heavy rains before the start of DIRT-IIIA and again before DIRT-IIIB kept the soil saturated and made trafficability difficult. On the morning of 12 April 1980, Fort Polk recorded about 14 cm of rainfall in 3 or 4 h. Five cm were recorded on 13 April 1980. A drying trend then prevailed until 17 April 1980 when thunderstorms moved through the area. Other periods of moderate to heavy rainfall occurred on 23 April and 25-27 April 1980. Light rain was recorded on 18, 21, 22, and 24 April 1980, and on 1 May 1980.

Between periods of heavy rainfall, the surface layer of soil began to dry. A few days after heavy rains, vehicles traveling on the dirt access road to the test area began to stir up dust. Detonations in very wet soil produced what appeared to be a gray smoke cloud. However, even the explosions in heavily saturated soil showed significant obscuration of visible and IR energy. Duration of obscuration was considerably less than was observed at DIRT-I and DIRT-II tests. Also, the wet soil provided strong backscatter and attenuation for the 95-GHz radar for both on-axis and off-axis shots.

8. DATA

Figure 5 through 13 show preliminary data from DIRT-III.

TABLE 1. INSTRUMENTATION SUPPORT FOR DIRT-III

Instrumentation	Agency	In Support of DIRT-IIIA	In Support of DIRT-IIIB
95 GHz radar	Night Vision Electro-Optics Laboratories	X	X
0.55μm, 1.06μm, 10.37μm transmissometer	Naval Research Laboratory	X	X
32-m meteorological tower	ASL	X	X
4-m meteorological tower	ASL	X	X
2-m meteorological tower	ASL	X	X
Scintillometer	ASL	X	X
Forward scatter meter	ASL	X	X
Rain rate, drop size	ASL	X	X
Rawinsonde	Fort Polk Metro Team	X	X
Visibility	ASL, Naval Research Laboratory	X	X
Surface observation, forecast	Air Weather Service	X	X
Acoustic sounder	ASL	X	X
Tethered meteorological balloon	CSU	X	
20-m meteorological tower	CSU	X	
Digital imagery	ASL and WSMR	X	X
Cloud particulates	ASL	X	X
Soil shockwave transmission	WES	X	
Survey	WES	X	X
Soil characteristics	WES, ASL	X	X
Crater measurements	WES	X	X
Photography	WES	X	X
38- and 60-GHz attenuation	Communications R&D Command	X	

TABLE II. SUMMARY OF DIRT-IIIA

DIRT-IIIA TEST SCHEDULE

TEST	DATE	TIME CST	TYPE	LOCATION X	LOCATION Y	AWS DATA* T°C	KT	DIR	DP	RH	REMARKS
A1	4-14-80	1119	155 ST	70	20	17.2	8	320			
C1	4-14-80	1222	C4, 26½ lb, ST	60	20	17.8	8	290			
A2	4-14-80	1338	155 ST	70	10	16.4	7	290			
A3	4-14-80	1541	155 ST	70	0	17	10-17	300	10	38	
C2	4-14-80	1638	C4, 26½ lb, ST	65	10	17	5	300	6	42	
C3	4-15-80	1116	C4, 26½ lb, ST	60	10	19	5	295	11	44	
B2	4-15-80	1259	105 ST	50	10	23	4	290	11	35	
B3	4-15-80	1349	105 ST	50	0	24	5	280	6	33	
D2	4-15-80	1459	122 ST	40	10	25		CALM	10	39	
D3	4-15-80	1543	122 ST	40	-3.5	24	7	300	11	43	
D7	4-15-80	1651	122 STB	30	0	23	2	330	10	43	
B1	4-16-80	1335	105 ST	50	20	26	5	140	11	39	
F1	4-16-80	1424	122 ST	40	20		3	270	11	35	
E1	4-16-80	1513	152 ST	80	20	26	4	160	13	45	
E4	4-16-80	1559	152 ST	90	20	26	5	190	13	45	
E2	4-16-80	1642	152 ST	80	30	26	2	180	13	45	
E3	4-16-80	1717	152 ST	80	40	26	5	180	13	45	
A4	4-17-80	1239	155 STB	100	20	23		CALM	15	61	
D4	4-18-80	0908	122 STB	110	20	16	8	290	9	63	
A5	4-18-80	0953	155 STB	90	10	18	5	300	8	54	
A6	4-18-80	1034	155 STB	90	0	19	7	290	8	49	
A8	4-18-80	1116	155 SB	100	0	19	5	300	8	49	0.46 m to base; 0.76 m to CG
C7	4-18-80	1203	C4, 15 lb, SB	100	10	19	8	320	10	56	0.58 m to charge; 0.72 m to CG
D5	4-18-80	1332	122 ST	30	20	18	5	31	10	59	
D6	4-18-80	1413	122 STB	20	20	17	5	320	12	72	
C5	4-18-80	1451	C4,15 lb, STB	30	10	19	6	330	8	49	
C4	4-19-80	1150	C4,15 lb, STB	0	20	25	3	20	7	32	
B4	4-19-80	1226	105 STB	10	20	25	4	360	10	39	
B6	4-19-80	1327	105 STB	20	11	24	2	10	9	38	
B7	4-19-80	1415	105 STB	20	0	24	3	90	12	47	
D9	4-19-80	1601	122 STB	15	11	24	5	100	11	44	
C6	4-21-80	1312	C4, 15 lb, SB	130	20	28	2	340	11	35	0.61 m to charge; 0.75 m to CG
A7	4-21-80	1356	155 SB	120	20	27	4	290	11	37	0.51 m to base; 0.81 m to CG
B8	4-21-80	1500	105 SB	120	10	27	6	330	11	37	0.53 m to base; 0.73 m to CG
E7	4-21-80	1536	152 STB	130	10	27	2	290	11	37	
E8	4-21-80	1615	152 STB	130	0	26	3	290	13	44	
E5	4-21-80	1658	152 STB	110	10	26	CALM		12	42	
B5	4-22-80	1212	105 SB	140	10	28	CALM		11	35	0.38 m to base; 0.58 to CG
D8	4-22-80	1403	122 SB	140	20	30	5	250	12	33	0.51 m to base; 0.74 m to CG
E6	4-22-80	1524	152 STB	150	10	29	5	240	11	33	
A9	4-22-80	1614	155 DB	150	0	26	3	270	14	47	1.22 m to base; 1.52 m to CG
B9	4-23-80	0937	105 DB	105	20	23	CALM		15	51	0.86 m to base; 1.06 m to CG
C8	4-23-80	1015	C4, 15 lb, DB	100	30	25	CALM		16	58	1.37 m to base; 1.61 m to CG
C9	4-23-80	1052	C4, 15 lb, DB	110	30	27	4	200	15	48	1.03 m to base; 1.17 m to CG

*Temperature °C

KT - windspeed - knots
DIR - wind direction - degrees
DP - dew point
RH - relative humidity
CG - center of gravity

TABLE III. CHARACTERISTICS OF AMMUNITIONS AND HIGH EXPLOSIVES USED DURING DIRT-IIIB

Characteristic	Munition or Charge				
	M1	M107 105 mm	OF462 155 mm	OF540 122 mm	C-4 152 mm
Projectile weight, kg	15.0	44.00	21.76	40.00	-
Charge weight, kg	2.3	6.76	3.68	6.93	6.8 & 11.9 kg
Charge type	Comp B*	TNT	Amatol/ TNT, 80/20	TNT	Cyclonite

*60% C-4, 39% TNT, 1% desensitizer

TABLE IV. SUMMARY OF DIRT-IIIB

DIRT-IIIB TEST SCHEDULE

TEST	DATE	TIME CDT	TYPE	LOCATION X	Y	AWS DATA T	KT	DTR	DF	RH%	REMARKS
TS 1	4-28-80	1031	Dry Clay	0	0	20	6	300	9	49	NOTE: All charges 5 lb (2.27 kg) unless otherwise noted. Dimensions 3-1/4 x 3-1/8 x 12 in (8.25 x 7.94 x 30.5 cm). All detonation ST unless noted.
2	4-28-80	1055	Dry Clay	5	20	21	7	310	9	46	
9	4-28-80	1123	Clay/Sand, Dry	25	0	21	7	320	9	46	
10	4-28-80	1145	Clay/Sand, Dry	25	20	22	5	300	8	41	
5	4-29-80	0734	Clay, Dry	0	0	15	Calm	Calm	10 10	73	
6	4-29-80	0758	Clay, Dry	5	20	16	Calm	Calm	10	68	
14	4-29-80	0821	Clay, Sand, Dry	25	20	18	Calm	Calm	9	56	
13	4-29-80	0843	Clay, Sand, Dry	25	0	19	3	210	9	52	
4	4-29-80	0913	Silt, Dry	85	20	21	3	210	10	49	
3	4-29-80	0935	Silt, Dry	85	0	22	6	260	11	49	
11	4-29-80	0956	Silt, Sand, Dry	65	0	23	6	280	11	47	
12	4-29-80	1025	Silt, Sand, Dry	65	20	24	6	280	11	44	
7	4-29-80	1216	Silt, Dry	85	0	26	6	290	11	39	
8	4-29-80	1239	Silt, Dry	85	20	27	5	270	11	37	
15	4-29-80	1306	Silt, Sand, Dry	65	0	27	6	280	10	35	
21	4-29-80	1337	Sand, Dry	45	0	28	5	270	10	33	
22	4-29-80	1402	Sand, Dry	45	20	28	5	270	11	35	
16	4-29-80	1429	Silt, Sand, Dry	65	20	27	3	270	10	35	
45	4-30-80	0736	Silt, Dry	65	20	18	Calm	Calm	16	88	
24	4-30-80	0807	Sand, Dry	45	20	18	Calm	Calm	16	88	Heavy haze and fog
23	4-30-80	0833	Sand, Dry	45	0	19	Calm	Calm	16	83	Fog dissipating
33	4-30-80	0901	*	25	0	20	Calm	Calm	16	77	
34	4-30-80	0923	*	25	20	21	2	200	18	83	
18	4-30-80	0957	Silt, Moist	85	20	21	3	170	18	83	
20	4-30-80	1041	Silt, Moist, 10 lb	85	20	22	4	190	18	78	4.54 kg; 9.5 x 14 x 30 cm
17	4-30-80	1122	Clay, Moist	5	20	27	5	160	21	70	
19	4-30-80	1233	Clay, Moist	5	20	28	7	180	22	70	
46	4-30-80	1304	Sand, Dry	45	20	28	8	210	19	58	
39	4-30-80	1328	**	25	20	25	7	170	16	57	
36	4-30-80	1344	Sand, Moist	45	20	25	5	150	16	57	
38	4-30-80	1404	Sand, Moist	45	20	26	5	180	16	54	
26	5-01-80	0750	Clay, Wet	5	20	17	Calm	Calm	14	83	
30	5-01-80	0830	Clay, Wet	5	20	19	5	120	16	83	
28	5-01-80	0858	Silt, Wet	85	20	20	6	170	15	74	
32	5-01-80	0924	Silt, Wet	85	20	21	6	180	15	70	
35	5-01-80	0955	Sand, Moist	45	30	22	6	170	16	68	
37	5-01-80	1023	Sand, Moist	45	30	23	5	170	17	69	
43	5-01-80	1057	Silt, Sand, Dry, STP	65	20	24	6	190	18	69	
44	5-01-80	1120	Silt, Sand, Dry	65	20	25	7	160	18	65	0.11 m to top of charge; 0.15 m to CG
42	5-01-80	1241	Silt, Sand, Dry	65	20	27	4	180	18	62	
27	5-01-80	1308	Silt, Wet	85	30	27	4	160	17	55	
31	5-01-80	1339	Silt, Wet	85	0	28	4	200	18	54	
25	5-01-80	1418	Wet	0	30	28	6	170	18	54	
29	5-01-80	1442	Clay, Wet	0	30	28	Calm	Calm	19	57	

*Kaolin on Clay, Sand, Dry
**Kaolin on Clay, Sand, Moist

SPECIAL ATMOSPHERIC TESTS

DATE	TIME	DESCRIPTION
4-17-80	1300-1405	Rain test with combined measurements by ASL, NVL&EOL, and NRL
4-21-80	1326	Vehicular dust transmission measurement by NRL.
4-22-80 4-23-80	Sunset - Sunrise	Natural environment monitoring by ASL, NVL, and CSU.

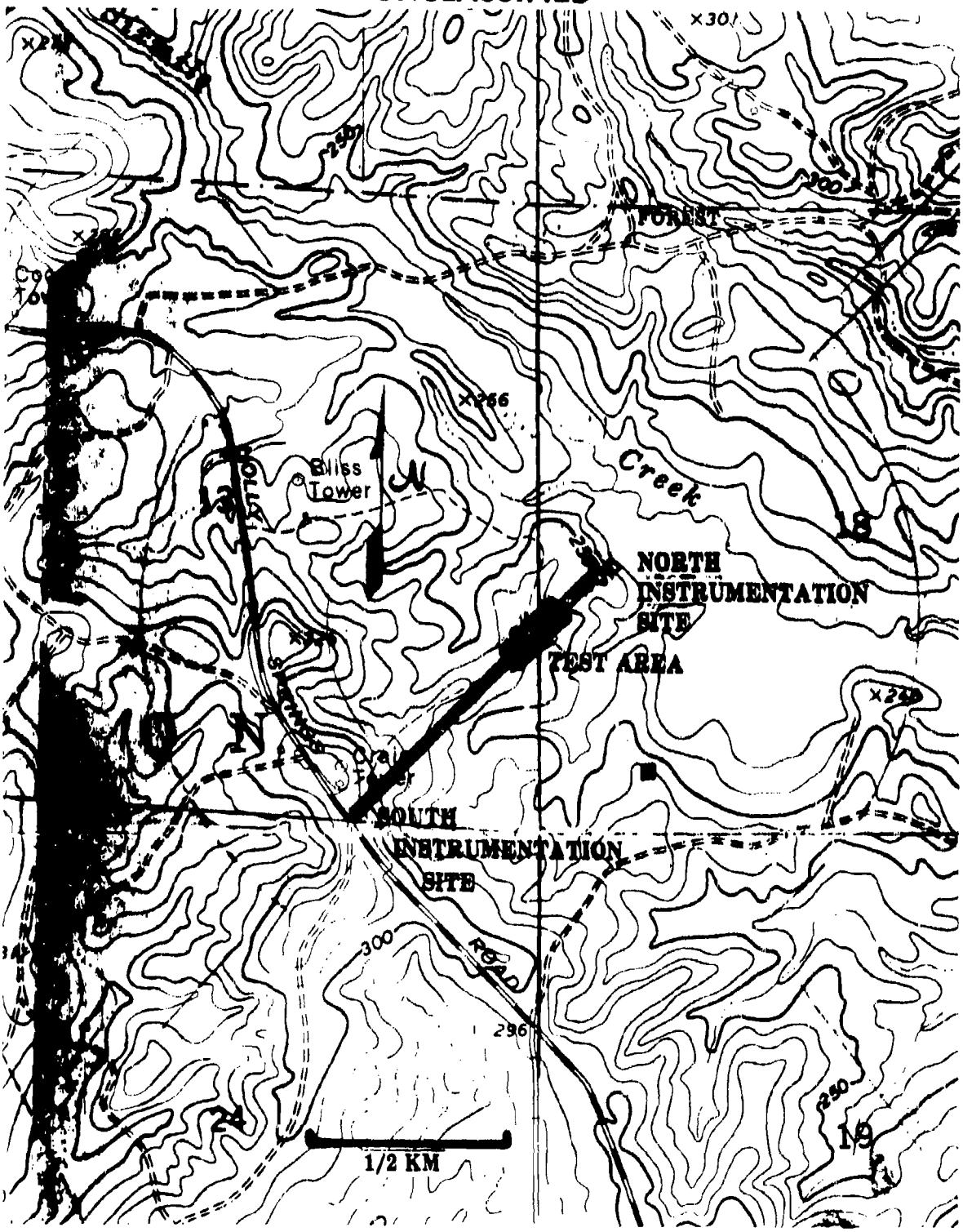

FIGURE 1. LAYOUT OF DIRT-III TESTING AREA, RANGE 37, FORT POLK.

UNCLASSIFIED

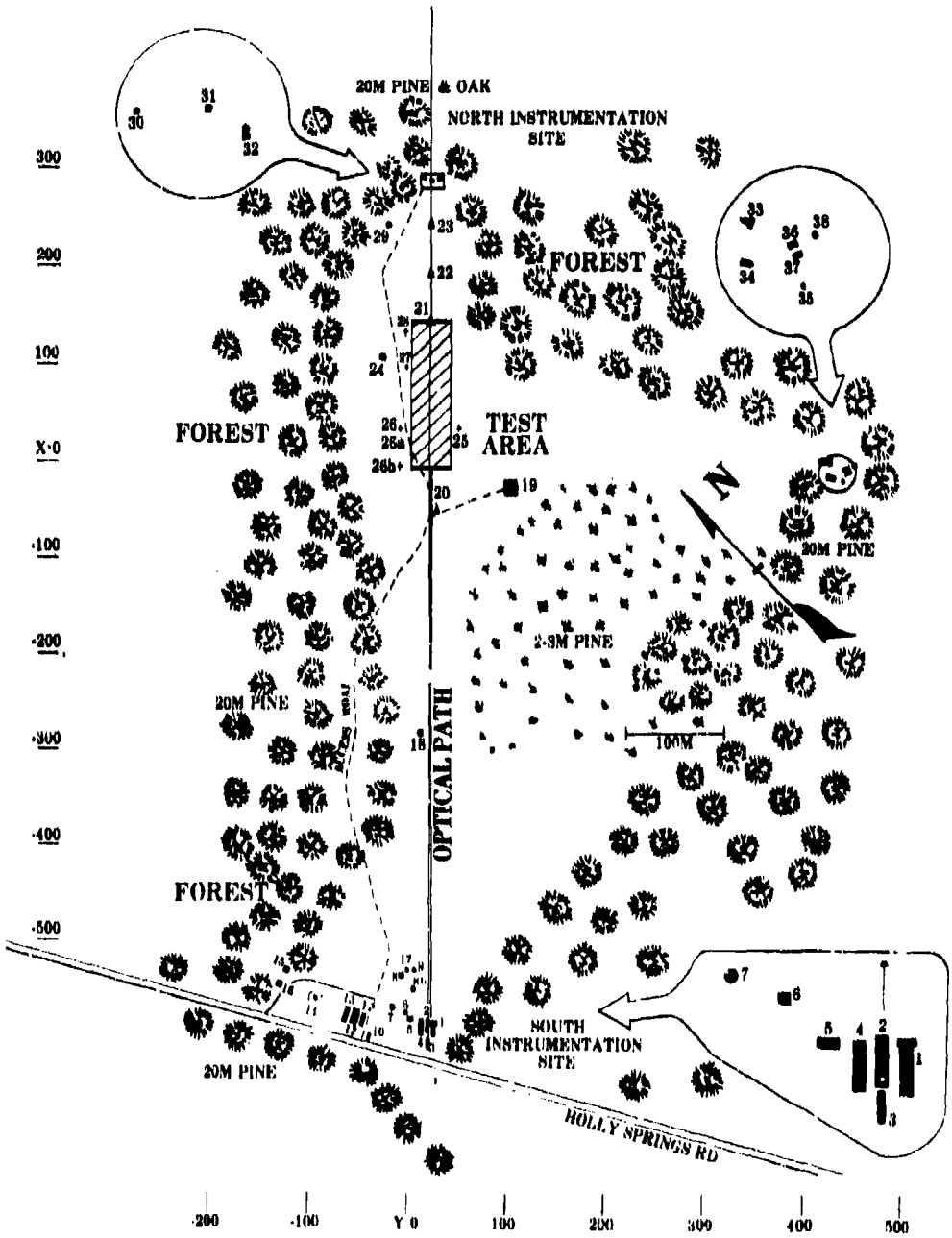

FIGURE 2. DETAILED LAYOUT OF INSTRUMENTATION LOCATIONS FOR DIRT-III. Tree locations and forest boundary are estimated.

UNCLASSIFIED

LEGEND FOR FIGURE 2

Legend		Coordinates (m) X	Y	Remarks
1.	NVL 95-GHz radar	-574.24	25.62	
2.	NRL filter transmissometer	-572.71	20.00	
3.	WES instrumentation trailer			
4.	ASL instrumentation van (digital imagery system, 38- and 60-GHz experiment, particulate data processing equipment and laboratory	-572.87	15.18	
5.	TACS M109 van	-572.76	6.76	
6.	T-9 mount with Knollenberg sensors	-564.58	0.95	
7.	32-m meteorological tower	-560.31	-11.61	
8.	Acoustic sounder	-523.33	-5.9	
9.	Forward scatter meter	-521.35	7.41	
10.	60-kW power generator			
11.	ASL shop van			
12.	AWS observation location	-550.0	-50.0	Estimate
13.	WES van			
14.	GMD and balloon release area	-546.21	-94.85	
15.	Division artillery Metro Section	-517.15	-118.92	
16.	Latrine			
17.	Scintillometer receiver	-520.5	0.72	
18.	Scintillometer transmitter	-273.86	13.22	
19.	WES concrete building	-17.08	96.56	
20.	NVL corner reflector	-39.86	20.76	
21.	NVL corner reflector	148.27	18.56	
22.	NVL corner reflector	200.18	17.58	
23.	NVL corner reflector	244.87	16.56	
24.	2-m meteorological tower	82.99	-33.81	
25.	Optical target	39.1	49.89	Faces south
26.	Optical target	39.31	-12.34	Faces south
26a.	Optical target	40.38	-11.21	Faces east
26b.	Optical target	-0.48	-11.26	Faces east
27.	Optical target	100.67	-10.10	Faces east
28.	Optical target	141.42	-9.96	Faces east
29.	4-m meteorological tower	252.61	-23.39	
30.	Power generator			
31.	NRL transmitter (searchlight)	296.95	20.47	
32.	2-ton van (NRL cavity)	290.31	28.27	
33.	CSU tethered balloon			
34.	Digital imagery system	-12.04	420.36	
35.	Power generator			
36.	CSU van			
37.	CSU trailer			
38.	20-m meteorological tower	425.0	0.0	Estimate
*Rain gauge		-538.19	5.88	No number on layout
*Radiometer		-551.46	5.57	No number on layout

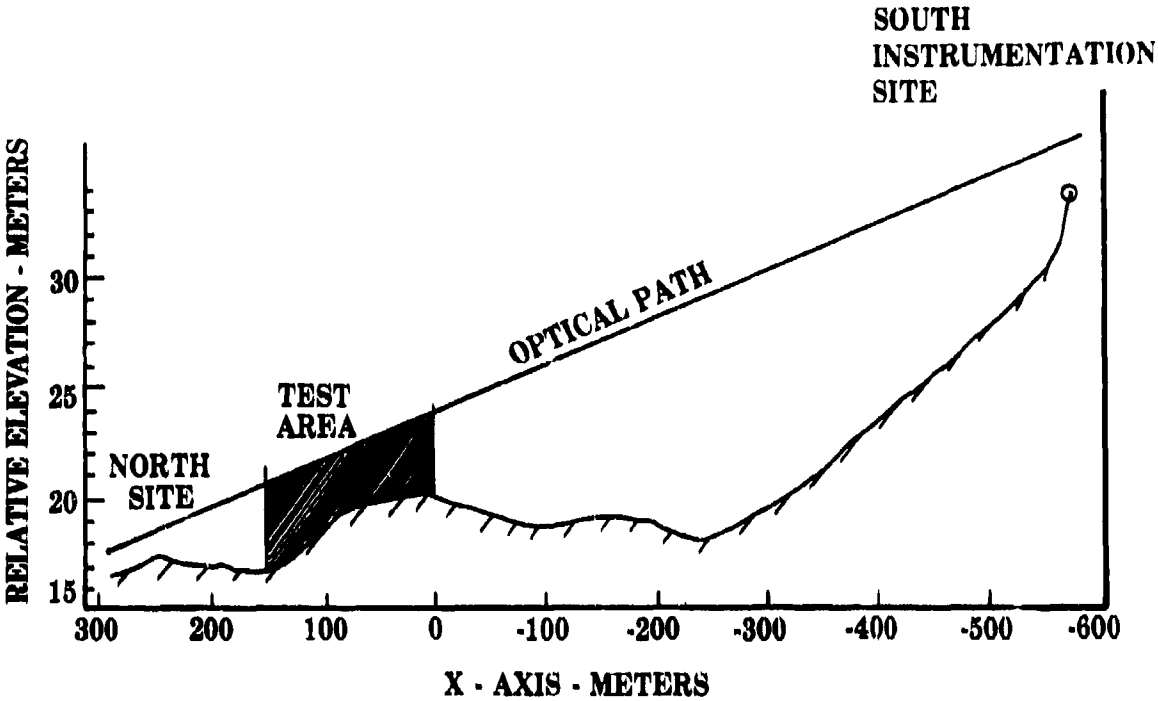

FIGURE 3. ELEVATION CROSS SECTION ALONG OPTICAL PATH. Vertical scale is exaggerated.

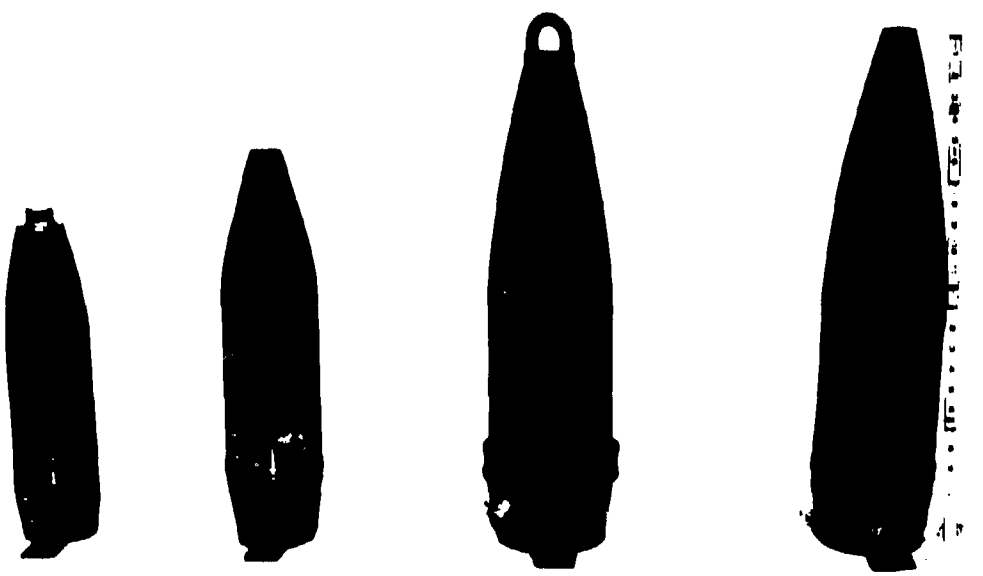

FIGURE 4. MUNITIONS USED DURING DIRT-IIIA TESTS.
Left to right: 105 mm, 122 mm USSR, 155 mm, and 152 mm USSR.

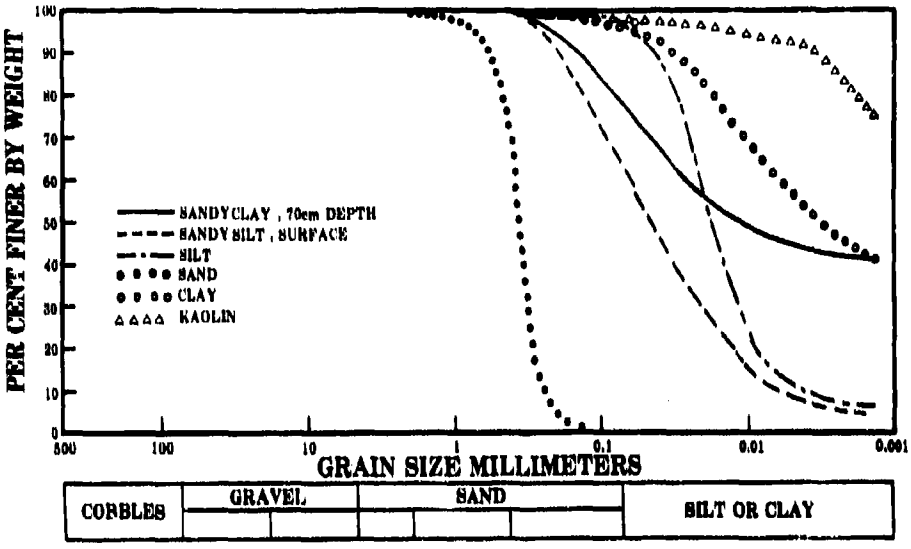

FIGURE 5. SOIL TYPES ENCOUNTERED OR TAILORED DURING THE DIRT-III PROJECT: (1) Natural surface, dark brown sandy silt; (2) natural soil, 70 cm deep, reddish sandy clay; (3) kaolin, tailored soil test; (4) sand tailored soil test; (5) clay, tailored soil test; (6) silt, tailored soil test.

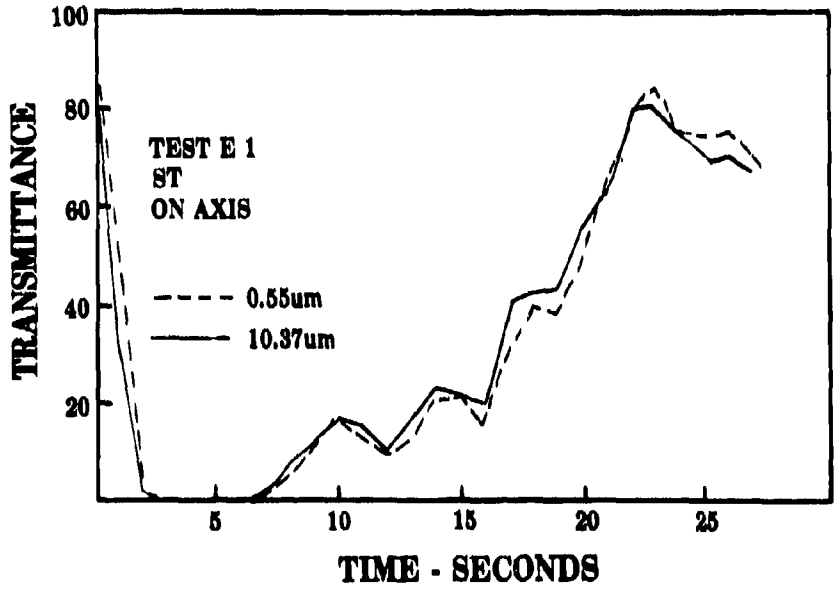

FIGURE 6. TRANSMITTANCE MEASURED AFTER THE DETONATION OF AN ST SOVIET 152-mm PROJECTILE ON AXIS. Differential transmission is negligible and was dominant on most ST tests.

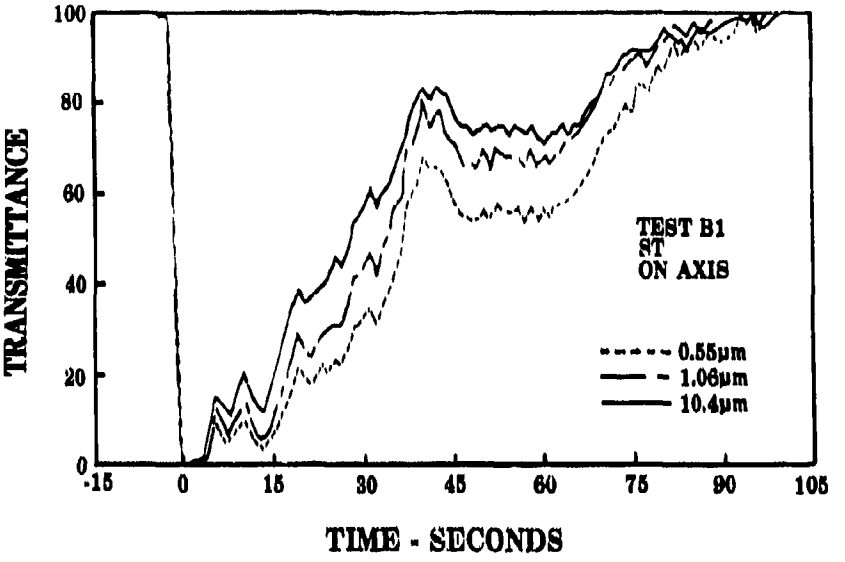

FIGURE 7. THE TRANSMITTANCE MEASURED THROUGH A DUST CLOUD PRODUCED BY A 105-mm PROJECTILE TANGENT TO THE SURFACE ON AXIS.
Note that the visible energy is attenuated more than the near or far infrared.

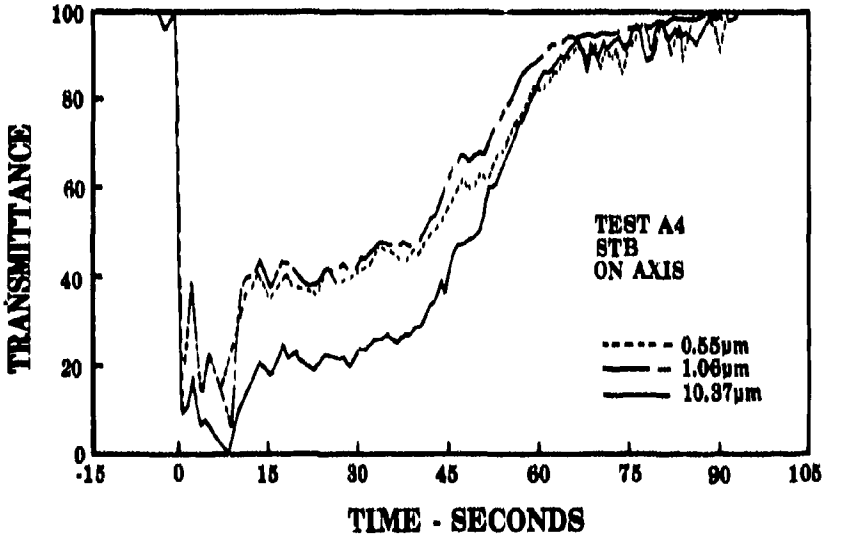

FIGURE 8. TRANSMITTANCE THROUGH DUST CLOUD PRODUCED BY A BURIED 155-mm PROJECTILE ON AXIS.
Note that the far infrared is attenuated more than visible or near infrared.
This phenomenon seemed to occur most frequently, but not always, in buried rounds.

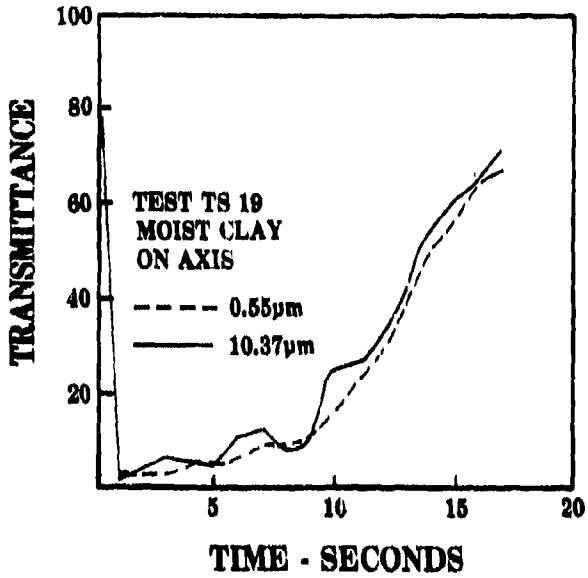

FIGURE 9. TRANSMITTANCE THROUGH DUST CLOUD OF MOIST CLAY PARTICLES USED FOR TAILORED SOILS. There is little or no wavelength dependence for this or dry clay soils.

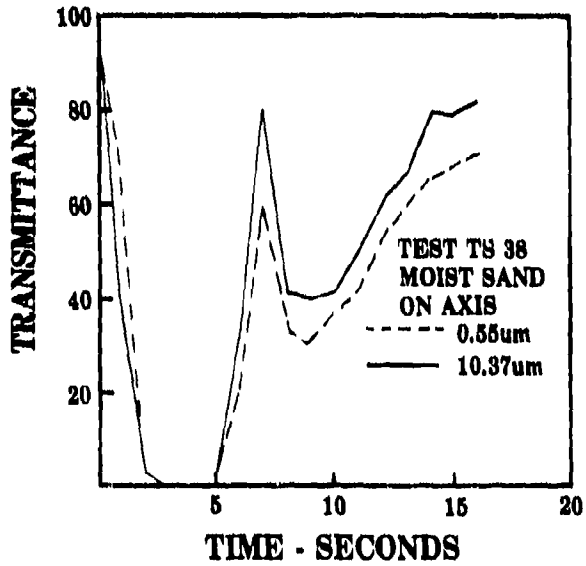

FIGURE 10. TRANSMITTANCE THROUGH DUST CLOUD OF MOIST SAND. Wavelength dependence is observed on this and dry sand tests more frequently than through clay or silt.

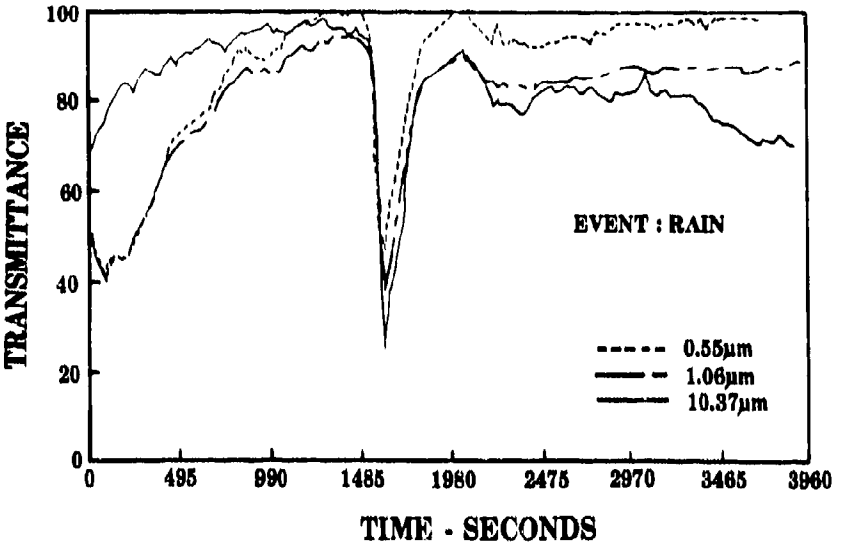

FIGURE 11. TRANSMITTANCE THROUGH RAINFALL.
The attenuation of infrared with respect to visible reversed positions during and after the period of intense showers.

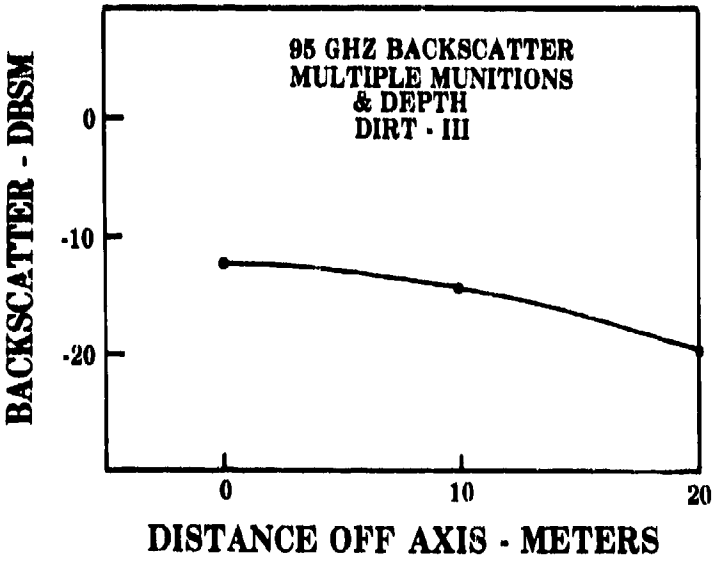

FIGURE 12. PEAK VALUE OF 95 GHz BACKSCATTER AVERAGED FROM ALL MUNITIONS FOR ALL DEPTHS FOR DIRT-IIIA. The individual values ranged from -1 dB for a buried round on axis to -31 dB for buried round 20 m off axis.

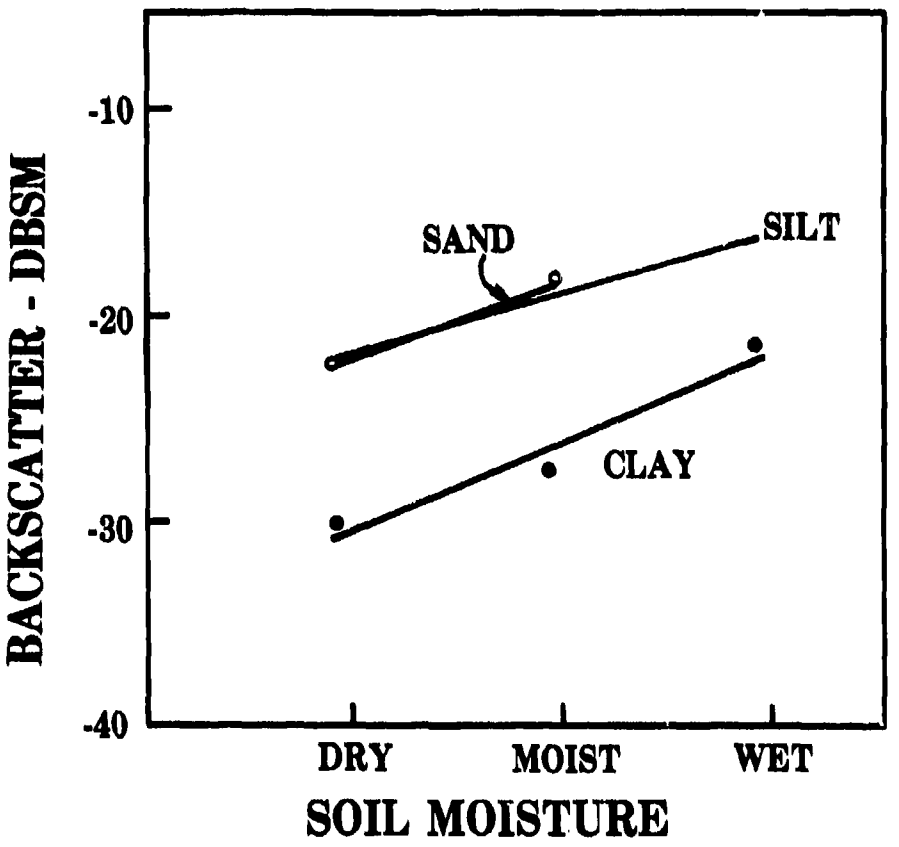

FIGURE 13. PEAK VALUE OF 95 GHz BACKSCATTER FOR TAILORED SOILS, DIRT-IIIB, ON AXIS TESTS ONLY.

ESTIMATION OF PRECISION OF SMOKE/OBSCURANT MEASUREMENTS AND PRODUCT VARIABILITY

James F. O'Bryon
Army Material Systems Analysis Activity
(Smoke Aerosol Working Group)
Aberdeen Proving Ground, MD

ABSTRACT

An understanding of the precision of measurement (or imprecision of measurement) of various parameters measured during smoke/obscurants testing is of paramount importance. Apparent disagreement in results between tests of like munitions under like conditions can be attributable to a number of factors, not the least of which is the measurement error of the various pieces of instrumentation being used. A statistical technique and computer model are presented which allow for the estimation of measurement error when simultaneous measurements of successive occurrences of the same phenomena are made by two or more instruments. The technique also provides an estimate of the real product variability. Outlier techniques and significance tests are also incorporated to endable the user to apply the methodology under a number of testing situtations.

1. INTRODUCTION

Smoke/Obscurant testing is "nonreplicatable". Obscurants are destructively tested and cannot generally be retrieved for supplementary analyses. Hence, one must rely on whatever data can be obtained in real time (and subsequent analysis) to determine cloud size, transport, transmission through it and other parameters.

More and more instruments are being manufactured which can measure a wide range of obscurant characteristics using a variety of physical techniques. With this comes the promise of obtaining estimates of how well the instruments themselves are behaving in regard to their bias errors and random imprecision.

The methodology presented here was originally developed for use in estimating the precision of measurement of velocimeters used to measure muzzle velocities of artillery shells and is contained in Reference 1. The same methodology can be applied to smoke/aerosol measurements, provided the test procedures described herein are applied.

When one is taking measurements with the same instrument of successive occurences of the same phenomena, one can then compute the variance and mean of the sample. If the measuring instrument has some sort of measurement error, this error becomes part and parcel of the sample's statistics unless one can somehow "strip out" this error from the real variability (product variability) and real mean of the phenomena being measured. This task is complicated further if the phenomena are non-replicatable, as is the case with destructive testing.

When, however, two or more instruments independently and simultaneously measure successive occurrences, it is possible to estimate both the true product variability and the precision (or imprecision) of measurement of each instrument used. These methods have been published by Grubbs.[2]

These methods were later expanded to the case where one wishes to determine whether a given measuring instrument is operating as consistently as two other known instruments.[3] The nomenclature in this report is consistent with that found in the referenced reports.

A minimum of two instruments simultaneously measuring is needed. If three or more instruments are used, estimates of measurement can be made which are totally free of the variability of the phenomena observed. This results in more direct comparison of the errors of measurement of each instrument. The procedures discussed here involve:

(1) The estimation of the precision of measurement,

(2) Estimation of product variability and,

(3) Significance tests for comparing the precisions of measurement of N instruments ($2 < N < 10$) and determining whether a given instrument has a bias which is so large compared to that of the other measuring devices that the instrument needs calibration.

2. STATISTICAL OVERVIEW

A. Statistical Assumptions

The following statistical overview is reproduced from References 2 and 3 to enable the computer program user to understand the functioning of the program. References are made in the examples to equations discussed here. For a comprehensive understanding of the statistical basis for the program, the reader is encouraged to study the referenced publications.

We shall first define some basic terminology. Below we see tabulated pairs of data points measured simultaneously by two instruments, I_1 and I_2,

---

[1] O'Bryon, J. R., "Estimation of Precision of Measurement and Product Variability: A Computer Model," ARBRLMR No. 2778, Aug. 1977.

[2] Grubbs, F. E., "On Estimating Precision of Measuring Instruments and Product Variability," Journal of the American Statistical Association, Vol. 43, p 243-264, June 1948.

[3] Grubbs, F. E., and O'Bryon, J. F., "The Statistical Comparison of Measuring Instrumentation,", BRL ARDC Technical Report No. 11 (AD 732 428), July 1971.

Measurements by I_1	Measurements by I_2
$x_1 + e_{11}$	$x_1 + e_{12}$
$x_2 + e_{21}$	$x_2 + e_{22}$
.	.
.	.
.	.
$x_i + e_{i1}$	$x_i + e_{i2}$
.	.
.	.
.	.
$x_n + e_{n1}$	$x_n + e_{n2}$

where x_i = the true value of the characteristic considered, where i represents the ith item in the sample,

e_{ij} = the error in measurement of the ith item by the jth instrument, I_j.

It is assumed that both the characteristic being measured and the errors of measurement are normally distributed and that the absolute values of the characteristic measured and the errors of measurement are statistically independent, i.e.,

$$E(x_i^p \cdot e_{ij}^q) = E(x_i^p) \cdot E(e_{ij}^q).$$

In addition, it is assumed that the error of measurement of the different instruments are statistically independent of each other, i.e.,

$$E(e_{ij}^p \cdot e_{ik}^q) = E(e_{ij}^p) \cdot E(e_{ik}^q) \qquad j \neq k .$$

It is also assumed that the errors of measurement are significantly smaller than the real value of the characteristic being measured.

B. General Case: Estimation of Precision of Measurement and Product Variability:

The basic way in which the computer program is used is in estimating the precision of measurement and product variability given observations from 2 to 10 instruments simultaneously.

Since the statistical treatment is somewhat different for the two instrument case, this statistical summary is presented in two parts.

(1) Two Instrument Case. For this case, there are two methods for estimating precision of measurement.

We take as an estimate of the variance in errors of measurments of instruments I_1,

$$\text{est. } (\sigma_{e1}^2) = S^2_{x+e1} - S_{x+e1,x+e2} \qquad (1)$$

where
$$S_{x+e1,x+e2} = \frac{1}{n-1} \sum_{i=1}^{n} \left\{(x_i + e_{i1}) - (\bar{x} + \bar{e}_1)\right\} \left\{(x_i + e_{i2}) - (\bar{x} + \bar{e}_2)\right\}$$

$$= \frac{1}{n(n-1)} \left\{ n \sum_{i=1}^{n} (x_i + e_{i1})(x_{2i} + e_{i2}) - \left[\sum_{i=1}^{n} (x_i + e_{i1})\right]\left[\left(\sum_{i=1}^{n} (x_i + e_{i2})\right)\right] \right\}$$

and as an estimate of the variance in errors of of measurement of instrument I_2, we compute

$$\text{est. } (\sigma_{e2}^2) = S^2_{x+e2} - S_{x+e1,x+e2} \qquad (2)$$

and
$$E(S_{e1}^2) = \sigma_{e1}^2$$

$$E(S_{e2}^2) = \sigma_{e2}^2$$

where the estimates of the covariances

$$E(S_{x,e1}) = E(S_{x,e2}) = E(S_{e1,e2}) = 0 \qquad \text{under the assumptions.}$$

It is remarked in passing that a technique of working with differences in corresponding measurement of the two instruments is of some interest. That is, if the measurements of I_2 are subtracted from corresponding measurements of I_1, the result gives

$$e_{11} - e_{12}$$

$$e_{21} - e_{22}$$

$$\vdots$$

$$e_{i1} - e_{i2}$$

$$\vdots$$

$$e_{n1} - e_{n2}$$

thus eliminating the true value of x_{ij}, the characteristic measured. Using the above differences, an estimate of σ_{e1}^2 is given by

$$\text{est. } (\sigma_{e1}^2) = \frac{1}{2}\left\{S^2_{x+e1} - S^2_{x+e2} + S^2_{e1-e2}\right\} . \qquad (3)$$

It is easy to see that estimate (3) is hence precisely that given by (1).

$$S^2_{e1} + S_{x,e1} - S_{x,e2} - S_{e1,e2}$$

In order to estimate the amount of variability in the product being measured, we may first add corresponding measurements of the two instruments, obtaining

$$\begin{array}{c} x_1 + e_{11} + x_1 + e_{12} \\ \vdots \\ x_i + e_{i1} + x_i + e_{i2} \\ \vdots \\ x_n + e_{n1} + x_n + e_{n2} \end{array}$$

The variance of the above sums of readings is

$$4S_x^2 + S_{e1}^2 + S_{e2}^2 + 4S_{x,e1} + 4S_{x,e2} + 2S_{e1,e2}$$

An estimate of the variability in the product, σ_x^2, is then given by

$$\text{est. } (\sigma_x^2) = \frac{1}{4}\left\{S^2_{x+e1+x+e2} - S^2_{e1-e2}\right\}, \qquad (4)$$

The estimate of σ_x^2 is given by the covariance of the readings of I_1 and I_2:

$$\text{est. } (\sigma_x^2) = S_{x+e1,x+e2} \qquad (4a)$$

(Equation 4 and 4a are identical).

Estimate (4) or (4a) is unbiased and can be shown to be the maximum likelihood estimate.

The variance of the estimate, est. (σ_{e1}^2) or est. (σ^2_{e2}), depends on (A) σ_x^2, the variance in the characteristic measured, (B)σ^2_{e1}, the variance of the errors of measurement of Instrument I_1, (C) σ^2_{e2} the variance of errors of measuremrnt of Instrument I_2 and (D) n, the number of observations or the sample size. Therefore, in order to obtain a precise estimate of σ^2_{e1} when using only two instruments, the variation in the characteristic measured, i.e., σ_x^2, should be held to a reasonable minimum or the sample size, n, should be sufficiently large.

Sometimes, the estimated variance in errors of measurement may turn out to be negative. This may be due to small sample size, bad observations, errors in recording, outlying observations, etc. Since it is physically impossible for a true variance in errors of measurement to be negative, one suggestion is to add the absolute value of the negative variance to the estimated variance in error for the other instrument for an overall estimate of instrument error. The computer program prints negative as well as positive variances and stores these values to compute pooled estimates of variance in precision error for each instrument if multiple cases are input back-to-back using the same instruments. However, to avoid negative square roots, the program lists $\sigma_e = 0$ when taking the square root of a negative variance. See References 2, 3, and 5 for further information on the treatment of negative estimates of variance.

If the variation in the characteristic measured is zero (or if we measure the same item over and over again) i.e., if $\sigma_x^2 = 0$, then one could compute

$$\frac{1}{n-1} \sum_{i=1}^{n} (e_{i1} - \bar{e}_1)^2 \qquad (4b)$$

directly, and this would give an estimate of σ_{e1}^2 with variance equal to

$$\frac{2}{n-1} \sigma_{e1}^4 \qquad (4c)$$

Apparently, in employing two instruments, there are only two computational procedures of interest for separating the variability in the product from the variance in the errors of measurement, and both methods give the same estimate. In using either method, however, it is possible to estimate σ_{e1}^2, σ_{e2}^2, and σ_x^2 and thus determine from the relative order of magnitude of these quantities whether the instruments are sufficiently precise to be used in taking the required measurements.

(2) Three or More Instrument Case ($3 \leq N \leq 10$).* Since the nomenclature has been established in the two instruments, this description of the $N \leq 3$ case will be limited to the basic equations solved by computer program. As was stated earlier, using three or more instruments permits precision of measurement estimates totally free of the product variability itself.

---

[5] Thomson, W. A., Jr., "The Problem of Negative Estimates of Variance Components," Annals of Mathematical Statistics: Vol. 33, pp 273-288, 1964.

The following equation is used to estimate precision of measurement of Instrument I_1 ($2 \leq i \leq 50$ data points)

$$\text{est. } (\sigma^2_{e1}) = S^2_{x+e1} - \frac{2}{N-1} \left\{ \sum_{r=2}^{N} S_{x+e1,x+er} \right\} + \frac{2}{(N-1)(N-2)} \left\{ \sum_{2\leq j<k}^{k=N} S_{x+ej,x+ek} \right\} \quad (5)$$

Estimates of all other instruments can be made by obvious rotations of the subscripts. The real product variability (stripped of measurement error) is estimated

$$\text{est. } (\sigma^2_x) = \frac{2}{N(N-1)} \sum_{1\leq r<s}^{s=N} S_{x+er,x+es} \quad (6)$$

Sample problems and complete computer listing in FORTRAN IV are contained in Reference 1.

3. SUMMARY

The methodology presented is effective provided that the smoke/obscurant data are collected in such a way that spatial (both time and distance) errors are minimized and multiple instruments are used. Test instrumentation configurations should permit lines of sight which are as coincidental as possible to allow measurement of the same phenomena simultaneously.

Data collection using such aprocedure will allow for the performance evaluation of various types of instrumentation and allow the smoke/obscurant modelers and developers to determine the confidence bounds of their observations.

*N is limited to 10 and n to 50 only because of the dimensions of the program's storage. The equations, of course, are valid for any $N \geq 3$, $n \geq 2$.

A DATA REDUCTION TECHNIQUE FOR FIELD DATA

Marvin D. Smith, Keith Jones and P. Kittikul
Division of Engineering, Technology and Architecture
Oklahoma State University
Stillwater, OK 74078

ABSTRACT

Prior to analyzing data from field tests such as Smoke Week I and II the information must be put into perspective. A technique has been developed to assist in this effort. Due to the spatial separation of instrument lines of sight the relationship between variables such as concentration-length and transmittance cannot be made with respect to the common time base that is published in the reports. A technique is presented to determine which values of transmittance and concentration-length should correspond by shifting the data in time. Two assumptions are made, frozen flow occurs between lines of sight and data scatter is minimized at the correct time shift. Coefficients for a model relating the logarithm of the transmittance and concentration-length (CL) is determined by a regression analysis. An optimization program is used to control the regression program and determine the time shift values used to arrive at the minimum value for the error term.

The technique was tested using laboratory data which was artificially offset. The optimum time shift for this data would be expected to be zero. Program results showed optimum time for two white phosphorus tests to be .004 seconds and .003 for two FE tests. The error terms for the tests were .042, .173, .996, and .082 respectively. These values represent the sum of the weighted errors for each time.

This technique was used on Inventory Smoke Munitions Tests, Smoke Week I and Smoke Week II tests. Time shifts concurred with the relative spatial separations of the various lines of sight. Significance of these modifications to the published data are realized when it is seen that CL data changes by a factor of 100, in some cases, over the span of a designated time shift.

1. INTRODUCTION

Essentially all smoke obscuration test data taken to date follows the general methodology outlined in reference (1). The instrumentation and mode of reporting are similar in each case too. This paper involves data from Inventory Smoke Munition tests, Smoke Week I and Smoke Week II tests (2-4). Data from these tests require adjustments to account for differences in sample time among the various instruments. After this is taken into account the data can be analyzed.

Instrumentation interference requires a certain distance to be maintained between adjacent instruments throughout the lines of sight for each measuring device. Because of this physical separation, the relationships between the measured values from each instrument do not correspond with the same mass of smoke for a given time. Therefore it is not valid to relate, for example, transmittance at time t with concentration-path length at the same time. If smoke is blowing across the line of sight for concentration measurements and towards the line of sight for visual transmittance measurements, then the concentration path length at time t would correspond to the transmittance at time $t + \Delta t$. The value for Δt is dependent on the rate of smoke propagation and the distance between lines of sight. An estimate for Δt can be obtained by dividing the average distance between

the lines of sight in question by the average wind velocity. This is tantamount to assuming steady laminar flow with smoke propagation at the same speed as the wind velocity. Since the flow is unsteady and turbulent, the approximation could be improved upon by relying on the behavior of the data as outlined in the next section.

2. CORRELATION TECHNIQUE

The Beer-Lambert Law suggests that a straight line relation should result if -ln T is plotted against the concentration-path length (CL). When this occurs it is expected that a good correlation exists for that set of data. As was noted previously (5), the data in many cases develops a loop rather than a straight line. It was shown that this loop was a result of the differences in sampling time between T and Cl data. Also shown was the fact that a linear relation does not exist between -ln T and Cl even after a correction for sampling time is made. This implies a non-constant extinction coefficient or a constant influence on transmittance from some undefined source. This source could be a function of Cl, relative humidity, velocity or other similar parameters. Taking this information into account, it was determined that an extension to the Beer-Lambert Law would be utilized for correlation purposes.

The basic premise for correlation is that a minimum amount of scatter would exist for the correlation model when the proper shift in sampling time was found. This shift in the sampling time should be relatively close to the value obtained by dividing the average distance separating the lines of sight of the instruments by the average wind velocity vector which is perpendicular to the lines of sight. A regression analysis is used to determine the coefficients for the model.

Once a model is determined, the following procedure is used to determine the shift in sampling time and obtain the final set of coefficients for a given trial and a given wavelength. Figure 1 shows the flow diagram which is followed.

Each trial has transmittance data for four different wavelengths, visual, 1.06 μm, 3.44 μm and 9.75 μm versus time. Also, Cl data is available as a function of the same time intervals. These data are inputs to the program. An optimization program, Golden Search (6), is used to select the time shift applied to the transmittance data. The optimization parameter is the error value generated in the MARQ program (7) which is a non-linear least squares solution technique for determining the coefficients for the model. The Golden Search program is the executive program which guides the selection of time shift values to modify the correspondence between transmittance and Cl values which

will enable the minimum error value to be found. An interpolation routine is used to change the time base for transmittance data according to the time shift selected by Golden Search. These sets of transmittance and Cl values are input to the MARQ program and a set of coefficients and an error value is found. Two other indications of errors are also calculated but not used in the optimization analysis. When the search "time envelope" gets sufficiently small, then the last value calculated is defined as the minimum error value.

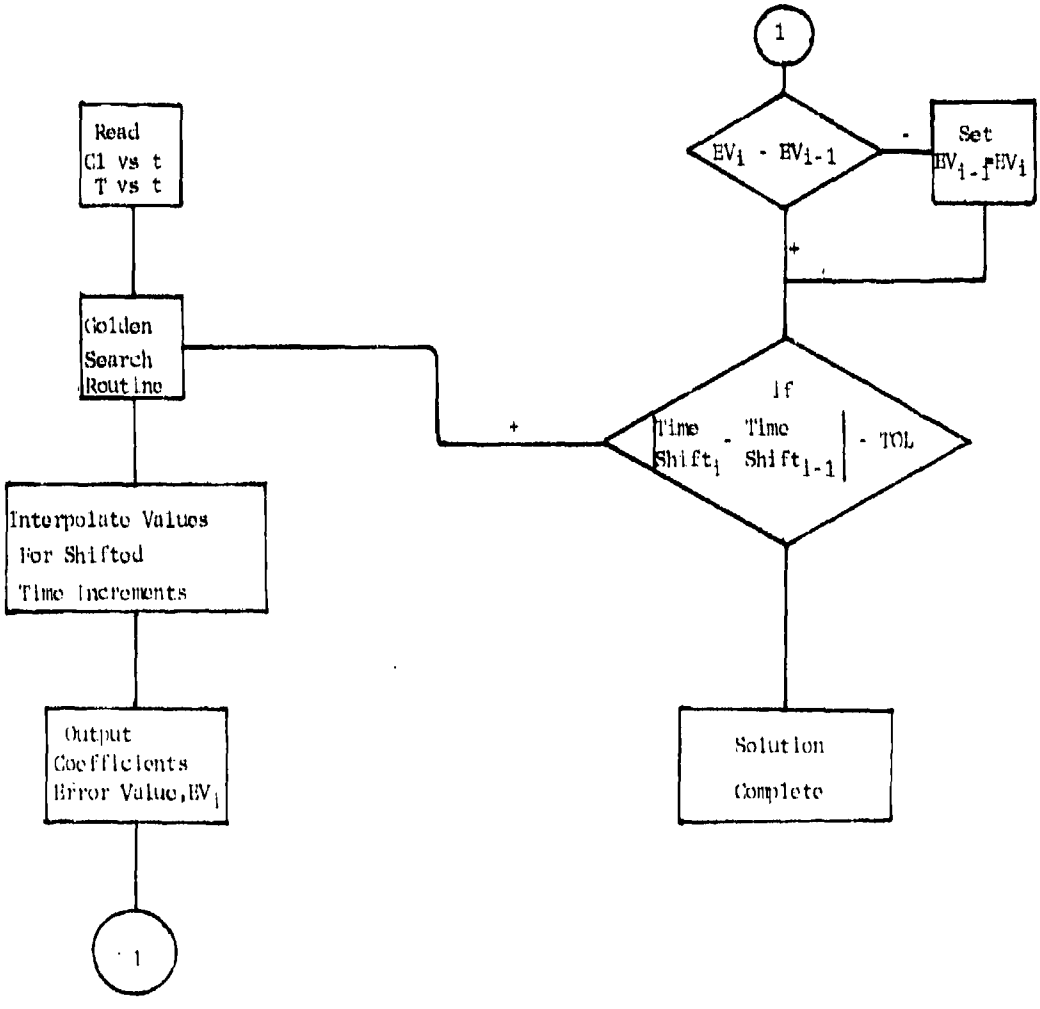

FIGURE 1. ANALYSIS FLOW DIAGRAM.

3. MATHEMATICAL MODELS

Several models were attempted to relate transmittance to C1. Some were chosen because of their simplicity and others were based on models that would satisfy certain characteristics that were observed in the data. The initial model that was used was a simple third order polynomial.

$$-\ln (T) = X(1) + X(2)\ C1 + X(3)\ C1^2 + X(4)\ C1^3$$

This model would reduce to the Beer-Lambert Law if the values for X(1), X(3) and X(4) were to go to zero. Characteristics of the model were that it was underdamped and it tended to overshoot the data. This model was abandoned.

A second model was a power model of the form

$$-\ln (T) = X(1) + X(2)\ (C1 - X(3))^{X(4)}$$

which was chosen to allow the log of transmittance to approach an asymptotic value. Results of this model were not good because of the pole that developed.

Another model which is an extension of the Beer-Lambert Law was of the form

$$T = X(3) + X(2)\ e^{-X(1)\ C1}$$

This showed promise for the data which had a low asymptotic value for transmittance and significant data points near C1 equal to zero. Otherwise the curve would not approach T equal to one and therefore would not represent the data well. The X (3) term would allow the curvature on a semilog plot to be fit. A modification to this model was made to try to circumvent this problem. The new form was to take into account the two limits: at C1 equal to zero the transmittance would be one and at large values of C1 the transmittance would approach an asymptotic value. This form is

$$T = \frac{X(2)\ C1}{X(3) + C1} + e^{-X(1)\ C1}$$

and it resulted in the best fit of all the models. The problem with some data was that the term X (3) would go negative. This would cause a discontinuity in the middle of the data. Even for the data where the discontinuity occurred, the model in general fit well. Since the discontinuity is unacceptable, another model was formulated.

The model used in this report is a modification to the previous two models and satisfies the two end points. It is

$$T = X(2) + (1-X(2))\ e^{-X(1)\ C1}$$

where the X (2) values cancel when C1 is zero and the second term goes to zero for large values of C1. Also, the extinction coefficient remains constant as in the Beer-Lambert Law. Quite recently W. Michael Farmer of the University of Tennessee Space Institute did work which indicates that the extinction coefficient is not constant but a function of time. At this time, it is difficult to determine whether the extinction coefficient is time dependent, or whether transmission varies with respect to influences other than a changing extinction coefficient.

The error value that is used to optimize the regression analysis is defined as

$$\phi = \sum_{i=1}^{n} \frac{(T_{mi} - T_{pi})^2}{\sigma_i}$$

where

T_m = measured transmittance data

T_p = predicted transmittance values

σ = error weighting factor.

The term σ can be chosen as a constant or a function. For this work σ was defined as

$$\sigma_i = T_{mi}$$

which allows a larger error for the larger values of C1.

Another guide to determining the degree of correlation in this model is the correlation coefficient defined as (8):

$$r = \frac{N \Sigma XY - \Sigma X \Sigma Y}{(N \Sigma X^2 - (\Sigma X)^2)^{\frac{1}{2}} (N \Sigma Y^2 - (\Sigma Y)^2)^{\frac{1}{2}}}$$

where

$X = T_m$

$Y = T_p$

N = Number of data points

When r equals one the correlation is perfect and when r equals zero no correlation exists. It should be pointed out that the correlation coefficient does not relate to the amount of scatter in the data as

does the error value, but it shows whether the correct model was chosen.

A term defined as the fit factor was used to see how well the model followed a quasi-centroid of the data. This is expressed as

$$F = \frac{\frac{1}{N-1}\sum_{i=2}^{N} a_i}{\left\langle \frac{1}{N-1}\sum_{i=2}^{N} a_i \right\rangle}$$

where

$$a_i = \begin{cases} 1, & \text{Sgn (Error}_{i-1}) \neq \text{Sgn (Error}_i) \\ 0, & \text{Sgn (Error}_{i-1}) = \text{Sgn (Error}_i) \end{cases}$$

$\langle\ \rangle$ = Expectation Value.

For this case the expectation value was assigned a value of 0.5, which means that it is expected that there are as many points above the curve as below it. If F is one, then the expectation was fulfilled.

4. REGRESSION ANALYSIS RESULTS

Several runs were made on the computer to check the models and the analysis technique. Figure 2 shows the results of the curve fit for data obtained by Stuebing (9) in a smoke chamber. The transmittance was artificially shifted 2 seconds and model number 5 was used (in conjunction with the regression analysis and the golden search) to select the final time shift. In this run, the data was shifted back to time equal to zero, as it should be, and the model correlation was excellent. The error value ϕ was 0.043. The operational aspects of the program being accepted as valid, other trials of interest were run.

Table I lists the runs that were made using model 5 and results of the program such as the time shift, the error terms and the values for the coefficients. These data were separated in groups of ammunition types including WP, HC and Wicks and Wedges of both RP and WP.

It is well established that the extinction coefficient (9) is a function of wavelength and relative humidity. The coefficient X(1) is the extinction coefficient for the model used in this analysis. It has the dimensions of m^2/mg. According to the model used, X(2) must be dimensionless.

STUEBING DATA TABLE V

TYPE OF SMOKE: HC WAVELENGTH: 7-12

LABORATORY DATA MODEL 5

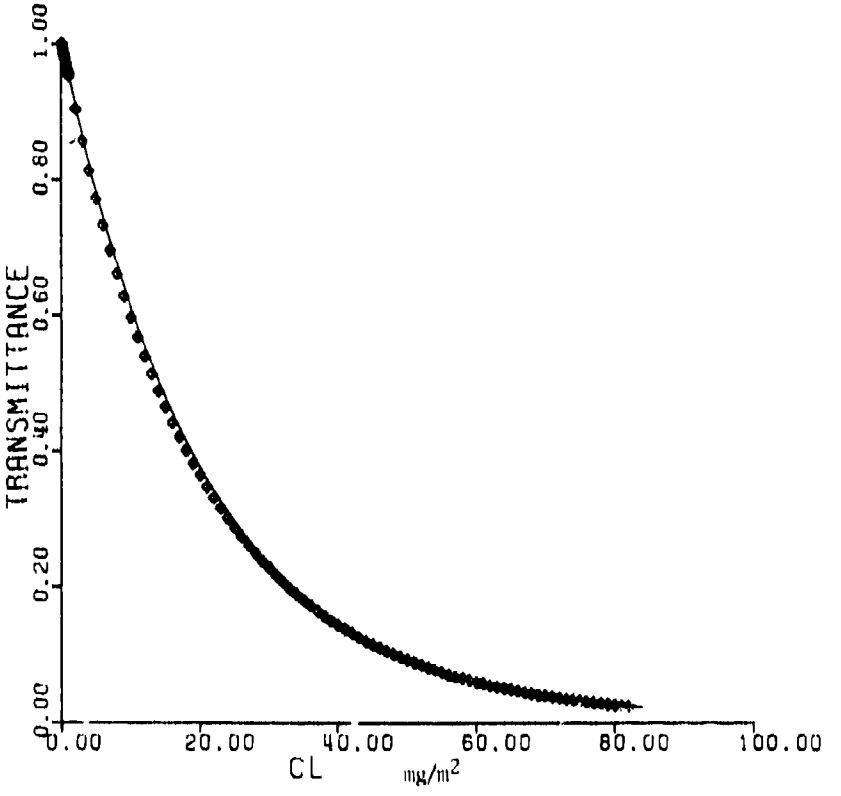

FIGURE 2. CURVE FIT FOR STUEBING DATA.

UNCLASSIFIED

TABLE 1. SMOKE TRIAL DATA, CORRELATION COEFFICIENTS AND ERROR VALUES

TEST DESIGNATION AND TRIAL NUMBER	WIND VELOCITY m/s	RELATIVE HUMIDITY %	NUMBER OF ROUNDS	TYPE OF AMMUNITION	WAVE LENGTH	TIME SHIFT (SEC)	ESTIMATED TIME SHIFT (SEC)	ERROR TERMS ϕ —	F —	r^2 —	X (1) m^2/mg	X (2)
SPIIA-T-3	4.4	19	18	105 mm, HC	VIS	1.35	.57	6.34	.1556	.9807	-.0079	.00962
					1.06	2.54	.98	15.08	.3012	.975	-.00126	.00804
					3.44	2.57	1.7	.3963	.4484	.6561	-.00075	.850
					9.75	5.76	1.9	.4286	.4	.9262	-.000303	.559
SWI-T-4	4.0	36.5	36	105 mm, HC	VIS	0.0	.63	53.477	.54545	.84202	-.00667	.01709
					1.06	.27	1.1	13.6417	.56566	.97691	-.001133	.01502
					3.44	3.54	1.9	3.2519	.15385	.94118	-.000151	.15953
					9.75	1.42	2.1	.53256	.19289	.89706	-.000187	.64281
SWI-T-24	4.4	36.2	12	155 mm, WP	VIS	.27	.6	6.3748	.62626	.98805	-.00314	.01173
					1.06	.22	1.0	6.7667	.58586	.97965	-.001161	.00742
					3.44	1.66	1.7	17.9204	.48731	.88032	-.000205	.00245
					9.75	2.02	1.9	34.724	.37755	.82793	-.000221	.00588
SWI-T-33	2.3	26.5	18	105 mm, HC	VIS	1.39	1.1	15.511	.41624	.95286	-.007117	.00975
					1.06	1.45	1.9	11.499	.38579	.979685	-.001497	.01265
					3.44	5.45	3.2	.67557	.38342	.93987	-.000267	.33114
					9.75	5.58	3.6	.21338	.52849	.79507	-.000452	.79521
SWI-T-34	4.9	35	6	155 mm, WP	VIS	.22	.51	15.535	.68687	.97906	-.00288	.01165
					1.06	.42	.88	9.2352	.54545	.96426	-.000809	.01021
					3.44	2.47	1.5	5.0284	.53061	.96942	-.000179	.0216
					9.75	2.36	1.7	5.1818	.43878	.97637	-.00022	.0299
SWII-T-1	4.1	52	15	155 mm, HC	VIS	1.74	1.3	115.99	.20213	.5615	-.04038	.00146
					1.06	2.75	1.6	73.575	.16484	.59053	-.02496	.00806
					3.44	1.55	.66	12.088	.31285	.40434	-.04552	.79759
					9.75	1.33	.83	.70555	.30864	.22127	-.06032	.85791
SWII-T-3	5.7	48	12	2.75 inch, WP (Wick)	VIS	1.53	1.5	49.342	.2987	.56102	-.04943	.00158
					1.06	.34	1.8	20.961	.3125	.83221	-.00174	.01853
					3.44	0.0	.73	3.4807	.26531	.81854	-.0006505	.34525
					9.75	.16	.92	2.7214	.34595	.7968	-.00106	.36707
SWII-T-8	2.4	52	3	155 mm, WP (Wick)	VIS	1.64	2.3	95.613	.18994	.84731	-.01078	.00209
					1.06	1.56	2.8	32.995	.2125	.82848	-.003464	.02332
					3.44	0.0	1.1	3.5765	.19192	.83478	-.001299	.3979
					9.75	0.0	1.4	3.0078	.43478	.878904	-.001351	.37167

TABLE 1. CONTINUED

TEST DESIGNATION AND TRIAL NUMBER	WIND VELOCITY m/s	RELATIVE HUMIDITY %	NUMBER OF ROUNDS	TYPE OF AMMUNITION	WAVE LENGTH	TIME SHIFT (SEC)	ESTIMATED TIME SHIFT (SEC)	ERROR TERMS ϕ —	F —	r^2 —	X (1) m^2/mg	X (2)
SWII-T-8	3.4	55	6	122 mm, WP	VIS	2.69	1.7	34.112	.27027	.911373	-.0038	.00708
					1.06	2.05	1.9	68.227	.243245	.76697	-.0018	.00966
					3.44	1.58	.82	10.665	.36145	.80583	-.00037	.2231
					9.75	1.75	1.0	8.8441	.231405	.858956	-.00034	.2231
SWII-T-17	3.2	48	16	155 mm, HC	VIS	2.54	.7	46.6795	.23669	.90478	-.01046	.001643
					1.06	2.62	2.1	23.76	.28877	.94458	-.005341	.0057
					3.44	1.22	.8	1.2613	.13198	.98818	-.000287	.09142
					9.75	1.35	1.1	.76792	.14444	.98107	-.000181	.59602
SWII-T-18	1.9	72	6	155 mm, RP (Wedge)	VIS	0.0	3.0	107.03	.236025	.26295	-.06586	.001217
					1.06	.18	3.5	65.949	.14583	.45908	-.01358	.05071
					3.44	.19	1.5	2.9846	.16667	.4151	-.00484	.5384
					9.75	0.0	1.8	6.9997	.21714	.4987	-.005375	.4899
SWII-T-20	2.5	53	6	120 mm, WP	VIS	4.6	2.3	60.048	.375	.76043	-.0163	.00171
					1.06	.67	2.6	71.83	.28571	.69243	-.00884	.00543
					3.44	.41	1.3	4.8683	.26866	.75941	-.001679	.25217
					9.75	.61	1.4	4.3168	.30075	.77323	-.00168	.27115
SWII-T-24	4.0	71	6	155 mm, WP (Wedge)	VIS	2.29	1.4	109.72	.29213	.8465	-.011735	.001814
					1.06	2.10	1.6	50.382	.438503	.96206	-.00451	.005545
					3.44	0.0	.7	12.451	.34682	.95022	-.000452	.02607
					9.75	0.0	0.9	15.925	.433386	.96697	-.000331	.02494

Effectively, this coefficient represents the minimum transmittance attained for a given run.

Examples of run results are seen in Figures 3 and 4. Figure 3 is representative of WP trials and the variation in the characteristics of the curves for wavelengths in the visual, 1.06 μm, 3.44 μm and 9.75 μm ranges. As seen in the figure, a considerable amount of scatter exists. Even so, the correlation of this data was relatively orderly. In Figure 4, the data for HC is more orderly but, ironically, the correlation with velocity and relative humidity data was not as good as for the WP data.

A plot of the coefficients versus wavelength for WP smoke is shown in Figure 5. Presentation of the data was improved by plotting the logarithms of the coefficients. As seen in the figure, a trend, varying in magnitude, is followed by each set of data. SWII-T-15 data have an anomaly in the X(1) data at the 1.06 μm wavelenght. By revieiwng the curve fit for that run, it is easy to justify changing the coefficient to fit the trend. Also, a plot of the coefficients versus wind speed with wavelength held constant, Figures 6 through 9, shows additional justification for changing it. Each of the X(i) plots correlates well with a straight line except for the SWII-T-15 1.06 μm point. If it were shifted up to a value of 5.5 to correspond to a point on the line which correlates X(1) and velocity then it would also fit the trend in Figure 5. The X(2) coefficients as functions of wavelength do not represent such a consistent trend as the X(1) coefficients as seen in Figure 5. If the curves were drawn through the X(2) points in Figures 6 through 9 by ignoring the points which do not follow the trend in Figure 5 then a linear relationship would also exist between -ln(X(2)) and wind velocity. These results are encouraging in that coefficients can be determined as a family of curves which are functions of velocity and wavelenth.

In figures 10 through 13 the coefficients were plotted versus relative humidity for constant values of wavelength. These correlations are not as good as those for the velocity data but an apparent trend exists. The X(1) data shown in Figure 11 show a good linear relationship with respect to humidity without modifying the point for SWII-T-15 which makes data interpretation more difficult. Velocity is independent of humidity but the effective humidity of the smoke cloud could depend on the transport of the cloud through the atmosphere. This would help explain how average wind velocity can affect transmittance other than through the distribution of the cloud concentration.

Figure 14 is a plot of the correlation coefficients as functions of wavelength for HC smoke. This family of curves is not as well behaved as the corresponding family for WP smoke. A general trend still exists, but the spread is greated and more cross over is seen. Scatter in the plots of the coefficients versus velocity and relative humidity were too large to allow conclusive results. As

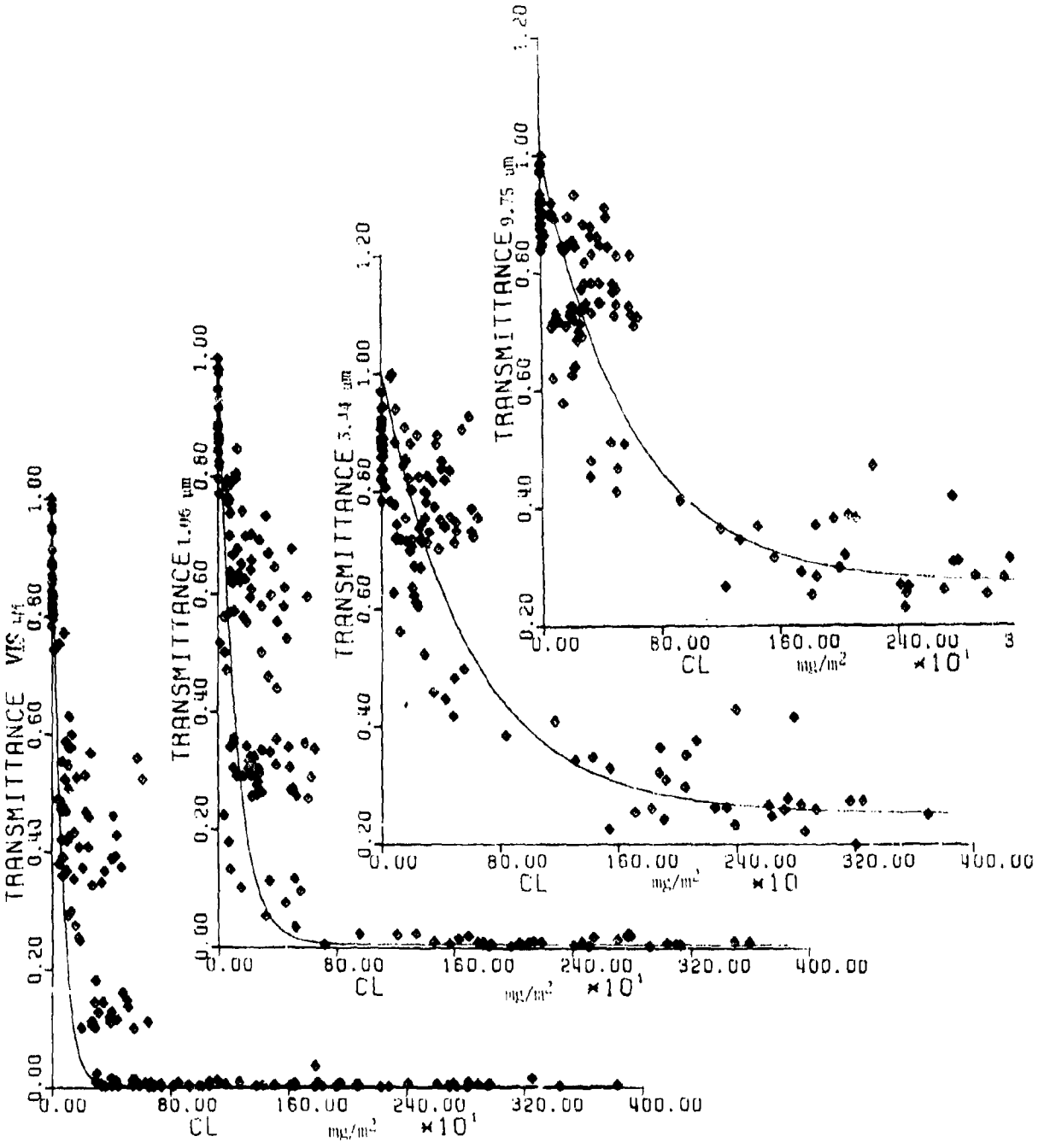

FIGURE 3. CURVE FIT FOR SWIT-T-20 WP SMOKE

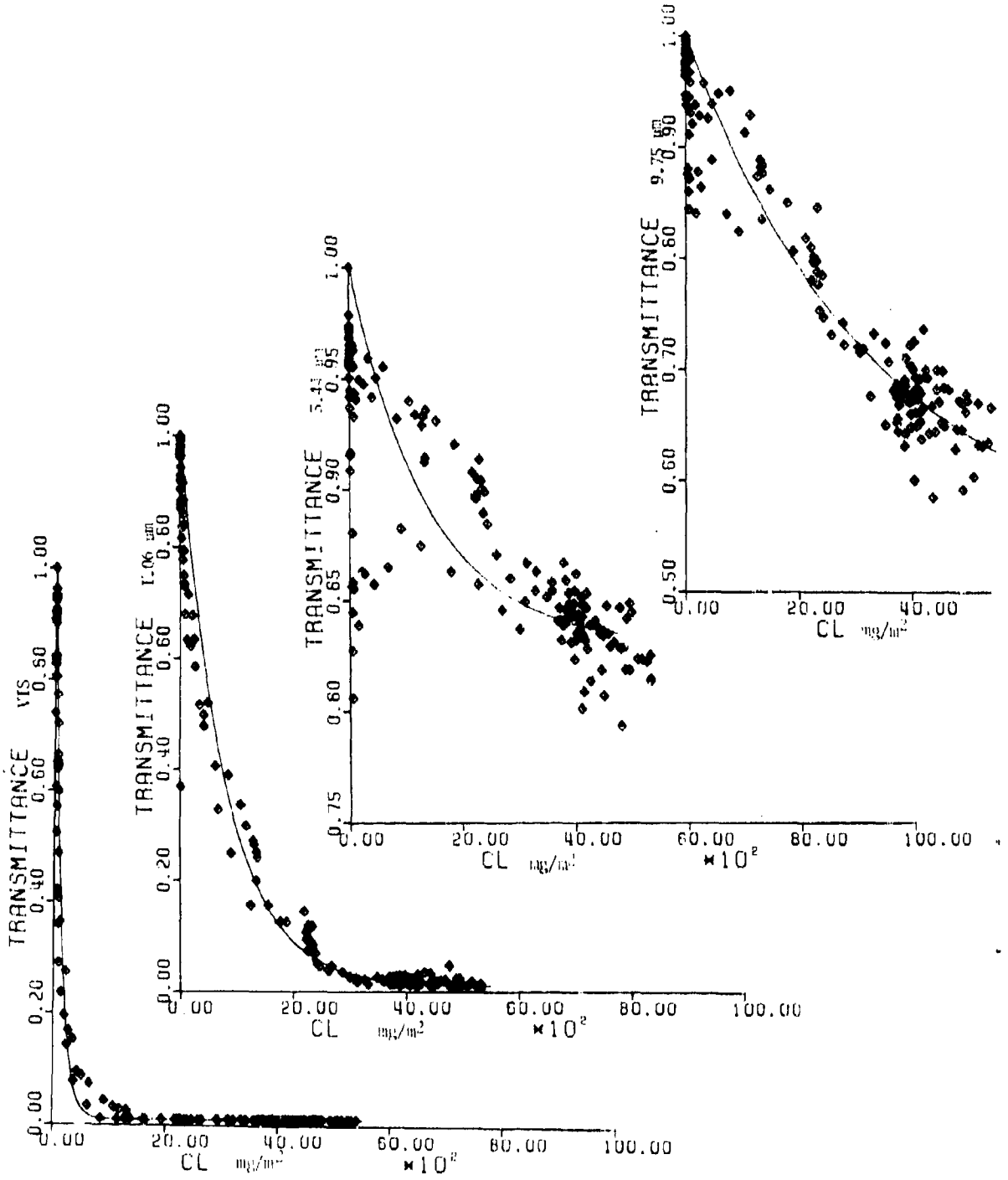

FIGURE 4. CURVE FIT FOR SPITA-T-3 HC SMOKE.

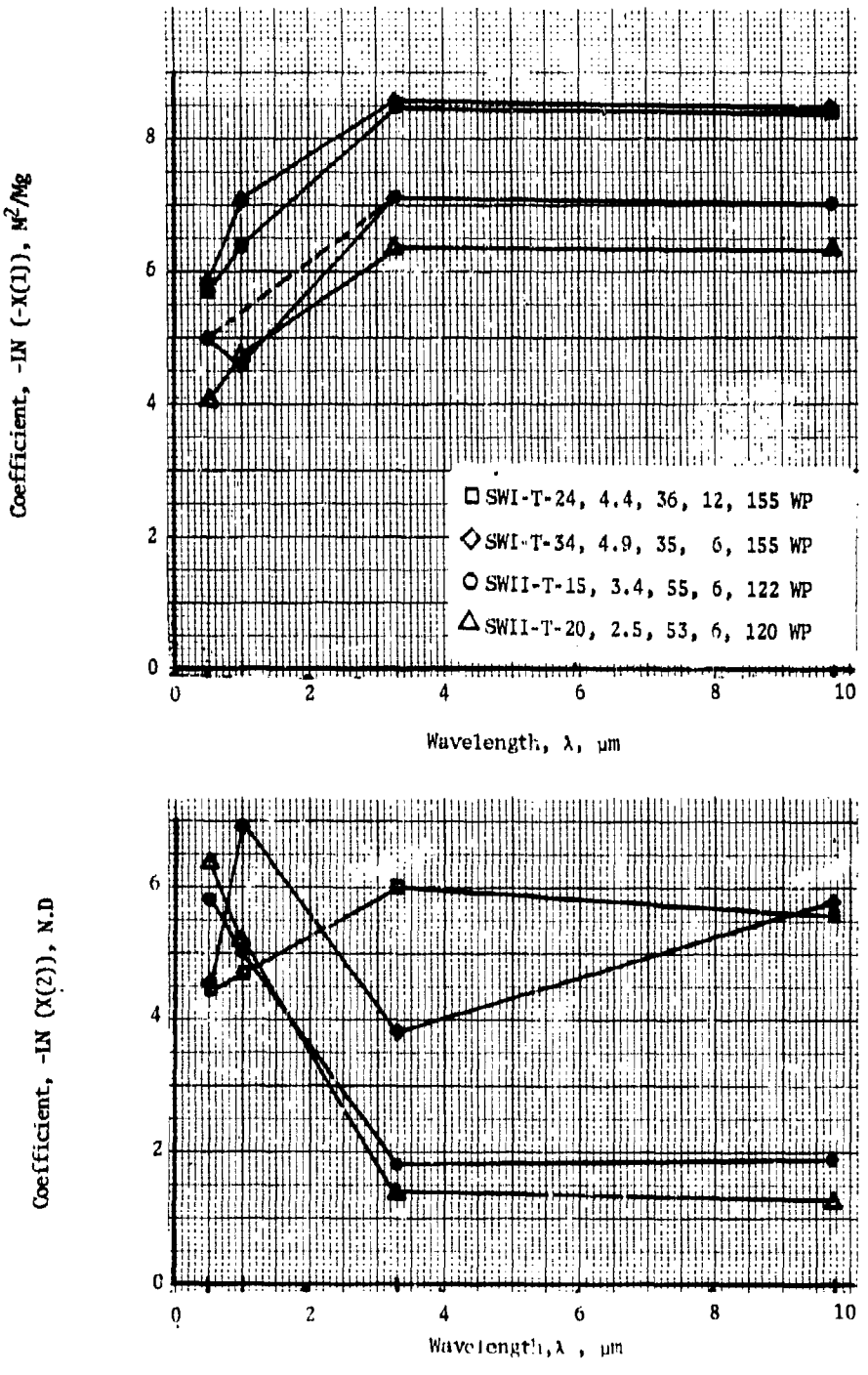

FIGURE 5. CORRELATION COEFFICIENTS FOR WP SMOKE AS A FUNCTION OF WAVELENGTH

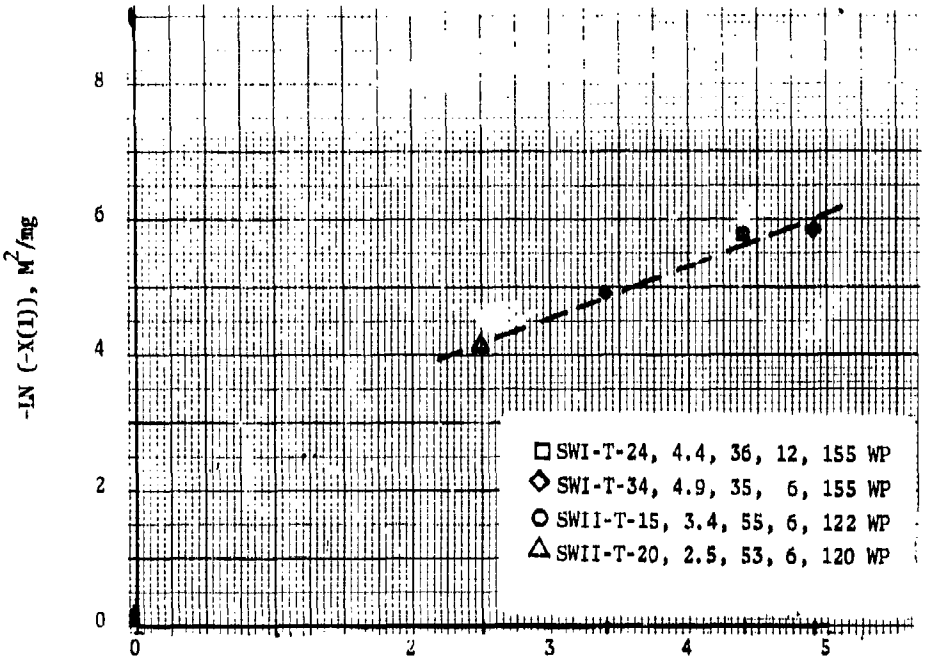

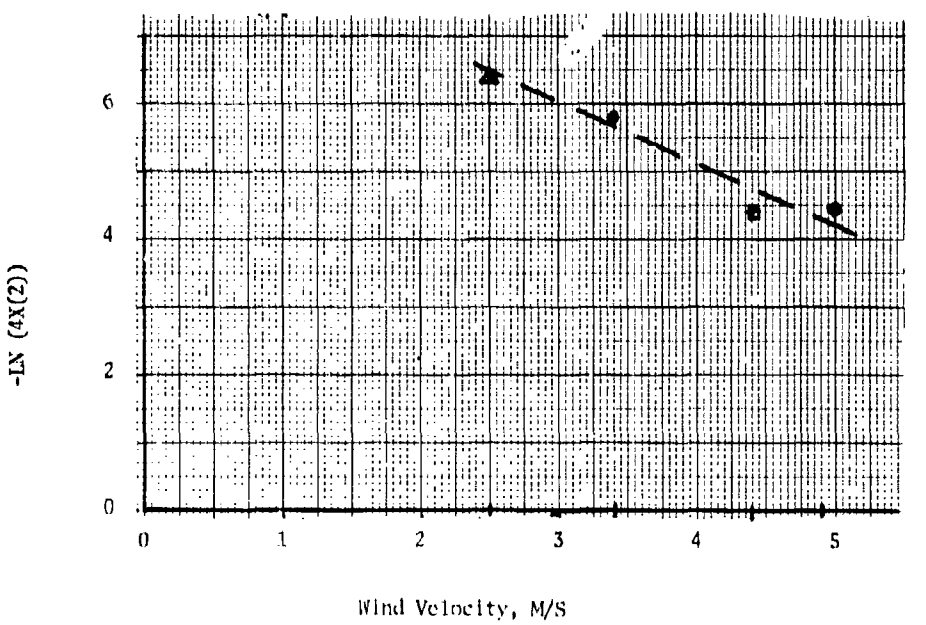

FIGURE 6. CORRELATION COEFFICIENTS VERSUS WIND VELOCITY FOR WP SMOKE AT (0.4 to .7) μm

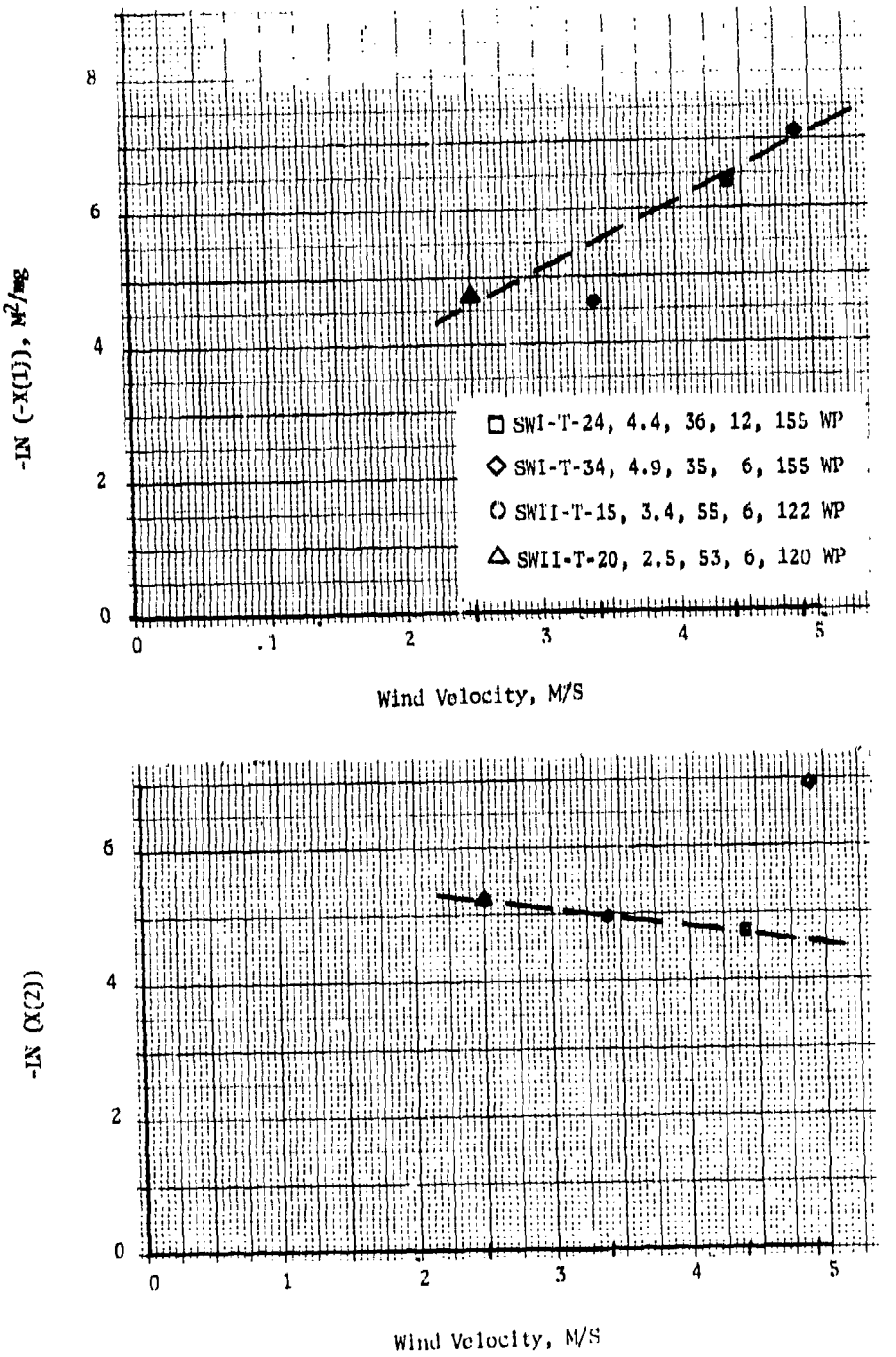

FIGURE 7. CORRELATION COEFFICIENTS VERSUS WIND VELOCITY FOR WP SMOKE AT 1.06 μm

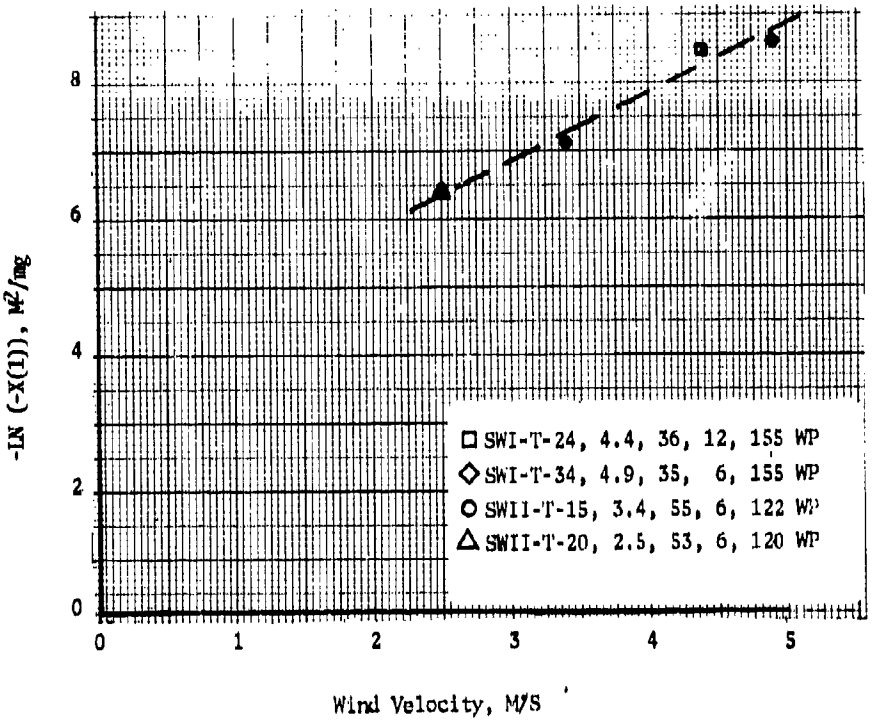

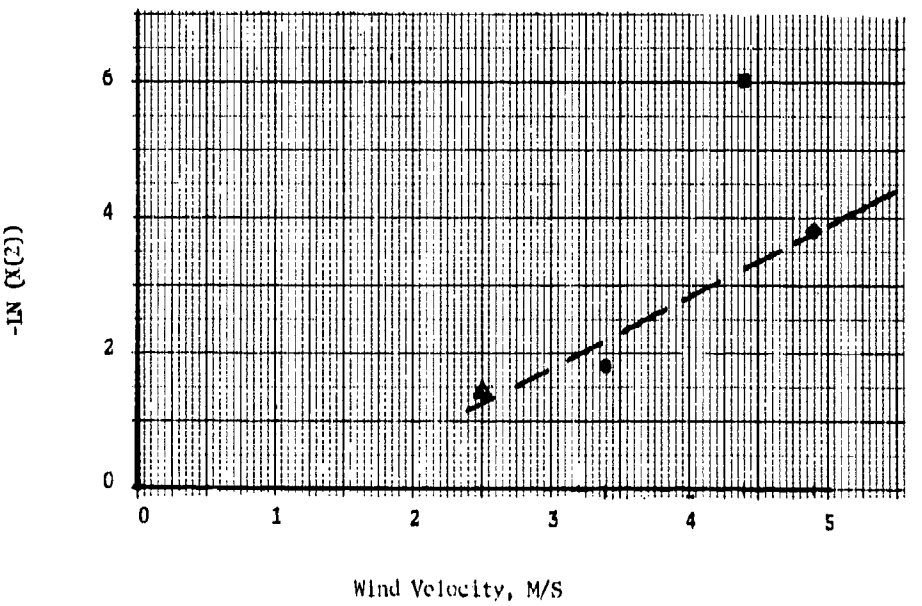

FIGURE 8. CORRELATION COEFFICIENTS VERSUS WIND VELOCITY FOR WP SMOKE AT 3.44 μm.

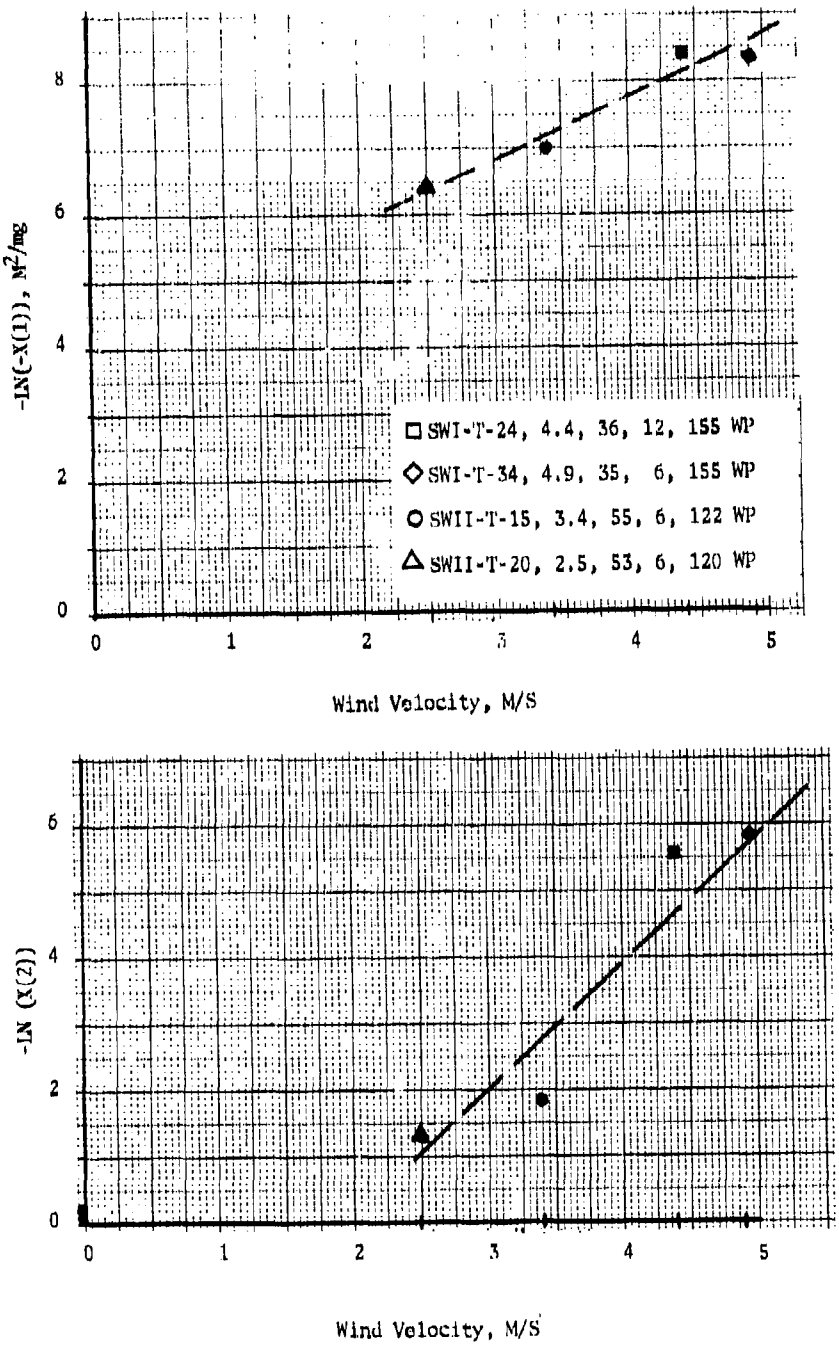

FIGURE 9. CORRELATION COEFFICIENTS VERSUS WIND VELOCITY FOR WP SMOKE AT 9.75 μm.

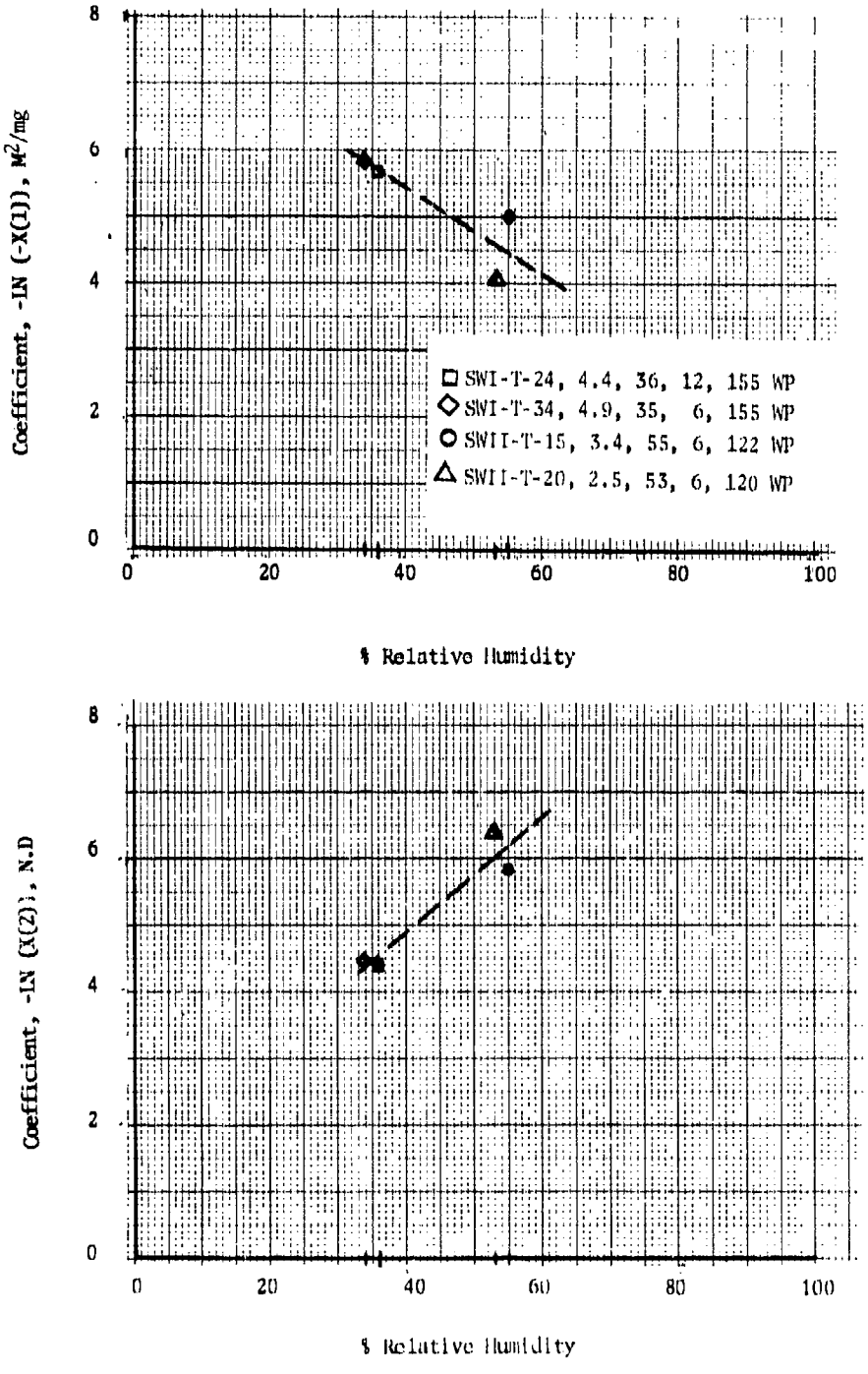

FIGURE 10. CORRELATION COEFFICIENTS VERSUS RELATIVE HUMIDITY FOR UP SMOKE AT (.4 to .7) μm

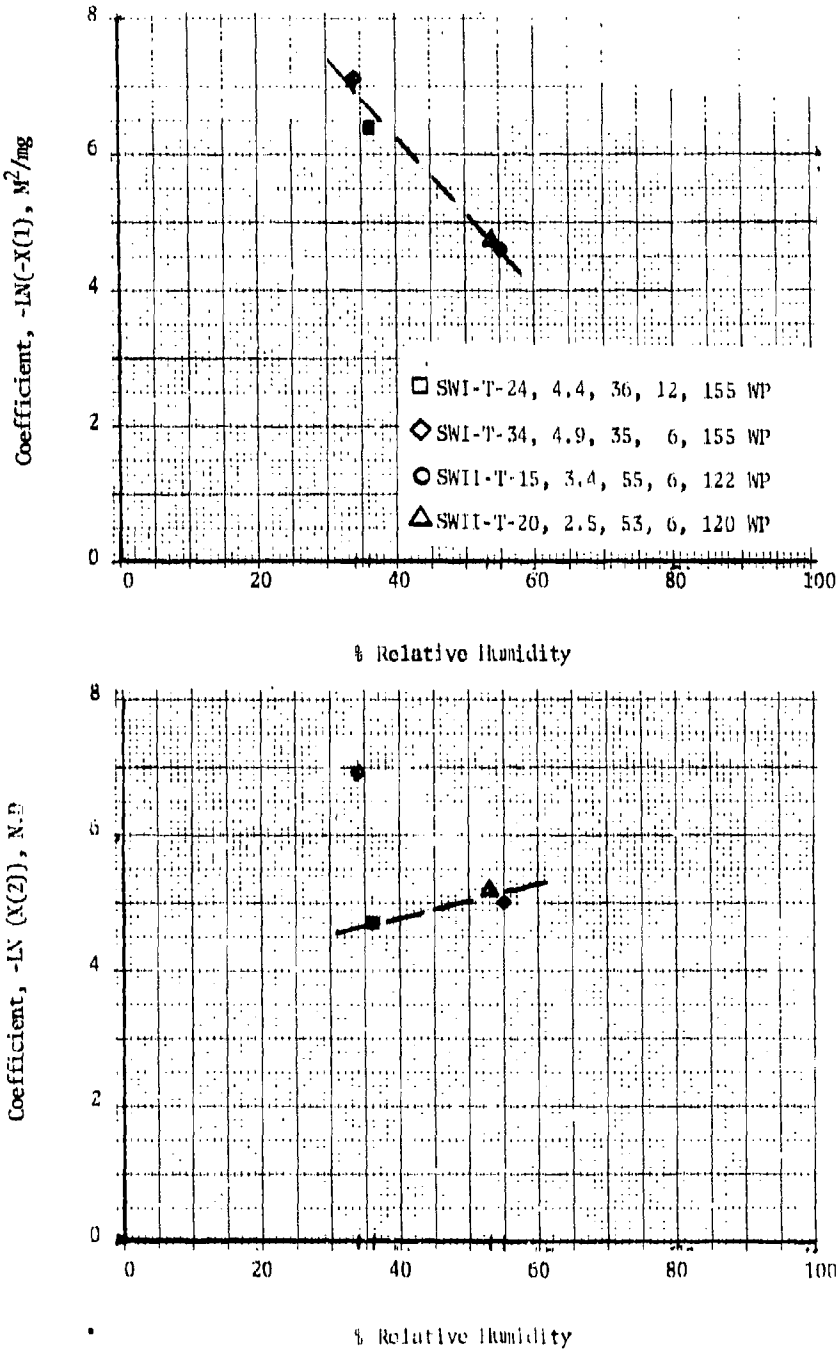

FIGURE 11. CORRELATION COEFFICIENTS VERSUS RELATIVE HUMIDITY FOR WP SMOKE AT 1.06 μm.

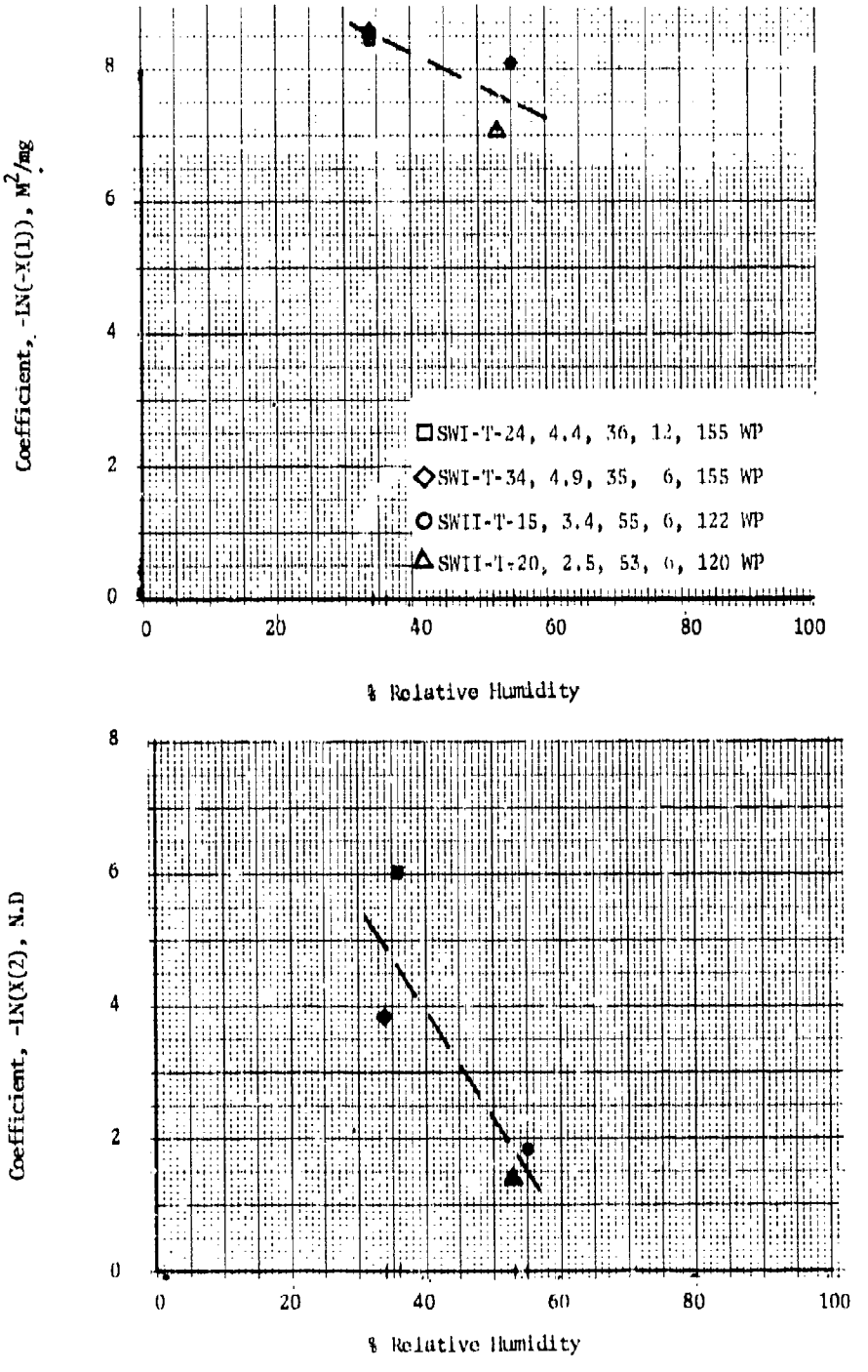

FIGURE 12. CORRELATION COEFFICIENTS VS RELATIVE HUMIDITY FOR WP SMOKE AT 3.44 μm.

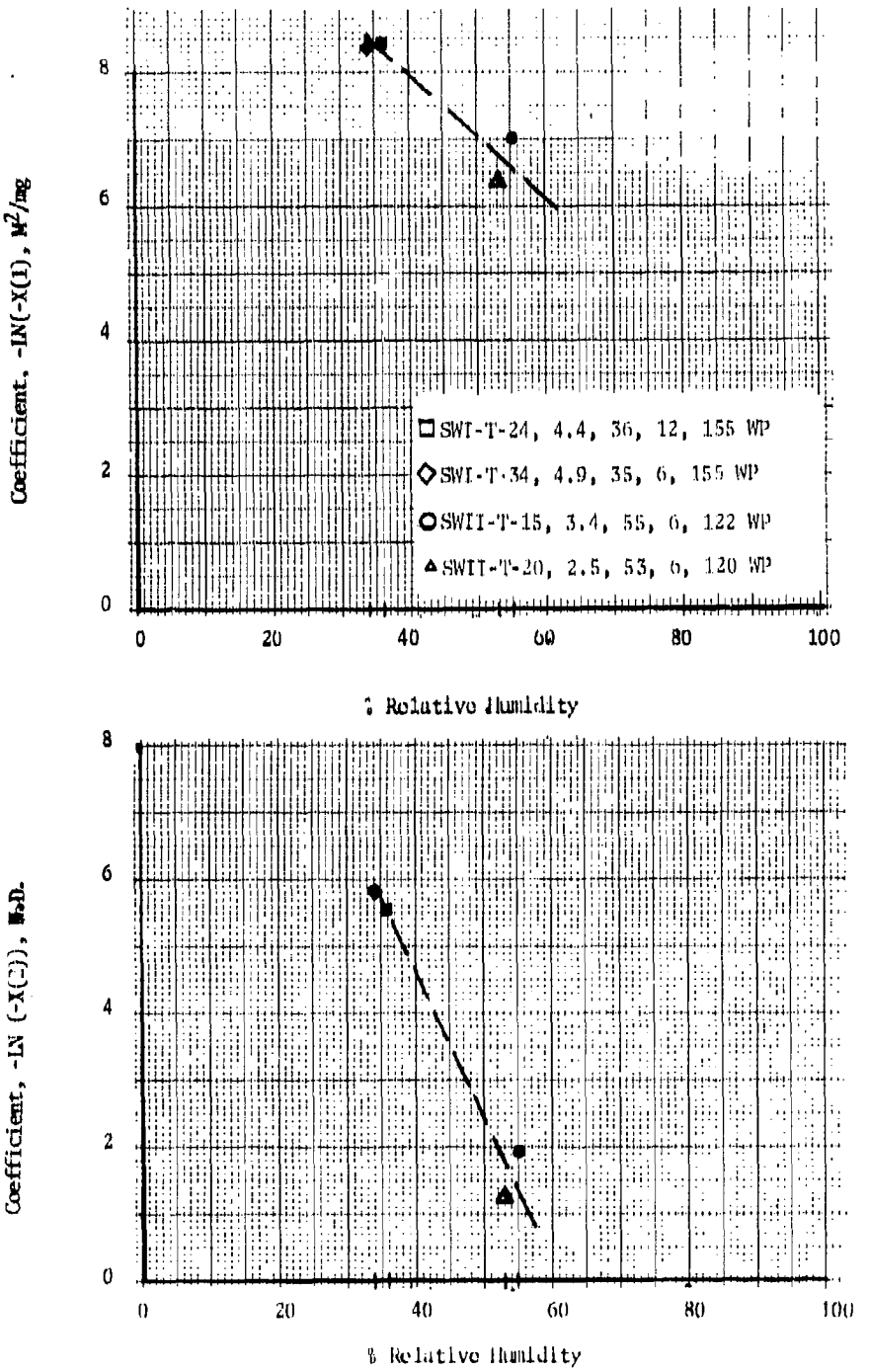

FIGURE 13. CORRELATION COEFFICIENTS VS RELATIVE HUMIDITY FOR WP SMOKE AT 9.75 μm.

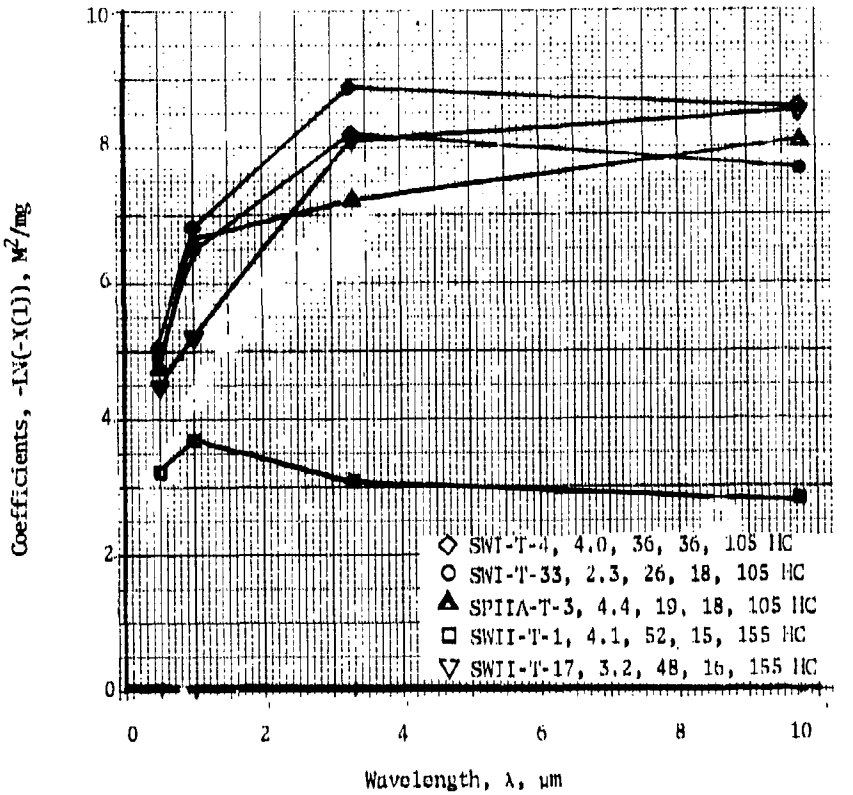

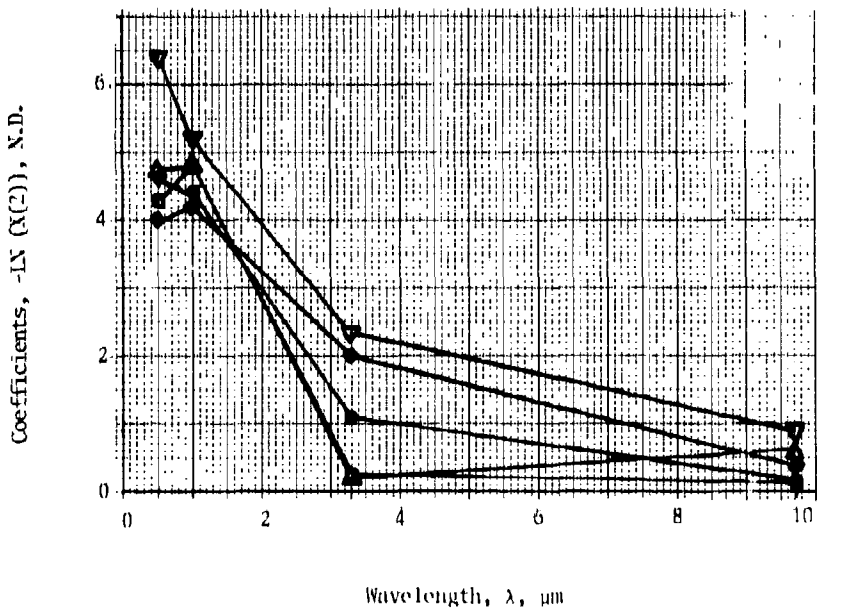

FIGURE 14. CORRELATION COEFFICIENTS VERSUS WAVELENGTH FOR HC SMOKE. (U)

(Unclassified)

forthe WP smoke curves, if the points in Figure 14 were adjusted to show a consistent trend, then the velocity would be linear with respect to the coefficients. A fairly close approximation to a straight line representation exists for both velocity and humidity in the 9.75 μm case. These are shown in Figures 15 and 16 respectively. The best resolution of cloud characteristics occur at the longer wavelengths, since the instruments are not defeated. As seen in these figures, the SWII-T-1 test point is considerably below the others. It is postulated that the level of concentration would influence the values of the coefficients, too. The maximum Cl values for each run were recorded. In this case the Cl values were 1172 for SWII-T-1, 5226 for SWI-T-33, 5498 for SPIIA-T-3, 1375 for SWI-T-4 and 14,139 for SWII-T-17. The units on Cl are mg/M^2. The magnitudes of the -Ln (-X(1)) coefficients corespond to magnitudesof the Cl values. Therefore it is concluded that the magnitude of Cl should be considered as one of the correlating parameters.

Tests run at Smoke Week II using WP Wicks and Wedges of WP and RP were included in the analysis. Figure 17 shows the relationship among the coefficients and wavelengths. These data are more orderly than the HC smoke data. The two lower wavelengths are not ordered but the two upper wavelengths are, and plots of the correlation coefficients versus velocity for thelonger wavelength values tend to be linear relations as shown in Figure 18. This is not true for the coefficients versus relative humidity plots as seen in Figure 19. Three of the points follow a linear relation but the fourth point is far from the curve. The three points in line are from tests having smaller maximum Cl values than the point off the curve. Maximum Cl values for SWII-T-18, 8B and 3 are 4398, 5165 and 5811 respectively whereas SWII-T-24 has a maximum Cl of 24,127 mg/m^2. Again, it is evident that the level of Cl must be taken into account when models are developed to describe the data.

5. CONCLUSIONS

The data reduction technique developed in this paper is general enough to apply to other time-varying situations. In analyzing the results of the technique, it is seen that a definite set of trends is present in the data and, except for some cases, the coefficients are predictable. Improvements in the model can be made which should reduce the scatter in the data.

Results of the data reduction tend to show that the coefficients are functions of (at least) velocity, relative humidity and the maximum level of Cl. Because of the relations among the variables, it is expected that an empirical relation for predicting the coefficients using these parameters is attainable.

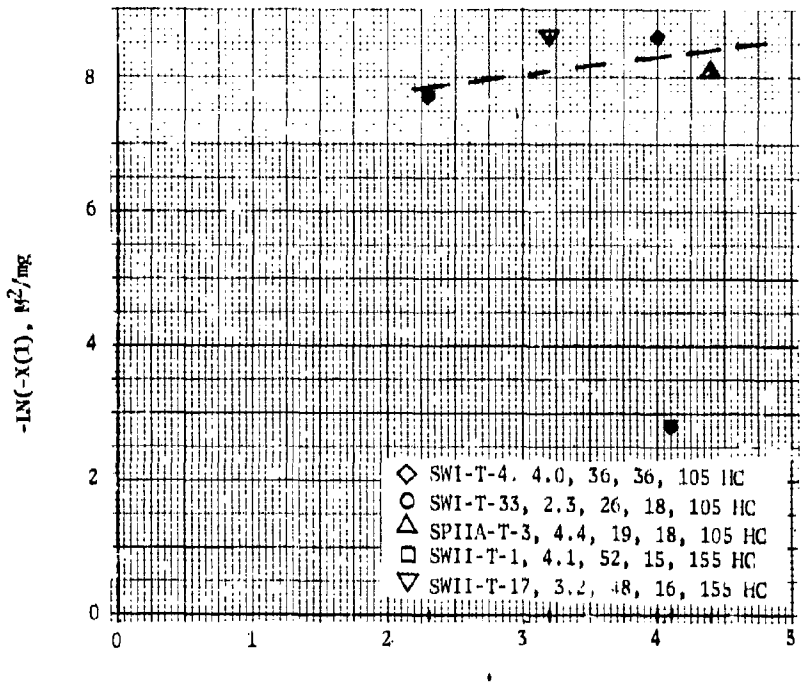

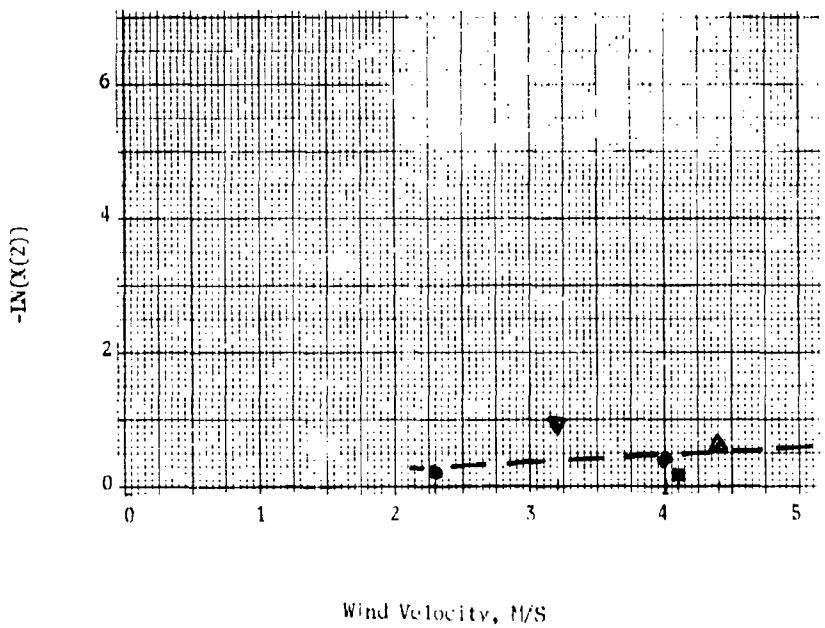

FIGURE 15. CORRELATION COEFFICIENTS VS WIND VELOCITY FOR HC SMOKE AT 9.75 μ.

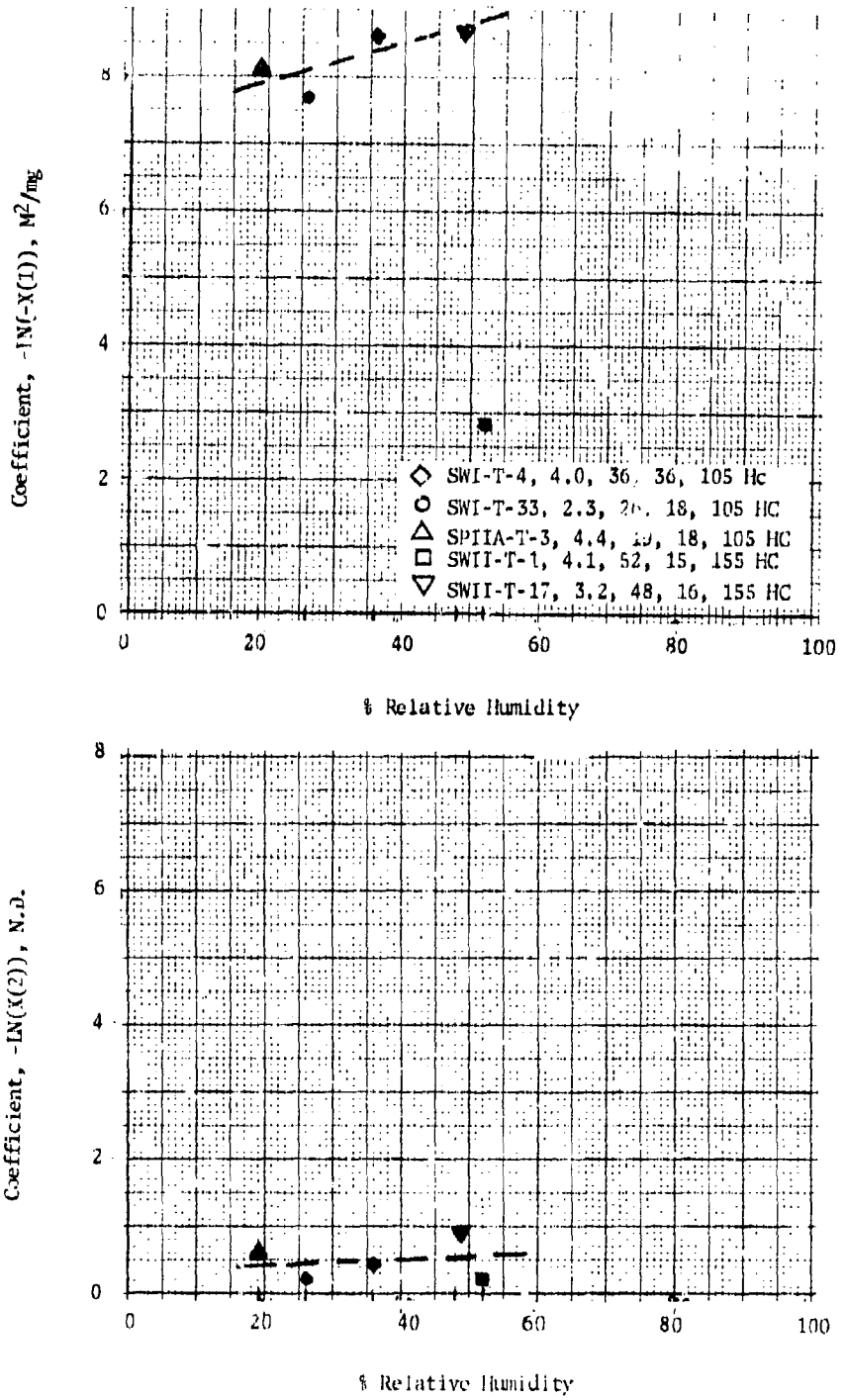

FIGURE 16. CORRELATION COEFFICIENTS VS RELATIVE HUMIDITY FOR HC SMOKE AT 9.75 μm.

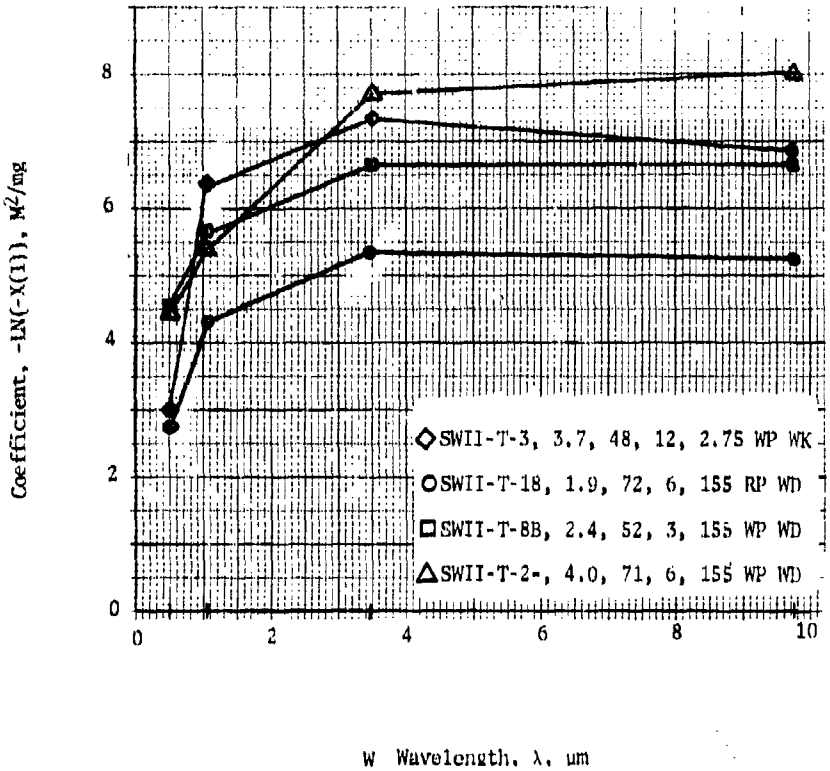

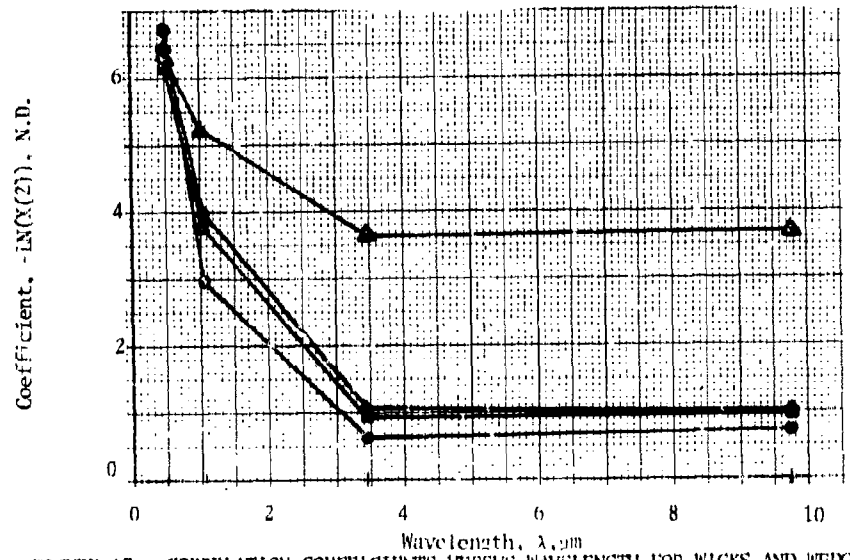

FIGURE 17. CORRELATION COEFFICIENTS VERSUS WAVELENGTH FOR WICKS AND WEDGE SMOKE

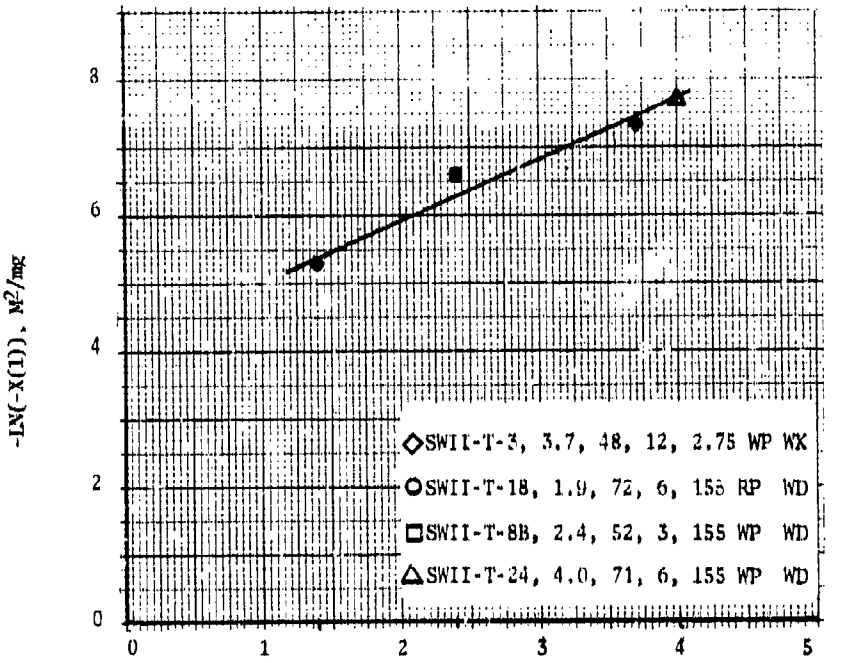

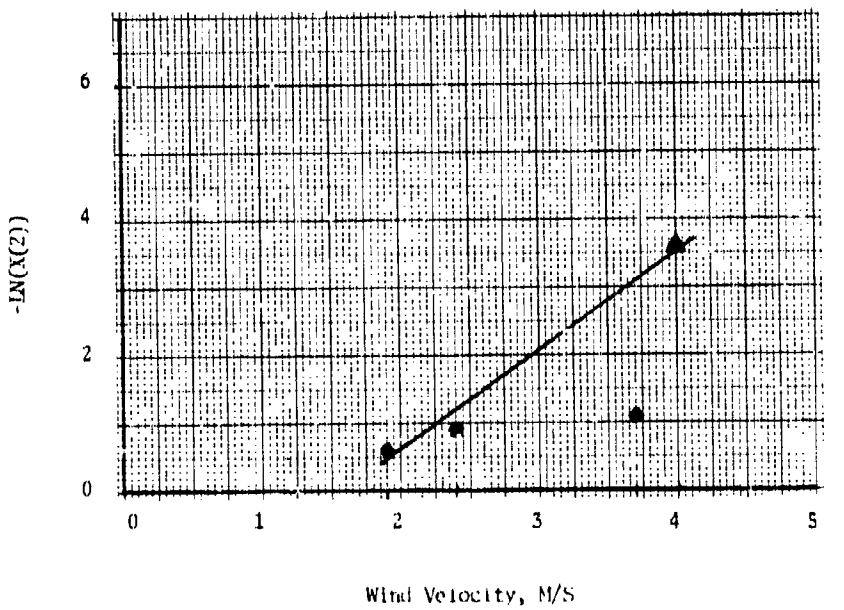

FIGURE 18. CORRELATION COEFFICIENTS VERSUS WIND VELOCITY FOR WICKS & WEDGES.

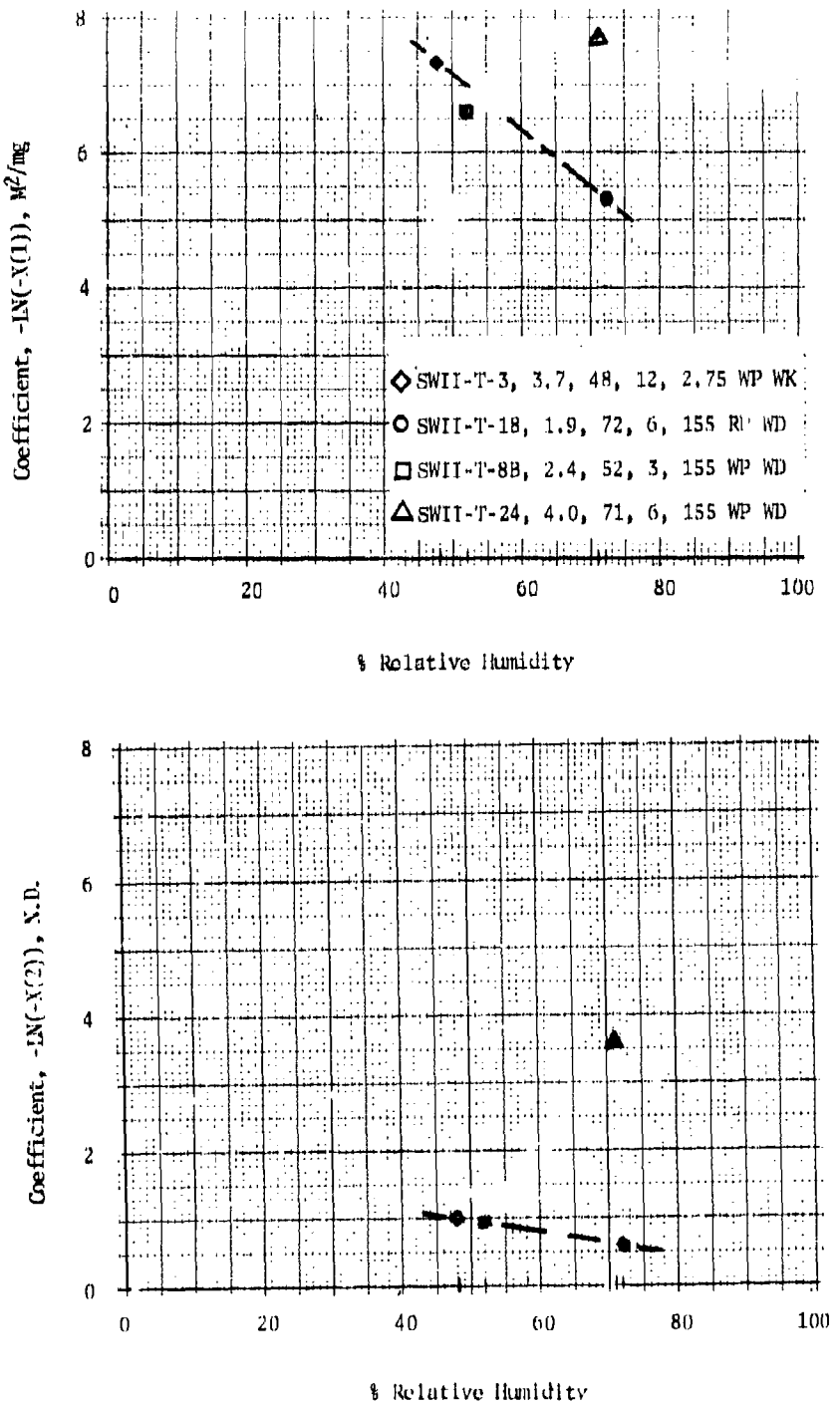

FIGURE 19. CORRELATION COEFFICIENTS VERSUS RELATIVE HUMIDITY FOR WICKS & WEDGES.

6. REFERENCES

1. Methodology Investigation for Testing Effectiveness of Smoke/Aerosol Munitions Pilot Study, Final Report, DPG Document No. DPG-FR-76-701. Dugway Proving Ground, UT, October 1977. (U)

2. Inventory Smoke Munition Test - Phase IIa, Final Test Report, Volumes I and II, DPG Document No. DPG-FR-77-314 (DDC Nos. ADBO 31191L, ADBO 31192L), Dugway Proving Ground, UT, June 1978. (U)

3. Smoke Week I, Electro-Optical (EO) Systems Performance in Characterized Smoke Environment at Dugway Proving Ground, UT-Nov. 77 (U), DRPCM-SMK-T-002-78 (DDC No. ADCO 15328), Aberdeen Proving Ground, MD, April 1978. (Confidential)

4. DPG Final Test Report on Smoke Week II at Eglin AFB, FL, Volumes I and II, DPG Document No. DDPG-FR-78-317, Dugway Proving Ground, Ut, 1979. (Confidential)

5. Marvin D. Smith, Ping Shih and P. Kittikul,"A Transmittance-Cl Relationship Based on Field Test Data," Proceedings of the Smoke/Obscurant Symposium IV, Harry Diamond Laboratories, Adelphi, Md, April 22-23, 1980. (U)

6. Morten M. Denn, "Optimization by Variational Methods" McGraw-Hill Book Co., NY, NY. 1969. (U)

7. John P. Chandler,Quantum Chemistry Program Exchange, QCPE No. 307, Indiana Univ., Bloomington, IN. (U).

8. Hugh D. Young, "Statistical Treatment of Experimental Data" McGraw--Hill Paperbacks, NY, NY. 1962. (U)

9. E.W. Stuebing, "Relative Humidity Dependence of the Infrared Extinction by Aerosol Clouds of Phosphoric Acid," Proceedings of the Smoke/Obscurant Symposium III, Harry Diamond Laboratories, Adelphi, Md., April 24-25, 1979. (U)

THE INSTRUMENTATION CLUSTER CONCEPT IN OBSCURANT FIELD TESTING

W. M. Farmer
The University of Tennessee Space Institute
Tullahoma, Tennessee

ABSTRACT

Recent research has indicated that, for hygroscopic smokes, significant variances exist between extinction coefficient measurements obtained with long transmission paths and those localized measurements obtained from particle size distribution data. Furthermore, uncertainties in the long path measurements due to such factors as atmospheric scintillation and the lack of correlation with other kinds of measurements make error estimates in the determined optical properties difficult, if not impossible, to compute. During Smoke Week III, in addition to long path measurements of concentration and transmittance, data on the physical properties of the tested obscurants are obtained in a localized area with a cluster of instruments. Sufficient redundancy existed in the instrumentation to determine data consistency and instrument stability. In many trials, sufficient data existed to estimate the uncertainty in the determined optical properties. This paper will discuss the instrumentation cluster concept and its significance in field testing. Instrumentation used in the Smoke Week III cluster will be described. Examples of data consistency tests will be given. Examples of data from the instrumentation will be presented and limitations and improvements in the instrumentation cluster concept discussed.

1.0 INTRODUCTION

Prior to Smoke Week III, a reasonably large body of data had been obtained which was used to describe the optical characteristics of a variety of materials used to produce obscurant clouds. These materials included phosphorus, hexachloroethane, fog oils, and a variety of experimental powders and liquids. However, close examination of these data for hygroscopic smokes such as phosphorus revealed a serious discrepancy in values for such fundamental parameters as the mass extinction coefficient and the particle size distribution.[1] It was found, for example, that the mass extinction coefficient, when computed using particle size distribution data, differed markedly from that obtained using field methodology which had been in use for several years. Furthermore, even when comparisons were made between data obtained by different instruments for such fundamental parameters as particle size distributions, poor agreement was found. The degree to which such disagreement existed is aptly illustrated by Figure 1 which plots the mass extinction coefficient for a wavelength of 3.4 micrometers as obtained from a variety of tests and measuring instruments. As the figure shows, the mass extinction coefficient calculated from particle size distribution data is significantly different from that obtained through computations using dosage and transmittance data as was typically done in large field tests such as Smoke Weeks I and II.

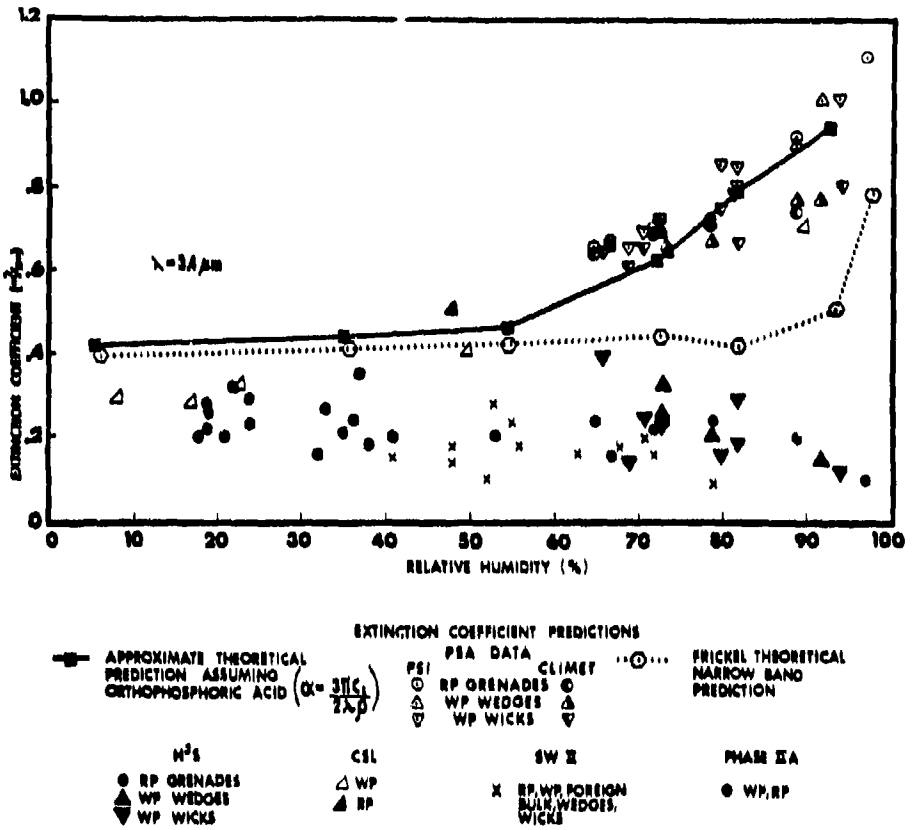

Figure 1. Extinction coefficients measured by different agencies and by different techniques for several field and laboratory trials.

The discomfiture of such discrepancies is further compounded when the results from these tests are evaluated in terms of measurements uncertainty. There are, in fact, very few uncertainties quoted for any measurement such as particle size distribution, mass concentration, or transmission when measured in the field. Very often it is not quoted or known for comparative laboratory data. Thus while, as figure 1 shows, there is a broad discrepancy between the two sets of measurements, neither set can be called correct because it is not known to what degree of accuracy, precision, or consistency any one set of measurements has been made either in the laboratory or the field. A method proposed and adopted for the elimination of many of the uncertainties which have arisen in past measurements was implemented during Smoke Week III. The approach during SWIII was to cluster a number of different kinds of instruments which could be used to compute identical obscurant parameters in a localized position exposed to the obscurants tested during the field trials. The objectives of this cluster of instruments were:

1. to obtain redundant measurements of the same parameter in order to determine the potential spread of data values and to determine the data consistency among the various techniques

2. to develop independent means of estimating parameters from several different instruments which had not been used in past field tests

3. to increase present instrumentation capabilities by developing a data base against which new instrument results could be compared.

As a by-product of this approach, it was hoped that sufficient instrumentation could be used to identify sources of discrepancies in past measurements and possibly identify sources of erroneous data in past tests. In this paper, the cluster of instruments used in Smoke Week III will be called, simply, the instrumentation cluster. It was located very near the center of the sampling grid and contained instrumentation which was capable of 1) determining spectral transmission, 2) measuring particle size distribution, 3) determining aerosol concentration, and 4) determining the turbidity absorption characteristics of various obscurants at a wavelength of 10.6 micrometers. Only the hardware and measurement approaches will be discussed in the present work. A detailed discussion of results obtained with the cluster data is presented elsewhere.[2]

2.0 DESCRIPTION OF INSTRUMENTATION CLUSTER USED DURING SMOKE WEEK III

Table I is used to identify and summarize the basic characteristics of the instruments which were in the instrumentation cluster during Smoke Week III. Table I provides an acronym or three-letter identification for each instrument, the agency which operated the instrument, the measured variable, and the variable range over which the instrument can function. The following discussion briefly describes each instrument and why it was included in the instrumentation cluster.

2.1 INSTRUMENTS USED IN THE INSTRUMENTATION CLUSTER

2.1.1 Short Path Transmissometer

The short path transmissometer (SPT) was operated by the University of Tennessee Space Institute in conjunction with the Barnes Engineering Company, which provided the instrument for the test. The optical path length for this transmissometer was 5m. The transmissometer provided by Barnes was capable of obtaining over 200 transmittance values per second for a range of wavelengths between 2.5 and 14 μm. UTSI provided a microprocessor data acquisition system which was used to acquire data from the transmissometer receiver. Because of limited memory capacity, only thirty seconds of data could be obtained before the data was transferred to magnetic disks, after which the transmissometer was returned to a data acquisition mode. Normally, in many of the trials, sufficient time existed to allow the acquisition of four 30-second samples. Prior to each trial, 30 seconds of clear air measurements

were obtained in order to determine the statistical variation of transmittance with wavelength. These data were used to estimate the uncertainty in transmission for a particular wavelength. The source for the transmissometer was a 1000°K blackbody chopped at 1 KHz rate. The SPT control system and computer memory were housed in a data acquisition system (DAS) box placed in the instrumentation cluster. In order to maintain proper operating temperatures, the DAS box was air-conditioned and sealed during each trial. Instruments operating on the cluster and connected to computers in the DAS box were operated remotely through the computers by terminals located in the University of Tennessee Space Institute (UTSI) instrumentation van. This approach minimized long cabling necessary to operate the cluster instruments.

TABLE I

SUMMARY OF INSTRUMENTS LOCATED IN INSTRUMENTATION CLUSTER

CLUSTER INSTRUMENT	IDENTIFICATION	OPERATING AGENCY	MEASURED VARIABLE	RANGE OF MEASURED VARIABLE	RANGE IN UNCERTAINTY OF MEASURED VARIABLE (% OF MEASURED VALUE)
SPECTRAL TRANSMISSOMETER (SHORT PATH TRANSMISSOMETER)	SPT	UNIV. OF TENN. I.	TRANSMITTANCE	0.01 - 1	40.2 - 1.5% (DEPENDS ON WAVELENGTH)
QUARTZ CRYSTAL MASS MONITOR	QCM	UNIV. OF TENN. I.	CONCENTRATION	10^{-1} - 10^{1} mg/m^3	+1% @ 1000 mg/m^3 +10% @ 1 mg/m^3
ELECTRIC AEROSOL ANALYZER	EAA	UNIV. OF TENN. I.	SIZE DISTRIBUTION NUMBER DENSITY	0.005 - 1 µm 2×10^{3} - 5×10^{7} @ 0.01 µm 5×10^{1} - 10^{6} @ 0.1 µm 10^{1} - 10^{5} @ 0.5 µm	+50% OVER SIZE RANGE GREATER THAN 0.024 µm
ELECTRIC CASCADE IMPACTOR	ECI	UNIV. OF TEXAS	SIZE DISTRIBUTION NUMBER DENSITY	0.25 - 20 µm 10^{-1} - 10^{3} cm^{-3} (3-5 RANGE/INSTRUMENT RELIED)	±5 - 10%
CLINIC PARTICLE SIZE ANALYZER	PSA	UNIVERSITY OF [illegible]	SIZE DISTRIBUTION NUMBER DENSITY	0.1 - 10 µm 10^{2} - 10^{3} cm^{-3} WITH DILUTION	+10 - 100% DEPENDING ON SPECIFIC SIZE
PARTICLE SIZING INSTRUMENTATION	PSI	UNIV. OF TENN. I.	SIZE DISTRIBUTION NUMBER DENSITY	0.2 - 5.0 µm / 0.25 - 20 µm 10^{-1} - 10^{3} cm^{-3}	+10% @ 0.5 µm +1% @ 5.0 µm
FAR-IR SPECTROMETER	FIS	AIR FORCE, NAVY, NASA,	ABSORPTION COEFFICIENT	[illegible] FAR-INFRARED WAVELENGTH	
[illegible]	[illegible]	AIR FORCE, NASA,	SIZE DISTRIBUTION NUMBER DENSITY RANGE	[illegible]	[illegible] SPECIFIC SIZE
RAMAN SCATTER SPECTROMETER	RSS	NASA, NAVAL RESEARCH LAB.	RAMAN SCATTER INTENSITIES CROSS SECTIONS DEPOLARIZATION RATIOS	[illegible] FREQUENCY RESPONSE	[illegible] OVER FULL RANGE FREQUENTLY REQUIRED FREQUENTLY UNDETERMINED
ATMOSPHERIC PHOTOMETER	AP	UNIVERSITY OF [illegible]	CONCENTRATION	[illegible]	5% IN SAMPLE ACQUISITION 5% COLLECTION EFFICIENCY 5% CHORDAL ARRAY (Pi, Ri) 5% CHORDAL ARRAY (Dm, Dil, Di+1, AND Pi+1 2001
[illegible]	[illegible]	UNIVERSITY OF [illegible]	SIZE DISTRIBUTION CONCENTRATION	[illegible]	5% IN SAMPLE ACQUISITION 5% COLLECTION EFFICIENCY 5% CHORDAL ARRAY (Pi, Ri) 5% CHORDAL ARRAY (Dm, Dil, Di+1, AND Pi+1 2001
[illegible]	[illegible]	UNIVERSITY OF [illegible]	[illegible]	[illegible]	5%
[illegible]	[illegible]	AIR FORCE, NASA,	[illegible]	[illegible]	[illegible] OF DIAMETER WHEN PARTICLES ARE LESS THAN [illegible] IN DIAMETER

[illegible]

2.1.2 Quartz Crystal Mass Monitor

The quartz crystal mass monitor (QCM) is a commercially available device (model 3205) from Thermo Systems Inc.[3] It operates on the principle that mass concentrations sampled at a fixed flow rate can be detected by measuring frequency shifts caused by mass accumulations on a quartz crystal which is vibrated at a fixed frequency. The QCM as used on the instrumentation cluster was used with a 100:1 diluter built by the Royco Company and loaned to UTSI by the Aerosol Research Division of CSL. The QCM with the diluter was capable of measuring concentrations up to 1000 mg/m^3 with a resolution of 0.1 mg and it recorded the concentration once per second during the trial. The QCM was housed in the DAS box in order to maintain thermal control of the mass detection crystals thus preventing evaporation of hygroscopic aerosols accumulated on the crystal. The QCM and the electric aerosol analyzer (see section 2.1.3) shared a common data acquisition system which was also located in the DAS box, and both instruments were controlled by remote terminals located in the UTSI van.

2.1.3 Electric Aerosol Analyzer

The electric aerosol analyzer (EAA) is a commercially available device (model 3030) constructed by Thermo Systems Inc., owned by the Chemical Systems Laboratory, and was operated by UTSI. The EAA is capable of measuring the electrical mobility of particles ranging in size from 0.005 μm to 1.0 μm in diameter. Measurement of the electrical mobility allows determination of the particle diameter.[4] The EAA shared the same sampling line as the QCM and was also located inside the DAS box. The EAA requires a two-minute cycle time in order to obtain a size distribution from 0.005 μm to 1.0 μm and is normally too slow to use reliably without a "bag" system in order to trap an aerosol sample from an inhomogeneous cloud. However, because many of the aerosols which were measured during Smoke Week III were hygroscopic, it was felt that a bag system would distort any measured size distribution. It was decided, therefore, to allow the instrument to cycle as necessary through the very dense clouds and merely use the device as an indicator of the range over which small particles might exist in such clouds. Fortunately, during one trial the smoke was sufficiently homogeneous during the sample time that a size histogram was obtained which is believed to be a reasonable representation of the small particles present in the cloud.

2.1.4 Electric Cascade Impactor

The electric cascade impactor (ECI) was constructed and operated by the University of Texas.[5] The cascade impactor is a device which is commonly used to determine the aerodynamic diameter of aerosols through inertial impaction in well defined aerodynamic flows. The University of Texas has modified this basic approach by replacing the mechanical collector normally used to collect the aerosol with an

electrical charging system that can charge the aerosol with reasonable reliability. The amount of aerosol on a particular impaction stage is thus determined through direct measurement of the current imparted to that stage. The ECI was located near the center of the SPT transmission path and used a nominally isokinetic sampling system. It measured a size range wherein the last impaction stage used a filter to cover particle sizes from approximately 0 to 0.25 μm. Additionally, six stages sampled up to a maximum size of approximately 20 μm.

2.1.5 Climet Particle Size Analyzer

This particle size analyzer system was operated by Dugway Proving Grounds and was constructed by the Climet Corporation (model 208).[6] This PSA covers a size range of 0.3 μm to 10 um in 16 size increments and is capable of producing a size distribution once per second. This device measures sampled and diluted aerosols. It determines particle size through pulse height analysis. The measured size distribution is an equivalent latex sphere distribution. Previous studies have indicated that when the aerosols have only real indices of refraction, the particle size range is essentially independent of the index of refraction and the measured sizes should correspond to true sizes.[7]

2.1.6 Particle Sizing Interferometer

The particle sizing interferometer (PSI) was constructed and operated by the University of Tennessee Space Institute.[8] Two PSI systems were used during Smoke Week III. One PSI system was located near the center of the instrumentation cluster,while a second PSI covering the same size range was located approximately 30m off the main grid line (near the secondary sampling line) and was used to study the spatial variations, size distribution, and concentration which might exist in an obscurant cloud. The PSIr were adjusted for two different size ranges during Smoke Week III. Normally, they were operated in a mode such that the size range was approximately 0.2 - 6 μm with size resolution ranging from approximately 0.3 - 6 μm in 21 size increments. The PSI does not require aerodynamic sampling from the cloud and has been shown to be relatively insensitive to particle index of refraction. It is capable of measuring number densities as high as 10^6/cc without dilution.

2.1.7 Laser Spectrophone

The laser spectrophone was constructed and operated by the Atmospheric Sciences Laboratory and utilized a wavelength of 10 6 μm.[9] This device was used to determine the absorption component of the cloud turbidity (i.e. the product of mass extinction coefficient and concentration). It can also be used as a short path transmissometer to determine the mass extinction-concentration product (turbidity).

2.1.8 Particle Measurement Systems Size Analyzer

A Particle Measurement Systems (PMS) particle size analyzer was operated by the Atmospheric Sciences Laboratory.[9] This device covers a range of particle sizes between approximately 0.1 and 10 μm and normally uses illumination from a laser system. It does not sample an aerosol with dilution and can determine number densities to the order of $10^5 cc^{-1}$. The PMS systems were located very near the laser spectrophones on a 3m elevated position in the instrumentation cluster.

2.1.9 Backscatter Nephelometer

A backscatter nephelometer was constructed and operated by Harry Diamond Laboratories.[10] It is designed to determine the backscatter extinction coefficient, turbidity, and depolarization ratio for two different wavelengths by ratioing the backscatter signal for two different solid collection angles. It has been used in several different tests including Smoke Week III.

2.1.10 Integrating Nephelometer

Two integrating nephelometers were operated by the Atmospheric Sciences Laboratory. These devices are commercially available from Meteorology Research Inc. (model 1550). These devices measure the scattered irradiance in the visible over scattering angles ranging between approximately 8 - 170°. These devices produce measures of turbidity and are normally calibrated to read mass concentration.[11]

2.1.11 Aerosol Photometer

The aerosol photometer (AP) was operated by Dugway Proving Grounds.[12] It is available commercially from the Climet Corporation (model 2600). It is designed to determine aerosol concentration through optical scatter magnitude as a function of time by calibration against chemical impinger measurements for known dosages. This device requires aerosol sampling.

2.1.12 Chemical Impinger

The chemical impinger (CI) is a mechanical sampling device operated by Dugway Proving Grounds.[12] It is used to sample and collect an aerosol at a known flow rate for chemical analysis after a particular test. Its resultant output is dosage or time integral values of the concentration.

2.1.13 Mechanical Mass Sampler

The mechanical mass sampler was a high volume sampler operated by Dugway Proving Grounds. It collects a large volume of aerosol on a collection filter for weighing after a test.

2.2 INSTRUMENT ARRANGEMENT

Figure 2 shows how the instrumentation was arranged in the cluster. The measured location coordinates of each instrument is indicated by a dot. The instruments were clustered on a concrete pad which measured 15 x 30 ft. Commercial power was used to drive all instruments in the cluster. This eliminated any measurement uncertainties due to power surges. The instruments were arranged on the concrete pad to take advantage primarily of prevailing winds from the south. The data acquisition box proved to be a major contributor to turbulence around the cluster as did the barrel stands for some of the instruments in the cluster.

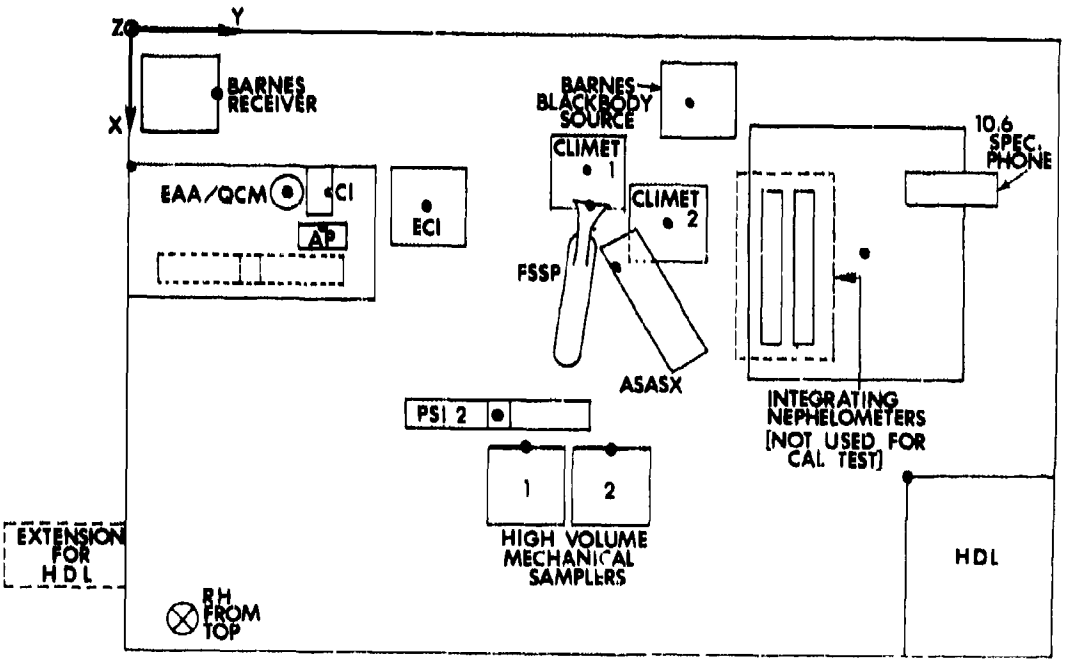

Figure 2. Instrument arrangement on test pad.

2.3 SELECTED EXAMPLES OF DATA OUTPUTS

Of the instruments which were listed and briefly described in section 2.2, the spectral transmissometer, the quartz crystal mass monitor, and the electrical aerosol analyzer are relatively new instruments and have not been used to any significant extent in obscurant field tests. Therefore, examples are presented of the data outputs from these instruments to illustrate their present and potential capabilities.

2.3.1 Spectral Transmissometer

Figure 3 shows a typical wavelength versus transmittance spectrum obtained with the SPT during Smoke Week III. The plot is for a white phosphorus smoke. The blank interval occurring between approximately 5.8 and 6.3 μm corresponds to a change in the response function of the transmissometer's sandwich detector. These data are plotted as a continuous function with linear interpolation between the discrete points. The passband for any one wavelength is approximately 1% of the center wavelength.

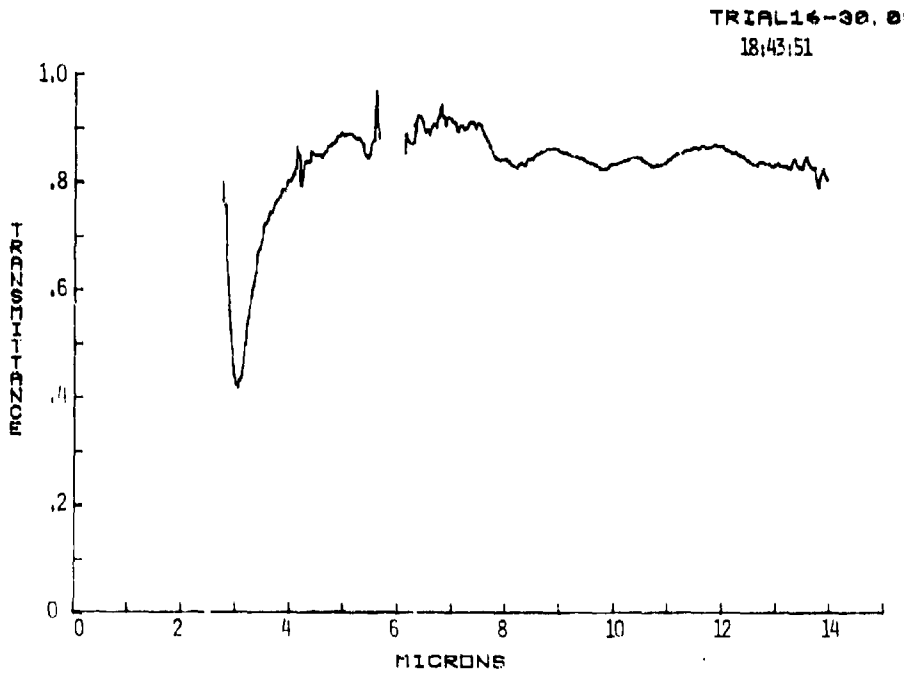

Figure 3. Transmittance spectrum for white phosphorus at 100% RH.

The data shown in figure 3 were acquired in 1 second. For the 30-second block of SPT data, any combination of transmittance as a function of time and wavelength is thus obtainable. These kinds of data were found to be most conveniently represented on the kind of three-dimensional plot shown in figure 4 which will be referred to as a T/t plot, i.e. transmittance, wavelength, and time. By examining these plots, those samples in the particular time sequence can be readily identified for a more detailed study of the type of spectral data indicated in figure 3. The power of this type transmissometer for the kinds of measurements taken in Smoke Week III resides in the fact that the spectral distribution of transmittance is measured over a very broad band of wavelengths of interest. With this data, particular wavelength regions which might be exploited using narrow wavelength devices such as lasers can be identified.

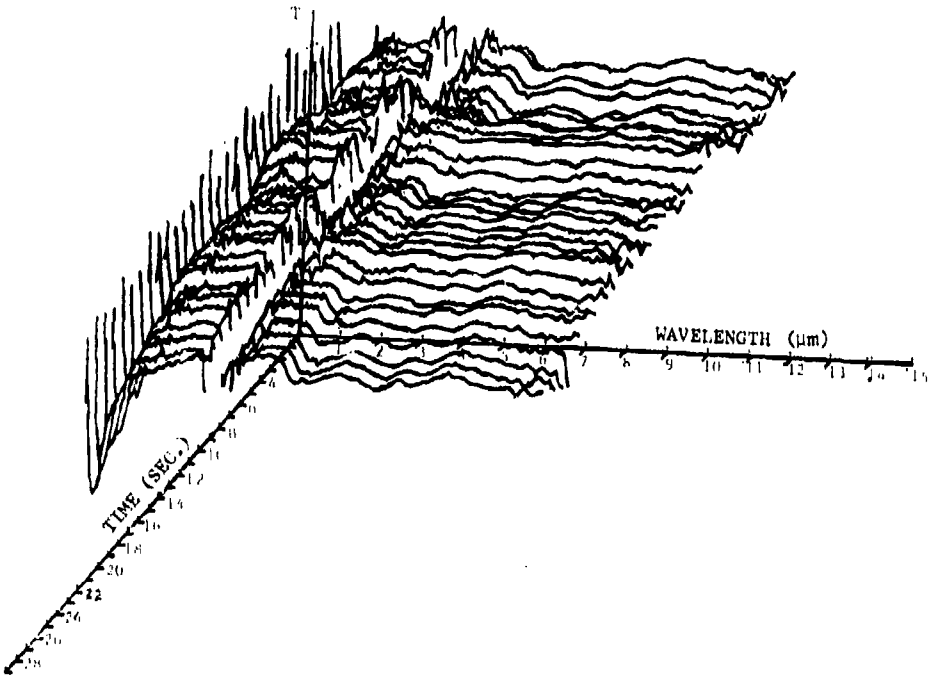

Figure 4. Transmittance, wavelength, time (Tλt) plot for white phosphorus - trial 16 (100% RH).

Identifying such regions cannot be done with broadband transmissometers. However, when it it desired, broadband transmittance can be estimated with the spectral transmissometer by integrating the detailed spectrum over the range of interest. By choosing a transmittance at some reference wavelength and computing ratios of ln(T) to the reference transmittance, data of this kind can be exploited to determine virtually any relative mass extinction coefficient in the full range from the near to far IR.

2.3.2 Quartz Crystal Mass Monitor

An example of the type of data which was obtained with the QCM is shown in figure 5. Figure 5 plots the accumulative mass concentration measured with the QCM as a function of time. The accumulative concentration measured over the entire trial time is identical to the parameter commonly referred to "dosage". Figure 5 also plots the instantaneous concentration as a function of time for 1-second averages as measured by the QCM. By using data such as is illustrated in figure 5, yield factors which are directly applicable to those dosages obtained with mechanical mass samplers can be determined directly in the field experiment.

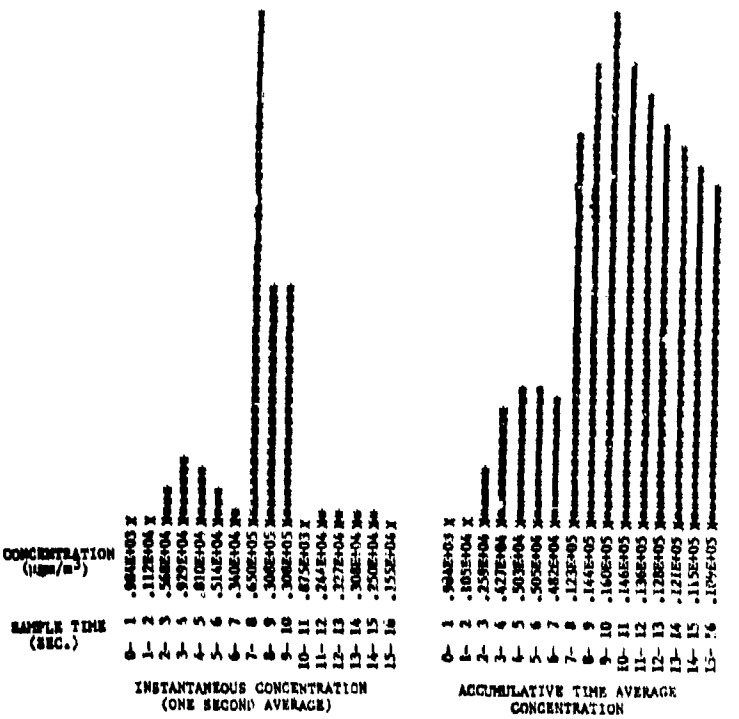

Figure 5. Examples of QCM output.

2.3.3 Electrical Aerosol Analyzer

Figure 6 plots a particle size distribution which was obtained for white phosphorus using the electrical aerosol analyzer. This size distribution was the only full distribution obtained during the Smoke Week III tests using the EAA because of its relatively long two-minute cycle time. Numerous data were obtained for the larger size increments measured by the EAA because the sample time for the larger size increments only corresponds to roughly 1/4 that of the entire cycle.

3.0 MEASUREMENT COMPARISONS

In this section, it is shown how the various measurements obtained in the instrumentation cluster can be used to compute the basic quantities needed to optically characterize an obscurant cloud.

3.1 EXPRESSIONS FOR THE BASIC PARAMETERS

3.1.1 Mean Extinction Cross-Section

The mean extinction cross-section may be determined either from size distribution measurements when the extinction efficiency is known or from transmittance values and number density estimates.

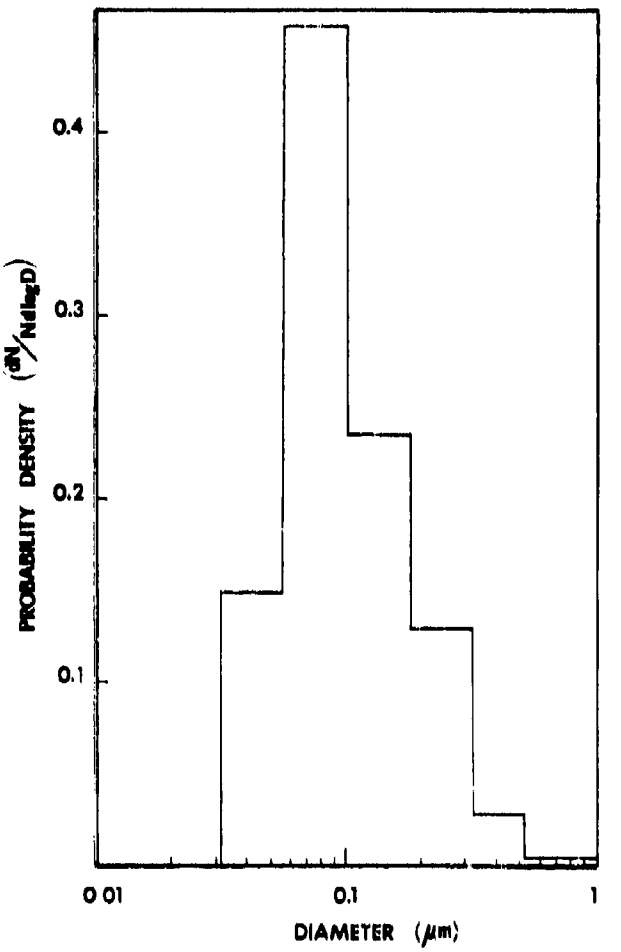

Figure 6. 0.007 - 1 μm particle size distribution probability density function measured by EAA for trial 18, white phosphorus .

Consider first how size distributions are used to estimate the mean extinction cross-section. Suppose a particle size analyzer obtains the size distribution in "n" discrete size increments; then, assuming that the aerosol is sampled randomly, the probability, f_I, of obtaining a particular measurement in the Ith size interval is given by

$$f_I = \frac{n_I}{N} \qquad (1)$$

where

$$N = \sum_{i=1}^{n} n_i \tag{2}$$

and n_i is the number of measurements in the ith size interval. The mean extinction cross-section, $\bar{\sigma}$, can then be written as

$$\bar{\sigma} = \frac{\pi}{4} \sum_{i=1}^{n} Q_{Ei} D_i^2 f_i \tag{3}$$

where Q_{Ei} is the extinction efficiency for the largest particle diameter, D_i, in the ith size interval. Q_{Ei} can be computed for spherical particles from Mie scattering theory when the index of refraction of the obscurant material is known.

Most particle size analyzers can determine particle number density, ρ_N, independently of the measured size distribution. This can be achieved by counting particles at a fixed flow rate (PSA) or by determining particle coincidence in a small sample volume optically placed in a large unperturbed volume of the aerosol. Examination of the Beer-Bougher law as expressed in the equation

$$T = e^{-\bar{\sigma}\rho_N L} \tag{4}$$

where T is the transmittance and L is the transmission path, shows that a number density and transmittance measurement also yields $\bar{\sigma}$, i.e.

$$\bar{\sigma} = \frac{-\ln(T)}{\rho_N L} \tag{5}$$

Hence, $\bar{\sigma}$ can be estimated directly using two relatively independent experimental measurements -- transmittance and number density.

3.1.2 Mass Extinction Coefficient

The mass extinction coefficient, referred to simply as the "extinction coefficient", is often used to characterize the optical characteristics of an obscurant rather than $\bar{\sigma}$. The mass extinction coefficient, α, is defined as

$$\alpha = \bar{\sigma} / \frac{\pi}{6} \rho_o \mu_3 \tag{6}$$

where ρ_o is the material density of the obscurant and μ_3 is the third moment of the particle size distribution or, equivalently, $\pi/6\ \mu_3$ is the mean particle volume. α is thus the mean extinction cross-section per mean particle mass. α can be computed using particle size analyzer data by computing $\bar{\sigma}$ as indicated in section 3.1.1, equation 3. The third moment of the size distribution can be computed

according to

$$\mu_3 = \sum_{i=1}^{n} f_i D_i^3 \tag{7}$$

Then, when ρ_o and Q_{Ei} are known, data from the particle size analyzer can be used directly to estimate α.

α can also be determined from transmittance values when the aerosol concentration, C, is known. In this case, the Beer-Bougher law can be expressed as

$$T = e^{-\alpha CL} \tag{8}$$

which can be solved to yield

$$\alpha = \frac{-\ln T}{CL} \tag{9}$$

Hence, independent measurement of C and T can be used to measure α values independently of the size distribution. Historically, this has been the approach to determine α, since C was believed to be more easily and more reliably measured than ρ_N.

3.1.3 Mass Concentration

Mass concentration is also considered a basic obscurant paramter which should stand on the same footing with α. This follows from the fact that, even though the α values of an obscurant may be relatively small, that obscurant might be generated in sufficient quantitites to more than offset a small α value. The QCM was used to provide a direct measure of mass concentration as a function of time. The particle size analyzers were also used to estimate concentration through the relationship

$$C = \frac{\pi}{6} \rho_o \mu_3 \rho_N \tag{10}$$

Equation 10 shows that if C is measured independently, then the consistency of the PSI, $\mu_3\rho_N$ measurement can be tested when ρ_o is known.

3.1.4 Particle Size Distribution Moments and Means

As the previous sections have indicated, particle size analyzers can be very powerful instruments in characterizing aerosols. The size distribution of the aerosol is itself a fundamental characteristic needed to describe its optical properties. To obtain comparative measures, the size distribution of the measured aerosols can be characterized by various means and moments obtained from the distribution. The kth moment, μ_k, of the size distribution is defined through

$$\mu_k = \sum_{i=1}^{n} f_i D_i^k \tag{11}$$

Using this relationship a number of different mean sizes can be defined. These means are:

1. Arithmetic average diameter, D_A:

$$D_A = \mu_1 \tag{12}$$

2. Sauter Mean Diameter (volume to area mean), D_s:

$$D_s = \mu_3/\mu_2 \tag{13}$$

3. Volumetric Mean Diameter, D_v:

$$D_v = \mu_3^{1/3} \tag{14}$$

3. Mass Mean Diameter, D_{mm}:

$$D_{mm} = \mu_4/\mu_3 \, . \tag{15}$$

Additionally, a log-normal size distribution is often assumed to apply to these data, in which case the geometric mean diameter, D_g

$$D_g = \exp\left[\frac{1}{N}\sum_{i=1}^{n} f_i \ln D_i\right] \tag{16}$$

and the geometric standard deviation σ_g

$$\sigma_g = \exp\left[\frac{1}{N}\sum_{i=1}^{n} f_i \ln^2(D_i/D_g)\right] \tag{17}$$

are the pertinent parameters. Comparison of the means, moments, and mode locations provides a convenient reference point for comparing distributions from different instruments.

3.2 POSSIBLE DATA COMPARISONS

One of the major objectives in using a number of different instruments in the instrumentation cluster was independent determination of many of the parameters described in section 3.1. Thus tests of internal data consistency and cross-checks of the various parameters which might be determined using the calculational procedures indicated in sections 3.1.1 through 3.1.4 can be created. Table II summarizes how the various instruments could be used to estimate the parameters of interest from data which could be collected from the instrumentation cluster. The instruments are indicated by row and the parameter of interest is indicated by column. Combinations of particular instruments are indicated which can be used to yield the parameter of interest. For example, the column headed by (SPT, QCM) shows that the mass extinction coefficient could be estimated from the data obtained using these two instruments with equation 9. The summary of individual estimates indicated in Table II provides an intrinsically enlightening look at the power of the optical and cascade particle size analyzers. It will be noticed

that, potentially, these devices can determine every parameter indicated in the left hand column when the particles can be assumed to be spheres and the index of refraction and material density are known.

TABLE II

METHODS USED IN SMOKE WEEK III
FOR ESTIMATING OBSCURANT OPTICAL PARAMETERS

INSTRUMENT OR METHOD / PARAMETER	SPT	QCM	SPT, QCM	OSA	CSA	SPT, OSA	SPT, CSA	QCM, OSA	QCM, CSA
MEAN PARTICLE DIAMETER				X	X[2]				
PARTICLE NUMBER DENSITY				X	X[2]			X[2]	X[2]
MASS CONCENTRATION	X[1]	X		X[2]	X[2]				
MEAN EXTINCTION CROSS-SECTION				X[2,3]	X[2,3]	X	X[2]		
MASS EXTINCTION COEFFICIENT			X	X[2,3]	X[2,3]	X[2,3]	X[2,3]		
TURBIDITY	X			X[2,3]	X[2,3]	X[2,3]	X[2,3]		
MEAN PARTICLE VOLUME				X	X[2]			X[2]	X[2]

1. WHEN MASS EXTINCTION COEFFICIENT IS KNOWN
2. WHEN MATERIAL DENSITY IS KNOWN
3. WHEN PARTICLES ARE SPHERES AND INDEX OF REFRACTION KNOWN

SPT: Short Path Transmissometer
QCM: Quartz Crystal Mass Monitor
OSA: Optical Size Analyser
CSA: Cascade Size Analyser

3.3 PARAMETER ESTIMATION LIMITATIONS

The approach which has been discussed for the instrumentation cluster alleviates many of the limitations encountered in past field measurements (e.g. insufficient instrument redundance and unknown errors). However, there are at least four major limitations which will restrict the potential utility of this approach in obscurant field characterization. These limitations are 1) different ranges in the parameters mensured, 2) different sampling times, 3) different spatial locations, and 4) different volumes of aerosol examined by the different instruments.

It should be clear that identical answers should not be expected from instruments which have different ranges of comparison or measure over different ranges. Thus, it is necessary to carefully choose instruments for the comparisons in which the ranges of the parameter to be determined significantly overlap. In the final analysis, the potential errors which are introduced into the separate sets of

measurements by ignoring the data values beyond the range of each instrumental measurement should be examined. This becomes particularly apparent when particle size analyzers are considered. For example, it often occurs that measured particle size ranges do not overlap, the histogram size increments are not the same, the aerosol is sampled differently, and significantly different volumes of aerosol are examined.

If the instruments used to measure a smoke cloud do not sample at the same rate or sample in an on/off sequence such that the sampling times do not correspond to observation of identical parts of the obscurant clouds, obvious discrepancies in the data may arise. This difficulty can be alleviated in part by looking at long time averages of the data such that short variations due to time lags between instruments may be reduced to insignificant quantities. Additionally, techniques exist and have been applied which tend to remove the effects of sample acquisition time and spactial location of the instruments if it can be assumed that, eventually, the instruments will sample the same portion of the cloud even though at different times and even though the equivalent sample response times are known.[2]

The problem of physically locating the sampling instruments such that the physical presence of one instrument does not interfere with the aerosol being sampled by another instrument is one which can lead to errors and which must be examined carefully. These errors are of two types. First, disturbances are introduced into the wind flow carrying the aerosol to the instruments. Second, lag times are introduced into the sampling system of the instrument. As a result, when data are considered for identical sample times, the instruments are actually responding to significantly different portions of the cloud. The problem of lag times is one which requires additional study, although there presently appears to be reasonably straightforward solutions to eliminating this difficulty. The problem of flow interference can be solved by careful studies of the location of the instruments for various wind directions and choosing to place the instruments on support structures which will not block or deviate the wind flow.

The limitation introduced by the fact that each instrument can potentially sample a significantly different volume of aerosol bears additional evaluation. For example, the short path transmissometer examined a volume of aerosol which corresponded to cylinder having a cross-sectional area defined by the diameter of the transmitted beam (10 cm) and by the 5m path. If the wind direction is assumed normal to the line of site the sampled volume is the product of this cross-sectional area multiplied by the wind velocity and sample time. (For a 30-second sample time and 3m/sec. winds this could correspond to a volume of 4.5 m^3. On the other hand, the particle size analyzers of the Climet type withdraw an aerosol at a fixed flow rate which is typically of the order of litres per minute. This volume obviously corresponds to a volume approximately 10^{-5} times smaller than that defined by the

SPT. Additionally, the QCM will also examine a much smaller volume of aerosol. Thus, an assumption must be made that the volumes sampled by the low volume instruments are reasonably representative of the much larger volume sampled by the SPT. A method for circumventing this difficulty is to use a number of different instruments such that 1) reliable statistics can be obtained for a given kind of instrument, and 2) a significantly larger spatial sample of the aerosol will be examined by a single kind of instrument.

4.0 SUMMARY AND CONCLUSIONS

Results obtained from the instrumentation cluster described elsewhere show clearly that clustering such instruments has yielded valuable data not obtained before. These data have shown, for example, a temporal dependence of the mass extinction coefficient for hygroscopic smokes that has provided a possible explanation of why the mass extinction coefficient obtained with particle size analyzers is usually significantly larger than that obtained by long path transmission-chemical impinger data.[2] The consistency and expected spread of measurements which can be expected for a given set of measurements has been demonstrated. Lastly, the spectral dependence of the extinction coefficient for a broad range of wavelengths between 2.5 and 14 μm has been obtained.

It has been found that the optical size analyzer, QCM, and SPT systems are powerful combinations of instruments for determining mass extinction coefficient, mean extinction cross-section, concentration, and spectral transmittance, and for parametric comparisons of data consistency.

The Smoke Week III test was the first attempt at using a cluster of instruments to obtain the type of data which has been provided by widely spaced instruments in the past. It has been obvious from analysis of the data that greater care should be paid to instrument arrangement and flow patterns around the instruments in future work. The value of the short path transmissometer data is obvious. However, in future tests, it is most desirable to be able to run the transmissometer continuously with a much expanded computer memory. It is also desirable to sample at even a higher rate than 200 wavelengths per second in order to determine the upper limit at which the mass extinction coefficient may fluctuate.

It is also recommended that an effort be made to require that the instruments function in a common sampling sequence and to further increase the data redundance by using more than one particular kind of instrument in order to cross-check the potential variations which might be introduced due to sampling different volumes of the flow and potential measurement errors by a given instrument.

A fundamental problem encountered in clustering the instruments in a localized area was the subjection of the test to the variability of the wind, e.g., if the wind changed such that the obscurant was not blown past the cluster, then the test had to be delayed until the wind was in a suitable direction. This difficulty can be overcome by utilizing a mobile system which could be positioned at

advantageous points during a particular trial for optimal wind location. It may be desirable to place such a unit at various downwind positions for the same type of obscurant in sequential trials to determine how the obscurant changes relative to cloud dispersion.

ACKNOWLEDGMENT

The authors wish to acknowledge the invaluable support provided by personnel in the Gas Diagnostics Division of UTSI during preparation of this paper. Ms. Edna Stallings and Mr. J. O. Hornkohl prepared the computer computations for the data reduction and Ms. Susan Carpenter prepared the manuscript. Many helpful comments and suggestions pertinent to this work were provided by Mr. Gary Nelson of the PM Smoke Office. However, the authors are solely responsible for its contents. This work was supported under US Army Contract DAAK11-80-C-0002.

REFERENCES

1. W. M. Farmer, "A Summary and Evaluation of Data Obtained in the H^3S Test" Final Report, UTSI-GD-TR-80-14. Prepared for the PM Smoke Office, Aberdeen, MD. 30 June 1980.

2. W. M. Farmer, et.al., "Data Obtained from the Smoke Week III Instrumentation Cluster" Smoke Symposium V, Harry Diamond Laboratories, Adelphi, MD. April 24-26, 1981.

3. Lundgren, et.al., Aerosol Measurement University Presses of Florida, Gainesville, FL (1979), pp. 119-131, 672-687.

4. Reference 3, pp. 341-497.

5. J. R. Brock and P. J. Kuhn, "Smoke Week III Electronic Cascade Impactor Measurements" Technical Report Prepared for PM Smoke Office, Aberdeen Proving Ground, MD. 3 October 1980.

6. Reference 3, pp. 219-260.

7. Deery D. Cooke and M. Kerker, "Response Calculations for Light Scattering Aerosol Particle Counters" Applied Optics 14, 734 (1975).

8. W. M. Farmer, "A Comparison of Data from Particle Size Analyzers Used to Measure Hygroscopic Smokes" Smoke Symposium IV, Harry Diamond Laboratories, Adelphi, MD. April 1980.

9. Smoke Week III data to be published by R. Pinnick and G. Bruce, Atmospheric Sciences Laboratory, White Sands Missile Range, NM, 1981.

10. Smoke Week III data to be published by Z. G. Sztankay, Harry Diamond Laboratories, Adelphi, MD, 1981.

11. B. Y. H. Lui, Fine Particles Academic Press, Inc., New York (1975), pp. 511-535.

12. "Field Characterization of Smoke and Obscurants" Final Test Report, Dugway Proving Ground Document No. DPG-FR-T-701, November 1978.

DATA OBTAINED FROM THE SMOKE WEEK III INSTRUMENTATION CLUSTER

W. M. Farmer, F. A. Schwartz, R. D. Morris,
M. A. Binkley and L. M. Boyd
The University of Tennessee Space Institute
Tullahoma, Tennessee

ABSTRACT

The instrumentation cluster used in Smoke Week III provided time-resolved, localized measurements of the optical characteristics of the obscurants tested. This paper will discuss some of the more important results obtained from these data. Chief among these are the time dependencies of the mass extinction coefficient and extinction cross-section, data consistency between different kinds of instruments, and the relative changes in the extinction coefficient for various wavelengths as a function of time and the uncertainties associated with these measurements.

1.0 INTRODUCTION

Serious discrepancies have been found to exist between laboratory and field measurements of the mass extinction coefficient of hygroscopic smokes.[1] Additional research has shown that the data differences could be traced to how the measurements were made in the field tests. When the extinction coefficient was computed using particle size distributions measured in field experiments, results reasonably consistent with laboratory measurements were obtained. However, when these results were compared to those obtained using long base line transmittance and chemical impinger data, significant differences were evident.[1] While the consistency of the laboratory and field determined extinction coefficients via size distribution argues strongly that those extinction coefficients determined by transmittance and chemical impinger data are erroneous, there is no a priori reason to assume this is so. A number of factors need to be considered and investigated before definitive conclusions may be drawn. The most significant of these are:

1. Apparently, very little attention has been given to the levels of uncertainty in extinction coefficients which have been determined in field or laboratory data.

2. It has been generally assumed that for the time scales present in field tests, the extinction coefficient is independent of time and is spatially constant. This is yet to be verified.

3. Generally speaking, there have been very few cross checks (with, perhaps, the exception of Particle Size Analyzers) of data from different kinds of instruments used to determine the same parameter.

4. Munition generated obscurants in field trials may have intrinsically different extinction coefficients from those generated in laboratory tests using small samples of the same material.

Thus, definitive comparisons between laboratory and field measurements cannot be made unless 1) some quantitative level of confidence is established for both sets of measurements both in terms of

statistical confidence and instrument to instrument data consistency, 2) fundamental assumptions have been verified, and 3) it is clear how laboratory and field data should be compared. During Smoke Week III, measurements were made with the intent of generating data to help resolve these questions. These data were provided by a localized set of instruments called the "instrumentation cluster" placed on a concrete pad near the test grid center. Among the parameters measured by these instruments were 1) particle size distribution, 2) particle number density, 3) aerosol mass concentration, and 4) transmittance over a 5m path for over 200 wavelengths between 2.5 and 14 μm. In a number of test cases, there was sufficient redundance in the instrumentation and in the measurements to determine data consistency and range of variation in the measurement. A description of the instrumentation cluster, its arrangement, hardware, and possible data correlations available with the measurements are discussed elsewhere.[2] The purpose of this paper is to discuss the most significant results obtained from the instrumentation cluster.

2.0 TIME DEPENDENCE OF THE MASS EXTINCTION COEFFICIENT

A major conclusion to be drawn from data obtained from the instrumentation cluster is that the mass extinction coefficient can often be a time dependent variable and not a constant as is often assumed. In this section, the analysis and the experimental data leading to this conclusion are presented.

2.1 TEMPORAL SPECTRA OF MASS EXTINCTION COEFFICIENTS

A primary limitation of any analysis which attempts to estimate a parameter from two separately sampled instruments is the accurate correlation of sampling times. For example, a cloud parameter such as the mass concentration, C, measured between times t_1 and t_2 will not directly correspond to the same portion of the cloud measured over the same time interval at a different spatial location. Even for the same location, instrument response times could be different. Previous analysis has attempted to circumvent this problem by examining time integral values of the parameters.[3] In the case of the mass extinction coefficient, α, it was necessary to assume α was independent of time. It is thus desirable to test this assumption by examining the temporal characteristics of α indicated by the instrumentation cluster data. Fourier transform theory can be used to reduce or eliminate the uncertainty arising from unknown shifts in sample times. It also provides a convenient means of examining temporal dependences in α.

Suppose α and C are functions of time given by $\alpha(t)$ and $C(t)$; then, the instantaneous transmittance as a function of time T(t) for the short path transmissometer (SPT) can be written as

$$-\ln T(t) = \alpha(t)\, C(t) L \qquad (1)$$

Assume that the cloud is sufficiently homogeneous that

$$C(t) = C_m(t + t_o) \tag{2}$$

where $C_m(t + t_o)$ is the measured concentration at some later time $t + t_o$, and t_o is a delay in the sampling time which is proportional to the instrument's spatial separation, atmospheric winds and turbulence, and the response time of the sampling instrument. Substituting equation 1 into equation 2 and integrating over the sampling interval τ yields:

$$-\int_0^\tau \ln(T(t))dt = L\int_0^\tau \alpha(t)C_m(t + t_o)dt \tag{3}$$

where L is assumed constant. The right hand side of equation 3 may be recognized as the cross correlation of α and C_m in the limit as τ approaches ∞. The Fourier transform of a function f(t) can be written as

$$F(f(t)) = \int_{-\infty}^{\infty} f(t)e^{-i2\pi wt}dt \tag{4}$$

Applying the Fourier transform to both sides of equation 3, it can be shown that

$$F(-\int_0^\tau \ln(T(t))dt) = F(\alpha(t))F(C_m(t))L \tag{5}$$

Solving equation 5 yields

$$F(-\int_0^\tau \ln(T(t))dt)/F(C_m(t))L = F(\alpha(t)) \tag{6}$$

An inverse Fourier transform can be applied to equation 6 to yield $\alpha(t)$, thereby eliminating the errors which may arise from an unknown t_o. An inverse transformation is not necessary, however, since all necessary information is contained in $F(\alpha(t))$. Methods of extracting the necessary information depend on Parseval's theorem, which can be written as

$$\int_{-\infty}^{\infty} |\alpha(t)|^2 dt = \int_{-\infty}^{\infty} |F(\alpha(t))|^2 dw \tag{7}$$

If $\alpha(t)$ were a quantity such as voltage, then equation 7 could be interpreted as a statement of conservation of energy. The root-mean-square of $\alpha(t)$, α_{RMS}, is defined as

$$\alpha_{RMS} = \left[\frac{1}{\tau} \int_{o}^{\tau} |\alpha(t)|^2 dt \right]^{1/2} \tag{8}$$

On using equation 7 in equation 8 and making suitable adjustments for finite time records of length, τ, there results

$$\alpha_{RMS} = \left[\lim_{\tau \to \infty} \frac{1}{\tau} \int_{-\tau/2}^{\tau/2} |F(\alpha(t))|^2 dw \right]^{1/2} \tag{9}$$

Hence, the Fourier transform may be used directly to compute the RMS value of $\alpha(t)$. It is straightforward to show that the zeroth frequency component of the Fourier expansion of some function $f(t)$ corresponds to the time average of $f(t)$, $< f(t) >$, where

$$< f(t) > = \frac{1}{\tau} \int_{o}^{\tau} f(t) dt \tag{10}$$

Thus, if the square root of the zeroth frequency component of $|F(\alpha(t))|^2$ is computed, the time average defined by equation 10 is obtained.

The integrand on the right hand side of equation 7 is often used in the analysis of time dependent systems. It is called the "power spectrum" of the function, and is written $S(\omega)$

$$S(\omega) = |F(\alpha(t))|^2 \tag{11}$$

If $\alpha(t)$ were a voltage, then, for unit resistance, $S(\omega)$ would show how the power or energy is distributed in terms of frequency. For example, $S(\omega)$ as a function of ω for a constant frequency sinusoid with amplitude A and frequency ω_o would be a spike of amplitude $|A|^2$ located at ω_o. (Equation 11 predicts a second spike at $-\omega_o$ which is usually ignored for physically real systems since there are no negative frequencies.) No physical explanation is presently offered for the meaning of the "power spectrum" of the extinction coefficient. It will be presented here merely as a convenient computational device for examining the temporal characteristics of α.

Figure 1 shows the set of power spectra computed for α for trial 16 using the spectral transmissometer data at 3.4 micrometers and the quartz crystal mass monitor (QCM) concentration data. Both sets of data were acquired using a once per second sampling rate. Contrary to expectations and assumptions made in numerous past analyses, α has an obviously strong temporal dependence. The temporal character changes for the 4 sets of data. This implies that α has a nonstationary mean, i.e. the mean changes on time scales at least of the order of the time separating the transmissometer samples (approximately 30 seconds).

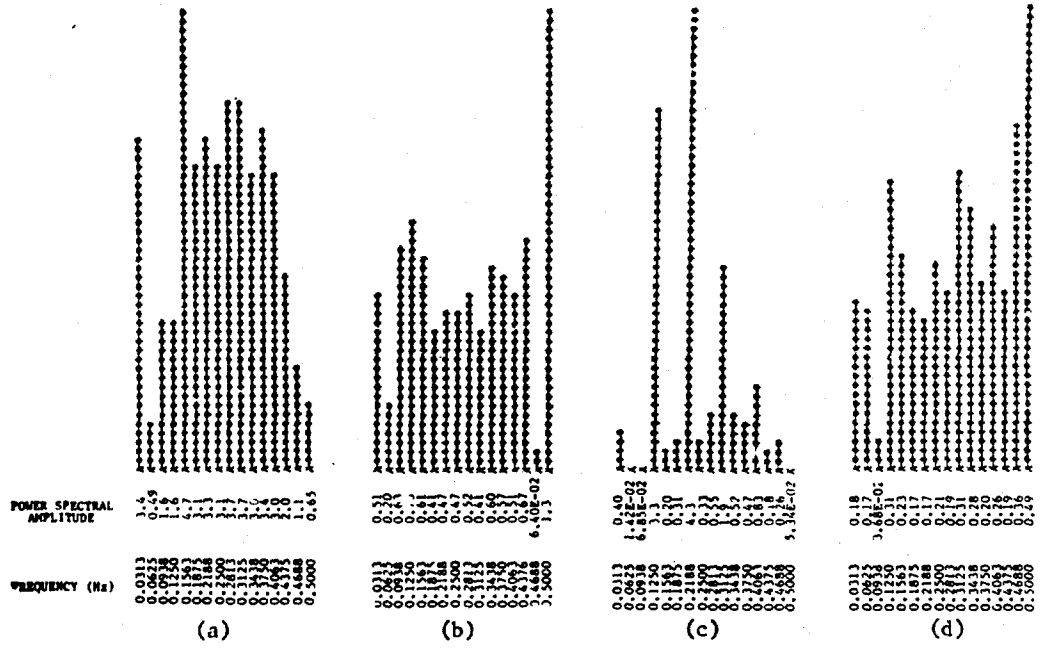

Figure 1. Power spectrum for mass extinction coefficient for phosphorus smoke at 100% RH (trial 16). Relative time sequence is a-d.

Figures 1a-d clearly show that the quoted value of $\alpha(t)$ will depend on how the data are averaged with respect to time. Table I compares the arithmetic and RMS time averages obtainable from these data, the maximum and minimum values of α, (α_{max}, α_{min}) shown in the power spectrum, and the frequencies (ω_{max}, ω_{min}) at which they occur. Additionally, the power spectrum for the entire ensemble of data has been computed as though it were a continuous time record. The result is shown in Figure 2. The time average of successive data sets in Figure 1 shows a steadily decreasing trend which is stronger than the RMS decrease. There is no obvious trend in the maximum or minimum values except that the maximum values seem to occur at higher frequencies than the minimum values.

TABLE I

MASS EXTINCTION VALUES DETERMINED FROM POWER SPECTRA FOR A PHOSPHORUS AEROSOL NEAR 100% RELATIVE HUMIDITY

TRIAL NUMBER	RELATIVE HUMIDITY (%)	$<\alpha(t)>$	α_{RMS}	α_{MAX}	α_{MIN}	ω_{MAX}(Hz)	ω_{MIN}(Hz)
16.1	100	1.84	1.15	2.17	0.70	0.1563	0.0625
16.2		0.71	0.50	1.15	0.25	0.50	0.468
16.3		0.63	0.67	2.07	0.12	0.2188	0.0625
16.4		0.42	0.33	0.70	0.19	0.500	0.0938
{ 16 }		0.35	0.41	1.41	0.01	0.500	0.4922

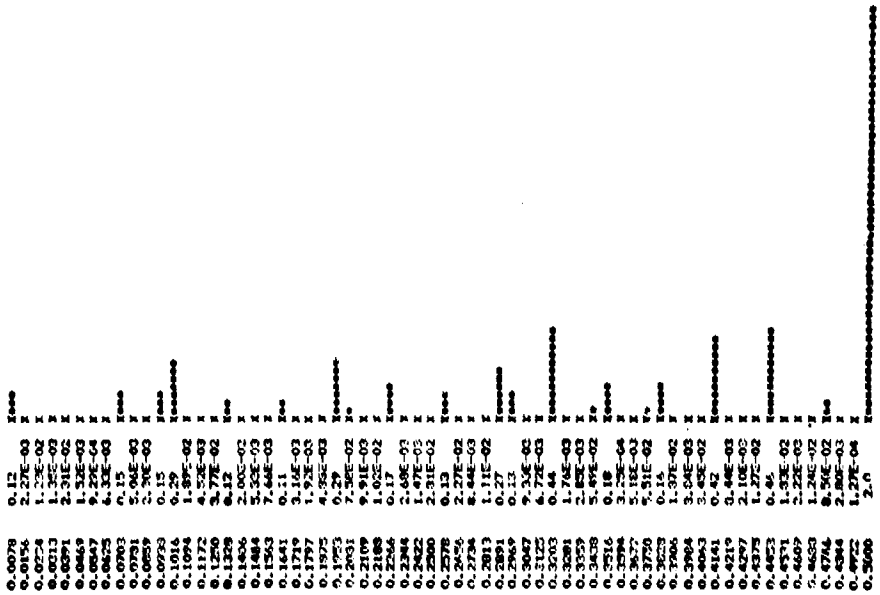

Figure 2. Power spectral density for the mass extinction coefficient using the total time record of the spectral transmissometer.

These data provide a possible clue as to why there exists a significant difference in α values measured using time-integral concentration and transmission values and those measured in the laboratory or field using particle size analyzers. The entry labeled { 16} in Table I shows that the average values of α over the long time record are significantly smaller than those computed for the shorter sample times. Thus, aside from the fact that α apparently cannot be assumed constant in time for the hygroscopic smokes, the mean value of α over the trial decreases.

The usefulness of this approach for estimating α is further illustrated when the temporal spectrum of nonhygroscopic clouds are examined. For example, compare the power spectra shown in Figure 3 obtained from the XM49 generator dispensing IR #1 at two different operational periods where the generator is operating near the instrumentation cluster. Figure 3a corresponds to initially reasonably stable operation,although the spectral distribution shows a broad range of values. In this case, RMS values of α are about 75% of the magnitude of the time averaged values. Figure 3b corresponds to a case near the end of the same trial when the output from the generator is apparently strongly periodic with the extinction coefficient having a time period between 2.6 and 2.9 seconds. Comparison of the power spectrum magnitudes shows that it is roughly 7 times greater in magnitude than the time average value. If the source of this periodicity in α could be identified then,obviously,the possibility exists for improving the characteristics of α through generator or obscurant modification to obtain the

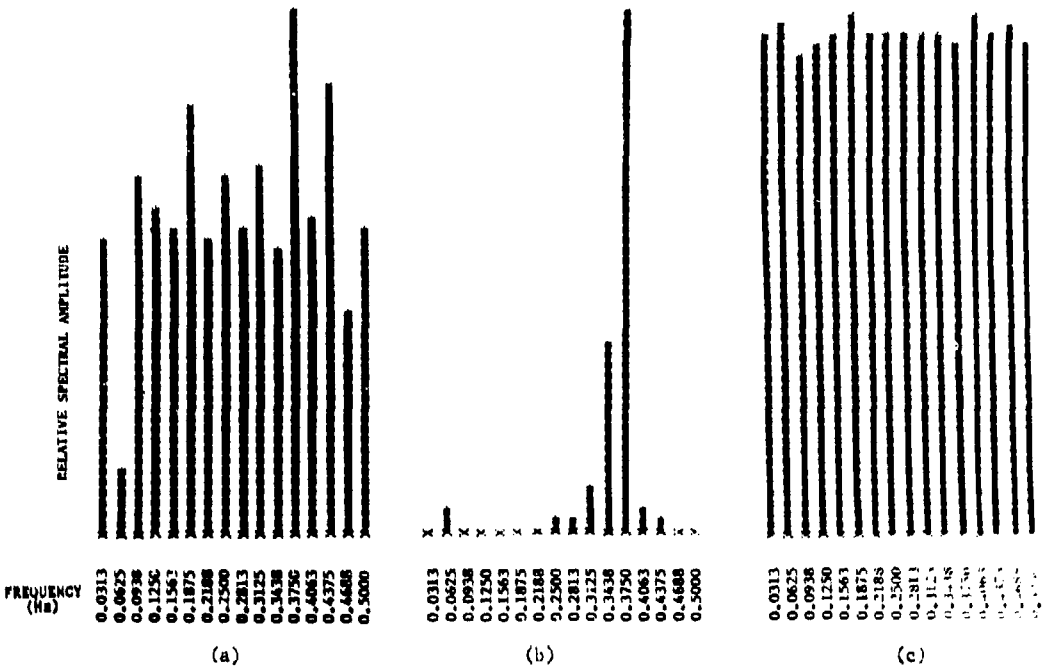

Figure 3. Mass extinction spectra for IR #1. a) Normal generator operation, b) extraordinary generator operation, c) dispersion from a helicopter for IR #1 mixed with fog oil.

desired result. Figure 3c shows the relative power spectrum for IR #1 mixed with fog oil after dispersion from a helicopter. By comparison with the ground generated cloud, this power spectrum is much more uniform in amplitude. Only a 4% difference exists between the maximum and minimum values of α at any one frequency. This is interpreted to indicate a well-mixed cloud with no predominant sources of α.

2.2 MASS EXTINCTION COEFFICIENT DETERMINATION USING PARTICLE SIZE DISTRIBUTION DATA

The time dependent character of α indicated by the Fourier analysis of transmission and concentration data has been found consistent with determinations of α made using particle size distribution data. The mass extinction coefficient can be computed directly from particle size distribution data when the extinction efficiency, Q_E, and material density, ρ_o, are known. The mass extinction coefficient defined as

$$\alpha = \overline{\sigma}/\frac{\pi}{6}\,\rho_o\mu_3 \qquad (12)$$

where $\overline{\sigma}$ is the mean extinction cross-section and μ_3 is the third moment of the size distribution. In this section, α values for phosphorus are reported which were obtained using particle size distribution data measured with a particle sizing interferometer (PSI). Figures 4-9 plot the computed extinction

coefficients for 3.4 micrometers and trials 16, 25, 32, 18, 30, and 24. Values for ρ_o as a function of relative humidity were computed using the expressions given in reference 5. The extinction efficiency was computed assuming that these smokes had the same index of refraction as orthophosphoric acid. Data from two PSI systems are given. PSI 1 was located 30m from PSI 2 which was positioned in the instrumentation cluster. PSI 1 was usually positioned nearest the munition detonation point.

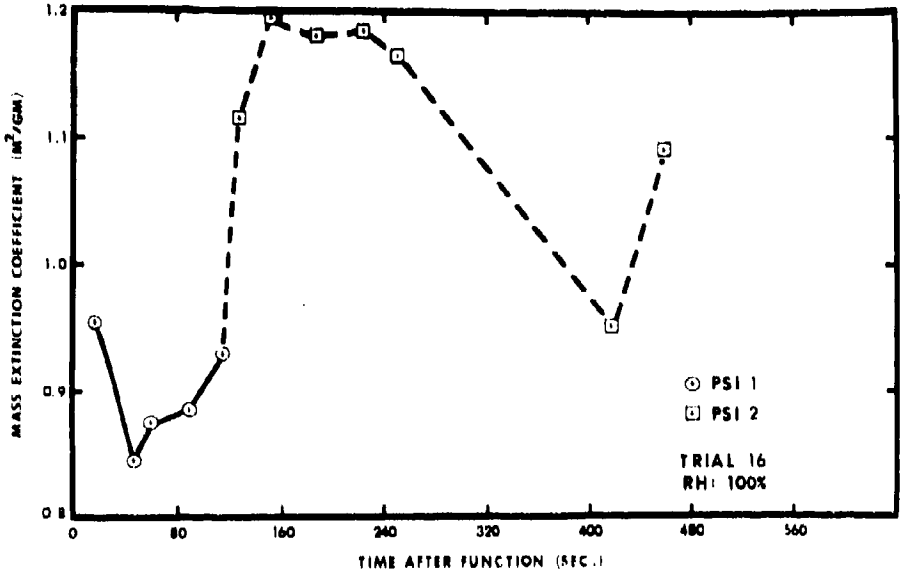

Figure 4. Mass extinction coefficient as a function of time after munition detonation for trial 16.

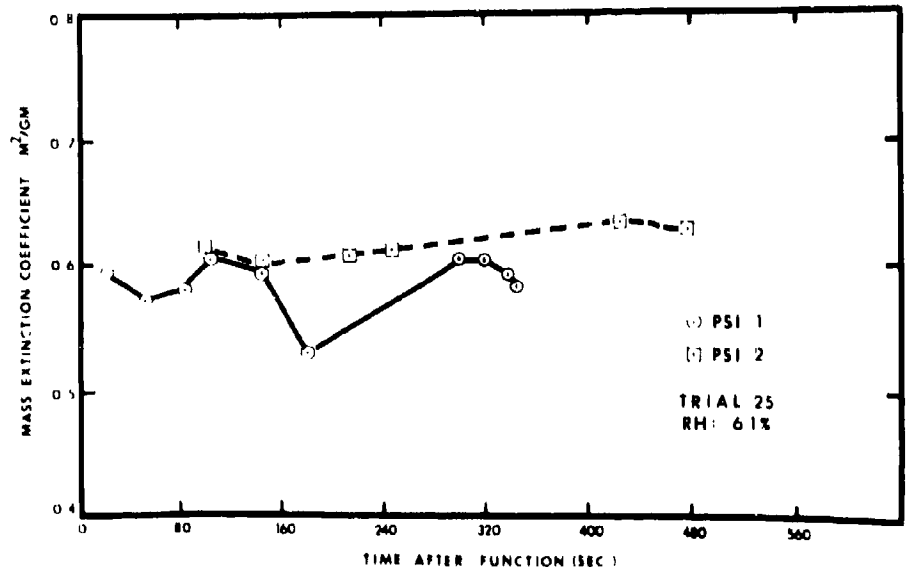

Figure 5. Mass extinction coefficient as a function of time after munition detonation for trial 25.

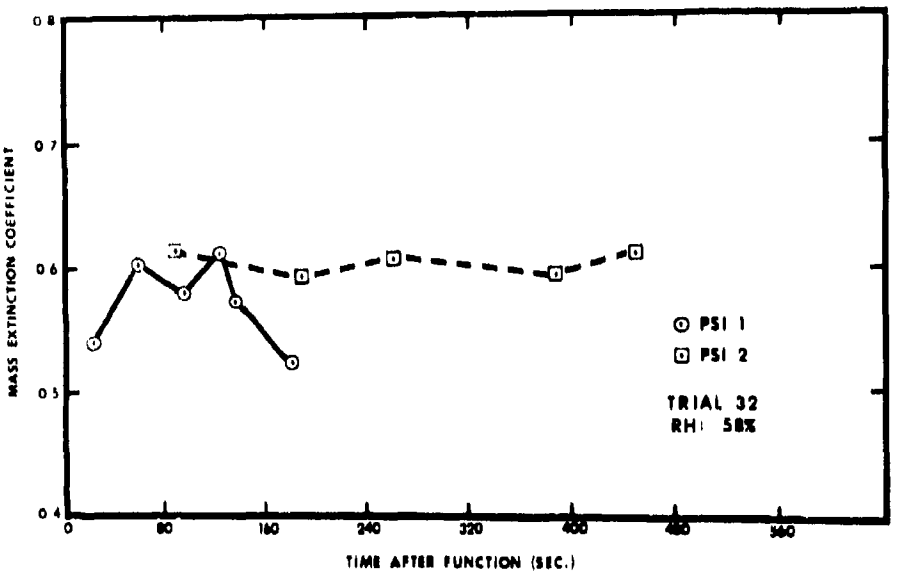

Figure 6. Mass extinction coefficient as a function of time after munition detonation for trial 32.

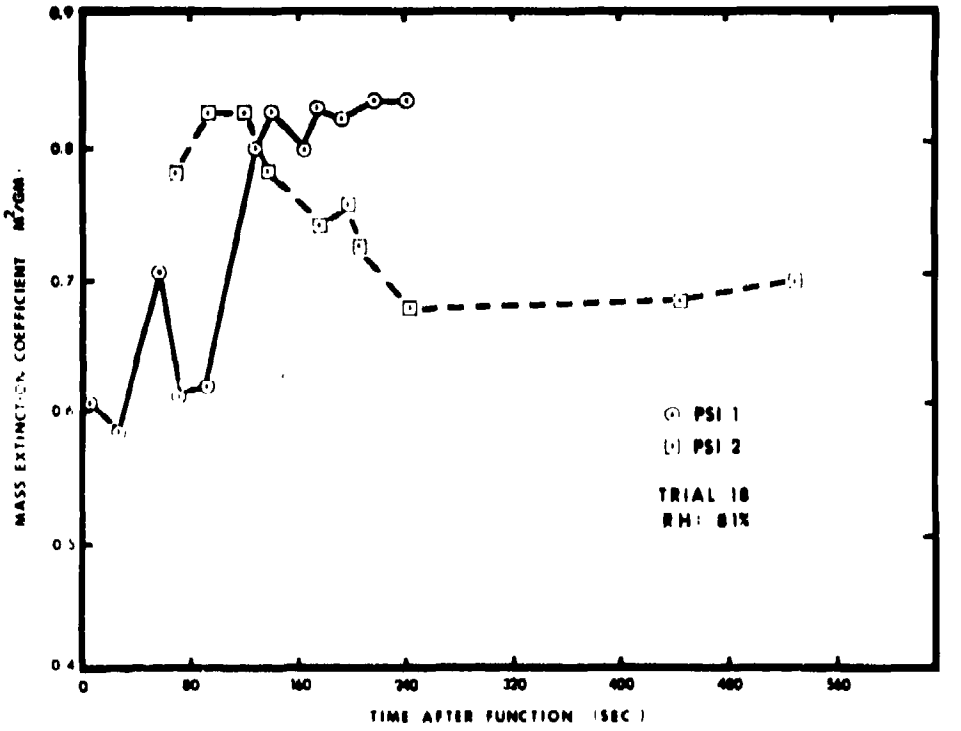

Figure 7. Mass extinction coefficient as a function of time after munition detonation for trial 18.

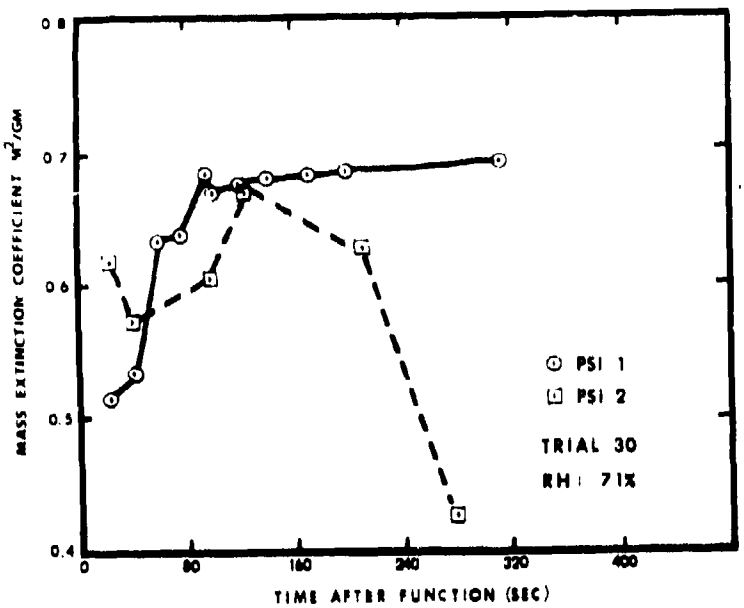

Figure 8. Mass extinction coefficient as a function of time after munition detonation for trial 30.

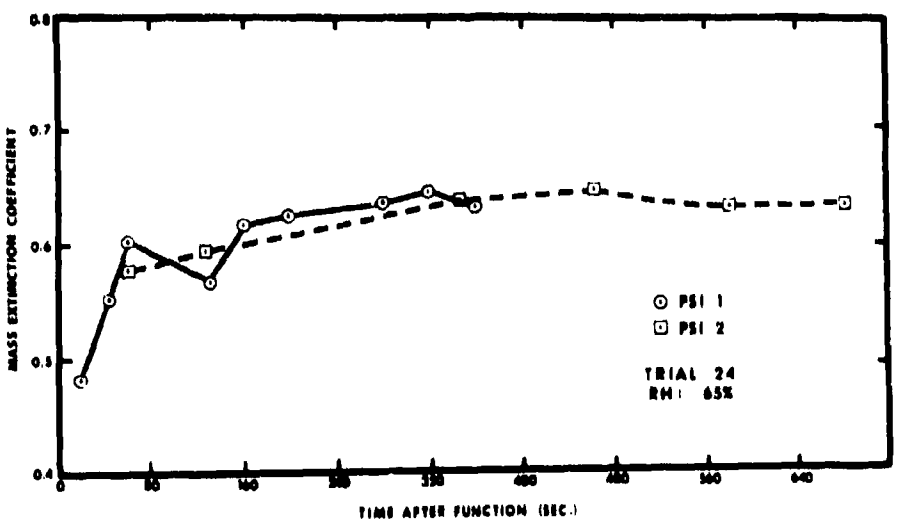

Figure 9. Mass extinction coefficient as a function of time after munition detonation for trial 24.

Figures 4-9 clearly show that in at least the first 240 seconds after detonation the extinction coefficient is time dependent and that the range of variation is consistent with that shown in Table I. A primary reason for the variation in α with time is found when values of $\bar{\sigma}$ as a function of time are considered. Only trial 18 will be considered here for purposes of illustration. Detailed comparisons may be found in other reports.

$\bar{\sigma}$ can be computed for an "η" interval particle size distribution histogram using equation 13

$$\bar{\sigma} = \frac{\pi}{4} \sum_{i=1}^{\eta} f_i Q_{Ei} D_i^2 \qquad (13)$$

where Q_{Ei} is the extinction efficiency for the D_ith particle diameter and f_i is the probability of occurrence. Figure 10 plots $\bar{\sigma}$ for trial 18 as a function of time. Note that during the trial $\bar{\sigma}$ changes by nearly three orders of magnitude. Additional data points obtained with the spectral transmissometer (SPT) and PSI and PSA derived number densities, ρ_N, are also plotted in figure 10.[4]

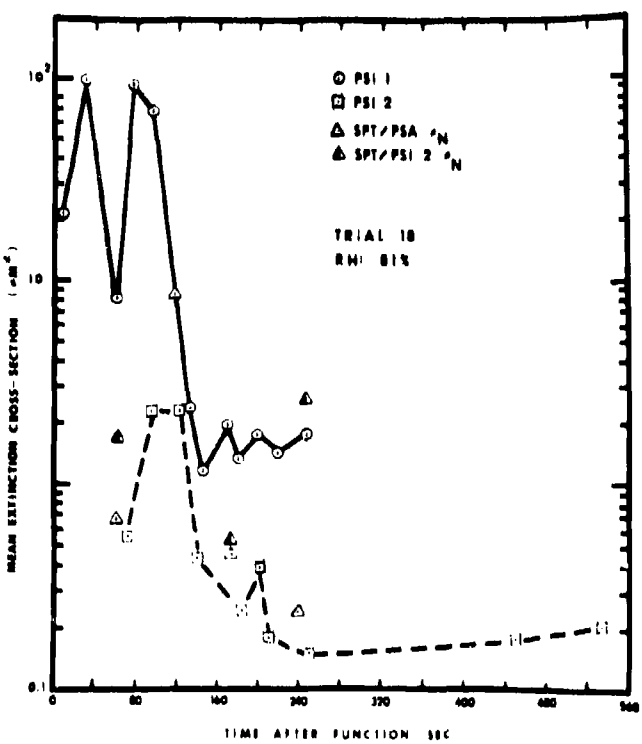

Figure 10. Mean extinction cross-section as a function of time after munition detonation for trial 18.

The broad range of values of $\bar{\sigma}$ with time are to be expected when the particle size distribution measurements are examined. Data obtained from Smoke Week III shows that the size distributions have spatial

and time dependences which presumably can be correlated through considerations involving atmospheric turbulence and wind velocity. Consider the evolution of the mass distributions as shown in Figure 11 from the PSI 2 (i.e. the PSI operated on the instrumentation cluster). These data show an initial distribution of small particles which shifts to larger sizes, then a decrease in size as test time increases. This effect is reflected in the $\bar{\sigma}$ plot shown in Figure 10. Also, note the increase in the small size mode as time increases. The bimodal mass distribution is consistent with observations made in the H^3S test.[1] Secondly, consider how this data compares with that obtained from PSI 1 located 30m from PSI 2 and much nearer the munition detonation point. It is more likely to detect explosive debris. The initial histograms shown in Figure 12 show sizes significantly greater than those initially measured in the cluster by PSI 2. There is a time differential of 60 seconds between the start of PSI 1 and PSI 2. As time evolves, the distribution measured by PSI 1 shifts toward smaller sizes.

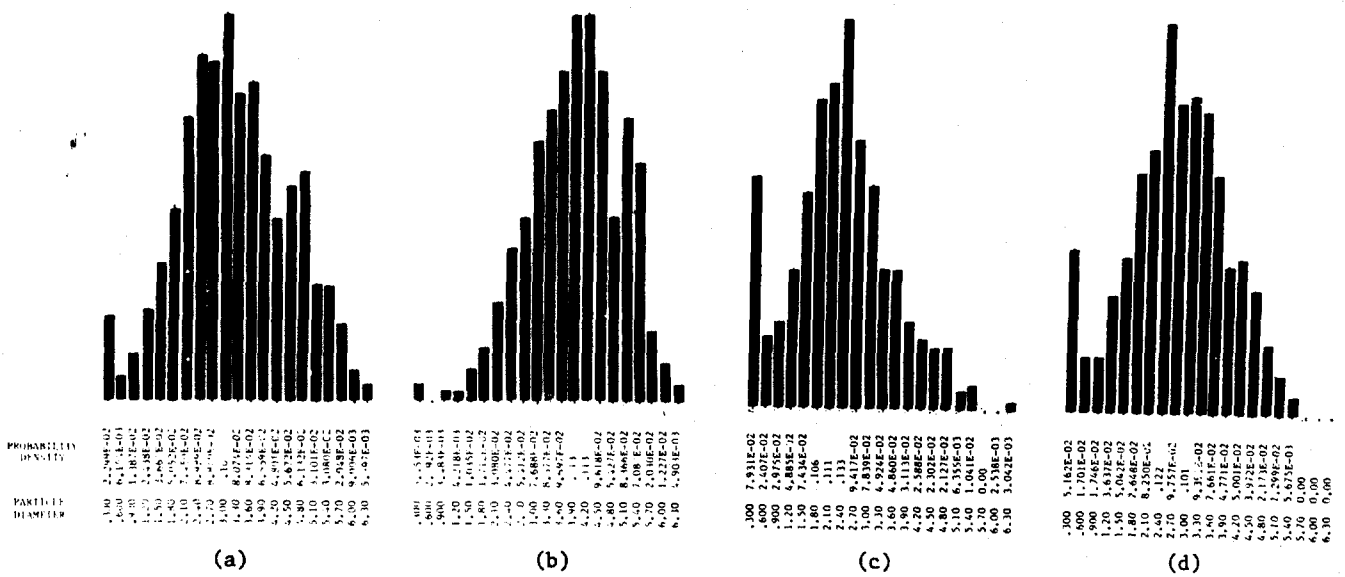

Figure 11. Examples of the evolution of the mass distribution with time during trial 18 for WP (CBU 88 Bomblet, RH = 81%) as measured by PSI 2.

These data seem to suggest that PSI 1 nearest the detonation point initially measured numerous large bits of elemental WP or debris which had not yet produced smoke. PSI 2, being further away, measured only true phosphorus smoke, which was much smaller. As test time increased, smoke was observed which was much smaller in size. PSI 2 was able to sample the cloud over a significantly longer period of time than PSI 1 because of cloud drift. These phenomena were observed for several trials during Smoke Week III. The extinction cross-section and mass extinction coefficient depend on the size distribution. The observed spatial and temporal differences in the measured distributions suggest that the extinction cross-section and, thus, the mass extinction coefficients are also spatially and temporally dependent.

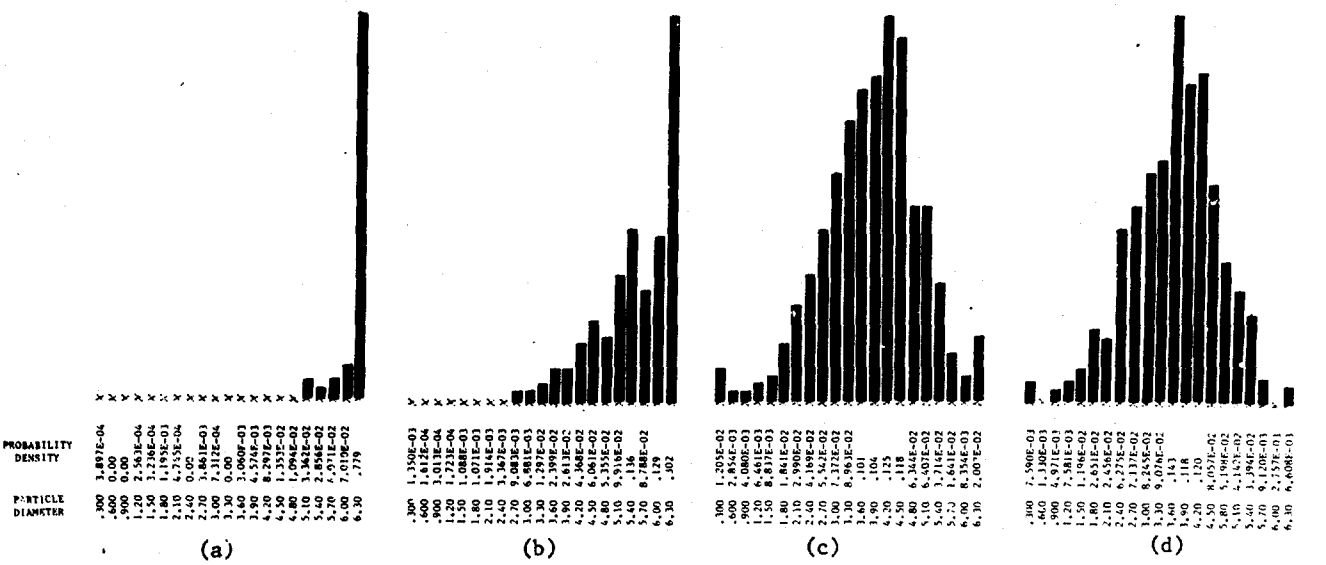

Figure 12. Evolution of mass distribution for trial 18 as measured by PSI 1.

3.0 COMPARISON OF DIFFERENT EXTINCTION COEFFICIENT DETERMINATIONS

A number of different instrumentation outputs obtained on the instrumentation cluster could be combined to yield an estimate of the extinction coefficient. It is of interest, therefore, to compare these values with those determined by the PSIs and obtain an estimate of the spread in the instrumental measurements. For reasons which will become apparent in section 4.0, these comparisons will be for the α value at a wavelength of 3.4 micrometers. Because the various instruments are spatially separated, values of α would apply for different sampling times. As the previous sections have shown, the method of averaging the data is significant even over short time intervals. Hence, in these comparisons entire trial averages will be presented without any attempt to weight the data in terms of sampling intervals or to correlate the data with time.

The primary instrument involved in these measurements was the SPT. This instrument was used to provide transmittance values at 3.4 micrometers which could be entered in the equation

$$\alpha_T = \frac{-\ln(T(3.4\ \mu m))}{CL} \tag{14}$$

where α_T is understood to mean α determined using transmittance values. It is assumed that the path length L (5m) was constant throughout the transmittance measurements (i.e. for times of approximately 30 seconds). C can be computed using particle size distribution and number density data or from QCM data which provides C directly as a function of time. A symbol convention is adopted wherein $<\alpha(PSI\ 2)>$ is understood to mean the trial time averaged value of α determined from PSI 2 data and equation 12.

$<\alpha_T$(PSI 2)> is understood to mean the trial time average of α as determined from equation 14, with PSI 2 data used to compute C. In cases where PSI 2 values did not overlap ln(T) values in time, samples were used which were a few seconds apart. A similar convention is adopted for data used from the Climet particle size analyzer operated by Dugway Proving Grounds. This instrument is identified as PSA. $\{<\alpha>\}$ should be understood to mean the ensemble average of the time average measurements which are within one standard deviation of the entire ensemble for a particular trial. $\Delta\alpha$ is the relative standard deviation for the population of measurements. Table II presents a summary of these results. It shows reasonably good agreement between the instruments in nearly all cases. The exceptions to good agreement are found when the uncertainties are large or sample time intervals do not overlap.

TABLE II

COMPARISON OF TIME AVERAGED α VALUES FOR PHOSPHORUS

TRIAL NUMBER	RELATIVE HUMIDITY (%)	$<\alpha$(PSI 1)> m^2/gm	$<\alpha$(PSI 2)> m^2/gm	$<\alpha$(PSA)> m^2/gm	$<\alpha_T$(PSI 2)> m^2/gm	$<\alpha_T$(PSA)> m^2/gm	$<\alpha_T$(QCM)> m^2/gm	$\{<\alpha>\}$ m^2/gm	$\pm\Delta\alpha$(%) m^2/gm
16	100	0.86	1.117	1.002	1.14	2.0[1]	0.87	0.93	10.6
21	93	0.97	0.75	0.8501	0.46[1]	1.607[1]	0.8342	0.85	10.6
7	83	0.80[1]	0.57	0.42	NO SPT DATA			0.53	17.6
18	81	0.63 (0.82)[3]	0.78 (0.68)[3]	0.84	0.33[1]	1.05	0.54	0.77	25.7
33	72	0.69	0.62	0.384	NO SPT DATA			0.56	28.5
30	71	0.66	0.63	0.785	0.38[1]	0.74	3.36[1]	0.70	10.1
24	65	0.63	0.63	0.74	0.3[1]	0.064		0.66	9.5
25	61	0.596	0.62	0.45	0.31[1,2]	0.31[1,2]	0.58[2]	0.56 (0.41)[2]	13.5 (39.)[2]
32	58	0.56	0.60	0.55	0.24[1,2]	0.17[1,2]	0.37[1,2]	0.57 (0.26)[2]	4.6 (39.)[2]

1. These data deleted from ensemble average.
2. α computed separately from α_T
3. Obtained early in trial.

4.0 WAVELENGTH DEPENDENCE OF MASS EXTINCTION COEFFICIENT

In this section, the wavelength dependence of the mass extinction coefficient is examined and a method is devised to estimate the minimum uncertainty in the estimate value.

A convenient method for examining the wavelength dependence uses only the spectral transmissometer data. It can be shown that over "reasonably" short time intervals where it can be assumed that the same path is observed for wavelengths λ and λ_R the following approximation will apply:

$$\frac{<\alpha(\lambda)>}{<\alpha(\lambda_R)>} \simeq \frac{\int_0^\tau \ln T(\lambda)dt}{\int_0^\tau \ln T(\lambda_R)dt} \tag{15}$$

Within the limitation indicated in section 2.1, it will be assumed that the 30 second sample time used by the spectral transmissometer in the instrumentation cluster is "reasonably short". The left hand side of equation 15 will be called the relative mass extinction coefficient, $\alpha_R(\lambda)$ and because of similar use in past tests, α_R will be chosen as 3.4 micrometers, i.e.

$$\alpha_R(\lambda) = \frac{<\alpha(\lambda)>}{<\alpha(3.4)>} \tag{16}$$

In order to express absolute time-averaged extinction coefficient values at wavelengths other than 3.4 μm, it is necessary only to measure $<\alpha(3.4)>$, which has been computed in detail for many of the obscurants in Smoke Week III, and multiply by $\alpha_R(\lambda)$.

Before proceeding with a detailed examination of $\alpha_R(\lambda)$ for a number of different obscurants, a method for estimating the uncertainty in α_R, $\Delta\alpha_R$, is presented which will allow some insight into the "quality" of the α_R measurement. The variation of any function $f(x_i)$ where x_i represents the "n" variables associated with f(x) may be computed from

$$\Delta f(x_i) = \sum_{i=1}^{n} \frac{\partial f}{\partial x_i} \Delta x_i \tag{17}$$

Applying equation 17 to $\alpha_R(\lambda)$ in equation 16 yields

$$\alpha_R(\lambda) = \frac{\Delta<\alpha(\lambda)>}{<\alpha(3.4)>} - <\alpha(\lambda)> \frac{\Delta<\alpha(3.4)>}{<\alpha(3.4)>^2} \tag{18}$$

Using equation 16, the relative variation in α_R, leads to

$$\frac{\Delta\alpha_R(\lambda)}{\alpha_R(\lambda)} = \frac{\Delta<\alpha(\lambda)>}{<\alpha(\lambda)>} - \frac{\Delta<\alpha(3.4)>}{<\alpha(3.4)>} \tag{19}$$

If it is assumed that $<\alpha(\lambda)>$ is uncorrelated with $<\alpha(3.4)>$, then the root mean square relative uncertainty can be written as

$$\left.\frac{\Delta\alpha_R}{\alpha_R}\right|_{RMS} = \pm\left[\left(\frac{\Delta<\alpha(\lambda)>}{<\alpha(\lambda)>}\right)^2 + \left(\frac{\Delta<\alpha(3.4)>}{<\alpha(3.4)>}\right)^2\right]^{1/2} \tag{20}$$

If the transmittance is written as

$$\ln(T) = <\alpha(t)> CL \tag{21}$$

then the RMS uncertainty in the time averaged values of α can be written as

$$\left.\frac{\Delta < \alpha >}{< \alpha >}\right|_{RMS} = \left[\left(\frac{\int_0^T \frac{\Delta T}{T}\, dt}{\int_0^T \ln T\, dt} \right)^2 + \left(\frac{\int_0^T \Delta C\, dt}{\int_0^T C\, dt} \right)^2 \right]^{1/2} \qquad (22)$$

Generally, the time integral uncetainty for ΔC is much less than it is in the transmission. Hence, the uncertainty in C will be ignored in the computation presented here for $\Delta < \alpha > / < \alpha >$, with the understanding that the computed uncertainties represent minimum values of uncetainty and that cases do exit where the actual uncertainty in the estimate can be much larger. With this understanding, $\left.\Delta <\alpha> / <\alpha>\right|_{RMS}$ can be approximated as

$$\Delta <\alpha> \approx \pm \frac{\int_0^T \frac{\Delta T}{T}\, dt}{\int_0^T \ln T\, dt} \qquad (23)$$

$\Delta T/T$ will be assumed to be independent of T for the computed values reported here. $\Delta T/T$ was estimated by averaging the transmittance at λ for 30 second (i.e. 30 transmittance values) in clear air and computing the standard deviation in these values. These values ranged from about 0.2% to slightly greater than 1.5%.

The above analysis has been used to compute α_R and $\Delta\alpha_R$ for the following wavelengths: 1) 6.98 μm, 2) 7.28 um, 3) 8.05 μm, 4) 8.58 μm, 5) 9.58 μm, and 6) 10.58 μm. 10.58 μm is the wavelength in the measured spectral transmittance closet to 10.6 μm, which is of interest because it is a laser wavelength. The remaining wavelengths correspond to maximum and minimum values in the mass extinction wavelength spectrum for laboratory measured values of red phosphorus smoke.[5]

Figure 13 plots the values of α_R as a function of λ for the 4 sets of spectral transmissometer data obtained for trail 16. The RH for this trial was 100% and the munition source was a set of XM825 WP wedges. The relative time sequence of the data sets is labeled 1-4. Those points with no indicated uncertainty range have values that are less than or equal to the symbol size locating the data point. Figure 13 clearly indicated significant changes in α as trial time increases. This is indicative of a nonstationary mean value. The general trend for the phosphorus trials is for α_R to be initially large, reduce to a smaller value, and stabilize.

Figure 14 plots α_R as a function of wavelength for one sample set each of trials 21 and 24. The RH for trial 21 is 93% while that for trial 24 is 65%. The effect is startling but consistent with results obtained in the H^{3}S test. Those results which showed that below roughly 71% RH, the integrated extinction coefficient for the 8-12 micrometer band should be greater than that at 3.4 μm. For the

conditions present in these trials, the H^3S data suggested that α_R for the 8-12 μm band should increase by a factor of about 2.5 as the RH decreases from 93-65%. These data seem reasonably compatible with that expectation.

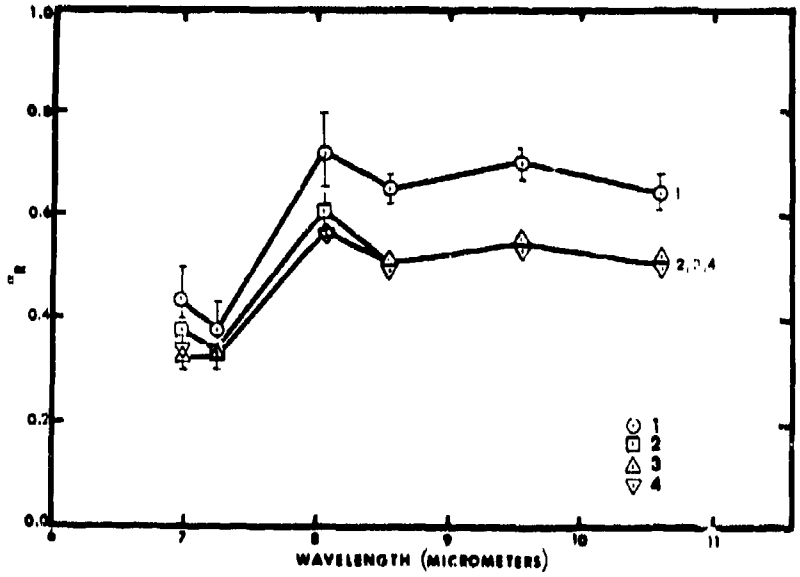

Figure 13. Relative mass extinction coefficient for phosphorus between 6-12 micrometer wavelengths at 100% RH in relative time sequence 1, 2, 3, 4.

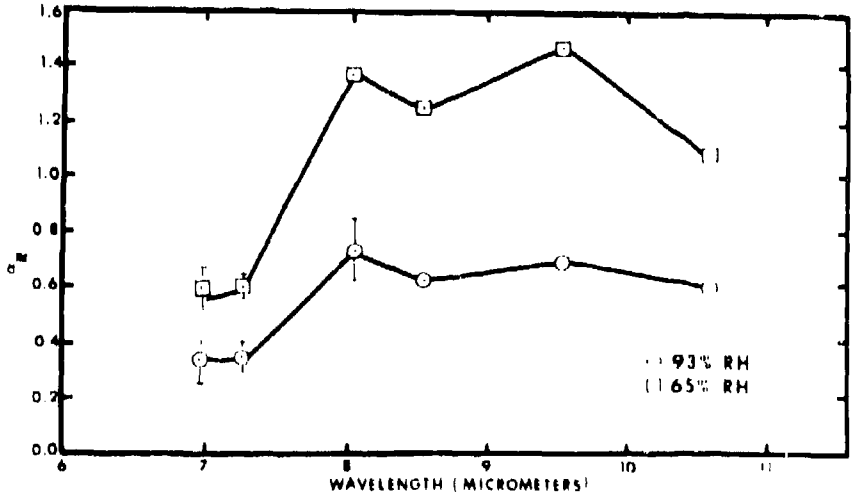

Figure 14. Comparison of relative mass extinction coefficient for phosphorus between 6-12 micrometer wavelengths for relative humidities of 93 and 65%.

Data examined via α_R suggest that the method of dissemination can have a significant effect on the magnitude of α_R. Figure 15 plots α_R for a data set from trial 24 and trial 25. Three 5" Zuni bulk-filled WP rounds were used in trial 24. Trial 25 used two rounds of XM825 WP wedges. Trial 24 was conducted at 65% RH, trial 25 at 61% RH. The data sets were chosen as those having the least uncertainty in α_R. Figure 15 shows that α_R for the bulk-filled round (trial 24) is slightly larger than for the wedge-filled round.

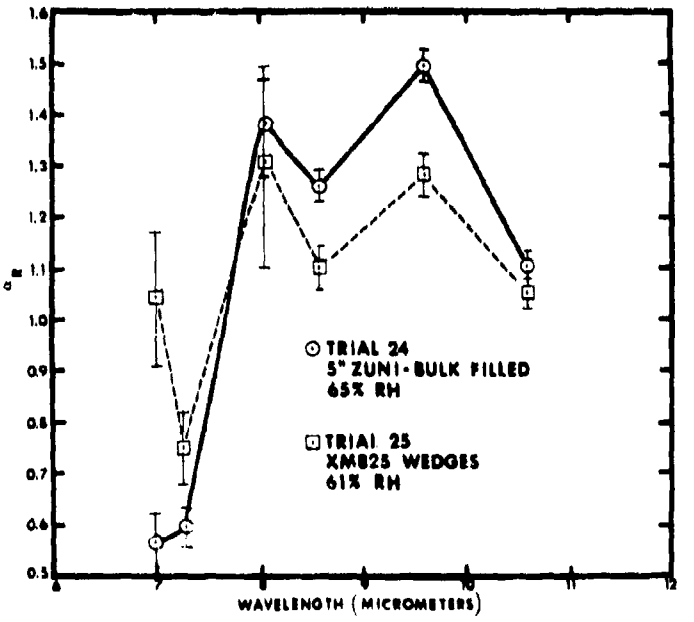

Figure 15. Comparison of relative mass extinction coefficient for phosphorus using two different methods of dissemination.

α_R has been computed for a number of other kinds of obscurants observed during Smoke Week III. Examples of these data are plotted in Figures 16 and 17 for fog oil and HC. Figure 16 shows that α_R even for fog oil smokes may be strongly dependent on the generator. In these data the M3A3 generator was not in stable operation and produced a cloud which had relatively large numbers of fog oil droplets. In this way, the extinction coefficient in the 6-12 micrometer range could be made quite large as compared to that for the VEESS generator, which produced few oil droplets after stabilized operation. Figure 17 shows that HC yields an extinction coefficient which is comparable to that for phosphorus for relative humidities less than 70%. The large uncertainties in these data arise from the relatively poor extinction by these smokes. α_R has also been computed for the broadband IR screeners examined during Smoke Week III. These data are classified and presented elsewhere.[6]

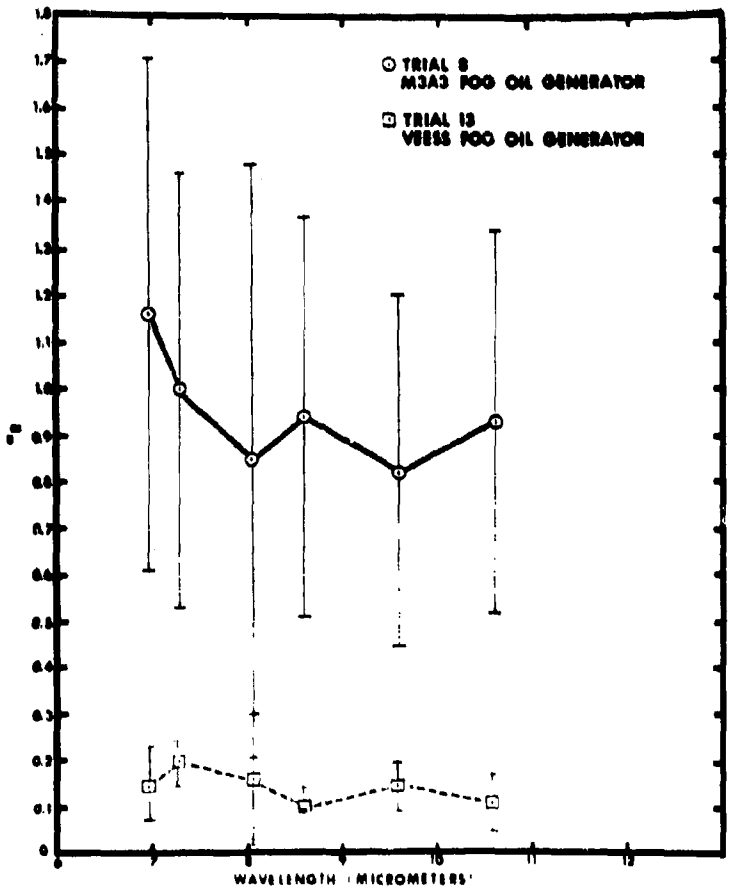

Figure 16. Comparison of relative mass extinction coefficient for fog oil for two different generators. (note: trial 8 corresponds to unstable generator operation, trial 13 corresponds to normal generator operation).

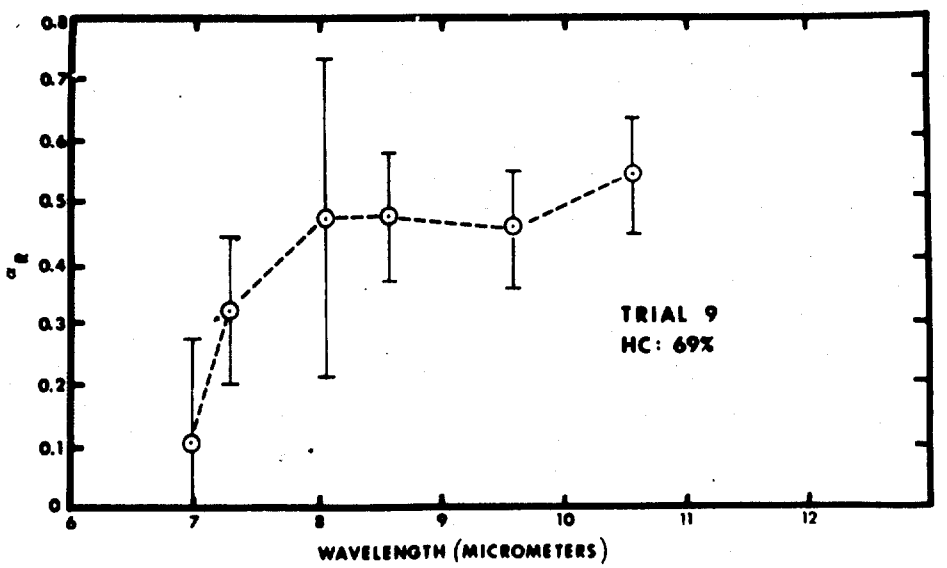

Figure 17. Relative mass extinction coefficient as a function of wavelength for hexachloroethane.

5.0 SUMMARY AND CONCLUSIONS

Many data obtained from the cluster of instruments operated during the Smoke Week III trials have been found to be internally consistent and consistent with data obtained during the H^3S trials. However, because of the increased instrumentation capability available with the instrumentation cluster, considerable insight has been gained into the range of values which can be generated through the use of different kinds of instruments to sample the same cloud. Furthermore, because much of the instrumentation provided time resolved measurements, new information has been obtained which will provide a greater understanding of the dynamic properties of obscuration clouds.

Mass extinction coefficients were computed using particle size distribution data and the same assumptions used to compute $\bar{\sigma}$. These data, like those for $\bar{\sigma}$, also show a time dependent character. Variations in α as determined by various instruments are not nearly as large as those observed for $\bar{\sigma}$. The trial average values measured for phosphorus are in reasonable agreement with those measured in the H^3S test.

α values for 3.4 micrometers computed for phosphorus smokes from the particle size distributions were compared with those values determined from time averaged concentration and short path transmittance measurements. Altogether, 6 independent estimates were compared for this study. It was usually necessary to remove 1 or 2 estimates which were significantly different from the ensemble. (This is not to say that the measurement was erroneous -- only that it was not consistent with the time averages obtained with other values.) The average variation in the ensemble of measurements in this case was about 13% and ranged between 4.5 and 26%. The greatest discrepancies found in the α values computed from the size distributions and the concentration-transmittance values occurred at relative humidities below

about 70%.

Differences in spatial locations of two or more instruments may lead to errors when their data are used to compute the extinction coefficient. If the measurements are acquired at a uniform rate, then Fourier analysis can be used to eliminate or reduce the error. The Fourier temporal spectrum of the extinction coefficient was computed using the short path transmittance for 3.4 micrometers and the quartz crystal mass monitor data. The results of this analysis show a broad range of values of α. α was found to vary significantly not only over the entire trial time, but also over intervals as short as 2 seconds. The value obtained for α was found to depend strongly on how the measurements were averaged in time, e.g., the arithmetic time average was usually found to be larger than the root-mean square average. The length of the time record was also found to significantly affect the time average. The longer time records yielded values smaller than the short time records. This result suggests that a reason for past field methodology yielding values significantly different than those measured on a short time basis such as might be achieved with a particle sizing system is that α is a function of time with a non-stationary mean.

This method of data analysis was also found useful for obscurants produced by mechanical generators. In some cases, apparent generator effects on α values or cloud uniformity were apparent.

The short path transmissometer data were used to compute the variation of the mass extinction coefficient as a function of wavelength relative to that for 3.4 micrometers. These results also show a time dependence of the extinction coefficient for wavelengths other than 3.4 micrometers.

The RH dependence for XM825 WP wedges was found to be consistent with that observed in the H^3S test (α in the 8-12 μm band is smaller than 3.4 μm until an RH of 71% is reached, at which point it is larger). α for phosphorus as a function of wavelength was also found to be dependent on the method of dispersal.

α for fog oil and HC was found to be roughly 10-20% that of WP in the range between 8 and 12 micrometers.

A method for estimating the minimum uncertainty in the relative extinction coefficient was developed. This uncertainty typically was found to run about 10% but some values were greater than 100%. This method provides a logical approach to estimating the quality of the measured values.

ACKNOWLEDGMENT

The authors wish to acknowledge the invaluable support provided by personnel in the Gas Diagnostics Division of UTSI during preparation of this paper. Ms. Edna Stallings and J. O. Hornkohl prepared the computer computations for the Fourier spectra and Ms. Susan Carpenter prepared the manuscript. Many helpful comments and suggestions pertinent to this work were provided by Mr. Gary Nelson

of the PM Smoke Office. However, the authors are solely responsible for its contents. This work was supported under US Army Contract DAAK11-80-C-0002.

REFERENCES

1. W. M. Farmer, "A Summary and Evaluation of Data Obtained in the H^3S Test" Final Report, UTSI-GD-TR-80-14. Prepared for the PM Smoke Office, Aberdeen, MD. 30 June 1980.

2. W. M. Farmer, et.al., "The Instrumentation Cluster Concept in Obscurant Field Testing" Smoke Symposium V, Harry Diamond Laboratories, Adelphi, MD. April 24-26, 1981.

3. "Field Characterization of Smoke/Obscurants" Final Test Report, Dugway Proving Ground Document No. DPG-FR-T-701. November 1978.

4. NOTE: This $\overline{\sigma}$ estimate is computed by rewriting the Beer-Bougher law as $T = \exp(-\overline{\sigma}\rho_N L)$. The equation is then solved to yield $\overline{\sigma} = -\ln(T)/\rho_N L$.

5. R. H. Frickel, G. O. Rubel, and E. W. Stuebing, "Relative Humidity Dependence of the Infrared Extinction by Aerosol Clouds of Phosphoric Acid" Proceedings of Smoke/Obscurant Symposium III, Harry Diamond Laboratories, Adelphi, MD. April 24-25, 1979. p. 571.

6. W. M. Farmer, et.al., "IR Extinction Coefficients Determined in Smoke Week III" Smoke Symposium V, Harry Diamond Laboratories, Adelphi, MD. April 24-26, 1981.

BATTLEFIELD SMOKE AND DUST PARAMETERS MEASURED IN SITU USING SPECTROPHONES

C. W. Bruce
Y. P. Yee
L. M. Moore
US Army Atmospheric Sciences Laboratory
White Sands Missile Range, New Mexico 88002

A. V. Jelinek
OptiMetrics, Incorporated
White Sands Missile Range, New Mexico 88002

N. Richardson
Physical Science Laboratory
New Mexico State University
Las Cruces, New Mexico 88003

ABSTRACT

Absorption to extinction ratios for experimental countermeasure "smokes" and soil-based dust lofted by high explosives were measured at 10μm wavelengths during the tests of Smoke Week III by using specially designed field spectrophones. These ratios permit contrast modeling of the effects on Electro-Optical (EO) systems by providing accurate proportions of total absorption and scattering. The spectrophones, which have an inherently high dynamic range, are not hampered by saturation effects and thus provide a time history of the magnitude of the absorption within the smoke clouds for media which absorb at 10μm. The magnitudes, which ranged downwards from about 10^2 km^{-1}, and the fluctuational properties are described in this paper.

1. INTRODUCTION

Our problem, in general terms, is the effect of the gases/aerosols of the tactical battlefield, natural and countermeasure, and gaseous and particulate, on EO systems. When the objective is to learn how aerosol clouds disperse for the formulation or validation of models which extend prediction of behavior to other spatial and time domains and not simply for the binary question of screening effectiveness, actual and accurate magnitudes of the aerosol parameters are required. To obtain these quantitative values for propagation parameters and correlative source densities, spatial and temporal resolution (in situ measurements) as well as a large dynamic range are required. Ideally one would use a remote sensing, raster scanning lidar with high spatial resolution capable of uniquely identifying constituent sizes, densities, and propagation properties. Such a system is clearly in the future and probably will require multiple wavelengths and possibly bistatic geometry.

Transmissometers, which are particularly relevant to the binary question of screening effectiveness, (assuming relevant spectral response) are not nearly as well suited to the determination of magnitudes. The transmissivity, T, may be converted through Beer's law to the propagation coefficients which in turn are closely related to the aerosol densities and thus mass loading. Limitations on this procedure are several and depend on integrated path length, obscurant cloud depths, and instrumental

accuracies. The latter leads to a limited credible dynamic range in T (less than one order of magnitude [Myers, 1980]) and to quite a variable dynamic range in the propagation coefficients. To summarize, for short obscurant cloud depths, low coefficients are not measureable. For example at 10^{-2} km, by the above criterion, the extinction coefficient which could be measured would start at > 10 km^{-1}. For longer obscurant cloud depths, for example, greater than 10^{-1} km, the dynamic range is much too small to encompass realistic obscurant magnitudes, that is, 1 to > 100 km^{-1}. Further, if the spatial profile of the source density is not well-known through other (multiple) measurements, that error in the exponent will yield relatively large errors in the determination of the propagation coefficients. Finally, optical turbulence and ambient fluctuations in the extinction over the entire optical pathlength may degrade data severely while temporal smoothing must be limited for dynamic events.

Spectrophones and particle counters as a correlative pair offer a currently available alternative. The measurement of each is related to the aerosol mass loading. Spectrophones measure a quantity which is proportional to the absorption coefficient and

a. are in situ, real-time measurements

b. are point samplers

c. have very high dynamic range

d. may be operated at infrared (IR) window wavelengths with existing lasers, for example, 1.06μm, 1.1μm, 3.4μm, 3.5μm to 4.1μm, 9.2μm to 11.3μm, and near millimeter wavelengths.

Point measurements of the aerosol might be performed as the cloud is swept by the wind past the instrumentation as it was at Smoke III. If the cloud levelops slowly relative to the windspeed at the location of the instrumentation, cloud spatial profiles for the direction of cloud motion can be obtained with minimal instrumentation.

The integrated field spectrophones of this paper and in general field use by this group combine measurements of the absorption coefficents with a coincident short path transmissometer. These latter data are converted to extinction coefficients. This conversion provides the components of the extinction coefficient needed for contrast modeling, that is, the extinction, the absorption coefficient, and, by subtraction, the total scattering coefficient. This procedure provides a much stronger determination of the components than is possible with techniques employing transmission and scattering data.

The application of spectrophones to aerosols requires more caution than for gases because the time required for the energy transfer from the absorption process to kinetic energy in the gaseous medium may be relatively long, thus interacting with optical chopping frequencies and also causing decreased coupling to acoustical modes. The first order effects on time response depend on particle radius, absorption coefficients for the bulk material, and thermal diffusivities of the bulk material and the atmosphere. Because the models are quite complex, those chosen represent bounds for the problem. Aerosols are studied in the laboratory to verify operating parameters that accurately represent the absorption coefficients.

2. SPECIFIC APPLICATIONS

Prior to aerosol applications, spectrophones at the Atmospheric Sciences Laboratory (ASL) were developed and applied to gaseous absorption (for example, Bruce, 1975; Bruce, 1976a). Briefly, our first spectrophone measurements were intended to identify absorption coefficients for naturally occuring and trace pollutant gases at IR window wavelengths. These are listed in Table I.

TABLE I. SPECTROPHONE MEASUREMENTS OF ABSORBING GASES AT IR WINDOW WAVELENGTHS

(1μm)	(3μm to 4μm)	(9μm to 11μm)
trace gas survey	H_2O*	O_3*
	HDO*	NH_3*
	D_2O*	C_2H_4*
	CH_4*	H_2O*
	SF_6	

Following this series of measurements, concentrations of atmospheric gaseous constituents at the White Sands Missile Range remote sites were measured largely using these absorption spectra. The concentrations were determined by a self-consistency analysis based on the uniqueness and sharpness of the molecular spectra (Samuels et al, 1978).

*Reports or journal articles exist or are being prepared for these gases

Next, in situ spectrophones were applied to particulate aerosols, the first such published applications (Bruce, 1976b; Bruce and Pinnick, 1977). The interest was primarily battlefield aerosols.

Aerosols subjected to ASL environmental chamber measurements to date are (all at 9μm to 11μm wavelengths plus exceptions noted)

SiO_2, crystalline*

Calcite*

$(NH_4)_2SO_4$*

Dust of soil samples from Germany and various White Sands Missile Range, New Mexico, sites and depths*

Smoke of phosphorus (red phosphorus [RP]) (1.06μm, 3μm to 4μm, and 9μm to 11μm)

Hexachloroethane (HC) smoke.

The spectrophone systems and procedures used for the aerosol studies have been described in various publications (for example, Bruce, 1976a; Bruce, 1976b; Bruce and Pinnick, 1977; Bruce et al, 1978). Application of aerosol spectrophones to field measurements of absorption has also been reported by the authors (Bruce et al, 1980). Several systems have been designed for relatively specific applications.

The first field spectrophone system was quite elaborate and was designed to survey and separate gaseous and particulate absorption in the atmosphere. In the first field measurements, results were compared with those calculated on the basis of particle counter data. Sampling errors were indicated in windy situations and higher than expected ambient gaseous absorption may have resulted from the presence of operating personnel.

Following this, systems were designed specifically to study battlefield aerosols in situ under a wide dynamic range of mass loadings. Figure 1 is a schematic of such a system. This system was

*Reports or journal articles exist or are being prepared for these atmospheric particulates

designed for measurements at wavelengths between 10.3μm and 10.8μm and incorporates a CO_2 laser with line stabilization by optical feedback through an electronic servo loop controlling optical cavity length. This system will stabilize on any of about 5 to 7 laser lines (once an operational equilibrium is established) and will also cycle through any preselected sequence of these lines (up to four), remaining on each line for preselected periods. The beam chopper is a special unit designed by Bulova and is mounted in an acoustically isolated cell. Figure 1 also shows the beam path and the aerosol intake bell. The optical geometry of this latter section is designed to minimize disturbance of the intake airflow. The spectrophone houses an acoustically isolated resonant (longitudinal resonance) inner cavity with integral microphone diaphragm (Bruce, 1976a; Bruce et al, 1976). Windows (BaF_2) may be used in both ends of the spectrophone for baking and pumping cycles to eliminate system related trace absorption and also to allow calibration with premixed high purity gaseous mixtures. Figure 2 shows a premeasurement calibration in progress during the measurements taken at US Army Missile Command (MICOM) (Bruce et al, 1981). Calibration checks were also performed on site. Figure 3 is a schematic of the technique used for the Smoke Week III calibration and measurement cycles that were obtained simply by the indicated switching process, that is, either forward airflow through the intake bell or backflow through the system when the calibration mixture is selected. These results are occasionally compared with results of the fill-from-vacuum method of Figure 3.

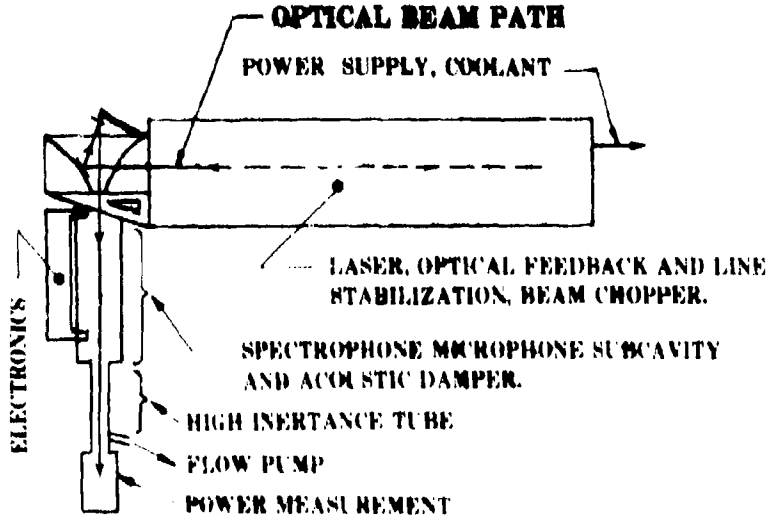

Figure 1. Schematic diagram of 10μm integrated field spectrophone system indicating beam path.

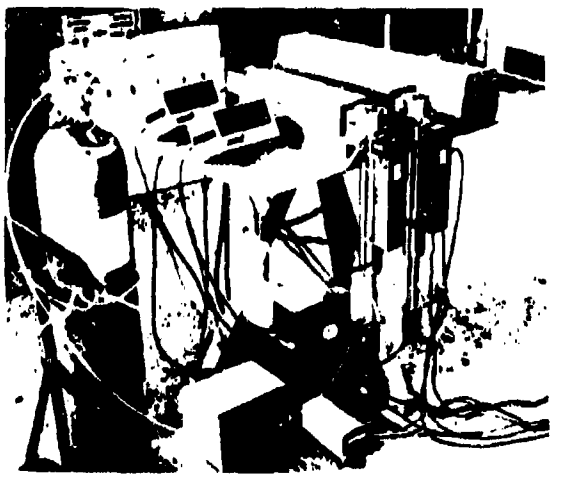

Figure 2. Calibration checkout at MICOM (July 1980) prior to field measurements.

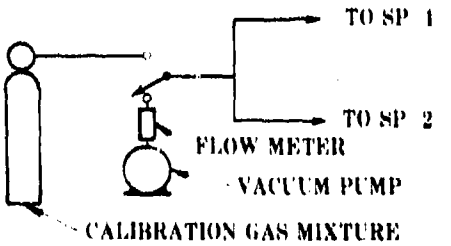

Figure 3. Schematic representation of field calibration procedure.

Figure 4 shows the measurement system at Smoke III. A spectrophone and various particle counters and nephelometers were mounted on the upper level at about 2.6 m above ground level. Another spectrophone was mounted about 1.2 m above the ground level (to the right of the photo).

Spectrophone data were limited to the 10μm window for these measurements. In this region, HC and diesel oil, for example, were known to be very weakly absorbing. Therefore, significant absorption was expected only for the smoke of phosphorus, the experimental smokes, and soil-based dust, if any.

Several general observations may be made concerning a comparison of the Smoke III data from the spectrophones at the 1.2- and 2.6-m levels. The spectrophone calibrations were performed separately and were not subsequently adjusted in any way. However, in every available case, the two peak absorption coefficients were quite close. The remainder of the profiles show more variable agreement although in.

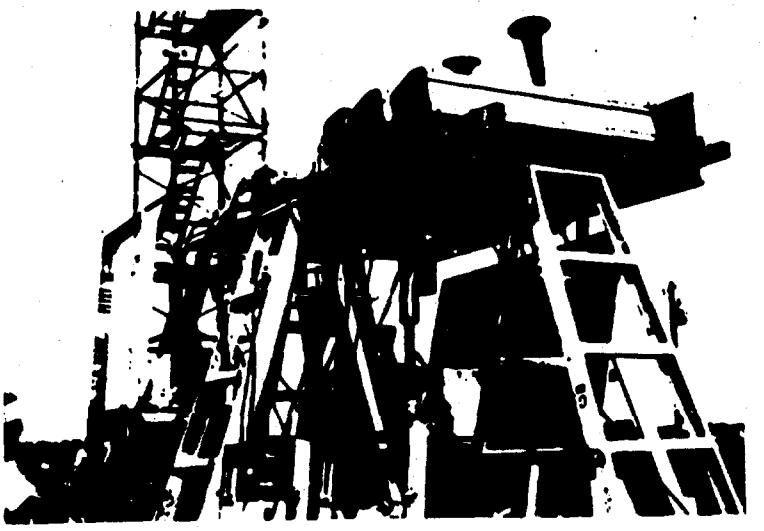

Figure 4. Spectrophone and particle counting systems at Smoke Week III.

each case most features are similar. Figure 5 shows typical examples of results for the smoke of phosphorus and for experimental smoke. The temporal correlation is quite good despite the separation and difference in height. Temporal correlation of the spectrophone and counter data will be presented in papers by Pinnick (1981) and Garvey (1981). Generally, agreement here is also fairly close. However, attempts to correlate these data with those of the ASL 10μm λ transmissometers (Butterfield, 1981) are less successful. Figure 6 shows examples of these attempts. The examples have been divided into two groups: those that correlate well temporally, and those that do not. In the latter category are examples for which the time span of the attenuation is the only point at which the agreement is even nearly approximate. Agreement in magnitudes is expected to occur for the smoke of phosphorus only, since, in this case, at 10μm λ, the extinction and absorption coefficients are very close (Bruce et al, 1980). In any case, the extinction coefficients should be greater than the absorption coefficients.

The log of the measured quantity is actually $-\int \varepsilon(x)dx$ integrated across the extent of the aerosol cloud along the line of sight for the transmissometer. Since there is insufficient data to evaluate this quantity for the appropriate dimension, the approximation $\langle\varepsilon\rangle$ L could be substituted. This approximation can, of course, be expected to be significantly in error for comparison of actual magnitudes at points within the cloud. The values of the outer scale on the ordinate for each graph of figure 6 represent this integral and are scaled for maximum correlation with the spectrophone results. The effective cloud depth apparently varies significantly (L_{cloud} of the order of 0.1 to 0.2 km is

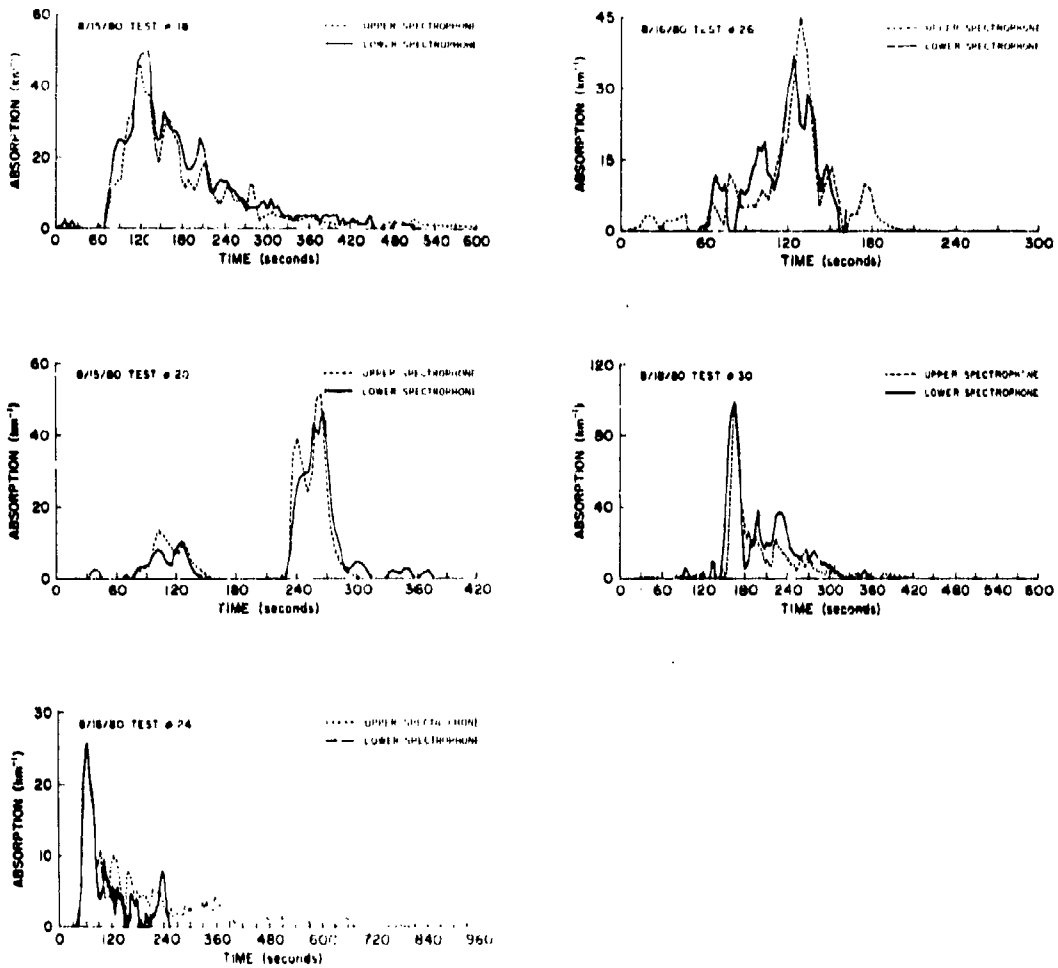

Figure 5. Spectrophone measurements of absorption coefficients for several tests of Smoke Week III at two sites separated by about 3 m at approximate heights of 1.2 m ("lower") and 3 m ("upper") above the ground level. Substances are identified in tables III and IV.

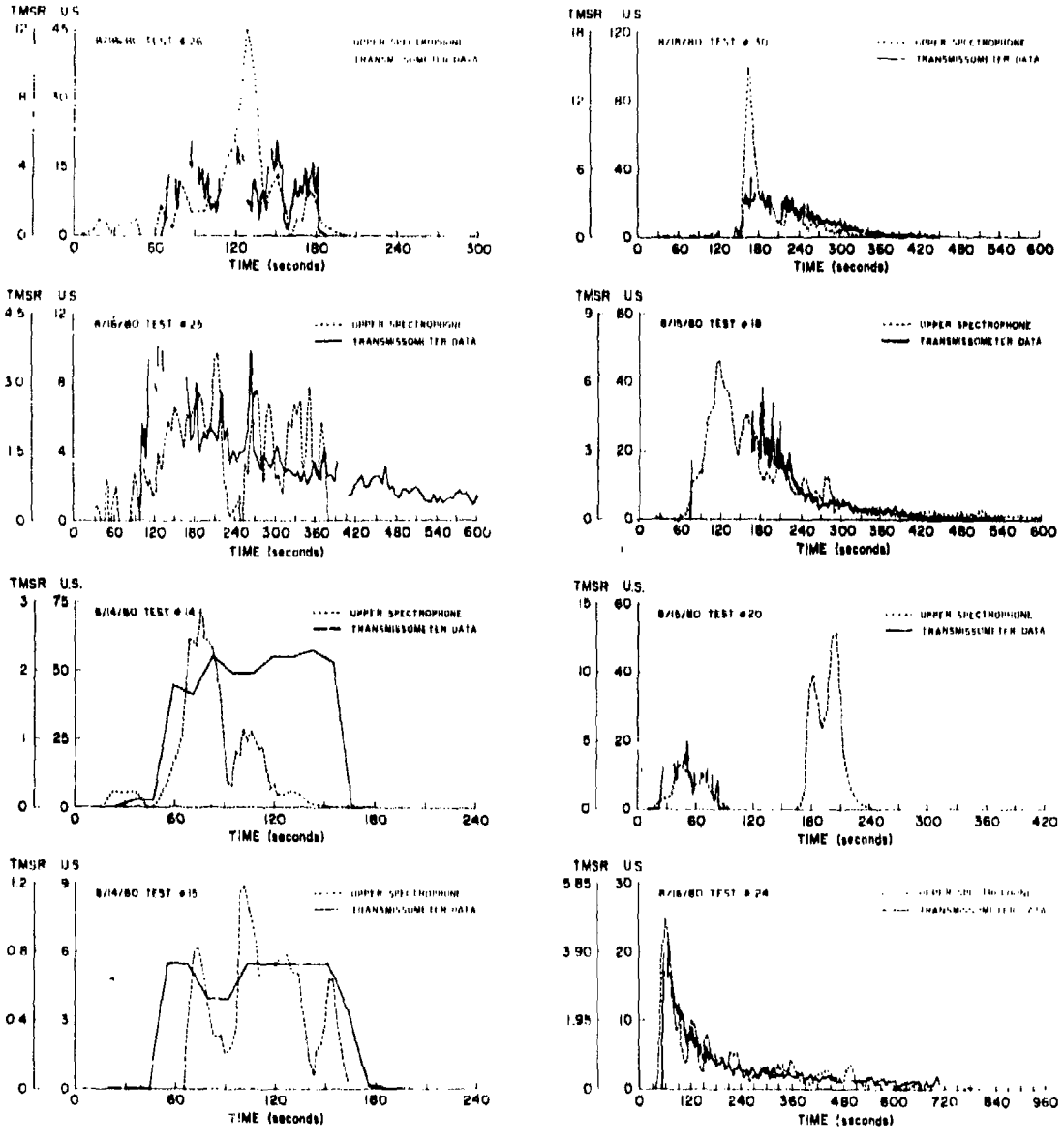

Figure 6. Superimposed log of transmissometer ($\int \varepsilon(x)dx$, unitless) and spectrophone (α, km^{-1}) measurements as functions of time for several Smoke Week III tests. Substances are identified in tables III and IV.

typical). For reasons that are not clear, these values are generally high. An extinction measurement which does not have the above mentioned problem of uncertain effective cloud depth is illustrated in figure 7 where plots for the upper and lower spectrophone and the extinction measured within the same system are shown. The three results are in fairly close agreement. Of course, the extinction values become much less accurate as the extinction coefficient decreases to lower values. The useful threshold here is about 20 km^{-1}, which is relatively low because the system is nearly closed and optical noise (for example, that due to turbulence and irradiance) is minimal and the duration of the signal is brief, so that baseline power drift is also minimal. Note that although the absorption and extinction coefficients may vary greatly with time, the particle size distribution is unlikely to fluctuate significantly; therefore, the ratio of the absorption to extinction coefficients will be nearly constant. This means that the ratio can be taken at high magnitudes of the extinction coefficients (when such occur), and the remainder of the profile is not needed. This measurement was obtained for two experimental smokes, IR 1 and 2, and soil-based dust. Table II shows the ratios for these tests and for Eglin soil-based dust from another test.

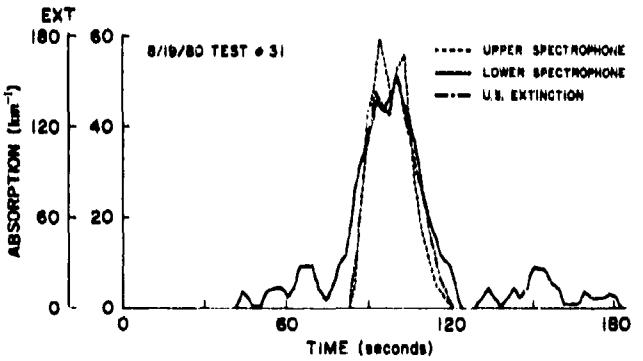

Figure 7. Extinction (upper spectrophone) and absorption coefficients (upper and lower spectrophones) as functions of time for Smoke Week III test number 31 (IR 2).

TABLE II. RATIO OF ABSORPTION TO EXTINCTION COEFFICIENTS FOR THREE AEROSOLS OF SMOKE WEEK III

Substance	Ratio	Expectation
IR-1	0.22	±7%
IR-2	0.37	±4%
Dust	0.19	±4%

Data for these tests are summarized in Tables III and IV. The smoke of phosphorus was expected to be quite effective for 10μm λ screening which is indicated from these field measurements. The particles are small (easily lofted and buoyant), have fairly high mass absorption coefficients, scatter a very small proportion at 10μm λ (about 4%), and are relatively easy to disperse. The ratio α/ε is just about reversed for WP and RP smokes in the visible where scattering predominates (reducing contrast though weakly absorbing). Table IV shows smoke density as measured on the instrumentation pad to be quite variable from cloud to cloud. A large part of this variability results from the fact that the aerosol clouds did not necessarily intersect the instrumentation pad, due either to lifting or changes in wind direction. At least 11 (of 42) test cases were observably in this category. Results for smokes other than that of phosphorus are included; for example, PEG 200 indicates a quite low peak absorption for the single test for which we had valid data. The alkali chloride tests yielded very low 10μm absorption coefficients despite the high relative humidity.

The dynamic range of the spectrophones is not challenged by the magnitudes encountered in these tests (having been used to measure absorption coefficients from less than 10^{-1} to more than 10^{3} km^{-1}) and the values of absorption coefficient for these tests are expected to be quite accurate with regard to peak magnitudes (within ±11 percent) and to be linear to within the same figure.

TABLE III. SUMMARY: DATA FOR TESTS INVOLVING IR 1, 2, 3

Date (Aug 1980)	Official Test Number	IR Number	Host	Value for Absorption to Extinction Coefficient Ratio (α/ϵ)	PMS Particle Counter Data?	Peak Absorption Coefficient	Upper/Lower Spectrophone, Nephelometer	Plot(s)
11	6	1	Fog Oil		Yes	11 km^{-1}	Upper	α
12	10	3			No	4.7, 8.8	Upper	
12	11	1		0.20	No	19 km^{-1}	Upper	α
14	14	2			Yes	73 km^{-1}	Upper	α
15	20	2		$\frac{0.34}{0.37}$	Yes	13, 52	Upper/ Lower	α
16	26	2			Yes	45	Upper/ Lower	α
18	27	2			No	0.27 km^{-1}	Nephe- lometer	
19	31	2		0.39	No	58	Upper/ Lower	α, ϵ
20	35	2			No	<0.02 km^{-1}	Nephe- lometer	
21	38	1		0.24	Yes		Upper	
21	39	2			Yes	>1.7 km^{-1} <3 km^{-1}	Nephe- lometer Upper	
21	40	2			Yes	0.05 km^{-1}	Nephe- lometer	
21	41	1	Fog Oil		No	2.9, 3.9 km^{-1}	Upper	
21	42	2			Yes	<3	Upper	

TABLE IV. SUMMARY: DATA FOR REMAINING OBSCURANTS

Date (Aug 1980)	Official Test Number	Obscurant	PMS Particle Counter Data?	Peak Absorption Coefficient	Upper/Lower Spectrophone, Nephelometer	Plot(s)
11	1	RP	No	>1.7 <3	Nephelometer Upper	
11	5	PEG 200	Yes	>1.7 <4	Nephelometer Upper	
12	7	PWP	No	>1.7 <2	Nephelometer Upper	
13	12	VEESS	Yes	2.97 km^{-1}	Upper	
14	15	PEG 200	Yes	9	Upper	a
14	15	PEG 200	Yes	9	Upper	a
15	16	WP	No		No	
15	18	HN	Yes	50	Upper/ Lower	a
16	21	WP	Yes		No	
16	23	RP	Yes	0.09	Nephelometer	
16	24	PWP	Yes	26	Upper/ Lower	
16	25	WP	Yes	10	Upper	
18	28	HE	No	17.8	Upper	
18	29	Vehicular Dust	No	<0.1	No	
18	30	RP	Yes	100	Upper/ Lower	a
19	32	WP	Yes	31.7*	No	a
19	33	WP	Yes	>1.7 <5	Nephelometer Upper	a
19	34	Alkali Chloride	No	<3	Upper	
20	36	Alkali Chloride	Yes	>1.7 <5	Upper	
20	37	HE Dust	Yes	0.85	Nephelometer	

*Absorption spike (at start) includes dust from detonation.

REFERENCES

Bruce, C. W., 1975, "Ozone Absorption at 9μm CO_2 laser wavelengths," J Opt Soc Am, 65:1163-1164A.

Bruce, C. W., 1976a, "Development of spectrophones for CW and pulsed radiation sources," ECOM-5802, Atmospheric Sciences Laboratory, US Army Electronics Research and Development Command, White Sands Missile Range, NM.

Bruce, C. W., 1976b, "Spectrophone for in-situ measurement of gaseous/particulate absorption," J Opt Soc Am, 66:1071A.

Bruce, C. W., B. Z. Sojka, B. G. Hurd, W. R. Watkins, K. O. White, and Z. Derzko, 1976, "Application of pulsed source spectrophone to absorption by methane gas at DF laser wavelengths," J Appl Opt, 15:2970.

Bruce, C. W., and R. G. Pinnick, 1977, "In-situ measurements of aerosol absorption with a resonant CW laser spectrophone," J Appl Opt, 16:1762.

Bruce, C. W., R. G. Pinnick, R. J. Brewer, Y. P. Yee, and G. Fernandez, 1978, "In-situ measurements of aerosol absorption with a resonant CW laser spectrophone," Proceedings 1978 Army Science Conference, United States Military Academy, West Point, NY.

Bruce, C. W., Y. P. Yee, B. D. Hinds, R. J. Brewer, J. Minjares, and R. G. Pinnick, 1980a, "Initial field measurements of atmospheric absorption at 9-11μm wavelengths," J Appl Meteorol, 19:997.

Bruce, C. W., Y. P. Yee, and S. G. Jennings, 1980b, "In-situ measurement of the ratio of absorption to extinction coefficient," J Appl Opt, 12:1893.

Bruce, C. W., Y. P. Yee, and S. Duran, 1981, "Evaporative clearing for a CO_2 high energy laser beam in white phosphorus smoke," symposium paper A-24.

Butterfield, J. E., 1981, private communication, Smoke Week III transmissometer measurements.

Garvey, D. M., G. Fernandez, C. W. Bruce, and R. G. Pinnick, 1981, "In-situ measurements of phosphorus smokes during Smoke Week III, symposium paper A-17.

Myers, J. F., editor, 1980, "Proceedings of workshop: atmospheric transmission and particle size measurements," AFWAL-TR-80-1086, Air Force Avionics Laboratory, Wright-Patterson Air Force Base, OH.

Pinnick, R. G., G. Fernandez, C. W. Bruce, D. M. Garvey, and B. D. Hinds, 1981, "Particle size and infrared absorption measurements of IR smokes during Smoke Week III," symposium paper A-19.

Samuels, C., C. W. Bruce, and R. J. Brewer, 1978, "Spectrophone analysis of gas samples obtained at field site," ASL-TR-0009, US Army Atmospheric Sciences Laboratory, White Sands Missile Range, NM.

IN SITU MEASUREMENTS OF PHOSPHORUS SMOKES DURING SMOKE WEEK III

D. M. Garvey,* G. Fernandez, C. W. Bruce, and R. G. Pinnick
US Army Atmospheric Sciences Laboratory
White Sands Missile Range, New Mexico 88002

ABSTRACT

The temporal variations in the size distributions of phosphorus smokes generated by a number of techniques during Smoke Week III were measured using a combination of optical particle counters manufactured by Particle Measuring Systems (PMS). Simultaneous measurements of the absorption coefficient at 10.6μm were made using a CO_2 laser spectrophone. Relative humidities during the sample period varied from 58 to 93 percent; peak mass loadings inferred from the measured size distributions ranged from 0.025 to 0.25 g/m^3. Mass loadings greater than 0.1 g/m^3 were found only during the first minute of about half the tests, and there was evidence that the submicron particle counters were saturated during these times. Generally both the number concentration and mean particle radius decreased thereafter. For tests in which the peak measured mass loading was less than 0.05 g/m^3, size distributions remained relatively constant and were similar to those found during the latter part of the tests with initially high mass loadings, namely, a principal mode at $r < 0.2\mu m$ and a secondary mode at $r \approx 2\mu m$. Time correlation of calculated mass loadings with the spectrophone measurements was generally good and indicated a mass absorption coefficient of the order of 0.5 m^2/g, though this value varied significantly from test to test.

1. INTRODUCTION

The amount of water absorption by hygroscopic smokes as a function of relative humidity can be predicted from empirical and theoretical considerations (Hänel, 1976; Fitzgerald, 1975), and the growth of phosphorus smoke particles, in particular, has been modeled by Frickel et al (1979), Hänel (1978), and Tarnove (1980), among others. Attempts to verify these growth models, particularly in field experiments (Farmer et al, 1980), have been hampered by a number of factors, including differences in the smoke generation procedures. The principal obstacle, however, appears to be the lack of a fast response particle measuring system which can consistently and accurately size particles of radii from ~0.05μm to 10μm in the very high concentrations (>10^6 cm^{-3}) characteristic of military smoke clouds.

To meet this need, we have assembled a system of three Particle Measuring Systems (PMS) optical particle counters, including the ASASP-X and the CSASP-100. These probes and their calibrations have been described by Garvey et al (1980) and Pinnick et al (1979). During Smoke Week III, this system of probes was used to measure the phosphorus smokes generated by a number of techniques. They were situated 2.5 m above the ground in close proximity to a CO_2 laser spectrophone operated at 10.6μm (see Bruce et al, 1981). The ranges of the probes were set so that particles from 0.1μm to 10μm in radius were sized and counted.

*National Research Council Senior Research Associate on leave from Department of Atmospheric Science, Colorado State University, Fort Collins, CO.

The principal objectives of the size distribution measurements were:

a. To determine the functional dependence of the particle sizes on time;

b. To determine the functional dependence of the particle sizes on relative humidity;

c. To obtain an analytic expression which accurately parameterizes the particle concentrations and sizes.

The simultaneous absorption measurements made with the spectrophone were used together with the optical particle counter results to yield experimentally determined mass absorption coefficients at 10.6μm. Since the extinction at 10.6μm is known to be absorption dominated, these values can be used to provide reasonable estimates of the mass extinction coefficients (Pinnick and Jennings, 1980).

2. SIZE DISTRIBUTION MEASUREMENTS

Size distributions of phosphorus smokes as a function of time were measured during seven trials of Smoke Week III. The size distributions (dN/dr) obtained by the three probes at a time close to that of maximum concentration for each trial are shown in figures 1 through 7. The discrepancy among the three probes is disturbing, particularly since the instruments were found to calibrate properly with polystyrene spheres prior to the start of the tests. Also evident from these figures is the deterioration in the response of probe B during the course of the tests. A feature which both probes A and B show in trials 18 and 30 (figures 1 and 5)--an apparent peak in the distribution for $0.3\mu m < r < 0.7\mu m$--has been found in laboratory tests with probe A to be an artifact caused by high concentrations of large particles saturating the probe amplifier. In figures 3, 4, 6, and 7, a mode (a plateau in the distribution) at $r \sim 2.0\mu m$ is evident. This feature also appears later during the other trials, as can be seen in figure 8, which shows the probe responses during trial 21, about 3 minutes later than those shown in figure 2. It has not been determined whether this mode is real or an artifact of the response curve of probe C.

In the analysis presented here, it is assumed that probe C accurately counts and sizes the particles with radii greater than 1μm. If it is further assumed that the concentration of submicron particles is not significantly greater than that implied by the peak concentration measured by probe A, then

undercounting of the submicron particles does not lead to serious errors in our estimate of an integrated quantity such as mass. However, undercounting of the submicron particles can lead to large errors in average quantities such as the mean volume radius.

A summary of the results from all of the trials is given in table 1.

3. TIME EVOLUTION OF THE PARTICLE SIZE DISTRIBUTIONS

We make three assumptions concerning the interaction of the phosphorus smoke with the ambient atmosphere:

a. The wind is relatively steady in both speed and direction so that the ventilation and dispersion rates are constant.

b. The smoke particles assume their equilibrium sizes in times short compared to the travel time from source to sensors.

c. The phosphorus is mixed with air in sufficiently low concentrations so that the local humidity is not significantly reduced. For the high ambient temperatures of Smoke Week III, this assumption is quite good, but this may not be true in colder environments. Using Tarnove's (1980) values for the equilibrium concentration of H_3PO_4 as a function of relative humidity and assuming no mixing of water vapor from the smoke-free air into the plume, we have calculated the local relative humidity as a function of the mass concentration of phosphorus, the ambient temperature, and the ambient relative humidity. The results shown in figure 9 indicate that for temperatures as low as 30°F and for phosphorus mass concentrations as high as 1g/kg of air, the reduction in the relative humidity can be very pronounced. Two factors which would mitigate this result are mixing of water vapor from the smoke-free air and production of water vapor in the source combustion process.

With these assumptions, the evolution of the particle sizes as measured at a point removed from the smoke source should depend primarily on the degree of coagulation among the particles. If the output rate of the smoke source remains constant, then the amount of coagulation, if any, also remains constant, and the particle size distribution should not change with time. If the output rate of the smoke source decreases with time, say exponentially, then the degree of coagulation, if initially significant, also decreases and the average particle size should decrease with time.

The evolution of the particle size distributions as measured by the PMS probes is consistent with these expectations. Figures 10 through 16 show the mass concentrations of the phosphorus smokes as determined from probes A and C for the seven phosphorus smoke trials. These figures also show values of the mean volume radii as a function of time. The mass concentrations were calculated from the probe response assuming that the particles were spherical and had a density (ρ) determined from the relative humidity using the results of Hänel (1978) (table 1). The ranges of the individual probes used in the calculation of the mean volume radii were:

Probe A	$0.12\mu m < r < 0.42\mu m$
Probe B	$0.42\mu m < r < 0.75\mu m$
Probe C	$0.75\mu m < r < 10\mu m$

The mass loading (M) and the particle concentration (N_p) are related through the mean volume radius (r_{mv}) as

$$M = N_p \frac{4}{3} \pi r_{mv}^3 \rho . \tag{1}$$

As might be inferred from figures 1 through 7, the particles counted by probe C generally dominate the mass calculations. The temporal correlation among the probes is very good in all cases where the measured mass is significant. The absolute values of r_{mv} are in error because of our incomplete counting of the submicron particles; but to the extent that N_p is dominated by probe A, and M by probe C, the relative values of r_{mv} were consistently determined from test to test.

Five of the tests show an exponential decay in the mass concentration with time (figures 10, 11, 12, 14, and 16). The two tests in which the source is indicated as WP wedge (trials 25 and 32) show long periods of relatively constant mass loadings (figures 13 and 15). For periods during which the mass loading is greater than $\sim 10^4 \mu g/m^3$, variations in the mass loading are reflected by corresponding variations in the mean volume radius. This is true of both the high frequency variations and the long time constant decay. Thus, trials showing a fall-off in the mass loading also show an initial fall-off in the value of the mean volume radius due to a proportionately greater number of large particles during times when the mass (and particle) concentrations are high. It is likely that this result is due to

coagulation of particles at high concentrations, but we cannot ignore the possibility that the undercounting of submicron particles is a contributing factor.

For all of the tests there is a period of time, which corresponds to mass loading of $10^3 \mu g/m^3 < M < 10^4 \mu g/m^3$, during which the mean volume radius is relatively constant, reflecting variations in the mass loading only slightly, if at all. These periods extend from at least 3 minutes (trial 21) to the entire duration of a test (trial 32). During these "steady state" periods, the form of the particle size distribution remained constant even though the total number of particles continued to fall off. The values of r_{mv} during these periods are given in table 1.

For mass loadings less than $10^3 \mu g/m^3$, the mean volume radius generally exhibited large fluctuations which did not necessarily reflect variations in the mass loading. This result is most pronounced for trials 21 and 24 (figures 11 and 12). The effect is almost certainly caused by statistically insufficient numbers of larger particles. It is worthy of note that the mass loadings in trials 25 and 32 never dropped below a level of $10^3 \mu g/m^3$.

4. EFFECT OF RELATIVE HUMIDITY ON PARTICLE SIZE

Theories of the growth of hygroscopic particles predict that the equilibrium radius (r) of a solution droplet at a given relative humidity (ψ) is equal to a multiplicative constant times the dry particle radius (r_o)

$$r = \alpha(\psi) r_o \qquad (2)$$

For dry particle radii $0.1\mu m \leq r_o \leq 1\mu m$, a linear relation is valid within 2 percent for relative humidities up to 95 percent. The functional dependence of α on ψ for phosphoric acid is shown for three models in figure 17 (Tarnove, 1980; Hänel, 1978; and Rubel, 1979). The model of Tarnove takes into account only the vapor pressure depression of water due to the presence of the phosphoric acid and not the vapor pressure enhancement due to the curvature of the particle. Since the latter represents a growth inhibition factor, Tarnove's model should represent an upper bound to expected particle growth. Hänel's values of α are identical to those of Tarnove for $0.4 \leq \psi \leq 0.8$. His value at $\psi = 0.2$ appears anomalously low. The model of Rubel falls below that of Tarnove for $0.2 \leq \psi \leq 0.8$. Hänel's and Rubel's

values, identical at $\psi = 0.9$ and $\psi = 0.95$, lie above the corresponding values of Tarnove. Except for Hänel's value at $\psi = 0.2$, all are in agreement within 6 percent.

Attempts to verify these growth models for distributions of dry particle sizes generated in field experiments have not been successful. Size distributions of phosphorus smokes generated by three different techniques during the High Humidity Hygroscopic Smoke (H^3S) field test are presented by Farmer (1980). The humidity in these tests varied from 73 to 97 percent, and yet the size distributions obtained with both a particle sizing interferometer and a Climet optical particle counter showed very little variation from one test to another. In fact, there is a suggestion that the mean particle size actually decreased with increasing relative humidity. It is apparent that if all of the particles in a distribution are counted and sized, mean values of the radius of that distribution will be equal to $\alpha(\psi)$ times the corresponding mean value of the dry particle distribution. Farmer's values of the mean volume radii of phosphorus smokes measured by the particle sizing interferometer and the Climet instrument are plotted in figures 18 and 19. To plot these data in the format of figure 17, each data set was divided by a somewhat arbitrarily chosen value of the mean volume radius of the dry particle size distribution (r_{mv_o}). (A limiting condition for r_{mv_o} was that all resulting values of α had to fall between 1 and 2.5). Note that the values of r_{mv_o} differ slightly for the two data sets, and that both data sets indicate that the mean particle sizes decrease with increasing relative humidity. Farmer suggested that this result might in part be due to the fact that particles with radii less than 0.15μm were not accurately sized or counted.

Laboratory verification of the phosphorus growth model has been somewhat more successful. Frickel et al (1979) have presented size distribution data for phosphorus smokes measured in a chamber with an Anderson impactor. The relative humidity in these tests varied from 0.12 to 0.51, and results are given in terms of a mass median radius (r_{MM}) and a geometric standard deviation (σ_g). The values of r_{MM} may be converted to r_{mv} using the relation given in the next section [equation (6)]. These values of r_{mv} divided by an appropriate value of r_{mv_o} are plotted in figure 20. It appears that at least two distributions characterized by two different values of r_{mv_o} were initially present, and that the one characterized by an r_{mv_o} of 0.25μm is in agreement with the growth model up to $\psi = 0.5$. Note that this value is less than that for either of the data sets of Farmer.

Values of the steady-state mean volume radius for the seven Smoke Week III trials determined as outlined above are plotted in figure 21. Again, the data set is divided by an appropriate value of

r_{mv_o}. The data do bear a general resemblance to the growth model, but there is too little data and too much scatter for any definitive conclusion. A reason for the relatively low value of r_{mv_o} is that the initially high values of r_{mv} measured during periods of high concentrations were not considered representative.

5. PARAMETERIZATION OF THE PARTICLE SIZE DISTRIBUTIONS

Typical size distributions obtained for the data sets used in plotting figures 18 through 20 are shown in figure 22. Note that the actual experimental data have been plotted for size measurements made with the particle sizing interferometer and the Climet optical particle counter, whereas the data obtained with the Anderson impactor had already been fit to a lognormal expression of the form

$$\frac{dM}{d \ln r} = \frac{M}{\sqrt{2\pi} \ln \sigma_g} \exp - \left[\frac{\ln^2 \frac{r}{r_{MM}}}{2 \ln^2 \sigma_g} \right] \tag{3}$$

To plot a distribution of this form as dN/dr, we note that the lognormal form remains unchanged

$$\frac{dN}{dr} = \frac{N_p}{\sqrt{2\pi} \ln \sigma_g} \exp - \left[\frac{\ln^2 \frac{r}{r_g}}{2 \ln^2 \sigma_g} \right] \frac{1}{r}, \tag{4}$$

that σ_g is the same for both expressions, and that

$$r_{MM} = r_g \exp (3 \ln^2 \sigma_g) \tag{5}$$

(Patterson and Gillette, 1977).

The mass loading (M) and total particle concentration (N_p) are related by equation (1) where

$$r_{mv} = r_g \exp(1.5 \ln^2 \sigma_g) = r_{MM} \exp(-1.5 \ln^2 \sigma_g) \tag{6}$$

(Lindauer and Castleman, 1971).

Frickel et al (1979) emphasize an important property of a distribution having this analytical form, namely, that for particle growth satisfying equation (2), the form of the distribution will remain unchanged for changes in the relative humidity; N_p and σ_g remain constant and

$$r_g = a\, r_{g_o} . \tag{7}$$

Comparing the distributions of figure 22, we note that both the PSI and the Climet instruments yield broader distributions than the Anderson impactor and that they show no indication of a peak in the distribution at $r \sim 0.2\mu m$. The Climet data exhibit a power law distribution

$$\frac{dN}{dr} = cr^{-\nu} \tag{8}$$

over the range $0.15\mu m < r < 1.5\mu m$ where $\nu \approx 2$. The PSI determined distribution is very flat over this range with a mode at $r \sim 2.0\mu m$, a relatively steep fall-off for $r > 2.0\mu m$, and a large number of particles with $r < 0.15\mu m$. Neither the Climet- nor the PSI-determined distribution appears to be lognormal in character.

Only relative values of dN/dr are to be compared in figure 22. Actual number (or mass) concentrations are not available for either the Climet data or the Anderson impactor data. The plots are presented as typical distributions obtained with the respective instruments, even though our analysis of the data for Smoke Week III shows the form of the distributions to be a function of the number concentration or mass loading. In general, the greater the mass loading the broader the distribution—a property which we have attributed to coagulation. Thus, in parameterizing the data obtained with the PMS probes we have chosen two forms of the particle size distribution: one representing the maximum measured concentration and the other typical of the form of the distribution at mass concentrations less than $10^4 \mu g/m^3$. These are given together with the slightly modified probe responses with which they were fit in figures 23 and 24. No procedure was used to establish a best fit; single values of the parameters N_p, r_g, and σ_g were chosen which established a reasonable compromise between the responses of probes A and C. No attempt was made to parameterize the apparent 2μm mode in the distributions, though consideration was given to its effect in broadening the distribution.

It is seen that even the typical PMS-measured distribution is much broader (σ_g is bigger) than typical distributions obtained with the Anderson impactor, but that the number concentration falls off much more sharply with size over the range $0.15 < r < 1.5\mu m$ than do the distributions obtained with the PSI and the Climet instruments. It is further noted that the peak in the lognormal distribution is not actually measured; in this respect the results confirm those of the PSI and Climet instruments--the primary mode in the number size distribution is at $r < 0.2\mu m$. The mode at $r \sim 2.0\mu m$ found with the PSI instrument may be present, but its fractional contribution to the mass loading is not dominant.

A comparison was made between the values of M and r_{mv} calculated from the actual measurements and those obtained using the parameterized distributions of figures 23 and 24. It was found that the values of M obtained using the lognormal parameters are from 2.5 to 6 times lower than those calculated from the measurements. This is because the response of probe C is not given full weight in the parameterization. The values of r_{mv} are reduced both for this reason and because a greater number of particles are accounted for in the lognormal parameterization than are actually measured by the probes.

6. ABSORPTION AND EXTINCTION PROPERTIES OF THE PHOSPHORUS SMOKES

A comparison of spectrophone (Bruce et al, 1981) measurements of absorption at $10.6\mu m$ with calculated mass loadings is given in figures 25 through 28 for the four phosphorus smoke trials in which simultaneous measurements were made. The temporal correlation of the independent measurements was good, particularly so for trials 24 and 25. If the peak values of absorption and mass are compared, a mass absorption coefficient for each test can be inferred. These values (given in table 1) are in very rough agreement with theoretical predictions (Pinnick and Jennings, 1980) but show a significant variability from test to test.

7. SUMMARY OF RESULTS

The conclusions to be drawn from the work presented in this paper can be summarized as follows:

a. In general, the size distribution of the phosphorus smoke produced by a source exhibiting an exponential decay in its output rate is not constant with time. For mass concentrations greater than $\sim 10^4 \mu g/m^3$, the mean particle size decreases as the mass concentration falls off, apparently due to particle coagulation.

b. The experimental results of Smoke Week III are insufficient to verify models of particle growth as a function of relative humidity. For the relatively steady-state conditions achieved during the middle of the trials summarized here, larger particles are found during tests with high relative humidity, but the sources and ventilation rates were not sufficiently controlled to verify a growth model predicting r/r_o as a function of ψ.

c. The size distributions of the phosphorus smokes can be reasonably parameterized by the lognormal function [equation (4)], though the small particle "wing" of the distribution has not been adequately measured. Values of r_g in this parameterization do not vary greatly, a typical value being $r_g = 0.15\mu m$, and a value at a high mass concentration being $r_g = 0.20\mu m$. Values of σ_g (1.75 to 2.0) are larger than those determined from laboratory experiments (Frickel et al, 1979) and decrease as the mean particle size decreases.

d. Comparisons of mass loadings determined from the PMS-measured size distributions with spectrophone-measured absorptions show rough agreement with theoretical predictions. Discrepancies of a factor of 2 in the mass absorption coefficients can well be due to uncertainties in the measured size distribution.

8. REFERENCES

Bruce, C. W., Y. P. Yee, A. V. Jelinek, L. M. Moore, and N. Richardson, 1981

Battlefield smoke/dust parameters measured in-situ using spectrophones, Proceedings of Smoke/Obscurants Symposium V, Aberdeen Proving Ground, MD.

Farmer, W. M., 1980

A Summary and Evaluation of Data Obtained in the High Humidity Hygroscopic Smoke Test, Final Report to Project Manager/PM Smoke Office, University of Tennessee Space Institute, Tullahoma, TN.

Firzgerald, J. W., 1975

Approximation formulas for the equilibrium size of an aerosol particle as a function of its dry size and composition and the ambient relative humidity, J Appl Meteorol, 14:1044-1049.

Frickel, R. H., G. O. Rubel, and E. W. Stuebing, 1979

Relative humidity dependence of the infrared extinction by aerosol clouds of phosphoric acid, Proceedings of Smoke/Obscurants Symposium III, Aberdeen Proving Ground, MD 517-548.

Garvey, D. M., R. G. Pinnick, and C. W. Bruce, 1980

Calibration and application of two Knollenberg optical particle counters, Proceedings of the Eighth International Conference on Cloud Physics, Clermont-Ferrand, France, 677-679.

Hänel, G., 1976

The properties of atmospheric aerosol particles as functions of relative humidity at thermodynamic equilibrium with the surrounding moist air, Adv in Geophys, 19:73-188.

Hänel, G., 1978,

Private communication.

Lindauer, G. C., and A. W. Castleman, Jr., 1971

Initial size distributions of aerosols, Nucl Sci and Eng, 43:212-217.

Patterson, E. M., and D. A. Gillette, 1977

Commonalities in measured size distributions for aerosols having a soil-derived component, J Geophys Res, 82:2074-2082.

Pinnick, R. G., and H. J. Auvermann, 1979

Response characteristics of Knollenberg light-scattering aerosol counters, J Aerosol Sci, 10:55-74.

Pinnick, R. G., and S. G. Jennings, 1980

Relationships between Radiative Properties and Mass Content of Phosphoric Acid, HC, Petroleum Oil, and Sulfuric Acid Military Smokes, Technical Report ASL-TR-[illegible]052, US Army Atmospheric Sciences Laboratory, White Sands Missile Range, NM.

Rubel, G. O., 1979

An aerosol kinetic model for the condensational growth of a phosphorus smoke, Proceedings of Smoke/Obscurants Symposium III, Aberdeen Proving Ground, MD, 729-756.

Tarnove, T. L., 1980

Studies of the Chemistry of the Formation of Phosphorus-derived Smokes and their Implications for Phosphorus Smoke Munitions, Technical Report ARCSL-TR-80049, Chemical Systems Laboratory, Aberdeen Proving Ground, MD.

TABLE 1. SMOKE WEEK III: PHOSPHORUS SMOKE SUMMARY

Trial	Source Material	Wind (m/s)	Relative Humidity	Particle Density (g/cm^3)	Sample Duration (min)	Peak Mass Loadings ($\mu g/m^3$)	Peak Mean Volume Radius (μm)	Steady State Mean Volume Radius (μm)	Peak Absorption Coefficient (km^{-1})	Mass Absorption Coefficient (m^2/g)
18	HN Pellets	2	0.81	1.21	8.0	1.5×10^3	1.1	0.48	40	0.27
21	WP Rockets	1.5	0.93	1.10	9.0	2.0×10^5	1.0	0.70		
24	Zuni FWF	4	0.65	1.51	10.0	2.5×10^4	0.5	0.30	20	0.80
25	WP Wedge	3.5	0.61	1.33	12.25	5.0×10^4	0.65	0.46	8	0.16
30	WP Pellets	3.5	0.71	1.27	7.0	1.0×10^5	0.85	0.40	80	0.80
32	WP Wedge		0.58	1.35	13.25	1.0×10^4	0.45	0.37		
33	Foreign WP	3.5	0.72	1.27	4.75	8.0×10^3	0.45	0.35		

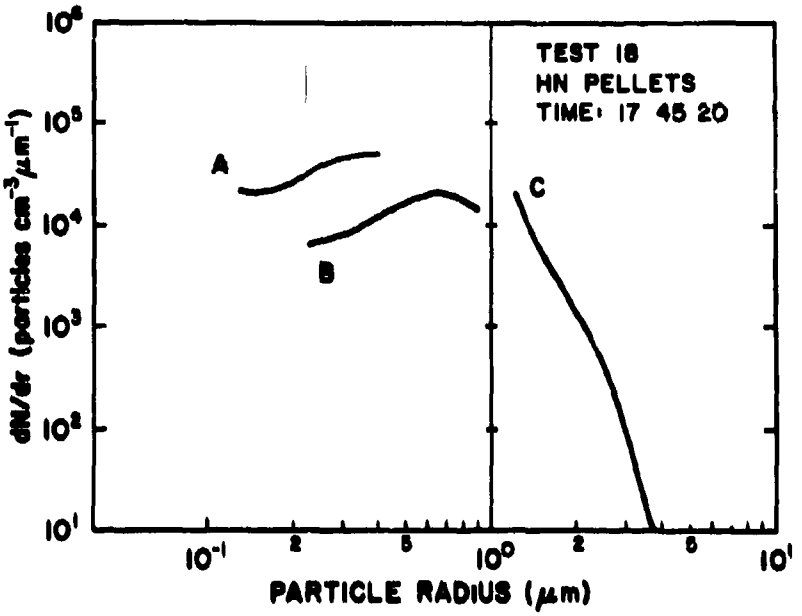

FIGURE 1. SIZE DISTRIBUTIONS OBTAINED BY THREE PMS PROBES NEAR TIME OF MAXIMUM SMOKE CONCENTRATION DURING TRIAL 18.
PROBE A:ASL ASASP-X, RANGE 1; PROBE B. DUGWAY PROVING GROUND ASASP-X, RANGE 1; PROBE C:ASL CSASP-100, RANGE 1.

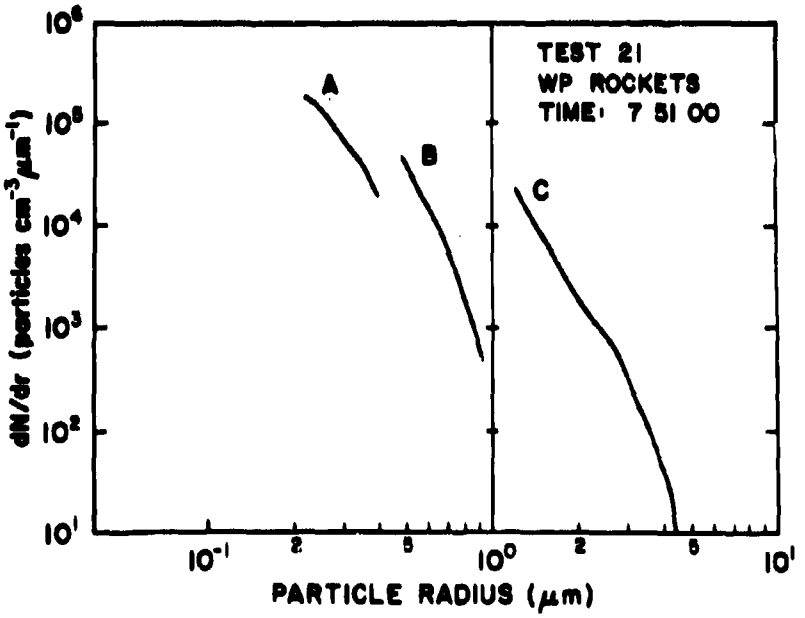

FIGURE 2. SAME AS FIGURE 1 FOR TRIAL 21.

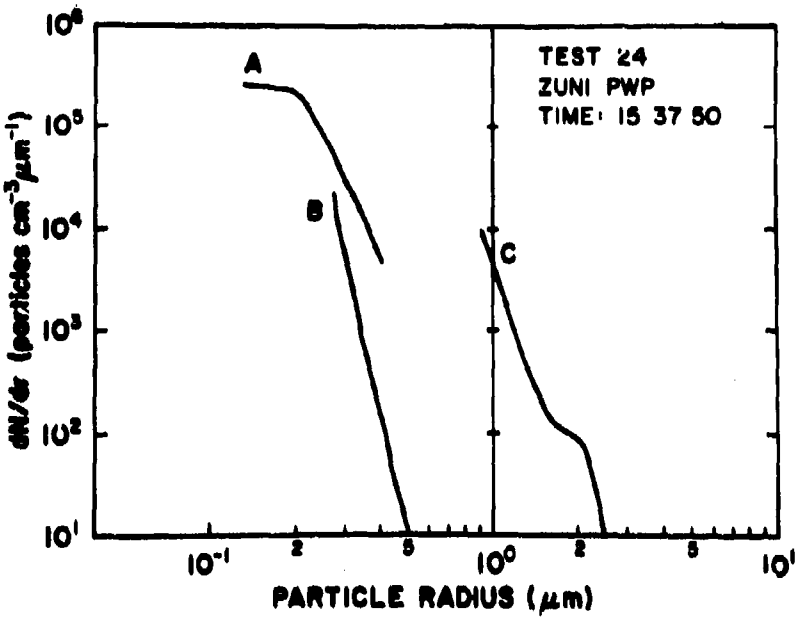

FIGURE 3. SAME AS FIGURE 1 FOR TRIAL 24.

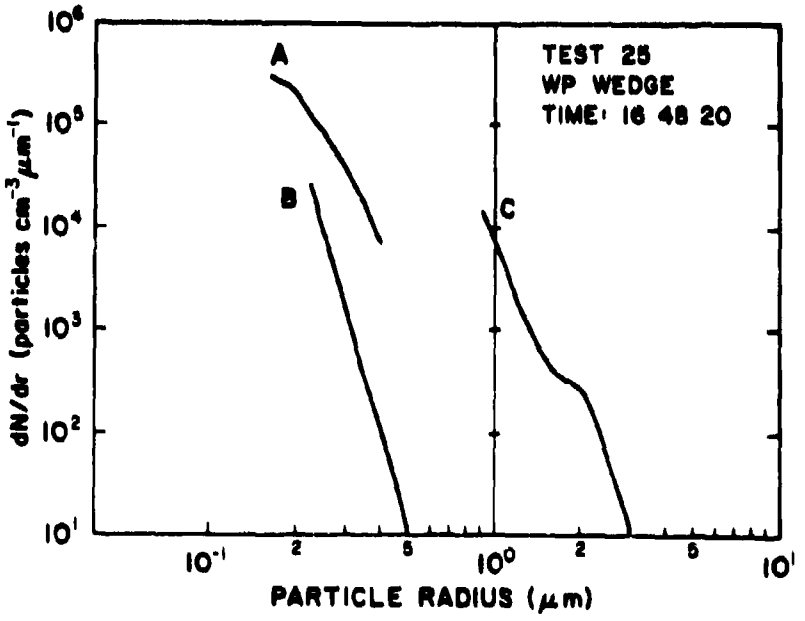

FIGURE 4. SAME AS FIGURE 1 FOR TRIAL 25.

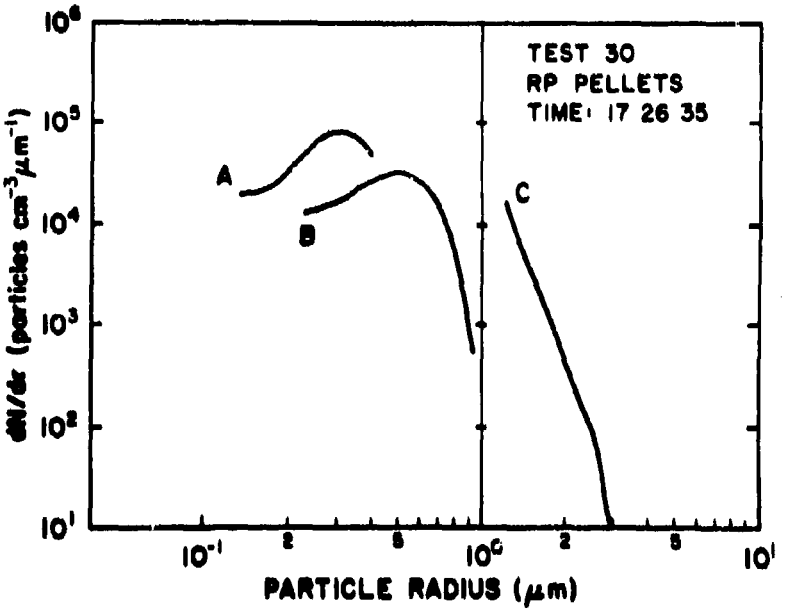

FIGURE 5. SAME AS FIGURE 1 FOR TRIAL 30.

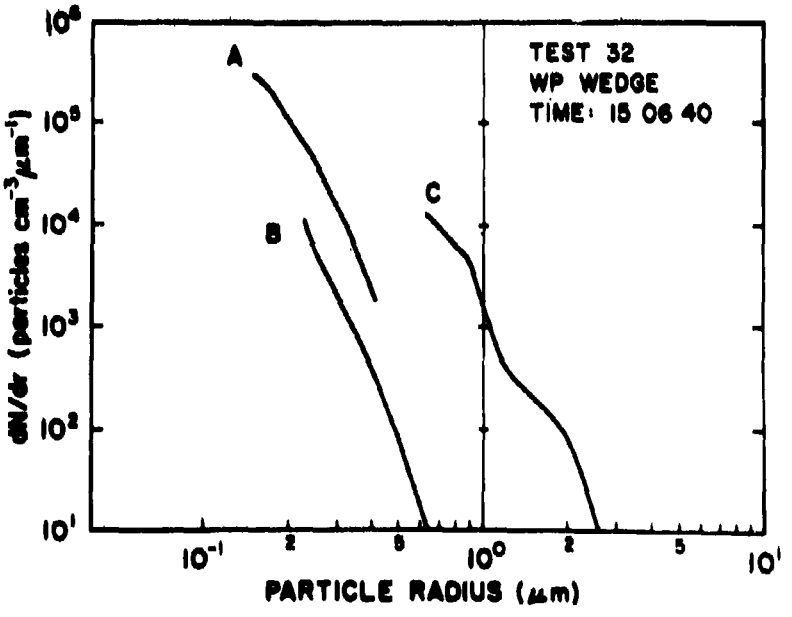

FIGURE 6. SAME AS FIGURE 1 FOR TRIAL 32.

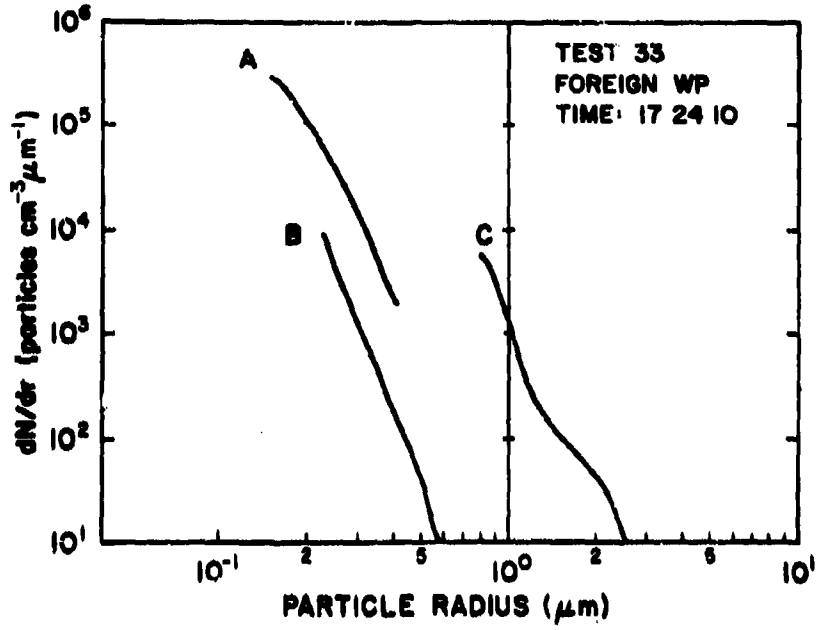

FIGURE 7. SAME AS FIGURE 1 FOR TRIAL 33.

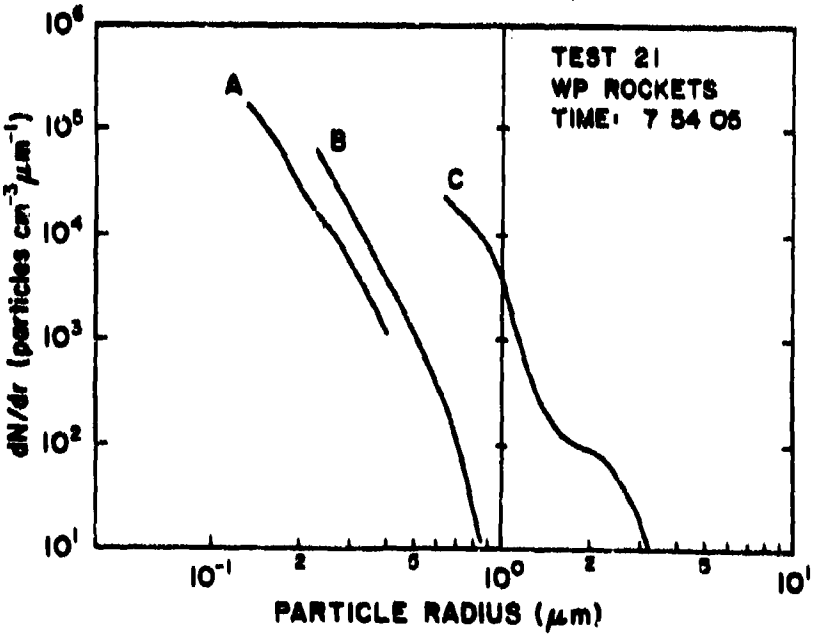

FIGURE 8. SIZE DISTRIBUTION OBTAINED BY THREE PMS PROBES AT A TIME DURING TRIAL 21 WHEN THE MEAN VOLUME RADIUS WAS RELATIVELY CONSTANT.

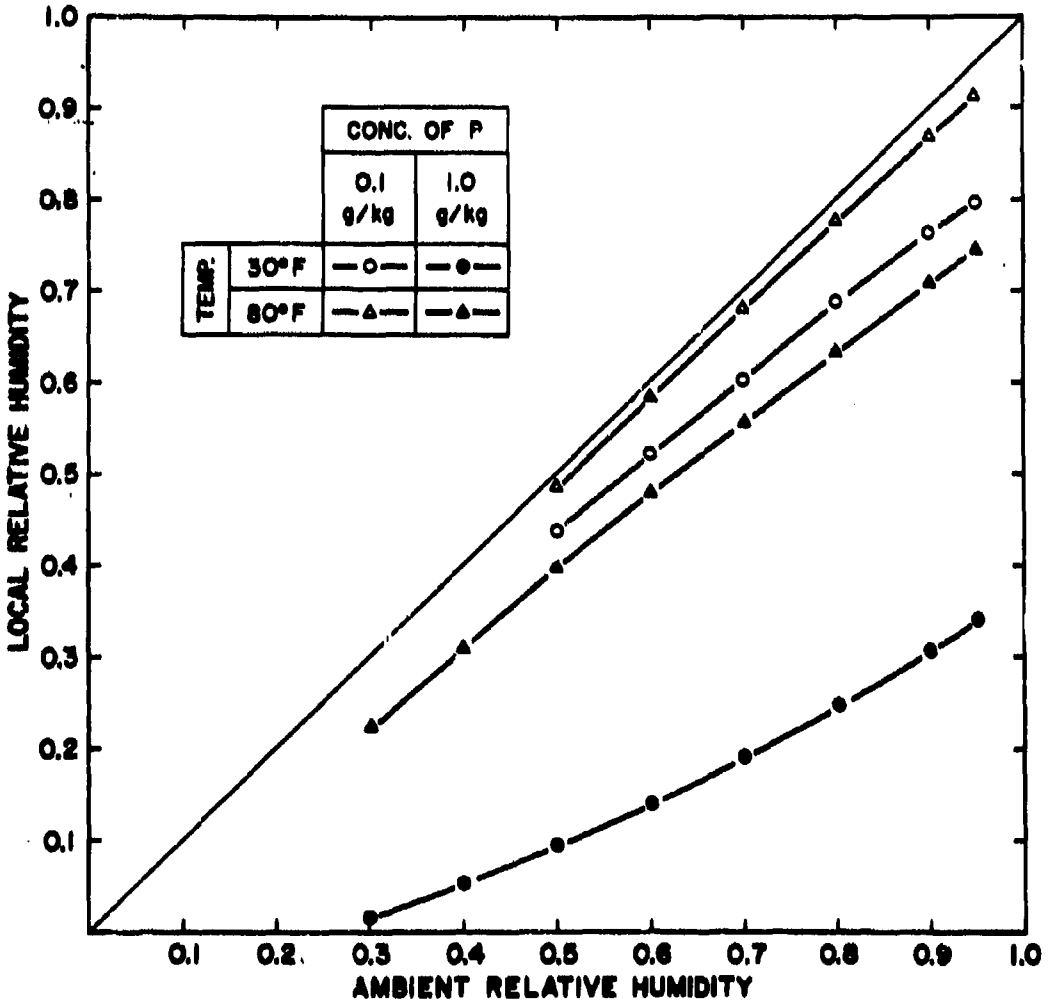

FIGURE 9. LOCAL RELATIVE HUMIDITY (WITHIN PHOSPHORUS SMOKE PLUME) AS A FUNCTION OF AMBIENT RELATIVE HUMIDITY FOR GIVEN VALUES OF PHOSPHORUS MASS LOADING AND AMBIENT TEMPERATURE. It is assumed that no mixing of water vapor from outside the plume has taken place and that the ambient pressure is 1000 mbar.

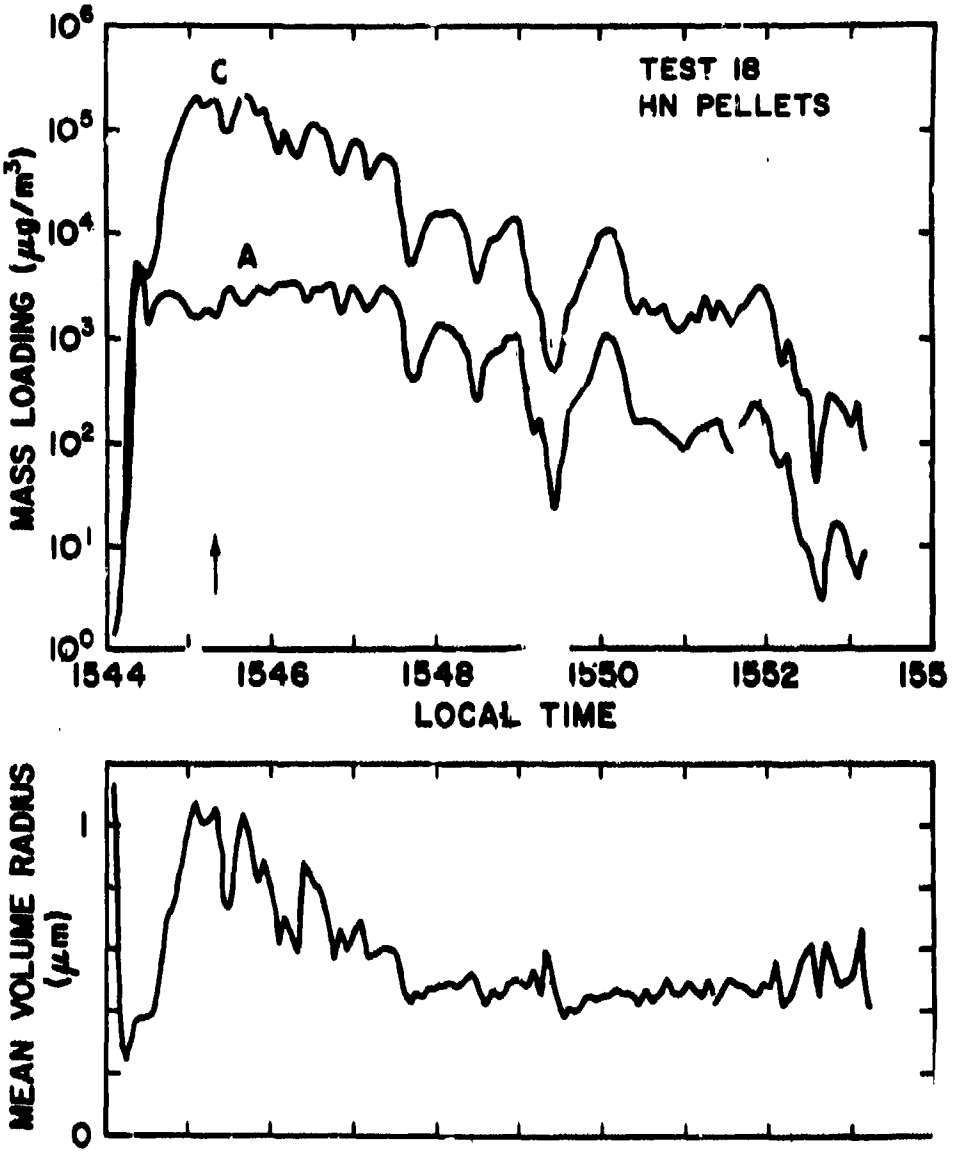

FIGURE 10. MASS LOADINGS OF PHOSPHORUS SMOKE DETERMINED FROM PROBE A (ASL ASASP-X, RANGE 1) AND PROBE C (ASL CSASP-100, RANGE 1) AS A FUNCTION OF TIME DURING TRIAL 18. Corresponding values of the mean volume radius calculated as described in the text are also given. Arrow indicates the time at which the probe responses given in figure 1 were obtained.

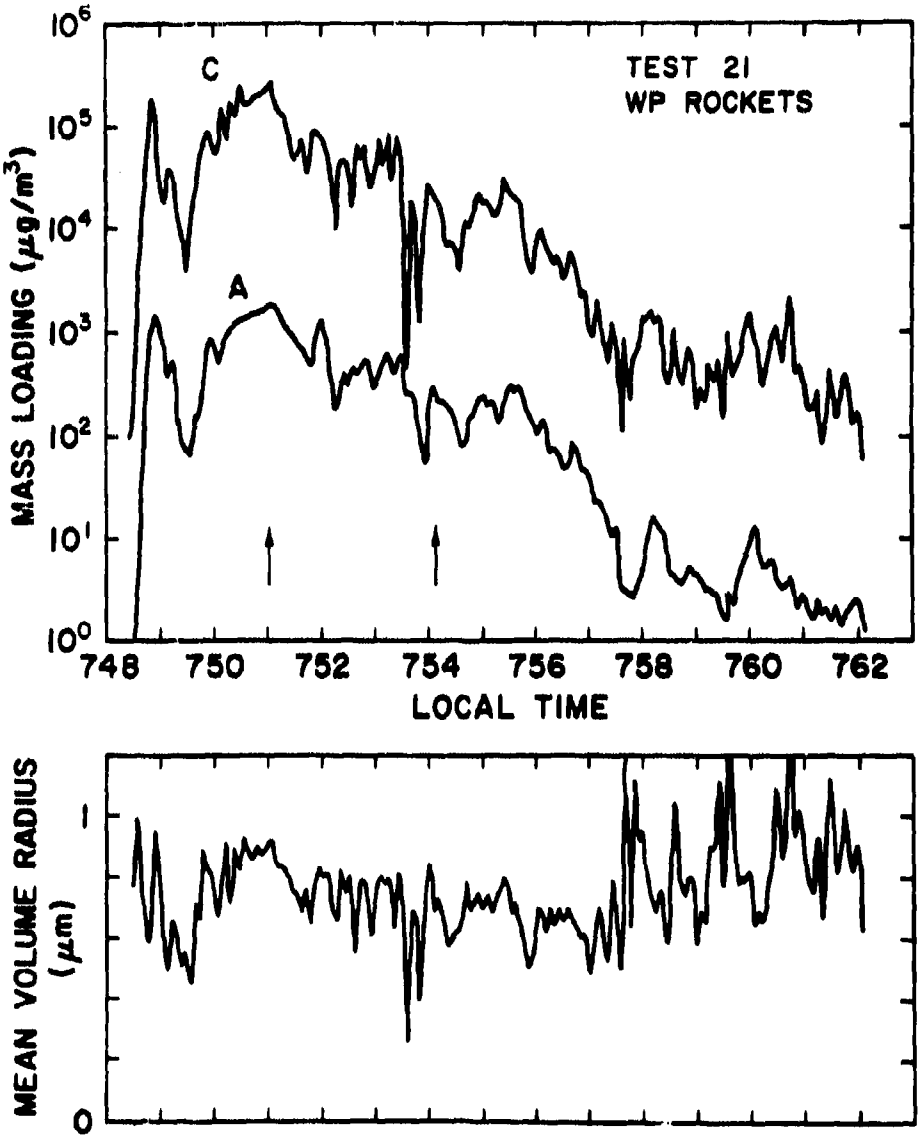

FIGURE 11. SAME AS FIGURE 10 FOR TRIAL 21. Arrows indicate the times corresponding to the probe responses given in figures 2 and 8.

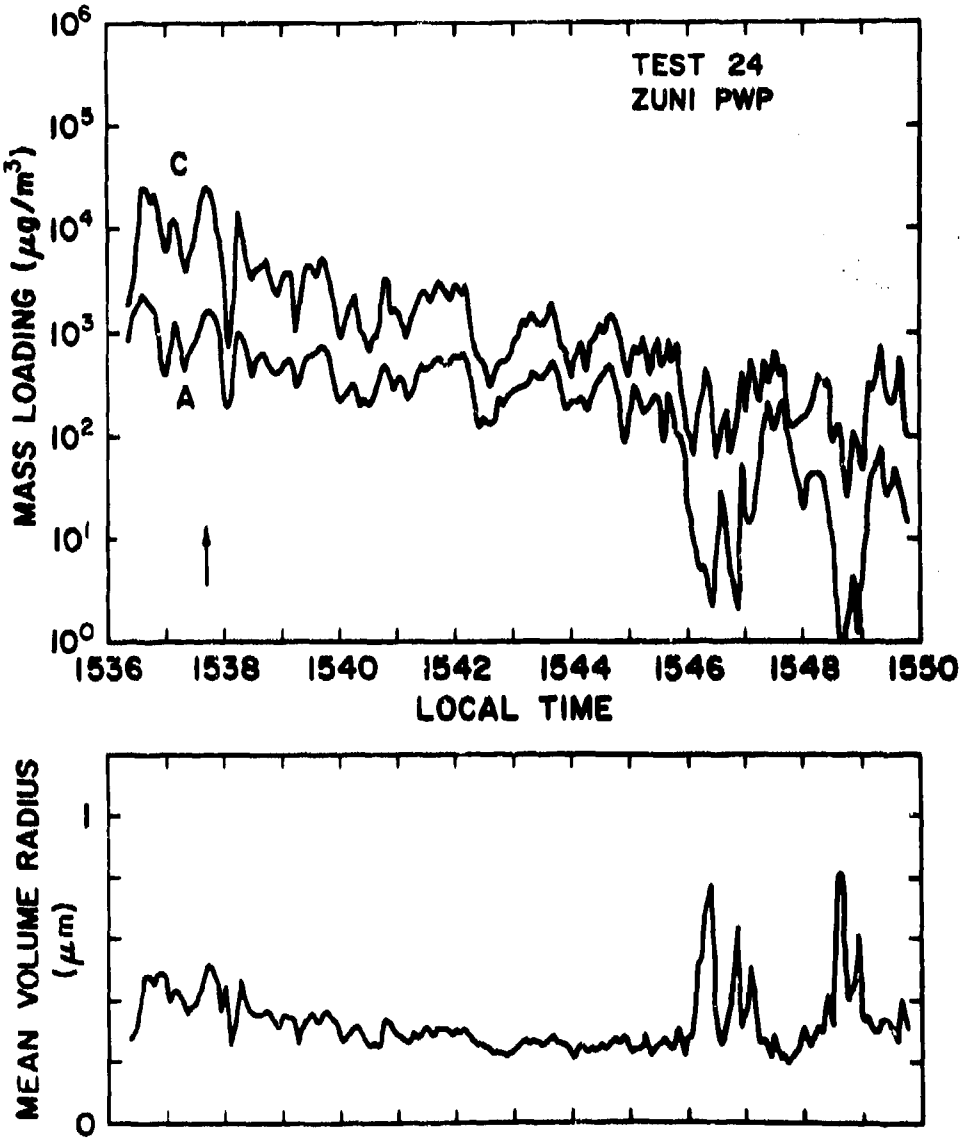

FIGURE 12. SAME AS FIGURE 10 FOR TRIAL 24.
Arrow indicates the time corresponding to the probe responses given in figure 3.

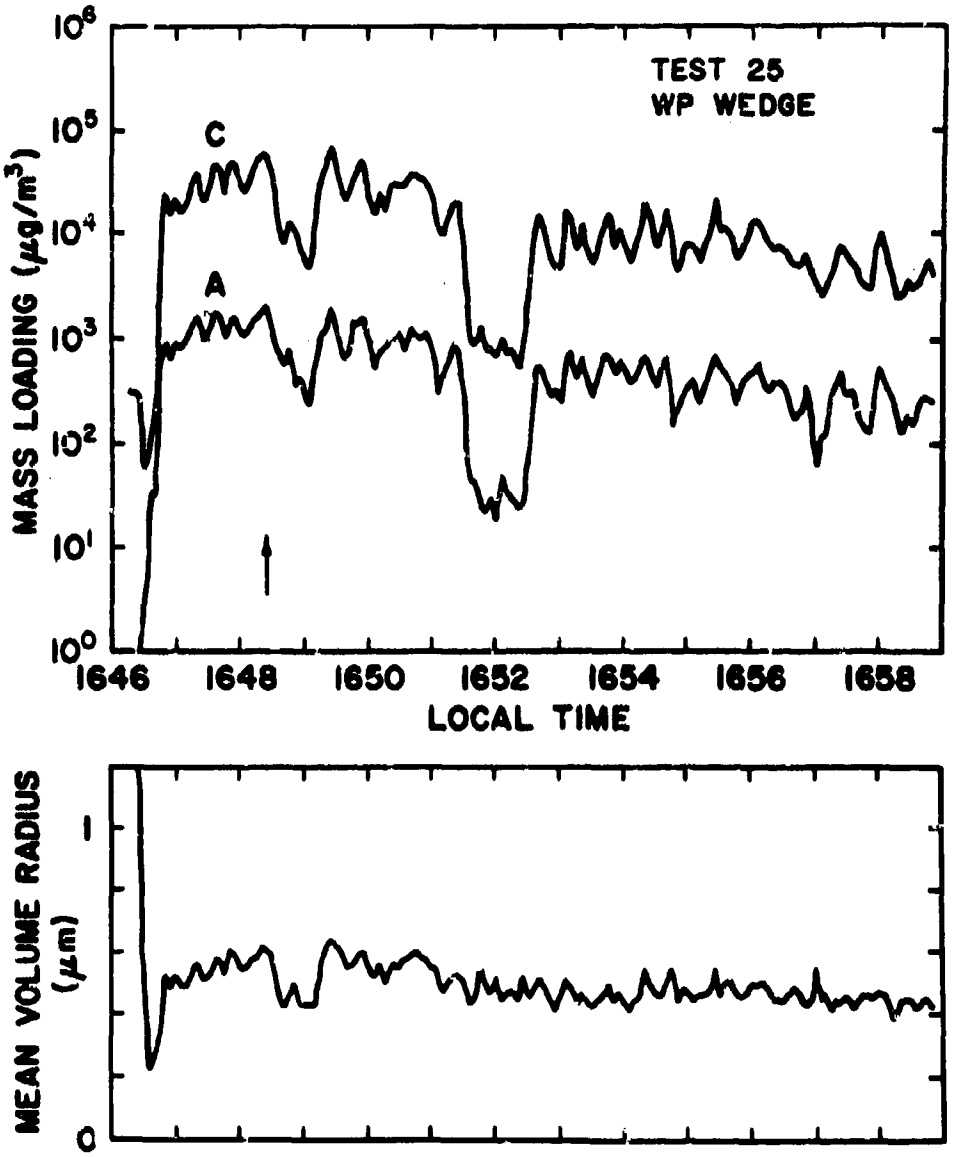

FIGURE 13. SAME AS FIGURE 10 FOR TRIAL 25. Arrow indicates the time corresponding to the probe responses given in figure 4.

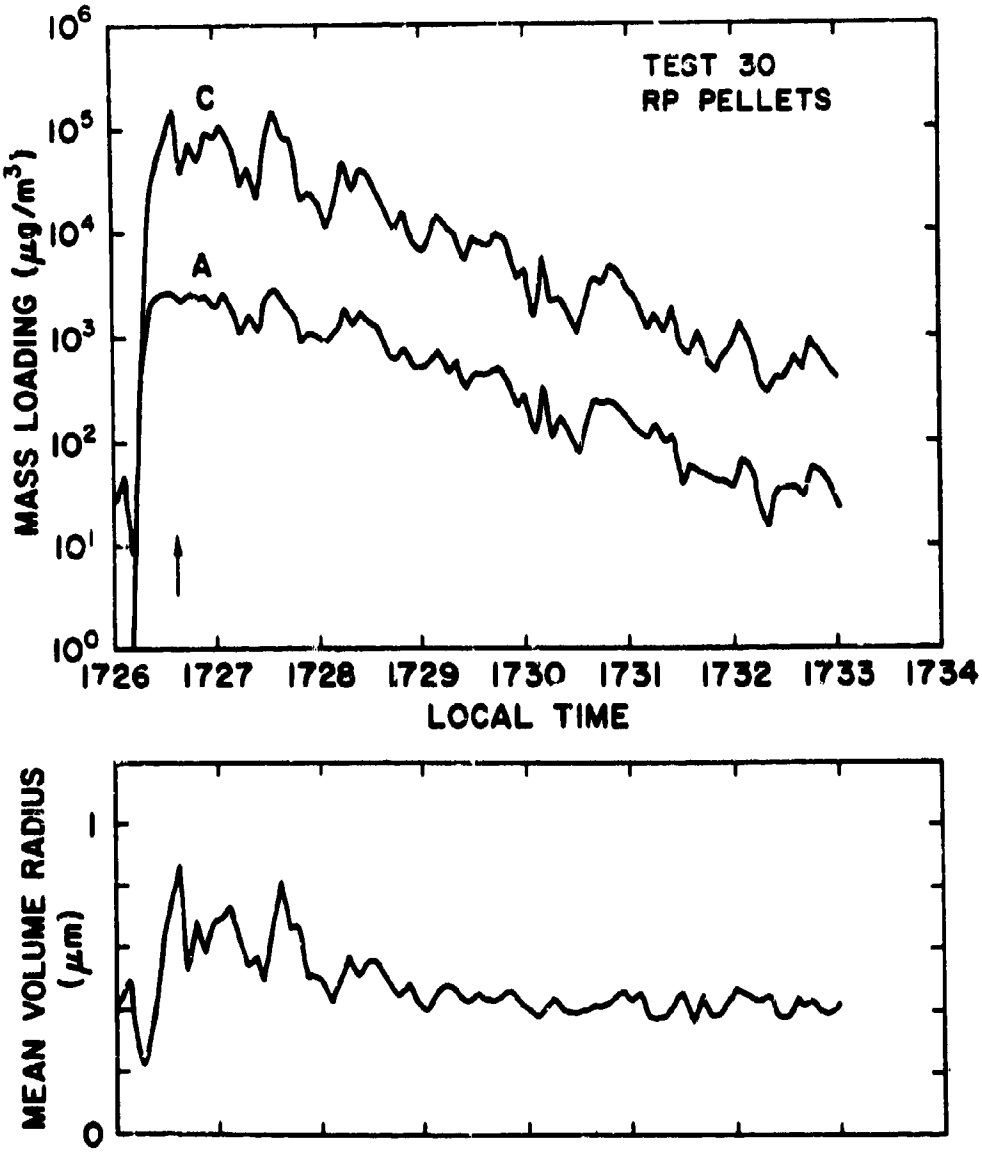

FIGURE 14. SAME AS FIGURE 10 FOR TRIAL 30.
Arrow indicates the time corresponding to the probe responses given in figure 5.

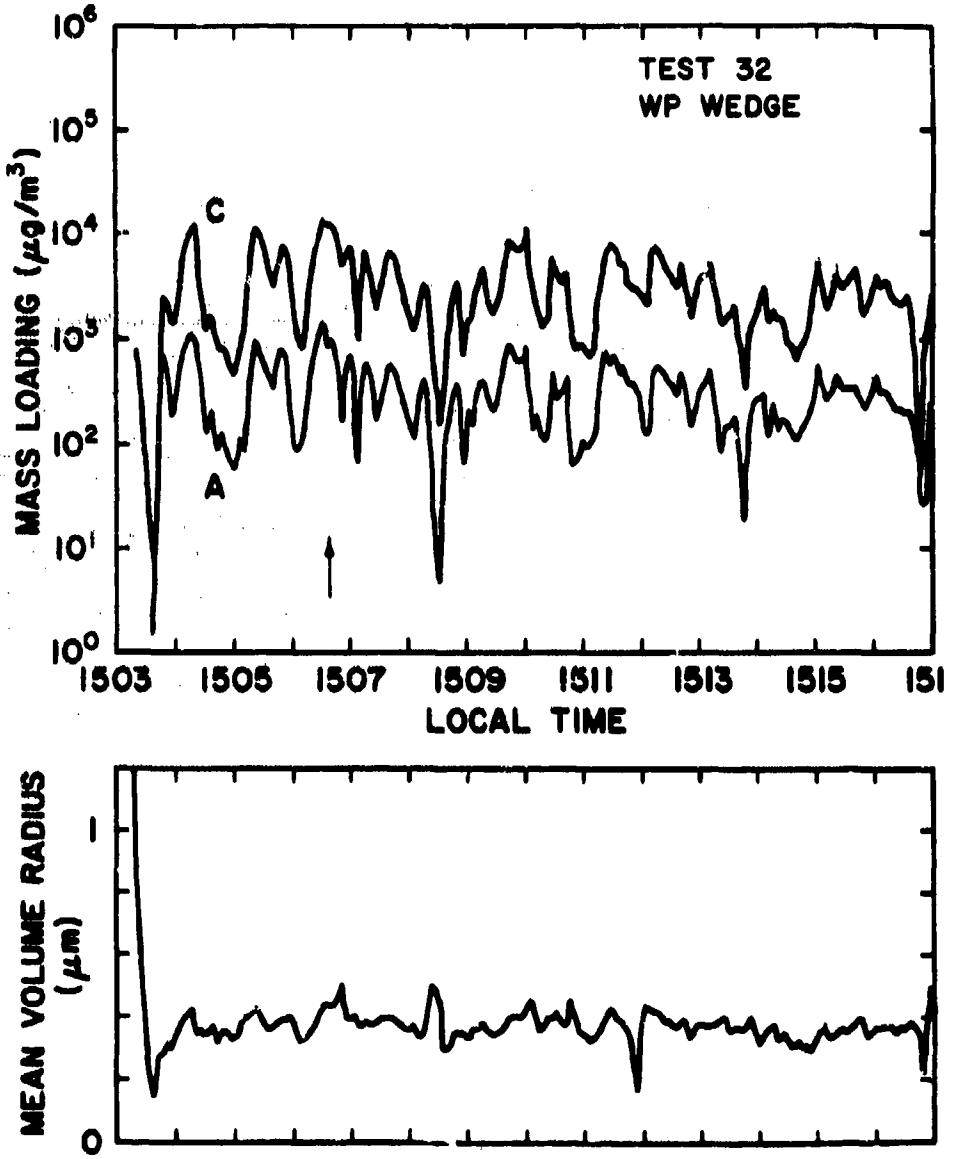

FIGURE 15. SAME AS FIGURE 10 FOR TRIAL 32.
Arrow indicates the time corresponding to the probe responses given in figure 6.

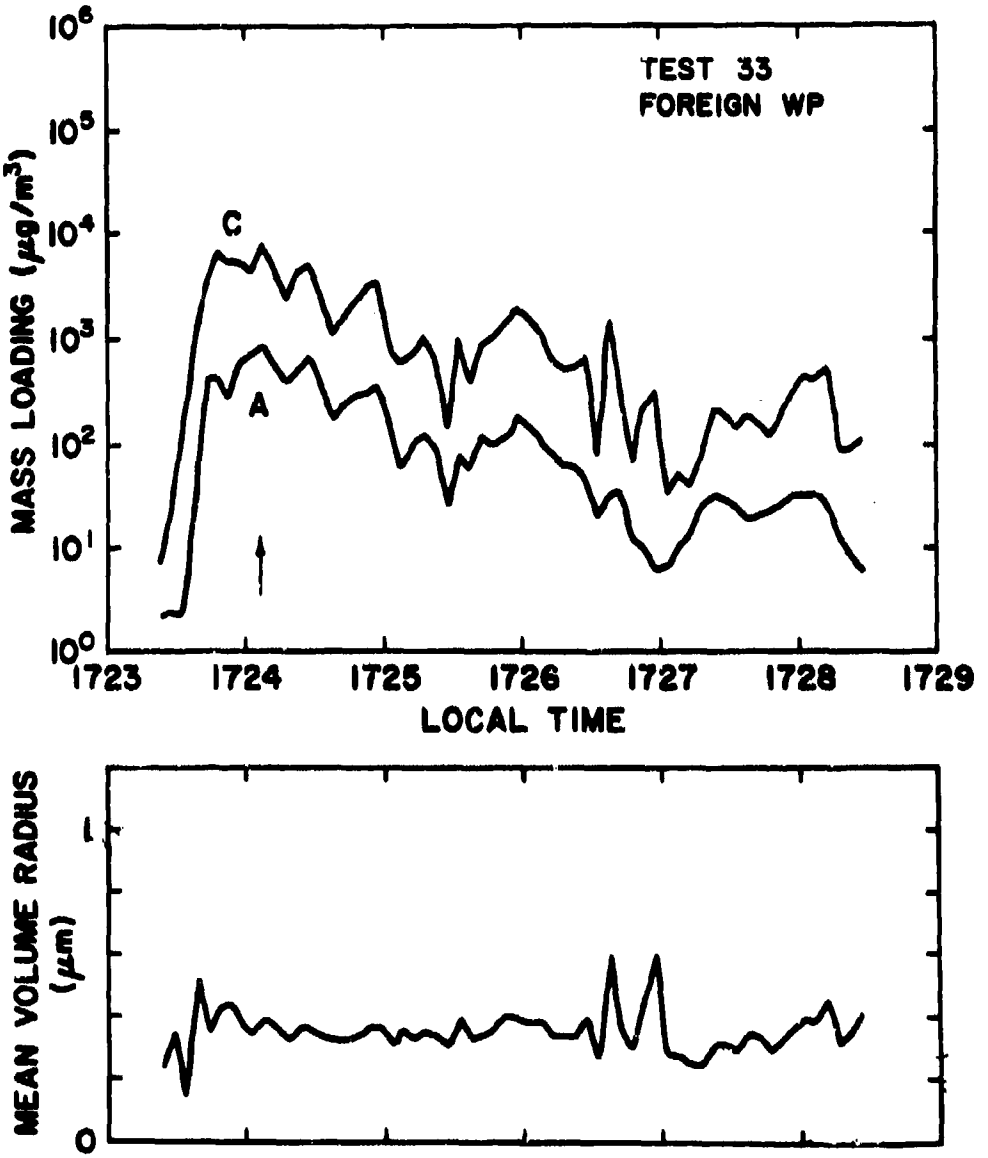

FIGURE 16. SAME AS FIGURE 10 FOR TRIAL 32.
Arrow indicates the time corresponding to the probe responses given in figure 7.

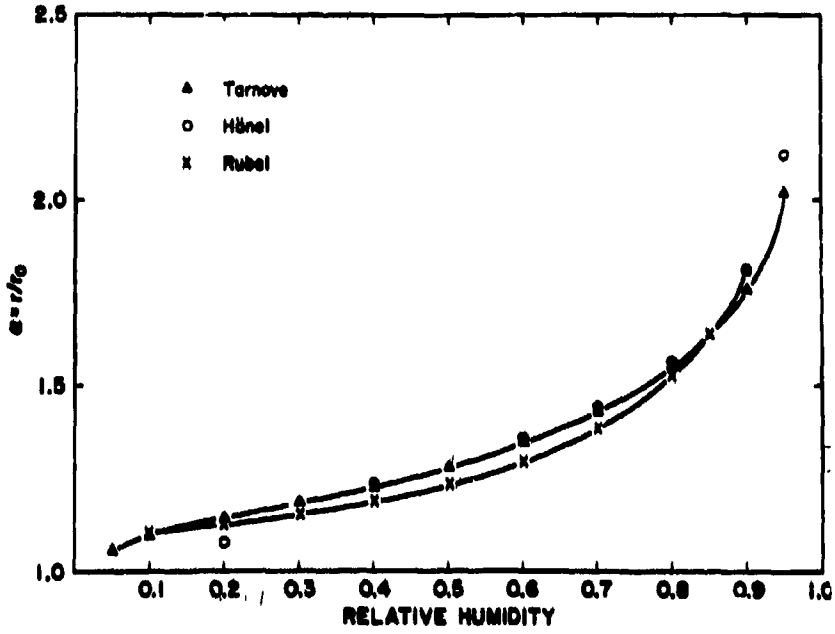

FIGURE 17. THEORETICAL MODELS OF PHOSPHORIC ACID PARTICLE GROWTH AS A FUNCTION OF RELATIVE HUMIDITY.
(Tarnove, 1980; Hänel, 1978; and Rubel, 1979).

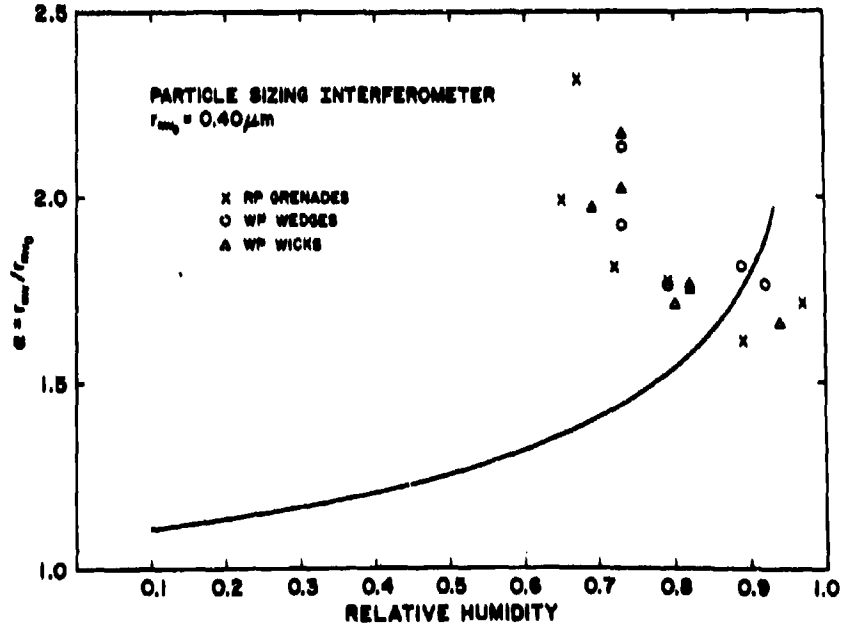

FIGURE 18. PARTICLE SIZING INTERFEROMETER DETERMINATIONS OF THE MEAN VOLUME RADII OF PHOSPHORUS SMOKES DURING THE H^3S FIELD TEST.
Values given by Farmer (1980) are normalized using a dry particle mean volume radius of 0.40μm.

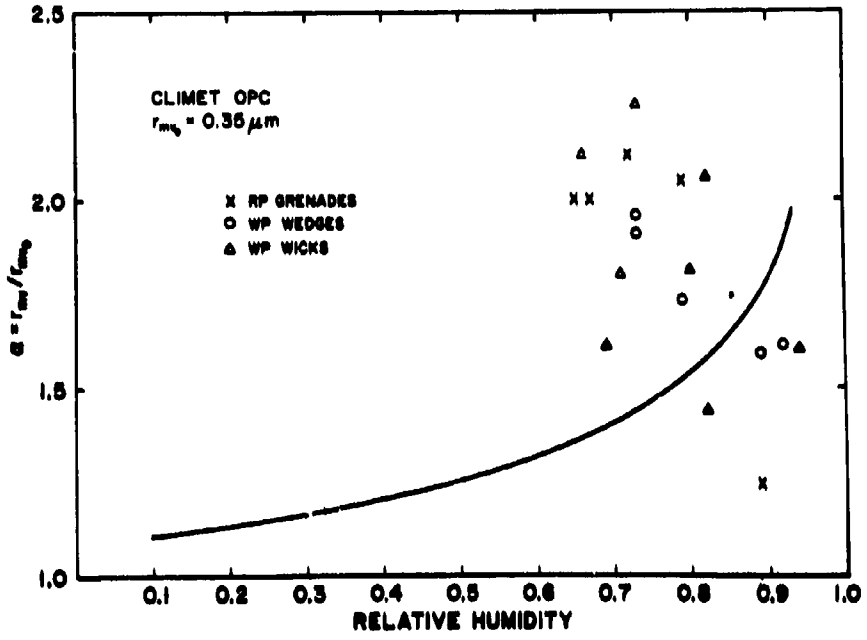

FIGURE 19. CLIMET OPTICAL PARTICLE COUNTER DETERMINATIONS OF THE MEAN VOLUME RADII OF PHOSPHORUS SMOKES DURING THE H^3S FIELD TEST. Values given by Farmer (1980) are normalized using a dry particle mean volume radius of 0.35μm.

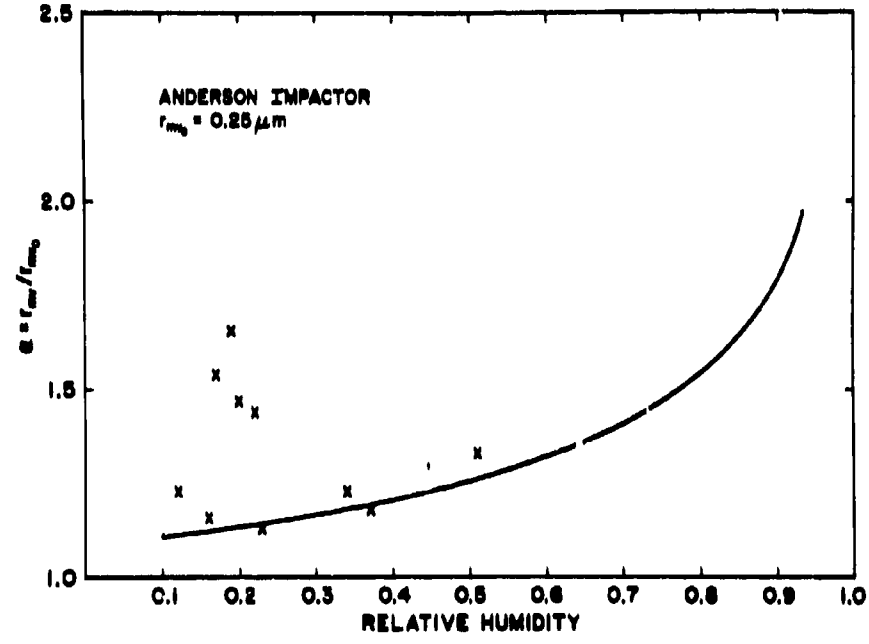

FIGURE 20. ANDERSON IMPACTOR DETERMINATIONS OF THE MEAN VOLUME RADII OF PHOSPHORUS SMOKES IN A LABORATORY CHAMBER. Values given by Frickel et al (1979) are normalized using a dry particle mean volume radius of 0.25μm.

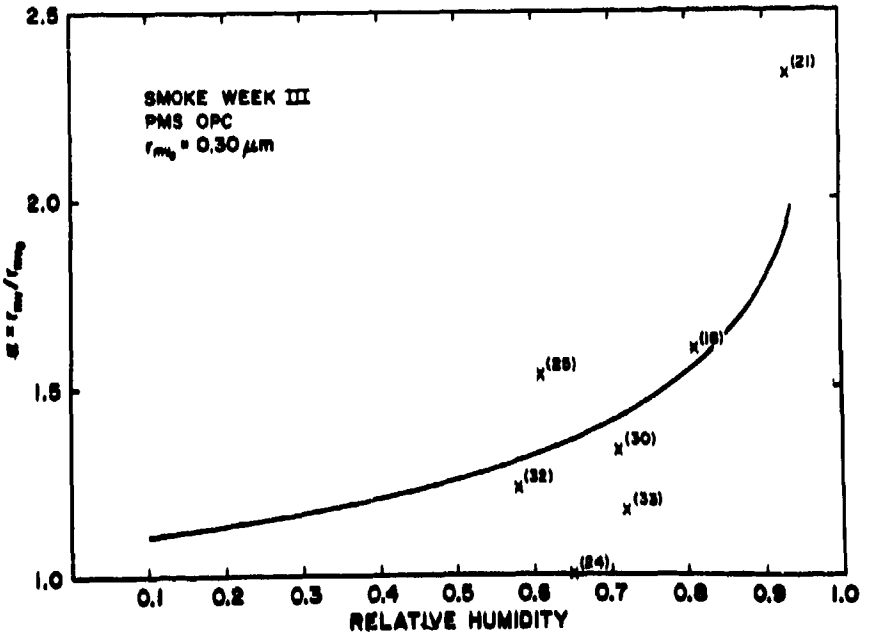

FIGURE 21. PMS OPTICAL PARTICLE COUNTER DETERMINATIONS OF THE MEAN VOLUME RADII OF PHOSPHORUS SMOKES DURING SMOKE WEEK III.
Values given in table 1 are normalized using a dry particle mean volume radius of 0.30μm.

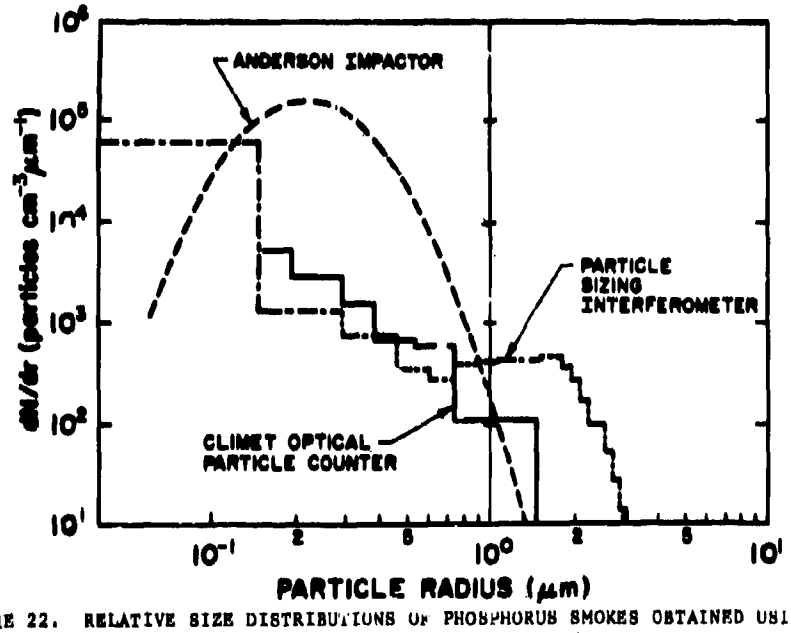

FIGURE 22. RELATIVE SIZE DISTRIBUTIONS OF PHOSPHORUS SMOKES OBTAINED USING THREE DIFFERENT INSTRUMENTS. Only relative values of dN/dr are to be compared. The Particle Sizing Interferometer and the Climet data are for trial 9 of the H^{3}S test (Farmer 1980). The particle concentration (N_p) used in plotting the distributions are 10^4 and 10^3 cm^{-3}, respectively. The Anderson Impactor data are for case 6 of table 1 of Frickel et al (1979). A value of 4×10^4 cm^{-3} is used for N_p

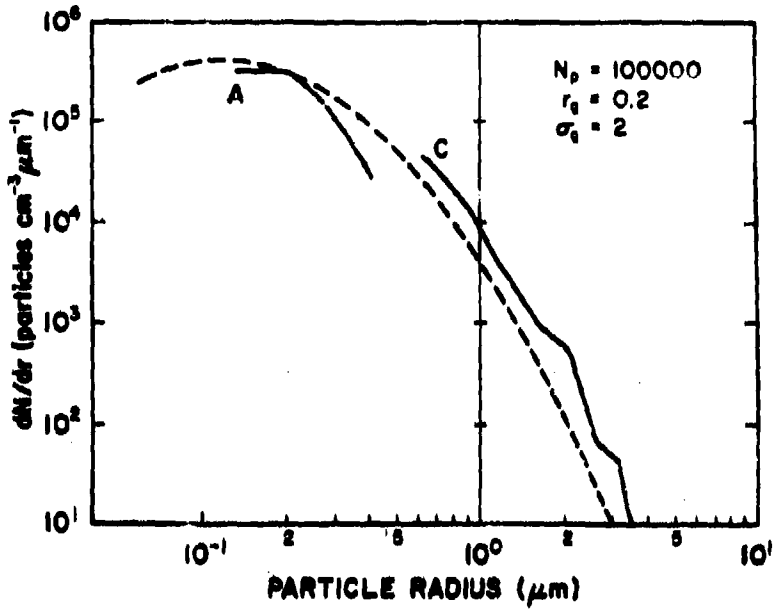

FIGURE 23. LOGNORMAL FIT TO PMS MEASURED SIZE DISTRIBUTION OF PHOSPHORUS SMOKE MEASURED DURING PERIOD OF MAXIMUM MASS LOADING DURING SMOKE WEEK III.

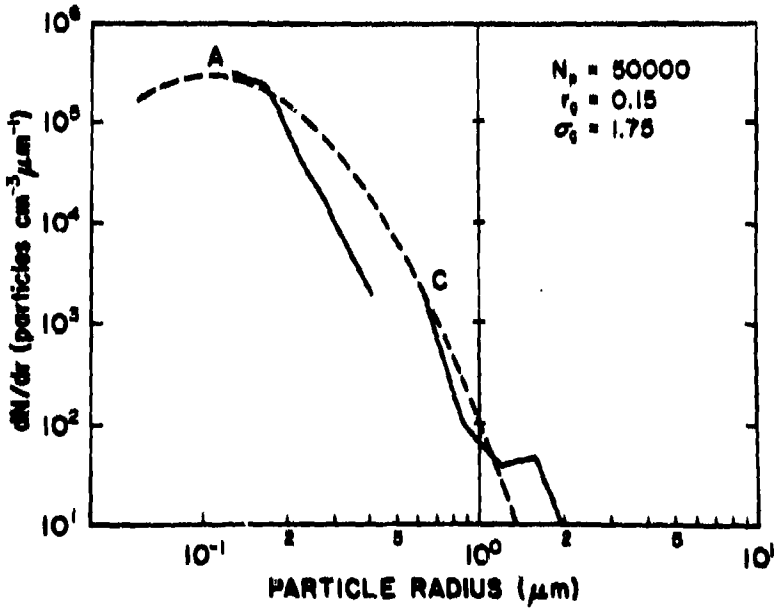

FIGURE 24. LOGNORMAL FIT TO TYPICAL PMS MEASURED SIZE DISTRIBUTION OF PHOSPHORUS SMOKE MEASURED DURING SMOKE WEEK III.

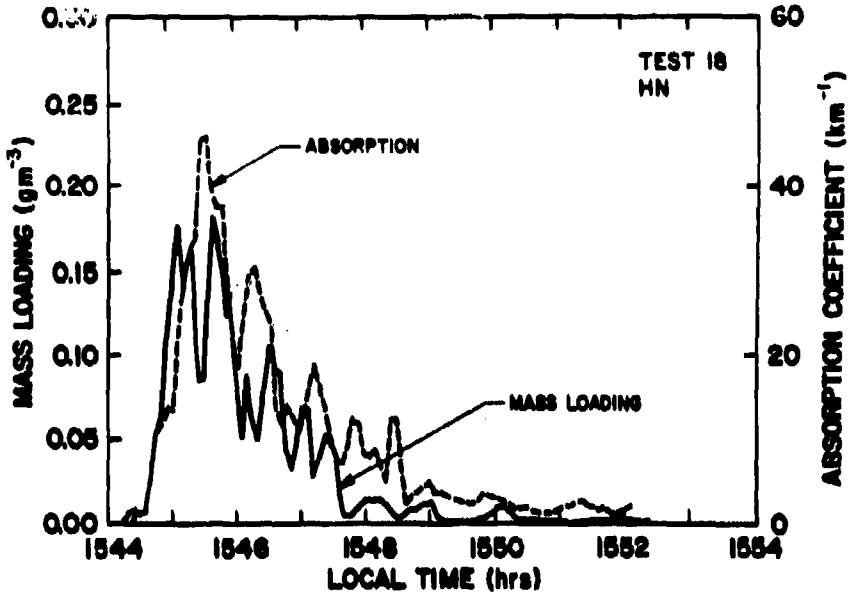

FIGURE 25. COMPARISON OF PMS-DETERMINED MASS LOADING AND SPECTROPHONE-MEASURED ABSORPTION AS A FUNCTION OF TIME DURING TRIAL 18.

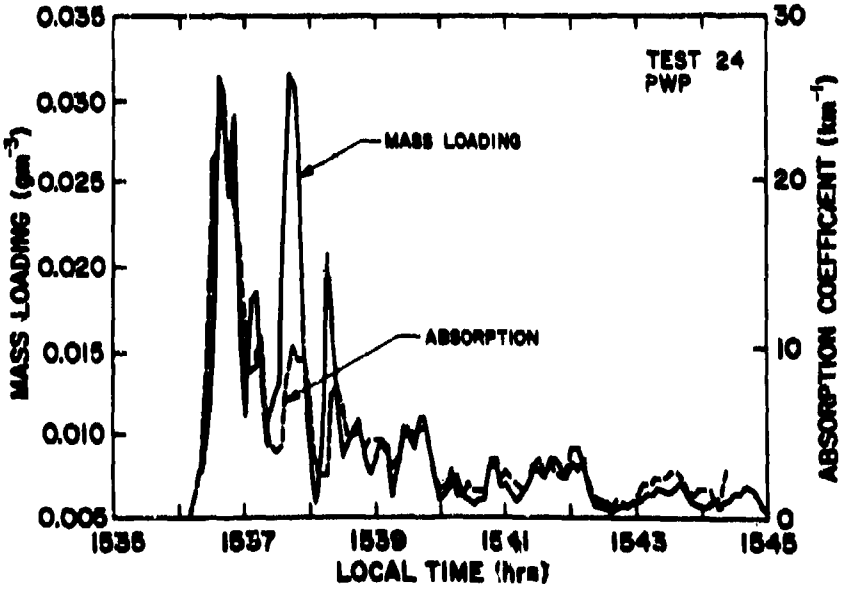

FIGURE 26. SAME AS FIGURE 25 FOR TRIAL 24.

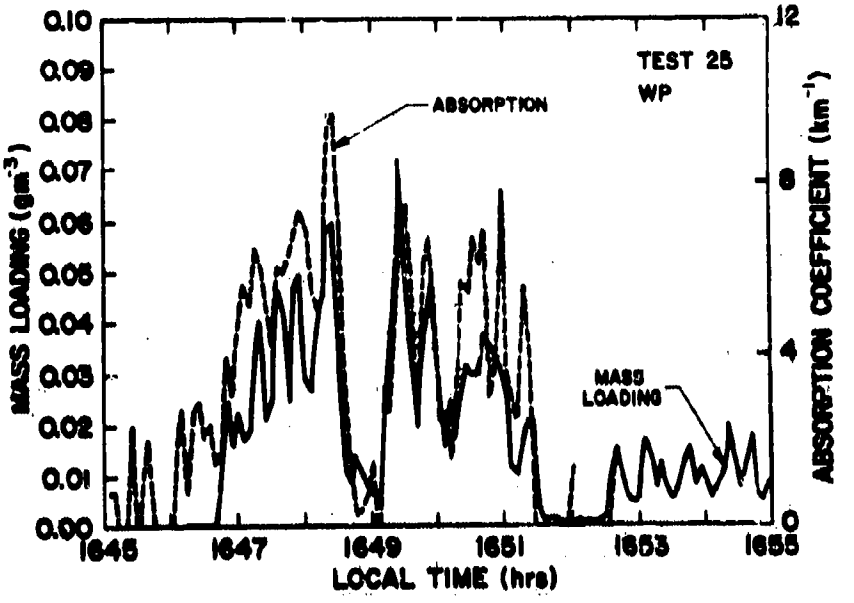

FIGURE 27. SAME AS FIGURE 25 FOR TRIAL 25.

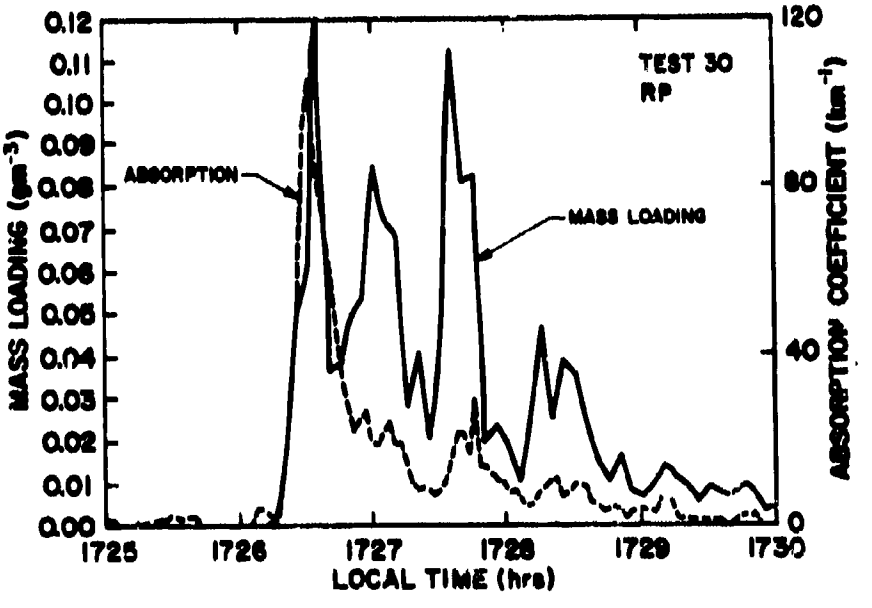

FIGURE 28. SAME AS FIGURE 25 FOR TRIAL 30.

PARTICLE SIZE ANALYSIS - THEORY AND DATA ON BIMODAL FOG OIL DISTRIBUTION

Robert W. Doherty and Robert H. Frickel
Chemical System Laboratory
Aberdeen Proving Ground, MD 21010

ABSTRACT

Preliminary data collected at the Obscuration Science Section of CSL at APG, MD using a light scattering optical particle counter of the PMS-CSASP type have shown evidence of multimodal structure in the particle size distribution of a vaporized/condensed aerosol of fog oil in the 0.3 μm < dia < 2.5 μm dia range. Assuming complete vaporization of the fog oil during dissemination, multimodal size distributions are not expected; however, under certain conditions of supersaturation, a bimodal size distribution is predicted by theory. Being investigated is the possibility that the observed aerosol distribution may be an artifact of the optical counter. The optical counter is designed to interpret light scattering signals in terms of a monotonic response function with respect to particle size independent of refractive index. The effects of a "fold over" in the optical system's response function in yielding multimodal distributions from unimodal log normal distributions will be demonstrated. A comparison of the observed particle size distribution with a conventional cascade impactor will also be presented.

INTRODUCTION

The purpose of this paper is to present a brief summary of some of the findings made at the Obscuration Sciences Section of CSL at APG on aerosols of vaporized/condensed fog oil (No. 100 PALE OIL). Specifically, some rather unexpected multi-modal peaks in the aerosol size distribution over the interval of measurement (i.e., 0.3μm <diameter <6.0μm were observed. An effort was then made to establish whether or not these peaks were real or were measurement system artifacts.

This paper presents the experimental findings on the time development of fog oil aerosols ranging from a mass concentration of 0.012gm/m^3 to 0.58gm/m^3, as well as a brief discussion on the theoretical development of a bimodal distribution from an originally unimodal distribution considering evaporation and condensation as the driving mechanisms.

EXPERIMENTAL FACILITIES

The experimental procedure utilized by CSL to perform the present experiments involved using a 12' x4' x5' plywood box with suitable exhaust and sampling ports. Dissemination of the smoke into the chamber was handled by a Burgess Jungle Fogger Model F-1442 made by the Burgess Vibrocrafters, Inc. located in Grayslake, Ill. Aerosol mass concentration measurements were made using Gelman 47 mm diameter, type A/E glass fiber filters.

Measurement of the aerosol size distribution was performed using both an Anderson Mark III cascade impactor available from Anderson 2000, Inc., Atlanta, GA and a Particle Measuring Systems CSASP-100-HC optical particle counter available from PMS, Boulder, Colorado. Analysis of the cascade impactor stages was performed gravimetrically, which limited the use of the impactor to aerosols with mass concentration exceeding 0.1 gm/m^3. The CSASP-100-HC optical size analyzer was used on both low

and high concentration aerosols with the understanding that for aerosols exceeding $\sim 10^4$ particles/cc, correction factors must be applied to the raw data to transfrom the observed relative size distribution into absolute size distribution.

In addition to total mass concentration and size distribution measurements, optical transmission measurements across the 4' dimension of the smoke chamber were made at the wavelengths $\lambda =$ 0.4416 μm 0.6328μm, and 1.15μm. A continuous record of the transmission levels monitored by SGD 100 A detectors for each of the laser lines was keep via strip chart recorders. The optical depth, τ, of the aerosols as a function of time was then obtained from the transmission charts using Beer's Law i.e.

$$I(t) = I_o \exp(-\tau)$$

where I_o corresponds to the initial transmission level through the chamber without smoke, and I(t) corresponds to the transmission level through the chamber with smoke at time 't'.

DATA FORMAT

Figures 1, 2 and 3 show the time history of the vaporized/condensed fog oil aerosol distribution with initial mass concentrations of 0.012 gm/m^3, 0.035 gm/m^3, and 0.58 gm/m^3 respectively. All measurements were made on the CSASP-100-HC optical particle counter. The reader is cautioned that the size distributions shown in Figures 1, 2 and 3 are not absolute size distributions, but only relative size distributions. An absolute size distribution implies that the amplitude as well as the location of the size peaks can be traced to a known volume of actual aerosol. A relative size distribution implies that the actual volume of aerosol sampled is not known, but that the size peak locations and relative amplitudes on any given run are accurately represented. Hence, comparison of the size distributions from moment to moment using our data does not provide the answer on an absolute basis to the net flux of particles into or out of a particular size interval, but it does provide information on changes in the location of the size peaks and their relative strengths at fixed times. As a reminder to the reader of the uncertainty in the placement of the vertical offset to the curves in Figures 1, 2 and 3, the vertical axis is shown as a staggered axis with only relative scale factors given. To have attempted to provide for a moment by moment absolute comparison of the size distribution curves would have required the use of large correction factors, each with a high degree of uncertainty. The empirical procedure for estimating the correction factors can be obtained from the manufacturer under the title "Activity and Its Influence on Instrument Measurements."

Figures 4, 5 and 6 demonstrate the optical depth, τ, and the aerosol mass concentration as functions of time for the aerosol of Figures 1, 2 and 3 respectively. Figure 7 shows a plot of cascade impactor data taken on the aerosol of Figure 3.

It should be noted that the times labeled t=0 are not the end points of the smoke generation, but the beginnings of the data collection. There may be a several minute gap between these two times. In addition, the rather rapid aerosol mass decay is due to the mixing fan used throughout the experiment to keep the cloud homogeneous rather than due to settling effects.

DATA ANALYSIS

(a) Low concentration Fog Oil - 0.012 gm/m^3: Examination of Figure 1 shows that, initially, the peak in the size distribution occurs somewhere below the lower level of particle detection for the CSASP-100-HC, i.e. below 0.3 μm diameter, but that there is a steep shoulder to the distribution at about 0.4 μm diameter and a weaker secondary shoulder at about 0.6 μm diameter. In time the 0.4 μm diameter mode develops into a definite peak while the 0.6 μm diameter mode becomes more pronounced. Hence, by 50 minutes into the test run, the data indicates a weak bimodality over the monitored portion of the particle size spectrum from 0.3 μm diameter to 6.0 μm diameter.

Figure 4 demonstrates a steady decay in both the optical depths measured at λ=0.4416 μm, 0.6328 μm and 1.15 μm and the aerosol mass concentration with increasing time. Notice that, although the optical depth at λ=0.4416 μm is 1.5 times larger than the corresponding optical depth at λ=0.6328 μm, the rate of decrease in the former is also greater such that the two values become equal at about 34 minutes into the test. Beyond 34 minutes the optical depth at λ=0.4416 μm drops below that of λ=0.6328 μm. The optical depth at λ=1.15 μm shows a steady decrease throughout the entire test, continually remaining the lowest of the three measurements.

(b) Medium Concentration Fog Oil - 0.035 gm/m^3: Examination of Figure 2 shows the peak in the initial aerosol size distribution occurs somewhere below the 0.3 μm diameter lower limit of the CSASP-100-HC with a steep shoulder at 0.4 μm and a second, weaker shoulder at about 0.65 μm, all of which is very similar to the t=0 plot of Figure 1. By 24 minutes into the test, Figure 2 shows that the shoulders at 0.40 and 0.65 μm diameter have become pronounced peaks and hence demonstrates a definite bimodality in the monitored portion of the size distribution. At 49 minutes into the runs, the peaks at 0.40 μm and 0.65 μm diameter are more evident with the 0.65 μm diameter peak having grown to a relative magintude of one third that of the main peak at 0.40 μm. This pattern remained unchanged to the end of the test at 68 minutes into the run.

The measurements of the optical depths at λ=0.4416 μm, 0.6328 μm and 1.15 μm and the aerosol mass concentration shown in Figure 5 are very similar to those of the low concentration fog oil test

shown in Figure 4 with the exception that the initial optical depth at λ=0.4416 μm is over 2 1/2 times that of λ=0.6328 μm, which is much higher than that of Figure 4 and suggests some mass concentration dependency to the initial size distribution.

(c) High Concentration Fog Oil ~ 0.58 gm/m^3: Unlike Figures 1 and 2, Figure 3 shows a pronounced peak in the initial aerosol distribution within the monitored size range, the peak being located at 0.44 μm diameter. It must be mentioned, however, that the aerosol of Figure 3 was produced by the generation and subsequent dilution of a much higher concentration aerosol (1 gm/m^3). This process took several minutes to accomplish, so that early development of the aerosol from a size mode below 0.3 μm diameter to that at t=0 may have taken place prior to our data gathering. By 25 minutes into the test, Figure 3 demonstrates a strong bimodality in the measurable portion of the size spectrum with peaks at 0.44 μm and 0.85 μm diameter. By 52 minutes into the run, the size distribution appears to be trimodal with the largest peak occuring somewhere below 0.3 μm and additional peaks at 0.54 μm and 0.85 μm diameter. At 144 minutes into the test, Figure 3 continues to show a trimodal size distribution, as seen at 52 minutes, but with some downward shifting of the peaks which can be attributed to fogging of the CSASP-100-HC probe lenses. Evidence supporting the downward shift seen in the size distributions from t=52 minutes to t=144 minutes via dirty probe lenses was obtained by observing a similar downward shift in the probe calibration using Dow Chemical polystyrene latex spheres run before and after the smoke test. In addition, the manufacturer of the CSASP-100-HC probe found it necessary to incorporate nonuniform voltage intervals for the scattering event pulse height analysis in order to provide uniform diameter intervals corresponding to these same channels. As a result, a 15% drop in the pulse height can readily cause a 2 channel downward channel assignment for particles at the upper end of a given probe size range, while it would require a 20% to 70% drop in signal strength to accomplish a similar shift in the smaller particle size, depending on the probe size range selected. For the size range in which the peaks of Figure 3 at t=52, 144 minutes are occuring, i.e. size range #3, the observed shifting in the t=52 minute and t=144 minutes curves is consistent with the observed shifting of the latex standards and the nonuniform voltage intervals established by the manufacturer. However, fogging over of the probe lens can not explain the disappearance of the 0.54 μm diameter peak as shown in the t=52, 144 minute curves, nor have we an alternative explanation

Figure 7 shows the results of cascade impactor tests run on the high concentration aerosol at t=9.5 minutes and again at t=52 minutes. The trend of the data is towards a higher mass median diameter with increasing time; however, we believe our experimental error is simply too great for

those particular test runs to provide quantitative information on a particle number basis for the verification of the multimodal distributions seen in the optical size distributions of Figure 3.

There are notable changes in the time history of the optical depth measurements of Figure 7 as compared to the optical depth measurements on the low and medium aerosol concentrations of Figures 4 and 5. Figure 7 shows that the optical depth at λ = 0.6328 μm remains greater than that of λ = 0.4416 μm for the first 70 minutes of the test. At 70 minutes into the test, all 3 wavelengths have converged to the same value of optical depth. This was not the pattern observed in Figures 4 and 5. Nor is the early increase in optical depth with time seen in Figure7 for λ = 1.15 μm comparable to the lower concentration tests.

The initial increase in the optical depth at λ = 1.15 μm would seem to indicate a significant corresponding change in the size distribution providing a more favorable scattering particle towards λ = 1.15 μm. However, the observed size distributions of Figure 7 at t = 0 and t = 11 minutes do not bear this out, at least not on a relative size basis over the size range monitored i.e. 0.3 μm $\leq$ diameter $\leq$ 6.0 μm. The change in the size distribution may, however, be taking place below the 0.3 μm diameter detection limit of the CSASP-100-HC. Support for this hypothesis is given by Figure 9, which demonstrates the relationship between the particle extinction coefficient and the size parameter, k, for a material with a refractive index n = 1.5 - 0 i. The large slope seen in Figure 9 for k $\leq$ 3 indicates that even a small increase in the particle size over this region of 'k' will result in a large change in the particle extinction coefficient with the greatest enhancement in the particle extinction coefficient taking place at the longest of the observed wavelengths, i.e. λ = 1.15 μm. Thus, one possible explanation for the initial increase in the optical depth at λ = 1.15 μm might be the formation of additional 0.45 μm diameter particles, the peak diameter seen in Figure 3 at the earlier times, along with the depletion of a possibly much larger number of particles less than 0.3 μm diameter, which are not seen by the present particle counter. The same aerosol behavior of small particle growth followed by the partial removal of the larger, more efficient scatterers would also explain the simultaneous decrease observed in the optical depths at λ = 0.4416 μm and 0.6328 μm. In effect, the optical depth at each of the 3 monitored wavelengths is the algebraic sum of the net gain in the more efficient 0.45 μm diameter scatterers minus the net loss of the less efficient scatterers smaller than 0.3 μm diameter. Table 1 presents an example demonstrating how such competing processes might operate on the optical depth. In Table 1, the distribution of particle sizes has been reduced to two sizes for the purpose of illustration.

EFFECTS OF A MULTIVALUED RESPONSE FUNCTION ON AN OPTICAL COUNTER'S PERFORMANCE

We have seen in the previous section of this report unimodal distributions of vaporized/condensed fog oil changing in time to form bimodal and even trimodal distributions. The question raised here is whether it is possible that some of the multimodal peaks might be artifacts of the optical counter.

In general, the signal strength registered by an optical counter for a particular scattering event can be plotted as a function of the actual particle diameter to form what is called the response function of the system. Unfortunately, the response function is often not just a function of the particle size, but also of many other factors including the particle shape, refrative index, light collection angle (s), beam profile and particle location within the sensing zone of the system. Even for spherical particles of known refractive index, the response function will still contain a region of non-uniqueness between response and particle diameter. Such a region, where the response is multivalued in terms of the particle diameter, is referred to as a "fold over" in the response function.

Figure 8 demonstrates the effect that fold over has on the interpretation of an originally unimodal log-normal particle size distribution. In the example of Figure 8, we have chosen as our test aerosol distribution a log-normal distribution with a geometric count median diameter of 1.0μm, a log-geometric standard deviation of 0.5, and a total number density of 10^7 particles/cc. The test aerosol distribution is shown as Curve A. Curve B of Figure 8 is the manufacturer's published response function for the CSASP-100-HC and represents the "averaged" response of the probe over many different refractive indices. It should be noted that Curve B has been defined by the manufacturer as a monotonic function, i. e. without a fold over. Let Curve C of Figure 8 represent the actual or calibrated response function of the CSASP-100-HC for the material comprising Curve A in our example. Curve C is not the response function of a real material, but has been chosen to illustrate the effects of a pronounced fold over on the interpretation of a given aerosol size distribution.

Table 2 lists the diameter intervals corresponding to the specific response intervals as established by the manufacturer for the CSASP-100-HC response function of Curve B. Also listed are the diameter intervals obtained from our assumed response function of Curve C, corresponding to these same manufacturer's specified response intervals. Table 2 can be broken into 3 diameter ranges with respect to Curve C as follows:

Range I - all particles below the fold over in Curve C

Range II - all particles encompassed by the fold over of Curve C, i.e. all particles with non-unique responses

Range III - all particles above the fold over in Curve C.

Closer examination of Table 2 demonstrates that all particles of the test aerosol of Curve A which fall in Range I will be oversized while those falling in Range III will be undersized, and further that all particles which fall in Range II will undergo a more complicated transformation with the net effect being a compression within this range of the actual size distribution. Curve D of Figure 8 shows how all the diameter interval mappings of Table 2 act on the test aerosol to produce a multimodal, non-log-normal distribution which would be seen on the display screen of the optical counter. Hence, at least for the case when there exists a pronounced fold over in the actual or calibrated response function, the displayed size distribution contains many peaks and other structures not contained in the actual size distribution.

At this point in our work, we simply can not state that the multivalued peaks observed in the experiments of Figures 1, 2 and 3 are or are not due to a fold over in the response function for fog oil similar to the one in our example case given above. However, based on the locations of the peaks in Figure 1, 2 and 3, the gradual "on-site" growth of the secondary peaks, where by "on-site" we refer to the lack of any steady progression of the peaks along the diameter axis, it is our opinion that the multivalued peaks of Figure 1, 2 and 3 are not due to a possible fold over in the response function for fog oil, but due to some other mechanism such as condensation or coagulation. Possible conditions for the formation of a bimodal distribution from a unimodal distribution will be discussed in the next section. We do expect, however, to observe a fold over in the response function for fog oil, as we have measured the refractive index for fog oil to be 1.51 on an Abbe-3L refractometer, and have observed fold overs in some preliminary experiments measuring the response functions for both polystyrene latex with a refractive index of 1.59 @ λ=5893Å and for Cargille type E/AA refractive index liquid with a refractive index of 1.45 @ λ=5893Å. Thus, it seems appropriate at this point to experimentally determine the extent of the expected fold over in the fog oil response function.

FORMATION OF A BIMODAL DISTRIBUTION: CONDENSATION AND EVAPORATION[1]

Calculations on the behavior of evaporating and/or condensing aerosols reveal mechanisms by which bimodal particle size distributions can develop in aerosols originally having single-mode distributions. One such mechanism is the interaction between Raoult's law governing such colligative properties as saturated vapor pressure depression and the Kelvin effect relating vapor pressure to particle surface curvature. The diameter growth rate, $\frac{dD}{dt}$, for a two-component particle consisting of a non-volatile solute in a volatile solvent is given by

$$1) \quad \frac{dD}{dt} = K \; F(K_n) \; (S_e - S)$$

where K is a constant involving physical characteristics such as the equilibrium vapor pressure of the volatile component, the diffusion coefficient of the vapor, etc; K_n is the Knudsen number (ratio of the mean free path to the particle radius); S is the ratio of saturated vapor pressure at the surface of the droplet to the saturated vapor pressure over a flat surface of the pure solvent; and S_e is the environmental saturation ratio with respect to pure solvent. The factor $K\ F(K_n)$ can be evaluated as

$$2) \qquad K F(K_n) = \frac{1.27\times10^{-3}(D+0.13)}{D^2+0.2223D+0.0225} = H(D, D_n)$$

where D is the droplet diameter in microns. The droplet saturation ratio S is governed by Kohler's equation combining Raoult's law and the Kelvin effect:

$$3) \qquad S = \frac{(D^3-D_n^3)\exp\left(-\frac{4\sigma V_w}{kTD}\right)}{D^3-\left(1-\frac{M_w}{M_n}\right)D_n^3}$$

where D_n is the diameter of a droplet which would contain only the solute present in a solution droplet of diameter D, σ is the surface tension, V_w is the solvent molecular volume, k is Boltzmann's constant and T is the absolute temperature. For typical values of physical quantities, Equation 3 becomes

$$4) \qquad S(D, D_n) = \frac{D^3-D_n^3}{D^3-\frac{1}{2}D_n^3}\exp\left(-\frac{0.0144}{D}\right)$$

where D and D_n are in micrometers.

Suppose that, initially, an aerosol is a log-normally size distributed collection of droplets of a given non-volatile solute mass concentration C_o in the volatile solvent in an environment slightly supersaturated with respect to the pure solvent. The droplet diameter D is related to the solute "diameter" D_n and the solute concentrations by

$$5) \qquad D = \left[1-\left(\frac{1}{C}-1\right)K\rho\right]^{1/3} D_n$$

where $K\rho$ is the ratio of this solute density to the solvent density (here taken to be 1.). Similarly,

$$6) \qquad D_o = \left[1-\left(\frac{1}{C_o}-1\right)K\rho\right]^{1/3} D_n = g_o D_n$$

where D_o is the initial droplet diameter (distributed log-normally over the aerosol). For a given droplet, C and D vary as evaporation and condensation occur, but D_n remains constant. It can be shown from equations 4 and 5 that, unless the given initial concentration C is equal to 1, that is the droplets are initially pure solute, the saturation ratio S for the smaller droplets is less than the ambient saturation ratio S_e, and they evaporate toward the equilibrium condition $S = S_e$, while for the larger droplets $S > S_e$ and they grow by condensation.

222

Equation 2 can be rewritten and integrated as follows.

$$7) \quad t = \int_{D_o}^{D_t} \frac{dD}{KF(K_n)(S_o - S)} = \int_{D_o}^{D_t} \frac{dD}{H(D)(S_o - S(D, D_n))}$$

where D_o is the initial particle diameter and D_t is the diameter at time t. Let the aerosol be sufficiently dilute that coagulation is negligible. Then, if the particle diameter distribution is initially

$$8) \quad \frac{dN}{dD_o} = f(D_o) \ ,$$

we can find a later distribution by

$$9) \quad \frac{dN}{dD_t} = \frac{dN}{dD_o} \frac{dD_o}{dD_t} = \frac{dD_o}{dD_t} f(D_o)$$

This equation relates the distribution function at diameter D_o at time 'O' to the diameter D_t at time 't,' where D_t is the diameter attained at time 't' by a particle whose initial diameter was D_o, and dD_t is the width of the diameter interval containing the dN particles per unit volume initially contained in the interval (D_o, $D_o + dD_o$). (Since there is no coagulation and no particle can disappear by evaporation since it contains a non-volatile component, dN does not change). Similarly, if the initial distribution is written

$$10) \quad \frac{dN}{d\ln D_o} = f(D_o)$$

then at time 't'

$$11) \quad \frac{dN}{d\ln D_t} = \frac{D_t}{D_o} \frac{dD_o}{dD_t} f(D_o)$$

Here, an initial log normal distribution has been assumed, so that

$$12) \quad f(D_o) = \frac{N_o}{\sqrt{2\pi}\ln\sigma_g} \exp\left(-\frac{1}{2} \frac{\ln(D_o/D_m)}{\ln\sigma_g}\right)$$

where N_o is the total number concentration, σ_g is the distribution standard deviation, and D_m is the initial number median diameter. The quantity dD_o/dD, representing the change from time 'O' to time 't' in the width of the diameter interval containing dN particles per unit volume, can be obtained by differentiating Equation 7. Let us first write

$$13) \quad G(D, D_n) = \frac{1}{H(D)(S_o - S(D, D_n))}$$

Then, Equation 7 becomes

$$14) \quad t = \int_{D_o}^{D_t} G(D, D_n)\, dD$$

Remembering that the differention is for a given value of 't,' we can write

15) $$0 = \left(\int_{D_o}^{D_t} \frac{\partial G}{\partial D_m} dD\right) dD_m - G(D_o, D_m)\, dD_o + G(D_t, D_m)\, dD_t$$

Since from Equation 6

16) $$dD_m = \frac{1}{g_o}\, dD_o ,$$

Equation 15 yields

17) $$\frac{dD_o}{dD_t} = \frac{G(D_t, D_m)}{G(D_o, D_m) - \frac{1}{g_o}\int_{D_o}^{D_t} \frac{\partial G}{\partial t} dD}$$

The aerosol has been assumed to be dilute, so that S_a is not changed appreciably by the addition or removal of vapor from the droplets; Equations 14 and 17 can then be integrated numerically for each initial particle size. The collection of values of D and dD_o/dD_t corresponding to a collection of initial values of D_o can then be used to calculate changes in the particle size distribution with time.

Integration of Equations 14 and 17 disclose that small particles approach their equilibrium diameter quickly while larger particles change more slowly; the range of diameters between the quickly and slowly changing particles is rather narrow and provides a sharply defined transition region which moves toward larger particle sizes as evaporation or condensation continue. Within this transition region, a small initial diameter interval corresponds to a large diameter interval at time 't,' that is D_o/D_t is small and the particle size distribution is depressed at this value of D_t. In some cases, this effect is pronounced enough to produce a trough in the distribution, that is, a bimodal distribution develops.

Figures 10, 11, 12 display the development of a bimodal distribution by this mechanism. Figure 10 shows this initial log normal distribution with NMD = .129 μm and $\sigma_g = 1.7$. Figures 11 and 12 show the distribution after 30 and 100 seconds respectively compared with the initial distribution (dashed lines). The rapid evaporation of the small particles and resulting development of the bimodal distribution is shown, as well as the shift toward larger particle sizes with the trough separating the two modes.

The bimodality peaks calculated here are at diameters substantially smaller than those observed experimentally, and may not represent the same mechanism. The calculations do show that bimodality is not an unexpected phenomenon for small diameters.

CONCLUSIONS AND RECOMMENDATIONS

In this report, we have presented some preliminary experimental data on vaporized/condensed clouds of fog oil. The data supports the hypothesis that the aerosol develops a bimodality with time, the effect being more pronounced at higher aerosol mass concentration. We have attempted to reduce the possibility that the observed bimodal distributions are artifacts produced in the optical counter as well as to stablish a theoretical basis for the formation of a bimodal liquid aerosol from an initially unimodal, log-normal distribution. We recognize that the assumptions employed in the theoretical development of the bimodal distribution were not met in the actual experiments and that the case against artifacts in the observed size distribution has not been completely closed. Work will continue in both of these directions.

In an effort to extend particle size measurements below the 0.3 μm diameter lower limit of the present optical counter, an Electrical Mobility Analyzer manufacturer by TSI, Inc., St. Paul, MN has been acquired. The EMA has an inherent size range of 0.003 μm $\leq$ diameter $\leq$ 0.75 μm and is being interfaced to our data acquisition system. The problem of shifting in the optical counter calibration as a result of fogging of the probe lenses can be greatly reduced by providing a clean air purge to the lenses when no sample is being taken. There is no "ready made" solution to the problem of saturation of the particle counter, but the possibility of high order dilution schemes will be investigated in a further attempt to arrive at the absolute rather than the relative size distribution. In addition, the present optical system's response function for fog oil will be experimentally determined using the vibrating orifice technique to control particle generation.

Combining the above into a more accurate representation of the vaporized/condensed aerosol with independent measurements of the refractive index for the recondensed fog oil at λ = 0.44 16 μm, 0.6328 μm, and 1.15 μm will allow a direct comparison of the observed optical depths with those predicted by Mie scattering theory.

LITERATURE CITED:

1. Friedlander, S. K. "Smoke Dust, and Haze." 1st Edition, Wiley Interscience, New York, New York, 1977.

FIG. 1: VAPORIZED/CONDENSED FOG OIL - LOW CONCENTRATION, SIZE DISTRIBUTIONS AS A FUNCTION OF TIME

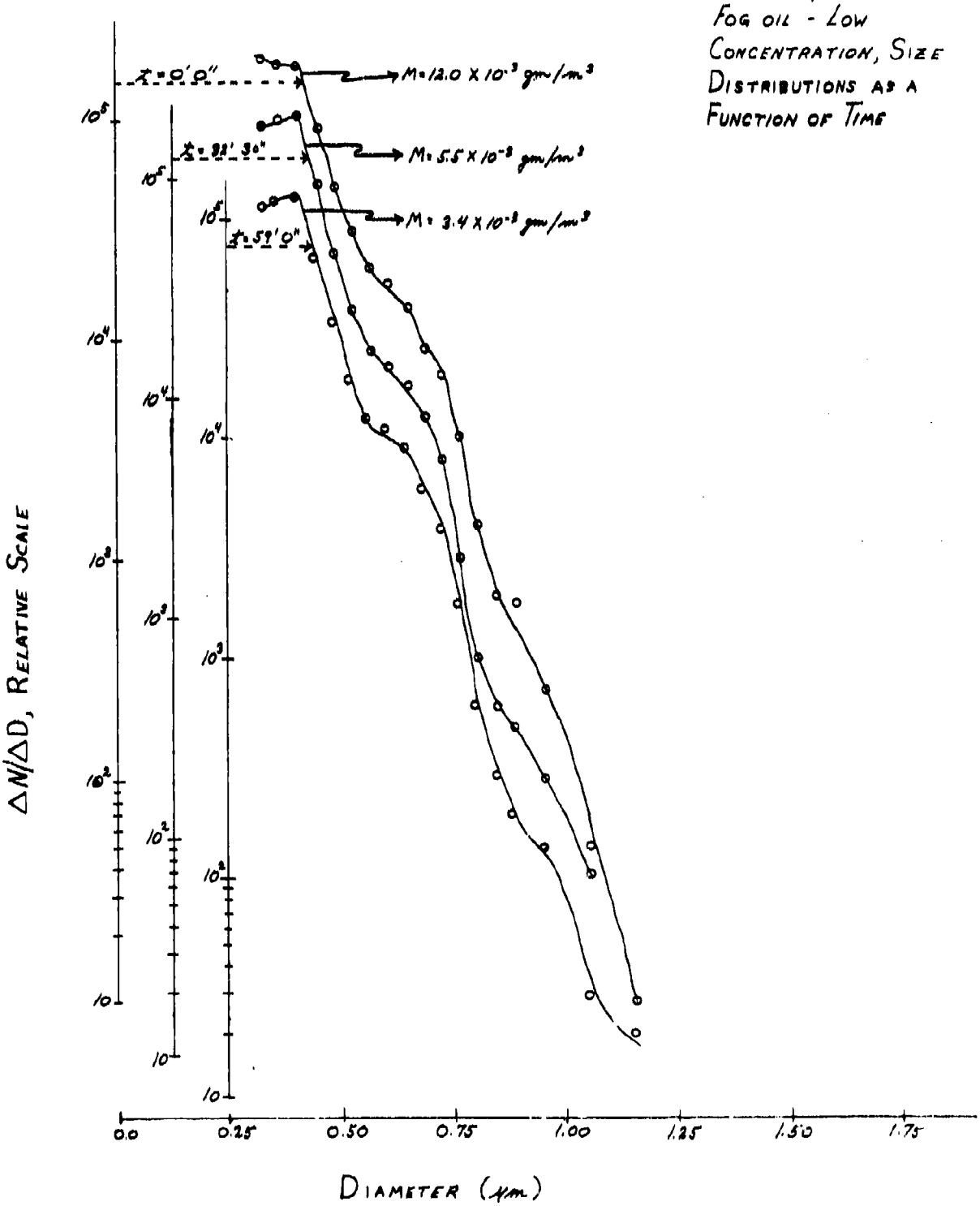

UNCLASSIFIED

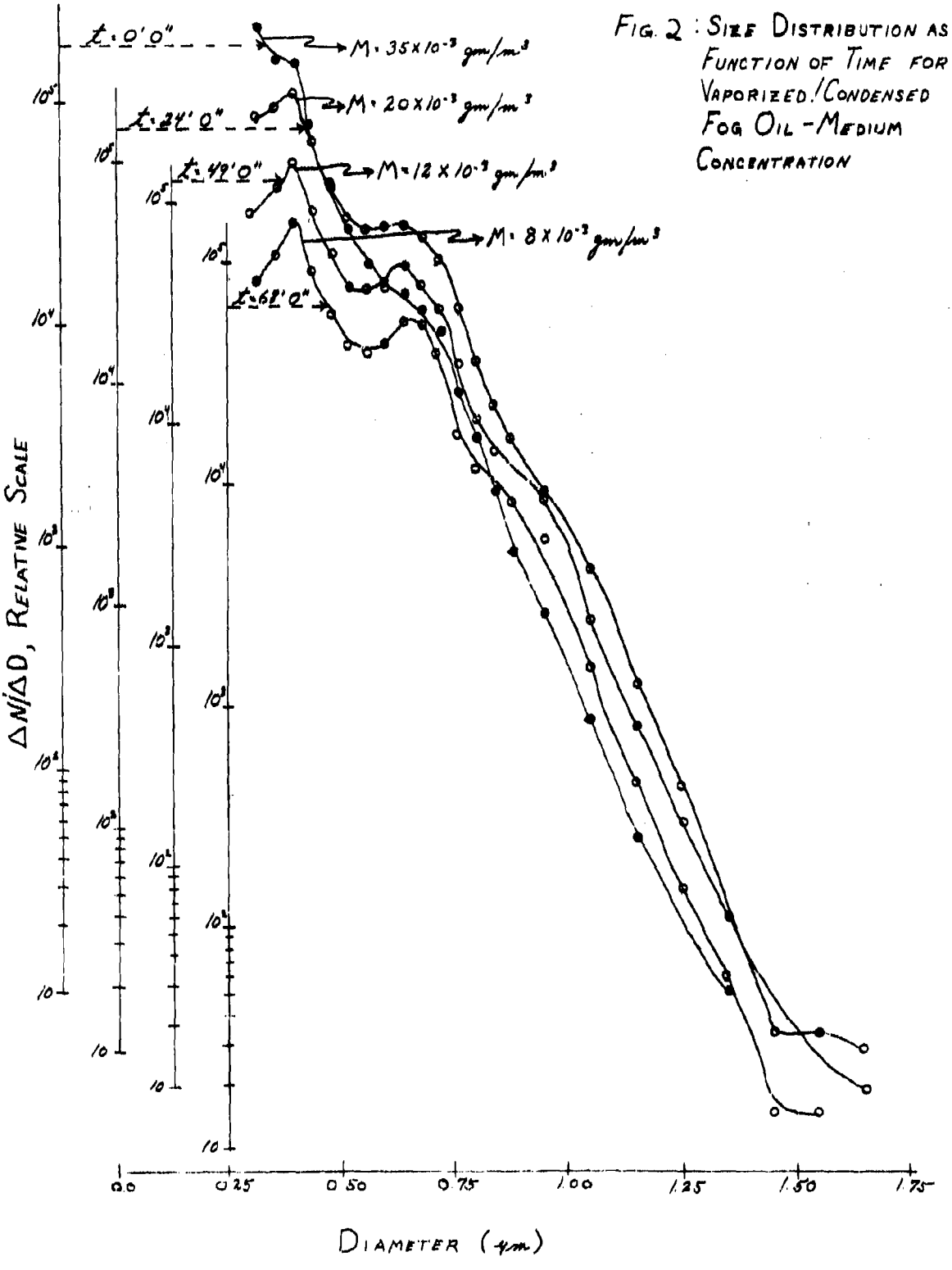

FIG. 2 : SIZE DISTRIBUTION AS A FUNCTION OF TIME FOR VAPORIZED/CONDENSED FOG OIL - MEDIUM CONCENTRATION

UNCLASSIFIED

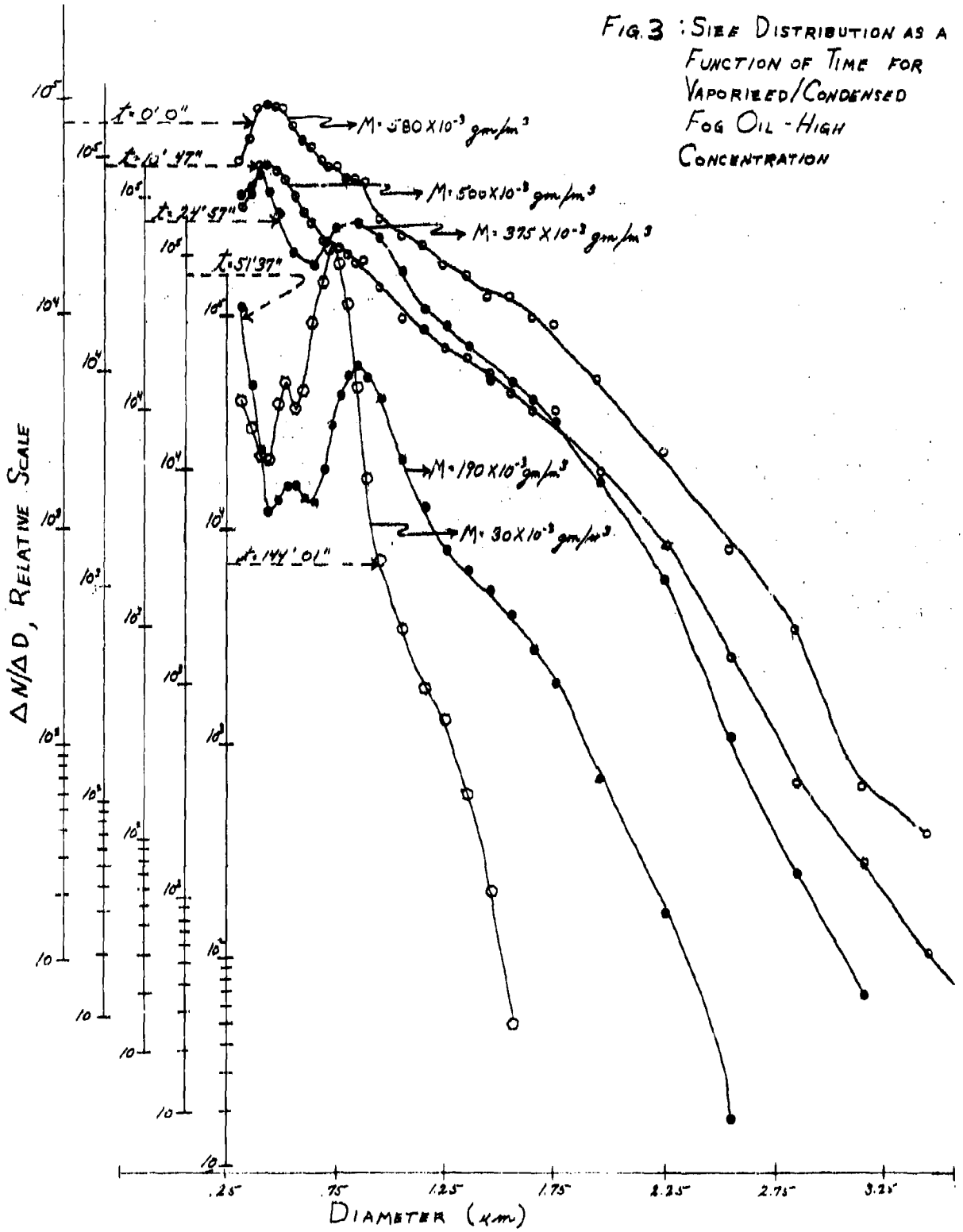

FIG. 3 : SIZE DISTRIBUTION AS A FUNCTION OF TIME FOR VAPORIZED/CONDENSED FOG OIL - HIGH CONCENTRATION

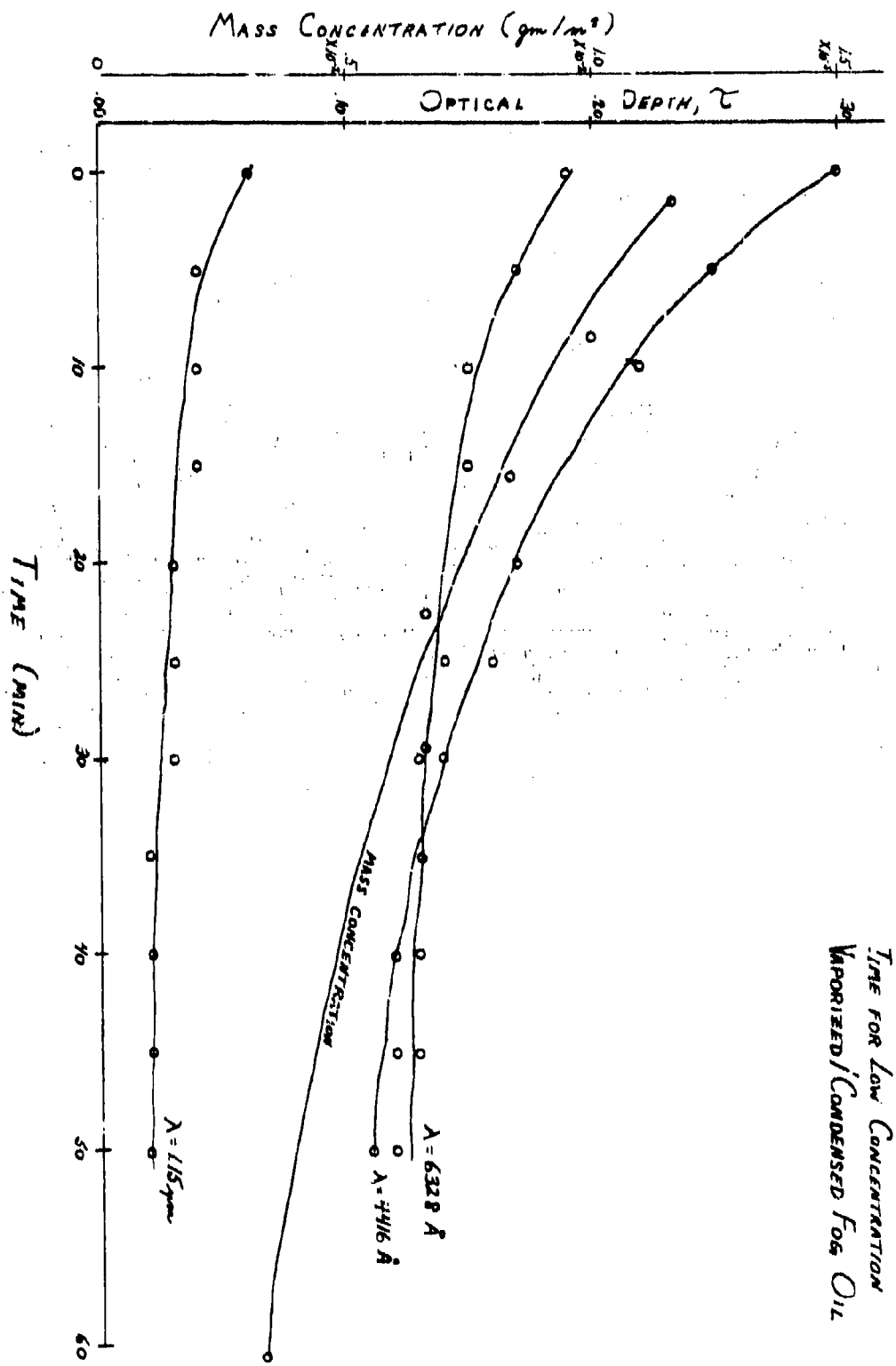

FIG. 4: OPTICAL DEPTH AND MASS CONCENTRATION AS FUNCTIONS OF TIME FOR LOW CONCENTRATION VAPORIZED/CONDENSED FOG OIL

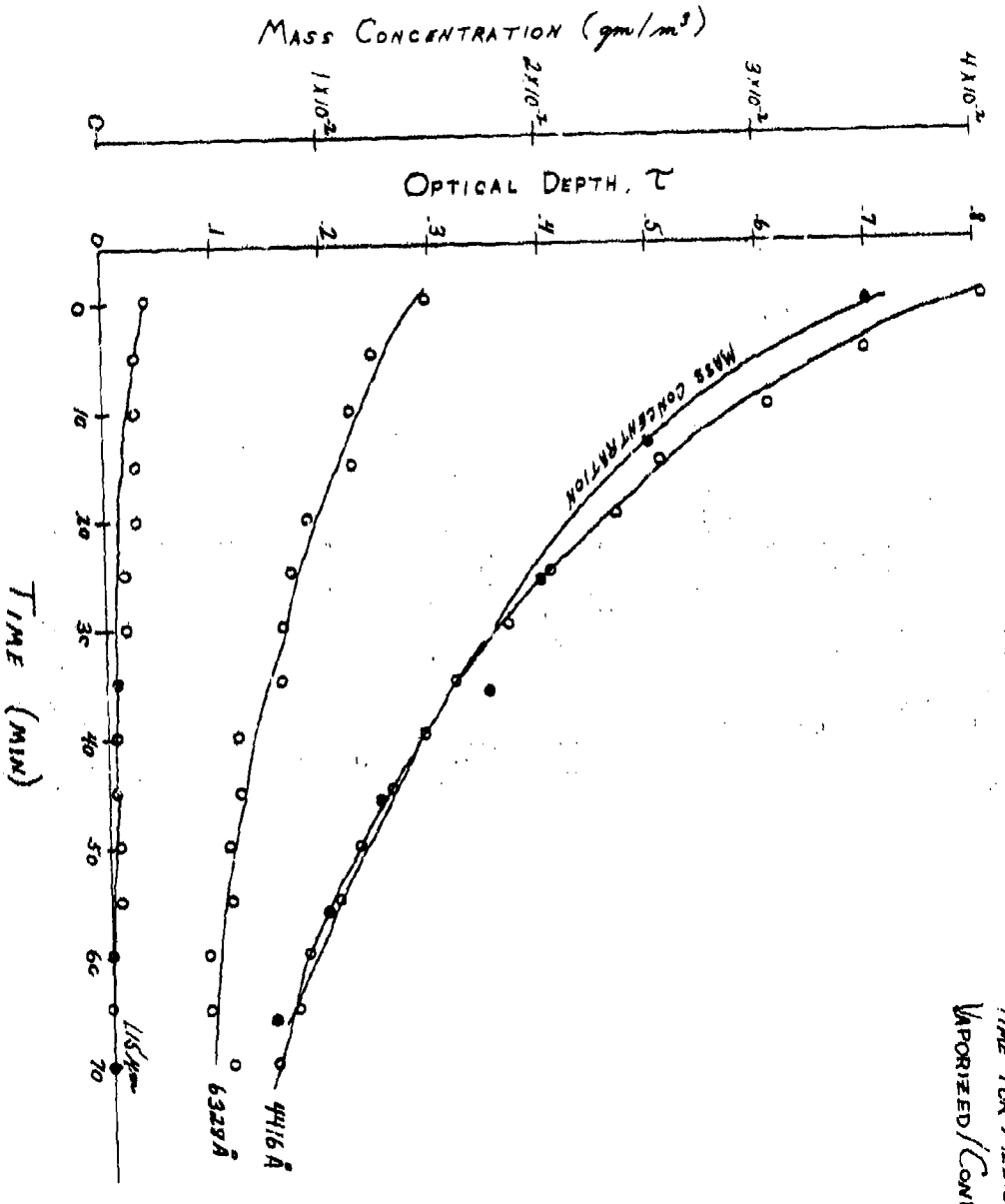

FIG. 5: OPTICAL DEPTH AND MASS CONCENTRATION AS FUNCTIONS OF TIME FOR MEDIUM CONCENTRATION VAPORIZED/CONDENSED FOG OIL

UNCLASSIFIED

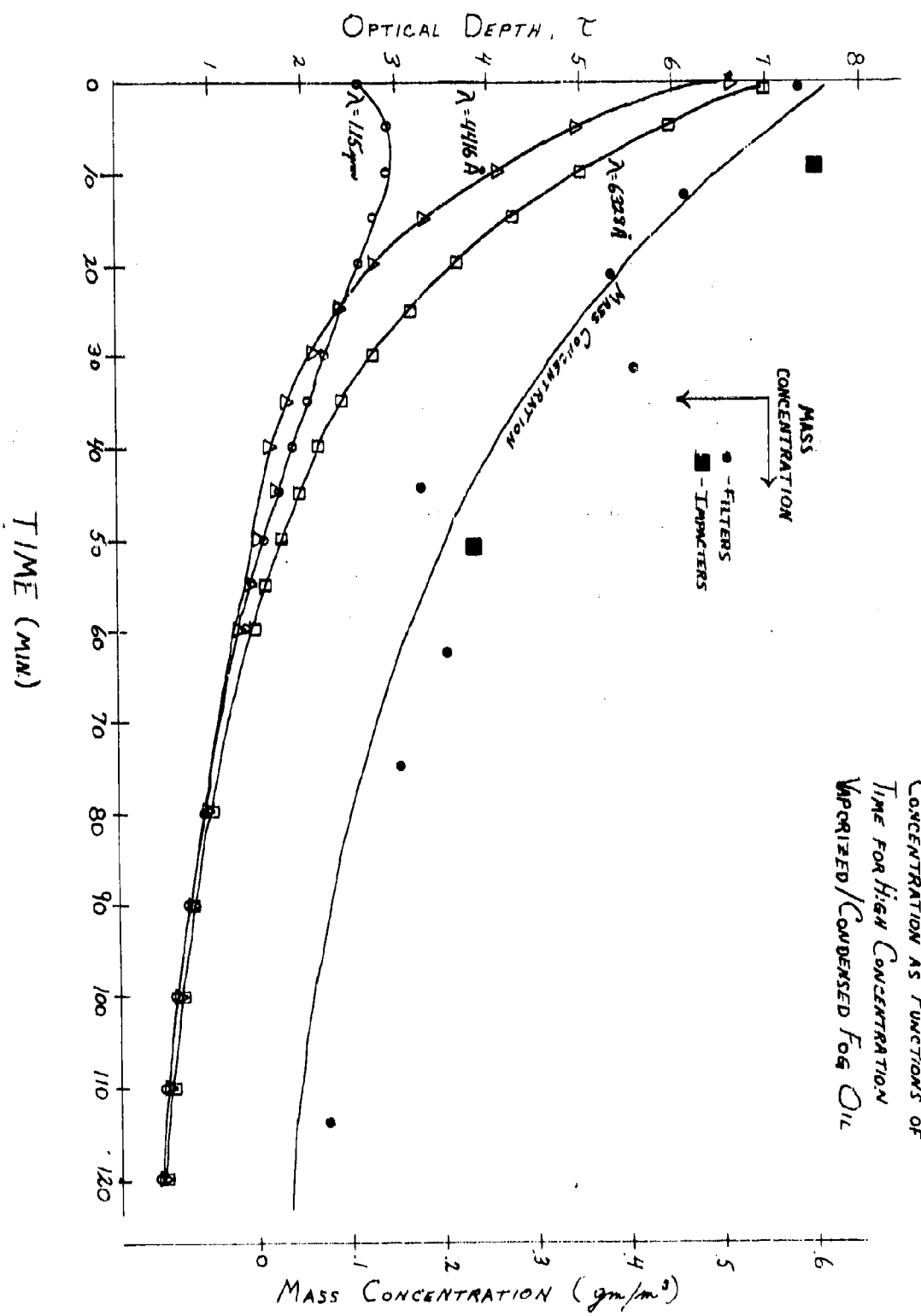

FIG. 6: OPTICAL DEPTH AND MASS CONCENTRATION AS FUNCTIONS OF TIME FOR HIGH CONCENTRATION VAPORIZED/CONDENSED FOG OIL

UNCLASSIFIED

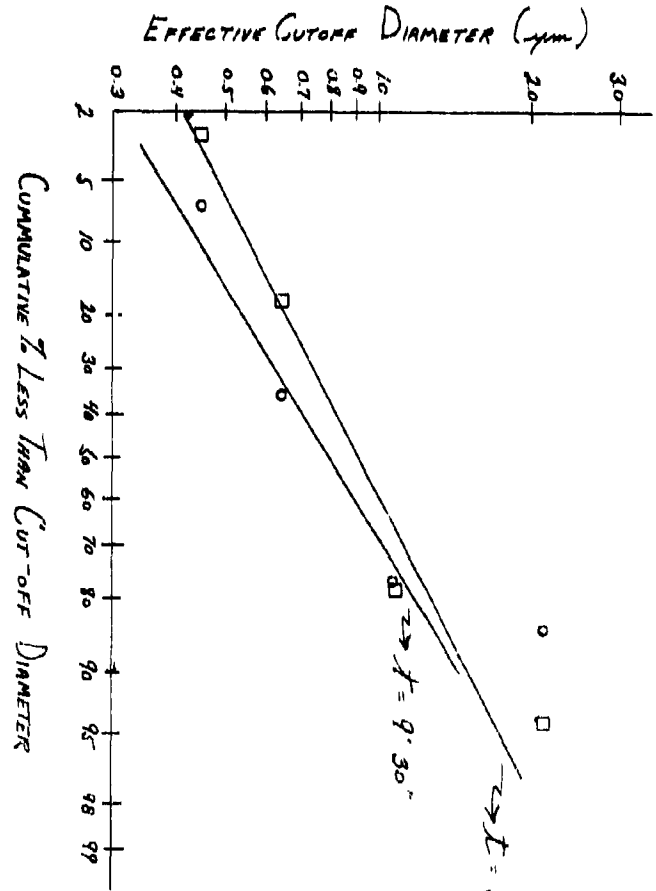

Fig. 7: Cascade Impactor Mass Distribution for High Concentration Vaporized Condensed Fog Oil

UNCLASSIFIED

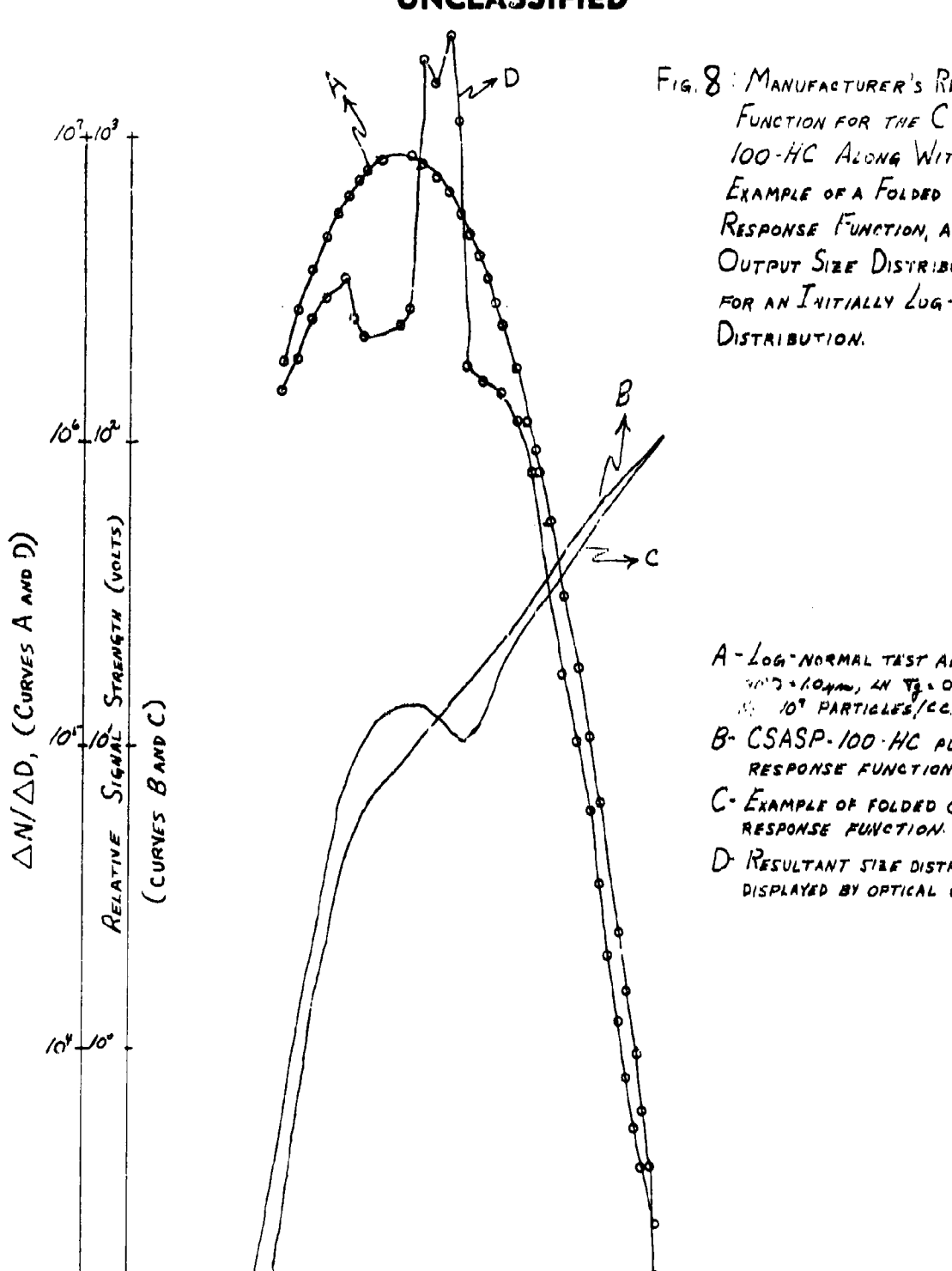

FIG. 8: MANUFACTURER'S RESPONSE FUNCTION FOR THE CSASP-100-HC ALONG WITH AN EXAMPLE OF A FOLDED OVER RESPONSE FUNCTION, AND THE OUTPUT SIZE DISTRIBUTION FOR AN INITIALLY LOG-NORMAL DISTRIBUTION.

A - LOG-NORMAL TEST AEROSOL $\bar{r}_g$ = 1.0μm, $\ln \sigma_g$ = 0.5 AND 10^9 PARTICLES/CC.

B - CSASP-100-HC PUBLISHED RESPONSE FUNCTION.

C - EXAMPLE OF FOLDED OVER RESPONSE FUNCTION.

D - RESULTANT SIZE DISTRIBUTION DISPLAYED BY OPTICAL COUNTER.

UNCLASSIFIED

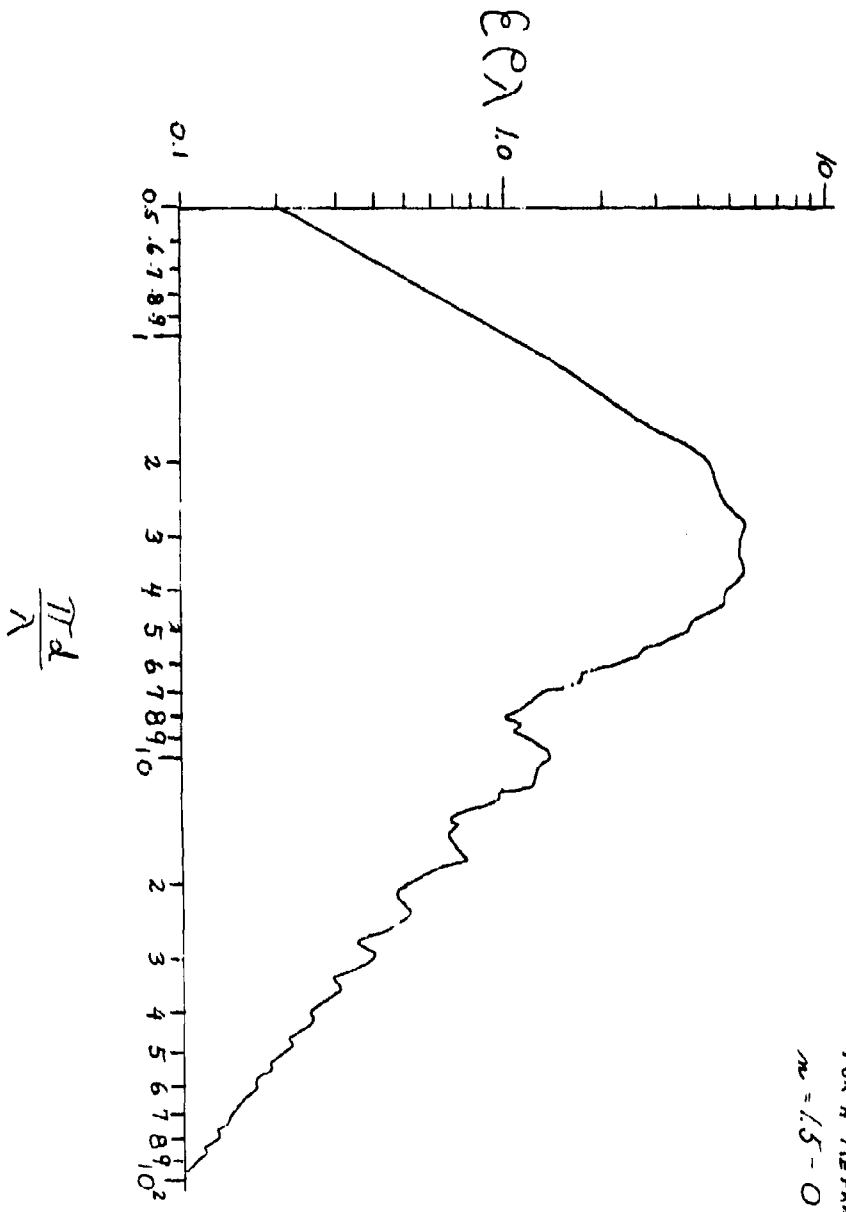

FIG. 9 : PARTICLE EXTINCTION COEFFICIENT X PARTICLE DENSITY X WAVELENGTH AS A FUNCTION OF THE SIZE PARAMETER FOR A REFRACTIVE INDEX OF $m = 1.5 - 0\,i$

FIG.10 INITIAL UNIMODAL LOG-NORMAL DISTRIBUTION WITH MMD = 0.30 σ_g = 1.7 AT A DROPLET CONCENTRATION RATIO C = 0.064 AND A SUPER-SATURATION RATIO SE = 1.001

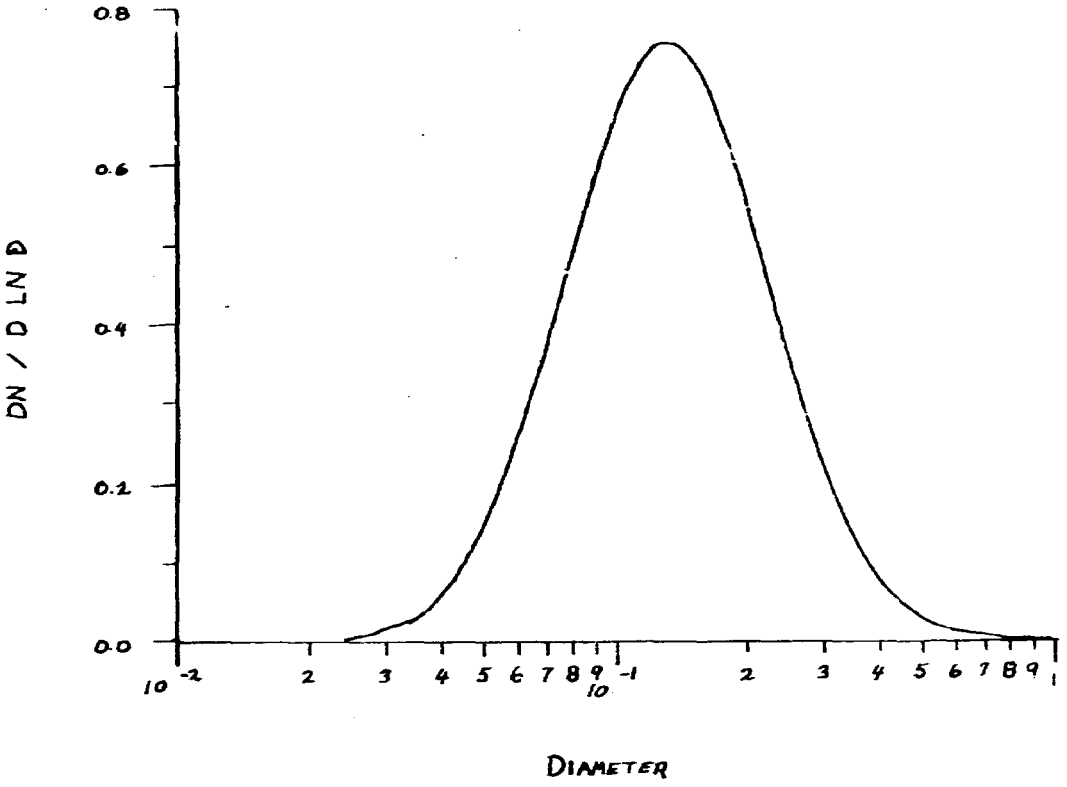

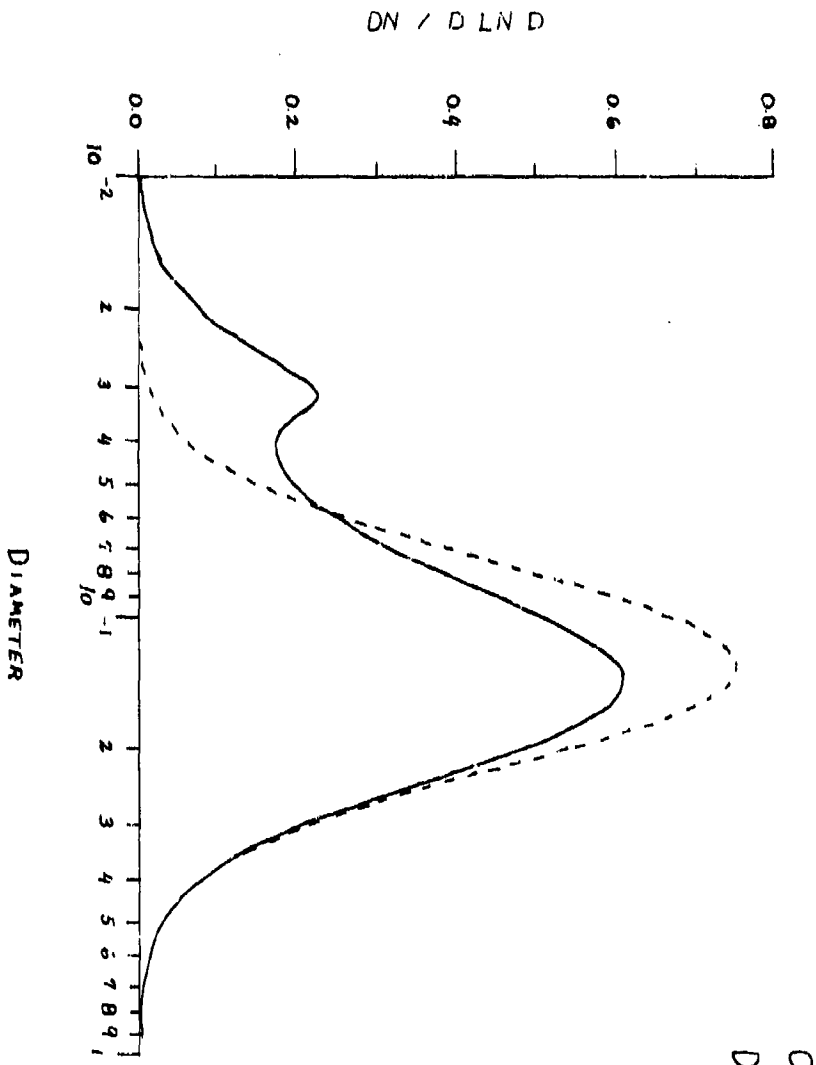

FIG. 11 : BIMODAL DISTRIBUTION AT 30 SECONDS INITIAL UNIMODAL LOG-NORMAL DISTRIBUTION OF MMD = 0.30, σ_g = 1.7 SHOWN AS DOTTED LINE.

FIG. 12: BIMODAL DISTRIBUTION AT 100 SECONDS. INITIAL UNIMODAL LOG-NORMAL DISTRIBUTION OF MMD = 0.30 AND σ_g = 1.7 SHOWN AS DOTTED LINE

N	λ = 1.15 μm		λ = 0.6328		λ = 0.4416 μm	
# particles	DIA = 0.25 μm	0.45 μm	DIA = 0.25 μm	0.45 μm	DIA = 0.25 μm	0.45 μm
1	0.38	1.57	2.94	7.99	7.84	13.31
2	0.76	3.14	5.88	15.98	15.68	26.62
3	1.14 A → B	4.71	8.82 A → B	23.97	23.52 A → B	39.93
4	1.52	6.28	11.76	31.96	31.36	53.24

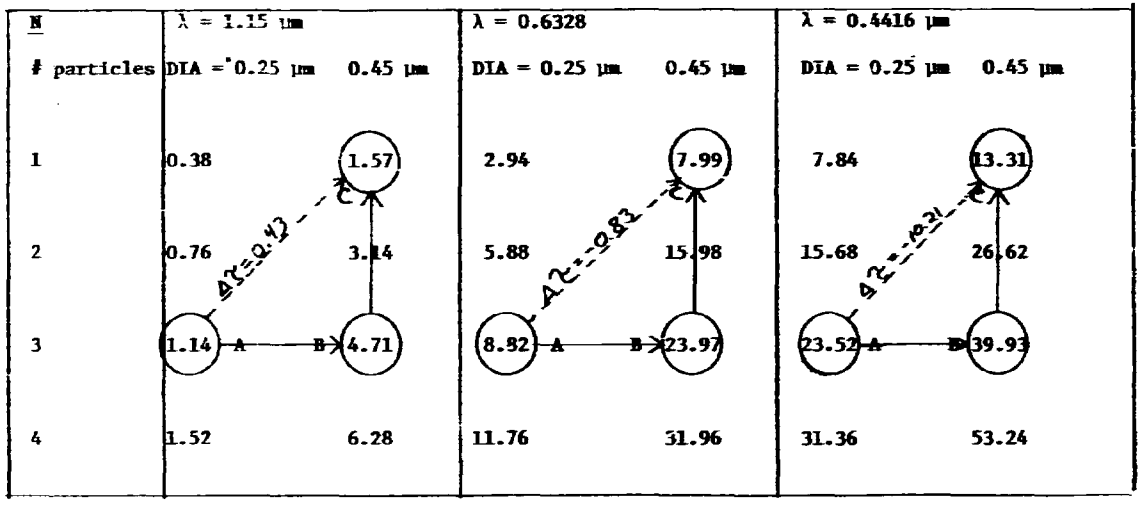

TABLE 1 : ε X N values where ε is the particle extinction coefficent for fog oil with a density of $\rho \sim 0.91 gm/m^3$ and an assumed refractive index of n = 1.5 − 0 i, and N is the # of particles. Example illustrates the net change in the optical depth, $\Delta\tau \equiv (\Sigma\varepsilon N)\Big|_A^C$ via growth from 0.25 μm to 0.45 μm diameter particles followed by partial removal of the larger particles. Note the net increase in τ @ λ = 1.15 μm along with the net decrease in τ @ λ = 0.6328 μm and τ @ λ = 0 .4416 μm.

DATA POINTS: Figure 8, Curve B CSASP-100-HC Response Function		Diameter Intervals on Curve C of Figure 8 Corresponding to the CSASP-100-HC Relative Signal Strengths in First Column	
Relative Signal Strength (VOLTS)	Diameter Range (μm)		(μm)
0.120V - 0.394V	.30 - .34		.247 - 0.303
.394 - .852	.34 - .38		.303 - .342
.852 - 1.56	.38 - .42		.342 - .379
1.56 - 2.50	.42 - .46		.379 - .413
2.50 - 3.55	.46 - .50		.413 - .441
3.55 - 4.60	.50 - .54		.441 - .469
4.60 - 5.38	.54 - .58		.469 - .487
5.38 - 6.05	.58 - .62	RANGE I	.487 - .502
6.05 - 6.68	.62 - .66		.502 - .517
6.68 - 7.28	.66 - .70		.517 - .531
7.28 - 7.88	.70 - .74		.531 - .545
7.88 - 8.45	.74 - .78		.545 - .559
8.45 - 8.99	.78 - .82		.559 - .572
8.99 - 9.50	.82 - .86		.572 - .585
9.50 - 10.00	.86 - .90		.585 - .600
10.00 - 11.36	.90 - 1.00		.600 - .647, 1.161 - 1.434
11.36 - 12.64	1.00 - 1.10	RANGE II	.647 - .718, 1.072 - 1.161, 1.434 - 1.508
12.64 - 13.91	1.10 - 1.20		.718 - .856, .967 - 1.072, 1.508 - 1.569
13.91 - 15.27	1.20 - 1.30		.856 - .967, 1.569 - 1.630

TABLE 2: List of corresponding diameter intervals taken from Figure 8 for the CSASP-100-HC and example response functions. Both sets of diameter intervals correspond to the same response signal level set by the manufacturer for the CSASP-100-HC.

DATA POINTS: Figure 8, Curve B CSASP-100-HC Response Function				Diameter Intervals on Curve C of Figure 8 Corresponding to the CSASP-100-HC Relative Signal Strengths in First Column		
Relative Signal Strength (VOLTS)		Diameter Range (μm)			(μm)	
15.27	- 16.70	1.30	1.40		1.630 -	1.693
16.70	- 18.17	1.40	1.50		1.693	1.758
18.17	- 19.74	1.50	1.60		1.758	1.830
19.74	- 21.36	1.60	1.70		1.830	1.908
21.36	- 23.04	1.70	1.80		1.908	1.997
23.04	- 27.96	1.80	2.10		1.997	2.301
27.96	- 34.57	2.10	2.40		2.301	2.705
34.57	- 41.08	2.40	2.70		2.705	3.032
41.08	- 47.59	2.70	3.00		3.032	3.338
47.59	- 54.10	3.00	3.30	RANGE III	3.338	3.651
54.10	- 60.39	3.30	3.60		3.651	3.967
60.39	- 66.26	3.60	3.90		3.967	4.265
66.26	- 71.92	3.90	4.20		4.265	4.545
71.92	- 77.23	4.20	4.50		4.545	4.798
77.23	- 82.48	4.50	4.80		4.798	5.039
82.48	- 87.71	4.80	5.10		5.039	5.271
87.71	- 93.26	5.10	5.40		5.271	5.511
93.26	- 99.66	5.40	5.70		5.511	5.780
99.66	- 104.90	5.70	6.00		5.780	5.996

TABLE 2 (Continued): List of corresponding diameter intervals taken from Figure 8 for the CSASP-100-HC and example response functions. Both sets of diameter intervals correspond to the same response signal level set by the manufacturer for the CSASP-100-HC.

THE INFRARED CHARACTERIZATION OF SMOKES AND OBSCURANTS UTILIZING THE HONEYWELL BACKGROUND MEASUREMENT SPECTRORADIOMETER

J. R. Bryson, M. J. Flanagan
Honeywell Tactical Support Operations
Clearwater, Florida

and

D. R. Snyder, III
USAF 3246 TEST WING
Eglin AFB, Florida

ABSTRACT

The smoke/obscurant data gathered in an extensive field measurement program and instrumentation utilized in the collection are discussed. Moderate ($4cm^{-1}$) resolution spectral data of smokes/obscurants were collected for use in detection algorithm training and testing as well as use in a scen[15] simulation model. Several representative samples of field measured data are presented.

1. INTRODUCTION

The technique of remotely sensing the atmosphere has in recent years become an extremely valuable tool for the detection and analysis of vapor or small aerosol clouds. Applications have included a variety of chemical substances, both natural and manmade. The Fourier Transform Infrared or FTIR spectrometer has proven itself a versatile instrument in field measurement because of sensitivity, resolution, and scan speed advantages. Honeywell Tactical Support Operations is currently developing the XM21 remote sensing chemical agent alarm for the U.S. Army Chemical Systems Laboratory. This instrument is a portable ruggedized FTIR spectroradiometer system capable of automatic detection of toxic vapor clouds.

In the course of development, a large spectal data base was required for the training and testing of detection algorithms. Among these data, a large requirement existed for the infrared spectral characteristics of smokes and obscurants against both natural and manmade backgrounds. By training the detection algorithms to reject the presence of spectral interferents, the probability of false alarm is greatly reduced.

2. EQUIPMENT

To collect the necessary field measured data, a prototype instrument, the Honeywell Background Measurement Spectroradiometer or BMS was constructed. This instrument is a single cube Michelson interferometer. The scanning mirror drive assembly is a flex pivot or "porch swing" type movement. These two features result in an extremely temperature and vibration resistant design, important considerations in a field instrument. ZnSe transmission optics, combined with a HgCdTe detector cooled to 77°K provide excellent sensitivity in the 1200 to 800 cm^{-1} (8.3 to 12.5 um) region. The reflective optics are diamond turned aluminum. All transmission optics are anti-reflection coated. The optical instrument head was manfactured at Honeywell Electro-Optical Operations in Lexington, Massachusetts. The servo and control electronics for the BMS were modified from a Nicolet Instrument Company MX-1 laboratory interferometer. The result has been an extremely reliable and versatile field instrument. The BMS is shown in figures 1 through 5. Figure 6 is a table of applicable sensor parameters.

The interferograms are generated by the sensor at a rate of seven scans per second. The signal is digitized into 1024 16 bit words and then recorded by Engineering Data Analysis system or EDAS. The EDAS consists of a ruggedized Honeywell Level 6/43 and various peripheral devices. The data are formatted by the EDAS and is collected real-time on 30 megabytes of disc storage. Experiments may be conducted from either a system CRT terminal or Hughes C3 graphics terminal. The high resolution graphics terminal allows examination of spectral data in the field. A full size line printer is used to print summaries of experimental and environmental conditions. An array processor (CDA) is linked to the EDAS to provide rapid processing (fourier transform) of the raw interferograms into spectra. The formatted data are stored on tape via a 9 track tape unit. A boresighted Panasonic video system provides a permanent record of the experiment on video tape.

To document the environmental conditions during these field measurements, a Climatronics electronic weather station was interfaced to the EDAS so that the meteorological conditions during each scan would be recorded. The parameters recorded were wind speed, wind direction, temperature, dew point, rainfall, barometric pressure, and solar radiation. The meteorological sensors were tripod mounted away from the influences of the data van.

The system is transported from site to site in a 34 foot Earth instrument van. This vehicle provides a sheltered environment for the data processing equipment. Large cargo doors on the sides and rear allow ease in loading and unloading as well as a sheltered area for recording during severe weather. The vehicle is self leveling, allowing for operation on rough terrain. Power for utilities is provided from two onboard 7.5 kw Kohler generators. A regulated 30 kw Kohler is trailered behind the van to provide "clean" power for the EDAS and instruments. In this configuration, up to 4 BMS's can be used to record data simultaneously. The van is shown in figures 7 to 9. Figure 10 shows the weather station rack with mainframe, digital displays, and chart recorders. Figures 11 and 12 show the system (van and BMS) collecting data.

3. DATA

The data are stored as digitized 1024 16 bit word interferograms on magnetic tape. Each experiment is formatted with a global file header (figure 13), subfile headers (figure 14), and interferograms (figure 15). The global file header is a documentation of the sensor, scene, and general meteorological conditions for each experiment. With each interferogram is a subfile header containing instantaneous sensor and meteorological parameters. The result is a sequential record of each experiment. In addition, 16 ambient and 16 LN_2 temperature blackbody scans are recorded prior to each experiment to allow calibration of the data by removing the instrument response. The normal collection sequence included 60 seconds of background, 90 to 120 seconds of dispersal, 30 seconds of trail-off, and a pause for clearing followed by a final 60 seconds of background.

A total of 306 experiments were conducted during the BMS phase of the XM21 system development. Of these experiments, 167 involved the presence of a natural or manmade obscurant. Many of these were in combination with DMMP, which is a toxic agent simulant. Observations were conducted at several sites throughout the U.S. during all types of weather, ranging from clear to heavily overcast and snowing. Backgrounds during this measurement program included sky, terrain, water, vegetation, building, roads, snow, ice, and other miscellaneous targets such as vehicles or aircraft. The following is a list of the types of smokes and obscurants observed:

Smoke/Obscurants Data Base

1. White Phosphorus - WP
2. Red Phosphorus - RP
3. Plasticized White Phosphorus - PWP
4. Alkali Chloride
5. Hexachloroethane - HC
6. PEG 200
7. Green
8. Red
9. Yellow
10. Violet
11. IR #1
12. IR #2
13. IR #3
14. Fog Oil
15. Dust (Kaolinite, Montmorillonite, Calcium Carbonate)
16. Rubber (Tire) Smoke
17. Fuel Oil (Diesel) Smoke
18. Aircraft Exhaust
19. Vehicle Exhaust

The field measured data from the above list was utilized in the training and testing of the detection algorithms' discriminants. Both singly and in combinations, interferents were processed, as well as weta interferents in combination with various concentrations of the toxic agent simulant DMMP. From this exercise, both the obscuration and spectral interferent effects on system performance could be gauged. Finally, the smoke/obscurant data gathered in the field were incorporated into a realistic scene simulation model.

The scene simulation model incorporates the Lowtran IV atmospheric propagation model with field measured backgrounds. This model has allowed us to fill in the gaps in our empirical data base. A file of reference absorptivity coefficients is used (via a Beer's law calculation) to generate several slabs of either obscurants or vapor

clouds in absorption or emission. The smoke/obscurant data recorded have been used to validate this function. In addition, the use of backgrounds with smoke and other obscurants presents a scene model which more realistically simulates conditions found on the battlefield. Given the variety and complexity of backgrounds that may be viewed by an IR sensor in the FEBA, it is not surprising that a primary weakness of many models has been the computing of realistic background radiances.

Several representative field measured spectra are shown in figures 16 to 25. These include spectra of Phosphorus , HC, Alkali Chloride, PEG 200, Red, IR screening, and several dust clouds. The final spectra (figures 26 to 28) illustrate the difficulties caused by interferents in the detection of a threat agent or simulant such as DMMP.

All the spectra shown are background subtraction plots. The spectra therefore represent the scene with the obscurant in the FOV minus the scene prior to the intervention of the target cloud. The spectra will show either emission or absorption features depending upon the relative temperatures of the target cloud and the background. The plots of spectra are in wavenumbers (cm^{-1}). Those plotted versus radiance values have the instrument response removed. Those plotted versus Arbitrary Units are not corrected for instrument self radiance and are intended to show relative spectral features.

Figure 16 is a typical white phosphorus spectrum in absorption. The broad peak centered at 1030 cm^{-1} is shown here in absorption. In most trials to date, this peak has been observed in emission as shown in figures 17 and 18. Some atmospheric fine structure is seen in the region greater than 1100 cm^{-1} as a result of the subtraction process. Figure 19 is the spectrum of an Alkali Chloride smoke dispensed at Smoke Week III. The very broad absorption is centered at approximately 1000 cm^{-1}. Instrument response roll-off with this particular instrument has magnified the structure below 850 cm^{-1}. Figure 20 shows the spectrum of PEG 200. The prominent feature at 1000 cm^{-1} to 1150 cm^{-1} displays sharp spectral features. Typical alcohols possess a strong peak in the 1050 to 1100 cm^{-1} region. The peak in this figure is presumably broadened by the polymeric nature of the PEG (polyethylene glycol) molecule. The effects of dusts as observed by the BMS is illustrated in figure 21. As the concentration of dust in

the instrument FOV increase (1-4) the obscuration effect correspondingly increases. HC is the only common military smoke we have found to be a significant obscurant in the 800 to 1200 cm^{-1} region of the spectrum. The very broad peak at 880 cm^{-1} (figure 22) has shown a tendency to significantly mask the features of other spectrally significant materials present. By contrast, the sharp peak at 990 cm^{-1} which results from red smoke (figure 23) can usually be observed only after signal averaging (coadding) to increase the signal to noise ratio. Figures 24 and 25 show the broad spectrally obscuring features of infrared screeners 1 and 3 as observed at Smoke Week III. A typical DMMP spectra is shown in figure 26. Figures 27 and 28 illustrate the degree of obscuration and spectral interference with which a discrimination algorithm must cope.

4. CONCLUSIONS

The field measurement program which we recently completed has shown the versatility of the FTIR spectroradiometer in field measurements. The characterization of the spectral and obscuration qualities of smokes and obscurants can be accomplished remotely by the use of an instrument like the BMS. The BMS has been demonstrated to be sufficiently rugged and reliable in extensive use in hostile environmental conditions. In fact, very few alignment adjustments of the interferometers were required despite the harsh conditions to which they were subjected (travel, handling, explosions, and temperatures from 0^{o} to $105^{o}F$).

The effect of smokes and obscurants on the performance of a tactically deployed IR system must be accounted for in the development process. By including well documented field measured smoke/obscurant data in our algorithm development data base and utilizing realistic smoke/obscurant backgrounds in our simulation model, we have achieved a high level of system performance. By consideration of these factors in development of this system, we have been able to minimize the response of the algorithms to spectral interferents and correspondingly reduced the number of false alarms.

While the study of the effects of these materials on the performance of our system is still in process, a few comments can be made regarding the general effectiveness of several obscurants. We have found HC and PEC 200 to be significant in

screening portions of the spectral region of interest (800 to 1200 cm^{-1}). When generated in sufficient quantities, WP, RP, and the infrared screeners provide a broad obscuration effect. The common military signal smokes we have observed have several spectrally interesting peaks but do not, in general, provide a significant level of obscuration.

The authors would like to acknowledge the participation and support of Ernest J. Webb of the Army Chemical Systems Laboratory, Remote Sensing Branch. This work was completed under contract number DAAK11-79-C-0051 for ARRADCOM, Chemical Systems Laboratory, Aberdeen Proving Ground (Edgewood Area) Maryland 21010.

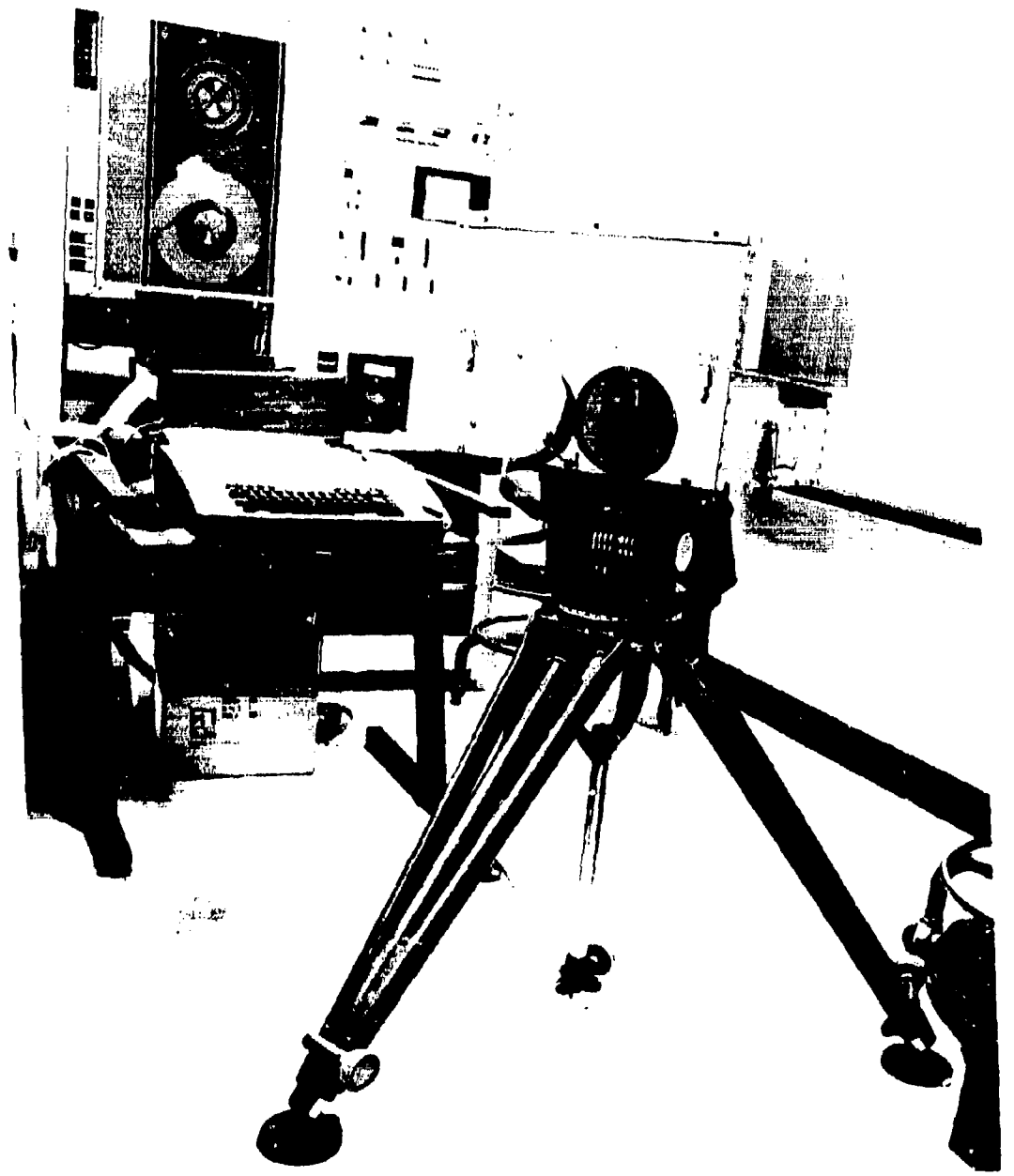

FIGURE 1. HONEYWELL BACKGROUND MEASUREMENT SPECTRORADIOMETER

FIGURE 2. BMS OPTICAL HEAD ASSEMBLY

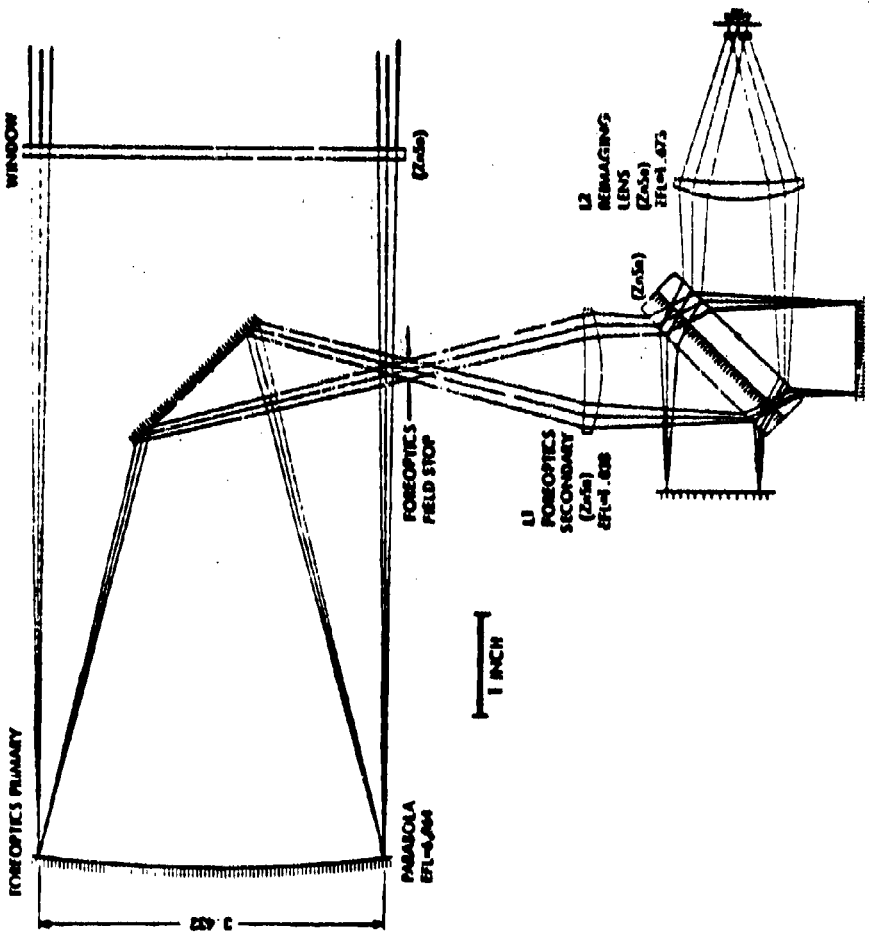

FIGURE 3. BMS OPTICAL DESIGN

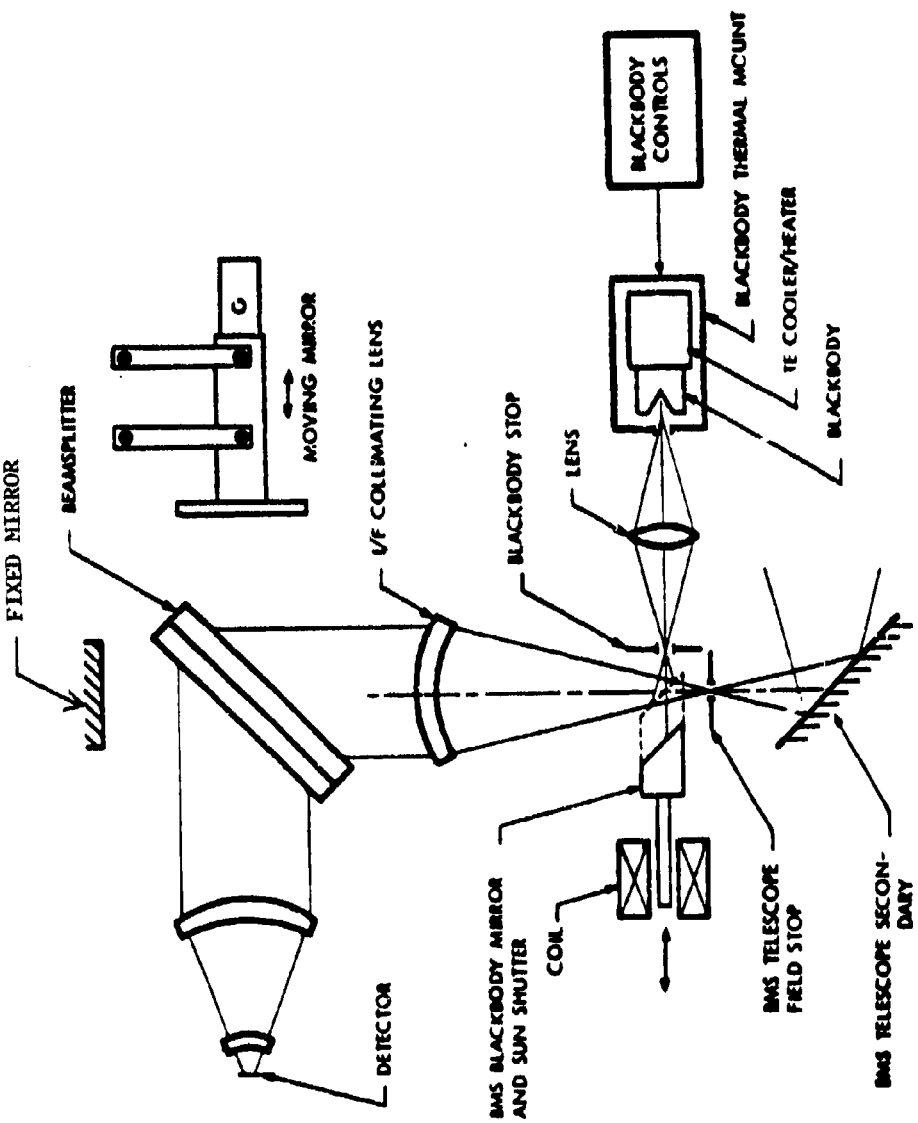

FIGURE 4. BMS OPTICAL HEAD LAYOUT

FIGURE 5. BORESIGHTING BMS VIDEO CAMERA

DETECTOR

TYPE - (Hg,Cd)Te

SIZE - 2mm x 2mm

DETECTIVITY - D^*_{PK} (11 μm, 2 kHz, 1 Hz) ≥ 3.5×10^{10} cm $Hz^{\frac{1}{2}}/W$

FIELD OF VIEW - 60°

D^*_λ (8 μm, 2 kHz, 1 Hz) ≥ $0.7D^*_{PK}$

D^*_λ (12 μm, 2 kHz, 1 Hz ≥ $0.5D^*_{PK}$

INTERFEROMETER

TYPE - MICHELSON

BEARING TYPE - FLEX PIVOT

MIRROR SIZE - 4.8 cm (1.9 in.)

USEABLE MIRROR SIZE - 2.54 cm (1.0 in.)

MIRROR AREA - 5.07 cm^2

INTERFEROMETER HALF ANGLE - 55×10^{-3} rad

MAXIMUM OPTICAL RETARDATION 0.5 cm (0.197 in.)

MAXIMUM PHYSICAL SCAN - 0.25 cm (0.098 in.)

WORKING RESOLUTION - 4 cm^{-1}

TELESCOPE

TYPE - NEWTONIAN

DIAMETER - 8.76 cm

AREA - 52 cm^2 (60 cm^2 - OBSCURATION)

MAXIMUM HALF ANGLE - 0.79°

FIELD OF VIEW - 0.5° x 1.5°

GENERAL PARAMETERS (SYSTEM)

RETARDATION RATE	- 2.5 cm/s
RETARDATION	- 0.25 cm
SCAN TIME	- 0.1 s
APPROXIMATE DUTY CYCLE	- 80%
SCAN RATE	- 8 scans/s
He-Ne REFERENCE FREQUENCY	- 39.51 kHz
SIGNAL FREQUENCY AT 8 μm	- 3.125 kHz
AT 12 μm	- 2.08 kHz

DATA FILE SIZE AT SAMPLE x 0.6328 μm FOR SINGLE SIDED INTERFEROGRAM

SAMPLE X	FILE SIZE	SHORT WAVE LENGTH
1 x 0.63 μm	4096	1.26 μm
2 x 0.63 μm	2048	2.5 μm
4 x 0.63 μm	1024	5 μm

FIGURE 6. TABLE OF RMS INSTRUMENT PARAMETERS

UNCLASSIFIED

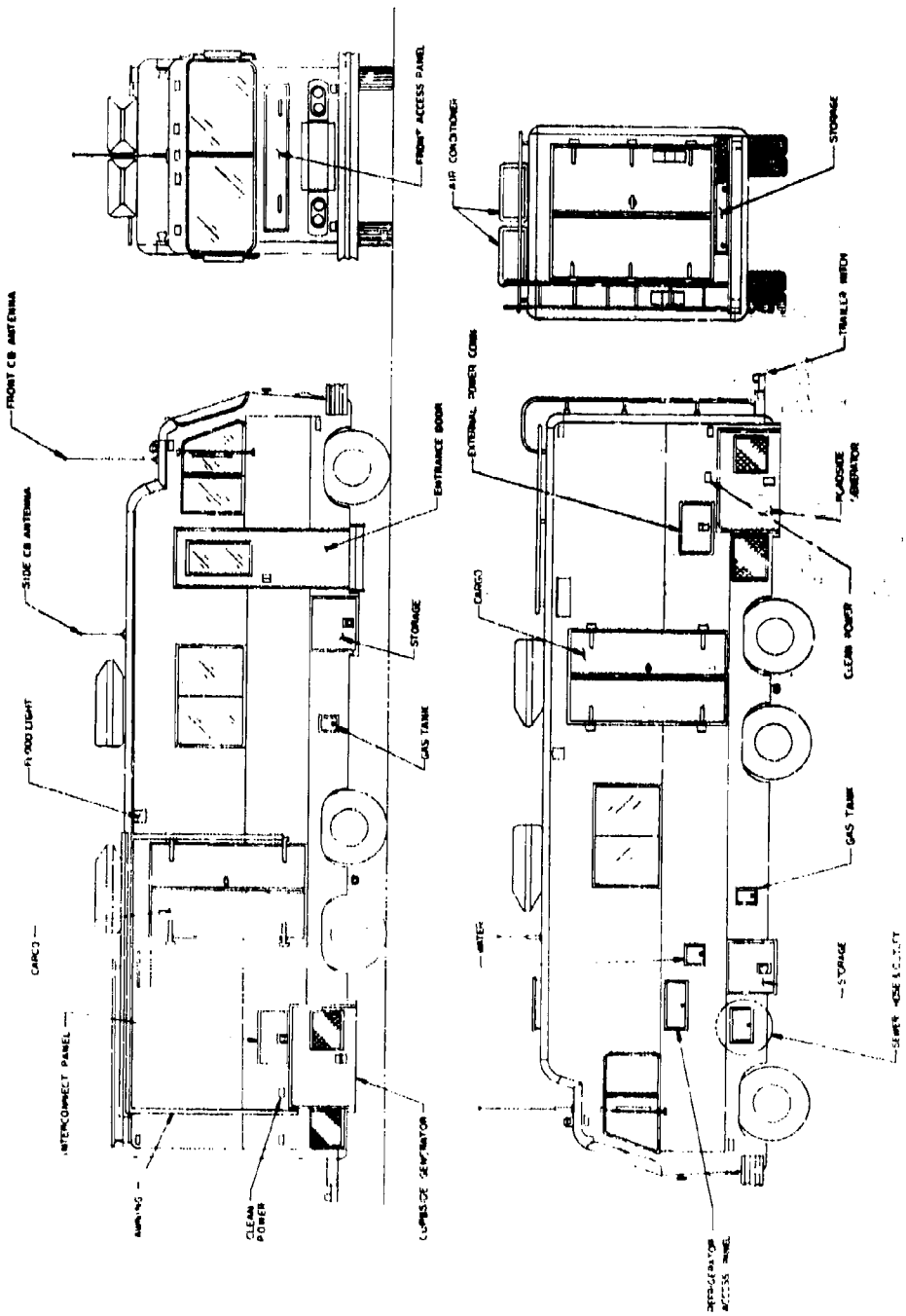

FIGURE 7. XM21 DATA VAN ELEVATIONS

FIGURE 8. XM21 DATA VAN & GENERATORS

FIGURE 9. XM21 DATA VAN INTERIOR

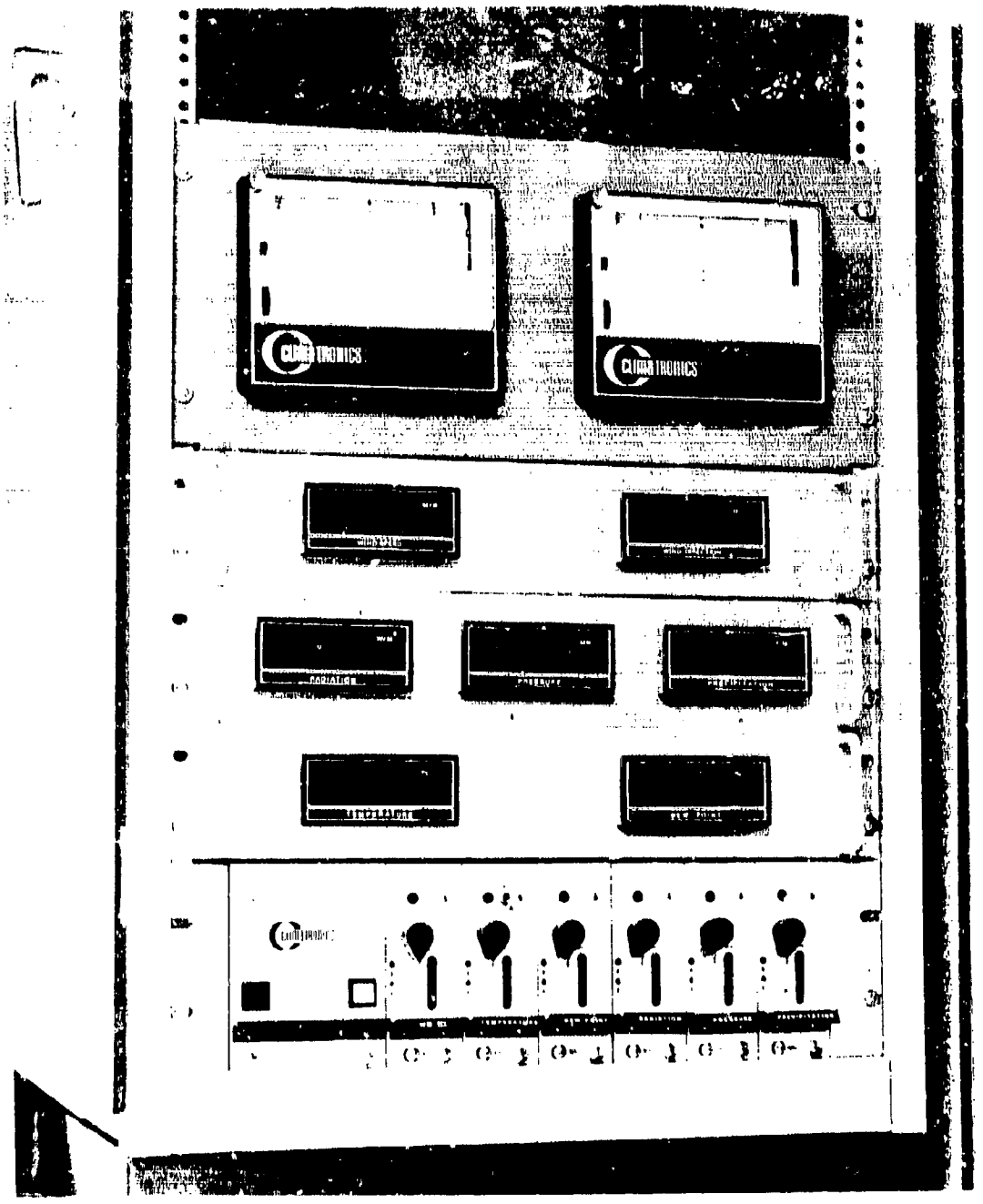

FIGURE 10. CLIMATRONICS ELECTRONIC WEATHER STATION

FIGURE 11. BdS OBSERVING SIMULANT CLOUD

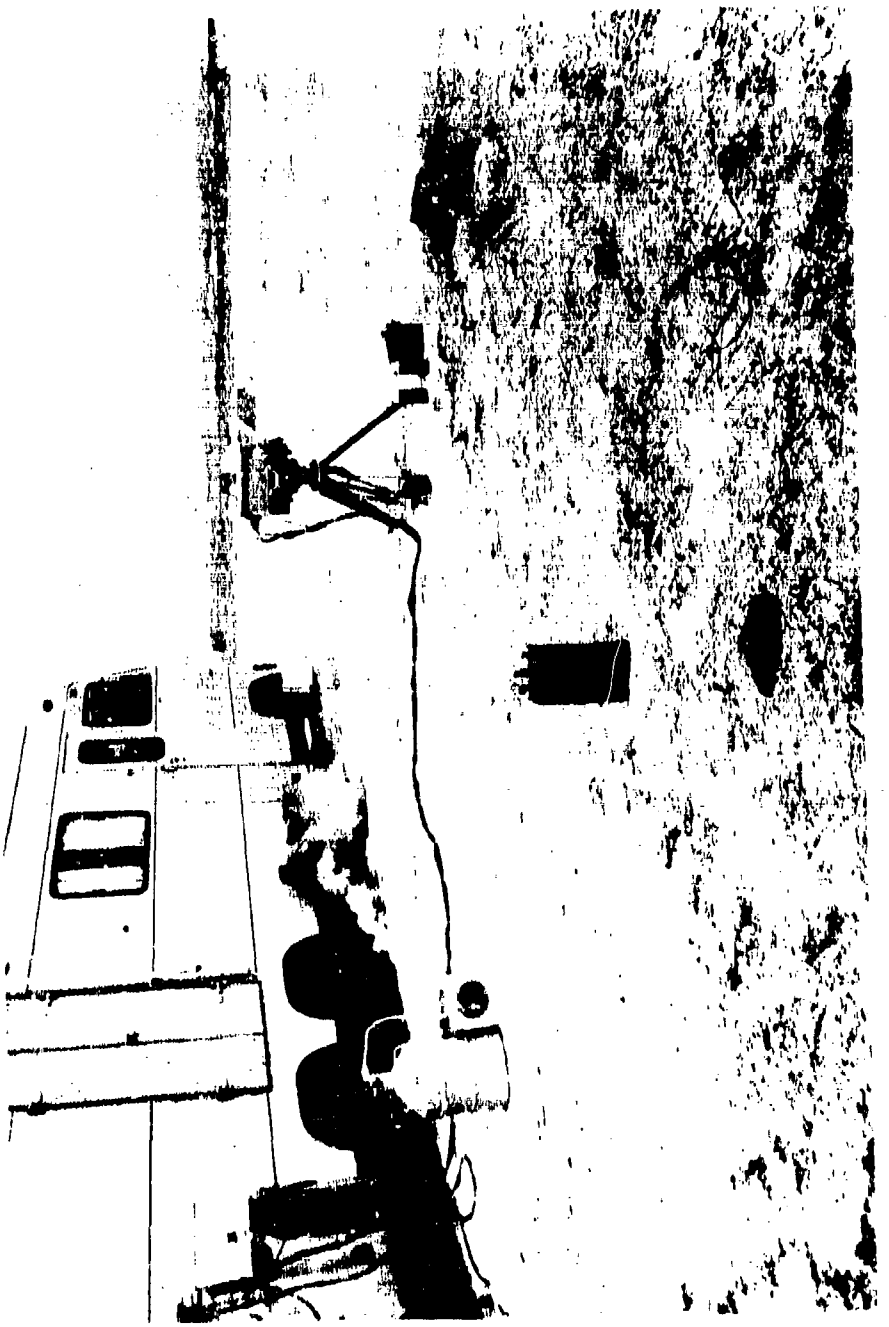

FIGURE 12. BMS RECORDING DATA IN ADVERSE WEATHER

PAGE 1 GLOBAL FILE HEADER LISTING YNC

RUN NUMBER: 12 FILE NAME: C30012.1.1.1

DATE: 1980/02/27 START: 1329:10.850 END: 1340:55.150

***** EQUIPMENT PARAMETERS *****

1.	SITE ID CODE	C3
2.	EDAS ID CODE	120
3.	TASK NAME	RECORD
4.	POINTS PER SCAN	1024
5.	SEQUENCE NUMBER OF FIRST SUB FILE	1
6.	SEQUENCE NUMBER OF LAST SUB FILE	2145
7.	DATA TYPE INDICATOR	1
8.	CALIBRATION SCANS PER BLACK BODY	16
9.	TEMP OF CALIB BLACK BODY 1 (DEG K)	77.0
10.	TEMP OF CALIB BLACK BODY 2 (DEG K)	275.0
****	REFERENCE SCANS VS SCENE SCANS PER GROUP:	
11.	NO OF SEQUENTIAL REF SCANS	0
12.	NO OF SEQUENTIAL SCENE SCANS	30
13.	DELAY BETWEEN SCAN GROUPS (SEC)	0
****	WAVE NUMBER CALIBRATION:	
14.	FREQUENCY OF FIRST POINT (CM**-1)	0.00000000E+00
15.	FREQUENCY OF LAST POINT (CM**-1)	0.19728213E+04
16.	RESOLUTION (CM**-1)	4.0
17.	RETARDATION RATE (CM**-1)	2.5
18.	STARTING SPECTRAL RANGE	800
19.	ENDING SPECTRAL RANGE	1200
20.	APODIZATION BREAK POINT	0.000
21.	ALTITUDE (METERS)	5
****	VIDEO TAPE RECORDER DATA:	
22.	CARTRIDGE NUMBER	1
23.	STARTING COUNTER NUMBER	462
24.	STOPPING COUNTER NUMBER	500
****	INTERFACE NO. 1 SENSOR DATA:	
25.	SENSOR AND ESIP ID CODE	B1E0
26.	AZIMUTH ANGLE (DEGS)	130.0
27.	ZENITH ANGLE (DEGS)	90.0

FIGURE 13. SAMPLE GLOBAL FILE HEADER

PAGE 2 GLOBAL FILE HEADER LISTING

***** SCENE PARAMETERS *****

28.	BACKGROUND TYPE CODE	ACQC6
29.	AREA TYPE CODE	T1C6G6CDGA
30.	TEST TYPE CODE	15
****	CONCENTRATION*PL (CL):	
31.	MG/M**2	9999
32.	MG/M**3	9999
****	MATERIAL 1 DATA:	
33.	MATERIAL 1 TYPE CODE	
34.	MATERIAL DISPERSION METHOD	
35.	DISPERSION RATE GAL/MIN	999.9
36.	DISPERSION RATE LBS/MIN	999.9
37.	RANGE TO TARGET (METERS)	9999
38.	FIELD OF VIEW COVERAGE (%)	0
****	MATERIAL 2 DATA:	
39.	MATERIAL 2 TYPE CODE	
40.	MATERIAL DISPERSION METHOD	
41.	DISPERSION RATE GAL/MIN	0.0
42.	DISPERSION RATE LBS/MIN	0.0
43.	RANGE TO TARGET (METERS)	0
44.	FIELD OF VIEW COVERAGE (%)	0
****	MATERIAL 3 DATA:	
45.	MATERIAL 3 TYPE CODE	
46.	MATERIAL DISPERSION METHOD	
47.	DISPERSION RATE GAL/MIN	0.0
48.	DISPERSION RATE LBS/MIN	0.0
49.	RANGE TO TARGET (METERS)	0
50.	FIELD OF VIEW COVERAGE (%)	0
****	MATERIAL 4 DATA:	
51.	MATERIAL 4 TYPE CODE	
52.	MATERIAL DISPERSION METHOD	
53.	DISPERSION RATE GAL/MIN	0.0
54.	DISPERSION RATE LBS/MIN	0.0
55.	RANGE TO TARGET (METERS)	0
56.	FIELD OF VIEW COVERAGE (%)	0

FIGURE 13. SAMPLE GLOBAL FILE HEADER (cont.)

PAGE 3 GLOBAL FILE HEADER LISTING

***** METEOROLOGICAL PARAMETERS *****

57.	MET STATION ID	1
58.	WIND DIRECTION (DEG)	240
59.	WIND SPEED (M/SEC)	1.5
60.	WIND DIRECTION TREND CODE	
61.	WIND SPEED TREND CODE	
62.	VISIBILITY (KM)	40.00
63.	PAST WEATHER CODE	2
64.	PRESENT WEATHER CODE	2
65.	BAROMETRIC PRESSURE (MB)	1008
66.	PRESSURE TENDENCY CODE	3
67.	AMBIENT TEMPERATURE	2.5
68.	DEW POINT TEMPERATURE (DEG C)	-10.3
69.	DEW POINT TEMPERATURE TREND CODE	1
70.	RELATIVE HUMIDITY (%)	34.2
71.	CLOUD COVER CODE	9
72.	LOW/MIDDLE CLOUD COVER CODE	9
73.	LOW CLOUD HEIGHT CODE	6
74.	LOW CLOUD TYPE CODE	5
75.	MEDIUM CLOUD TYPE CODE	0
76.	HIGH CLOUD TYPE CODE	3
77.	AMT OF PRECIPITATION LAST HOUR	0.0
78.	TIME PRECIPITATION STARTED	0
79.	TIME PRECIPITATION STOPPED	0
80.	AMOUNT PRECIPITATION DURING RUN	0.00
81.	PRECIPITATION RATE DURING RUN	0.00
82.	DEPTH OF SNOW (CM)	0
83.	ATMOSPHERIC STABILITY CODE	D
84.	SOLAR RADIATION (W/M**2)	211
85.	SUN AZIMUTH (DEG)	9.3
86.	SUN ELEVATION (DEG)	41.2
87.	DATA SOURCE DISTANCE (KM)	10

***** OPERATOR COMMENTS *****

EST ZONE VEHICLE IN FOV
TRUCK AT VARIOUS RANGES SEE VTR FOR DETAILS
TEMP. SENSOR SEEMS OK WIND SPEED IS INCORRECT WS APP 15 MPH

FIGURE 13. SAMPLE GLOBAL FILE HEADER (cont.)

FILE NAME: C30002.1.1.1		SUBFILE HEADER	
SUBFILE NO.	1	TIME	1980/02/20 1657:05.800
REFERENCE/SCENE FLAG.....	1	DATA TYPE CODE	0
APODIZATION BREAKPOINT	0	PEAK LOCATION	54
NO. OF SCANS COADDED.....	1	GAIN	8
SCALING EXPONENT = 2**N	-6	AZIMUTH ANGLE = DEG	0
WIND DIRECTION = DEG	164	WIND SPEED = M/SEC * 10	1
BAROMETRIC PRESSURE = MB	1011	AMBIENT TEMP = DEG C * 10	158
DEW POINT TEMP = DEG C * 10 .	-6	TOTAL PRECIP = CM * 10	0
SOLAR RADIATION = W/CM**2 *10	668	ALGORITHM OUTPUT (1)	0
ALGORITHM OUTPUT (2).....	0	ALGORITHM OUTPUT (3).....	0
ALGORITHM OUTPUT (4)	0	ALARM	0
NO CONTRAST	0	SENSOR ERROR CODE	0
A/D OVERFLOW	0	UNDEFINED	0
UNDEFINED	0	UNDEFINED	0
UNDEFINED	0	UNDEFINED	0

FILE NAME: C30002.1.1.1		SUBFILE HEADER	
SUBFILE NO.	2	TIME	1980/02/20 1657:05.750
REFERENCE/SCENE FLAG.....	1	DATA TYPE CODE	0
APODIZATION BREAKPOINT	0	PEAK LOCATION	54
NO. OF SCANS COADDED.....	1	GAIN	8
SCALING EXPONENT = 2**N	-3	AZIMUTH ANGLE = DEG	0
WIND DIRECTION = DEG	164	WIND SPEED = M/SEC * 10	1
BAROMETRIC PRESSURE = MB	1011	AMBIENT TEMP = DEG C * 10	158
DEW POINT TEMP = DEG C * 10 .	-6	TOTAL PRECIP = CM * 10	0
SOLAR RADIATION = W/CM**2 *10	668	ALGORITHM OUTPUT (1)	0
ALGORITHM OUTPUT (2).....	0	ALGORITHM OUTPUT (3).....	0
ALGORITHM OUTPUT (4)	0	ALARM	0
NO CONTRAST	0	SENSOR ERROR CODE	0
A/D OVERFLOW	0	UNDEFINED	0
UNDEFINED	0	UNDEFINED	0
UNDEFINED	0	UNDEFINED	0

FILE NAME: C30002.1.1.1		SUBFILE HEADER	
SUBFILE NO.	3	TIME	1980/02/20 1657:05.900
REFERENCE/SCENE FLAG.....	1	DATA TYPE CODE	0
APODIZATION BREAKPOINT	0	PEAK LOCATION	54
NO. OF SCANS COADDED.....	1	GAIN	8
SCALING EXPONENT = 2**N	-3	AZIMUTH ANGLE = DEG	0
WIND DIRECTION = DEG	164	WIND SPEED = M/SEC * 10	1
BAROMETRIC PRESSURE = MB	1011	AMBIENT TEMP = DEG C * 10	158
DEW POINT TEMP = DEG C * 10 .	-6	TOTAL PRECIP = CM * 10	0
SOLAR RADIATION = W/CM**2 *10	668	ALGORITHM OUTPUT (1)	0
ALGORITHM OUTPUT (2).....	0	ALGORITHM OUTPUT (3).....	0
ALGORITHM OUTPUT (4)	0	ALARM	0
NO CONTRAST	0	SENSOR ERROR CODE	0
A/D OVERFLOW	0	UNDEFINED	0
UNDEFINED	0	UNDEFINED	0
UNDEFINED	0	UNDEFINED	0

FIGURE 14. SAMPLE SUBFILE HEADERS

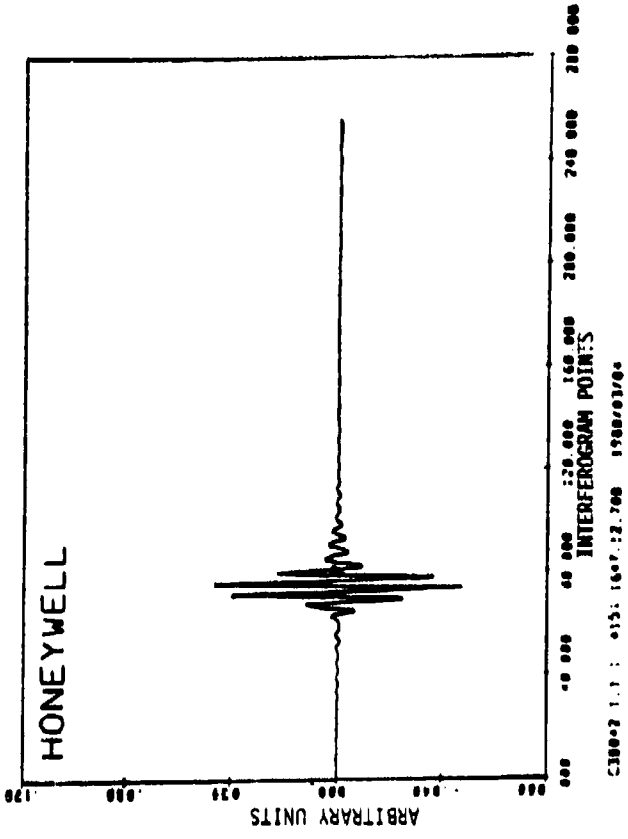

FIGURE 15. TYPICAL INTERFEROGRAM

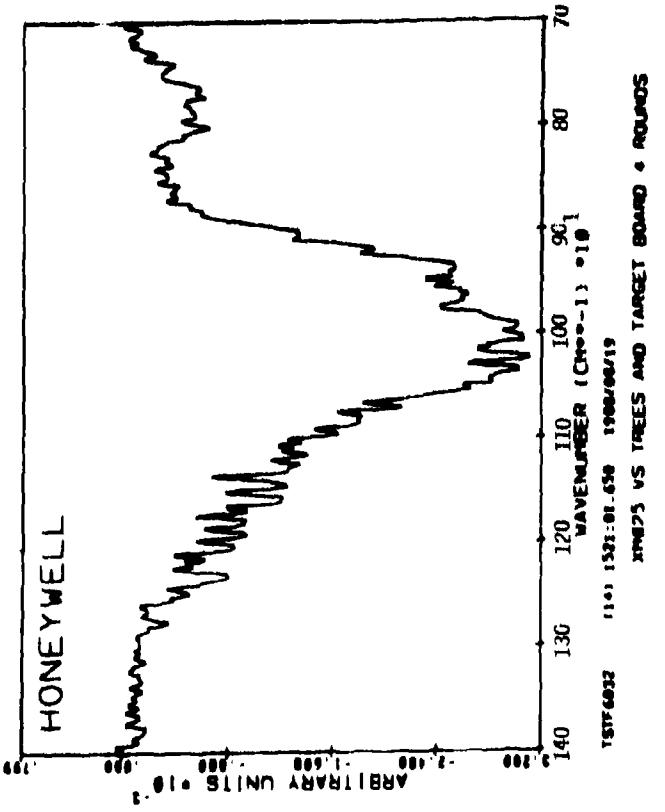

FIGURE 16. WHITE PHOSPHORUS (absorption)

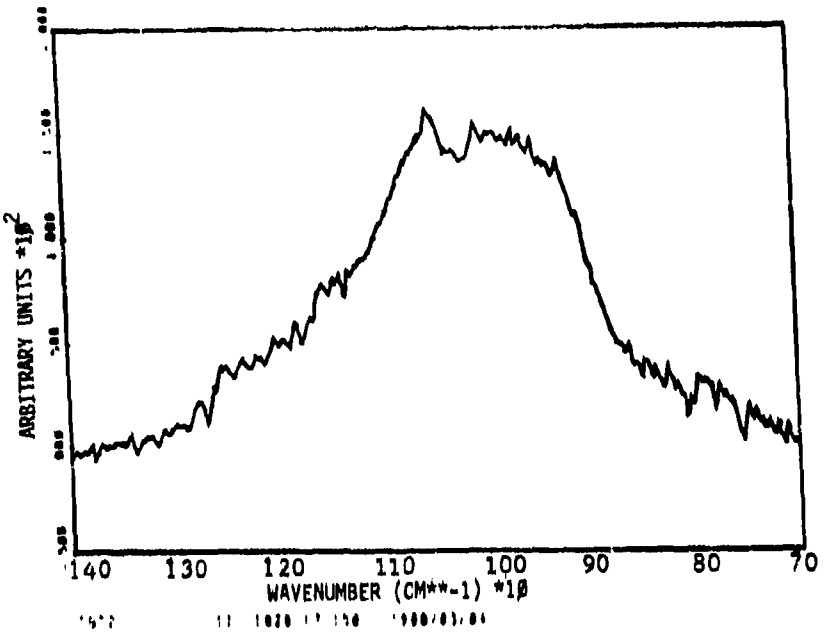

FIGURE 17. PHOSPHORUS VS. OVERCAST SKY (emission)

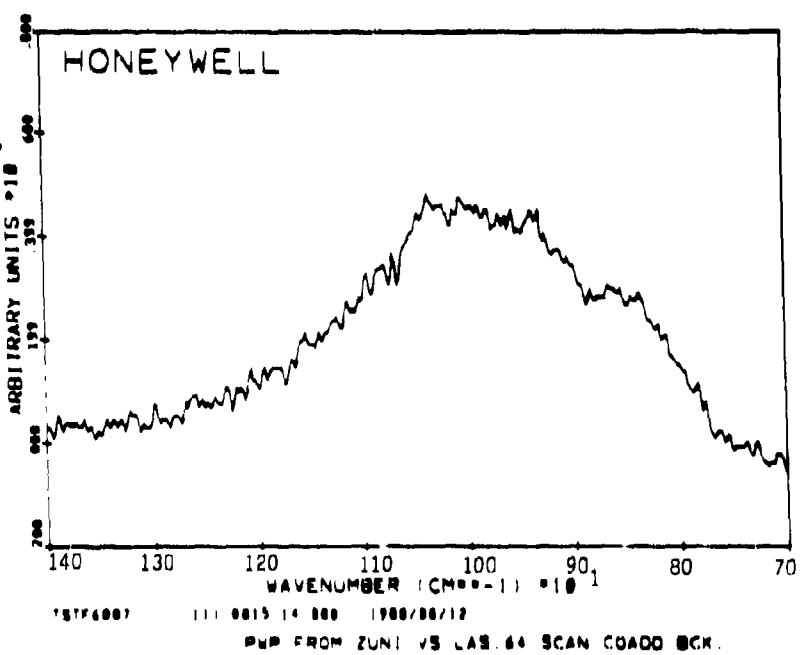

FIGURE 18. WHITE PHOSPHORUS VS. TERRAIN (emission)

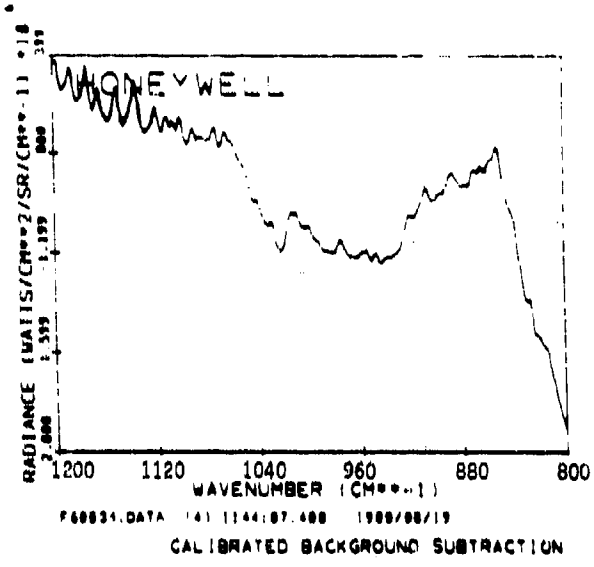

FIGURE 19. ALKALI CHLORIDE VS. TERRAIN

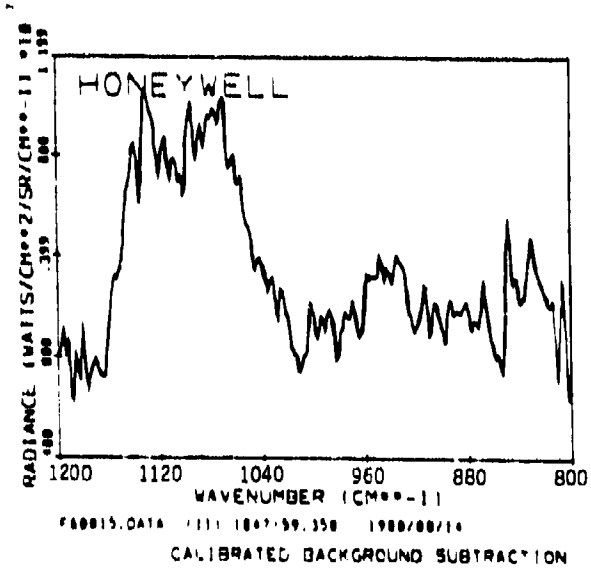

FIGURE 20. PEG 200 VS. TERRAIN

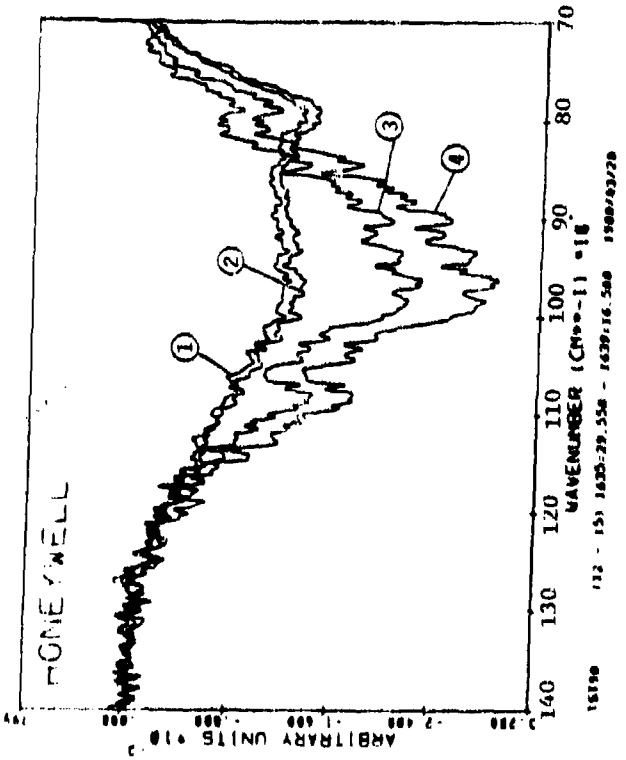

DUST VS. TERRAIN SERIES

FIGURE 21. INCREASING CONCENTRATIONS OF DUST IN THE FOV.

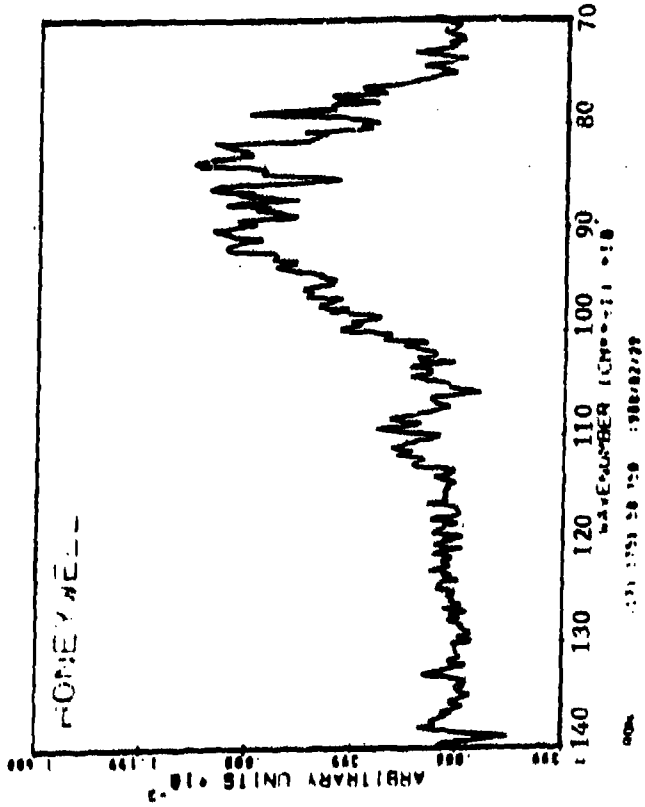

HC SMOKE vs. TERRAIN

FIGURE 22. HEXACHLOROETHANE SMOKE VS. TERRAIN

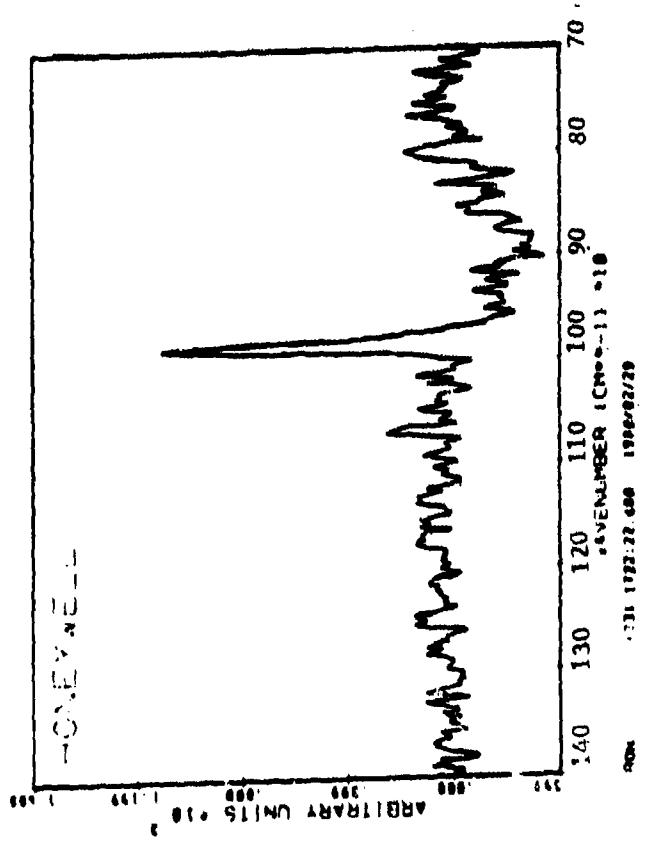

RED SMOKE VS. TERRAIN

FIGURE 23. RED SIGNAL SMOKE VS. TERRAIN

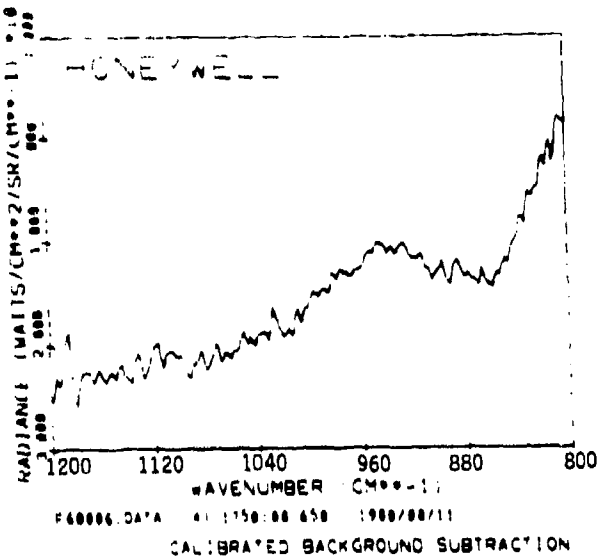

FIGURE 24. INFRARED SCREENING AGENT #1.

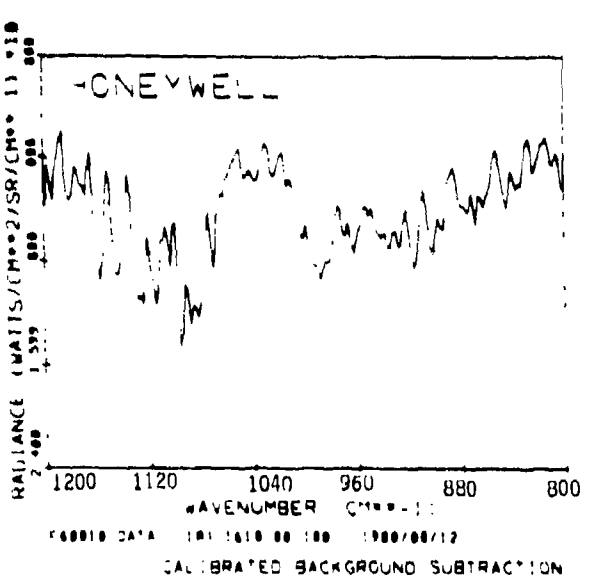

FIGURE 25. INFRARED SCREENING AGENT #3.

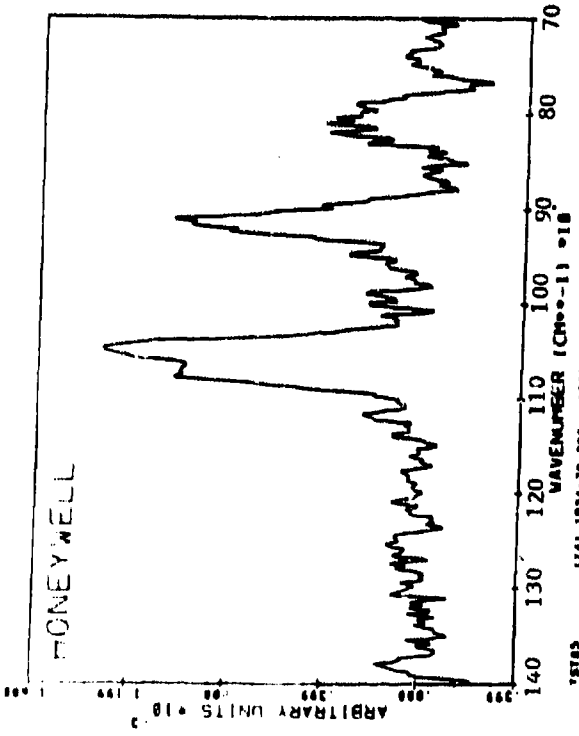

FIGURE 26. TYPICAL SPECTRA OF DMMP (dimethyl methyl phosphonate) VS. TERRAIN

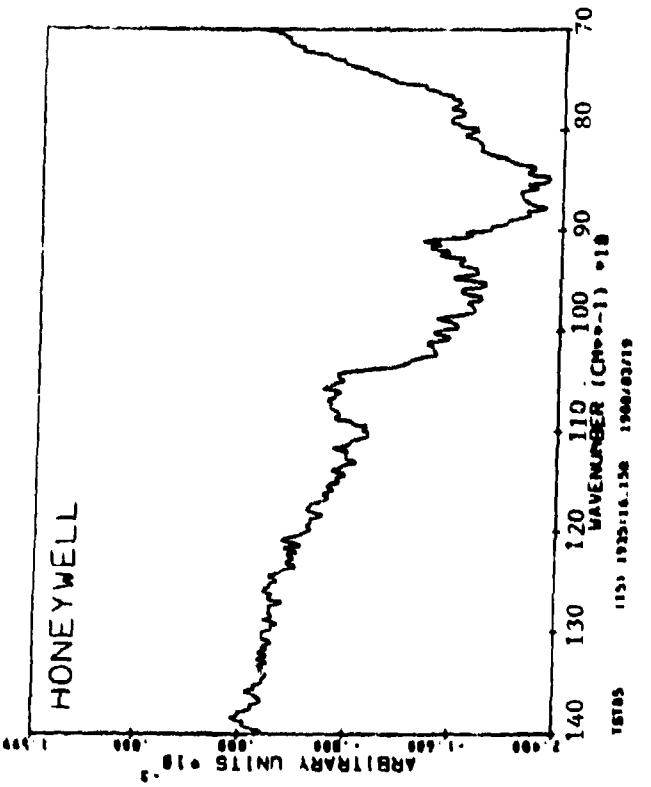

FIGURE 27. WHITE PHOSPHORUS AND DAMP VS. TERRAIN

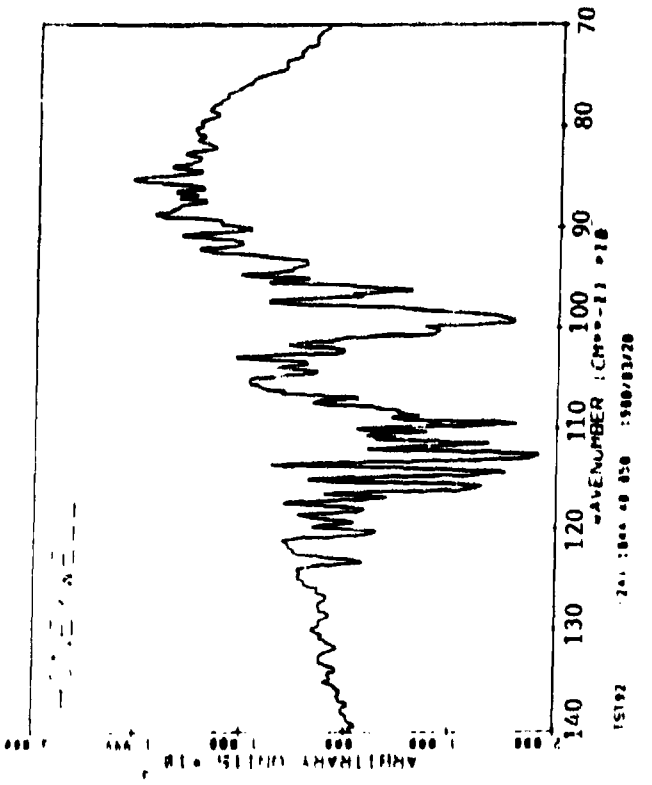

FIGURE 28. HC AND DAMP VS. TERRAIN

LIDAR EVALUATION OF SMOKE AND DUST CLOUDS*

Edward E. Uthe
Atmospheric Science Center, SRI International
Menlo Park, California 94025

ABSTRACT

Lidar provides the means to evaluate quantitatively the spatial and temporal variability of smoke and dust clouds as they are transported downwind from particulate sources. Quantitative evaluation of cloud optical and physical densities from cloud backscatter is complicated by effects from particle size, shape and composition and by attenuation and multiple scattering from dense clouds. Examples are presented that illustrate use of the lidar technique to provide useful evaluations of smoke and dust clouds.

*This paper is scheduled to appear in the 1 May 1981 issue of Applied Optics and therefore is not reprinted here.

PROPAGATION OF A HIGH POWER PULSED CO_2 LASER BEAM THROUGH BATTLEFIELD AEROSOLS*

Thomas G. Miller
Directed Energy Directorate
US Army Missile Laboratory
US Army Missile Command
Redstone Arsenal, AL 35898

ABSTRACT

1. INTRODUCTION

The propagation of a high power laser beam (either cw or pulsed) through the atmosphere is dependent on many factors. These factors include the laser phase distribution, laser amplitude distribution, laser wavelength, atmospheric turbulence, molecular absorption, molecular scattering, aerosol absorption, and aerosol scattering. If the power at the laser is sufficiently low such that no substantial heating of the atmosphere results, the power density at the target is proportional to the laser power and one is in the linear regime. However, if substantial heating of atmosphere occurs due to absorption of the laser energy by the atmosphere, an increase in the laser power beyond a certain critical value can actually result in a decrease in the power density at the target and one is in the nonlinear regime. This particular nonlinear effect is called thermal blooming. This research effort is concerned with such nonlinear effects. The purpose of these experiments was to assess experimentally, using a high power ($\sim 10^6$ joules/cm^2/s at the transmitter) pulsed CO_2 laser beam with a relatively large output aperture, the effects of transmission through an atmosphere contaminated with battlefield aerosols. Past experiments and associated theoretical treatments usually have been concerned with solid particles or water droplets, including clouds[1-18]. The present experiments were designed as semi-field experiments, i.e., the atmospheric parameters were partially controlled, to help ascertain the interaction between a high power pulsed CO_2 laser beam and a battlefield-contaminated atmosphere.

* These tests were conducted at Test Area 3, Redstone Arsenal. In addition to personnel from the Directed Energy Directorate, MICOM, personnel from T&E Directorate, MICOM, and White Sands Missile Range assisted in carrying out the tests. Personnel from Teledyne Brown assisted in data analysis. A document describing the tests in more detail is being prepared and will be published in the future.

2. EXPERIMENTAL PROCEDURE

2.1 Figure 1 shows the basic experimental strategy. A high power single pulse CO_2 laser (S^3 laser*) was directed downrange via a turning flat. The output distribution of the S^3 laser was a 10cm by 10cm beam with a 7.58cm X 7.58cm hole in its center. Its output energy was typically 200 joules for these experiments. The pulse width was typically 4μsec with a gain switch spike that was typically 4 times the average intensity of the main pulse. The gain switch spike was about 250ns wide.

2.2 The flat that turned the S^3 pulse downrange had a square hole in its center that was made to coincide with the hole in the S^3 beam as shown in Figure 1. A cw laser beam (Model 41 laser**) was directed downrange through the hole in the mirror. The two beams were colinear. As shown, the beams passed through artifically created aerosols and were incident either on a calorimeter to record the energy from the S^3 laser or on a diffuse reflector (target board) which recorded the image of the 41 laser via an IR scanning camera***. The Model 41 typically was operated at 200 watts.

2.3 It was possible to record the percent transmission of the pulsed laser by measuring the energy at the laser and the energy at the target site. It also was possible to detect changes of the index of refraction in the laser path caused by the pulsed laser by recording the cw laser's image before and after the laser pulse. Detection of punch through could be detected by either or both techniques.

2.4 Figure 2 shows an overall sketch of the experimental layout. It was decided that an enclosed path for the laser beams should be used so that the atmospheric variables could be monitored and controlled to a certain extent. Two MET Stations were located along the tunnel and were manned by the Atmospheric Sciences Laboratory. They measured

---

* The S^3 laser was manufactured by Systems, Science, and Software, San Francisco Division, P. O. Box 4803, Hayward, CA 94504

** Model 41 Laser was manufactured by Spectro-Physics, 1250 West Middlefield Road, Mountain View, CA 94042

*** IR Scanning Camera, Model APL-18, a pulsed laser data acquisition system, was manufactured by EG&G, Albuquerque Division, Government Services and Systems Operation, EG&G Incorporated, 9733 Coors NW, Albuquerque, NM 87114

absorption coefficients directly using spectrophones and measured particle size distributions, number densities, temperature and other parameters necessary for characterizing the aerosols. The door from the Beam Transmitter Room faced a small hill; for convenience a ditch was dug which served as a partially enclosed path for the laser beams. The top and ends of the ditch were covered with polyethylene, which provided an enclosed propagation path. Holes were cut in the ends which allowed the laser beams to pass. As can be seen from Figure 1, it was 135 meters from the Beam Transmitter Room to the target site. The distance from the Beam Transmitter Room to the entrance of the tunnel was 30 meters. The length of the tunnel was 100 meters; hence, it was 5 meters from the tunnel exit to the target recording site.

2.5 Figure 3 shows the experimental arrangement in the Beam Transmitter Room. As can be seen, in addition to the Model 41 and S^3, a low power cw laser (Model 42 laser*) was used as a monitor laser to continuously measure the extinction coefficient at 10.6 microns as a function of time. As will be mentioned later, this served as the primary source of information for determining when to fire the S^3 laser.

2.6 Figure 4 shows the experimental arrangement at the target site. The power meter measured the power collected from the Model 42 laser as a function of time. The beam from the Model 42 was split with a beam splitter at the Beam Transmitter Room; hence, by monitoring the power from the Model 42 at both the Beam Transmitter Room and the target site, any fluctuations in power of the Model 42 could be noted. The Model 42 was typically operated with a total output power of 20 watts, with 10 watts directed downrange with a telescope to the indicated detector. To view the image of the cw (Model 41) laser, its beam was allowed to impinge on a diffuse reflector and the resulting image was recorded by an IR-scanning camera. The highest camera speed was 500 frames/s, although for these experiments, the framing rate was usually 250 frames/s.

2.7 T&E Directorate, MICOM, also monitored C_n^2 and visible wavelength transmission during the tests using the indicated sources.

---

* Model 42 Laser was manufactured by Spectro-Physics, 1250 West Middlefield Road, Mountain View, CA 94042

2.8 Figure 5 shows a photograph of the enclosed Transmission Tunnel taken from the entrance end of the tunnel.

2.9 Figure 6 shows a photograph of the Beam Transmission Room. In the left foreground, one can see the Model 41 laser on the table along with the expansion telescope, which expanded and focussed the beam from the Model 41. The output beam from the Model 41 was approximately 5cm in diameter and was gaussian in shape. On the right of the picture one can see the exit window from the S^3. Also shown on the right is the output mirror with the hole where the two beams from the S^3 and Model 41 are combined and directed downrange. At the upper left one can see the monitor laser (42) which was used to continuously monitor the extinction coefficient in the Transmission Tunnel.

2.10 Figure 7 shows a block diagram of the laser firing sequence. The IR transmission was determined with no smoke present, using the Model 42. A background run also was made on the IR scanning camera. Smoke was released and, following the firing sequence as indicated in Figure 7, data were accumulated as a function of absorption coefficient.

3. RESULTS AND CONCLUSIONS

3.1 Figure 8 shows the diffraction pattern of the S^3 laser at (a) the laser, (b) the entrance to the tunnel, and (c) the target site, without smoke in the tunnel. As can be seen from the diffraction pattern at the entrance to the tunnel, the hole almost has filled, so that a moderately homogeneous beam existed at this point for the S^3 laser beam. As can be seen from the diffraction pattern at the target, the S^3 laser has an almost textbook far field diffraction pattern, thus indicating very good beam quality.

3.2 Figure 9 shows a plot of E/E_o vs. absorption coefficient for the pulsed laser, where E_o is the output energy of the S^3 laser and E is the energy in the pulse as recorded at the target site. The ratio E/E_o is a measure of the transmission through the aerosols. The solid curve is a theoretical plot of $E/E_o = e^{-\alpha z}$ where z is the path length, a constant. Clearly any indication of punch through will result in experimental measurements with points falling above this theoretical curve. As can be

seen, the measured points do fall above the theoretical curve, indicating some punch through or path clearing for white phosphorus. Within the experimental uncertainty of the measurements, there is complete clearing of the path for extinction coefficients of about 2.5 km^{-1} or less. The deviation from the theoretical curve becomes less at higher values of the extinction coefficient. This is as one would expect, since an increasing amount of energy is required to clear the path.

3.3 The dashed curve shows a theoretical fit to the data using analytical expressions[18] of Lee, Miller, and Jones developed for propagation of laser beams through a fog. They make the assumptions: (1) the laser beam is collimated, (2) absorption and extinction cross sections are linear functions of the droplet radius, and (3) volumetric conduction from the droplet can be neglected. One would expect the fit to be improved by adjustment of the analytic expression to account for focussed beams and to take into account the composition of the droplet* and not to assume they are composed of water. These improvements currently are being made.

3.4 If punch through does exist, one would expect to see an increase in the intensity of the Model 41 cw laser just after the S^1 pulsed laser. This in fact was observed. Figure 10 shows computer plots of frames from the IR Scanning Camera just before the pulsed laser and for 29 ms after the pulsed laser. These data were taken when the extinction coefficient was 24 km^{-1}. As can be seen, immediately after the S^1 pulse, several peaks occur in the recorded distribution which appear to die away as a function of time as one would expect as the punched holes fill due to thermal diffusion.

* Current estimates are that the droplets are phosphoric acid plus attached water molecules, depending on relative humidity.

UNCLASSIFIED

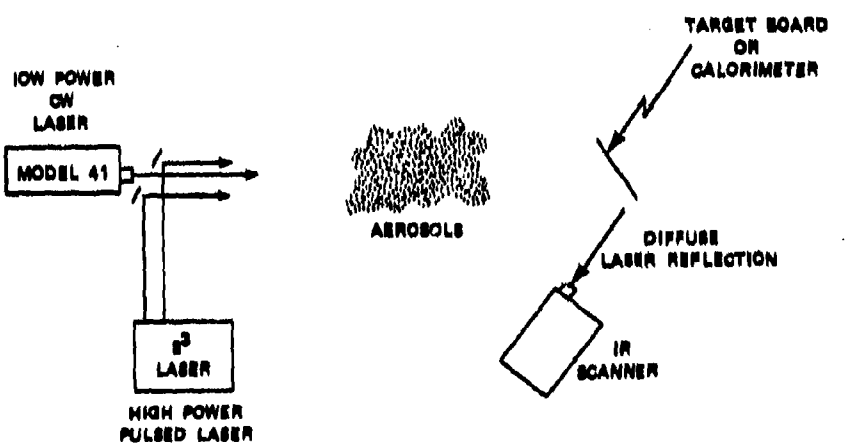

FIGURE 1. AEROSOL PROPAGATION EXPERIMENT.

UNCLASSIFIED

UNCLASSIFIED

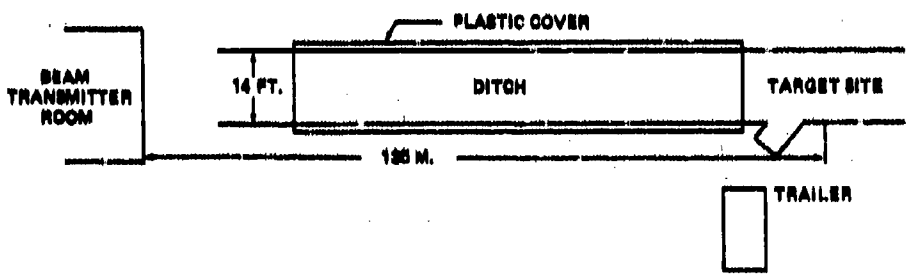

FIGURE 2. OVERALL SKETCH OF EXPERIMENTAL LAYOUT.

UNCLASSIFIED

UNCLASSIFIED

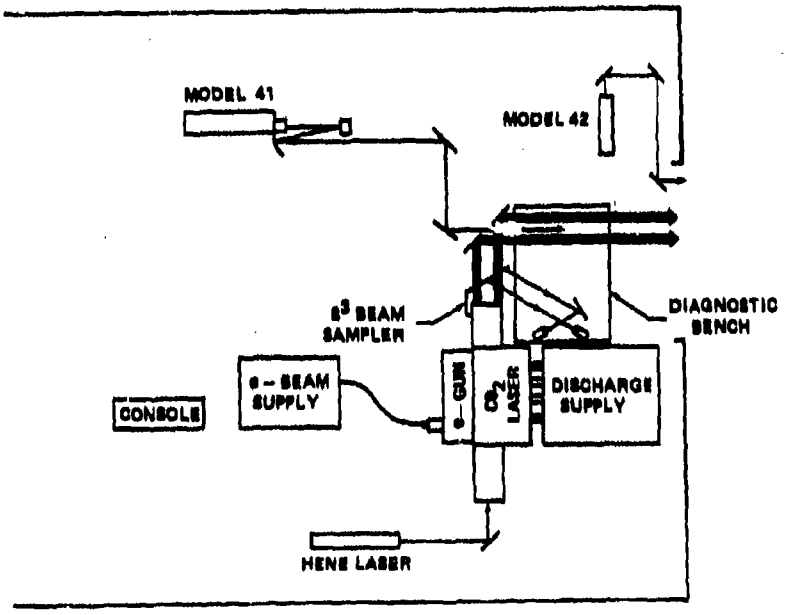

FIGURE 3. EXPERIMENTAL ARRANGEMENT AT THE BEAM TRANSMITTER ROOM.

UNCLASSIFIED

UNCLASSIFIED

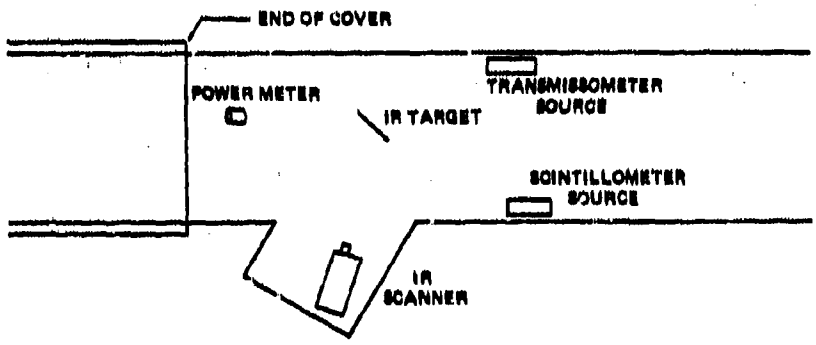

FIGURE 4. EXPERIMENTAL ARRANGEMENT AT THE TARGET SITE.

UNCLASSIFIED

FIGURE 5. VIEW OF ENCLOSED TRANSMISSION TUNNEL.

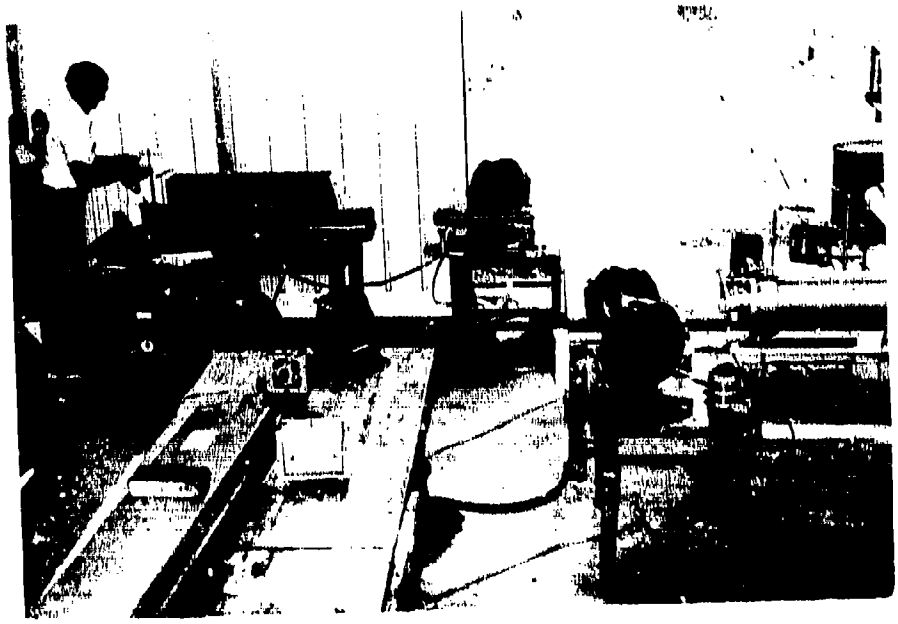

FIGURE 6. VIEW OF LASER TRANSMISSION ROOM SHOWING OPTICS LAYOUT.

UNCLASSIFIED

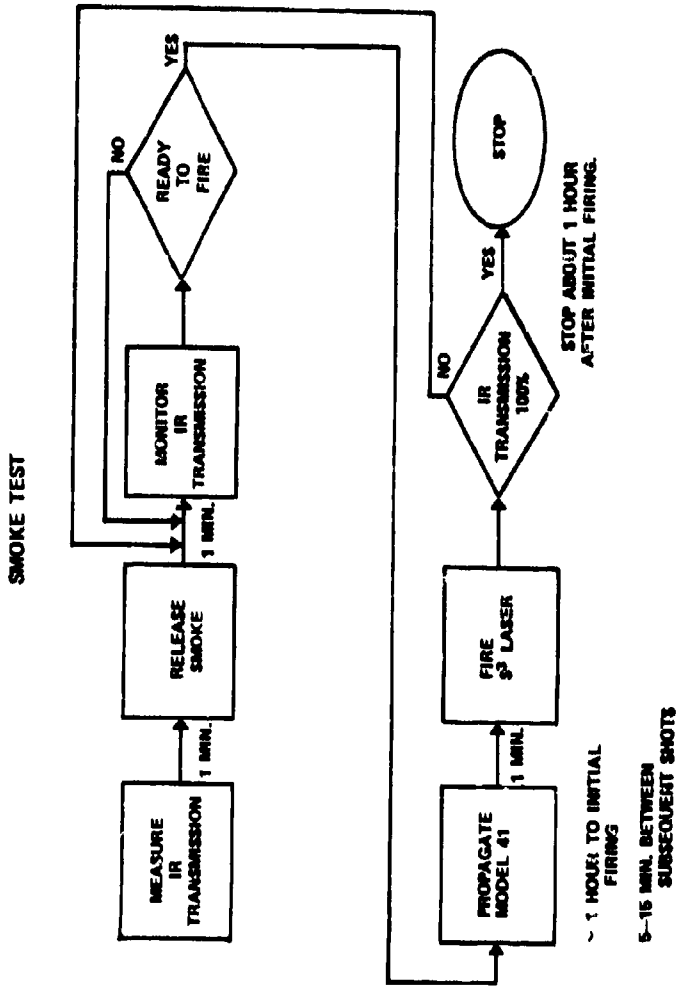

FIGURE 7. BLOCK DIAGRAM SHOWING LASER FIRING SEQUENCE.

UNCLASSIFIED

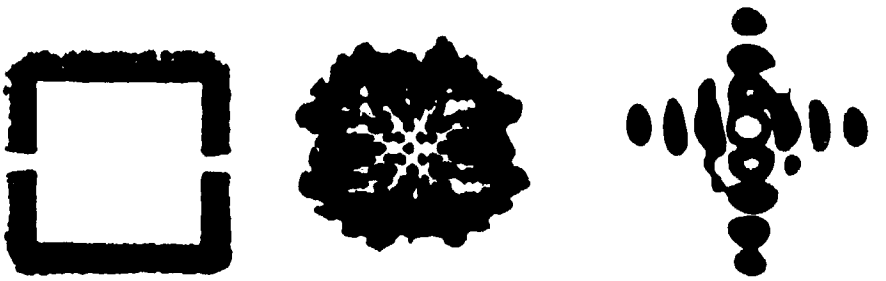

FIGURE 8. DIFFRACTION PATTERN OF PULSED LASER AT
(a) LASER, (b) ENTRANCE TO SMOKE TUNNEL, AND (c) AT TARGET SITE.

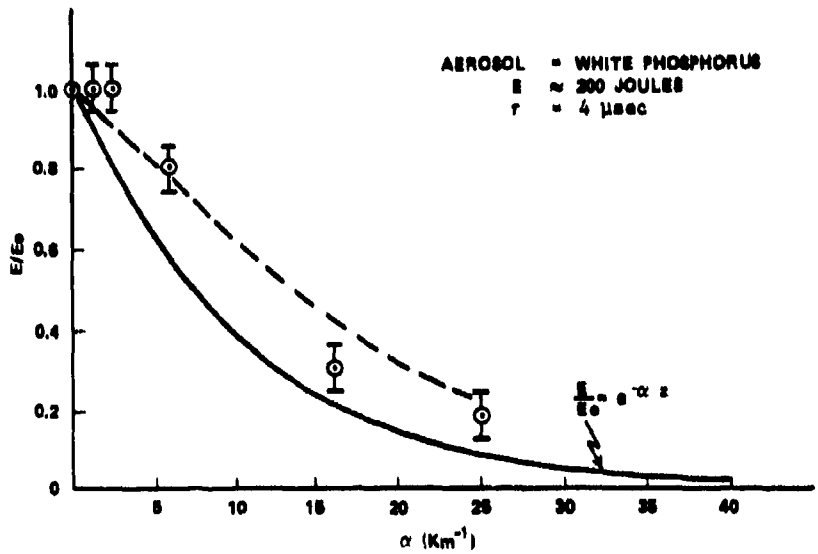

FIGURE 9. GRAPH SHOWING MEASUREMENT OF PERCENT TRANSMISSION OF THE PULSED LASER AS A FUNCTION OF EXTINCTION COEFFICIENT.

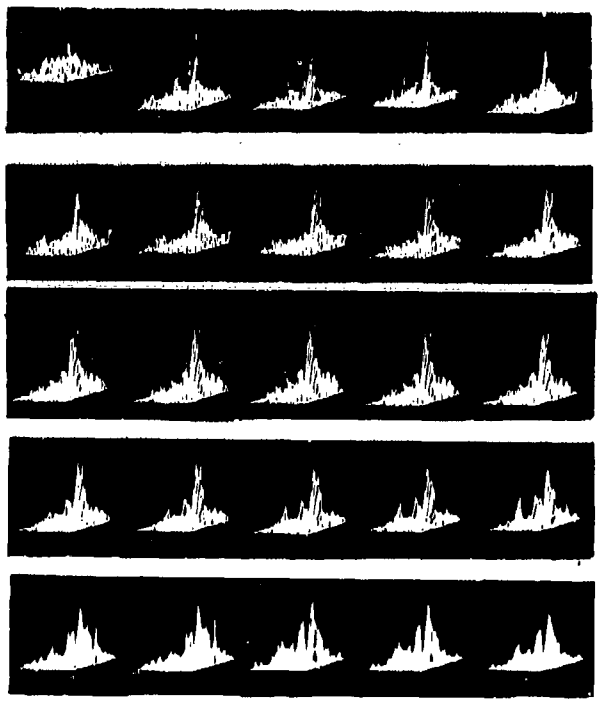

FIGURE 16. COMPUTER PLOTS OF FRAMES OF IR SCANNING CAMERA SHOWING IMAGE FROM LOW POWER CW LASER JUST BEFORE PULSED LASER AND 24 FRAMES AFTER PULSED LASER. THE TIME SPAN AFTER THE PULSED LASER EXTENDS FROM 0.17 msec TO 29 msec.

REFERENCES

1. Smith, D. C. and R. T. Brown, "Aerosol-Induced Air Breakdown with CO_2 Laser Radiation," Journal of Applied Physics, Vol. 46, No. 3, March 1975, pp. 1146-1153.

2. Lencioni, D. E., "The Limitations Imposed by Atmospheric Breakdown on the Propagation of High Power Laser Beams," AGARD Conference Proceedings, No. 183, Optical Propagation in the Atmosphere, 33-1 May 1976.

3. Lowder, J. E. and H. Kleiman, "Long-Range Breakdown with 10.6μm Laser Radiation," Journal of Applied Physics, Vol. 44, No. 12, December 1973, pp. 5504-5505.

4. Lencioni, D. E., "The Effect of Dust on 10.6μm Laser-Induced Air Breakdown," Applied Physics Letter 23, 1973; also D. E. Lencioni, et al, MIT Lincoln Lab Project Report LTP-20, 25 April 1973.

5. Lencioni, D. E. and J. E. Lowder, "Aerosol Clearing with a 10.6μm Precursor Pulse," IEEE Journal of Quantum Electronics, Vol QE-10, No. 2, February 1974.

6. Reilly, J. P., P. Singh, and S. Glickler, "Laser Interaction Phenomenology for Water Aerosols at CO_2 Laser Wavelengths," AIAA Paper No. 77-659, AIAA 10th Fluid and Plasma Dynamics Conference, Albuquerque, NM, June 1977.

7. Schlier, R. E., A. N. Pirri, and D. J. Reilly, "Air Breakdown Studies," AFWL-TR-72-74, AVCO Everett Research Lab, Everett, MA, Feb 1973.

8. Reilly, J. P., P. Singh, and G. Weyl, "Multiple Pulse Laser Propagation Through Atmospheric Dusts at 10.6 Microns," AIAA Paper No. 77-697, AIAA 10th Fluid and Plasma Dynamics Conference, Albuquerque, NM, June 1977.

9. Singh, P. I. and C. J. Knight, "Impulse Laser Induced Shattering of Water Drops," AIAA Paper No. 78-1218, AIAA 11th Fluid and Plasma Dynamics Conference, Seattle, WA, 10-12 July 1978.

10. Hull, R. J., D. E. Lencioni, and L. C. Marquet, "Influence of Particles on Laser Induced Air Breakdown," Laser Interaction and Related Plasma Phenomena, Ed. by H. J. Schwarz and H. Hora, Plenum Press, 1972, pp. 147-152.

11. Antric, M., J. P. Caressa, Ph. Bournot, L. Dufresne, and M. Sarazin, "Experimental Study on the Propagation of Pulsed Laser Energy Through the Atmosphere," AIAA Paper No. 80-1379, AIAA 13th Fluid and Plasma Dynamics Conference, 14-16 July 1980, Snowmass, CO.

12. Manlief, S. K., and A. P. Ferdinand, "Fog Blooming Measuremerts," Optics Research, MIT Lincoln Lab, Lexington, MA, 7 November 1975.

13. Glicker, S. L., "Propagation of a 10.6μ Laser Through a Cloud Including Drop Vaporization," Applied Optics, Vol. 10, No. 3, March 1971.

14. Sutton, G. W., "Fog Dispersal By High Power Lasers," AIAA Journal, v. 8, p. 1907 (1970).

15. Smith, D. C., "Gas-Breakdown Dependence on Beam Size and Pulse Duration With 10.6 Micron Radiation," Applied Physics Letters 19, 405 (1971).

16. Lowder, J. E., H. Kleiman, and R. W. O'Neill, "High Energy CO_2 Laser Pulse Transmission Through Fog," Journal of Applied Physics, Vol. 45, No. 1, Jan 1974, pp. 221-223.

17. Bedair, S. M. and S. S. Aly, "Fog Dissipation Using 10.6u Radiation," Vol. 15, Sep 1975, pp. 235-237.

18. Lee, C. T., T. G. Miller, and R. W. Jones, "Fog Dispersal by CO_2 Laser Pulses: An Exact Solution Including Pre-Vaporization Heating," to be published.

EVAPORATIVE CLEARING FOR A CO_2 HIGH ENERGY LASER BEAM IN WHITE PHOSPHORUS SMOKE

C. W. Bruce
Y. P. Yee
S. J. Duran
US Army Atmospheric Sciences Laboratory
White Sands Missile Range, New Mexico 88002

ABSTRACT

This paper describes a set of aerosol measurements to determine the effect of a countermeasure smoke, white phosphorus (WP), on a pulsed high-energy laser (HEL) beam. An analysis of the aerosol (gaseous and particulate airborne material) was used as the basis for calculations of evaporative clearing and application was made to a given specific test situation. Linear propagation properties forming the basis for the 10.6μm pulsed laser nonlinear effects are obtained relatively directly by using spectrophone absorption and extinction, a light scattering particle spectrometer and nephelometers (particle density as a function of radius and mass loading), and dew-point hygrometer (partial pressure of water vapor). General conclusions are that, for the smoke produced by burning WP, a CO_2 pulsed HEL beam can clear the optical path quite rapidly and efficiently. The absorption after clearing is caused by the residual vapors and is much lower.

1. INTRODUCTION

In this paper aerosol characterization measurements are analyzed for prediction of countermeasure aerosol effects on a high-energy laser (HEL) beam. Although the general principles are applicable for various beam parameters, our calculations will be oriented toward those of a pulsed CO_2 laser (10.6μm wavelength) with a pulse length of about 3μs and a total beam energy of about 200 J. The focus of this effort will be the effect due to evaporative clearing. The basis for thermal blooming (atmospheric lensing due to thermally created density gradients in the beam) (Gebhardt, 1976), the other major nonlinear effect, will be established by describing heating of the ambient gases and particles. Threshold calculations show that the 3μs pulse of these tests is short for strong blooming effects.

These measurements were performed in conjunction with a test of an HEL having the parameters described above. The beam traversed a trench approximately 100 m long. The trench was covered with polyethylene forming a relatively closed environment in which the smoke was dispersed and then measured as a function of settling time. Most of the characterization was performed at the midportions of the trench and assumed to approximate a spatial average since the smoke mixing, diffusing, and settling times were long at 1 to 2 h.

2. MEASUREMENT SYSTEMS

Table I lists the instrumentation used for the characterization.

TABLE I. WP CHARACTERIZATION INSTRUMENTATION

Measurement	System	Manufacturer
Extinction absorption, coefficients at 10.6μm	CO_2 laser spectrophone	ASL
Particle counting and sizing	Active cavity, light scattering single particle spectrometer, HeNe	Particle Measurement systems (Model ASASP-X)
White light volume scattering coefficients calibrated to measure absorption for the smoke of phosphorus	Nephelometer	Meteorological Research Instruments (Model 2050B)
Relative humidity and partial pressure of water vapor	Dew-point hygrometer, thermometer	Edgerton-Germehausen and Grier (Model 880)

Of the absorbing gaseous constituents at 10.6μm, water vapor was expected to be by far the strongest. The very high temperatures and dew points produced in the trench by the greenhouse effects resulted in relatively high partial pressures and thus high gaseous absorption coefficients. The Edgerton-Germehausen and Grier (EG&G) condensation plate dew-point hygrometer was used to obtain the water vapor partial pressures from which the water vapor absorption coefficients were computed. Although site-peculiar gases are possible contributors, contributions to the net 10.6μm absorption coefficient due to other ambient gases can be reasonably estimated. Relative humidity values obtained from the dew point and temperature data were also used to compute fractional water content of the very hygroscopic smoke of burning phosphorus. This computation, in turn, was used to determine the appropriate complex refractive index and other physical properties of the smoke.

The distribution of particles with respect to size is important since the calculations of the nonlinear effects are also generally size dependent. The instrument used (ASASP-X) had been subjected to laboratory tests, first with particles of known sizes to determine accuracy in sizing and then with the

294

smoke of phosphorus to determine response to high densities. Calibrations with respect to absolute density for each increment of particle radius are difficult to perform with accuracy and have not been accomplished for this instrument. As stated then, the form of the particle size distribution was the object of this measurement. The absolute magnitude of the absorption was obtained by using another technique--the spectrophone.

The authors' application of spectrophones to atmospheric gases and particulates is documented in the literature (Bruce and Pinnick, 1977; Bruce et al 1980) and in another paper of these proceedings (Bruce, Yee, and Duran 1981). In a more recent publication (Bruce and Yee, 1980), the authors discuss their spectrophone research on the smoke of WP. The particular system used for these measurements was designed for field use and is tunable and stabilized for several 10μm laser lines. Figure 1 shows a schematic cross section of this system.

3. AMBIENT ABSORPTION

The ambient gas and particulate absorption coefficients were measured before the tests. The particulate absorption was obtained indirectly by using particle counting results. Lorenz-Mie calculations were based on these data and complex refractive indices for soil-based (clay) dust. Though not really precise, this technique usually is accurate within a factor of three. The ambient level of particulate absorption (coefficient) was found to be approximately 10^{-3} km^{-1}. The total (gaseous and particulate) absorption coefficient as measured by the spectrophone was, as expected, much higher. Conditions within the trench were relatively repeatable from day to day. Typical parameters for calculations and calculated values are shown on table II.

TABLE II. CALCULATED RANGE OF GASEOUS ABSORPTION COEFFICIENTS, α, IN TRENCH (PRE-SMOKE TEST VALUES)

Date/ Time	Dew point Temperature (°C)	Partial Pressure H_2O (torr)	α_{H_2O} (km^{-1})	α_{CO_2} @330 ppm (km^{-1})	α Total (minus trace gases) (km^{-1})
28-29 Jul 4-5 pm	80	26.2	0.66	0.08	0.74
30 Jul 5 pm	89.0	35.0	1.11	0.08	1.19
3 Aug 11 am	88.8	34.8	1.09	0.08	1.17

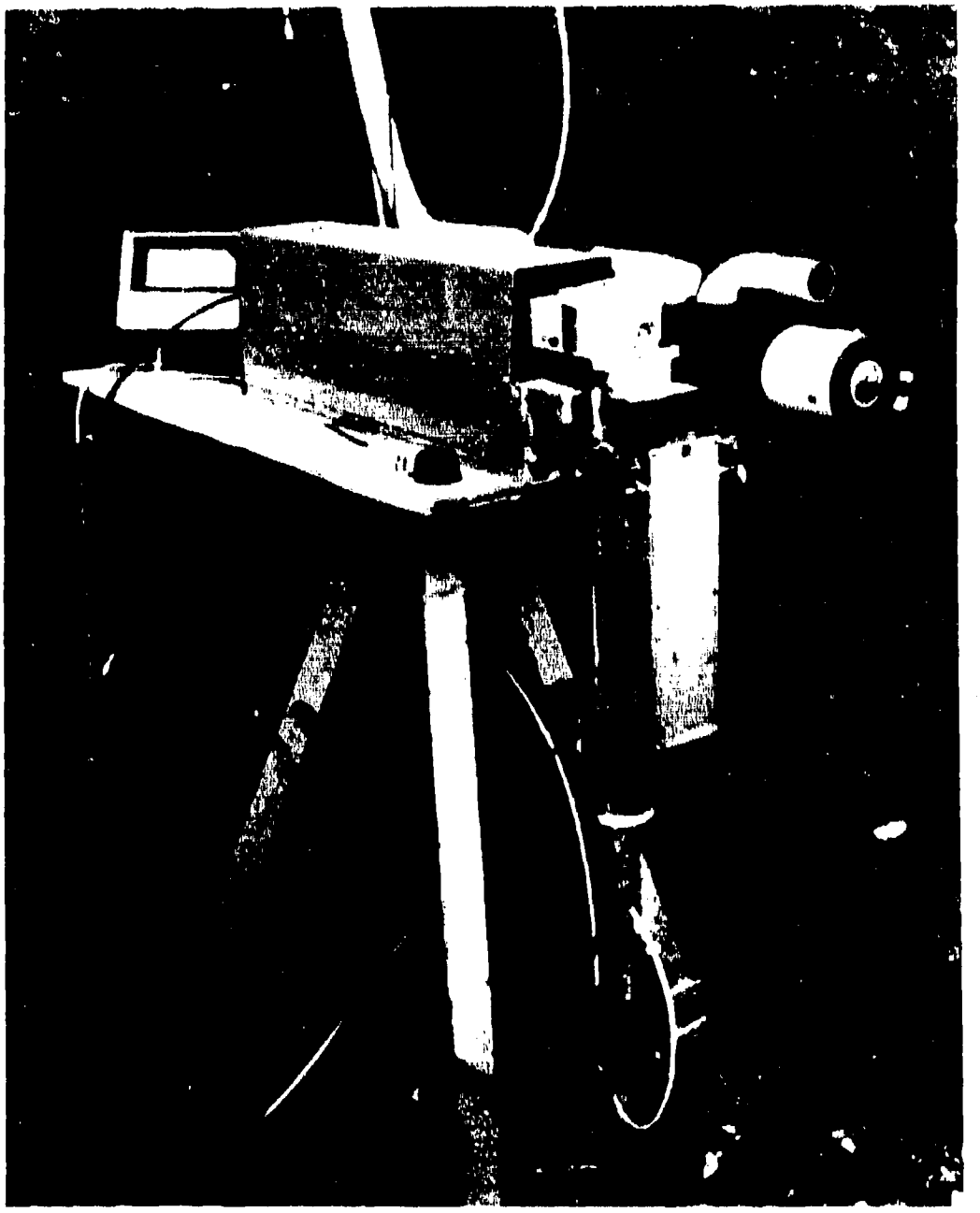

FIGURE 1. PHOTOGRAPH OF SPECTROPHONE AND NEPHELOMETER IN USE AT MIDDL.

The partial water pressure was based on extrapolations from the data of Yin et al (1968), and the results were based on data of Shumate et al (1976), about 11 percent lower for these partial pressures. One tunnel section (within 4 m of the measurement systems) was removed for the 28-29 August, 4 to 5 pm times. The section cover was reinstalled before the aerosol tests, and the data here for 30 July and 3 August are for completely covered trenches.

The measured gaseous absorption coefficient corresponding to the first example (data of 28-29 July 1980) was 1.1 km^{-1}. Probable error figures on this measurement are not precise but are estimated to be 0.2, largely because of temporal variations due to unknown source(s). Higher than predicted values of the absorption coefficient frequently occur in ASL field measurements of ambient absorption at 10μm wavelengths.

Absorption due to trace constituents could elevate the value considerably. A rough rule of thumb is that trace gas absorption (within an absorption band region) often reaches or exceeds 1 $(ppm\text{-}km)^{-1}$ and, of course, 1 ppm is not a high concentration.

4. AEROSOL CHARACTERIZATION FOR TESTS

Aerosol characterization for two test situations will be discussed. The dates and approximate starting times are listed as the latter two examples in table II (information for 30 July 1980 and 3 August 1980). The most notable difference in the conduct of these two tests is the time of day. Aerosol characteristics were similar, in the mean.

The procedure was to ignite phosphorous smoke grenades in the trench at about the one-quarter and three-quarter length positions. The smoke dispersed roughly over a 2-h period during which aerosol measurements were made. The data and analyses will be presented as functions of the evolving aerosol system and implications for nonlinear effects will be discussed.

Particle size distribution evolved generally as expected from prior laboratory measurements on the same aerosol; that is, the mean densities decreased and the peak moved to progressively smaller sizes.

Figure 2 represents a plot of the differential absorption based on the particle size distribution. The absorption peak occurs at a radius of about 1.2μm soon after the smoke is dispersed and

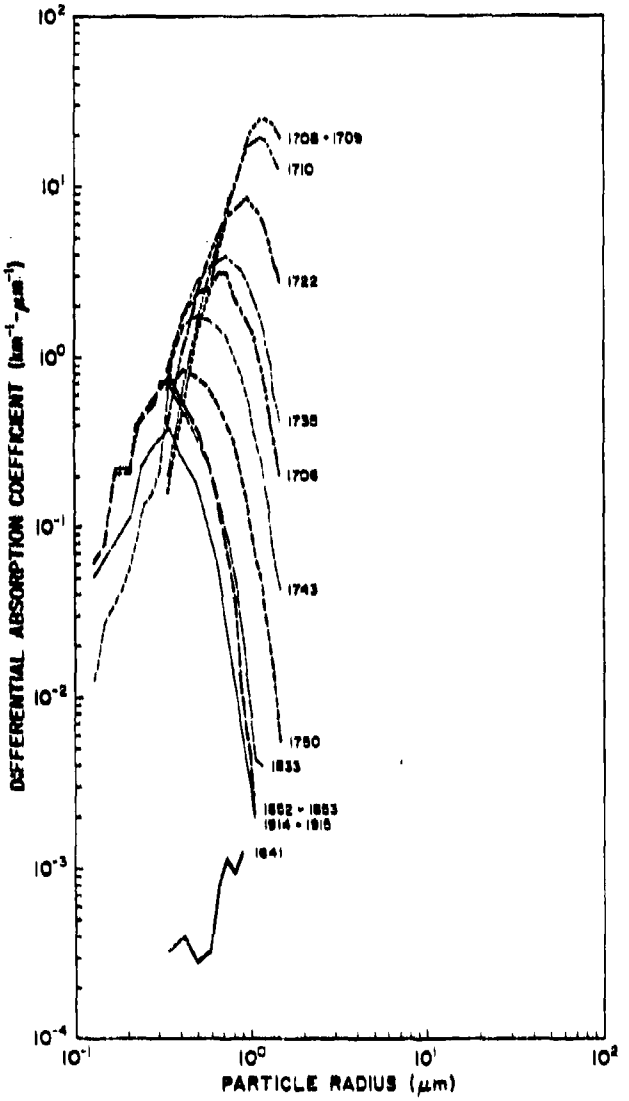

FIGURE 2. DIFFERENTIAL ABSORPTION COEFFICIENTS FOR THE FIRST TEST CALCULATED ON THE BASIS OF PARTICLE COUNTING AND SIZING DATA.

decreases relatively smoothly to about 0.4μm in roughly 2 h; in the same time the peak absorption level has dropped roughly two orders of magnitude. At the midpoint in this 2-h evolution, 80 percent of the absorption occurs within a radius span of approximately 0.30μm.

The background particulate absorption (~ 10^{-3} km^{-1}) is represented by the lowest curve labelud 1641, that is, before the smoke was released.

The total absorption coefficients as calculated from the particle size and density information are plotted as a function of time in figure 3. For this presentation, 1-min averages obtained at approximately 10-min intervals are connected by straight-line segments. These values are much lower than those of the spectrophone measurements. The spectrophone yielded absorption and extinction coefficient peak values (in separate measurements) of about 200 and 220 km^{-1}, while the particle counter result was much lower. This difference is believed to be due primarily to low counting efficiencies and sampling errors in unknown proportions. As the purpose of sizing and counting for these tests was to obtain measurements of the form of the size distribution as a function of time rather than absolute values, this difference is not a problem. Prior calibration of the counter using monodisperse aerosols precludes sizing as a prime source of error. Likewise, the optical constants and calculational scheme introduce uncertainties that are very small compared with the difference.

The largest size particles are most important in the calculation of the total absorption because of the rapid increase with particle radius of the Lorenz-Mie efficiency factor for the absorption cross section. Therefore, the apparent increase with time in the densities of the relatively small particles (whose signals are probably masked in the counter by those from the larger particles) is not of concern here. A designed-in characteristic of the counter is also partly at fault in this misrepresentation which causes a "tailing-off" effect in the signals representing progressively smaller sizes.

Calculations to follow are based on the peak absorption values which agree well with the author's previous predictions based on laboratory measurements (Bruce and Yee, 1980) (within 15 percent).

The measurement of extinction coefficient derived from power loss in the spectrophone is satisfactory at high values (early in the test) but is not useful below 10 km^{-1} due to the question of power meter drift. Figure 4 shows the extinction coefficient for the test of figure 3. The slope of the decreasing extinction coefficient with time, however, agrees well with that found by using the PMS particle counter data. An electronic problem, presumed to be overheating of system electronics prevents complete comparison of spectrophone absorption data for this test.

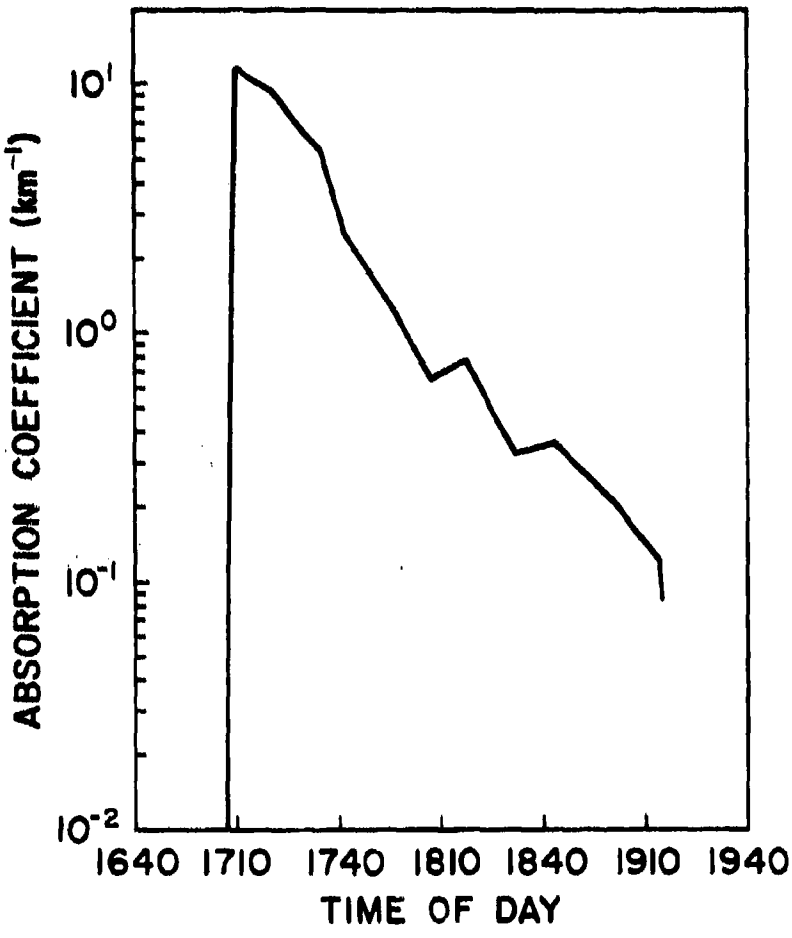

FIGURE 3. CALCULATED ABSORPTION COEFFICIENTS AT 10.6μm λ FOR SMOKE OF PHOSPHORUS DURING FIRST TEST.

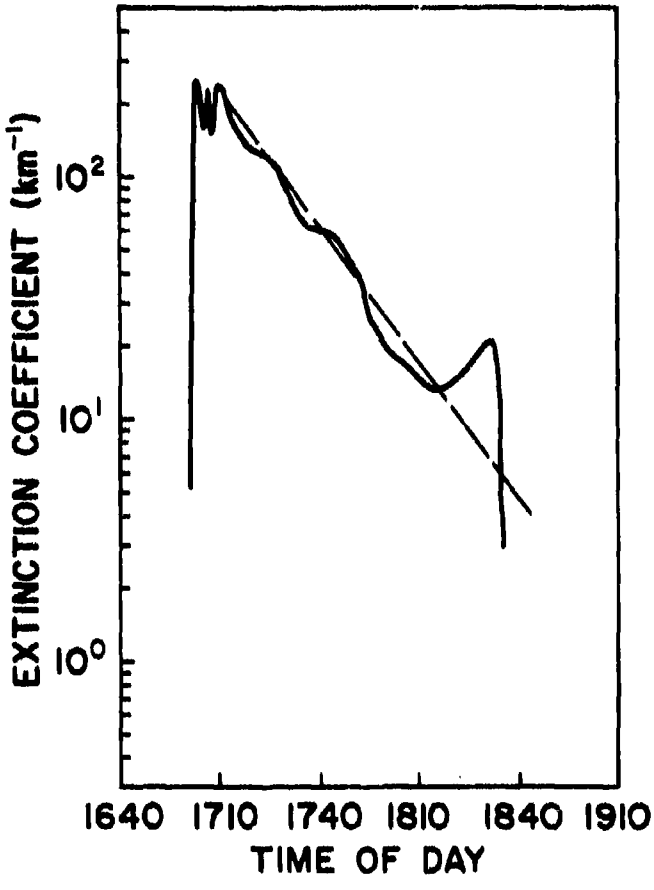

FIGURE 4. MEASURED EXTINCTION COEFFICIENT AS A FUNCTION OF TIME DURING THE FIRST TEST.

Time variations culled from the extinction, the density distribution, and the absorption measurements at the location of the apparatus were greater than a factor of five for integration times less than 3 s and about a factor 2 to 3 for integration times of 10 s. However, a spatial density average over as much as 10 percent or greater volume of the trench probably varies less than 20 percent.

Temperatures in the trench were somewhat lower than the temperatures in the first test even though the second tests were during midday (the 30 July test was later in the afternoon). Particle size distributions and their evolution in time were similar in form though the corrosive action of the smoke caused a reduction in particle counter laser power for this test. The spectrophone measured peak absorption and extinction values were virtually the same at 200 km^{-1}. Absorption coefficient as a function of time for this test is shown in figure 5. For a resolution time of about 2 s, the magnitude fluctuates by more than an order of magnitude. The same data, when averaged over about a minute for each of the sampling periods, yield a much more steady decrease. This decrease has nearly the same mean slope as that calculated from the particle counter data though the magnitudes are very different.

The reduction of the relative humidity resulting from the introduction of the smoke into the tunnel was calculated and a partial pressure change of less than 0.1 torr was obtained. This change is negligible for effects of interest here.

5. EFFECT OF EVAPORATIVE CLEARING ON HIGH POWER BEAMS

The tendency to punch-through the absorbing countermeasure aerosol WP is of prime interest here, and parameters from the two similar tests will be used as a basis. The thermodynamic and optical bases for the calculations will be applied by using laser beam parameters relevant to a system whose beam parameters are to be described (US Army Missile Command [MICOM] S^3 system). Glickler (1971) and Sutton (1978) used elaborate (but still inexact) integral solutions to describe clearing by fog.

6. CALCULATIONS, PART I: EVAPORATION OF SINGLE PARTICLES

Particles are first heated to boiling T, assuming spatially uniform heating of the particle, and then energy is added to evaporate them, that is

$$E_B = \left(\frac{4\pi}{3}\right) \frac{\rho_m R_p R_B^2 c}{Q_a(R_p)} \Delta T .$$

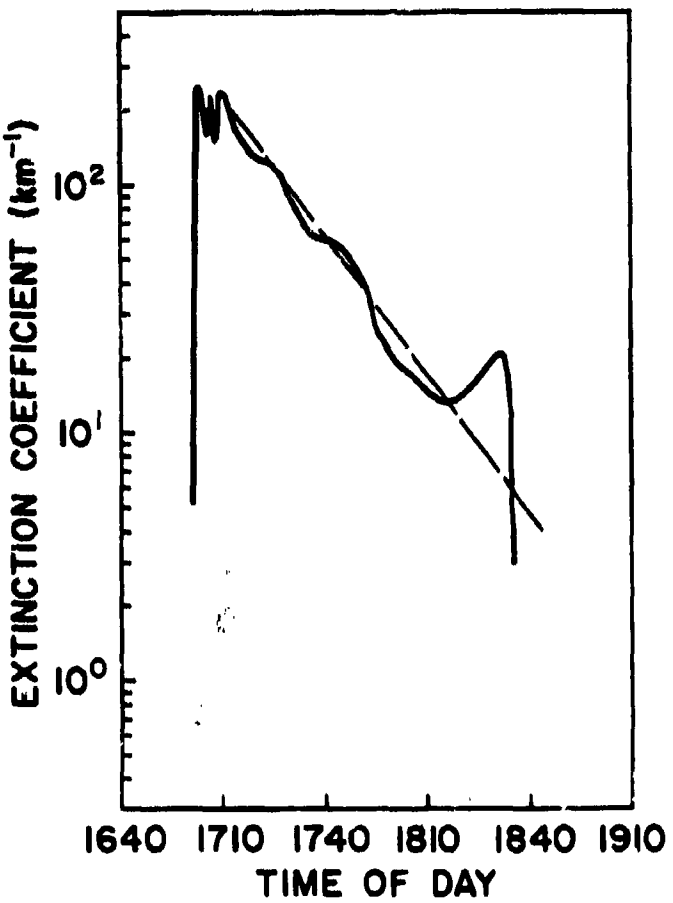

FIGURE 4. MEASURED EXTINCTION COEFFICIENT AS A FUNCTION OF TIME DURING THE FIRST TEST.

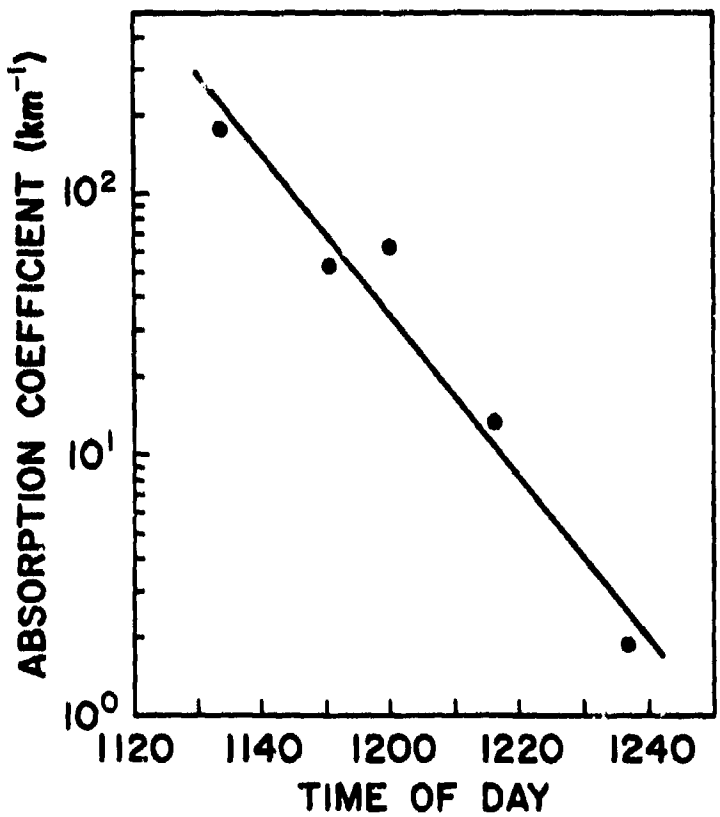

FIGURE 5. SPECTROPHONE MEASUREMENTS OF ABSORPTION COEFFICIENT AS A FUNCTION OF TIME FOR THE SECOND TEST.

and

$$E_{LHV} = \left(\frac{4\Pi}{3}\right) \frac{\rho_m R_p R_B^2}{Q_a\left(R_p\right)} H .$$

where

ρ_m = the bulk density of the phosphorous smoke

c = the specific heat of the bulk smoke material

R_p, R_B = the radii of particles and beam

Q_a = the Lorenz-Mie efficiency for the smoke particles

H = the latent heat of vaporization of the bulk smoke material

The sum of these two processes represents the total beam energy which has passed the plane of a particle of radius R_p at the time of evaporation, that is,

$$E_{cum}(R_p) = E_B(R_p) + E_{LHV}(R_p)$$

An examination of the S^3 laser pulse intensity profiles led to the suggestion that the pulse be modeled as triangular in time.*

Here it is assumed that the particle is vaporized and vaporous at time t'. The first simplifying assumption is justified since clearing is effective when particle diameters are reduced in boiling by considerably less than an order of magnitude (see figure 2). The second assumption follows from kinetic calculations showing that dispersal velocities are sufficient to form an effective vapor state within an interval very short compared with the pulse duration.

Figure 6 shows the problem schematically.

Then,

$$t' = t_{pulse} - \sqrt{t_{pulse}^2 - 2\left(\frac{E_{cum}}{P_{max}}\right)\left(t_{pulse}\right)} .$$

*Bill Jones, MICOM, private communication

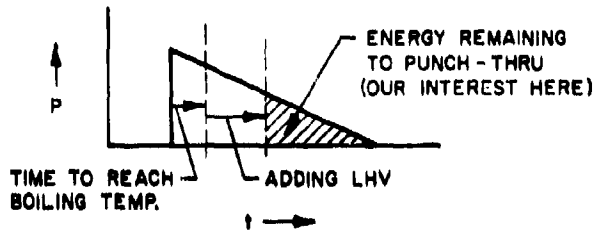

FIGURE 6. LASER PULSE: EXPENDITURE OF ENERGY.

Now the energy (or power) density distribution in the beam must be determined. The job is simplified since the laser output is a line-square, that is, two pairs of parallel slits in orthogonal directions. The approach is to estimate the distribution of energy in the far field pattern or that in the area under the twin slit intensity profile.

$$I \sim \frac{\sin^2\beta}{\beta^2} \times (\cos^2 u) ,$$

We use the far field burn pattern and the double-slit part of the calculation to find the critical dimension, that is, $\beta = 4.535 \times 10^3$.

The distribution of energy in the lobes is given in table III.

TABLE III. DISTRIBUTION OF ENERGY IN FAR FIELD BEAM LOBES FOR S^3 LASER

Lobe* Number	Percent E per Lobe	Percent E per Lobe / Lobe Area (cm^{-2})	Energy Density per Lobe for E_{total} = 200 J (J/cm^2)
0	18.7	7.19	14.4
1	8.5	4.47	8.94
2	6.3	3.32	6.64
3	3.7	1.95	3.90
4	1.5	0.79	1.58
5	0.3	0.16	0.32

*Increasing away from center

The time for individual particles to evaporate and the fractional energy remaining to be transmitted after clearing will be calculated. The clearing effect as a function of the total smoke absorption will then be obtained.

The clearing process effectively reduces the absorption to gaseous levels which are much lower, that is, to near normal atmospheric levels. The scattering is, of course, also greatly reduced; however, for the smoke of WP, the fraction of CO_2 laser beam energy scattered to that absorbed is less than 10 percent. The atmospheric propagation is therefore related to the punch-through effect in a form illustrated in figure 7.

Tables IV and V show rapid and effective clearing as a function of smoke particle size for a relative humidity of 35 percent. Earlier data show that very few particles are larger than $R_p \approx 4\mu m$ and that the clearing efficiency is almost independent of size to that point because of the increase in Lorenz-Mie efficiency with radius (up to $R_p = 4\mu m$) in spite of the growing mass to be evaporated. Coincidentally, this convenient independence disappears for the larger particles. The last column represents the single particle efficiency of punch-through or, in other words, the percentage of energy available after evaporation. The transmission is not unity at that point (as was mentioned) but reverts nearly to the pretest levels.

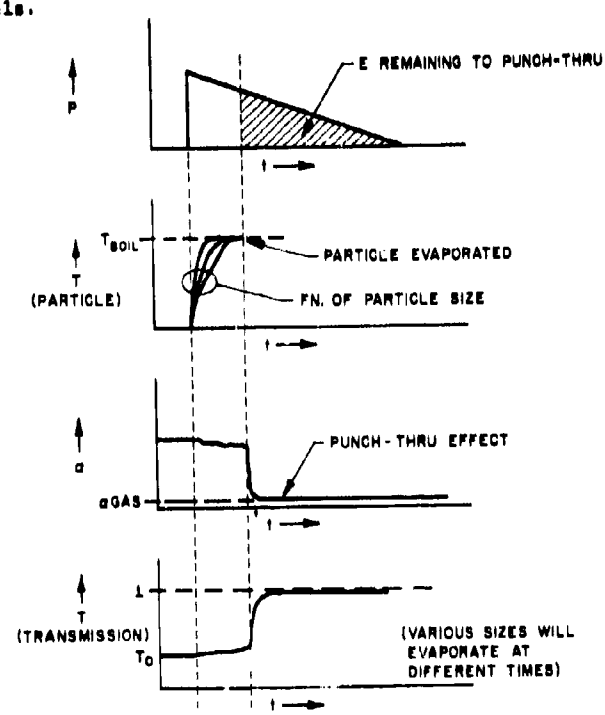

FIGURE 7. ILLUSTRATION OF RELATIONSHIP BETWEEN LASER PULSE AND PROPAGATION PARAMETERS

TABLE IV. PARAMETERS OF SINGLE PARTICLE CLEARING AS FUNCTIONS OF PARTICLE SIZE AND BEAM LOBE NUMBER FOR E_{TOTAL} = 200 J AND T_{PULSE} = 3.2μs

Center Lobe (0)

Energy = 40.0 J

R_p (μm)	Q_a	Time to Evaporate (μm)	Fraction of Energy in Remaining Portion of Pulse
0.01	0.00202	1.68×10^{-1}	0.90
0.05	0.0101	1.68×10^{-1}	0.90
0.10	0.0203	1.67×10^{-1}	0.90
0.15	0.0305	1.67×10^{-1}	0.90
0.20	0.0511	1.32×10^{-1}	0.92
0.40	0.0828	1.64×10^{-1}	0.90
0.60	0.127	1.60×10^{-1}	0.90
1.0	0.222	1.52×10^{-1}	0.91
2.0	0.490	1.38×10^{-1}	0.92
4.0	0.904	1.50×10^{-1}	0.91
8.0	1.217	2.25×10^{-1}	0.87
10.0	1.265	2.72×10^{-1}	0.84
15.0	1.2600	4.20×10^{-1}	0.76
20.0	1.2123	6.00×10^{-1}	0.66

7. CALCULATIONS, PART II: COLLECTIVE EFFECT

From these results one can calculate the net clearing effect on the beam. This phenomenon will be illustrated in the following calculations. For this purpose the particle size corresponding to the peak absorption for selected settling times will be used.

The expenditure of energy as a function of aerosol loading can be calculated from

$$E(L) \simeq e^{-uL} \int_0^{t'} P(t)dt + \int_{t'}^{t_{pulse}} P(t)dt ,$$

TABLE V. PARAMETERS OF CLEARING FOR SPECIFIC CONDITIONS (SECOND TEST) AND USING PARTICLE RADII OF PEAK ABSORPTION

Time: 1159

Run Number 7716

t_{max} = 3.0μs

E_{total} = 144.9 J

R_p = 1.0μm

Q_α = 0.2217

Beam Lobe Number (from center)	P_{max} (W)	Time to Boil and Evaporate (μs)	Fraction of Energy in Remaining Portion of Pulse
0	1.81×10^7	2.12×10^{-1}	0.86
1	8.21×10^6	3.50×10^{-1}	0.78
2	6.09×10^6	4.83×10^{-1}	0.70
3	3.57×10^6	8.90×10^{-1}	0.49
4	1.45×10^6	>3.0	0.0
5	2.90×10^5	>3.0	0.0

where t' is the time to evaporate and t_{pulse} is the total pulse duration. Here t' will have been increased over that of the single particle function as a result of the mass loading. For particles of given size and composition, t' is an inverse function of P_{max}. (L) represents the path length within the aerosol medium. The time to evaporate at a given position along the trench is now dependent on that position although the above equation is written as though it depends only on the end point. This simplification does not significantly alter the results here. For the calculations to follow, open air dispersal of WP was assumed; therefore, the peak absorption is for particles of 1μm to 1.2μm radius (see early-time data of figure 2). The relative improvement in the energy transmitted when punch-through occurs is shown in table VI. The improvement in energy transmitted is truly significant (compare columns 4 and 8)--even though the pulsed laser on which the calculated parameters were based on a relatively small one. The smoke of phosphorus clears significantly for a fairly broad range of aerosol absorption coefficients (or alternatively a range of aerosol mass loading values). For relatively low absorption coefficients, clearing can, of course, do little to enhance the total energy transmitted. The enhancement due to clearing determined by the above presentation extends to absorption coefficients of several tens per kilometer (typical field values) for even the relatively low energy system of these

tests. Clearing continues to be significant for this (and other volatile) aerosols to, ro[illegible] loading at which beam energy is consumed in the evaporation process. Screening of available energy for particles farther from the source causes a significant increase in t' at about 25 km^{-1} though the increase depends somewhat on factors such as particle size and relative humidity.

Generally, thermal blooming and evaporative clearing effects are interactive; that is, the power density is affected by the thermal blooming which in turn affects the evaporative clearing. Thermal blooming depends on beam parameters (power density, pulse length, and pulse shape) and atmospheric parameters (gaseous and particulate absorption, crosswinds, and turbulence). Blooming effects on the test beam have been calculated not to be strong for the given beam parameters; therefore, for this analysis, these effects have been ignored.

8. CONCLUSIONS

Aerosol characterization performed on the smoke of WP was used to calculate punch-through or evaporative clearing on a pulsed CO_2 laser beam. This effect can be significant for HEL use. High energy pulsed CO_2 laser beams can effectively penetrate phosphorus (red phosphorus and WP) countermeasure smoke, though the degree of efficiency depends on beam and aerosol parameters. This effectiveness is related to the volatility and absorbing qualities of the smoke particles. Repetitive and/or long pulses can encounter strong thermal blooming which counteracts the clearing effect due to the high level of aerosol absorption. This report discusses the development of an analytical model and its application to aerosol parameters that derive from measurements in an extended enclosure at the MICOM in Huntsville, AL, and then to aerosol parameters that are more typical of atmospheric dispersion of the smoke (represented primarily by relatively large diameter particles). The laser beam parameters in both cases are relevant to the MICOM high energy research laser. The aerosol absorption measurement systems employed in situ aerosol spectrophones developed at ASL. Thermal blooming is calculated to be minimal for the beam parameters of the MICOM (S^3) laser as used in these tests and therefore is not expected to significantly affect the calculations of the clearing phenomenon.

TABLE VI. PARAMETERS SHOWING EFFICIENCY OF PUNCH-THROUGH FOR E_{TOTAL} = 40 J FOR CENTER LOBE

(1) α, Aerosol Absorption Coefficient (km^{-1})	(2) $\alpha \times L$ ($L = 10^{-1}$ km)	(3) t' Time to Evaporate Aerosol	(4) On-Target Energy Without Clearing, E/40 for $\alpha \times L$	(5) $\frac{t_{pulse}-t'}{t_{pulse}}$	(6) $\frac{t' \times 40}{t_{pulse}}$ (J)	(7) (5) x 40 (J)	(8) On-Target Energy With Clearing (6) + (7)/40
0.0	0.0	1.52×10^{-7}	1.00	0.953	1.9	38.1	1.00
0.1	0.001	1.54×10^{-7}	0.99	0.952	1.91	38.08	1.00
0.5	0.05	1.60×10^{-7}	0.99	0.950	1.9	38.00	1.00
1.0	0.10	1.68×10^{-7}	0.90	0.948	1.89	37.90	0.99
1.5	0.15	1.78×10^{-7}	0.86	0.944	1.91	37.80	0.99
2.0	0.20	1.87×10^{-7}	0.82	0.942	1.92	37.70	0.99
2.5	0.25	1.97×10^{-7}	0.78	0.938	1.92	37.50	0.98
3.0	0.30	2.08×10^{-7}	0.74	0.933	1.92	37.40	0.98
4.0	0.40	2.30×10^{-7}	0.67	0.930	1.93	37.20	0.98
5.0	0.50	2.56×10^{-7}	0.61	0.920	1.95	36.80	0.97
10.0	1.00	4.34×10^{-7}	0.37	0.864	2.01	34.60	0.92
15.0	1.50	7.56×10^{-7}	0.22	0.764	2.08	30.60	0.82
20.0	2.00	1.41×10^{-6}	0.14	0.559	2.47	22.40	0.62
21.0	2.10	1.63×10^{-6}	0.12	0.491	2.45	19.60	0.55
22.0	2.20	1.92×10^{-6}	0.11	0.400	2.64	16.00	0.47
23.0	2.30	2.34×10^{-6}	0.10	0.269	2.93	10.80	0.34
23.5	2.35	2.70×10^{-6}	0.095	0.156	3.21	6.24	0.24
23.7	2.37	2.97×10^{-6}	0.093	0.072	2.45	2.88	0.16
23.8	2.38	$>3.2 \times 10^{-6}$	0.093	----	----	----	----
24.0	2.40	$>3.2 \times 10^{-6}$	0.091	-----	----	----	----

REFERENCES

Bruce, C. W., and R. G. Pinnick, 1977, "In-situ measurements of aerosol absorption with a resonant CW laser spectrophone," Appl Opt, 16:1762.

Bruce, C. W., Y. P. Yee, B. D. Hinds, R. J. Brewer, J. Minjares, and R. G. Pinnick, 1980, "Initial Field Measurements of Atmospheric Absorption at 9-11μm Wavelengths," J Appl Meteorol,19:1997.

Bruce, C. W., and Y. P. Yee, 1980, "In-situ measurement of the ratio of aerosol absorption to extinction coefficient," Appl Opt, 19:1893.

Gebhardt, F. G., 1976, "High power laser propagation," Appl Opt, 15(6):1479.

Glicker, S. L., 1971, "Propagation of a 10.6μm laser through a cloud including droplet vaporization," Appl Opt, 10:644.

Shumate, M. S., et al, 1976, "Water vapor absorption of carbon dioxide laser radiation," Appl Opt, 15:2480.

Sutton, G. W., 1978, "Fog hole boring with pulsed high energy lasers: An exact solution including scattering and absorption," Appl Opt, 17:3424.

Yin, P. K. L., and R. K. Long, 1968, "Atmospheric absorption at the line center of P(20) CO_2 laser radiation," Appl Opt, 7:1551.

Bruce, C. W., Y. P. Yee, and S. J. Duran, 1981, "Battlefield smoke/dust parameters measured in-situ using spectrophones," symposium paper A-16.

NEAR-IR EXTINCTION, BACKSCATTER, AND DEPOLARIZATION OF SMOKE WEEK III AEROSOLS

Z. G. Sztankay, D. McGuire, J. Griffin, W. Hattery, G. Martin and G. Wetzel
US Army Electronics Research and Development Command
Harry Diamond Laboratories
Adelphi, MD

ABSTRACT

The 0.9 μm extinction coefficient, backscatter coefficient, and depolarization were measured at Smoke Week III in various conventional and experimental smokes. The laser instrumentation was situated near the middle of the main sampling line and provided localized measurements of these parameters as a function of time. The spatial resolution of the measurements was about 1 m.

The backscatter properties of WP, RP, HC, fog oil, various experimental IR screeners, and other aerosols are compared. Some of the IR screeners were found to have very high depolarization, in contrast to negligible depolarization for the conventional aerosols. The backscatter-to-extinction ratios for some of the IR screeners were also found to be significantly higher than for the conventional smokes or the cumulus and stratus clouds measured previously.

1. INTRODUCTION

The Harry Diamond Laboratories (HDL) performed 0.9 μm extinction coefficient, backscatter coefficient, and depolarization measurements at Smoke Week III.[1] The HDL short-range laser backscatter probe (or nephelometer) makes local measurements of these parameters, as a function of time, at its position in the aerosol cloud. The probe was in the instrument cluster area[2] that was near the 32-m tower, where it was planned to have the center of the aerosol cloud drift for each trial. The HDL measurements and data analysis were partially supported by PM Smoke/Obscurants and Naval Weapons Support Center.

Knowledge of the extinction coefficient is, of course, necessary to determine the thickness of an aerosol cloud through which a system can see a target. The backscatter coefficient is important for determining the signal magnitude backscattered into a system such as a fuze or target designator; this signal may cause false target indications.[3,4] The ratio of the extinction to backscatter coefficients is an important parameter that, under most conditions, determines the maximum aerosol backscattered signal for a given system from a particular aerosol type, independent of concentration.[5] One possible method for discriminating between an aerosol backscattered signal and a legitimate target signal is based on polarization effects.[3] The measurement of depolarization effects of aerosols is important to assess the feasibility of such techniques. Both the extinction to backscatter ratio and the depolarization of the aerosols can also provide information about the aerosol particles themselves, such as asphericity. Such information may be important in the development of new types of screening aerosols.

2. DESCRIPTION OF THE EXPERIMENT

The laser-backscatter probe is a short-range lidar system comprising a 0.9 μm GaAs injection laser transmitter and two nearly identical receivers. The transmitter 3-dB pulse width is around 5 ns. The receivers employ narrowband optical filters, avalanche photodiodes, and wideband amplifiers (risetime <2 ns). They are located close to and on either side of the transmitter. The transmitter optics form a narrow pencil beam having a divergence of about 15 mrad; the fields of view of the receivers are

25 mrad.

At Smoke Week III, the transmitted radiation was linearly polarized by means of a sheet polarizer. One receiver had no polarizer while the other had a linear sheet polarizer that was crossed with respect to the transmitter polarizer. The two receivers were symmetrically located and aligned with respect to the transmitter so that they had nearly identical sensitive regions. The alignment of the system at Smoke Week III is illustrated in figure 1; the range-response function for the two receivers, which may be obtained by walking a diffuse target towards the transceiver, is shown in figure 2. Thus the two receivers observed the total and the cross-polarized aerosol backscatter from the same ≈0.8 m 3-dB width region in the aerosol. Actually, the scattering angle of the received radiation was 177.3±1.9 deg, rather than pure backscatter.

A diffusely reflecting target was positioned in the beam 3.2 m from the probe (see figure 1). At this distance, the system sensitivity to aerosol backscatter is very low (see figure 2), but because the target reflectivity was high (≈50 percent), the signal reflected from the target could be readily observed. Furthermore, the system response time was sufficiently fast to separate this signal from the aerosol backscatter signal peaked at 1.5 m.

The system has an internal reference feature which provides pulse-to-pulse monitoring of system variations. The light from the laser is coupled by fiber-optic cables both to the transmitter optics and directly to the detectors. The extra length of the cable to the transmitter optics provides a 10-ns delay between the system monitoring reference pulse and the aerosol return pulse. This delay is sufficient to resolve the two pulses in time so that no overlap occurs. Absolute calibration of the backscattered signal is obtained by measuring the return at the peak of the range-response function (1.5 m) from a standard reflector before and/or after the aerosol measurements.

The received pulses are amplified and input to a Tektronix R7912 Transient Digitizer. In part because it is desired to run at pulse rates higher than the 8 Hz that the digital mode of this instrument allows, the R7912 is used as a scan converter, whereby the video pulse return data are read in TV format. For each frame, the laser is pulsed twice 31 ms apart, the two receiver channels alternately feeding the R7912. An example of a frame as observed on a TV monitor is shown in figure 3. The two traces run from top to bottom instead of left to right because of a modification of the R7912 made at HDL to simplify subsequent digitization. The time axis thus runs downward, while signal deflections from the baseline are to the left. The trace on the right is for the unpolarized receiver; that on the left, for the cross-polarized receiver. Each trace contains three sequential but resolved pulses: the reference signal, the aerosol backscattered return from 1.5 m, and the target return from 3.2 m. Each frame is also provided with a frame code (not seen in figure 3). The data are recorded on video tape and later digitized and entered into a minicomputer for data reduction, display, and processing.

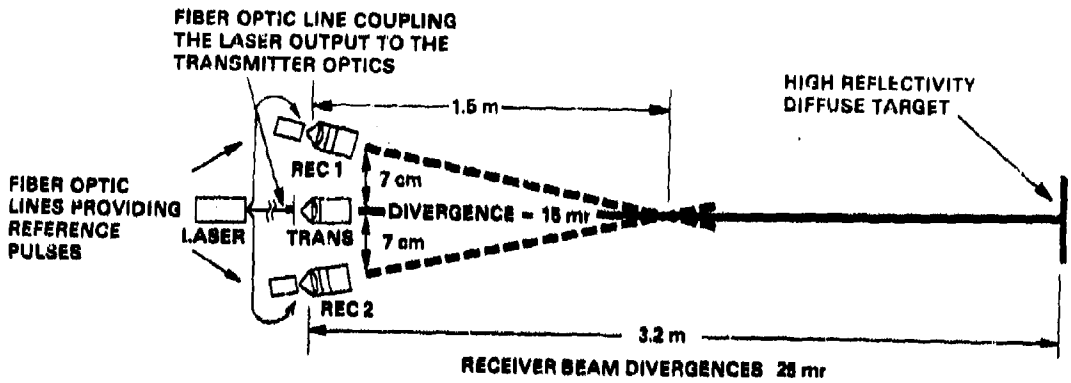

FIGURE 1. LASER BACKSCATTER PROBE CONFIGURATION AT SMOKE WEEK III.

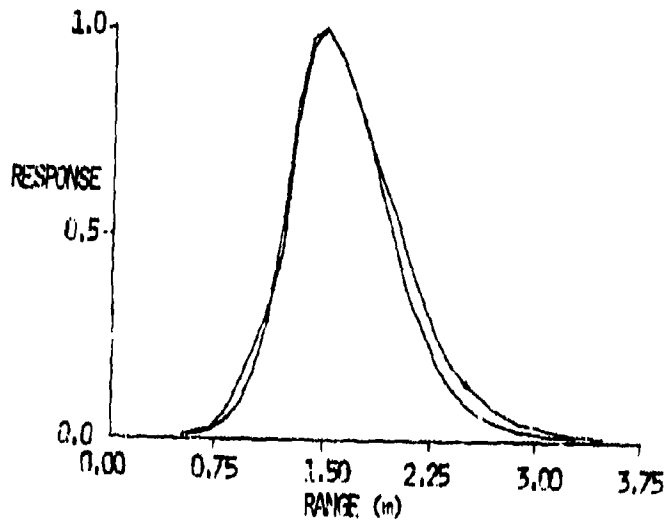

FIGURE 2. SYSTEM RANGE-RESPONSE FUNCTION. Response of the two receivers to a diffuse target as a function of range, normalized to unity at peak.

FIGURE 3. TV MONITOR DISPLAY OF A DATA FRAME. The time scale runs downward and spans 50 ns; signal deflections are to left. Unpolarized receiver trace is on right, cross polarized on left. Signal deflections, in sequence, are the reference pulse, the aerosol backscatter pulse, and the diffuse target pulse. Frame is from trial 14.

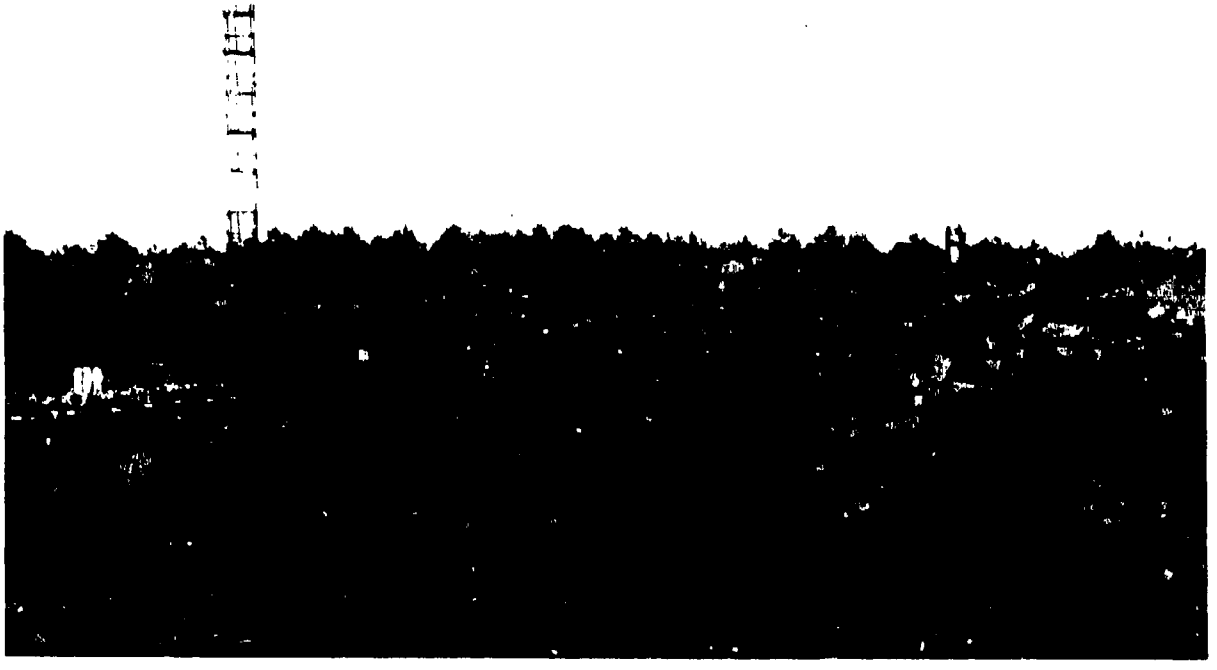

FIGURE 4. AEROSOL IR#2--TRIAL 14. The aerosol is being generated to the right of the photograph and is drifting towards the HDL instrumentation in the shiny foil-covered large box visible at the far left.

Figure 4 is a photograph taken during Smoke Week III, trial 14. The experimental aerosol IR#2 is being generated by an XM49 smoke generator to the right of the photo, and is drifting north toward the main sampling line (aerosol concentration and size distribution measuring instruments mounted on barrels), the 32-m tower, and the instrumentation cluster. The laser backscatter probe is contained within the shiny foil-covered 1.5 m x 1.5 m x 3 m box visible to the left of the large tower and just above the sampling line, and is not yet immersed in the aerosol cloud. The box is insulated and air-conditioned and contains the probe, other HDL instrumentation, and the data recording equipment. The laser beam emerges at a height of ≈3 m from a window in the back of the box (not seen) and is aligned parallel to the sampling line, and thus approximately perpendicular to the direction in which the aerosol particles are drifting with the wind.

The backscatter probe was located ≈11 m west and ≈7 m north of the test grid center. The latter point was on the main sampling line very near the 32-m tower. For all the smoke trials discussed in this paper except trial 9, the aerosol was generated on a line parallel to and 70 m south of the main sampling line; the position of the smoke generator along this line was chosen with the goal of having the wind blow the center of the aerosol cloud to the grid center. Thus the HDL position was ≈80 m from the smoke generator. For trial 9, the source of the smoke was distributed at six positions from 80 to 105 m south of the main sampling line.

The aerosol concentration observed at the HDL position was quite variable, sometimes changing rapidly with shifts in the wind direction. This was especially true for the trials where the amount of aerosol generated was not large, as was the case for the experimental smokes like the one shown in figure 4. For some trials only the edge of the aerosol cloud hit the HDL position, and for some others the aerosol missed the position altogether. Thus the magnitude of the measured extinction and backscatter coefficients depended on these factors as well as on the concentration of the aerosol generated and on the efficiency of the aerosol as a scatterer of 0.9 μm radiation.

The extinction coefficient was determined from the attenuation of the signal from the diffuse target at 3.2 m. The spatial resolution in the beam direction of this measurement is therefore 3.2 m. The backscatter coefficient was determined basically from the signal measured in the unpolarized receiver from the aerosol backscatter in the region, centered at 1.5 m, where the system response was significant. The depolarization was determined from the ratio of the 1.5 m backscattered signals of the cross-polarized and unpolarized receivers. The resolution of the latter two measurements in the beam direction is therefore roughly 1 m.

The spatial resolution available in the direction perpendicular to the beam, and therefore approximately in the direction of advance of the aerosol cloud, depends on the pulse repetition rate and wind velocity. The repetition rate used at Smoke Week III was 30 Hz. This corresponds to a 0.1 m resolution

of the aerosol nonuniformities in the direction of a 3 m/s wind perpendicular to the sampling line. To increase the signal-to-noise ratio and to average nonuniformities in the aerosol cloud in the direction of the wind that are of a smaller scale than the system resolution in the direction of the beam, a number of frames were usually averaged together before the scattering parameter calculations. For the above example, if 10 frames are averaged together, the time resolution degrades to 1/3 s and the spatial resolution in the wind direction to ≈1 m, compatible with the resolution in the perpendicular direction.

3. CALCULATION PROCEDURE

3.1 EXTINCTION COEFFICIENT

The extinction coefficient σ is defined from Beer's law describing the attenuation of a collimated light beam:

$$\frac{I}{I_0} = e^{-\sigma L}, \tag{1}$$

where I is the intensity after traversing a distance L of aerosol, and I_0 is the initial intensity. Both absorption and scattering account for the attenuation; however, in the near-infrared region, absorption may be neglected for most aerosols, and σ taken to describe attenuation by scattering. The mass attenuation coefficient, α, which is independent of the aerosol concentration, is related to σ by

$$\sigma = \nu\alpha ,$$

where ν is the aerosol concentration.

The extinction coefficient was determined at Smoke Week III from the ratio of the signal reflected from the target at 3.2 m with aerosol present to that signal before and/or after the test. The value of σ obtained is thus the average over the 3.2 m path length, and is given by

$$\sigma = \frac{1}{2L} \ln\left(\frac{T_0}{T}\frac{C}{C_0}\right), \tag{2}$$

where

T = amplitude of signal observed from the diffuse target at 3.2 m in the presence of aerosol,

T_0 = amplitude of that signal immediately before or after the presence of the aerosol,

C = amplitude of the reference pulse signal when T is measured,

C_0 = amplitude of the reference pulse signal when T_0 is measured, and

L = distance to diffusely reflecting target (3.2 m).

3.2 BACKSCATTER COEFFICIENT

The volume scattering coefficient $\mu(\theta)$ is the power scattered per unit solid angle at an angle θ from the incident beam direction, per unit power density, per unit volume. The backscatter coefficient $\mu(\pi)$, or simply μ, is the volume scattering coefficient for $\theta = \pi$. The backscattered signal as a function of time, P(t), may be written as

$$P(t) = \frac{K\mu}{r_o^2} \int_0^\infty e^{-2\sigma r} f(r)\, p\left(t - \frac{2r}{c}\right) dr , \tag{3}$$

where

$$f(r) = \frac{P_t(r)}{P_t(r_o)} , \tag{4}$$

K = a constant depending on the optical and electronic parameters of the system,

$p(t)$ = shape of transmitted pulse as detected by the receiving system viewing a diffuse target, normalized to unity,

$P_t(r)$ = peak return from a diffuse target at range r,

r_o = range at which maximum signal is received from a diffuse target, and

c = speed of light.

Defining

$$D(\sigma,t) = \int_0^\infty e^{-2\sigma r} f(r) p\left(t - \frac{2r}{c}\right) dr, \tag{5}$$

we may write

$$P(t) = \frac{K\mu D(\sigma,t)}{r_o^2} . \tag{6}$$

Both $f(r)$ and $p(t)$ may be experimentally determined for a particular system and alignment. We are interested in the peak value of the backscattered signal, so we perform the convolution indicated by equation (5) to obtain the peak of $D(\sigma,t)$, denoted by $D(\sigma)$, for all values of σ of interest, and store the results in the computer. For the Smoke Week III alignment, D is approximately constant at 0.67 m for $\sigma < 0.1\ m^{-1}$.

Replacing the time-dependent values with the peak values, we see from equation (6) that μ is given by

$$\mu = \frac{r_o^2 P}{K\, D(\sigma)} . \tag{7}$$

We can recast equation (7) in terms of easily measurable parameters if we calibrate the system by measuring P_t, the clear air signal from a diffuse reflector of known reflectivity ρ placed at r_o:

$$P_t = \frac{K_t \rho}{\pi r_o^2} .$$

The system constant K_t will in general differ from K because of transmitter or receiver system changes caused by temperature variations or other factors. Because these changes are reflected in the reference signals, we may write

$$\frac{K_t}{K} = \frac{C_t}{C} ,$$

where C_t is the peak of the reference pulse signal while the calibration target is observed. It now follows that

$$\mu = \frac{\rho}{\pi b(\sigma)} \frac{C_t}{C} \frac{P}{P_t} . \tag{8}$$

Because σ is known from the attenuation of the 3.2 m target signal, μ may be calculated from equation (8).

3.3 SCATTERING FUNCTION

Having independently determined σ and μ, we may find the scattering function for 180-deg scattering,

$$F = \frac{\mu}{\sigma} . \tag{9}$$

F for a given wavelength depends on the particle-size and -shape distribution and index of refraction, but, to a first approximation, is independent of aerosol concentration.

3.4 DEPOLARIZATION

The intensity and polarization state of a light beam can be described as follows. The total intensity, I, consists of a polarized part, I_p, and an unpolarized part, I_u, so that $I = I_p + I_u$. The polarization vector (the electric field vector, say) of the I_u-component has a completely random direction in a plane perpendicular to the propagation direction, while that of the I_p-component traces out an ellipse (the polarization ellipse) in the same plane as time passes. The values of I_p and I_u together with some geometrical specification of the polarization ellipse constitute a complete mathematical description of the intensity and polarization state of the beam. Such a description is provided by the so-called Stokes vector,[6] which has the four components (I, M, C, S) and is referred to a spatial coordinate system (x, y, z) in which the z-axis points in the direction of propagation. I gives the total intensity of the beam and $I_p^2 = M^2 + C^2 + S^2$. The polarization ellipse is determined as follows. Let ψ ($0 \leq \psi < \pi$) be the angle between the major axis of the polarization ellipse and the x-axis. Then

$$\tan 2\psi = \frac{C}{M} .$$

Let $\tan \chi$ ($-\frac{\pi}{4} < \chi \leq \frac{\pi}{4}$) give, in absolute value, the ratio of the minor-to-major axis lengths of the polarization ellipse, where the sign gives the sense of circulation ($\chi > 0$ corresponds to right-handed and $\chi < 0$ to left-handed circulation). Then

$$\sin 2\chi = S/I_p$$

An important computational convenience of the Stokes vector description is that the effect of propagation through a linear optical element is described by a matrix equation of the form

$$\begin{bmatrix} I_e \\ M_e \\ C_e \\ S_e \end{bmatrix} = \begin{bmatrix} & & & \\ & 4 \times 4 \text{ matrix} & & \\ & & & \\ & & & \end{bmatrix} \begin{bmatrix} I_i \\ M_i \\ C_i \\ S_i \end{bmatrix}$$

where the e and i subscripts refer to the emergent and incident beams, and the elements of the 4 x 4 matrix are determined by several transmission coefficients of the optical element. For example, if the optical element is a linear sheet polarizer perpendicular to the beam propagation direction and has its easy and hard directions coincident with the x- and y-axes respectively, then the matrix in the foregoing equation has the form

$$\frac{1}{4}\begin{bmatrix} (K_1 + K_2) & (K_1 - K_2) & 0 & 0 \\ (K_1 - K_2) & (K_1 + K_2) & 0 & 0 \\ 0 & 0 & 2\sqrt{K_1 K_2} & 0 \\ 0 & 0 & 0 & 2\sqrt{K_1 K_2} \end{bmatrix},$$

where K_1 is the intensity transmission coefficient of the element to plane polarized light whose polarization vector points fixedly along the x-axis (i.e., in the easy direction), and where K_2 is the similar coefficient for plane polarized light whose polarization vector points along the y-axis. An ideal or perfect linear sheet polarizer would have $K_1 = 1$ and $K_2 = 0$. An imperfect polarizer has K_1 somewhat less than unity and K_2 somewhat bigger than zero.

In our experiments two independent measurements are made pertaining to the intensity and polarization state of the backscattered beam. In general, four suitably chosen independent measurements are needed to determine the Stokes vector; however, the two measurements are sufficient to determine the depolarization caused by aerosol backscatter if two assumptions hold.

The crucial assumption we make is that the backscattered beam's polarized part is linearly polarized in the same direction as the transmitted beam. An evaluation of the correctness of this assumption would require knowledge of the constitution of the various aerosols measured and a specific analysis of the scattering mechanisms. We have found the assumption useful for analyzing polarization effects in previous experiments[3,7,8] with backscatter from water clouds and diffusely reflecting rough surfaces. The hygroscopic aerosols tested at the several smoke weeks are believed to have scattering properties that are similar to those of water clouds, especially under high humidity conditions where the water scattering is dominant. For spherical droplet water clouds, Mie theory predicts that the polarization state of the backscattered beam is the same as that of the transmitted beam, provided that multiple scattering effects are negligible.[9] Thus, for water clouds, the depolarizing mechanism arises from droplet asphericity and multiple scattering. One would expect an approximately random distribution of aspheric droplet orientations in many cases and would consequently expect the depolarizing effect in these instances to be a transformation of incident polarized light to randomly polarized or unpolarized light. Our basic assumption about the smoke backscatter could be phrased similarly, namely, that the smoke depolarizes the incident beam by changing part of it to a randomly polarized beam.

To proceed with the analysis, we first quantify the polarization state of the transmitted beam.

The radiation from the source GaAs laser has been verified by measurement (of the optically collimated beam) to be randomly polarized. The transmitted beam is vertically polarized by a sheet polarizer in its output optics. Let $K_1 = t_1$ and $K_2 = t_2$ for the transmitter polarizer, taking the x-axis to be vertical (i.e., $t_1 \approx 1$ and $t_2 \approx 0$). The Stokes vector of the beam incident upon the aerosol is therefore $\left[\frac{1}{2} I_t(t_1 + t_2), \frac{1}{2} I_t(t_1 - t_2), 0, 0\right]$ *, where I_t denotes the transmitter intensity prior to polarization. In accordance with our basic assumption, we take the Stokes vector of the backscattered beam to be of the form $(I_R, M_R, 0, 0)$. The total incident and backscattered intensities are related by

$$I_R = \frac{\rho_o}{2} I_t(t_1 + t_2)$$

for some constant $\rho_o < 1$; also, $I_R - M_R = I_{Ru}$ gives the unpolarized part of the backscattered intensity. Thus

$$I_{Ru} = \frac{\rho_o}{2} I_t(t_1 + t_2) - M_R$$

and

$$I_{Rp} = M_R,$$

where I_{Rp} is the polarized part of the backscattered intensity.

One of the two receivers has no polarizer in its collection optics and so will give a peak signal voltage V_u proportional to I_R. Let C_1 denote the proportionality constant so that $V_u = C_1 I_R$. The other receiver has a sheet polarizer with $K_1 = r_1$ and $K_2 = r_2$. Since this polarizer is crossed with respect to the transmitter polarizer, $r_1 \approx 0$ and $r_2 \approx 1$. The Stokes vector of the beam received in this cross-channel is (after passing through the polarizer) therefore

$$\left[\tfrac{1}{2}(r_1 + r_2)I_R + \tfrac{1}{2}(r_1 - r_2)M_R, \tfrac{1}{2}(r_1 - r_2)I_R + \tfrac{1}{2}(r_1 + r_2)M_R, 0, 0\right],$$

so that the peak received signal voltage V_x is given by

$$V_x = \tfrac{1}{2} C_2 \left[(r_1 + r_2)I_R + (r_1 - r_2)M_R\right],$$

where C_2 is a proportionality constant similar to C_1. The quantity $s = C_2/C_1$ gives the ratio of the sensitivities of the two receiver channels, both without polarizers. It is therefore possible to measure

$$\frac{M_R}{I_R} = \frac{\frac{2}{s}\frac{V_x}{V_u} - (r_1 + r_2)}{r_1 - r_2},$$

which gives the fraction of the smoke-backscattered intensity that is polarized. Were the incident transmitter beam totally polarized,

* Note that the Stokes vector of an unpolarized beam of intensity I is (I,0,0,0).

$$D_u = \frac{2\left(\frac{V_x}{V_u} - s\, r_1\right)}{s(r_2 - r_1)} \times 100\% \qquad (10)$$

would give the percentage extant to which the smoke depolarizes a linearly polarized incident beam. Denote the latter percentage by D_c.

An estimate of D_c in terms of D_u and the transmitter polarizer coefficients t_1 and t_2 is

$$\frac{D_c}{100\%} = \frac{\frac{D_u}{100\%} - d_1}{1 - d_1}, \qquad (11)$$

where

$$d_1 = \frac{2t_2}{t_1 + t_2}. \qquad (12)$$

This estimate becomes exact if it is assumed that the unpolarized part of the incident transmitter beam remains unpolarized after backscatter from the smoke. This is the second assumption referred to earlier.

4. DISCUSSION OF RESULTS

4.1 DATA AND ERRORS

Because of problems with the minicomputer that is an integral part of the digitization and data reduction process, data from only five trials have been reduced so far: experimental smokes IR#1, IR#2, and IR#3 dispersed with the XM49 smoke generator (Smoke Week III trial nos 11, 14, and 10 respectively); fog oil generated with the M3A3 smoke generator (trial 8); and 24 canisters of HC, simulating 6 155-mm shells (trial 9). Good data were obtained during many of the other trials; these data will be reduced later.

Plots of σ, μ, and F versus time from the official start of the trials ($z = 0$ in the test nomenclature) and plots of σ versus μ are given for trials 8, 9, 11, and 14 in figures 5, 6, 7, and 8. The plots of σ and μ versus time (graphs A and B of the figures) show how these parameters vary as the smoke cloud is blown past the measurement apparatus. This variation is primarily the result of variation in the smoke concentration, which can be quite rapid.

Graphs C and D of the figures concern the scattering function F. The variation of F with time is plotted directly in graph C, while μ is plotted versus σ in graph D. The slope of the latter graph gives an average of F for a trial. Variations of F are an indication of changes in the particle-size, -shape, or index of refraction distribution or of multiple scattering effects. The latter can be important at high aerosol concentrations. Because multiple scattering would tend to decrease the measured value of σ and increase that of μ, its presence would tend to be indicated by an upward curve of the points in the plot of μ versus σ at high σ. An absence of a trend in a μ versus σ plot would

tend to rule out multiple scattering as significant. If in such a case the F versus time plot showed variations that were not due to noise, one would attribute those variations to changes in the particle-size, -shape, or index of refraction distribution.

For trial 10, plots of σ and F are given in figure 9 (A), while μ and D_c are plotted in figure 9 (B). Depolarization results for trials 11 and 14 are plotted in figures 11 and 12, respectively.

The limits of the measurement at low signal values derive from the noise in the measurement system, the recording process, and the digitization. Based on this noise, the rms uncertainty in σ at low values is about $\pm 0.001\ m^{-1}$ without averaging. At higher values of σ, this uncertainty is multiplied by $e^{2L\sigma}$, which is ≈ 2 at $\sigma = 0.1\ m^{-1}$, and ≈ 10 at $\sigma = 0.4\ m^{-1}$. The maximum observable σ without averaging is $\approx 0.7\ m^{-1}$. The rms uncertainty in μ, also without averaging, is $\approx \pm 0.00004\ m^{-1}sr^{-1}$. The maximum observable μ depends on σ and adjustable system parameters; as a practical matter this limit is not reached. The uncertainty in F depends on those of σ and μ; it becomes large when σ and μ are near their minimum observable values. The uncertainty in D_c depends similarly on the signal levels in the unpolarized and polarized receivers. All the uncertainties are reduced by averaging a number of frames before the calculations, as long as the variation in the parameters is not too rapid.

There are, of course, other errors associated with the measurements, such as errors in calibration and in measuring the system parameters such as $D(\sigma)$. For μ, there is an additional error when σ is higher and nonuniform, because the σ used in the μ calculation (equation 8) is the average σ over the 3.2 m path of that measurement, which is not necessarily applicable to the path over which μ is measured. In addition, equation 3 and thus the entire μ calculation assumes a uniform aerosol from the transceiver to the far limit of significant response, a distance of ≈ 2 m.

The apparent noise in the data for all the trials except 14 may be somewhat greater than suggested by the foregoing. The reason is that for trials 8, 9, 10, and 11, an R7912 borrowed from Army Missile Command was used for the data acquisition because our unit malfunctioned. Because the substitute instrument was not modified to rotate the display as required by our digitizing system, the tapes could not be processed through the digitizing hardware and software developed for that purpose. The peaks of the signals were therefore laboriously measured by hand, a process that is more noisy than the machine digitization. As it happened, because of the aforementioned problems with the minicomputer, these are the only data to be processed so far, except for data of trial 14. Those data were acquired using the modified R7912 and processed by the normal procedure prior to the problems with the minicomputer.

4.2 DISCUSSION OF σ, μ, AND F

For trial 9, HC smoke (figure 5), significant smoke concentrations occurred at the HDL measurement site only from 71 to 198 s from initiation of the test, the time period covered by the graphs. A 16-frame average was used for most of this trial, although during some periods of rapidly varying smoke

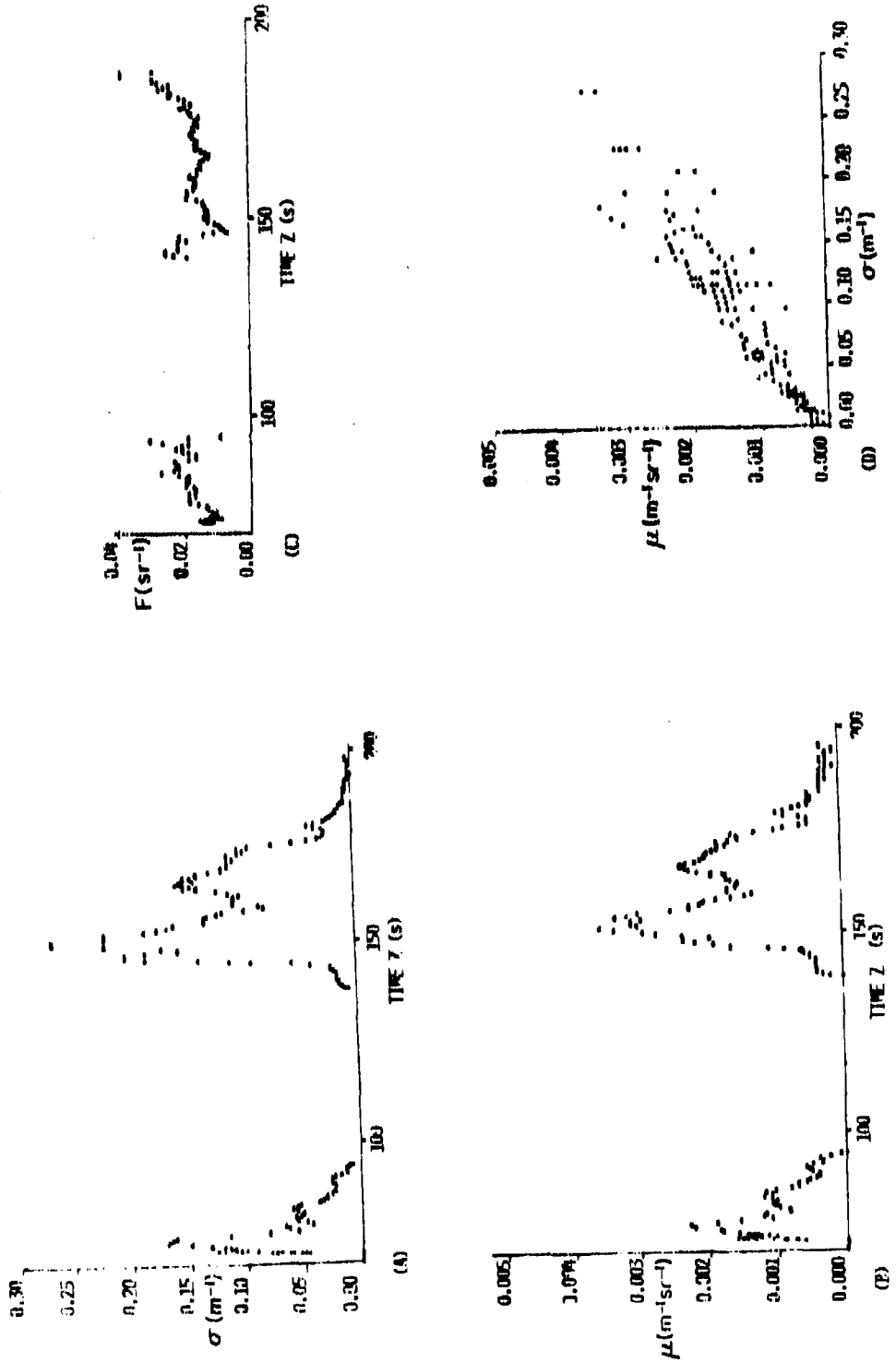

FIGURE 5. AEROSOL PARAMETERS FOR TRIAL 9, 24 CANISTERS OF HC: (A) Extinction coefficient σ versus time, (B) Backscatter coefficient μ versus time, (C) Scattering function F versus time, and (D) μ versus σ. At trial start z = 0.

concentration an 8-frame average or no averaging was used. With the 3 to 4 m/s mean wind speed during this trial, the 16-frame, or ≈0.5 s, average provides ≈1.9 m resolution in the smoke cloud in the wind direction.

A significant feature of the σ and μ plots for trial 9 is their rapid variation with time. For example, for the first cloud section, σ rises from zero to ≈0.05 m^{-1} from one frame to the next, corresponding to ≈0.1 m of cloud depth. This is all the more remarkable when we consider that the measured σ is the average value over ≈3 m of distance perpendicular to the wind direction. Over the next ≈2 m, σ rises to ≈0.1 m^{-1}, and peaks at ≈0.17 m^{-1} after ≈5 m more of smoke drifts by.

The μ/σ ratio F was plotted only to z = 187 s because the probable error for this ratio is very high for the last 11 s, where both μ and σ are small ($\sigma \lesssim 0.005\ m^{-1}$) and subject to large uncertainty. With the possible exception of a few isolated points, the variation of F with time shown in C is real and probably caused by variations in the size distribution of the particles. Multiple scattering would tend to be ruled out as a cause by the lack of correlation of F with the concentration. Both C and D indicate that, for $\sigma \gtrsim 0.05\ m^{-1}$, $F \approx 0.014 \pm 0.005\ sr^{-1}$. This compares well with our previously reported value of 0.012 sr^{-1} for HC from Smoke Week II, where the same laser backscatter instrumentation was used in a different configuration without a fixed target to determine the feasibility of its use in routine aerosol measurements.[10]

The fog oil data, trial 8 (figure 6), consist mainly of ≈10-to 20-m long patches of smoke blowing through the instrumentation site, as seen clearly in the σ and μ plots. No averaging was used during the rapidly changing regions which comprise the peaks in σ and μ, but 10 or more frames were averaged during some low concentration, slowly varying segments of the test. With the 2 m/s mean wind for this test, the resolution in the wind direction is ≈0.07 m in regions with no averaging. Rapid changes of σ and μ were also observed for this test, with σ increasing from ≈0.04 m^{-1} to over 0.2 m^{-1} in ≈2 m near the front of the densest patch.

All points with $\sigma < 0.005\ m^{-1}$ were omitted from the F versus time plots because of the large uncertainty in the ratio. However, in no case where the σ and μ data were above the peak noise level did F exceed 0.1 sr^{-1}. In the regions of relatively dense smoke, with $\sigma \gtrsim 0.03\ m^{-1}$, F ranged from 0.012 sr^{-1} to 0.027 sr^{-1}, with a mean value of 0.018 sr^{-1}. The latter value is confirmed by the slope of the μ versus σ plot. The variability of F for this smoke is illustrated, however, by a relatively solid region of smoke at z ≈ 370 s, where $\sigma \approx 0.02\ m^{-1}$ with a mean value of F of 0.036 sr^{-1}. These results are consistent with the F values of 0.02 sr^{-1} and 0.03 sr^{-1} reported for two trials of Smoke Week II.[10]

Only about a 25-s segment of the experimental aerosol IR#1 was observed in trial 11 by the HDL instrumentation. These data (figure 7) were not averaged, resulting in ≈0.1 m resolution in the direction of the 2.5 m/s mean wind. No points were omitted from any of the plots for this test. The maximum

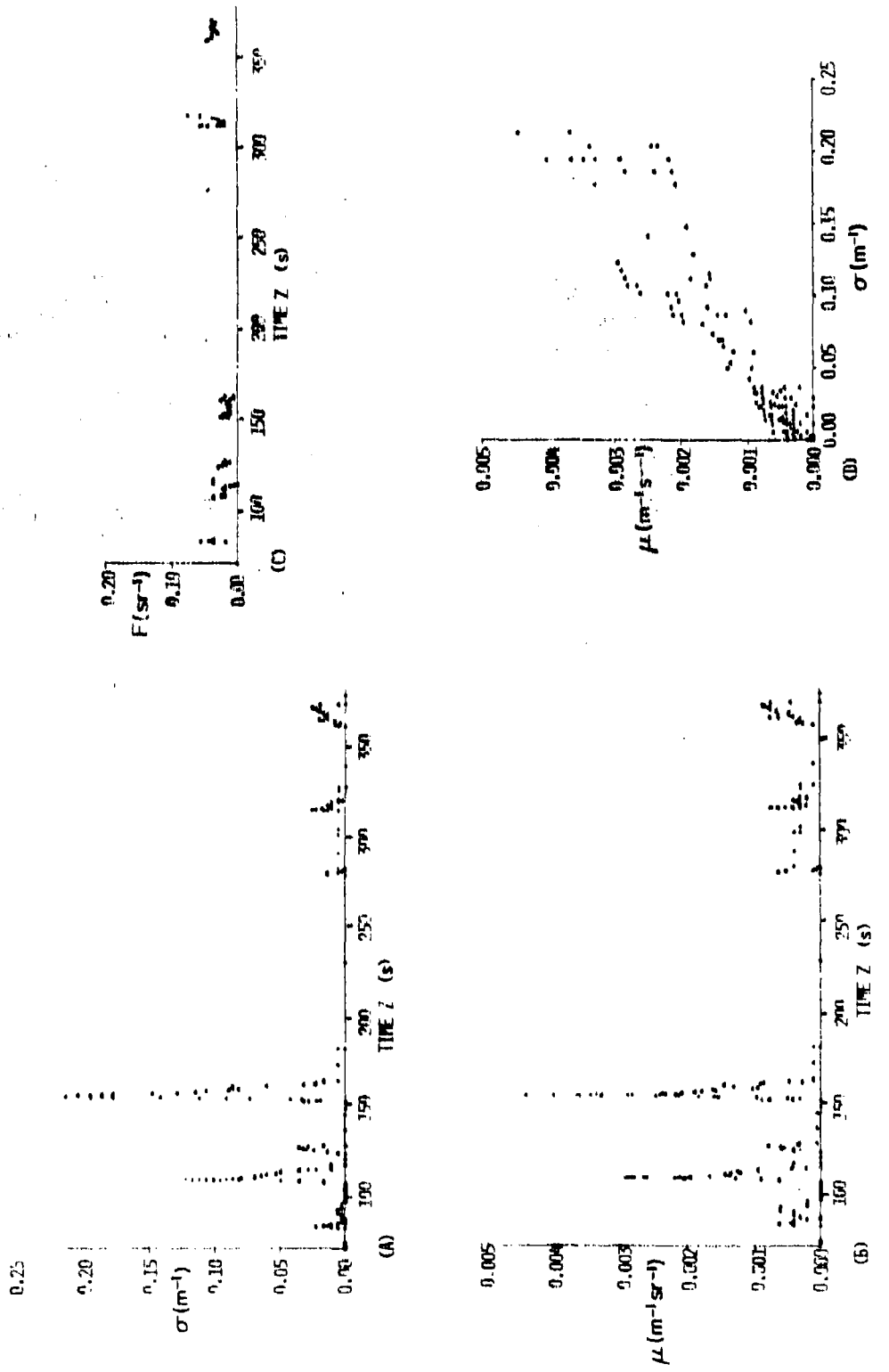

FIGURE 6. AEROSOL PARAMETERS FOR TRIAL 8, M3A3 w/Fog Oil: (A) Extinction coefficient σ versus time, (B) Backscatter coefficient μ versus time, (C) Scattering function F versus time, and (D) μ versus σ. At trial start $Z = 0$.

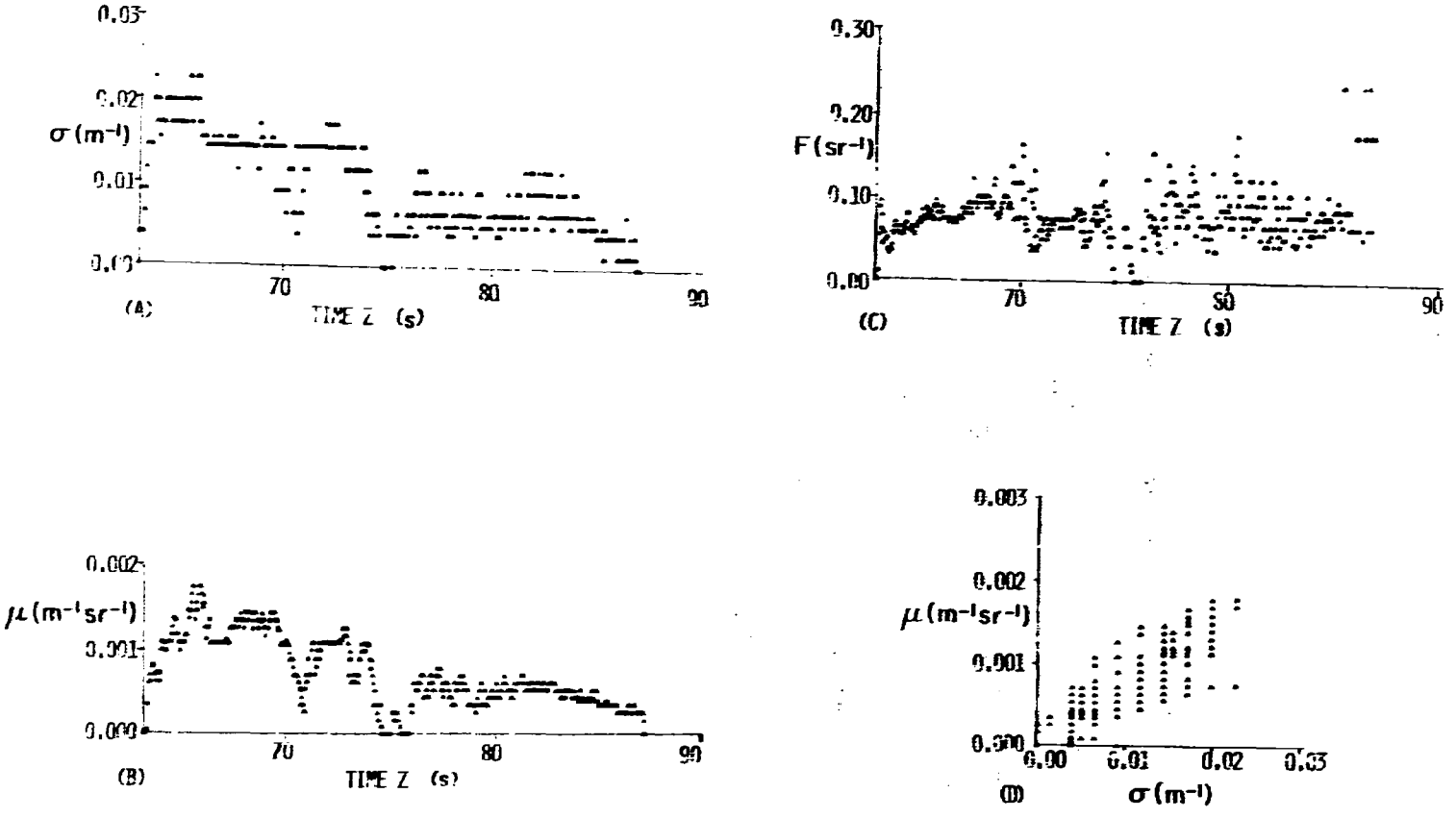

FIGURE 7. AEROSOL PARAMETERS FOR TRIAL 11, XM49w/IR#1: (A) Extinction coefficient σ versus time, (B) Backscatter coefficient μ versus time, (C) Scattering function F versus time, and (D) μ versus σ. At trial start z = 0.

value of σ observed for this aerosol was only $\approx 0.02\ m^{-1}$, about an order of magnitude lower than for HC and fog oil. The low value of σ, together with the lack of averaging, resulted in the noise apparent in figure 7 (A). Contrastingly, μ was relatively higher; therefore the plot in B is smoother.

The plot of F is also relatively low in noise for the first 10 s where σ and μ are reasonably high, but becomes quite noisy in the later, low concentration segments. In the first 10 s, F appears to have a real, although small, variation with time, with an average value of $0.08 \pm 0.03\ sr^{-1}$. This value is confirmed by the μ versus σ plot, which has a heavy concentration of points along the $F=0.08\ sr^{-1}$ slope.

The results for the experimental aerosol IR#2, trial 14, are plotted (figure 8) using an 8-frame average throughout for a $\approx$1/2 m resolution with the 2 m/s mean wind speed. All the points were retained in these plots also. The maximum σ was reasonably high for this aerosol, while the maximum μ, $0.010\ m^{-1}sr^{-1}$, was considerably higher than for the other aerosols at Smoke Week III for which our data have been reduced, although not as high as some μ's in fog oil measured at Smoke Week II.

The relative smoothness of the F plot, figure 8(C), is an indication that the fluctuations in the σ and μ plots result from real concentration variations, not noise. However, the behavior at $z \approx 170$ s results from the large uncertainty in F when σ and μ are low. From this plot, as well as figure 8 (D), we conclude that $F \approx 0.09 + 0.02, -0.04\ sr^{-1}$, with the lower values, down to $F \approx 0.05\ sr^{-1}$, for $\sigma \gtrsim 0.07\ m^{-1}$. The decrease in F at high σ, which is also apparent from a comparison of figure 8 (A) and (C), is opposite what one might expect from multiple scattering. The variations in F are therefore likely caused by changes in the particle sizes, shapes, or indices of refraction.

For the experimental aerosol IR#3, trial 10 (figure 9), significant concentrations were observed for only $\approx$7 s, starting at $z \approx 213$ s. With the 3 m/s mean wind, the 10-frame average used resulted in a $\approx$1 m resolution in the wind direction. The data for this test were plotted by hand and all points were kept. The maximum values for both σ and μ were lower for this trial than for the other Smoke Week III trials examined so far. This may be due to low scattering in the near IR by this aerosol, low concentrations generated, or the bulk of the aerosol missing the HDL measurement site. The low values of σ and μ result in a large uncertainty in F. However, in the regions where $\sigma \gtrsim 0.005\ m^{-1}$, $F \approx 0.13 \pm 0.04\ sr^{-1}$, which is higher even than IR#2, and at least twice as high as any F for conventional smoke, dust, or natural cloud that we have observed in any of our previous aerosol testing.[3,8,10,11] The indicated uncertainty in F is based on the spread of the F values in figure 9 (A) in the region where $\sigma > 0.005\ m^{-1}$. An analysis based on the noise in the σ and μ values, similar to that done for depolarization in Appendix A, indicates a standard deviation of from $+0.04\ sr^{-1}$ to $+0.07\ sr^{-1}$ for the individual points, with an average of $+0.05\ sr^{-1}$. This is consistent with the indicated uncertainty, but suggests that the variation of F with time implied by figure 9 (A) is not statistically significant.

UNCLASSIFIED

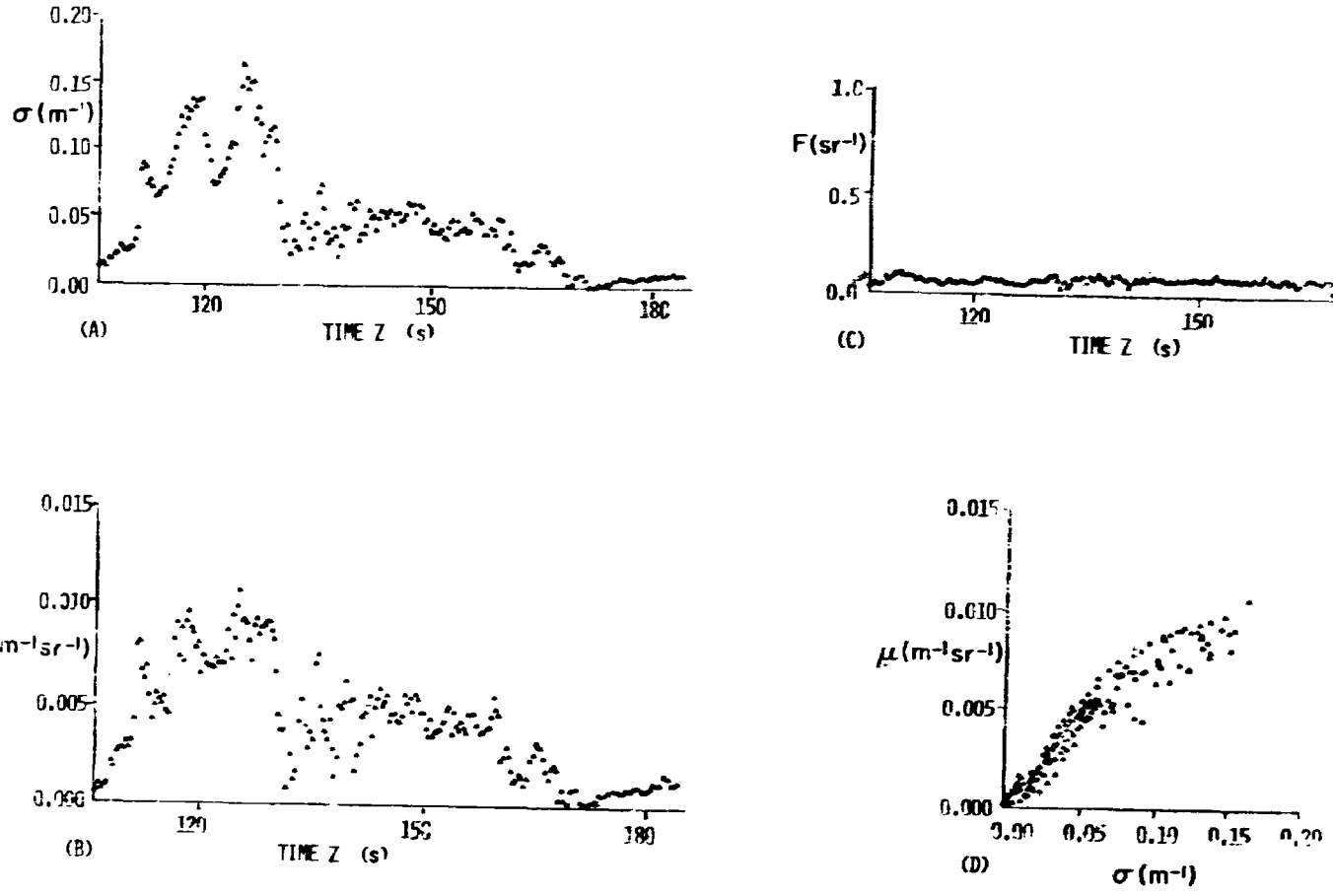

FIGURE 8. AEROSOL PARAMETERS FOR TRIAL 14, XM49w/TR#2: (A) Extinction coefficient σ versus time, (B) Backscatter coefficient μ versus time, (C) Scattering function F versus time, and (D) μ versus σ. At trial start z = 0.

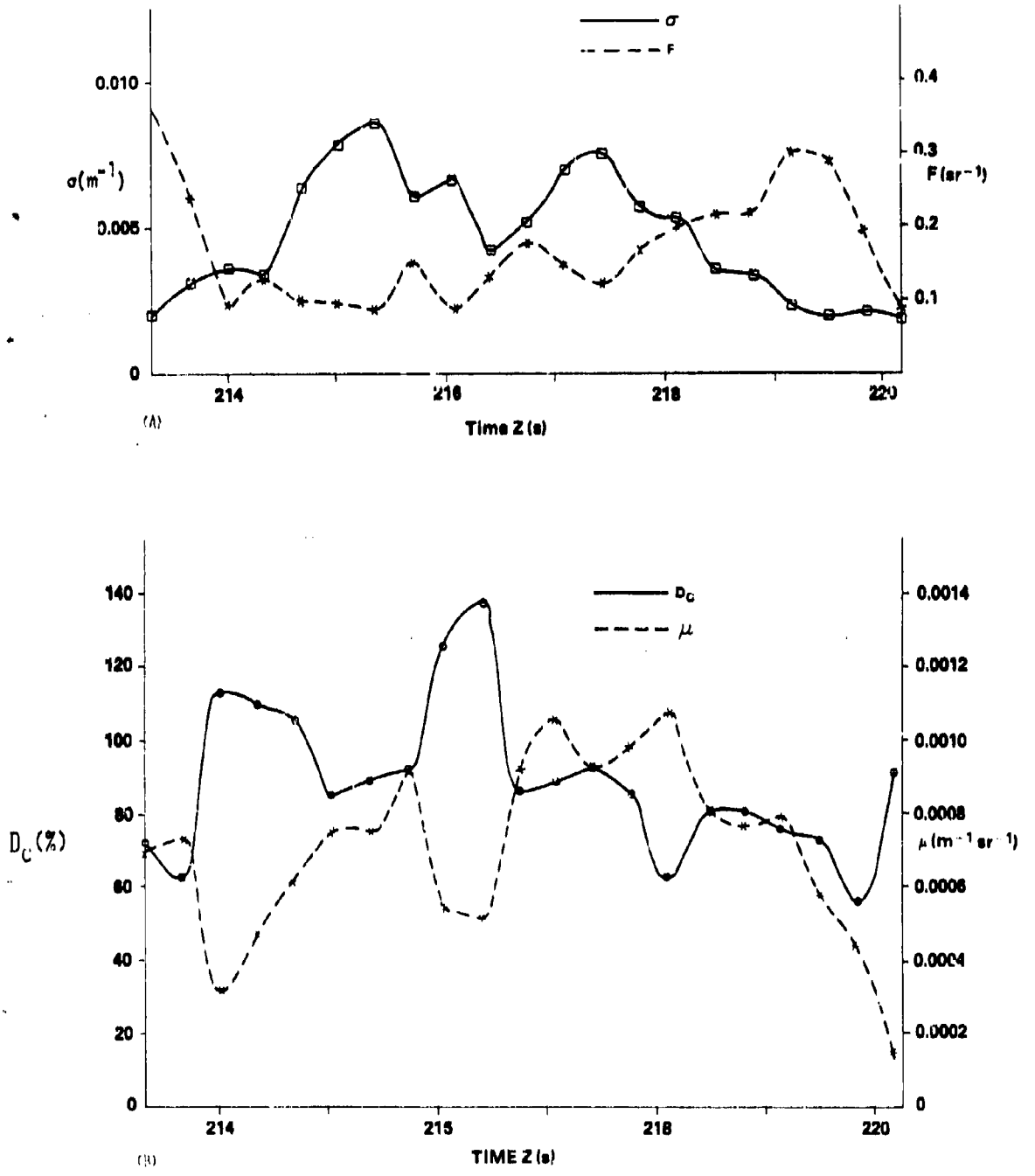

FIGURE 9. AEROSOL PARAMETERS FOR TRIAL 1C, XM49w/IR#3: (A) Extinction coefficient σ and scattering function F versus time, and (B) Backscatter coefficient μ and Depolarization D_c versus time. At trial start z = 0.

4.3 DISCUSSION OF D_c

There was no discernible backscatter signal in the cross-polarized receiver channel for the HC and fog oil trials. A determination of the rms noise level in this channel was used to place an upper limit on the cross-polarized return signal. Under conditions producing the largest backscatter signals in the other receiver channel, the maximum indicated depolarization for both HC and fog oil was less than 4 percent.

The depolarization shown in figure 9 for IR#3 appears at first to be somewhat bizarre because of the two excursions of the curve above 100-percent depolarization. We are convinced that these results are not caused by measurement errors, and in fact show that the polarization state of the backscatter in this case is qualitatively different from what we assumed in our data analysis. Recall that in obtaining D_c it is assumed that the backscatter is a mixture of unpolarized light and linearly polarized light with the same polarization direction as the incident transmitter beam. This assumption is correct if the smoke has no preferred optical direction in a plane perpendicular to the incident beam, but could be false if either the individual particle scattering mechanism or a collective alignment effect among oblong particles were to produce a preferred direction. We believe that the polarized part of the IR#3 backscatter was either rotated with respect to the transmitter polarization or was in some unknown state of elliptical polarization. A possible source of directionality is the lining up of a substantial number of the oblong population of this aerosol in the direction of the prevailing wind.

To convince ourselves that the depolarization results exceeding 100-percent depolarization were not caused by measurement error, several lines were pursued. First, data based on relatively low signal levels were omitted. These omissions were done systematically by using a sequence of increasingly severe signal-to-noise ratio (SNR) criteria to discard points. While this procedure did eliminate a number of the high depolarization values, substantial data higher than 100 percent (up to 200 percent) remained even after discarding signals that were up to six-times the rms noise levels.

The data just referred to correspond to single frames. The depolarization curve of figure 9 was obtained by averaging the results of 10 consecutive frames. Even with such averaging, depolarization levels up to almost 140 percent are obtained, as figure 9 shows.

An analytical formula showing the effect of noise in the measurement of the cross-polarized and unpolarized signal levels, V_x and V_u, on the calculated values of D_c was also developed. The result is

$$p_3(D_c) = \frac{1}{\sqrt{2\pi n^2 Q^3}} \exp\left[\frac{1}{2n^2}\left(\frac{S^2}{Q} - v_o^2\right)\right], \qquad (13)$$

where $p_3(D_c)$ is the probability density of depolarization values, n is the rms receiver noise level,

$S = V_{xo}(D_c + b) + aV_{uo}$, $Q = (D_c + b)^2 + a^2$, $v_o^2 = V_{xo}^2 + V_{uo}^2$, V_{xo} and V_{uo} are respectively the true or mean values of the cross-polarized and unpolarized signal levels (n, V_{xo}, and V_{uo} have the same units), and the positive constants a and b arise when D_c is expressed in the form $D_c = (aV_x/V_u) - b$ by using equations (10) through (12). This result is derived in Appendix A. Equation (13) can be used to determine the expected spread in D_c values for specific data V_{xo}, V_{uo} in terms of the known rms receiver noise level n. Two examples are shown in figure 10, which plots p_3 versus D_c for two individual data frames typical of those averaged together to produce the two largest relative maxima in the D_c-curve of figure 9; the figure 10 (A) plot corresponds to the lower D_c value in figure 9. The respective 30- and 20-percent spreads at the half-maximum points in figure 10 seem hardly sufficient to account for the many individual data points which we observe between 100- and 200-percent D_c levels (after considerable omission of data arising from low to moderate SNR). In addition, since the D_c spreads to be expected after a 10-frame average are smaller than the single-frame spreads by roughly a factor of $10^{1/2}$, it seems clear that the D_c curve of figure 9 represents a reasonably accurate measurement; error bars about the two largest maxima would be roughly 10-percent wide.

A main source of potential systematic error lies in the transmission coefficients of the sheet polarizers used in the transmitter and cross-polarized receiver. The Polaroid HR-3 infrared sheet polarizers we use are known to change their transmission characteristics upon extended exposure to ultraviolet light. Care must be taken to shield them from light when not in use, and occasional measurement of their transmission coefficients is required. Measurements immediately after Smoke Week III gave the values t_1=0.64, t_2=0.0012, r_1=0.0046, and r_2=0.68. These values, which were used for our data analysis, can be compared with t_1=0.69, t_2=0.0018, r_1=0.0042, and r_2=0.72, obtained several months before Smoke Week III. Were the latter values used for the data analysis, about 10-percent lower D_c's would have resulted at the maximum of the figure 9 curve. A 10-percent lowering of D_c would not materially alter our conclusions, however. Also, based on the history of the sheet polarizers between the two measurements, the transmission coefficients at Smoke Week III were likely decidedly closer to, if not virtually the same as, the post-test measured ones.

Post-test measurements of the receiver sensitivity ratio s were also performed to determine an accurate value for use in the data analysis. The value of s depends on the bias voltages used to set the avalanche gains of the receiver photodiodes. For the IR#1, IR#3, HC and fog oil trails, the bias levels were the same and s was measured to be 1.43; for the IR#2 run s was 1.78.

A final noteworthy feature of the IR#3 results is shown in figure 9, where the corresponding variation of the volume backscatter coefficient μ is also plotted. The precision of the μ measurement is estimated to be $\pm$ 0.2 x $10^{-4}m^{-1}sr^{-1}$ for the 10-frame average case shown. The evident correlation between high depolarization and low backscatter is noteworthy and suggests that the high depolarization

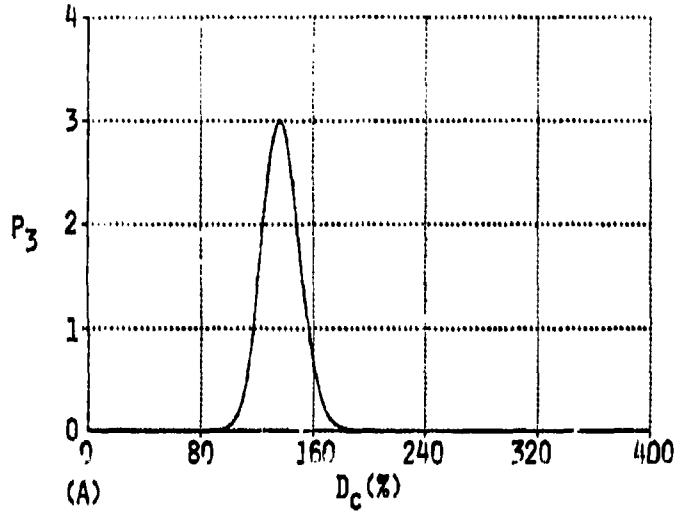

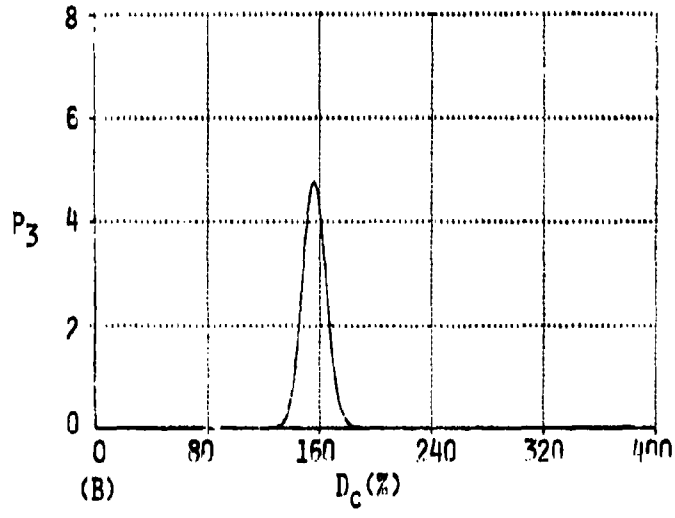

FIGURE 10. PROBABILITY DENSITY OF D_c ACCORDING TO EQUATION (13): (A) For typical data frame of those averaged to obtain the second highest D_c maximum in figure 9, (B) For typical data frame of those averaged to obtain the highest D_c maximum in figure 9.

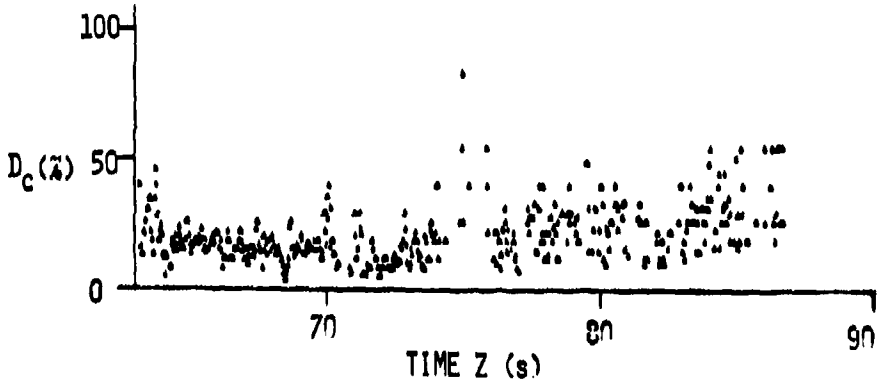

FIGURE 11. PERCENT DEPOLARIZATION VERSUS TIME FOR TRIAL 11, XM49w/IR#1. At trial start z = 0.

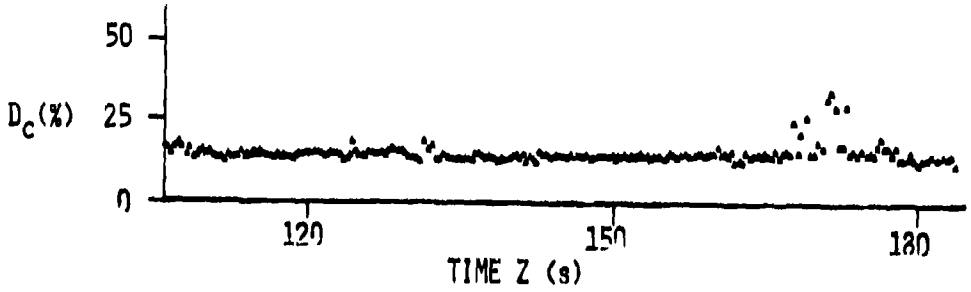

FIGURE 12. PERCENT DEPOLARIZATION VERSUS TIME FOR TRIAL 14, XM49w/IR#2. At trial start z = 0.

values may be associated with low smoke densities.

For the depolarization versus time plot for IR#1 (figure 11), each point corresponds to a single frame of raw data. The scatter in the data shows a marked increase beginning in the maximum D_c region at about z=75 s; low SNR is the main cause of the wider variations. The maximum D_c region at z=75 s coincides with the region of lowest signal levels where the backscatter return went virtually to zero for a brief period. Comparison of figure 11 with figure 7 reveals that the high scatter region of D_c coincides with the lower levels of σ and μ and with the high scatter region of F. The high D_c's at the very beginning of the plot are also likely due to low SNR. Similarly, the somewhat wider variations at about z=70 s and a little later coincide with local minima in σ and μ.

The sharp minimum in D_c a second or two before z=70 s seems to be an actual variation in the depolarizing effect of the aerosol; the data in this region are among the highest in SNR for the entire run. Also noteworthy is the fact that the minimum coincides with a definite but somewhat less pronounced minimum in the plot of F versus time in figure 7. Apart from the minimum in question, the depolarization in the higher SNR regions is fairly uniform and equals 15 ± 8 percent.

The plot of D_c versus time for IR#2 (figure 12) is from an eight-frame average of the data. The results are indeed remarkable, for a steady value of D_c = 15 ± 2 percent is indicated for the entire run, in spite of the fact that substantial variations in the smoke density and other parameters occurred during the run (cf. figure 8). The brief region of higher scatter near the end of the plot is an effect of low signal levels. The pronounced constancy of D_c in the face of significant variations in aerosol density suggests that multiple scattering plays only a small role as a depolarizing mechanism for IR#2.

5. CONCLUSION

A summary of the results of the Smoke Week III trials reduced so far is given in Table I. It is apparent that the IR screeners differ considerably from the conventional smokes. This conclusion is unlikely to change once data for phosphorous smokes from Smoke Week III are also reduced. Previous measurements of white and red phosphorous smokes (WP and RP) have shown them to have quite similar scattering properties at 0.9 μm to HC.[10] The depolarization was not measured in these experiments; however, since WP and RP, as well as HC, consist of spherical droplets containing mostly water, one would not expect them to depolarize radiation except through multiple scattering at high densities.

The IR screeners, on the other hand, do depolarize radiation significantly. Because this depolarization appears independent of the concentration, it is likely due to asphericity and alignment effects, not multiple scattering. The IR screeners also have significantly higher scattering functions than the conventional smokes or previously measured natural water clouds ($F \simeq 0.05 - 0.06\ sr^{-1}$)[3] and dust ($F \simeq 0.02 - 0.04\ sr^{-1}$).[10] At high concentrations, the higher F's would lead, under the single-scattering

approximation, to higher maximum aerosol backscatter signals for systems such as near-IR fuzes or target designators. Our data also show that F in a given trial can vary considerably for both the conventional and experimental aerosols. Fog oil shows the largest variation. This variation is sometimes independent of the concentration, but can also be quite dependent on it, such as the decrease in F with concentration for IR#2. This decrease contrasts to the increase previously observed in cumulus and stratus clouds and attributed, at least partially, to multiple scattering effects.[3] The constancy of D_c for IR#2 also indicates that multiple scattering was not important. The change in F would appear to be a size or index of refraction effect, because shape changes would be expected to be reflected in changes in D_c.

TABLE I. SUMMARY OF AEROSOL PARAMETERS

Smoke Week III trial number	Aerosol type	Maximum σ (m^{-1})	Maximum μ ($m^{-1}sr^{-1}$)	F (sr^{-1})	D_c (percent)
9	HC	0.28	0.0036	0.014±0.005	<4
8	Fog oil	0.22	0.0045	0.02±0.01*	<4
11	IR#1	0.02	0.0018	0.08±0.03	15±8
14	IR#2	0.16	0.011	0.08±0.03	15±2
10	IR#3	0.01	0.0010	0.13±0.04	60-140

* for $\sigma > 0.03\ m^{-1}$

IR screeners 1 and 2 appear quite similar in their 0.9 μm scattering properties, whereas IR#3 is obviously different. IR#3 has both the highest F and the highest D_c of all the aerosols we have so far measured. The very high depolarization of this aerosol would render any target/aerosol discrimination technique based on linear polarizers ineffective. The low values of σ and μ are likely a result of the low concentrations in trial 10, either because of limited generation or wind direction. The differences in σ and μ observed between IR screeners 1 and 2 are probably similarly caused, rather than resulting from differences in the single-particle scattering efficiency.

The depolarization data for IR#3 show that in some instances a more complete measurement of the polarization state of the backscattered beam is required. A complete measurement requires four rather than two backscatter signal determinations. A suitable set of measurements would include three with different orientations of the sheet polarizer axis and one with both a fixed sheet polarizer and a quarter-wave plate in the receiver channel. The resulting determination of four linearly independent linear combinations of the Stokes parameters of the backscattered beam would enable finding these Stokes parameters by solving four simultaneous linear equations. The measurement could be accomplished with our laser probe during smoke-week-type tests by using a small synchronous motor (synchronized to the laser pulse rate) to rotate a polarizer in front of one receiver and equipping the other with a suitable fixed polarizer/quarter-wave plate combination.

REFERENCES

1. "An Overview of Smoke Week III," G. Nelson, paper A-3, these proceedings.

2. "The Instrumentation Cluster Concept in Obscurant Field Testing," W. M. Farmer, paper A-14, these proceedings.

3. "Backscatter in Clouds at 0.9 μm and its Effects on Optical Fuzing Systems," Z. G. Sztankay and D. W. McGuire, Proceedings of the Seventh DOD Conference on Laser Technology, November 1977.

4. "Clutter Rejection Techniques for Laser Semi-Active Systems," H. F. Anderson, paper C-11, these proceedings.

5. "Analysis of a Slant-Range Optical Proximity Sensor," Z. G. Sztankay, Harry Diamond Laboratories, HDL-TR-1625, July 1973.

6. Polarized Light and Optical Measurements, D. Clark and J. F. Grainger, Pergamon Press, 1971.

7. "Measurements of the Directional Reflectivity and Depolarization Characteristics of Typical Military Targets at 0.9 μm (U)" D. W. McGuire and R. J. Wellman, Proc. of JTCG/MD/WPFF Tri-Service Optical Fuze Technology Symposium, NWC TP 5871, Part I, pp 95-114, Oct 1976 (Confidential).

8. "Measurements of Backscatter Effects in Clouds at 0.9 μm (U)," D. W. McGuire, H. M. Smalley, and Z. G. Sztankay, Proc. of JTCG/MD/WPFF Tri-Service Optical Fuze Technology Symposium, NWC TP 5871, Part I, pp 45-74, Oct. 1976 (Confidential).

9. Principles of Optics, M. Born and E. Wolf, pp 630-661, Pergamon Press, 1959.

10. "Backscatter and Extinction Measurements at Smoke Week 2," Z. G. Sztankay, J. Nemarich, J. Griffin, W. Hattery, and G. Wetzel, Proceedings of the Smoke/Obscurants Symposium III, DRCPM-SMK-T-002-79, June 1979.

11. "Measurement of the Localized Optical Characteristics of Natural Aerosols, Smoke, and Dust," Z. G. Sztankay, Proceedings of the Smoke Symposium II, DRCPM-SMK-T-004-78, June 1978.

APPENDIX A

PROBABILITY DENSITY OF DEPOLARIZATION VALUES

In the body of this paper, a method for determining the extent to which smoke scattering depolarizes an incident linearly polarized light beam in the backscatter direction was discussed. The discussion led to an equation of the form

$$D_c = a\frac{V_x}{V_u} - b \tag{A1}$$

for determining the percent depolarization, D_c, from two measured signal levels, V_x and V_u; a and b are positive constants. This appendix analyzes the effect of noise in measuring the two signal levels on the corresponding values of D_c. Equation (13) of the main text, which was used there to discuss measurement errors for specific data, is derived.

The noises in the two receiver channels which measure V_x and V_u are assumed independent, so that V_x and V_u can be considered as statistically independent random variables with respective probability density functions $p_1(V_x)$ and $p_2(V_u)$. Since the receivers are physically distinct devices, the only potentially correlated noises are those due to background light, which, under aerosol measurement conditions, are small compared with the noise arising in the receiver amplifiers. Because virtually all noise sources are of the Johnson or shot-noise type, both p_1 and p_2 are Gaussian densities in good approximation. The receivers are, additionally, of nearly identical construction, and their rms noise levels under the same measurement conditions are, not surprisingly, nearly the same. Accordingly, we take

$$p_1(V_x) = \frac{1}{\sqrt{2\pi}n}\exp\left[-\frac{(V_x - V_{xo})^2}{2n^2}\right],$$

and

$$p_2(V_u) = \frac{1}{\sqrt{2\pi}n}\exp\left[-\frac{(V_u - V_{uo})^2}{2n^2}\right], \tag{A3}$$

where n is the common variance and V_{xo}, V_{uo} are the means of V_x and V_u, respectively.

The probability density $p_3(D_c)$ of depolarization values can be determined from standard probability theory. First one finds the probability P(z) that $D_c \leq z$ for arbitrary real z, then $p_3(D_c)$ is determined as the derivative of P(z) at $z = D_c$. Because V_x and V_u are statistically independent,

$$P(z) = \iint_{\Gamma_z} p_1(V_x)\, p_2(V_u)\, dV_x\, dV_u\,, \tag{A4}$$

where the integration region Γ_z in the V_xV_u-plane is the image of the set $\{D_c : D_c \leq z\}$ under equation (A1). It is readily seen that Γ_z is all points lying on or above the line $V_u = aV_x/(z + b)$. Thus

$$P(z) = \int_{-\infty}^{\infty} dx\, p_1(x) \int_{\frac{ax}{z+b}}^{\infty} du\, p_2(u) \,, \tag{A5}$$

where the dummy variables x and u have been used in place of V_x and V_u.

Taking the derivative of equation (A5) with respect to z and evaluating at $z = D_c$ results in

$$p_3(D_c) = \frac{a}{(D_c + b)^2} \int_{-\infty}^{\infty} x p_1(x) p_2\left(\frac{ax}{D_c + b}\right) dx. \tag{A6}$$

Let

$$\lambda = \frac{a}{D_c + b} \,, \tag{A7}$$

$$p = \frac{1 + \lambda^2}{2n^2} > 0 \,, \tag{A8}$$

and

$$q = \frac{V_{xo} + \lambda V_{uo}}{2n^2} \,. \tag{A9}$$

Substituting equations (A2), (A3), and (A7) through (A9) into equation (A6) then gives

$$p_3(D_c) = \frac{1}{2\pi n^2} \frac{a}{(D_c + b)^2} \exp\left[-\frac{V_{xo}^2 + V_{uo}^2}{2n^2}\right] \int_{-\infty}^{\infty} x\,dx \exp(-px^2 + 2qx). \tag{A10}$$

The integral in equation (A10) is expressable in terms of elementary functions;[A1] it equals

$$\sqrt{\frac{\pi}{p^3}}\, q \exp\left(\frac{q^2}{p}\right).$$

Thus

$$p_3(D_c) = \frac{aS}{\sqrt{2\pi n^2 Q^3}} \exp\left[\frac{1}{2n^2}\left(\frac{S^2}{Q} - v_o^2\right)\right] \,, \tag{A11}$$

where

$$S = V_{xo}(D_c + b) + aV_{uo} \,, \tag{A12}$$

$$Q = (D_c + b)^2 + a^2 \,, \tag{A13}$$

and

$$v_o^2 = V_{xo}^2 + V_{uo}^2 \,. \tag{A14}$$

Equation (A11) is equation (13) of the main text.

A1 Tables of Integrals Series and Products, I. S. Gradshteyn and I. M. Ryzhik, p 337, Academic Press, 1965.

DEGRADED VISIBILITY TESTING AT THE ELECTRO-OPTICAL TEST FACILITY

CPT William M. Decker IV
US Army Electronic Proving Grounds
Fort Huachuca, Arizona 85613

ABSTRACT

The Electro-Optical Test Facility (EOTF) has been developed for testing Army devices working in the visible and infrared portions of the spectrum under conditions of obscuraton due to fog, smoke and dust and in the presence of interfering sources, such as flares, battlefield fires and active countermeasures from both coherent and incoherent sources. The EOTF contains a fog chamber, a smoke/dust chamber and an interference simulator which together give the Army the capability of testing the effects of many different types of countermeasures, both passive and active, quickly and inexpensively.

INTRODUCTION

The US Army Electronic Proving Grounds, located at Fort Huachuca, AZ, has had the mission to perform Electromagnetic Compatability and Electromagnetic Vulnerability (EMC/EMV) testing for the Army. Until recently, this testing was confined to the radio frequency portion of the spectrum. Several years ago, several test officers had the foresight to realize that EMC/EMV testing was also required in the optical and infrared portions of the spectrum if our systems are to be fielded with the fewest problems possible. As a result, the Electro-Optical Test Facility (EOTF) was designed and constructed. This facility can test the Army's electro-optical systems in a simulated dirty battlefield environment quickly and at low cost. Typically, the cost of testing an electro-optical system in the EOTF is ten percent the cost of performing equivalent field tests. As the environment is completely controlled, the same conditions can be repeated at will and, in the case of a prototype competition test, the same situations presented to the system under consideration.

DESCRIPTION OF THE EOTF

The EOTF is a wooden structure 200 feet long and 16 feet square in cross-section. The optical path length is approximately 160 feet. The facility has been constructed of wood to allow EMC/EMV testing in millimeter wave portion of the spectrum. The EOTF is not currently instrumented for this testing. The facility has been designed to be operated completely from the control area as shown at the lower right hand corner of Figure 1. This minimizes the number of technicians needed and reduces the eye harzard in the case where lasers are used either by the item under test or as an interference source.

Figure 1 shows a terrain model located at the far end of the facility. Targets will be presented to the item under test that are appropriate for that system. For example, an anti-tank missile night sight would be tested while looking at model tanks on a terrain background. Reference 1 contains additional information on the construction and spectral accuracy of the scale targets that will be presented to the systems under test. If a laboratory type of test is desireable, minimum resolvable temperature (MRT) targets can be presented. As most of the testing will be done with the operator in the loop, it is envisioned that realistic model targets will be used most of the time. Also located at the far end of the facility is the interference projection system.

Between the control area and the target area are located the intervening environmental simulators, the fog and smoke/dust chambers. These chambers enable the EOTF to recreate a typical dirty battlefield environment.

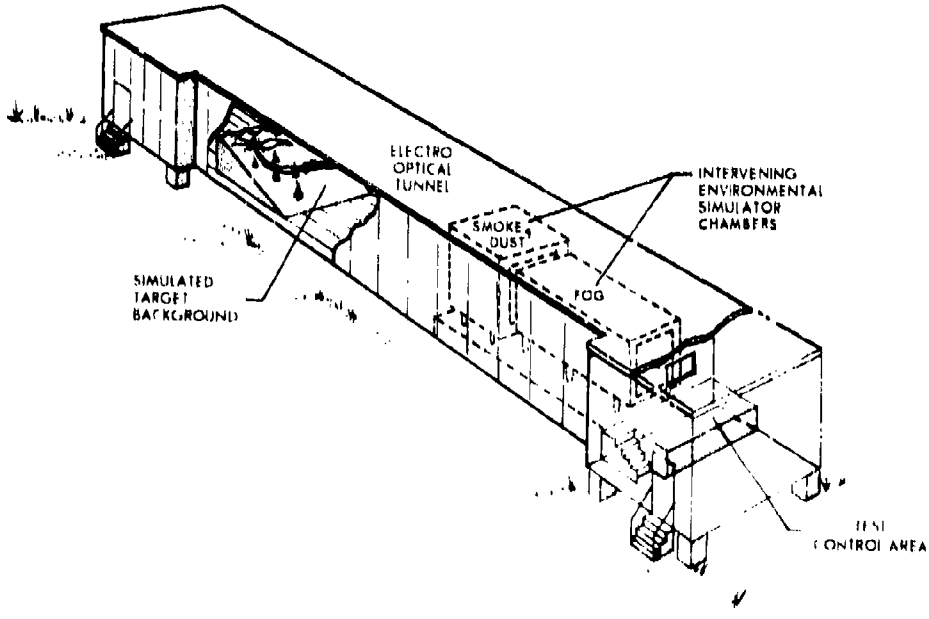

Figure 1. Electro-Optical Test Facility

FOG CHAMBER

In the fog chamber (Figure 2), fog is created very much as it is created naturally. Water in the chamber is heated up, evaporates and saturates the air above the water. The air is quickly cooled by liquid nitrogen flowing through the cooling coils located at the top of the chamber. This condenses the water in the air, forming fog. The particle size distribution, water content and the radius of the most frequently occuring particles (R-max) can be controlled by careful control of the water temperature, air temperature and the flow rate of the liquid nitrogen. To determine the nature of the fog in the chamber, a transmissometer is set up to view through the fog. The receiver is filtered so as to measure transmission at four different wavelengths: 0.46, 1.26, 3.9 and 11.3 microns. The output from the transmissometer is fed through an analog to digital converter to our minicomputer. The computer (Figure 3) uses a modified Mie scattering routine to determine the water content, particle size distribution, R-max and equivalent meteorological visibility. The output is available within 15 seconds of the transmission measurements, allowing near real-time information on the nature of the fog in the chamber. As the fog chamber can be recycled in less than thirty minutes, little testing time is lost if the fog fails to meet the required parameters.

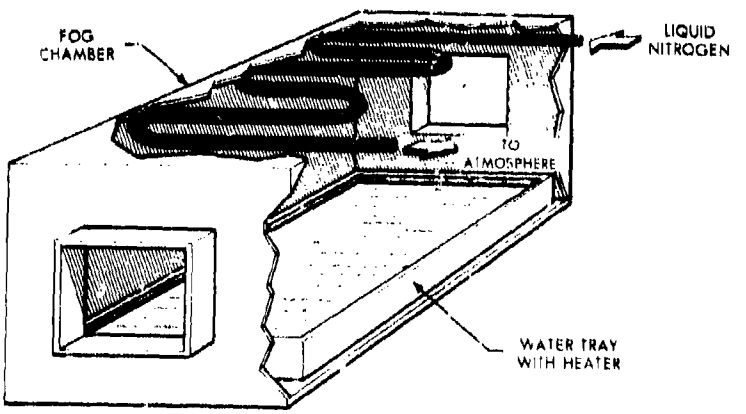

Figure 2. Fog Chamber

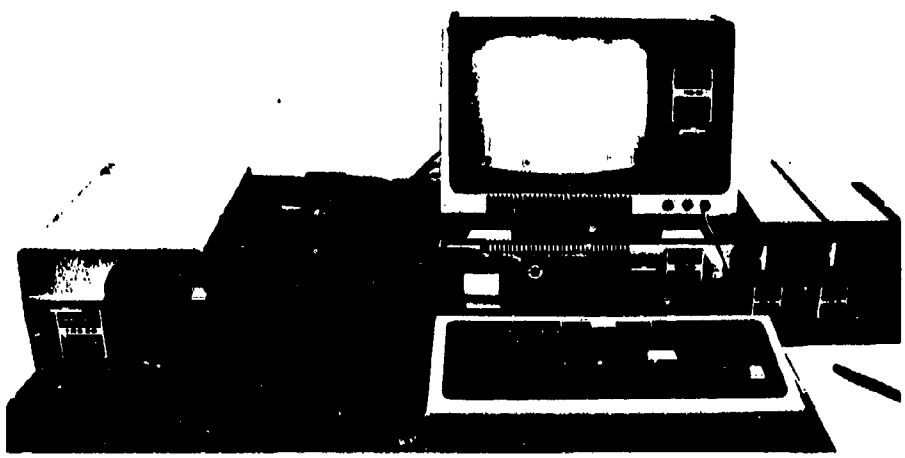

Figure 3. TRS-80 Minicomputer

In general, the formation of fog in nature involves the condensation of water from the air on either particulate nuclei, such as dust (heterogeneous fog), or spontaneously produced water nuclei (homogeneous fog). In either case, the air must contain a certain amount of water vapor, usually reaching supersaturation, before appreciable condensation will begin. The amount of saturation, usually denoted by "S", is inversely related to the temperature of the air. Thus, given an air mass with a certain amount of water vapor present, a decrease of air temperature below a critical point will result in fog formation. The rate of change of S and the magnitude of S determine the type of fog particles most likely to form. At the EOTF, it has been possible to produce fog particle sizes in three different ranges: particle radii of approximately 1 micron, radii on the order of 2-5 microns, and radii on the order of 8-14 microns. Further information concerning the calculations used to obtain the particle size distribution and other information from the transmissometer data are contained in References 2 and 3. The techniques and results are as follows.

SUB-MICRON RADII FOG

Due to the mechanical characteristics of the fog chamber and the cooling mechanism, the rate at which the air is cooled and the amount of saturation possible usually results in fogs of 2-5 micron particle radii. Once the fog is formed, discontinuing the heating of the water at the bottom of the chamber, and thus decreasing the water vapor present in the air, causes fog particles to begin evaporating, becoming smaller in size. In addition, other processes occur which result in the remaining fog being composed of smaller particles. This type of fog takes approximately 30 minutes to form and can last for approximately 10-15 minutes. A typical sub-micron particle size distribution produced along with other pertinent information is presented in Figure 4. This type of fog is typical of fogs that have been measured over dry land at several locations in Europe. One similar fog was measured at Grafenwohr in 1976.

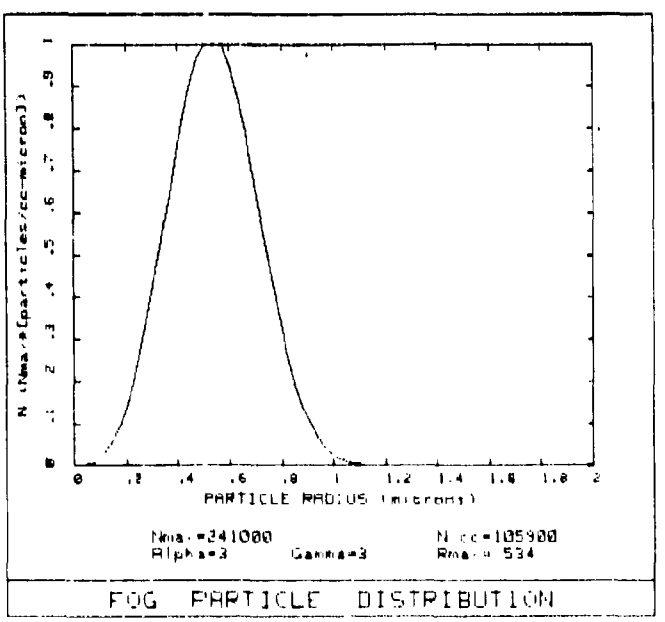

Figure 4 Sub-micron Fog Particle Size Distribution

2-5 MICRON RADII FOG

As described above, 2-5 micron radii fog is most easily formed, due to the fog chamber operating characteristics. It has been possible to produce this type of fog at various temperatures with the ability to "maintain" the fog with periodic heating and cooling cycles, so as to maintain the fog for as long as 2-3 hrs. Typical results are presented in Figure 5. Fogs of this type are most typically found in a marine environment. The fog shown in Figure 5 is similar to the fog measured off the California coast in 1975.

8-14 MICRON RADII FOG

In order to produce larger particle size fog it is necessary to change S slowly. This can be done by either lowering the temperature slowly or increasing the water vapor pressure slowly. Working within the constraints of the fog chamber, it has been found that increasing the water vapor pressure by prolonged heating of the water at the bottom of the chamber will result in fogs with particle sizes on the order of 10 microns. This procedure takes roughly 90 minutes to perform at room temperature and the fog lasts for approximately 20 minutes. Further work is being done to expedite this procedure by cooling the chamber with refrigeration units and thus decreasing the amount of water vapor pressure needed before fog formation will occur. Figure 6 displays a typical 8-14 micron fog produced at the EOTF. This large particle fog is similar to a fog measured at Fort Rucker, AL in 1975. The fog at Fort Rucker was formed due to the nighttime radiation of the heat of the earth and the subsequent cooling of the ground and the water vapor in the atmosphere immediately above the ground.

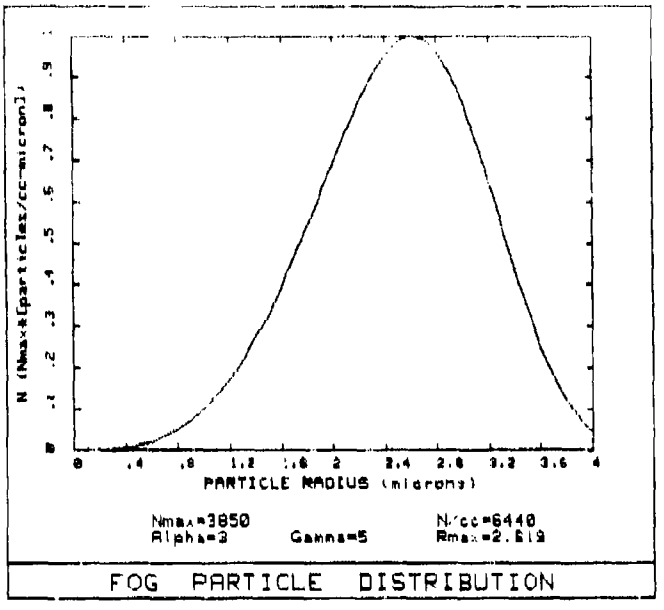

Figure 5 2-5 micron Fog Particle Size Distribution

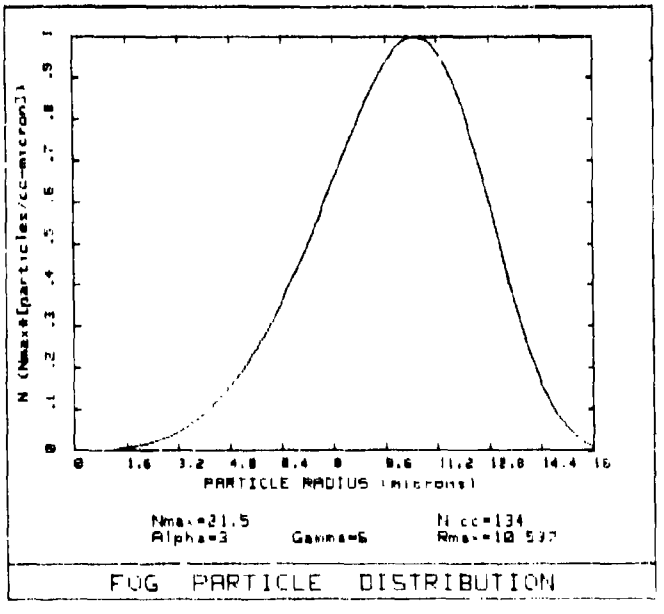

Figure 6 8-14 micron Fog Particle Size Distribution

SMOKE CHAMBER

As this paper is written, the smoke chamber is under construction. The EOTF smoke chamber (Figure 7) has been designed to handle the currently identified threat smokes, dust and haze. The primary smokes that are planned to be presented to the items under test are hexachloroethane (HC), white phosphorus and fog oil. The smokes will be characterized by measuring the spectral transmission of the smokes using a General Dynamics spectral radiometer with the Nicolet FFT processor and by making mass concentration measurements using the Anderson impactor. The optical and physical properties of the smokes will be compared to the results from the Smoke Week tests and other field tests to validate the accuracy of the smoke conditions generated in the EOTF. The smoke chamber is of the static type with the smoke generated within the chamber. Lights are being mounted within the chamber to simulate the interference effects of the ambient sunlight when scattered off the smoke. The smoke chamber will have air curtain windows at the ends of the chamber to provide a clear optical path through the chamber. This will eliminate smoke deposits on the windows as a source of error in testing.

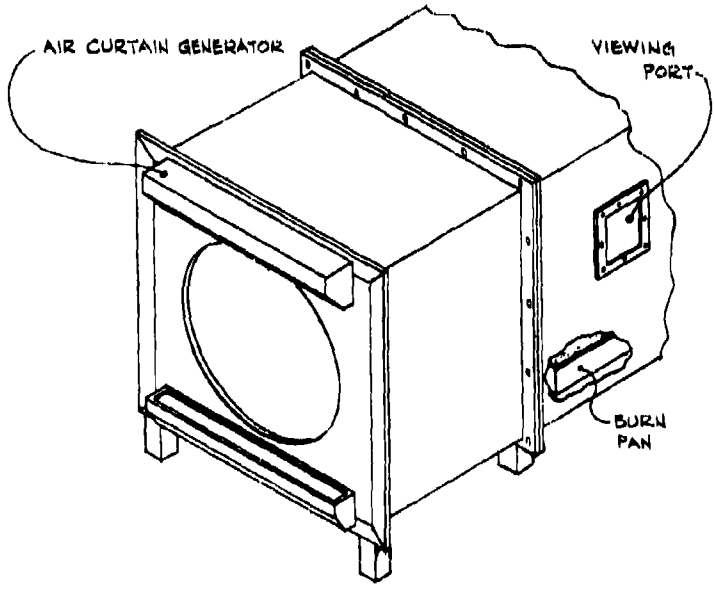

Figure 7 Smoke Chamber

INTERFERENCE SIMULATION SYSTEM

In order to simulate the effects of active interference sources on the electro-optical systems under test, the EOTF has an interference simulation generator (Figure 8). This system consists of visible, infrared and laser sources operating through a shutter system to control the duration of the interference and irises to control the intensity of the sources such as flares, battlefield fires, artillery rounds, mortars and muzzle flashes (Ref. 4 and 5). These will be used to reconstruct the interference source and present it to the system being tested. The mirrors on the X-Y traveling table allow the apparent source of the radiation to be moved very close to the target or quite far away with an accuracy of better than 0.03 degrees. Laser sources covering the visible and near infrared are currently on hand, and a tunable, high-power carbon dioxide laser is on order. A detailed discussion of the interference projection system is contained in Reference 6. The interference generator gives the EOTF the capability of simulating a wide variety of interference sources and countermeasures.

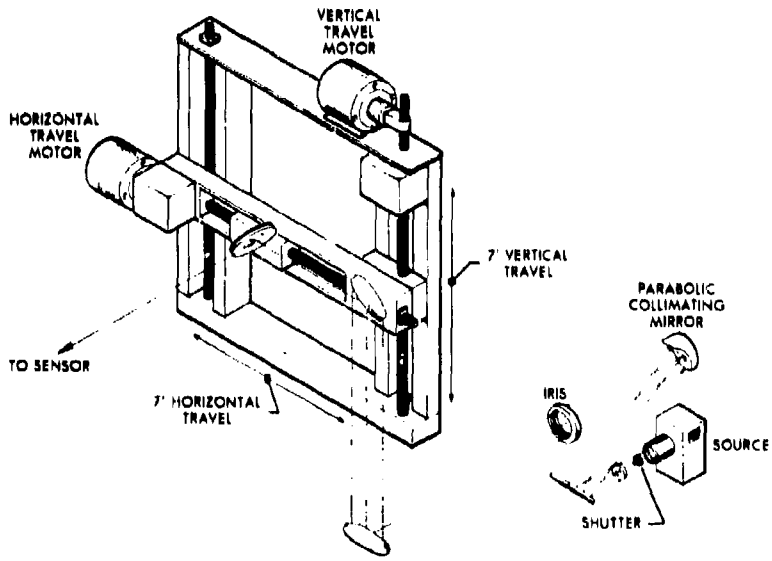

Figure 8. Interference Simulator Projection System

SUMMARY

The Electro-optical Test Facility gives the Army a testing tool that will allow quick, inexpensive testing of electro-optical systems. This testing will not replace field testing, but rather will enhance its effectiveness by highlighting those areas requiring detailed study in a field environment. In cases where insufficient funds preclude field testing in a degraded environmet, the EOTF can provide project managers definitve data concerning the performance of the system under less than ideal conditions. This same data can be used by commanders to insure that these electro-optical systems are employed to maximum advantage in the dirty battlefield environment.

REFERENCES

1. Crowe, Devon G., "Scaled Infrared Targets and Backgrounds for the Electro-Optical Test Facility", Infrared Physics, Vol. 20, pp. 29-31, (1980).

2. Crowe, Devon G., Cohen, D. K., and Dereniak, Eustace L., "Infrared Propagation and Performance Modeling at the Electro-Optical Test Facility", Applied Physics, Vol. 19, No. 12, pp 1953-1958, (1980).

3. Cohen, D. K., "Analysis of Fog Generated at the Electro-Optical Test Facility", to be published.

4. Davis, R. M., "Some Infrared Measurements of Weapon Shellburts", Avco Corporation, Electronics Division, Cincinnati. Report No. 2708, 1969.

5. Nanevicz, J. E. and R. C. Honey, "Thermal Imaging Camera Observations for Mortar and Artillery Firings", Stanford Research Institute, Menlo Park, CA. Meeting of IRIS Specialty Group on Infrared Imaging, February 1976.

6. Crowe, Devon G. and Nowak, Thomas M., "An Active Interference Projector for the Electro-Optical Test Facility", Infrared Physics, Vol. 20, pp 299-308, (1980).

PLANS FOR THE EVALUATION OF SMOKE MUNITION EXPENDITURE MODELS

Bernard F. Engebos
Atmospheric Sciences Laboratory
White Sands Missile Range, New Mexico

ABSTRACT

Attenuation of electromagnetic radiation is dependent upon such factors as scattering by aerosols and precipitation and crosswind integrated concentration of the plume of smoke deliberately injected into the line of sight of an electro-optical device. The amount of chemically produced smoke (munition expenditures) required to screen/obscure such a device can be derived.

This paper presents the details of two planned experiments to evaluate and verify smoke munition expenditure models. The first test is scheduled during April 1981 at WSMR and the second in Germany in the Spring of 1982.

DUST OBSERVATIONS IN THE BATTLEFIELD ENVIRONMENTS WITH TAILORED SOILS (BETS) SERIES

James B. Mason, Katherine S. Long, and Lewis E. Link
U. S. Army Engineer Waterways Experiment Station
Vicksburg, Mississippi

ABSTRACT

The generation of dust by combat activity is a subject of work now in progress at the U. S. Army Engineer Waterways Experiment Station (WES). The work has involved participation with other Army laboratories in field exercises as well as in-house testing to determine soil and terrain properties affecting atmospheric loading by explosives. The extreme difficulty of obtaining representative measurements of explosive dust clouds is a major obstacle making it necessary to consider alternative approaches.

This paper describes the results obtained at WES under the Battlefield Environments with Tailored Soils (BETS) test series. A qualitative model of the loading process with some energy considerations is included. Different methods for measuring mass loading are compared. Finally, observations with different soil types and properties and their effects on dust generation are discussed.

1. INTRODUCTION

The U. S. Army Engineer Waterways Experiment Station (WES) is conducting a series of experiments for the study of battlefield environments using tailored soils. The objective of BETS is to determine those terrain properties that influence the production of dust by high explosives (HE) and other activities on the battlefi d. The need for such tests stems from the fact that the performance of many weapons systems is severely degraded in optically obscured environments.

1.1 PURPOSE

Models of weapons systems environments, like the EOSAEL of the Atmospheric Sciences Laboratory (ASL) [Reference 1], and weapons systems performance, like BELDWSS of the U. S. Army Missile Command [Reference 2], incorporate dust generation features. However, there is a need for more accurate relations to describe the amounts of dust or atmospheric loading produced by combat activities as functions of terrain conditions. The development of such relations and of methods for their use in battlefield equipment performance evaluations is the goal of the BETS series.

1.2 SCOPE

Efforts to date have been confined to the effects of real and simulated munitions bursts. Future plans include investigations of the effects of muzzle blasts, vehicles and aircraft. In this paper we describe the underlying theory and features of burst phenomena and discuss related test results. Since the WES has supported several recent battlefield environment tests the observations made herein incorporate those results as appropriate.

2. BACKGROUND

2.1 EXPLOSION PROCESS

Atmospheric loading by the interaction of HE with the terrain is a complex process. The brief description which follows will serve to illustrate the separate loading mechanisms and to identify the controlling terrain properties. It is restricted to an uncased HE detonated at the surface above a level homogeneous terrain medium.

The process consists of: (a) the conversion of the HE mass to a superheated gas which expands rapidly to an equilibrium volume, (b) the development of two hemispherical shock fronts, one in the air and the other in the soil medium, (c) the excavation of solid material as kinetic energy is transferred from the expanding gas to the soil medium, and (d) the disturbance of the surrounding surface by the shock fronts and by impacting ejecta. Three sources of dust may be identified, the moving surface of the developing crater during the excavation process, the exposed surfaces of ejected material, and the surrounding terrain surface. The relative contribution from each of these depends upon the physical properties of the terrain and the size and configuration of the blast.

Note that we have not included in this description the development of buoyancy and entrainment in the atmosphere. Here we are concerned only with the deposition of dust in the air. Descriptions of bouyancy and entrainment are given in References 3 and 4 and more detailed discussions of explosive cratering may be found in Reference 5.

2.2 LOADING MECHANISMS

EXCAVATION. The active mechanism on the expanding crater surface during the excavation process is primarily wind erosion However, the standard theory may not be applicable because of the extreme velocities and pressures experienced. Eroded material moves along the surface and is ejected at the rim in a thin conical sheet. The process is illustrated in Figure 1. The ejection angle remains fairly constant and depends on soil density, water content and charge placement [Reference 6]. It may also be related to the angle of repose.

Ejection velocities diminish from an initial peak until the process ends with a massive slumping of material over the rim of the crater. This is consistent with an increasing surface area and mass over which the kinetic energy from the expanding gas is being distributed. The ejecta having the

highest velocities have been found to originate nearest the original surface [Reference 5]. Most of the dust from this process is probably deposited in the early stage. Grain sizes, plasticity, and water content are believed to be the properties controlling this process.

ABLATION. As larger fragments of ejected material pass through the air, particles are ablated from their surfaces. Examples of this process may be seen in photographs of such diverse events as the Mt. St. Helens eruption [Reference 7], nuclear simulations [Reference 8], and our own tests [Figure 1]. The separation of individual dust particles is thought to be due largely to aerodynamic erosion but may also involve thermal and outgasing effects. Water content, plastic and cohesive properties, and grain sizes are considered dominant controlling properties.

PORE AIR. A substantial deposit of dust is often observed along the terrain surface to considerable distances from a blast. This material appears sometime after the blast and rises very slowly, usually to no more than 2 or 3 meters in height. It is caused chiefly by the expansion of pore air in the soil following passage of the shock front, and to lesser degree by the impacts of ejecta. The air in soil pore spaces is compressed during the overpressure phase, and rapidly expands in the rarefaction phase to separate and impart small initial upward velocities to soil grains at the surface which are then lifted farther by turbulence. Soil moisture and porosity as well as vegetation are believed to dominate this process.

2.3 THEORETICAL BACKGROUND

Before discussing the test results, a brief comment on the distribution of deposited material may be helpful.

GAS EXPANSION. The distance to which the initial gas expansion extends may be estimated roughly from the gas law. For one kilogram of TNT with a heat of combustion of 1100 calories per gram and for total mass conversion and a specific heat of unity, the resulting gases will expand to a radius of 0.82 meters. This is of the same order of size as the crater radius in loose soil.

EJECTA DYNAMICS. The distance to which ejecta will travel for a given charge weight may be derived from observations of ejection angles by Andrews [Reference 6] and ejection velocities by Seebaugh [Reference 9]. Seebaugh provides the empirical relation

$$v_{ej} = 566\, W^{1/6} \quad ms^{-1} \tag{1}$$

where yield, W , is in megatons. The result for a 1 kilogram charge at the surface is $18.2\ ms^{-1}$. For an ejection angle of 45°, which is typical, the range of impact for a simple ballistic trajectory in vacuum would be 47.7 meters. Of course the actual value will be reduced by drag forces.

AERODYNAMIC EFFECTS. We may estimate the distances to which individual dust particles are deposited from energy considerations by employing Stokes' formula. The rate at which the velocity of a particle of radius R falling through a fluid of viscosity μ is diminished by aerodynamic drag is

$$\frac{dv}{v} = -6\pi\mu k dt \tag{2}$$

Integrating and setting $v = v_{ej}$ at $t = 0$ yields

$$v = v_{ej}^{-6\pi\mu Rt} \tag{3}$$

from which we may compute the time required to attain the settling velocity, v_s . In turn, integrating v dt yields the distance traveled by the particle before v_s is reached.

Representative travel distance values are given in Table I. As an example, a 0.01 particle of quartz will travel only 0.032 cm before being dominated by the air stream.

TABLE I

Particle Radius mm	Travel Distance in cm by Particle Type		
	Quartz	Mica	Charcoal (pine)
0.01	0.032	0.035	0.0043
0.1	3.23	3.53	0.426
1.0	323	353	42.6

It is clear that individual dust particles will become captives of the flow regime soon after they are separated from the mass. Thus, individual dust particles swept from the surface by the initial expansion will not be deposited appreciably beyond the expansion radius.

SUMMARY OF VARIABLES. Dust particles cohere to the soil mass because of electrical and chemical forces and a significant mechanical action is required to separate them. One important

factor influencing cohesion is water which forms a film on grain surfaces. It follows that particle surface area, and hence size and shape, is important. From such considerations, the soil properties believed to most significantly influence or correlate with dust loading are the grain size distribution, water content, bulk density, porosity, Atterburg limits and clay minerology. Descriptions of these properties and their measurements may be found in Reference 10. Additional terrain factors that must be considered are the vegetation type and amount, vegetation root density, sod depth (depth of the A horizon), and the mechanical state of the surface.

3. BETS

3.1 DESCRIPTION OF TESTS

The concept of the BETS series is to conduct explosive tests on specially prepared soil beds in which the properties just identified can be controlled. In FY-80, tests were conducted at three locations (Table II). The B series was conducted in cooperation with the ASL's DIRT-III series and with the WES, Structures Laboratory's Munitions Bare Cased Equivalence tests. The C portion was a joint effort with the Tropic Test Center, Panama.

TABLE II. BETS-80 OBSCURATION TESTS

Designation	Location	Date	Objective
BETS-80 A	Vicksburg, MS	Continuing	Soil type, moisture, strength, and vegetation effects
BETS-80 B	Ft. Polk, LA	April	Optical propagation effects
BETS-80 C	Ft. Clafton, Panama	August	Moisture, vegetation effects

Test beds were prepared as shown in Figure 2 with soils selected according to their grain size distribution. Three principal soils were chosen to reflect a wide range of terrain conditions. A heavy clay with 90-95 percent by weight consisting of particles less than 0.01 mm in diameter provides a highly cohesive and plastic soil, and washed sand with 0-10 percent less than 0.01 mm provides a non-cohesive, nonplastic soil. Intermediate conditions are provided by a silt of 45-55 percent less than 0.01 mm. Gradation curves for these materials are shown in Figure 3. Moisture content and density were controlled by thoroughly mixing measured amounts of water and dried soil materials and packing the resulting soils in the test beds.

3.2 DESCRIPTION OF MEASUREMENTS

Tests were conducted with HE of 0.227, 0.454, 2.27 kg yields placed on test beds in surface tangent (ST) and surface tangent buried (STB) configurations (cf. Figure 2). Measurements at each test included soil properties, ejecta mass distribution, crater depth and diameter, and the resulting dust cloud. Soil measurements, includingwet and dry density, water content, cone index, and remolding index, were made following procedures described in Reference 10. Meteorological data consisting of temperature, wind, humidity, and insolation were also measured at the sites.

The measurement of the dust clouds has posed a particularly difficult problem. Because of the severe environment, conventional samplers cannot be placed near the blast, and the transient nature of the events makes it difficult to collect sizeable samples. We have used impact samplers coated with adhesive tape and photographic imagery, both with limited success. At Ft. Polk, La., optical transmission data and conventional samples were obtained by the ASL, but results are not yet available. The photographic coverage was generally obtained using dual 70 mm Hulcher sequencing cameras operated stereographically with a sequence interval of one second. However, the stereographic feature has not been utilized. Ejecta samples were obtained in ordinary 23 cm pie pans and on 60 by 120 cm flat panels positioned at measured intervals around the point of burst (POB) as shown in Figure 2.

3.3 ANALYSIS AND RESULTS

EJECTA. In BETS-80 B where 2.27 kg explosive charges were used, ejecta samples were collected from 26 events using pans and from 11 events using panels. In BETS-80 A, with 0.227 kg charges, 12 events were sampled with each method. The results of test A are summarized in Figure 4. They are presented as reduced depth, De, and reduced radius, Re, for purposes of validating the sampling procedure against published data. Linear regression results are found to agree well with results of Rooke (Reference 11) and with Andrews (Reference 6) who used a continuous sampling method with an efficiency approaching unity. His curve can be seen to have a similar slope, but displaced to much higher values; reflecting the lower efficiencies of the pan and panel collectors. The resulting linear regression equations shown in the figure can be adjusted by a simple constant multiplier to produce results that approximate near 100 percent sampling efficiency.

We have determined the ejecta mass distributions obtained from BETS-80 A data with this sampling procedure (Figure 5a), and integrated the results about the axes of the craters to obtain totals

of mass ejected. These mass values were divided by the mean in situ bulk density to yield ejecta volumes which are compared to computed apparent crater volumes in Figure 5b. It can be seen that significant differences exist. In view of the earlier discussions of dust deposition it is clear that there is some risk associated with relating ejecta measurements directly to mass loading in the cloud, but this method is considered to be an improvement over that which uses only crater volume.

Grain sizes in the ejecta will tend to be larger than in the in situ material due to the removal of fines to form the cloud. A sieve analysis of pan samples is shown for silt in Figure 3 where it can be seen that the quantity of fines is substantially reduced. Test data that will be analyzed in the near future should provide more information on how to relate in situ grain size distribution to those of the dust cloud. These relationships can be used directly to estimate the portion of ejecta mass that composes the cloud mass.

DUST CLOUD. Samples of the airborne dust can be obtained on adhesive impactors placed around the POB. Such devices were used in tests A and C. The impactors were mounted on electron microscope stubs and analyzed by photographing the sample and counting the particles. Figure 6 shows an example of the data (inset) and the results from test A. Sampling efficiency again must be considered (see Appendix A for a discussion of this), and sampling time, which is necessary, is difficult to measure accurately. The concentrations for diameters ranging from 0.003 to 0.3 mm were obtained by estimating the sampling time from photographs and assuming a homogeneous distribution throughout the cloud.

In an effort to evaluate relative mass loading from various sized events for which samples are not available, the duration of the visible dust cloud was considered. Sequenced photographs from DIRT-II and BETS-80 B were used. We found that the clouds from tests on wet or moist soils sometimes outlasted those on dry soils, suggesting that substantial portions of the clouds may have been composed of water droplets. In general, however, clouds from larger events and from dryer sites were most persistent. Figure 7, which includes data from DIRT-II, summarizes the results. When tests from dry sand, silt, and clay pads under identical conditions with moist terrain surface (to minimize dust skirts) were compared, the clouds for silt and clay were found to be about equal in persistence at about twice the value for sand.

An interesting result seen in the imagery from BETS-80 B is the dust skirt that surrounds the blast but remains near the surface. The humidity during that series was typically higher in the morning but diminished as solar insolation increased each day. Figure 8 shows clouds at T + 10 seconds

for three events conducted on dry soils at different times on 30 April. In the morning when surface moisture was highest the cloud is in the form of a vertical column and is confined to the vicinity of the burst (Figure 8a). In the afternoon at the same location the cloud rose from the surface to considerable distances from the POB (Figure 8c). The incorporated material clearly did not originate in the crater (excavation process). Since it forms a substantial portion of the cloud, it is also clear that the tailored soil in this particular event was not accurately represented, because much of the resulting obscuration arose from this skirt and hence was native soil.

The event depicted in (Figure 8b) is a graphic example of an early morning shot for which the surface was moist. Note the small plume to the right of the burst. This proved to be the site of a bed prepared with dry clay and the plume has been raised by the shock front. On other shots, similar results were observed above the dirt road to the left of the site but not over the more vegetated area on the opposite side.

4. SUMMARY AND CONCLUSIONS

From the BETS series data, the following conclusions can be drawn:

(a) Substantial portions of dust can be generated from the surface around a POB.

(b) Soil moisture and vegetation conditions have a large impact on dust contribution.

(c) Sandy soils are less productive of dust than silts or clays.

(d) Clays do not appear appreciably more productive than silts, probably due to the cohesiveness of clay.

Unanswered questions remain regarding actual amounts and size distributions of airborne material; however, sampling methods have been developed that offer promise for solving this problem. Modifications of particle size distributions due to blast effects may be significant in some soils; this phenomenon bears further study. Measurements of loading by pore air expansion in relation to terrain surface conditions are desirable; this should be equally true for muzzle blast loading.

Crater volume as an indicator of loading has been largely ignored in this series because of the

uncertainties associated with soil compaction and back filling. However, the modeling of the excavation process is needed to properly describe the deposition of material and the effects of variations in munition size and placement. To date, munitions effects have been explicitly omitted in the BETS series because of the desire to assess terrain effects. However, munitions effects will be examined later in the series.

REFERENCES

1. Duncan, L. D., ed, EOSAEL 80, 2 Vols., U. S. Army Electronics Research and Development Command, Report No. ASL-TR-0072, January 1981.

2. Leonard, J. P., R. E. Yates, and C. L. Lewis, Laser Designator/Weapons System Simulation FY-77 Executive Summary, U. S. Army Missile Research and Development Command, Technical Report No. TG-77-9, 3 July 1977.

3. Thompson, J. H., ASL-DUST: A Tactical Battlefield Dust Cloud and Propagation Code, 2 Vols., U. S. Army ERADCOM, Report No. ASL-CR-80-0143-1, June 1980.

4. Ebersole, J. F., R. Vaglio-Laurin, and D. S. Dvore, Optical and Fluid Dynamic Properties of Explosion-Produced Dust Clouds, U. S. Army ERADCOM, Report No. ASL-CR-80-0043-2.

5. Roddy, D. J., R. O. Pepin and R. B. Merrill, eds., Impact and Explosion Cratering, Pergamon, New York, 1977.

6. Andrews, R. J., "Characteristics of Debris from Small-Scale Cratering Experiments," pp 1089-1100, D. J. Roddy et al., eds. op. cit.

7. Findley, R. "St. Helens, Mountain with a Death Wish," National Geographics Mag., Jan 1981, p 3.

8. Wisotski, J., "Dynamic Ejecta Parameters from High-Explosives Detonations," p 1116 FF., D. J. Roddy, et al., Eds., op. cit.

9. Seebaugh, W. R. "A Dynamic Crater Ejecta Model," pp 1043-1054, D. J. Roddy et al, eds., op. cit.

10. U. S. Army Office of the Chief of Engineers, Engineer Manual EM1110-2-1906: Laboratory Soils Testing, May 1965.

11. Rooke, Jr., A. D., et al., Cratering by Explosions: A Compendium and an Analysis, U. S. Army Engineers Waterways Experiment Station, Technical Report N-74-1, January 1974.

APPENDIX A. DISCUSSION OF THE COLLECTION EFFICIENCY OF IMPACT SAMPLERS

The velocity v, at which a spherical particle of density ρ, and radius r, will fall in a fluid is given by Stokes' formula;

$$v = \frac{2}{9} r^2 \frac{\rho g}{\mu} \tag{1}$$

where g is the accelerating force (gravity) and μ is the viscosity of the fluid. For a quartz particle in air at standard pressure, $\rho = 2.65$ gm/cc and $\mu = 1.79 \times 10^{-4}$ (centimeter-gram-second units) so that for a 1.0 μm radius particle the fall velocity, $v = 0.032$ cm sec^{-1} and for a 10.0 μm particle, $v = 3.23$ cm sec^{-1}.

If we expose a horizontal surface of area A, for a time T in still air containing a uniform dispersion of N_c m^{-3} of particles of 1.0 μm radius falling under the force of gravity, the exposed surface will accumulate these particles at a rate

$$\frac{dN_c}{dt} = N \cdot v \cdot A \tag{2}$$

where N_c is the number of particles collected. As shown in Figure A1a all particles lying within the vertical cylinder above A will be intercepted by area A. However, since the area will only be exposed for a finite time T, there is some distance $D(=vT)$ for which particles lying above D at initial exposure (time = 0) will not be collected because they will not reach the surface in time T. Conversely, a volume is identified by DA(or vTA) in which all particles are collected.

Now suppose the air is in uniform horizontal motion, V, to the right (in the figure). Then all of the particles in the original cylinder will not be intercepted by A. The particle indicated by B for example will pass to the right of A. A new sample volume is defined as in Figure A1b. The height of this volume is still D and the volume still equal to AD. A different set of particles will be collected but, since we specified a uniform concentration N, the total will be the same.

Next let us suppose that the particle distribution is confined to a fixed region of the moving air, say a vertical sheet of thickness W, and instead of an exposure time T we simply allow the passage of the contaminated volume to determine T. The time required for this passage will be $T = W/V$ sec when the test surface A is within the volume. The sampled volume is found to be AD where $D = vT$ and we have redefined T as W/V hence,

Sample volume = AvW/V (3)

The total number of particles collected will be $N_c = NAvW/V$ from which

$$N = \frac{N_c V}{AvW} \tag{4}$$

Thus we need to measure (1) the velocity of flow, V and (2) the width of the region, W in the direction of V in order to determine the concentration N .

To apply this equation in a realistic setting we must consider that particles of varying sizes will exist in different amounts. Thus v , a function of particle radius r, is not a constant. It is then necessary to integrate or sum eq (4) over the range of r . Noting that N_c is also a function of r and with substitution from (1) into (4),

$$N_r = N_{cr} \left(\frac{V}{AW}\right)\left(\frac{9\mu}{2\rho_g r^2}\right)$$

Thus the size distribution of the medium, N , is related to that of the sample by a constant term $\left(\frac{2\rho_g}{9A\mu}\right)$, a measured quantity $\left(\frac{V}{W}\right)$ and the function $\frac{1}{r^2}$.

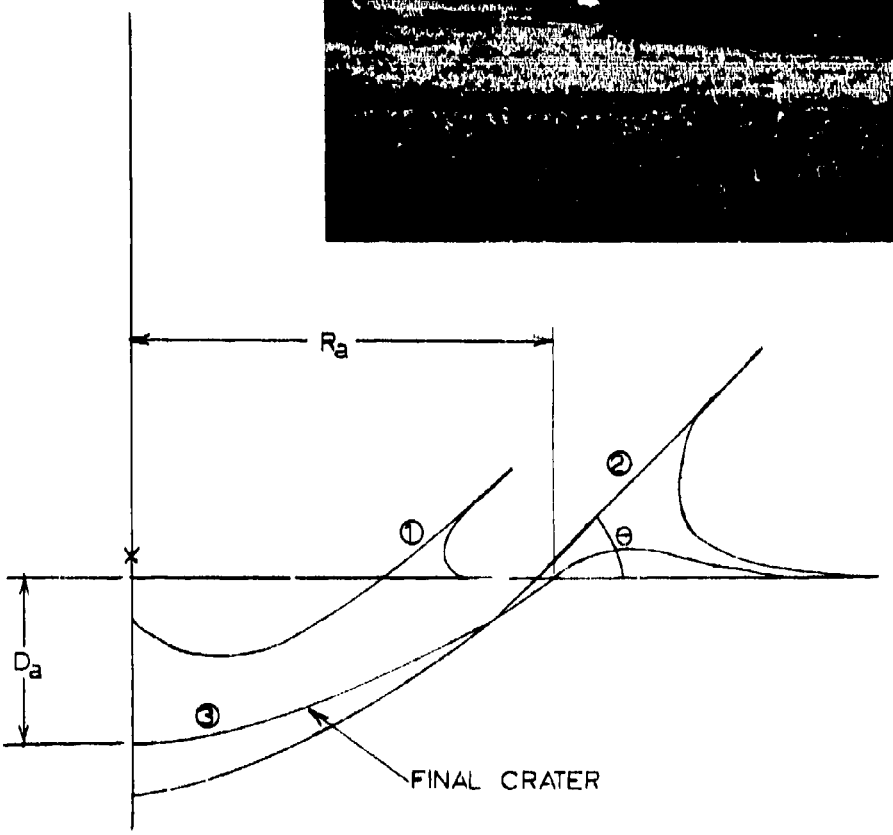

Figure 1. This schematic drawing depicts a half-section view of the explosive crater in three separate stages of development. The point of burst (POB) is indicated by (x). Positions (1) and (2) show successive stages of the advancing crater surface with ejecta exiting at a relatively constant angle at the rim. Position (3) is the final surface of the apparent crater. Note the backfill at the bottom and the raised lip. The apparent depth, Da, and apparent radius, Ra, are measured in explosive tests. The photograph shows a surface detonation on dry silt. Note the ejecta spears with trailing dust.

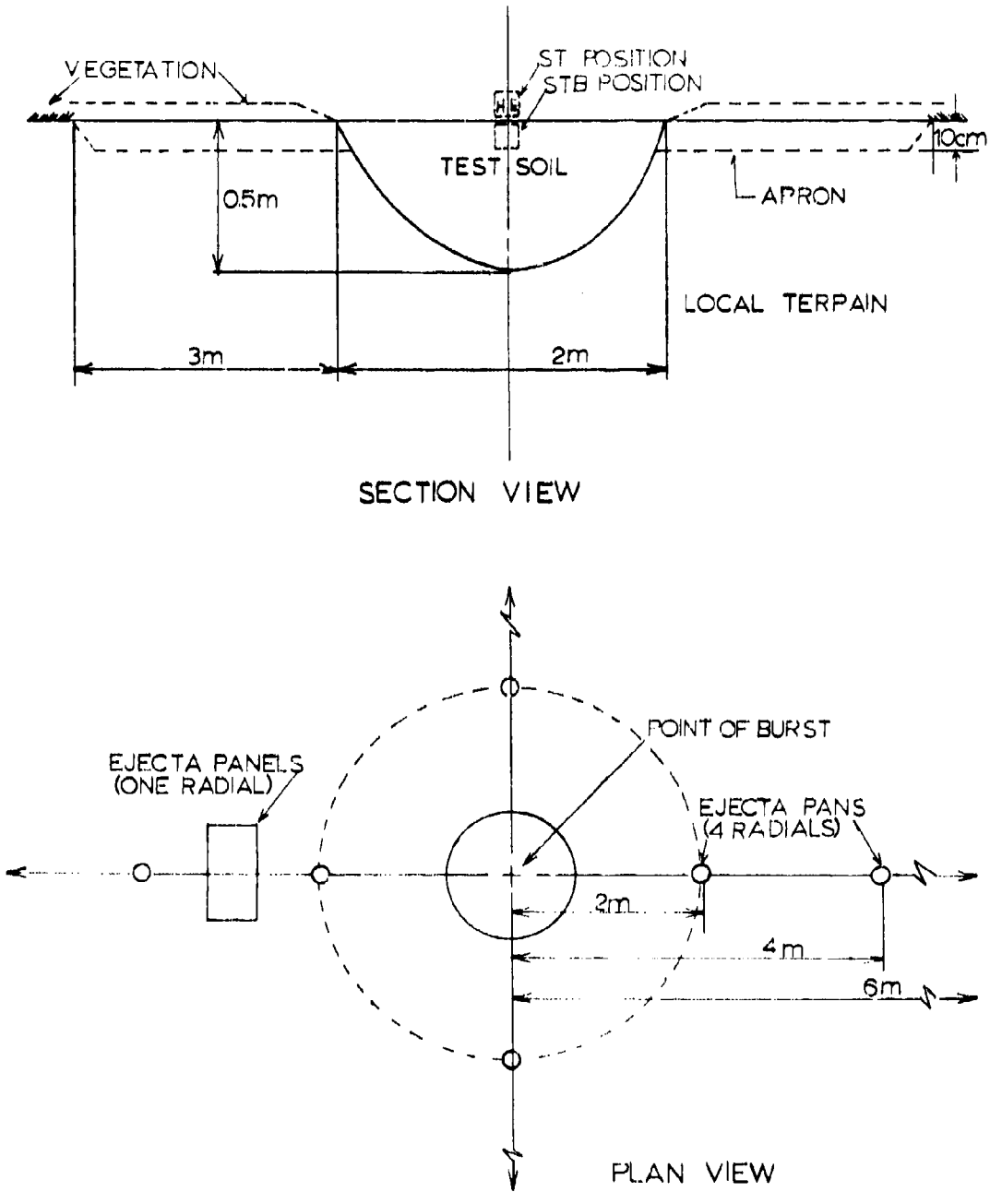

Figure . The test arrangement for BETS is indicated in these diagrams. Note the difference in scales. The section view shows the manner in which material is removed to allow placement of the test soil. The plan view indicates the positions of samplers. At least three pans are placed on each radial.

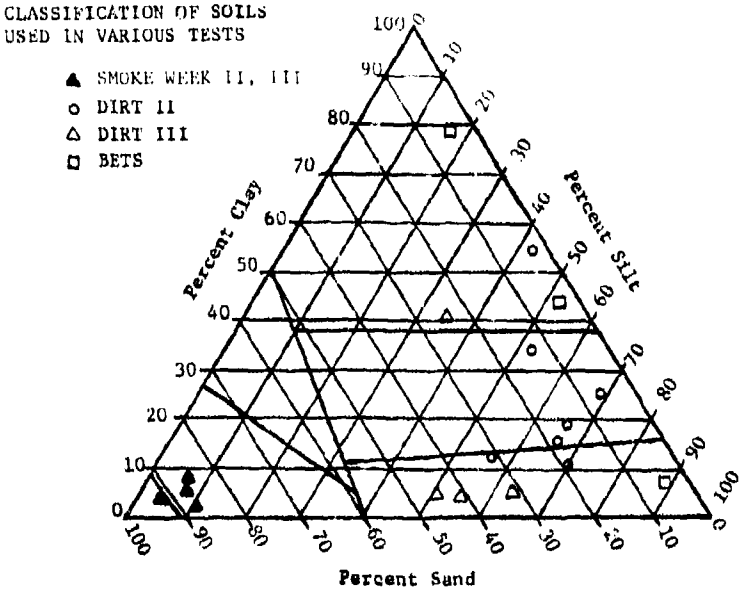

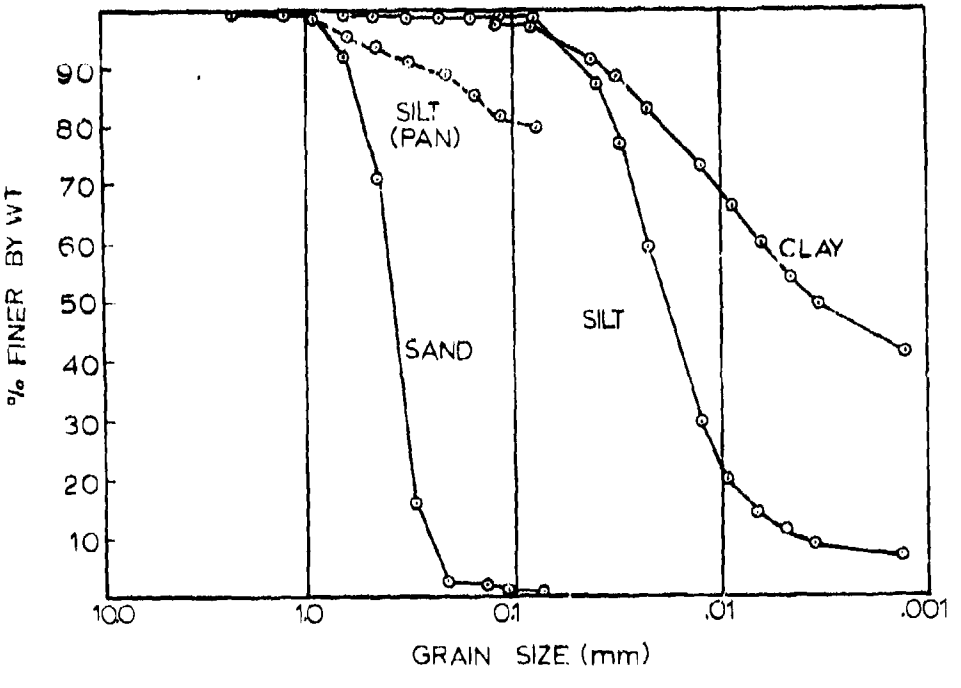

Figure 3. Grain size analyses for the three BETS soils are shown. The dashed silt curve is the result of a sieve analysis of the material collected in ejecta pans after a test.

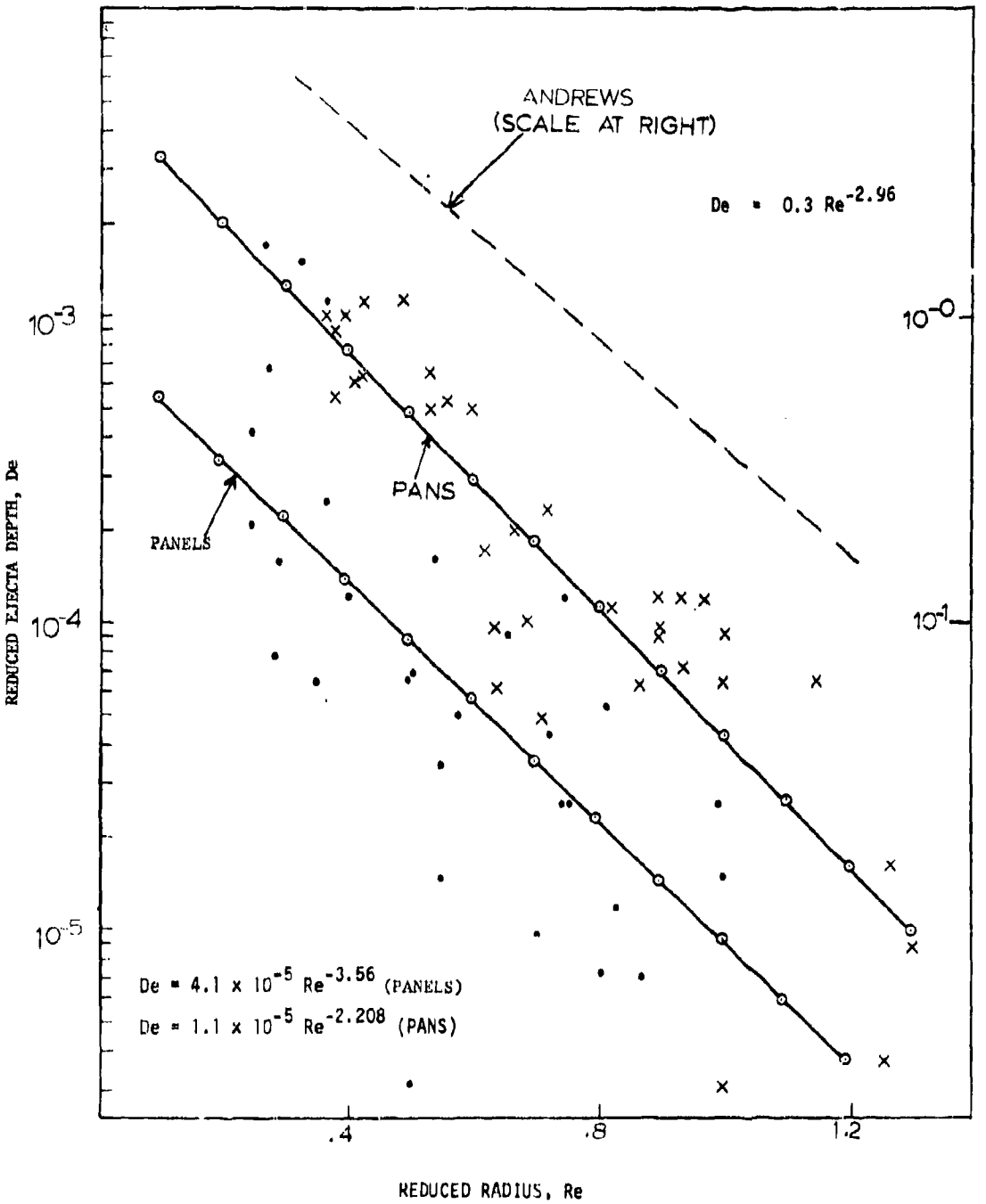

Figure 4. The reduced ejecta depth (depth divided by crater volume to the one third power) is plotted against reduced radial distance for both pan and flat panel collectors from the BETS-30 A slit tests. Andrews (Reference 6) results from sand are shown for comparison.

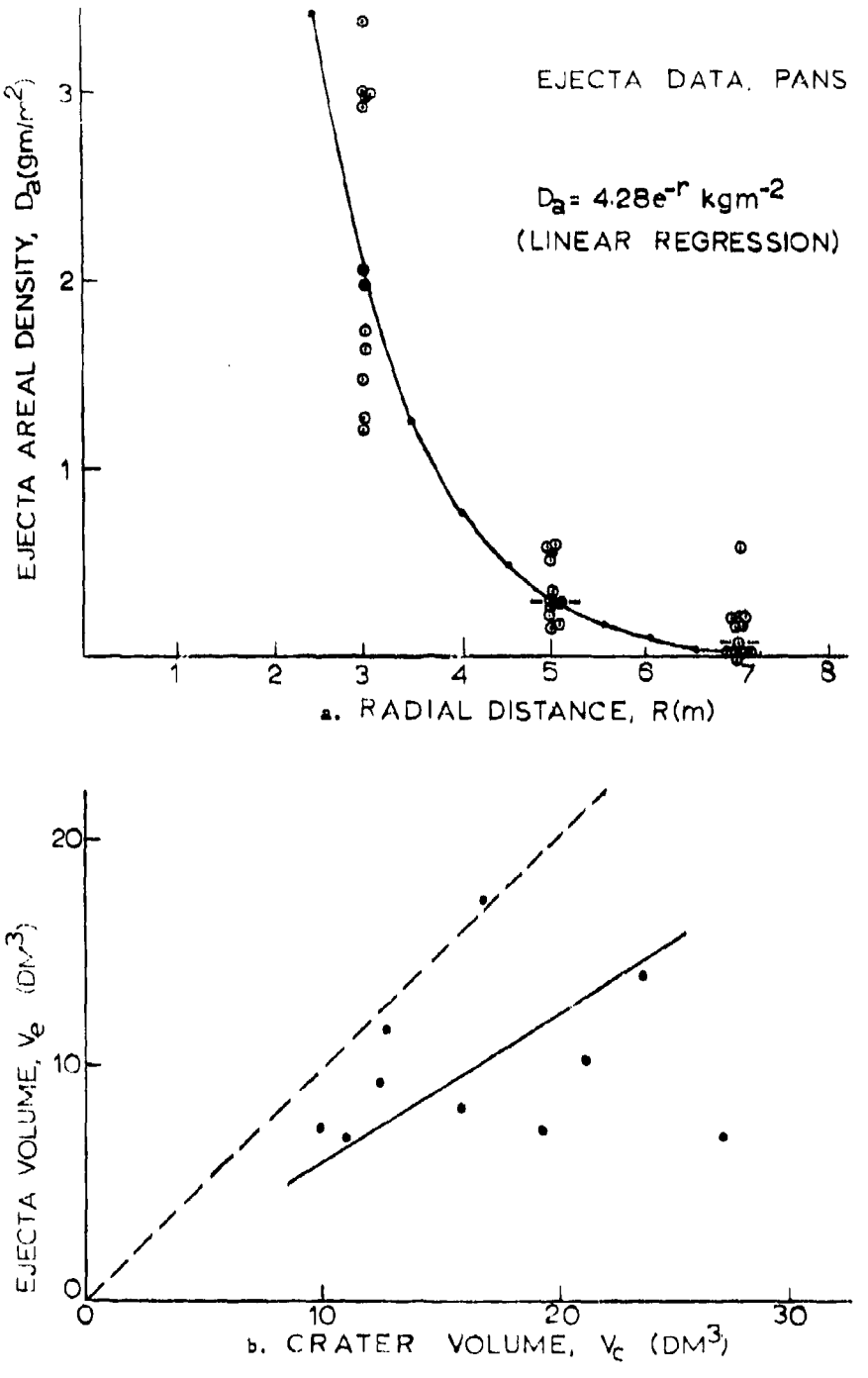

Figure 5. The measurements of ejecta material collected in 23 cm diameter pans are illustrated (top) in terms of areal density vs. radial distance. A linear regression provided the curve shown which was then integrated to yield total ejecta volume. The comparison of that volume to apparent crater volume for several events is shown at bottom.

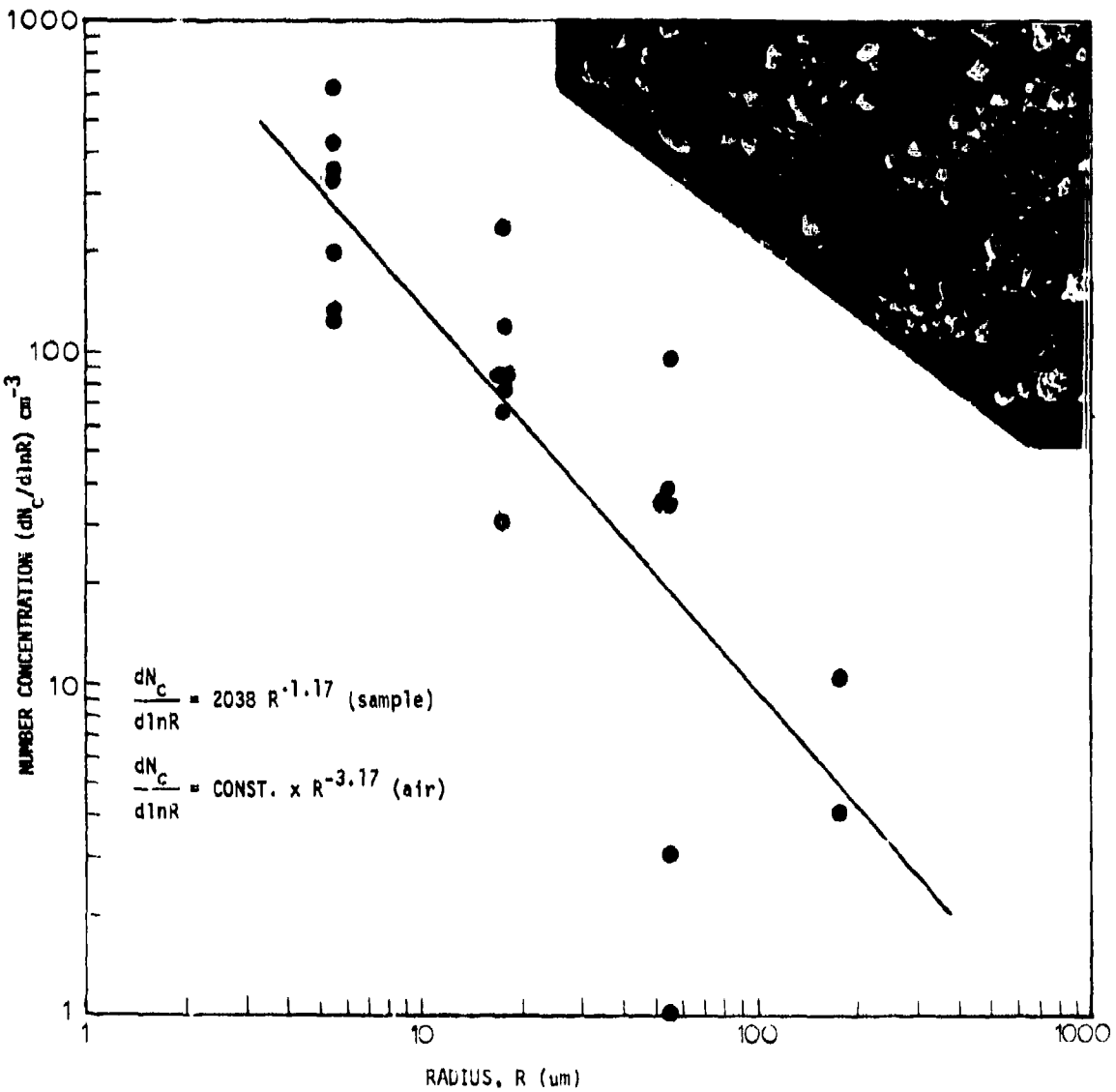

Figure 6. A size distribution analysis of dust samples collected on adhesive impactors is shown. The results were obtained by counting from electron micrographs such as that shown; original magnification is x100.

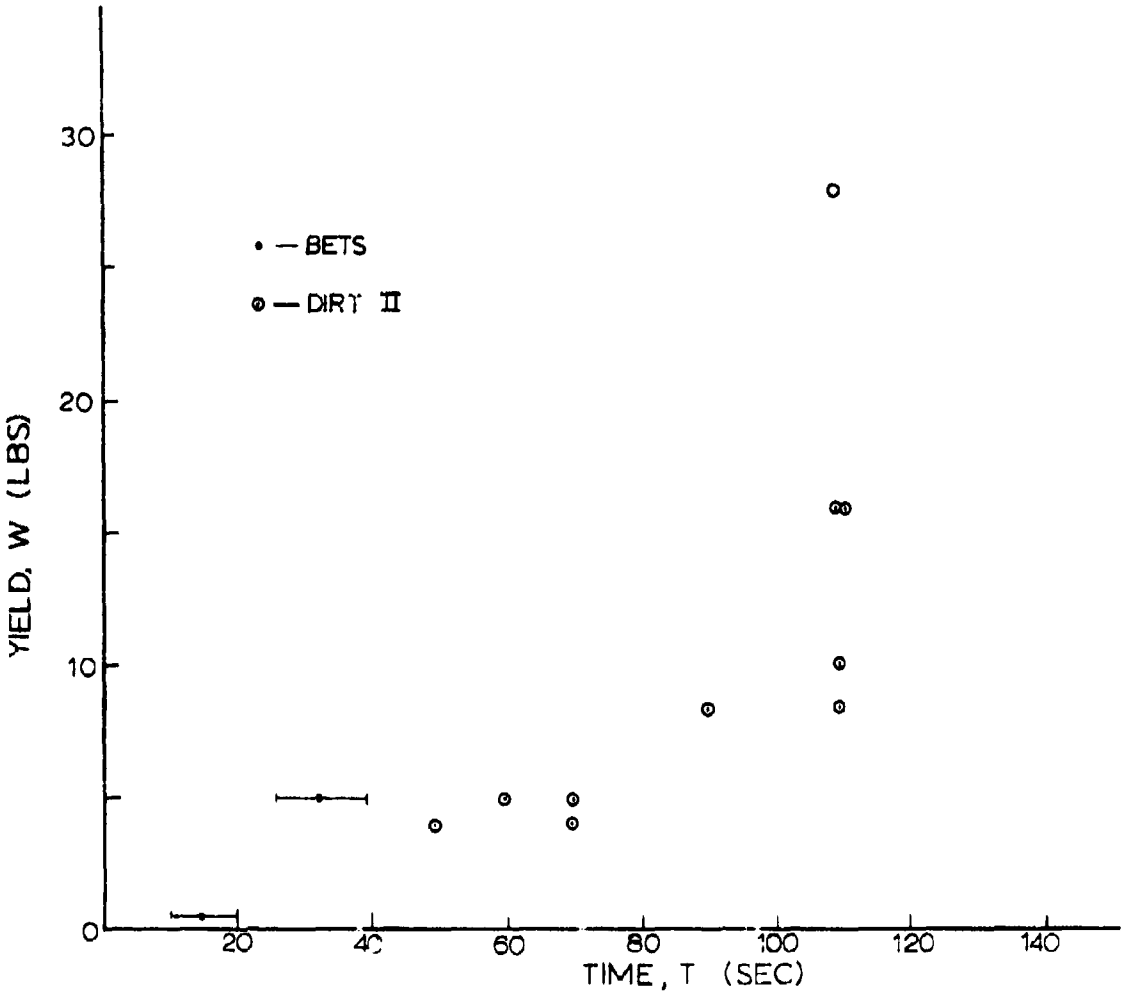

Figure 7. Dust cloud durations as determined from photographs are plotted vs. explosive yields for tests from the BETS and the DIRT-II series.

a. 0730

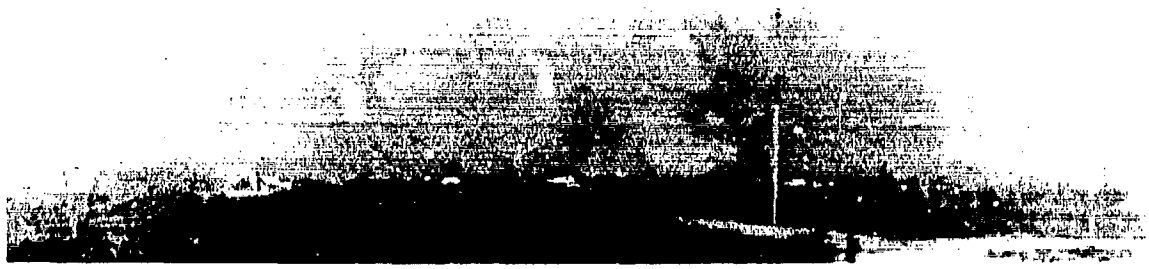

b. 1030

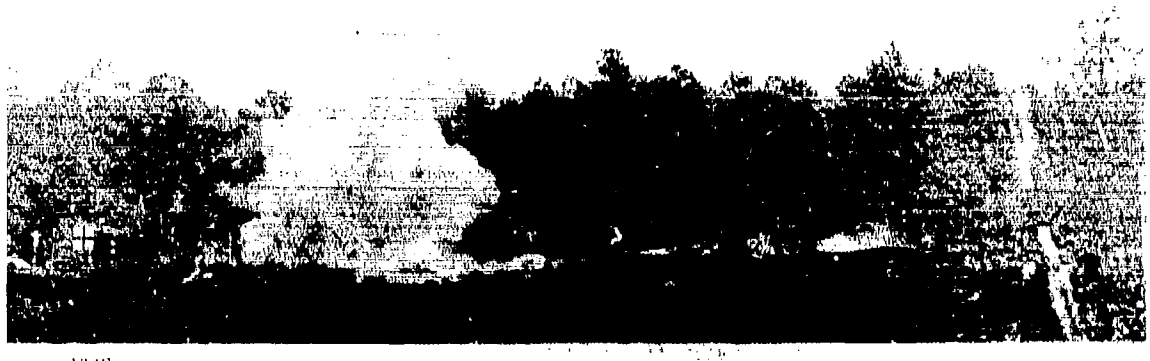

c. 1230

Figure 8. These photographs show examples of dry soil tests at 0730, 1030 and 1230 illustrating the contribution of the surrounding terrain surface to the dust cloud. In 'a' the surface is dense and humidity is high and dust is confined to the test plot. In 'c' a substantial dust skirt has been raised. Note in 'b' the small patch of dust to the right of the main column. This has been raised from an adjacent dry test plot by the shock wave. Times for all photographs are [illegible] after detonation.

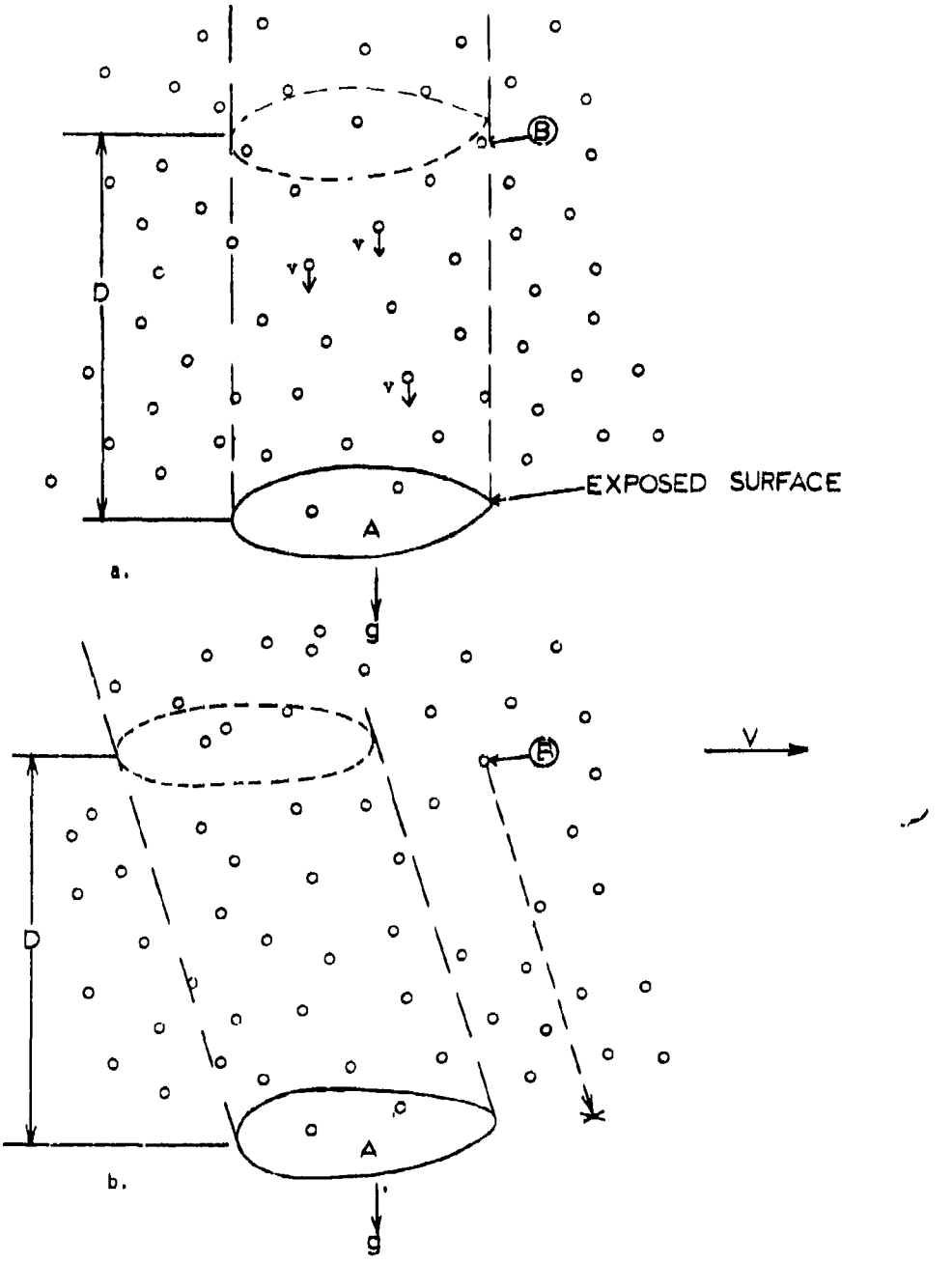

Figure A1. The collection of particles falling without lateral motion (top) and with (bottom) in a gravity field on a horizontal surface, A.

CORRELATIONS BETWEEN SOIL PARAMETERS AND OBSCURATION FEATURES OF CLOUDS PRODUCED BY MUNITIONS IN THE HUMID TROPICS

Mr. Robert J. Fuchs
CPT Marie Martinucci
US Army Tropic Test Center
Fort Clayton, Republic of Panama

ABSTRACT

Field trials in battlefield obscuration were conducted jointly by the US Army Tropic Test Center (USATTC) and US Army Waterways Experiment Station (USAWES) in the Republic of Panama during July and October of 1980. The objective was to determine the relationship between soil parameters and obscuration features of clouds produced by munitions and explosives in the humid tropics. A combined total of sixty-six 155- and 105-millimeter ammunition rounds and 15-pound TNT charges were detonated statically in varying types of soil and tropic vegetation. Obscuration areas during cloud growth stages were digitized from video recordings of each detonation. Correlations between obscuration parameters and soil/vegetation parameters were weak. Obscuration was due mainly to smoke rather than dust, and was minimal during the wet season in the humid tropics.

1. BACKGROUND AND OBJECTIVE

The performance of many modern weapons systems can be affected adversely by heavy concentrations of dust and smoke in the air. In recent years, a systematic effort has been underway to assess such effects, both in the field and through mathematical computer models, to meet the need for a more realistic battlefield representation. Because much of the obscurant material on the battlefield originates in the soil and is raised by battle activity, the link between obscurant material and terrain must be understood properly.

USAWES and USATTC conducted a cooperative research project in the humid tropics of the Republic of Panama from July through October 1980. The objective was to determine the relationship between soil parameters and obscuration features of clouds produced by munitions and explosives in the humid tropics. A combined total of sixty-six 105- and 155-millimeter ammunition rounds and 15-pound TNT charges were detonated statically in various types of vegetation at three sites, including an ocean beach site.

2. SUMMARY OF PROCEDURES

The test was conducted at Empire Range 6 (on the Pacific side of the Isthmus of Panama) and at Mindi Farm and Pina Beach (on the Atlantic side). In-place detonations of 155-millimeter rounds, 105-millimeter rounds, and 15-pound (6.8 kg) blocks of TNT were employed at Range 6 and Mindi Farm; only TNT was used at Pina Beach.

At Empire Range 6, three blast areas were used. Two of these areas were chosen because each area was covered by a different grass species: Gynerium sagittatum (3 to 4 meters high) and Panicum sp (1 meter high). The third area was under the jungle canopy. Half of the blast surface on each of the two grass areas was covered for several days to dry the soil. The covering was high enough above the ground to allow soil moisture to evaporate without destroying the vegetation. It was not removed until immediately before blasting to minimize exposure to rain. No attempt was made to dry the soil in the third (jungle canopy) area of Range 6. Three shots (one each of 155mm, 105mm, and TNT) were detonated statically in three different grass levels: uncut grass; grass cut to 0.3 to 0.5 meter; and bare soil cleared of all grass. The grass was not cut in the area under the jungle canopy. The 155- and 105-millimeter munitions were set, nose down, on the ground at a 30-degree angle of attack and detonated electrically. The TNT was placed so that the total charge detonated simultaneously.

At Pina Beach, eight TNT charges were detonated. The charges were set on the ground surface in six different areas: white, saturated sand (shoreline); white, wet (top centimeter partially dry) sand; black, wet (top centimeter partially dry) sand; Ipomoea pes-caprae (morning-glories); Hymenocallis americana (spider lily); and Panicum maximum (2 to 3 meters high). No munitions were detonated at the Pina Beach site and no artificial drying of the soil was attempted.

At Mindi Farm, the munitions and charges were detonated in three different levels of vegetation: Gynerium sagittatum (3 to 4 meters high), Gynerium sagittatum cut to 0.3 to 0.5 meter, and bare soil cleared of all vegetation. The explosives were set on the ground and detonated in the same manner as at Range 6.

At all sites, bulk soil samples were taken before and after the detonations. Cone index (CI) measurements were made, and moisture and density samples were collected. Crater measurements were made of symmetric and asymmetric craters. Blow-out material was collected at points 3, 6, and 9 meters from the center of the blast on the four points of the compass. (Jungle density precluded collecting

blow-out material for the jungle canopy area of Range 6.) Laboratory analyses were performed on the bulk samples and the blow-out material.

Still photograph and video tape records were made of all detonations at all sites. Analysis of video tapes provided data on cloud dissipation. Durand's Rule* was used to compute the obscured cloud area. Opaque cloud areas (through which jungle or background targets were visible) were not included in the obscured area computations.

3. SUMMARY OF RESULTS

TNT charges produced the largest obscuration areas for the longest time period, followed by 155- and 105-millimeter rounds (figure 1 and table I). The obscuration from TNT resulted mainly from the black, TNT-produced smoke, rather than from dirt or dust. Because of this, the cloud sizes at Pina Beach (TNT only) were comparable to those produced from TNT at inland tropic sites (figure 2).

Vegetation levels affected cloud sizes to some degree. Munitions detonated in high, uncut grass produced smaller clouds than did munitions in cut grass or bare soil (table II). The high grass probably had a dampening effect on the production of dust and other suspended particles in the air.

Crater sizes were largest at the Mindi Farm site where the soil was wettest. Resulting obscured areas were largest for the first 10 seconds following detonation, but fell off rapidly, leaving no obscuration by 20 seconds.

In general, correlations between obscuration parameters and soil parameters were weak. A matrix of linear correlation coefficients for the 105-millimeter data is presented in table III. Combinations of prediction variables (e.g., cone indexes, surface moisture, and Atterburg Limits) did fit a multiple regression model in adequately predicting cloud size. However, lack of consistency shows that the relationships are not strong enough to model without further data.

---

* The Chemical Rubber Company Standard Mathematical Tables, 20th Edition, Editor-in-Chief Samuel M. Selby, PhD., ScD, Cleveland, OH, 1972, p. 14.

4. CONCLUSIONS

Tropic wet season soils do not contribute greatly to obscuration. Nearly all obscuration was caused by the smoke from the munitions or explosive, and dissipated within 20 to 40 seconds. Tropic vegetation does influence the size of clouds produced—munitions produced smaller clouds in tall grass than in short grass or bare soil. A follow-up study in Panama is planned during the 1982 dry season to document effects of tropic soils on obscuration produced by munitions and explosives during the tropic dry season.

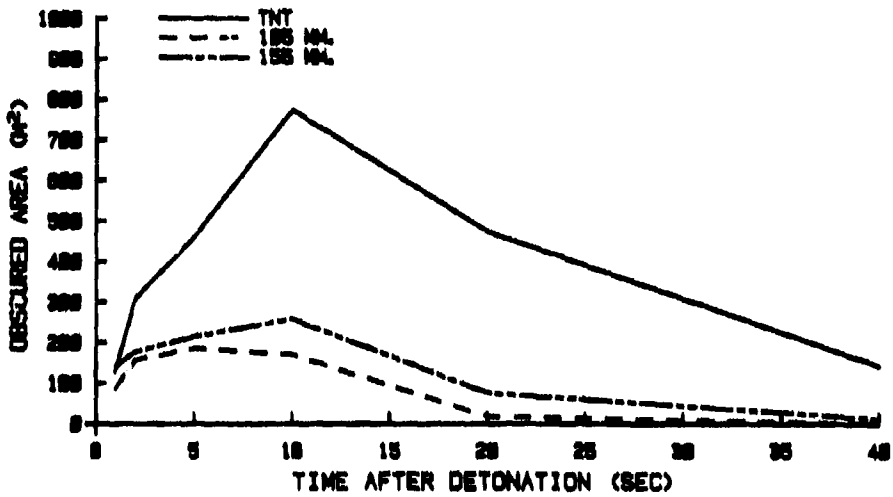

Figure 1. Obscured Area versus Time (Mindi and Empire Range 6 Data).

TABLE I. MEANS AND SIGNIFICANCE LEVEL OF CRATER AND CLOUD DATA FROM MINDI FARM AND RANGE 6, BY MUNITIONS TYPE

Munition	Number of Craters	Crater Volume	Obscured Area, Seconds After Detonation 1	2	5	10	20	Weight of Blow-out Material by Distance from Detonation 3m	6m	9m
		(m^3)			(m^2)				(g)	
TNT	16	0.339	130	308	458	774	475	5,257	1,436	370
105mm	12	0.210	87	157	187	171	18	2,914	834	336
155mm	15	0.531	143	177	215	259	76	7,176	2,313	974
Significance	—	<.001	NS	<.05	<.001	<.001	NS	<.001	NS	<.01

NS = Not Significant at the $\alpha = .05$ level.

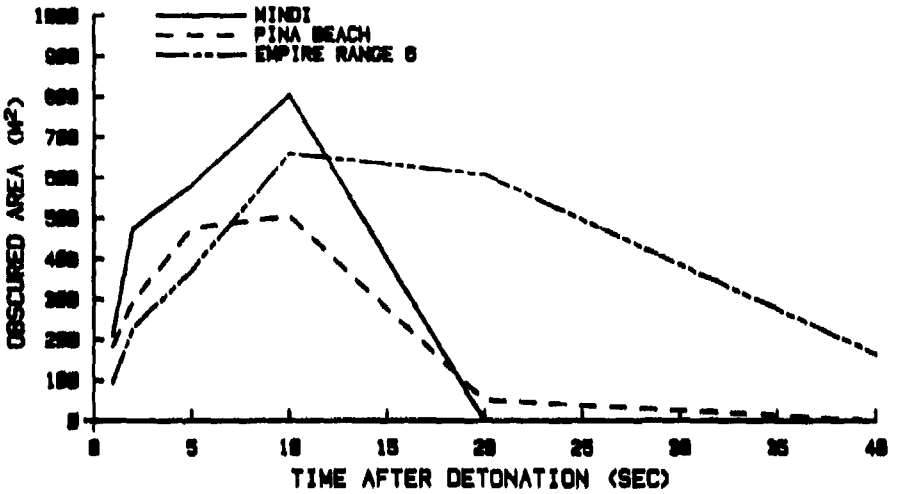

Figure 2. Obscured Area versus Time (TNT Data).

TABLE II. MEANS AND SIGNIFICANCE LEVEL OF CRATER AND CLOUD DATA FROM MINDI FARM AND RANGE 6, BY VEGETATION LEVEL

Vegetation Level	Number of Craters	Crater Volume	Obscured Area, Seconds After Detonation				
			1	2	5	10	20
		(m^3)			(m^2)		
Bare Soil	15	0.369	129	240	353	589	153
Cut Grass	14	0.340	134	268	290	406	287
Uncut Grass	14	0.369	103	151	246	272	190
Significance	—	NS	NS	<.01	NS	< 05	NS

NS = Not Significant at the $\alpha = .05$ level.

TABLE III. MATRIX OF CORRELATION COEFFICIENTS FOR 105-MILLIMETER DATA FROM EMPIRE RANGE 6 AND MINDI SITES

Variable	Crater Volume (m^3)	Crater Depth (m)	Obscured Area, Seconds After Detonation 1 (m^2)	2 (m^2)	5 (m^2)	10 (m^2)	20 (m^2)	Material Weight 3m (g)	6m (g)	9m (g)
Cone Index (kg/cm^2)										
Surface (Before Detonation)										
Surface layer	-.484 a/	-.340	-.029	-.345	-.248	-.339	.259	.303	-.251	.287
2-inch (51 mm) layer	-.606 b/	-.541 a/	-.178	-.382	-.311	-.301	.105	.159	-.313	.374
4-inch (102 mm) layer	-.277	-.582 a/	-.212	-.387	-.409	-.318	.027	-.076	-.518 a/	.093
6-inch (152 mm) layer	-.375	-.632 b/	-.283	-.357	-.345	-.319	-.031	.019	-.339	.272
Moisture Content Surface (%)	.204	.642 b/	.201	.424	.402	.393	-.132	-.423	.386	-.403
Density Dry (kg/m^3)	-.199	-.582 a/	.034	-.301	-.293	-.243	.227	.012	-.619 a/	-.056
Fines (%)										
0- to 6-inch (152 mm) Soil Layer	-.284	-.722 b/	.043	-.279	-.236	-.355	.322	.280	-.220	.472
Bottom of Crater	-.230	-.413	-.106	-.115	-.034	-.189	.020	.048	.154	.621 a/
Atterburg Limits										
Liquid Limit										
0- to 6-inch (152 mm) Soil Layer	.090	.093	.353	.173	.148	.115	.198	-.434	.018	-.438
Bottom of Crater	-.248	.246	.079	.737 b/	.778 b/	.719 b/	-.197	-.328	.131	-.026
Plastic Limit										
0- to 6-inch (152 mm) Soil Layer	.200	.024	.369	.053	.008	-.007	.242	-.469	.163	-.394
Bottom of Crater	.074	.417	.067	.176	.178	.254	-.145	-.532 a/	-.014	-.515 a/
Plastic Index										
0- to 6-inch (152 mm) Soil Layer	-.276	.081	-.213	.190	.246	.220	-.204	.089	-.224	.008
Bottom of Crater	-.303	-.233	-.009	.446	.481	.345	-.015	.265	.126	.507
Temperature (°C)	-.467	-.059	-.345	-.237	-.160	-.247	-.260	.040	.150	.277
Relative Humidity (%)	.504 a/	.140	.335	.240	.165	.246	.225	-.071	-.135	-.365
Wind Speed at Ground (knots)	-.157	.291	-.436	.193	.174	.206	-.535	.192	.565 a/	.329
Wind Speed at Tower (knots)	-.307	-.405	-.547	-.133	-.005	-.073	-.493	.375	.550	.717 b/
Material Weight (g)										
3 Meters	-.177	-.444	-.386	-.149	-.078	-.107	-.137	1.000	-.014	.683 b/
6 Meters	.291	.632 a/	-.080	-.182	-.218	-.271	-.160	-.014	1.000	.198
9 Meters	-.351	-.543 a/	-.427	-.187	-.063	-.199	-.198	.683 b/	.198	1.000

a/ Significantly different from zero at $\alpha = .05$ level
b/ Significantly different from zero at $\alpha = .01$ level

INFRARED MEASUREMENTS WITH THE MIDAS III RADIOMETER DURING SMOKE WEEK III TESTS

A.G. Geiser
Cincinnati Electronics Corporation
2630 Glendale-Milford Road
Cincinnati, Ohio 45241

1. SUMMARY

This paper summarizes the data obtained during Cincinnati Electronics Corporation's participation in the Smoke Week III tests at Eglin AFB, FL from August 8 to August 14, 1980. The data consists of measurements of infrared radiance of calibrated targets made with the MIDAS III scanning radiometer. These measurements were made in the spectral bands 3.2-4.77 um, 4.4-4.77 um, 3.8-4.2 um, 3.4-4.3 um and 8-12 um. The MIDAS III has an integration time of 0.3 milliseconds, a frame time of 100 milliseconds and the spatial resolution of 0.1 milliradians. A detailed description of the operation of the MIDAS III radiometer is presented along with details of system calibration.

Also included in this paper are descriptions of the test objectives, test site and measurement geometry.

A data log lists the test runs for which data was recorded and the obscurants, targets, and meteorological data. All data is permanently preserved on magnetic tape. Sample strip chart recordings of the raw data are presented. One segment of data from the IR No. 1 smoke test is analyzed. This data demonstrates the fine structured nonuniformities of the obscurant as it passed the target. These nonuniformities create false target temperature contrasts.

The MIDAS III can provide high spatial resolution irradiance difference data with a short integration time of any spectral band in the 3-5 um region and simultaneous data in the 8-12 um band. The system can also be used in a staring mode to measure signal fluctuations in the frequency range of 0.05 Hz to 6800 Hz. With addition of a chopper, reference source and associated electronics, the MIDAS will measure absolute radiance levels.

2. MIDAS SYSTEM DESCRIPTION

2.1 SCANNER AND CONTROL CONSOLE

MIDAS III is a banded radiometer used to gather target temporal and/or spatial data in several spectral bands. The system is modular and can be configured in a variety of ways. The MIDAS III System used for the Smoke Week III tests is shown in the block diagram in Figure 2.1.1. The system consisted o the scanner and control, monitoring and recording electronics and a mobile support van. An external vie of the scanner with the TV camera and sighting scope is shown in Figure 2.1.2. The UV sensor shown in Figure 2.1.1 was not used for the Smoke Week tests.

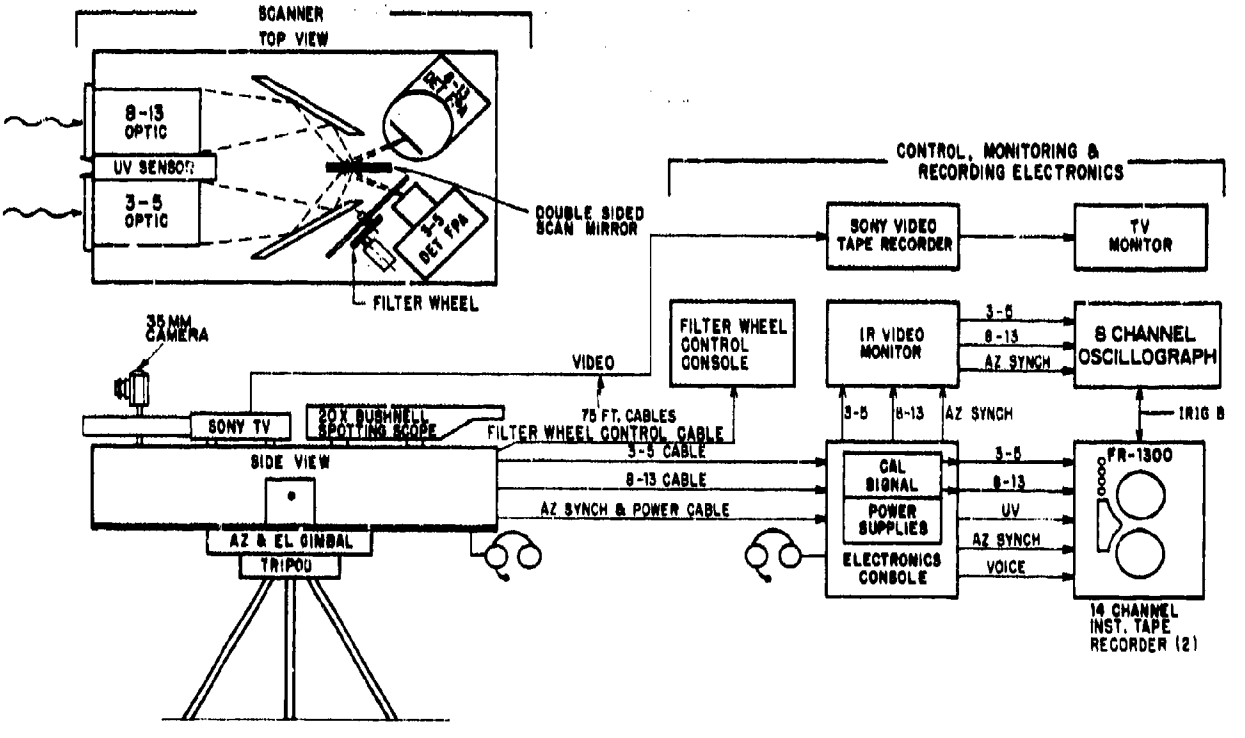

Figure 2.1.1. MIDAS III/UV System Block Diagram

The scanner unit contains two lenses side by side, a four-element germanium lens with an 8-13 um passband and a four-element (two germanium and two silicon) lens with a 3-5 um passband. Each of these lenses has a 7 inch aperture, a 21 inch focal length and a resolution of 0.10 milliradian. Behind each lens is a coated pyrex folding mirror which reflects the converging beams to opposite sides of the double sided coated aluminum scan mirror. The beam of the 8-13 um lens is reflected from the scan mirror

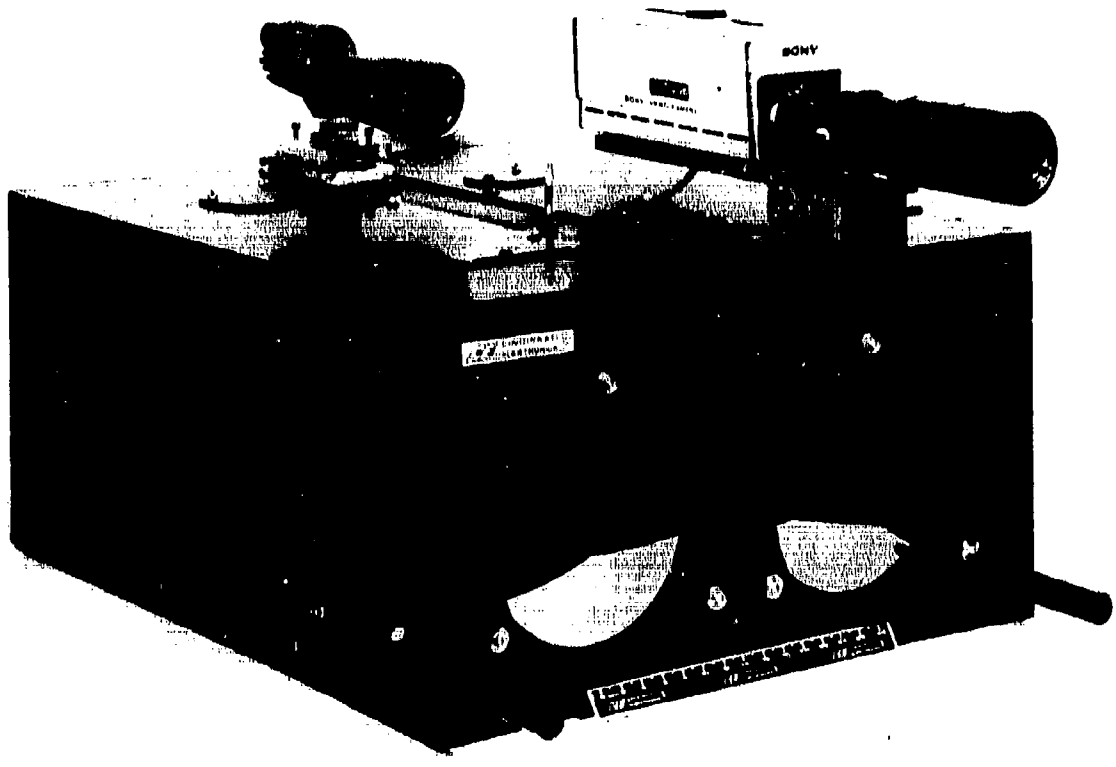

Figure 2.1.2. MIDAS III Scanner

to the 16 element mercury cadmium telluride (HgCdTe) detector located at the focal plane. The beam of the 3-5 um lens is reflected from the scan mirror to the 24 element indium antimonide (InSb) detector located at the focal plane. Both detectors have staggered arrays with 10 percent overlapping. Each element in the two arrays is 0.09 milliradian in azimuth by 0.11 milliradian in elevation. When convolved with the optical blur spot, the detector elements generate a system resolution of 0.1 milliradian in the azimuth direction by 0.12 milliradian in the elevation direction. The two staggered arrays in each detector are separated by 0.5 milliradian. Eight of the detector elements in each detector were used to record data. Thus, the total elevation field-of-view was 0.8 milliradian.

The 3-5 detector has a cold spectral filter which limits the passband to the region from 3.2 to 4.77 micrometers. A six-position filter wheel with warm filters was installed in front of the 3-5 detector in order to measure the spectral content of backgrounds at various passbands within the 3.2 to 4.77 region. Figure 2.1.3 is a photograph of the filter wheel. Only four of the available six positions in the filter wheel were used for Smoke Week measurements. The passbands for these four filters were wideband, 4.4-4.77 micrometers, 3.8-4.2 micrometers, and 3.4-4.3 micrometers. When the wideband

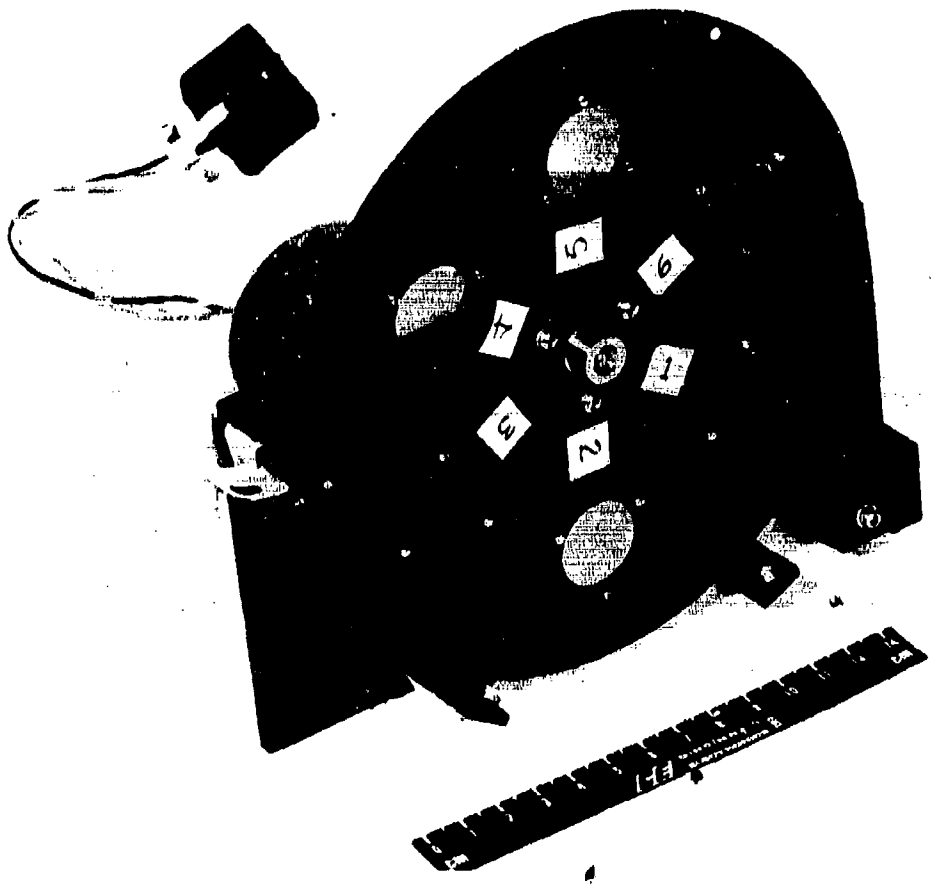

Figure 2.1.3. Filter Wheel Assembly

filter was in position, the measured spectrum was limited by the internal cold filter on the detector to the 3.2-4.77 micrometer passband. The number, sequence and dwell time for the selection of filters can be programmed for automatic operation or can be controlled manually.

The scan mirror is driven by a cam which produces a linear scan of 28 mrad from right to left in the object plane in 75 msec, followed by a retrace to the original position in 25 msec. Each detector element output connects to an analog preamp/postamp channel which produces an output signal corresponding to the spatial variation of infrared irradiance across the scanned field-of-view within the instantaneous angular field-of-view of the detector element. The resolution and sensitivity parameters are shown in Figure 2.1.4.

SYSTEM	LWIR DETECTOR	MWIR DETECTOR
SPECTRAL PASSBANDS	8-13 μm	3.2-4.8 μm
FIELD-OF-VIEW		
Azimuth	1.6° (28 mrad)	1.6° (28 mrad)
Elevation	0.8 mrad (Recorded Data) 1.6 mrad (Total FOV)	0.8 mrad (Recorded Data) 2.3 mrad (Total FOV)
RESOLUTION		
Azimuth	0.1 mrad	0.1 mrad
Elevation	0.12 mrad	0.12 mrad
FRAME RATE	10 Frames/Sec	10 Frames/Sec
ELECTRONIC BANDWIDTH	5-1900 Hz	0.05-1900 Hz
OPTICS		
SPECIFICATIONS	7" Diameter, f/3, 0.15 mrad Resolution 60% Transmission	7" Diameter, f/3, 0.15 mrad Resolution 70% Transmission
MATERIAL	4 Element Germanium	2 Germanium plus 2 Silicon Elements
DETECTOR		
TYPE	HgCdTe	InSb
NUMBER OF CHANNELS	16	24
$D^*_{\lambda p}$ (cm $Hz^{1/2}$ $Watt^{-1}$)	$2\text{-}3 \times 10^{10}$	$.7\text{-}20 \times 10^{11}$
SENSITIVITY		
NEI (Watts cm^{-2})	$2.5\text{-}5 \times 10^{-13}$	$0.7\text{-}3 \times 10^{-14}$

Figure 2.1.4. MIDAS III System Parameters

2.2 DATA RECORDING AND READOUT

The data recording and readout electronics consist of a 4 trace oscilloscope for direct monitoring of channel video signals, an 8 channel recording oscillograph for permanent visible records of direct or playback signals, and two FR-1300, 14 channel instrumentation tape recorders for permanent data records. In addition, there was a Sony video tape recorder and video monitor to record and display the picture from the TV camera on the scanner. All this equipment was located inside the mobile support van.

The two FR-1300 tape recorders were used in the FM mode except for the voice and IRIG time code channels, which were direct mode. The 3-5 channels (A1 through A8) were recorded on channels 1 through 8 of recorder A, and the 8-13 um channels (C1 through C8) were recorded on Channels 1 through 8 of recorder B. On each recorder, the IRIG time code, azimuth sync signals, and the voice channel were recorded on channels 12, 13 and 14 respectively. The tape channel format is tabulated in Figure 2.2.1.

RECORDER A

TAPE CHANNEL	MODE	DATA
1	FM	A1
2	FM	A2
3	FM	A3
4	FM	A4
5	FM	A5
6	FM	A6
7	FM	A7
8	FM	A8
9		
10		
11		
12	DIRECT	IRIG
13	FM	AZ SYNC
14	DIRECT	VOICE

TAPE DRIVE SPEED 7-1/2 IPS

RECORDER B

TAPE CHANNEL	MODE	DATA
1	FM	C1
2	FM	C2
3	FM	C3
4	FM	C4
5	FM	C5
6	FM	C6
7	FM	C7
8	FM	C8
9		
10		
11		
12	DIRECT	IRIG
13	FM	AZ SYNC
14	DIRECT	VOICE

TAPE DRIVE SPEED 7-1/2 IPS

Figure 2.2.1. Tape Recorder Channel Format

A Bell and Howell 5-134 Recording Oscillograph was used for direct recording of data for immediate analysis and for later playback. The oscillograph is capable of simultaneously reproducing 6 channels of data plus IRIG time code and azimuth sync. For both on-site data monitoring and post-test strip out for data reduction, the oscillograph was run at 20 inches per second. In almost all cases a gain of 0.2 volt per inch was used.

3. SYSTEM CALIBRATION

Radiometric calibration of the MIDAS III System was accomplished by measuring the response of the system to a source of known temperature, emissivity, and angular size. The calibration was done in the Cincinnati Electronics Corporation optical lab on a 16-inch Davidson reflecting collimator. An Infrared Industries blackbody set at 200°C was used as the infrared source. This source has an emissivity of 0.99 ± 0.01. The temperature was monitored by means of a thermocouple located in the cavity block. The measured temperature is believed accurate to ± 1.0°C.

Since the calibration needed is the large target radiance calibration rather than the point source irradiance calibration, an extended target should be used as a source. However, a 200°C large source will saturate the electronics. For this reason, a 1/20 mrad point source precision aperture was used, and the voltages measured were multiplied by the ratio of the large target signal to the 1/20 mrad target signal measured at a lower temperature where saturation did not occur. The reason that this measurement was not used as the actual large target calibration is that the low temperature could not be measured or controlled as accurately as the 200°C temperature. However, the ratios measured are accurate regardless of the actual temperature of the source. The ratio was found to be 12.30 for the 3-5 um channels and 17.67 for the 8-13 um channels.

The output signal pulse from the 1/20, 200°C source was observed on an oscilloscope and the difference in the signal voltage between the hot target and the ambient temperature aperture disk was recorded. The results were multiplied by the above ratios and averaged over the 8 channels and are shown in Figure 3.1.

The next step in the system calibration is to determine the radiance difference of the target for each filter. The effective radiance difference, $\Delta L_{eff}(\lambda_p)$, at wavelength λ_p is calculated from the equation,

$$\Delta L_{eff}(\lambda_p) = \rho_B \int \tau_A(\lambda) \frac{\tau_F(\lambda)}{\tau_F(\lambda_p)} \frac{R_S(\lambda)}{R_S(\lambda_p)} \left[L_\lambda(T_{BB}) - L_\lambda(T_L) \right] d\lambda$$

where ρ_B is the reflectance of the collimator mirror system,

$\tau_A(\lambda)$ is the spectral atmospheric transmission over the 21 foot collimator path length,

$\tau_F(\lambda)$ is the spectral transmission of the system filter at wavelength λ,

	SPECTRAL BAND (μm)	PEAK WAVELENGTH λ_p (μm)	VOLTAGE DIFFERENCE 200°C LARGE TARGET NO ATTENUATION (V)	RADIANCE DIFFERENCE ΔLeff 200°C TARGET, 24°C AMBIENT $\left(\frac{W}{cm^2 \cdot ster}\right)$	CALIBRATION FACTOR (RADIANCE DIFFERENCE PER VOLT) $\left(\frac{W}{cm^2 \cdot ster \cdot V}\right)$
1	3.2-4.77	4.5	13.40	6.953×10^{-3}	0.519×10^{-3}
2	4.4-4.77	4.5	7.99	3.082×10^{-3}	0.387×10^{-3}
5	3.8-4.2	4.0	4.00	2.243×10^{-3}	0.561×10^{-3}
6	3.4-4.3	4.0	6.78	3.505×10^{-3}	0.517×10^{-3}
	8-13	10.0	32.14	15.95×10^{-3}	0.496×10^{-3}

Figure 3.1. Calibration Factors

λ_p is a reference wavelength,

$R_S(\lambda)$ is the basic system spectral responsivity in centimeters squared volts per watt without the filter,

$L_\lambda(T_{BB})$ is the blackbody spectral radiance in watts per square centimeter per steradian per micrometer at the blackbody temperature T_{BB},

and $L_\lambda(T_L)$ is the blackbody spectral radiance at the laboratory ambient temperature T_L.

The spectral atmospheric transmission was calculated for the 21 foot Davidson collimator path length. The spectral transmission curves for the 4 filters used during the tests were measured with a Beckman IR-4 Spectrophotometer. The basic system spectral responsivity, $R_S(\lambda)$, was determined by using a series of spike filters covering the system passband in conjunction with the collimated blackbody source.

The overall system response (basic radiometer plus spectral filter) for the 3-5 channel is shown in Figures 3.2 through 3.5 for the various filters used. Filter No. 1 was broadband uncoated sapphire for optical path compensation, so that the overall system response is the same as the basic system response with no filter. The overall system response for the 8-13 channel is shown in Figure 3.6.

Figure 3.2. System Relative Spectral Response - Filter No. 1 (3.2-4.77 μm)

The spectral atmospheric transmission, system and filter spectral curves, and blackbody temperature were used in a previously developed computer program to calculate $L_{eff}(\lambda_p)$ for the various filters according to the above equation. These radiance difference values were then divided by the average measured signal voltage for all the channels in the 3-5 um array. Figure 3.1 also gives the radiance differences and the calibrated effective radiance difference per volt for each filter in the 3-5 um detector and for the 8-13 um detector.

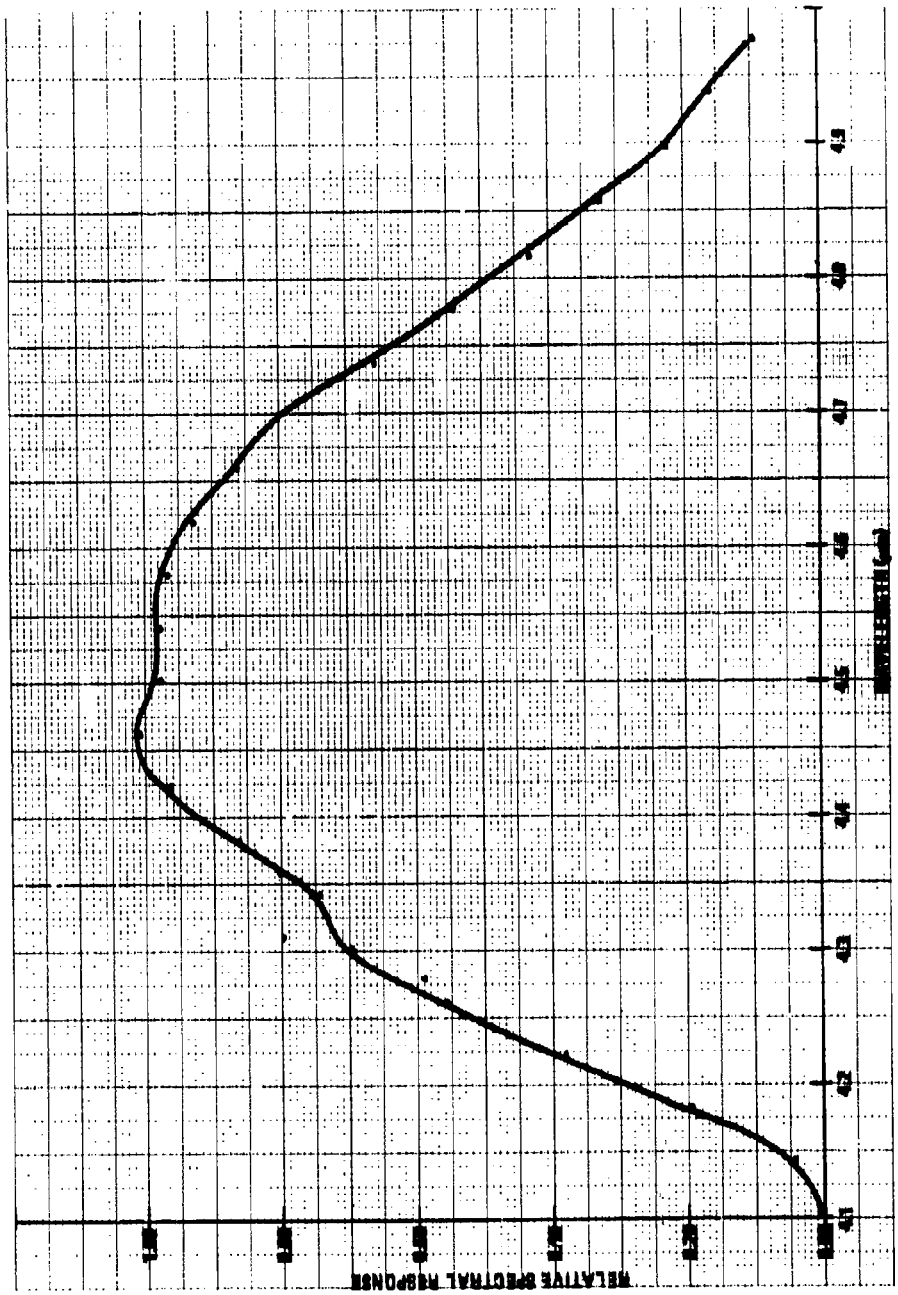

Figure 3.3. System Relative Spectral Response - Filter No. 2 (4.4-4.77 μm)

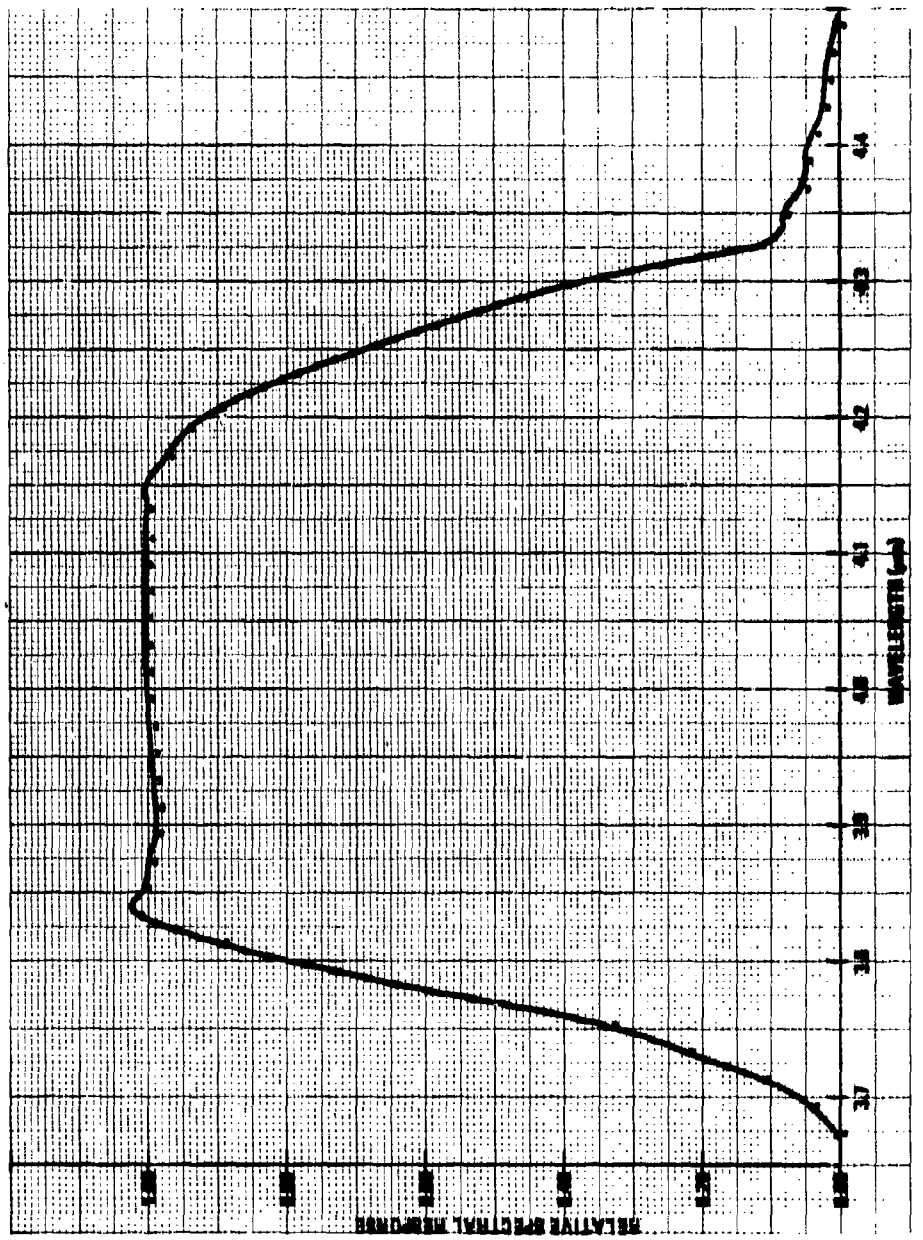

Figure 3.4. System Relative Spectral Response - Filter No. 5 (3.8-4.2 μm)

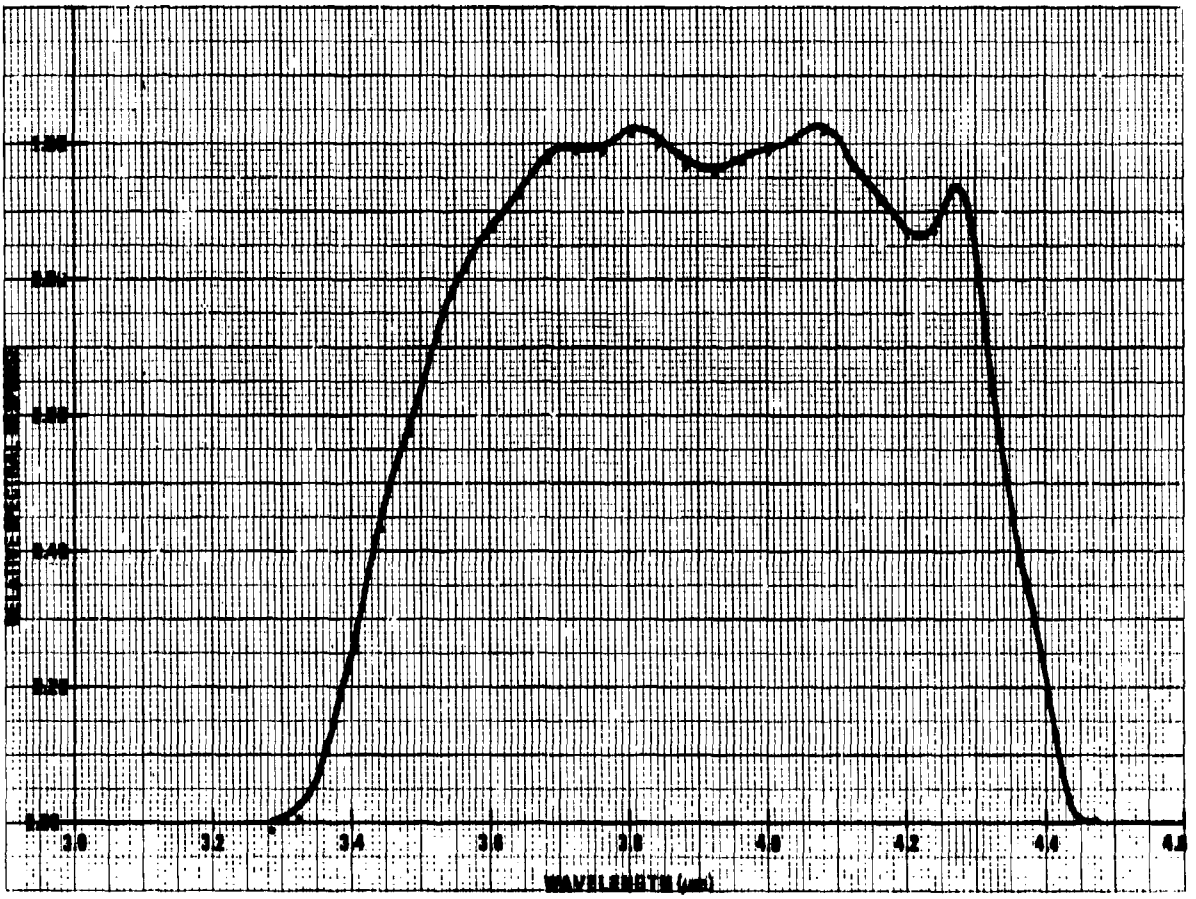

Figure 3.5. System Relative Spectral Response - Filter No. 6 (3.4-4.3 μm)

Figure 3.6. 8-13 System Response

4. SMOKE WEEK III TESTS

4.1 TEST OBJECTIVES

The Smoke Week III tests were held to provide developers and managers of electro-optical systems with an opportunity to evaluate developmental hardware under actual field conditions in a sub-tropical region. The systems tested included lasers, EO seekers, thermal imaging systems and radars.

The general objectives of the test were to:

(1) Determine the effectiveness of fielded, developmental and experimental EO systems against U.S. inventory, developmental, experimental and selected foreign obscurants.

(2) Determine the effectiveness of inventory, developmental, experimental and foreign obscurants against EO systems.

(3) Test new techniques and instrumentation for smoke/obscurant characterization under field conditions.

(4) Provide well characterized smoke/obscurant clouds under field test conditions which will assist obscurant/EO modelers in validating and/or improving their models.

(5) Determine the effect of humidity on the effectiveness of hygroscopic obscurants.

The specific objective with regard to the MIDAS III radiometer was to utilize its unique capabilities to measure the target radiance differences and path transmission with high spatial resolution (0.1 mrad), fast frame rate (100 msec), and multiple spectral bands.

4.2 TEST PROCEDURE

The test was conducted at Range C-52A at Eglin AFB, FL. The test layout is shown in Figure 4.1. The MIDAS radiometer was set up at the 800 meter point from the target area. This site was on an elevated mound giving a clear line of sight to the target area. At the target area a number of sources were set up, including a tank, a truck, and various point source and area source blackbodies. For almost all of the runs, the MIDAS system was positioned to scan across two blackbody panels, each three feet square, which were maintained at 10°C and 20°C above ambient temperature.

During a test run, smoke was generated at a point halfway between the target area and the 800M site and was carried across the line of sight from south to north by the prevailing wind. The smoke area and the line of sight through the smoke were heavily instrumented to fully characterize the smoke cloud.

4.3 DATA COLLECTED

The log of data collected is shown in Figure 4.2. All smoke runs from August 8 through August 14 were observed. Measurements were made before and after the smoke runs for calibration as well as during the time that the smoke was present. The four spectral filters used in the 3-5 um band were sequenced during the runs. The data was recorded on magnetic tape for permanent storage. Oscillograph charts of the data were also run at the time of the test for immediate visual output. A typical oscillograph chart is shown in Figure 4.3. The top trace is the azimuth sync pulse which identifies the scan portion of the video output. During this period the system scans from right to left through 1.6 degrees at a constant angular rate in 75 msec. The prominent feature to the right of center in these traces is the two heated panels. These targets were observed on nearly every run because they provided a consistent, calibrated source during the entire test.

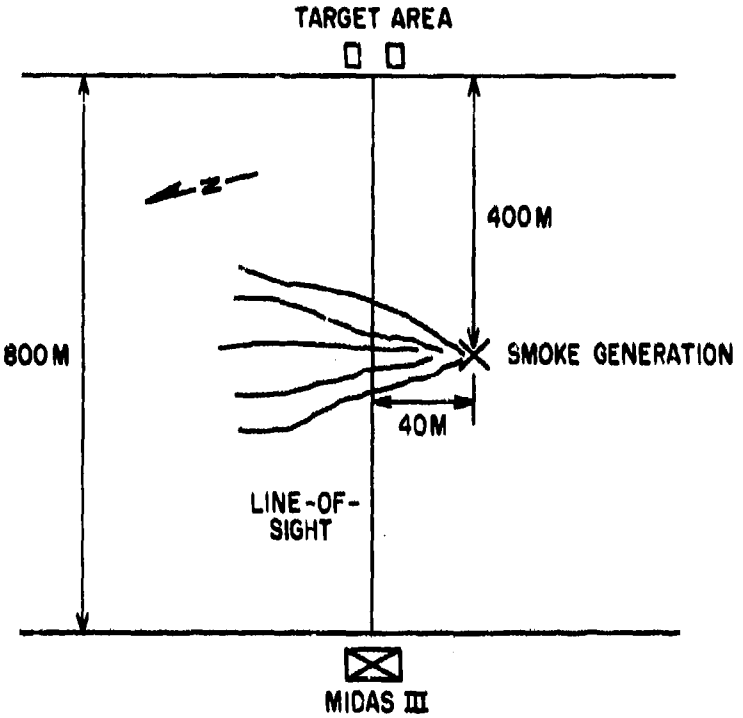

Figure 4.1. Test Layout

4.4 DATA ANALYSIS

The raw data of which Figure 4.3 is a sample was used to calculate smoke transmission versus time for the left and right panels separately. These curves are shown in Figure 4.4. The data selected for this analysis of IR No. 1 smoke was taken during a time when there appeared to be a reversal in the amplitude of the warmer and cooler panels. The transmission is seen to be changing rapidly and in an irregular manner. However, the situation becomes clear if we shift the curve for the 10°C panel to the left by 0.16 sec. This is shown in Figure 4.5, where it can be seen that the curves closely match. The interpretation is that the smoke cloud contains relatively small scale spatial structure and is drifting across the line of site, covering the 1.5 feet between the panel centers in 0.16 sec, a velocity of 9 feet per sec. This enables us to put a distance scale factor on the curve. The local non-uniformities in the cloud have a scale on the order of a few feet.

Another way of interpreting the same data is shown in Figure 4.6. Here, the difference in the signal from the 10°C and 20°C panels is expressed in apparent temperature difference. It can be seen

DATE	RUN	TARGET	OBSCURANT
8 AUG	1	TRUCK	NONE
	2	TRUCK	NONE
	3	TRUCK	NONE
11 AUG	1	MODULATED BLACKBODY	RED PHOSPHOROUS
	2	PANELS	XM49/FOG OIL
	3	PANELS	XM49/DIESEL & ADD.
	4	PANELS	M3A3/FOG OIL
	5	PANELS	XM49/PEG. 200
	6	PANELS	IR No. 1
12 AUG	1	TRUCK	5" ZUNI
	2	PANELS	M3A3/FOG OIL
	3	PANELS	HC CANNISTER
	4	PANELS	FOAM/IR No. 3
	5	PANELS	IR No. 1
13 AUG	1		VEESS
14 AUG	1		VEESS
	2		IR No. 2
	3	PANELS	XM49/PEG. 200
	4		

Figure 4.2. Smoke Week III Data Log

that the movement of the non-uniform smoke cloud sometimes causes a reversal in the apparent temperature contrast of the panels.

12 AUG 1980 RUN #5

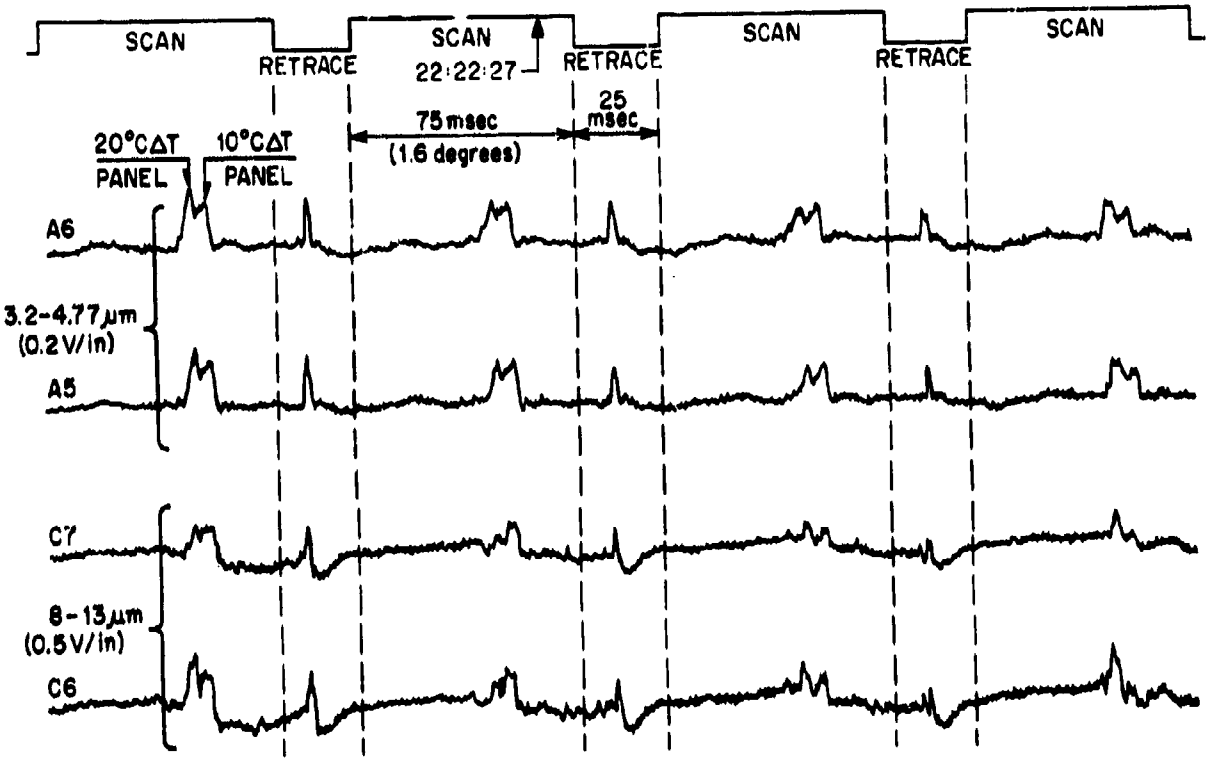

Figure 4-3. Channel Analog Data

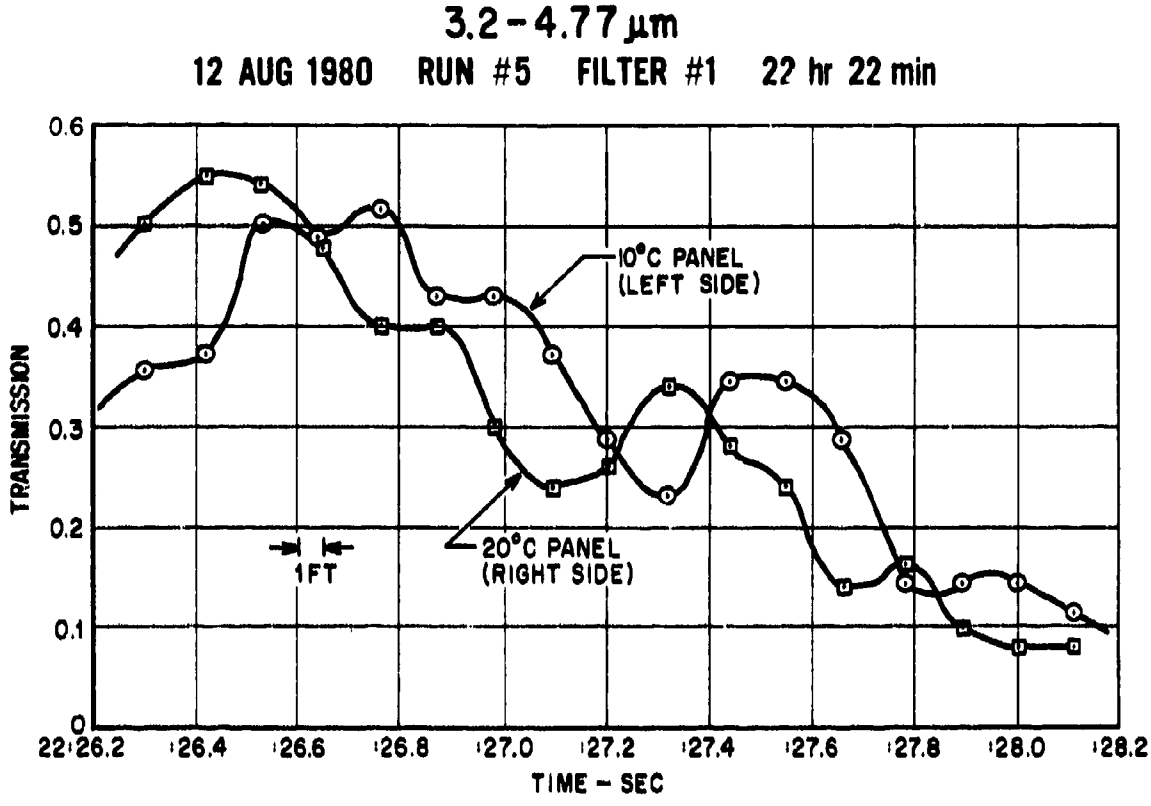

Figure 4-4. Transmission vs. Time

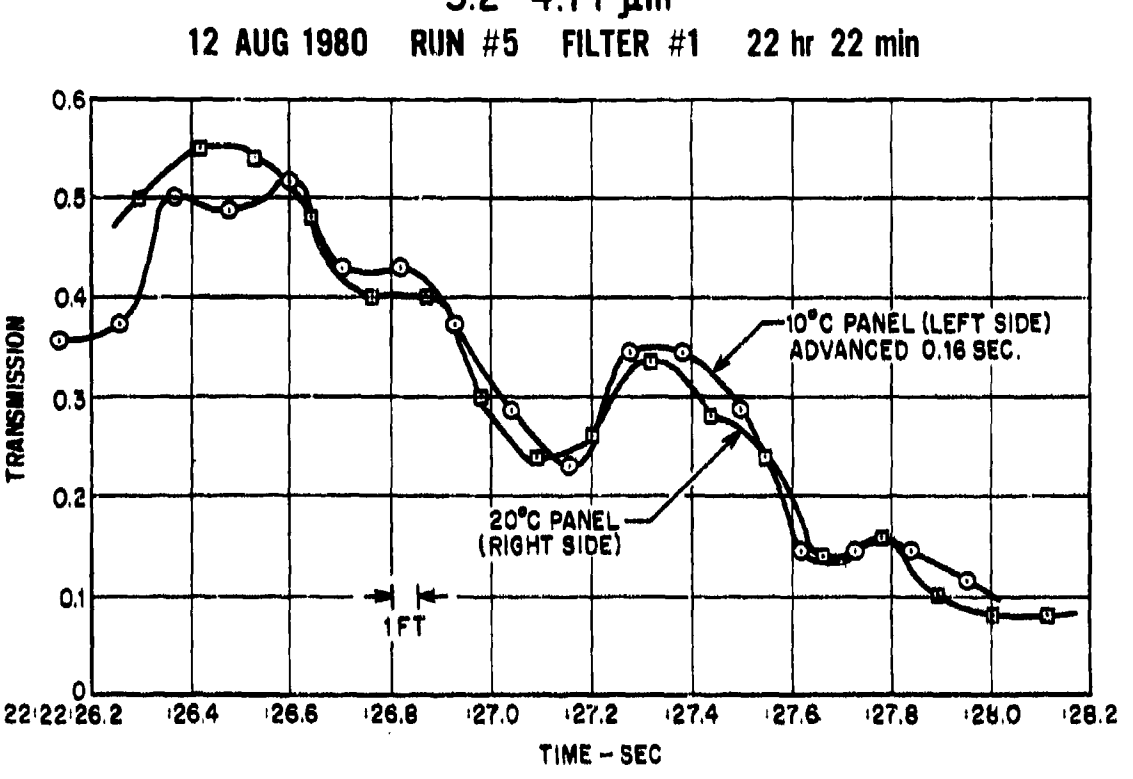

Figure 4-5. Modified Transmission vs. Time

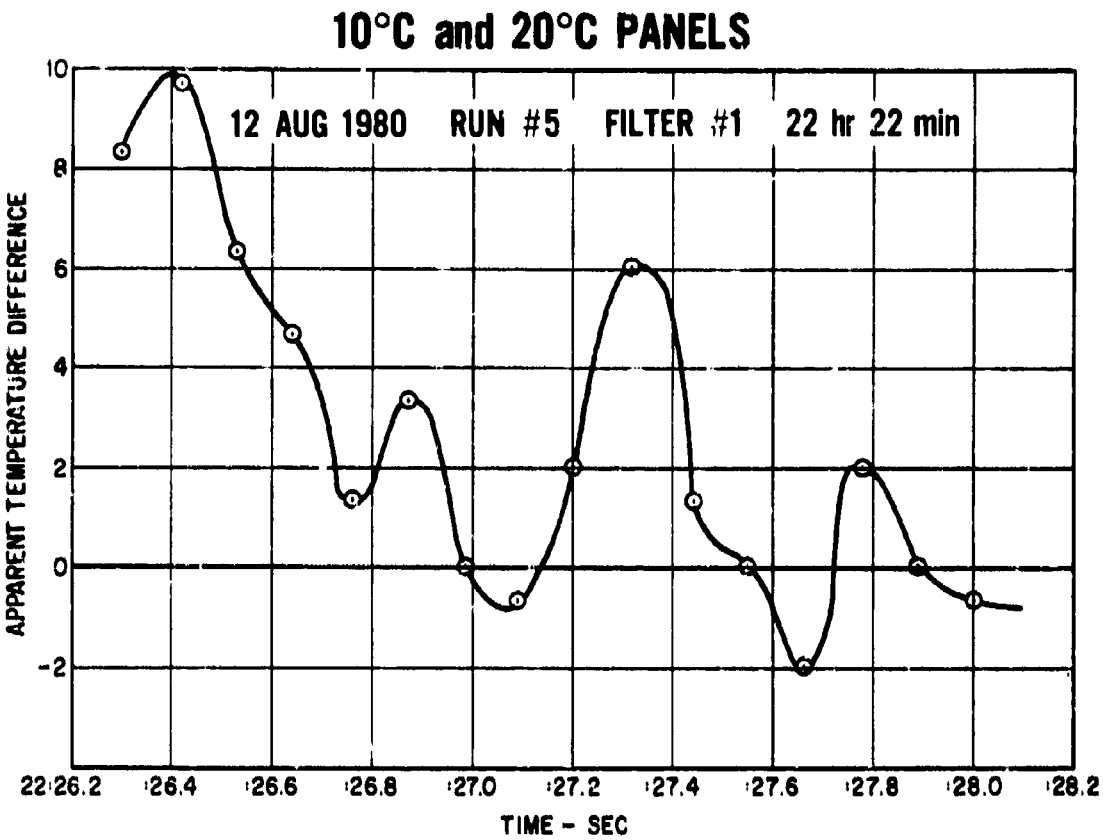

Figure 4-6. Apparent Temperature Difference vs. Time

5. RECOMMENDATIONS

Participation in Smoke Week III with the MIDAS III, tabulation of recorded data and reduction of a limited amount of data was performed under Cincinnati Electronics Corporation funding. The data reduced and analyzed showed some new and interesting characteristics of smoke due to the unique measurement characteristics of the MIDAS III. Figure 4.2 showed that recorded data is available for many obscurant types. Reduction of additional data would provide measurements of these various smokes and obscurants in the various 3-5 micrometer and 8-12 micrometer wavelength bands. In addition to providing general attenuation levels, the MIDAS data show the fine structure of the smoke clouds and their variation with time to 0.1 second resolution. The fine structure of the IR No. 1 smoke in the sample data presented in this report represents one short interval sample. Additional data should be reduced to further define this phenomenon and to determine its effect on various detection system concepts.

ATMOSPHERIC TRANSMISSION MEASUREMENT OF SMOKE AND OBSCURANTS

Leonard V. Lucia, William E. Surrette, Jr. and Frederic M. Zweibaum

Barnes Engineering Company

Stamford, Connecticut

ABSTRACT

This paper describes an instrument that measures the spectral transmission of the obscurant between the target and the measuring system. The instrument employs a microprocessor and solid-state memory to enable it to normalize the effects of the atmosphere so that only the effects of the obscurant are measured. The paper describes the instrument plus its capabilities and limitations in spectral resolution, high-speed spectral scanning and normalization. Also described are system deployment for field measurements during Smoke Week III.

1. INTRODUCTION

Defining the infrared thermal signature of military targets involves determining the target's self-emitted radiation after this infrared energy has traveled through the atmosphere in its path to the detection system. In the course of this transmission, radiation is absorbed and scattered by atmospheric constituents, by the contaminants normally present under battlefield conditions, and by additional smoke and obscurants that may be introduced deliberately to confuse identification by thermal signature. The atmosphere plus man-made smoke and obscurants alter the target's self-emitted radiation in a manner that is grossly non-uniform with wavelength and which seriously impedes the collection and interpretation of target thermal signatures.

Methodical collection of signature information should include an accurate evaluation of atmospheric spectral attenuation at the location and time of

the data collection. This permits atmospheric attenuation effects to be removed from the signature data. Moreover, in the case of evaluating the performance of tactical signature analysis equipment, it permits a standard performance factor to be assigned to the system itself. With the availability of such performance factors, the effects of development work can be evaluated on an absolute basis, and the performance of different systems can be compared realistically.

In the area of signature analysis, the more recent atmospheric transmission measurement systems are based upon the use of microprocessor-control. This enables them to perform the basic research required to develop data normalization techniques involved in removing the effects of atmospheric absorption so that man-made battlefield smoke and obscurants, can be spectrally analyzed. The end goal is to reveal the thermal signature of the targets of interest and to ascertain the effects of various obscurants.

2. TRANSMISSOMETER SYSTEM

2.1 MARK II SYSTEM

The Model 12-550 Mark II Research Radiometer shown in Figure 1 that is the basis of the transmissometer system used in Smoke Week has been described elsewhere (1) in detail. Only the outstanding characteristics of this instrument will be reviewed here.

The design philosphy was to achieve maximum flexibility by employing modularity of optics, electronics and mechanics, together with use of microprocessor and computer capabilities that are software-coupled to the application. In the mentioned paper the authors described a spectral radiometer optical system specifically designed to permit great ease and speed in interchanging detector-preamplifier and spectral-filter modules. In this arrangement, all detectors have aligned fields of view, and there is ample space to permit each module to be designed for maximum performance.

The above-mentioned optical system is insufficient to provide data that is easy

to process and reduce. The solution that the authors have designed is to install a microprocessor into the electronics system that processes the output signal from the radiometer optical head. As described in the referenced paper (1), the microprocessor has four powerful capabilities. First, it permits the incorporation of such capabilities as automatic gain control, normalization and sample averaging. Second, it provides control functions such as the automatic electronic switching of electrical attenuators, chopper speed control for maximum sensitivity of the detector in use; and the rotation of spectral filters, scanning mirrors and accessory devices according to requirements. Third, and most important, it integrates the first and second capabilities to the specific requirements of applications such as atmospheric transmission measurements, reflectivity measurements of a selected environment, or control of an industrial or scientific process. Fourth, the microprocessor processes input and output data to make it suitable for interfacing with selected data display and computer facilities. These four capabilites are provided primarily by software tailored to fit the requirements of the measurement mission.

2.2 USE AS A TRANSMISSOMETER

The spectral radiometer as described can also be used as the receiver section of an atmospheric transissometer system. All that is required is to aim the radiometer at a distant source of known radiation, or a suitable blackbody source equipped with a collimator as shown in Figure 2. Now the transmission characteristic of the intervening atmosphere can be measured directly in terms of percentage transmitted in any wavelength interval of interest. In such applications the instrument is operating as a single-beam spectrometer.

Such an instrument system is of vital importance on the military test range. Here the operation of many systems involves the detection of ultraviolet, visible or infrared radiation emitted or reflected by distant targets. Examples include laser ranging systems, FLIR systems, automatic target tracking, intrusion detection and target signature analysis systems. In these uses radiation is transmitted from a target through the atmosphere to the measurement system.

2.3 REQUIREMENTS FOR OBSCURANT MEASUREMENT

Making comprehensive spectral transmission measurements through dense obscurants requires that the following group of advanced characteristics be built into the measuring system:

1. High sensitivity
2. Fast Response
3. Full Spectral Coverage
4. Automatic Operation
5. Direct Interfacing with Data Logging Systems
6. Quick-Look Capabilities
7. Adaptability for Different Operational Modes and Spectral Regions
8. Elimination of Steady-State Signals and Instrument Calibration Constants by Normalization Techniques

2.4 DISCUSSION

Relatively fast response is required to analyze transient obscurant effects, as compared to slowly-changing atmospheric phenomena. To examine obscurant smoke effects comprehensively we must have full spectral coverage, and automatic operation is needed to monitor time-dependent effects. Recording on data logging equipment is important for processing, but a "quick look" by means of a real-time printer or analog X-Y recorder is of immense help to the field operator.

In measuring transmission through a normal atmosphere, the transmissometer will produce an output that is of little interest to this experiment. When no smoke is present, the atmosphere will produce some particular transmission percentage for a specific spectral region. It is helpful if the operator has the capability to normalize this percentage so that a transmission readout of 100 percent is produced. Then, any transmission percentage that is obtained in the presence of an obscurant is known to be due to the absorption of the obscurant alone. Details of the normalization procedure are described in Ref. (2).

If one can store clean-air normalizations for each filter used (be it a descrete filter or a position on a CVF), the system will produce an output giving the spectral transmission of the obscurants introduced into the atmosphere.

The same concept can be applied to an instrument employing a rotating filter wheel containing discrete elements or sections of continuously-varying filters.

2.5 SYSTEM TRADE-OFFS

The Mark II Radiometer System is modular in construction and offers a variety of detector packages, filter modules and collecting optics. The choice of specific components is dependent upon the following related measurement constraints:

1. Wavelength Region and Spectral Resolution
2. Spectral Scan Time, Affecting Information Bandwidth
3. Optical Path Length, i.e. Range
4. Transmission

The wavelength region determines the choice of detector package and filter, and the spectral resolution is determined by the filter selection. However, the spectral resolution determines the amount of radiation received from the Source/Transmitter and thus influences the signal-to-noise ratio.

Spectral scan time requirements are determined by the need for maintaining stable conditions during the spectral scan. A relatively steady condition can be scanned slowly, but a transient condition must be scanned sufficiently rapidly to record the nature of the changes. The rate of information transferred determines the bandwidth required to carry out the transfer with the required degree of accuracy. The required bandwidth is proportional to the rate of transfer. Noise, of course, is also dependent upon the bandwidth. Rapid data collection, then, requires a wide bandwidth which leads to more noise. In the interest of obtaining a better signal-to-noise (S/N) ratio, one may scan more

slowly, increasing the dwell time at each measurement wavelength. One may offset this increased scan time by making fewer measurements, perhaps using a wider wavelength window for each measurement. The latter thus improves the S/N first by decreasing the noise, and second by increasing the signal, at the cost of decreasing spectral resolution.

The range and absorption affect the amount of signal received. In a perfectly-transmitting medium the range attenuation for a given source will follow the inverse-square law. The transmission of the path will be given by the transmission per unit when raised to a power equal to the path length. Finally, the required signal-to-noise ratio of the system is affected by the required level of discrimination between transmission levels.

2.6 OPTICAL SYSTEM

In general, increasing the diameter of the projecting optical system in the source and the collecting optical system in the receiver will increase the signal level coming out of the detector. The fields of view of these optical systems can also be selected to best match the measurement program being planned. The radiation level from the source increases with source temperature (normally 500-1000 degrees C) and with the diameter of the source aperture itself (up to 0.5 inch). It will also increase with the area of the collimating optics adjusted for any throughput loss caused by obscuration by the additional mirror in an on-axis reflective system.

As far as the receiving system is concerned, for a given f/number, sensitivity will increase as the linear dimension of the collecting optic diameter, i.e., an 8-inch system will have approximately twice the sensitivity of a 4-inch system with the same field of view. Mark II radiometers have been produced with both 4-inch and 8-inch collectors. Source collimators are available with optical diameters of 4.7, 6, 10 and 16 inches.

2.7 DETECTOR SELECTION

2.7.1 CONVENTIONAL DETECTORS

Depending upon the needs of the measurement program, either conventional thermal or photo detectors can be chosen. Thermal detectors, such as thermistor bolometers and pyroelectrics depend upon heating the sensitive element and are largely independent of wavelength. The photo detectors are sensitive only to certain wavelengths as determined by the materials of which they are composed. Their peak response occurs near their long-wave limits, and their short-wave response falls off proportionally to wavelength, or even more rapidly. For example, a detector with peak response at 5 micrometers will have half the response, or less, at 2.5 micrometers. The longer-wavelength photo detectors require cryogenic cooling while the thermal detectors do not. The photo detectors are somewhat more expensive, but do have from 10 to 100 times greater detectivity at their peak wavelengths. The photo detectors have response speeds in the order of microseconds, while thermal detector response speeds are in the order of milliseconds.

2.7.2 SANDWICH DETECTORS

The Optical Head that has been designed makes it easy for the user to interchange detector-preamplifier modules with ease as required by the application. Regardless of how easy this may be, such interchange interrupts the measurements procedures and in certain research programs it may involve loss of data. This limitation has been overcome to a considerable degree by the development of the so-called "sandwich" detector.

In 1977 Barnes Engineering Company reported upon a technique (3) for producing photovoltaic sandwich detectors of InSb/PbSnTe where the two elements are physically separated. This technique has been developed and is now being used for the production of InSb/HgCdTe sandwich detectors. Also developed is a new package in which a liquid nitrogen dewar cooled sandwich detector with matching preamplifier is adapted to the Mark II Research Radiometer System.

Because of the microprocessor control capabilities built into the Mark II System, combined with the programmable spectral filter system, the outputs from both detectors can be used to their fullest advantage. As the spectral filter rotates, the microprocessor selects the detector output most appropriate for that particular spectral region and equalizes the gain of the amplifier system. The results produced are as from a single detector with the best qualities of both indium antimonide and mercury cadmium telluride.

The sandwich detector provides optimum sensitivity over the entire spectral range of interest in spectral signature studies of targets at ambient temperatures. This capability is useful in spectroradiometric, atmospheric transmissometer, and reflectometer applications related to environmental and ambient-temperature military targets.

In such applications the spectral filter wheel can be programmed to employ certain filter sequences with the output of one of the sandwich detectors and other filter sequences with the output of the other sandwich detector. In the same manner, and for each filter-detector combination, optimum amplifier gain and bandwidth settings can be employed. Moreover, the computation capabilities of the microprocessor can be employed to normalize the reduction, so that the spectral outputs and phasing of the two detectors are completely compatible.

2.8 ADDITIONAL CAPABILITIES

Performing transmission measurements through obscurants also requires automatic gain control (AGC), sample averaging and filter wheel control.

Automatic Gain Control (AGC) is selected by depressing Button #3 in the Output Mode section of the front panel. The purpose of AGC is to accommodate the full dynamic range of the instrument on the output display. AGC automatically selects the correct attenuator value for the signal presently being processed so that the output reading is approximately mid-range. The microprocessor reads the signal value from the analog to digital converter output and the present attenuator

value. The microprocessor central processing unit (CPU) then decides if the present signal reading has reached its minimum or maximum value for the present attenuator value. If it has, the CPU selects the next lowest or highest attenuator value as appropriate. The AGC setting is constantly updated to provide an accurate output.

The Signal Averaging function is activated by depressing a pushbutton in the Output Mode section of the front panel. The CPU then processes the signal and compares it to the noise, looking for a 100 to 1 ratio. If this ratio is met, the filter steps, and the front panel reading is updated. If the ratio is less than 100 to 1, 3 more samples are taken; and the ratio is checked again. This sample-taking process continues (1,4,8,16,32) until a maximum of 32 samples are taken. After the 32nd sample, the filter is stepped and the front panel is updated. At this time, the ratio may or may not be 100 to 1, but the Signal Averaging function has supplied the best available signal-to-noise ratio.

Filter wheel control is an important function supplied by the microprocessor, and converts the basic radiometer into a spectral-scanning radiometer or spectrometer. In one form the system employs a filter wheel with provisions for mounting up to 10 half-inch diameter discrete filters having any available wide or narrow-band spectral characteristics. Neutral density filters can also be installed and can be made to supply spectrally uniform optical attenuation in magnitudes up to 1000 to 1. This extends the instrument's total dynamic range to 10^6.

In an alternate arrangement the wheel can be fitted with one or more segments of a wedge type continuously-variable interference filter (CVF). In this arrangement the wavelength of the transmitted radiation varies gradually with angle of wheel rotation. It is possible to make combination filter arrangements in which there are CVF segments, discrete filters and neutral density filters. When equipped with either of these motor-driven filter options, the PCU is supplied with an accessory left control panel shown in Figure 1. This enables the operator to use the microprocessor's control capabilities to drive the filter to any selected position or to drive it automatically through any of 10 predetermined programs. In addition, the operator can modify any program according to the immediate needs of the phenomenon being measured, or create a brand-new program for the occasion. In such operations

the filter wheel can be driven through continuous scans at rates as fast as 2 scans per second or go through complex indexing patterns.

3. OBSCURANT MEASUREMENTS

3.1 FIELD APPLICATIONS

The microprocessor-based Model 12-550 Mark II Spectral Radiometer contains all that is required to make the obscurant emission and transmission measurements through a selection of spectral intevals and to process the resulting data to produce the desired results in real-time. The described system can be used as either a spectral radiometer, a spectral transmissometer, or as both a radiometer-transmissometer for making simultaneous emission-transmission measurements. For a discussion of simultanious emission-transmission measurements, see Reference (4).

3.2 TRANSMISSION MEASUREMENTS

As described earlier, the transmissometer is similar to the fundamental spectral radiometer, except that the modulator is embodied in the source/transmitter and the receiver is not chopped. The received signal is demodulated using the reference signal from the source modulation, assuring rejection of the radiation from the unmodulated background radiation. The direct transmission measurement is computed by normalizing each transmission measurement, using the data taken with a clear atmosphere path at the same range as that used during a calibration run. At each filter position, the calibration data is stored in the transmissometer's random-access-memory (RAM) for retrieval following each data measurement.

At slower scan speeds, i.e., one scan of 2.5 through 14 micrometers in 12-14 seconds, or longer, adequate time is available to permit the attenuation level of each filter point to be adjusted individually in proportion to the received signal intensity. At filter scan speeds up to one or two per second, a different technique is used. Advantage is taken of the fact that spectral responses rarely change at such rapid rates. It is acceptable to use attenuator settings for whole ranges of filter wavelengths. In this manner, it is possible to reduce the sampling period at each

filter step. With this technique, the filter is allowed to scan normally, during the calibration sequence, setting optimal attenuator settings in the AGC mode. During the succeeding scans, the attenuations are selected based upon the highest attenuator setting in preselected spectral bands. In the measurement mode, a different attenuation is set throughout each of 3 or 4 selected bands only, thus saving considerable time compared to reselecting attenuation before each filter position.

3.3 FIELD DEPLOYMENT

The transmissometer was utilized during the Smoke Week III exercises during the summer of 1980. During these exercises, high-speed atmospheric transmission measurements were made near the test point. This data was used to produce time-oriented transmission data such as that shown in Figure 3. In this illustration, the spectral transmission is illustrated as a function of time. Data shows the transmission spectrum of white phosphorus normalized to the clear atmospheric path of 5 meters. This illustration was supplied by Dr. M. Farmer of the University of Tennessee Space Institute and shows successive spectral scans during a period of 30 seconds, starting 2 minutes after the beginning of the test. Because of the small size of the illustration, the considerable spectral information in the 8 to 12 micrometer region is not readily visible, but it is revealed in detail by computer processing. This type of display is useful for a "quick look" because it shows both the spectral variations plus the magnitude of their variations with time.

Figure 4 shows the relative placement of the source and receiver Optical Head, and Figure 5 shows other views of the test setup. Both the source and the head were mounted in a protective shelter to reduce solar heating and provide protection from rain. In this exercise, the path length was very short (5 meters) and the aperture of the source was more than adequate to fill the field of view in the receiver. Accordingly, no collimator was required. Under this condition, measurements were made with a signal-to-noise ratio exceeding 200 in the 8-14 micrometer spectral range. The transmissometer was equipped with an InSb/HgCdTe sandwich detector providing spectral coverage in the overall band from 2.5 to 14 microns. A three-segment continuously variable filter (CVF) was installed, providing 243 point of data. This wheel offers bands and resolution as follows:

Segment	Band	Resolution (hbw)
1	2.5 - 4.5u	1.35%
2	4.4 - 8.0u	1.35%
3	7.9u - 14u	1.8%

The wheel was scanned in the high-speed mode at approximately 1 scan/second, providing for a rapid assessment of the concentration of the obscurant.

Control of the transmissometer was accomplished using the RS-232 data link, operated at 9600 baud, to a CRT terminal located at the trailer site some 200 yards up range. Using the remote control, it was possible to run the filter wheel up to speed, display the data output, and turn the wheel off at the end of the run. Calibration in Program 9 was accomplished locally and the receiver left in standby mode pending the initiation of the next run.

Data recording was accomplished by using an external dedicated Z-80-based microcomputer with 64K memory. Memory capacity was adequate for approximately 30 scans following which the data was dumped to a disc file. Data consisted of the filter wheel position attenuator setting, and data (12 bits). The unprocessed data output was taken from a parallel binary output, and in this instance, the final data reduction was performed on the raw data taken from the disc. Internal processing of data and display on the CRT provided a very efficient quick look capability.

Subsequent to these measurements, there was developed a technique for performing the complete data processing within the Mark II PCU. This technique enables the system to produce both normalized analog and digital information at a rate of 1 scan per second, and was later used for measurements during "Snow Week" to be described in a future paper.

System performance achieved the desired goals. Figure 6 illustrates a spectral scan made of a 0.3 mil sheet of polyethelene with a Perkin-Elmer Model 580B Infrared Spectro-photometer. Figure 7 shows a spectral scan of the same sheet made from reduced transmissometer data.

From a practical viewpoint, the system worked well. Problems were experienced twice with lightning strikes in the test vicinity, which knocked out data interface chips on the data link. The receiver worked well despite partial coating of some of the optical elements with certain obscurents. The calibration technique which normalizes the data to a clear atmospheric path allows recalibration prior to each run, and only occasional cleaning was necessary.

4. CONCLUSION

This paper has reviewed the major concepts and features concerning a spectral radiometer that has been custom-modified for studying the spectral transmission of obscurants used in Smoke Week II. Capabilities and limitations in spectral resolution, high speed spectral scanning and normalization have been described. Performance in spectral transmission analysis has been compared with a precision laboratory research spectrophotometer. System deployment for field measurements during Smoke Week II has been described, as well as a sample of the data recorded during these measurements. In the field, the system generally performed according to specifications in all modes of operation.

REFERENCES

1. F. Zweibaum et al. Design considerations for a microprocessor-based multipurpose spectral radiometer system. SPIE Proceedings Volume 230.

2. F. Zweibaum et al. On-line infrared process signature measurement through combustion atmospheres. SPIE Proceedings Volume 148.

3. W. Rolls, Two-color sandwich detector using InSb/PbSnTe, Infrared Physics, 1977, Volume 17, pp 419-421.

4. F. Zweibaum et al. Applying a microprocessor-controlled spectral radiometer to field measurements. SPIE Proceedings Volume 230.

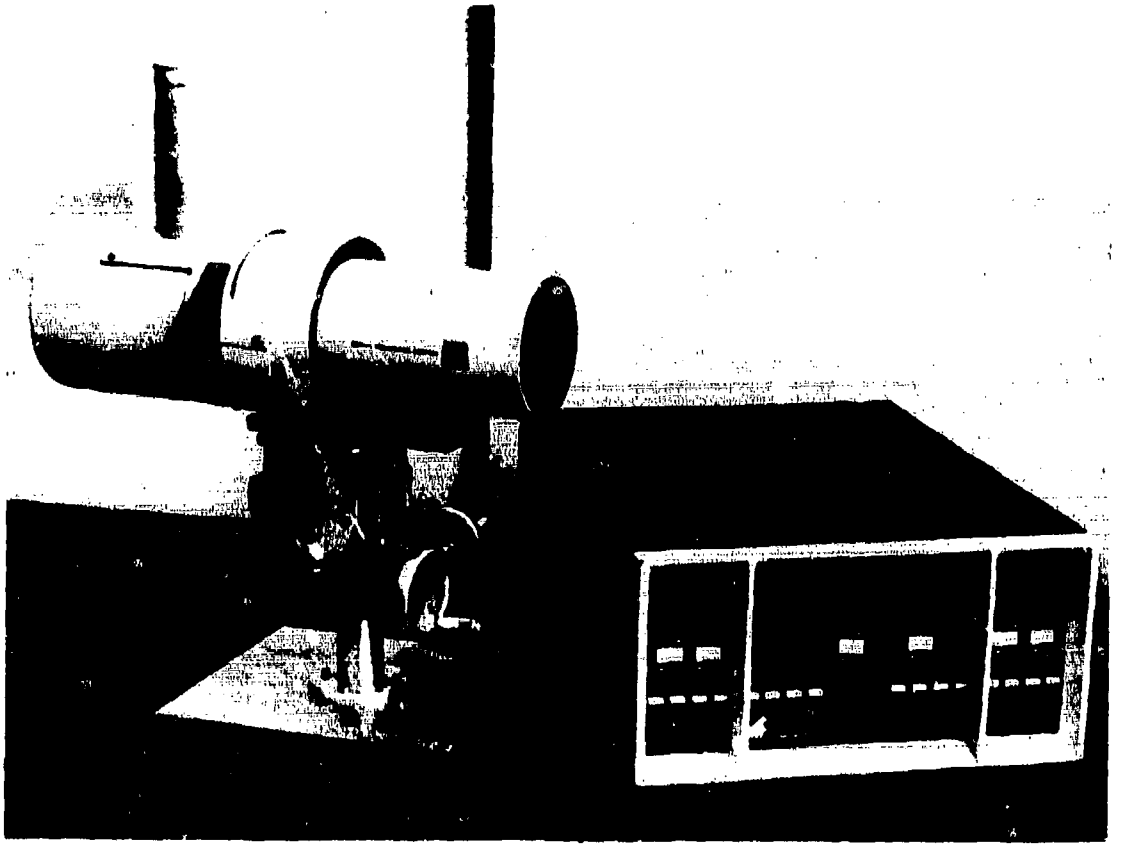

FIGURE 1. MODEL 12-550 MARK II RESEARCH RADIOMETER.

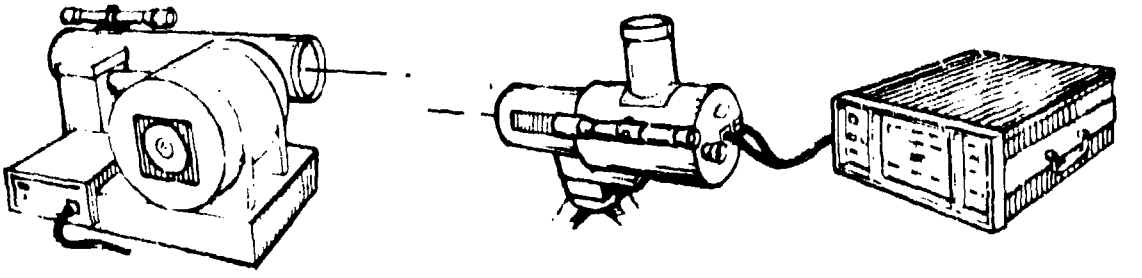

FIGURE 2. MARK II SYSTEM DEPLOYED AS TRANSMISSOMETER.

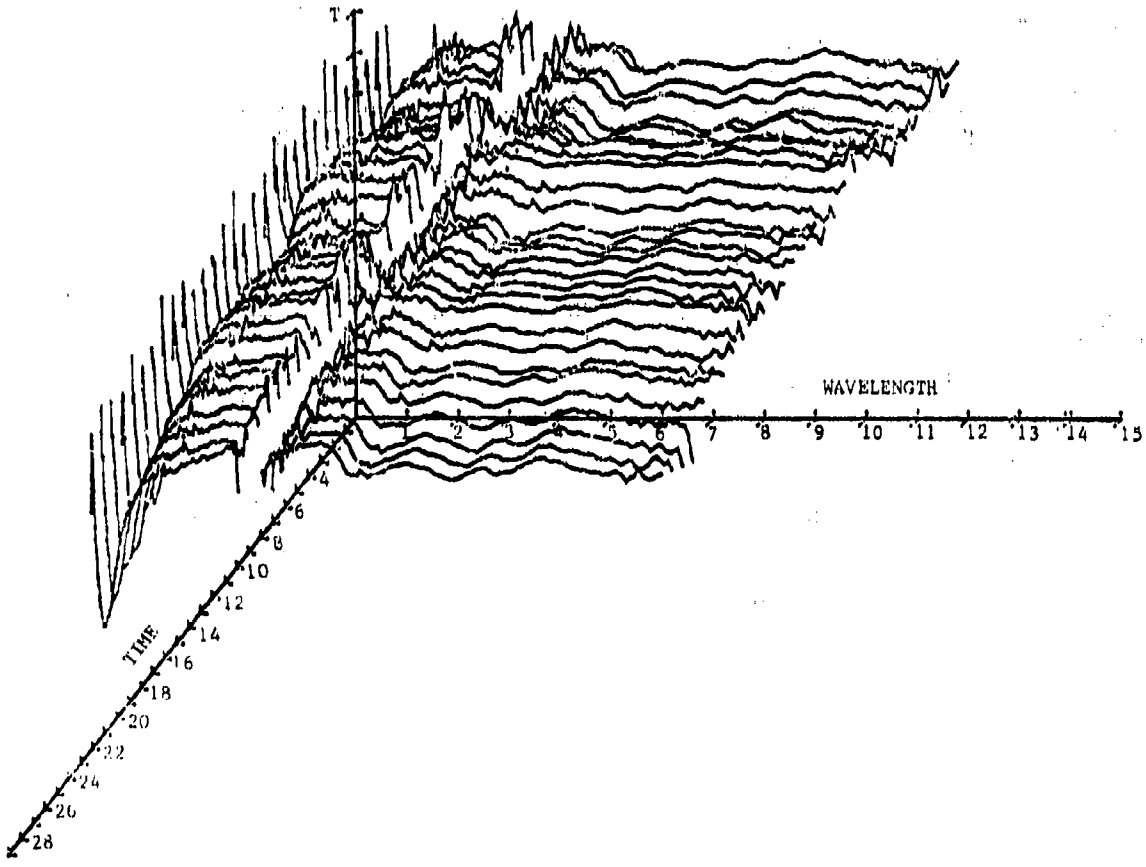

FIGURE 3. TRANSMITTANCE-WAVELENGTH-TIME DISPLAY. Illustration shows spectral scans during Trial 16, white phosphorus , 100% RH. Courtesy Dr. M. Farmer, The University of Tennessee Space Institute.

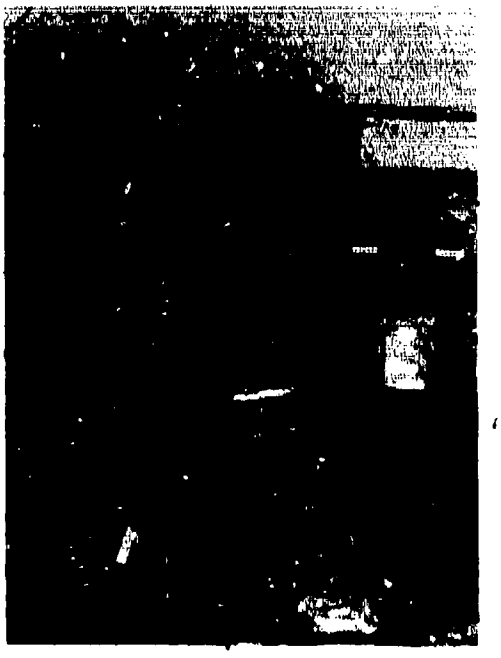

FIGURE 4. DEPLOYMENT OF TRANSMISSOMETER AT TEST SITE. (Top) Source at left and receiver optical head at right. (Lower Left) Closeup of source and temperature controller. (Lower Right) Closeup of Optical Head.

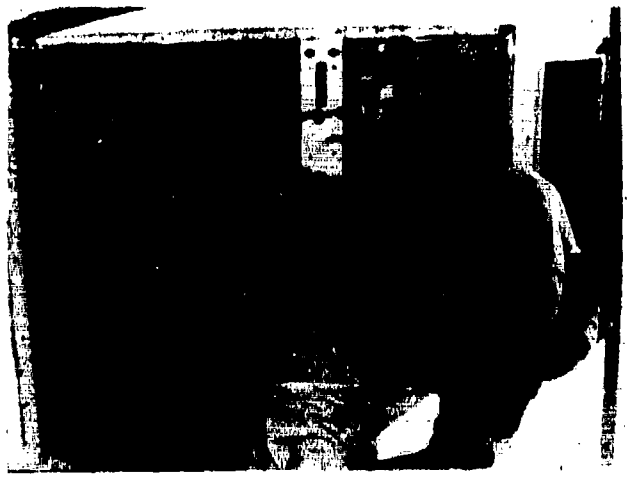

FIGURE 5. OTHER VIEWS OF TEST SITE. (Upper Left) Shelter for remote electronics units. Mark II PCU is seen under the arm of individual at left. Author Len Lucia is at right. (Upper Right) Closeup of Mark II PCU in Shelter. (Bottom) Remote video display array.

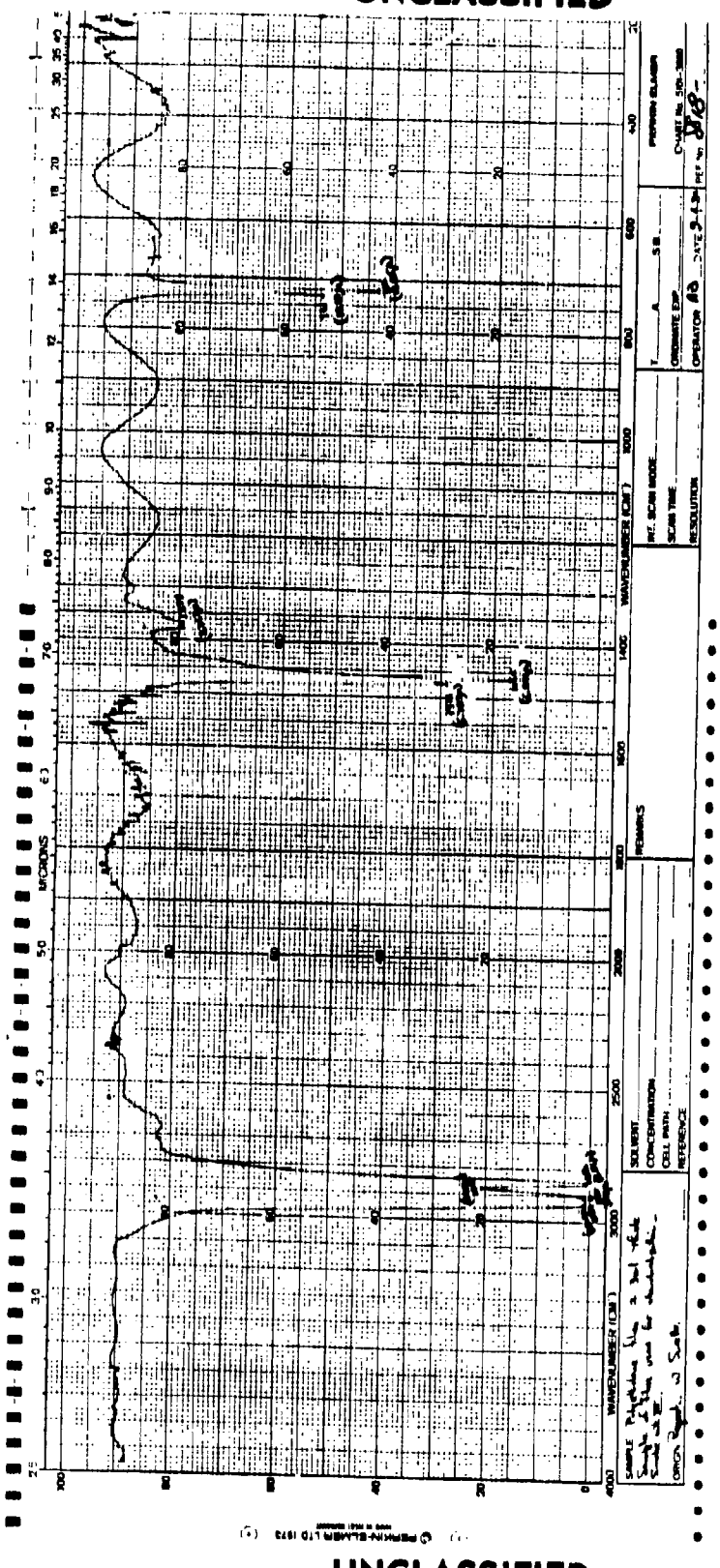

FIGURE 6. SPECTRAL SCAN OF 0.3 MIL POLYETHELENE. Scan was made with Perkin-Elmer Model 580B Infrared Spectrophotometer.

APOLY1-1. DAT

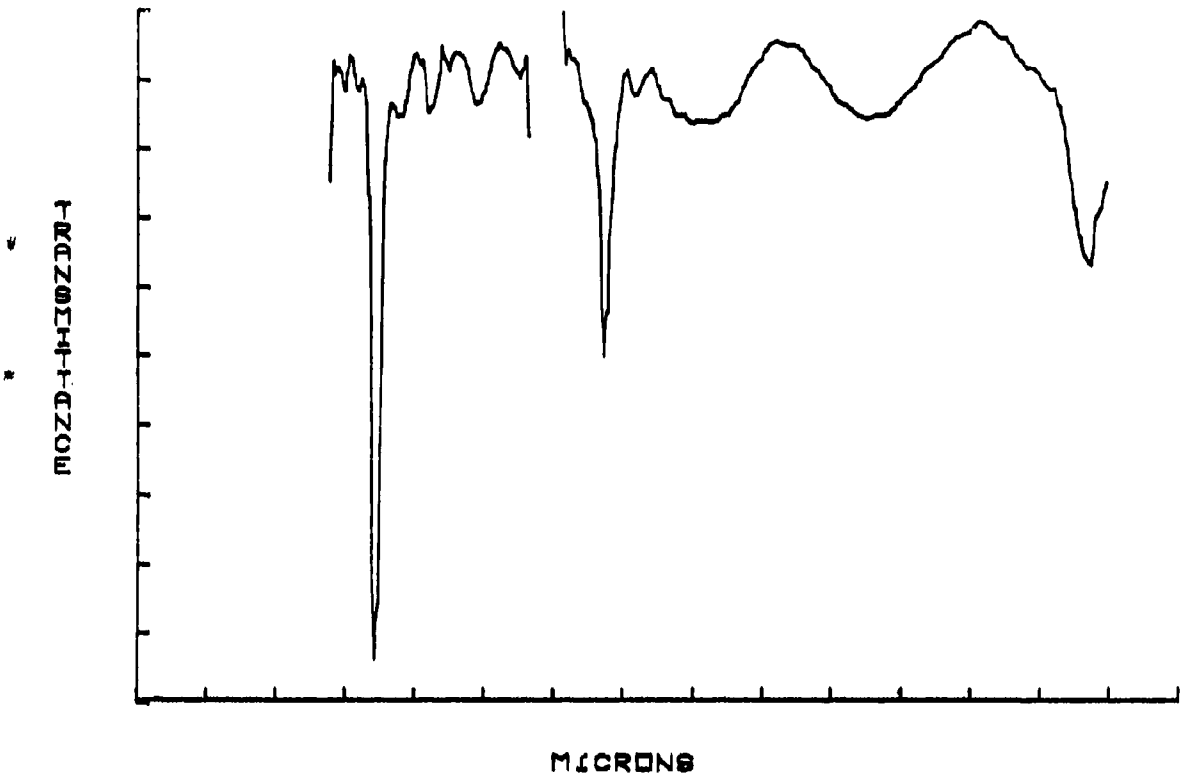

FIGURE 7. SPECTRAL SCAN OF SAME POLYETHELENE. Scan was made with Mark II transmissometer system.